

Editorial

Materials are a very important part of human life due to the fact that they are used on a daily basis. Materials are used for human things such as making buildings, creating films and forming fashionable clothing and what not. Every part of our body is a material. Bones, muscles, fingernails, hairs and skin are some examples. New materials are created all the time making new and fascinating things..

The properties of a material are important because they show you what it can and cannot be used for. There are two types of materials such as naturally found materials and manmade materials. From the beginning of time humans have used materials to survive. Materials have helped throughout the time and made it possible for people to contact each other across the world and travel great distances. Nevertheless before going to details of these materials we have to look for a quick history of materials

Ancient cultures began their existence making use of the stone, soil, plants and bones found in the environments. For nearly 2.3 million years humans lived using only these naturally occurring materials in a period known as the stone age. Normally this period counts from 15000 BCE to 7000 BCE.

Later humans learned how to convert copper and tin ore into metallic bronze and the stone age became the Bronze Age. Around 3000 BCE a technique of producing metal from mineral-rich ores was developed and then the Bronze Age started. The technique uses heat and chemical reactions to produce metal from the more complex mixture of minerals found in ore.

The discovery of a method for producing iron and steel from ore was developed around 1200 BCE and the Iron Age began. Making iron is a more complicated process than that for copper and

bronze. It requires a more consistent temperature. Agriculture development in the progress of human history has been practical since at least 1000 BCE. The wheel was developed around 4000 BCE and the first writing systems developed about 500 years later. The earliest method for producing glass from the melting of sand and other quartz based minerals was developed around 2500 BCE. Around 500 CE the middle ages began with the introduction of paper to Europe, which was first developed in China around 200 CE. Invention of printing press in 1450 was an important technological development in this period of time.

By the 1500s humans entered the Modern Age, when trade and technology reached new levels of complexity. The Industrial Revolution began around 1760 and developed the steam power, factory manufacturing and the use of iron and cement as structural materials.

More recent milestones include the development of synthetic plastics in 1907 and the identification of the first synthetic nanomaterials, the carbon fullerene in 1985. As these new materials have been developed, they have made new products and technologies such as computers, space crafts and robotics.

The polymer Age is also called the age of plastics. Thousands of polymers exist in nature. The natural polymer in the environment is cellulose, the major structural material of trees and other plants. The proteins that make up our body are also polymers which include deoxyribonucleic acid (DNA). In 1861 the British chemist Thomas Graham had noted that when he dissolved organic compounds in solutions, some of them would leave sticky residues when passed through a fine filter paper.

Many other 19th century scientists modified colloids and

natural polymers to form new materials. In 1870 the American inventor John Wesley Hyatt produced an astonishing new product called celluloid. Celluloid is a plastic made from natural cellulose and it could be used for everything from movie film to cricket balls. In 1907 American chemist Leo H. Baekeland took two ordinary chemicals phenol and formaldehyde, mixed them in a sealed vessel and subjected them to heat and pressure.

Nowadays people are not only using the materials for their modest living purposes but they are becoming the part and parcel of the human body. Stents used for blood flow, rods used to connect or replace the bone, thin membranes used as lenses in the eye etc are not the materials only but they become part of the human body. Advances in materials science made this possible and it has not been stopped. Overnight people around the globe are engaged in making the advances in materials science. A day is not far away that we may have all disposable kitchenware, foldable aeroplanes, hydrogen as an efficient and pollution-free fuel. We are already using non-tearable paper. We may have non-washable clothes too.

A lot can happen in the future and it is only due to the advances in Materials Science. In the history of human development humans have managed materials for their development. Now humans can't live without materials and a day will come in the future on which materials can manage humans also.

Dr. Shrikant R. Kokare,

Head and Convenor,
Post Graduate Department of Physics,

**Raje Ramrao Mahavidyalaya,
Jath (SANGLI)**

Email: kshirikant@yahoo.com

Phone: +91-9421219424

International Conference Organizing Committee	
Welcome	Invitation
<ol style="list-style-type: none"> 1) Prin. Dr. Abhaykumar Salunkhe 2) Prin. Shubhangi Gavade 3) Prin. Dr. S.Y. Honagekar 4) Dr. S.R. Kokare (Convener) 5) Dr. A.K. Bhosale (Co- convener) 6) Dr. S.S. Latthe (Secretary) 7) Mr. S.P. Dalawai (Treasurer) 	<ol style="list-style-type: none"> 1) Dr. S.R. Kokare (Convener) 2) Mr. K.K.Rangar 3) Mr. D.A. Kumbhar 4) Miss Deepali chougule 5) Miss A.N. Todakari 6) Miss A.S. Jagadale 7) Miss A.A. Kumbhar
Registration and Certificate Distribution	Stage and accommodation
<ol style="list-style-type: none"> 1) Mr. S.P. Dalawai 2) Dr. Shivaji Kulal 3) Mr.G.D. Salunkhe 4) Miss Vidya Mali 5) Miss Nikita Bobade 6) Mr. R.S. Sutar 7) Miss S.B Pawar 	<ol style="list-style-type: none"> 1) Dr. A.K. Bhosale 2) Mr. M.B.Sajjan 3) Mr. Khogare Balaji 4) Mr. M.A. Ankalagi 5) Mr. S.M. Jadhav 6) Mr. V.S. Kodag 7) Miss M.P. Mitkal
Publicity and paper presentation 7 – 8 December	Refreshment and Meals arrangement
<ol style="list-style-type: none"> 1) Dr. S.S. Latthe 2) Mr. P.B. Abhange 3) Mr. Y.A.Shinde 4) Mr. Mr.Sohan Thombare 5) Miss R.R. Patil 6) Miss P.P. Zambre 7) Mr. Sumit Vajrashetti 	<ol style="list-style-type: none"> 1) Mr. R.D. Karande 2) Mr.Suresh Bamane 3) Miss T.B. Bhutade 4) Miss D.R. Gade 5) Miss A.A. Kumbhar 6) Mr. A.N. Pasale 7) Miss T.B Shinde

Programme

Day and Date	Time	Programme
Wednesday, 7 th December 2016	11.00 – 12.00	Registration
	12.00 – 12.30	Inauguration
	12.30 – 01.30	Key Note Address Resource Person: Prof. Chiaki Terashima (Japan) Topic: Recent progress in Photocatalysis International Research Centre
	01.30 – 02.30	Lunch
	01.30 – 04.00	Technical Session I Resource Person: Prof. S W. Gosavi, Department of Physics, SSPU, Pune Topic: Development of functionalised Nano composite based VOCs (Volatile Organic Compound) Profiler: An aid on early Diagnosis of Cancer
	04.00 – 04.15	Tea
	04.15 – 05.45	Technical Session II Resource Person: Prof. P. S. Patil, Department of Physics, Shivaji University Kolhapur Topic: Emergence of Perovskite solar cells
	05.45 – 07.15	Technical Session III (Poster)
	07.15 – 08.00	Cultural
08.00 onwards	Dinner	
Thursday, 7 th December 2016	08.00 – 08.30	Breakfast
	08.30 – 10.00	Technical Session IV Resource Person: Prof. S.I. Patil, Department of Physics, SSPU, Pune Topic: Crystallographic Magnetic and Electrical properties of Hole doped manganites.
	10.00 – 11.00	Technical Session V Resource Person: Prof. B. J. Lokhande, Department of Physics, Solapur University, Solapur Topic: Electrochemical Properties of Spray pyrolysis Metal oxide thin film- A super capacitor approach Resource Person: Dr. Y.D. Kolekar, Topic: Tuning the structural, Dielectric and ferroelectric properties of lead free Ca modified BaTiO ₃ ceramics
	11.00 – 11.15	Tea
	11.15 – 12.45	Technical Session VI Resource Person: N. Venkataramani Metallurgical Engineering and Materials Science Department, Indian Institute of Technology Bombay, Mumbai 400076 Topic: Recent results in some Nano crystalline ferrite thin film systems
	12.45 – 01.30	Valedictory

INDEX

Sr. No	Authors	Title	Page No
1	Dr. Devanand Shinde	Vice-chancellor Message	iii
2	Prin. Abhaykumar Salunkhe	Chairman Message	iv
3	Prin. Shubhangi Gawade	Secretary Message	v
4	Prin S.Y. Hongekar	Principle Message	vi
5	Dr. S.R. Kokare	Convener Message	vii
6	Dr. S.S.Latthe	Secretary Message	viii
Key note Address			
1.	Chiaki Terashima	Recent Progress in Photocatalysis International Research Center	11
Invited Talk			
1.	Prof. (Dr.) Pramod S. Patil	Emergence of Perovskite solar cells	12
2.	Prof. N. Venkataramani (Prof. P.B. Joshi Memorial Lecture)	Recent results in some nanocrystalline ferrite thin film systems	13
3.	Prof. S.I. Patil	Crystallographic Magnetic and Electrical properties of Hole doped manganites	14
4.	Prof. B. J. Lokhande	Electrochemical Properties Of Spray Pyrolysed Metal Oxide Thin Films – A Supercapacitor Approach	15
5.	Prof. S. W. Gosavi	Development of Functionalized Nanocomposite based VOCs (Volatile Organic Compounds) Profiler: An Aid on Early Diagnosis of Cancer	16
6.	Dr.Y.D. Kolekar	Tuning the structural, dielectric and ferroelectric properties of lead free Ca- modified BaTiO ₃ ceramics	18
Research Papers (Volume – I)			
1	Yusei Sakurai, Yohei Harada, Chiaki Terashima, Hiroshi Uetsuka, Norihiro Suzuki, Kazuya Nakata, Ken-ichi Katsumata, Takeshi Kondo, Makoto Yuasa, Akira Fujishima	Rapid synthesis of boron-doped diamond by using in-liquid plasma	25
2	Aiga Hara, Chiaki Terashima, Norihiro Suzuki, Kazuya Nakata, Ken-ichi Katsumata, Takeshi Kondo, Makoto Yuasa, Akira Fujishima	Direct synthesis of ozone mist using boron- doped diamond electrode	26
3	Sanjay Latthe	Superhydrophobic Coatings Developed using Modified Alumina Nanoparticles for Self- Cleaning Applications	28
4	Uzma K.H. Bangi, Hyung-Ho Park	Influence of PVP concentrations on the microstructural characteristics of SrTiO ₃ and BaTiO ₃ nanoparticles: A comparative study	31
5	U.J. Chavan, A.A. Yadav	Supercapacitive performance of spray deposited Co ₃ O ₄ thin film	34

6	S. G. Deshmukh, A. M. More	Preparation, optical and structural properties of ZnO thin films by SILAR method	37
7	R. R. Tembhurne, S. P. Nanir, R. G. Pawar	Diversity of Fleshy Mushroom In Dry Deciduous Forest In Sangli District, Maharashtra. (India)	40
8	Kalyani Mitkari, Palak Shroff and Kamlesh Alti	Comparison of Electrowetting on Hydrophobic and Super Hydrophobic Surfaces	44
9	P.B. Abhange, V.C. Malvade, S. Chandralingam, S.R. Kokare	Studies on Complex Impedance of $BaNd_{2-x}La_xTi_3O_{10}$ and $BaNd_{2-x}La_xTi_4O_{12}$ Ceramic	46
10	Pravin S. Kadhane, B.G.Baraskar T.C.Darvade, Y.D.Kolekar and R.C.Kambale	Dielectric and Ferroelectric Properties of $Ba_{0.99}Ca_{0.01}Ti_{0.99}Sn_{0.01}O_3$ Lead-Free Piezoceramic	51
11	Pavan K. Pagare and A. P. Torane	Electrodeposition of low cost Cu_2O thin films for electrochemical sensor application	54
12	Sandip K. Jagadale, Popatrao N. Bhosale, Raghunath K. Mane	Novel approach for the synthesis of $CdZn(SSe)_2$ thin films and its photoelectrochemical application	58
13	Prakash Bansode, Gajanan Rashinkar	Preparation of Nanoparticles of Bioactive Compounds for Enhanced Anti-angiogenesis Activity	61
14	B. S. Kamble, V.J. Fulari, R. K. Nimat.	Structural and Morphological Study of LSM Thin Films as Cathode for SOFC	63
15	Shivaji V Bhosale, S.V.Bhoraskar, and V.L.Mathe	$CoFe_2O_4@SiO_2$ core shell magnetic nanoparticles as a novel adsorbent for aqueous heavy metal removal	66
16	A. V. Kadam, N.Y. Bhosale	Optimized thermal treatment for hydrothermally grown stabilized nanostructured WO_3 thin films in electrochromic applications	69
17	S. C. Yadav, M. D. Uplane	Photoluminescence Properties of ZnO thin films prepared by spray CVD technique	72
18	A.N. Tarale, V.L. Mathe	Effect of Pyrochlore Phase on Structural and Dielectric Properties of 0.75PMN-0.25PT	75
19	B. B. Dhale, S. H. Mujawar and P. S. Patil	An investigation of the electrochromic and optical transmittance of copper and copper oxide thin films prepared by vacuum evaporation technique	78
20	S. P. Dalawai, T. J. Shinde, A. B. Gadkari, P. N. Vasambekar	DC Electrical Resistivity of Ni-Zn Ferrite Thick Films	83
21	Rajaram S. Sutar, A. K. Bhosale, S. P. Dharigouda and Sanjay S. Latthe	Self-cleaning Superhydrophobic Silica Coatings Modified by Polystyrene	87
22	N.A. Kulkarni, B.D. Dangat, P.B. Teli, Y.S. Andoji	Selected Plants from Arid Zone Conditions as a Source of Novel Biometaterials	90
23	Takahiro Adachi, Chiaki Terashima, Kazuya Nakata, Ken-ichi Katsumata, Norihiro Suzuki, Takeshi Kondo, Makoto Yuasa, Akira Fujishim	Protection of lacquer materials from UV irradiation using the TiO_2/SiO_2 photocatalyst	96
24	Kensuke Katagishi, Asako Kuragano, Chiaki Terashima, Norihiro Suzuki, Kazuya Nakata, Ken-ichi Katsumata, Yoshinao Hoshi, Isao Shitanda, Takeshi Kondo, Makoto Yuasa, Masayuki Itagaki and Akira Fujishima	Structural Optimization and Improved Activity of Photoelectrochemical Glutathione Sensor by Electrochemical Impedance Spectroscopy	97
25	Kazuya Miyasaka1, Yusei Sakurai, Yohei Harada1, Chiaki Terashima, Hiroshi Uetsuka, Norihiro Suzuki3, Kazuya	Influence of solvent on diamond synthesis by microwave in-liquid plasma method	99

	Nakata, Ken-ichi Katsumata, Takeshi Kondo, Makoto Yuasa, Akira Fujishima		
26	A.D. Patil, S. M. Patange	Effect of Additives on the Structural and Magnetic Properties of Nano crystalline Spinel Ferrites	100
27	Bharat Govind Pawar	Sol-gel Synthesis of Crystalline SnO ₂ Nanopowder: Advantage of Sonochemical Method over Conventional Method	103
28	N.T. Padal, S. M. Salunkhe	Studies on New Perovskite Material for Pyroelectric Sensor Application	106
29	K. N. Patil, D. A. Kumbhar, S.S. Karhale, V.B. Helavi	Microwave assisted green synthesis of 1H-Pyrazolo [1, 2-b] Phthalazine-5, 10-Dione Derivatives with 5%CTAB capped ZnO nanoparticles as catalyst	108
30	C. R. Bobade, C. U.Mulik, M. D. Uplane	Synthesis and characterization of advance spray deposited Cu:CdO thin films and their LPG sensing performance	111
31	Shital Shinde, Gajanan Rashinkar, Rajashri Salunkhe	Bio-Polymer Entrapped Catalyst for Organic Transformations	115
32	A.R. Babar	Electrical properties of gallium doped zinc oxide thin films by spray pyrolysis	121
33	R.A. Bugad, T.R. Mane, B.B. Navale, J. V. Thombare, A.R. Babar, B.R. Karche	Structural And Magnetic Properties Of Lanthanum Substituted Mg-Zn Ferrite Nanoparticles Prepared By Co-Precipitation Method	123
34	P.P. Padghan and K.M. Alti	Calibration and testing of low cost optical phase shifter	126
35	Sunetra Dhere	Low density silica aerogel synthesized in less processing time via mechanical shaker	128
36	M. P. Yadav, A. A. Mane	Literature Survey on Study of Toxicity of Nanomaterials	130
37	A. L. Patil and U. B. Chanshetti	Optical, Structural and Spectroscopic Study of Metal Chalcogenide Doped Oxide Glasses: A Review	132
38	Pallavi Pawar, Swati Pawar, Shubhada More, Shubhangi Davale, Madhuri Varade,Prakash Patil, Raghunath Shinde, Bharat Pawar, Renukacharya Khanapure, Prakash Bansode	An Eco-friendly Green Route for Synthesis of Magnetite Nanoparticles using <i>Bryophyllum pinnatum</i> Aqueous Leaf Extract	135
39	Prakash Patil, Bharat Pawar, Sunil Mirgane	Chemical Synthesis and Characterization of Nano- Sized Ni _{0.75} Co _{0.25} Al ₂ O ₄	138
40	Ravi Kamble, Vijaya Puri, Smita Mahajan	Spectroscopic Studies on M-TiO ₂ (M = Mn, Ni and Fe) nanoparticles for degradation of malachite green dye	140
41	Vilas S. Hogade	An overview on Advances in material science research	144
42	S.N. Tambe, S.G. Chavan, S.R. Kokare, Y.D. Kolekar, D. J. Salunkhe	Synthesis and Propertise of (BSPT) Compositions Material	148
43	S. P. Patil, K. R. Sanadi, K. K. Patankar, V. B. Helavi	Effect of sintering temperature on structural and morphological analysis of Co _{0.50} Cu _{0.5} Fe ₂ O ₄ synthesized by sol-gel method	151
44	K.S. Pakhare, R.D Tasgaonkar B.D. Bhosale, S.N. Zende, B.M. Sargar	Synthesis and characterization of SnO ₂ by CBD method for LPG gas sensor	153
45	S. A. Khalate, R. S. Kate and R. J. Deokate	Studies on Nanosized Molybdenum Trioxide (α -MoO ₃) Thin Films	157

46	K. R. Sanadi, S. P. Patil, H. D. Dhayagude, G. S. Kamble	Influence of Cd substitution on structural and photocatalytic activity of copper ferrites synthesized by sol-gel auto-combustion method	159
47	J. S. Ghodake, T. J. Shinde, M. M. Sutar, P. K. Maskar	Infrared and Dielectric Study of Ti-Ni-Zn Ferrites	162
48	C.M. Kanamadi, A.A.Wali, V.P. Kothavale	Synthesis of High Dielectric Constant and Low Loss Lead Zirconate Titanate for By-Pass Capacitor in Microelectronics and Energy Storage Devices	166
49	Arjun Kokare, Sunil Zanje, Vishal Suryavanshi, Ganesh Kamble, Balasaheb kokare, Mansing Anuse	Extraction of ion-pair complex of mercury(II) and N-n-octylcyclohexylamine from hydrochloric acid : analysis of real samples	169
50	Anand Sawant, Rajaram S. Sutar	Transparent Nanocrystalline Zinc Oxide Thin Films by Double Pulse Method	175
51	S. S. Kumbhar, C. R. Bobade, S. T. Salunkhe, C. H. Bhosale	Preparation of Ni _x Zn _{1-x} Fe ₂ O ₄ thin films by spray pyrolysis method and to study their structural and electrical properties	180
52	Babasaheb Bhosale, Sunil Zende, Shashikant Sawant, Balasaheb Sargar, V. M. Gurame	Kinetics and Mechanism of Oxidation of Maltose by keggin type 12-tungstocobaltate (III) in hydrochloric acid medium	186
53	Babasaheb Bhosale, Sunil Zende Shashikant Sawant and Balasaheb Sargar	Surfactant Encapsulated Cobalt Complex Catalyst for Environmental Friendly Oxidation of Alcohols	190
54	Balaji T. Khogare Makarand K. Sakate, Pravina B. Piste, Balasaheb N. Kokare	Liquid-liquid extraction of ruthenium(III) from malonate media by novel 4-heptylaminopyridine: application to alloys and environmental analysis	192
55	S. T. Mane, R. S. Mane, D. G. Kanase L. P. Deshmukh	Studies on Nano Crystalline Co _{1-x} Cd _x S Thin Films	199
56	D.M.Chougule, A.S.Yadav, P.P.Zambre	Wetting properties of Rose petals	203
57	R. P. Patil, A.D.Pinjarkar, B.V.Jadhav, R.R.Sawant, S.B.Patil	Synthesis, characterization and photocatalytic application of Cr substituted ZnMnFeO ₄	204
58	Vaishali Mane, Swati Patil, Vijaya Puri	Microwave Permittivity for Sunflower Seeds Using Non Resonant Ag Thick Film Microstripline as a Sensor	209
59	P. M. Kulal, V. J. Fulari	Monitoring the physical properties of Bismuth Selenide thin films by electromagnetic wave as a special tool: Holographic Interferometry	213
(Volume – II)			
60	B. T. Khogare, S. R. Kulal, K. K. Rangar, G. D. Salunkhe, P. G. Pawar, M.H. Karenavar, P. M. Kadam and S. S. Latthe	A polystyrene modified sponges for effective oil/water separation	219
61	S. G. Kakade, R.C. Kambale and Y. D. Kolekar	Cobalt rich Ferrite for Magnetostrictive Sensor	220
62	S. K. Khade	Changes The Nano Particle (Zinc) During Leaf Senescence In Sericultural Crop Morus Alba Linn	222
63	A. R. Nimbalkar, N. B. Patil, M. G. Patil	Nitrogen dioxide sensing properties of nanostructured zinc oxide thin film grown by Sol-gel method	225
64	Shivaji R. Kulal, Krishna K. Ranagar, Vijay S. Jadhav, Dadasaheb V. Rupnawar, Vashistha M. Gurame, Dipak S. Rajmane, Ramchandra B. Patil	Synthesis and characterization of Dy Doped Co-Zn ferrite by sol-gel auto combustion method.	227

65	Tulshidas C. Darvade, P.S.Kadhane, B.G.Baraskar, Y.D.Kolekar and R.C.Kambale	Low Temperature Synthesis of CoFe_2O_4 Particles by Acrylic Acid – Glycine Assisted Sol-Gel Autocombustion: Structural and Magnetic Properties	230
66	Dattatray Sutrave, Bhanudas Karche. Sangam Gaikwad, Shahaji Madale, Sangeeta Jogade,	Ternary (Mn:Co:Ru) Oxides Thin films for supercapaitors	233
67	D. S. Gaikwad, K. A. Undale, D. M. Pore, S. N. Korade, S. A. Sonavane	Suzuki-Miyaura coupling catalyzed by Palladium nanoparticles generated from Multi functionalized ionic liquid	236
68	P.S Joshi, S.M. Jogade, S.D. Gothe and D.S Sutrave	A Comparative Study of Structural and Morphological Properties of Pristine and Mn Doped Ruthenium Oxide Thin Films.	241
69	Sangeeta Jogade, Preeti Joshi, Sagar Gaikwad, Sutrave. D. S	Mn Doped Co_3O_4 Thin Film Electrodes: CV Analysis for Supercapacitor Application	245
70	S. D. Chavan, R. M. Kharade, A. N. Tarale, S. G. Chavan, D. J. Salunkhe	Investigations on Ca and Zr Modified BaTiO_3 Ferroelectric Lead Free Ceramics	249
71	A. V. Thakur, B.Y. Fugare S. B. Ubale, B. J. Lokhande	Effect of molarity of cationic source on cyclic Voltammetry of Fe_3O_4 electrodes	251
72	V. V. Ganbavle	Enhanced NO_2 Sensing Properties of WO_3 Thin Film On Alumina Substrate	255
73	A.S. Jadhav,S.S. Karande, V. M. Bhuse	Chemical Bath Deposition of CuS/CdS Heterojunction for Photoelectrochemical Application	258
74	Madhushree G Bute, Geeta Sharma, Suresh W. Gosavi	Luminescence Properties of CaS:Ce Nanophosphors Embedded in PDMS Polymer Matrix	261
75	R. B. Waghmode, A. P. Torane	Synthesis of NiCo_2O_4 nanowalls for preparation of high performance supercapacitor electrodes	264
76	Sandip Patil, M R Shedam	Synthesis of Superhydrophobic Silica Coatings on Different Substrates	269
77	V. S. Jamadade, D. S. Gaikwad, C. J. Khilare, A. S. Burungale	Effect of Polyaniline Film Thickness on Rectifying Characteristics of Polyaniline Based Heterojunction	271
78	Sujit A.Kadam, G.B. Devidas and T.Sankarappa	Study the Structural, Optical and Morphological Properties of PbSe Thin Films prepared by Chemical Bath Deposition (CBD) method	273
79	S A Kulkarni, P S Sawadh,M G Gote, K K. Kokate, S E Bhandarkar	Synthesis and Chracterization of $\text{Fe}_3\text{O}_4/\text{PANI}$ Nanocomposite	277
80	Bhitre S. R	Synthesis and structural study of Al^{3+} substituted Cd ferrites	280
81	Shivani Gavande, Gouri Tuljalpurkar, Pooja Solapure Abhijit Nivargikar, S.S.Gavande	Synthesis and Structural Study of Cobalt Sulphide Thin Films By Chemical Bath Deposition	283
82	Ramchandra S Kalubarme, Suresh Gosavi	Simple Co-precipitation Synthesis of Nanostructured Tin oxide as an Anode for Li-ion Rechargeable Batteries	285
83	C. B. Mane, R. P. Pawar, D. D. Gaikwad, R. V. Khobare, A. P. Tayadec, K. D. Warad	Microstructural and Morphological study of SnO_2 nanoparticles	388
84	Sagar M. Mane, Chandrakant B. Kolekar, Shrinivas B. Kulkarni	Effect of sintering temperature on structural and dielectric properties of $\text{Ba}_{0.7}\text{Ca}_{0.3}\text{TiO}_3$ ceramic sintered by microwave technique	291
85	Bandgar Ramesh M.	Ultrasonic Distance Measurement Using Microcontroller 8051	295

86	S. A. Phaltane, S. S. Shinde, B. L. Kamble, P.S. Patil, L. D. Kadam	Hydrothermally synthesized CZTS: A potential candidate for methylene blue dye degradation	298
87	Shankar Kekade, S. I. Patil	Effect of sintering temperature on electrical and magnetic properties of $\text{La}_{0.7}\text{Ca}_{0.3}\text{MnO}_3$	302
88	N.L. Tarwal, A.M. Nalawade, S. A. Rasal, R.P.Bhosale, A.E.Korade, P.S. Patil, J.H. Jang	Fabrication and performance of the solar cell devices based on electrodeposited compact CZTS films	306
89	D. A. Kumbhar, A. M. Nalawade, R. A. Nalawade S. B. Raut	Study of Morphological Change in ZnO Nanoparticles by Capping Agents Using Sol-gel Method	309
90	Shriyog Kokare, Shrikant Kokare and Ashok Shinde	X-Ray Crystallography- A Tool For Material Characterization	313
91	Minakshi V. Patil, Laxman S. Walekar, Uttam R. Kondekar, Prashant V. Anbhule, Shivajirao R. Patil, Govind B. Kolekar,	Investigation to reveal the nature of interaction of human hemoglobin with Gibberillic acid	316
92	T.M. Khot, A.N. Pasale	Chemical Bath Deposition of Cd-Zn-S Thin Film of Solar Cell Application	317
93	S.S. Karande, S. A. Masti, M.S. Kavale, B.R.Karche	Coersivity, Magnetic moment, Remnent and Saturation magnetization of nanoparticle sized Aluminium substituted copper cobalt ferrites	319
94	S. H. Burungale, A.N. Bhingare	Column Chromatographic Separation of Iron and copper from Immobilization of Cation Exchanger Resin with derivatives of Phosphine Oxide	324
95	Dadaso B. Shinde, Popatrao N. Bhosale, Uday Patil, Raghunath K. Mane	Comparative study of TiO_2 , ZnO and hybrid TiO_2 -ZnO thin film composites prepared by hydrothermal technique	328
96	A.V. Thakur, Y. S. Kokare, S. R. Mane, B. J. Lokhande	Cyclic voltammetric study of Fe_3O_4 flexible electrodes in different electrolytes	330
97	S.G. Dhumal, D. S. Ghadage, S. M. Todkari, S. B. Kulkarni D.J. Salunkhe	Enhanced Magnetodielectric Properties of Nickel Doped $\text{Ba}_{0.7}\text{Pb}_{0.3}\text{TiO}_3$ Single Phase Multiferroic Compounds	333
98	V. L. Patil, P. M. Kadam, S. S. Kumbhar. S. A. Vanalakar, S.S.Shendage, J.H. Kime, P. S. Patil	Enhanced NO_2 gas sensing properties of flower-like ZnO microstructure	337
99	D. M. Pore, S. N. Korade	Glycine Nitrate Mediated Convenient Synthesis of Erlenmeyer Azalactone	343
100	Vidya C. Mali, Krinsha. K. Rangar, Rajendra A. Lavate, Dipak A. Kumbhar, Sanjay S. Sathe, and B. N. Kokare	Green Synthesis of Silver Nanoparticles From Plants.	347
101	A. R. Supale and G. S. Gokavi	Heteropoly acid catalyzed synthesis of amidoalkyl naphthols	352
102	S.G. Chavan, P. M. Kharade, S. N. Tambe, D. S. Ghadage, S. B. Kulkarni, D. J. Salunkhe	Hydrothermal synthesis and characterization of CNFO-BZT composites.	356
103	Sarika Jadhav, Ramchandra S. Kalubarme, and S.W. Gosavi	Hydrothermal synthesis of CobaltOxide/ Reduced Graphene Oxide Composite and their Electrochemical Investigations	359
104	D.S. Gaikwad and V. S. Jamadade	Identification of Bacterial Blight Disease on Pomegranate Fruit	362
105	S. P. Yadav, K.Y. Rajpure	Magnetic behavior OF (x) $\text{Co}_{0.8}\text{Mn}_{0.2}\text{Fe}_2\text{O}_4$ and (1-x) $\text{PbZr}_{0.52}\text{Ti}_{0.48}\text{O}_3$ magnetoelectric composites	364
106	S. R. Jigajeni, S. H. Kshirsagar,	Magnetodielectric properties of SBN–CMFO nanocomposites	367
107	K. K. Patil	Preparation and characterisation of lead iodide nanoparticles	370

108	Yogesh Waghadkar, Govind Umarji, Sunit Rane, Ratna Chauhan, and Suresh Gosavi	Solvothermal synthesis of hierarchical ZnO microsphere and its application in dye-sensitized solar cells	372
109	Jyoti Dhumal, E. K. Kore, S. S. Bandgar, J. A. Ukirade and G. S. Shahane	Structural and Magnetic Properties of $Fe_{0.5}Mn_{0.5}Fe_2O_4$ Ferrite Nanoparticles	375
110	T.S. Bhadrashetti, B.A.S. Sueba, R.A. Sayyad, M. S. Kavale,	Structural Study of Cobalt Sulphide Thin Films Synthesized By Successive Ionic Layer Adsorption Reaction Method	378
111	D.R. Mhamane, G.D. Pise, P.S.Shendage, T.S. Ghadge, S.S. Karande	Structural Study of Copper Hydroxide Thin Films By Electrodeposition	380
112	V.C.Malvade, P.B. Abhange, K.V.Rao and S.R. Kokare	Studies on $0.25(Ba_{0.7}Sr_{0.3}TiO_3) + 0.75(BaLa_2Ti_3O_{10})$ Polycrystalline Ceramic	482
113	Bhagyashri Bhangare, Suresh Gosavi	Studies on structural and optical properties of Zn doped CeO_2 nanoparticles	484
114	P. M. Kharade, S.G. Chavan S.S. Mane, S.D. Chavan, J.V.Thombare, T.R. Mane, S. B .Kulkarni, D. J. Salunkhe	Synthesis and characterization of Polypyrrole thin film for supercapacitor application	487
115	Kardele Sandeep Ambadas and Dhoble Vaishali Shankar	Synthesis and Charecterisation Of Zno Nanorods	390
116	Krishna Daware, Gaurav Lole, Suresh Gosavi	Synthesis of Trimetallic ($SiO_2@AuPtPd$) Core Shell Nanoparticles and its Structural Characterization	395
117	A M. Sargar, P.S. Dikule	Synthesis, Characterization and Photocatalytic activity of Fe_2O_3	398
118	Raviraj S. Kamble, N. Viswanadham, Tanaji S. Patil, Vijay P. Kothavale, Rajan S. Kamble	Study of Activity of H-ZSM-5 Catalysts for Light Alkane Aromatization	401
119	V.P. Kothavale, T.S.Patil, R.S.Kamble, C.M. Kanamadi, C. H. Bhosale	Structural and Optical Study of Titanium Dioxide Thin Films by Chemical Spray Pyrolysis	405
120	Vidya Kalyankar, Mahesh Salukhe, Prashant More, Heena Meroliya, Sharada Dagade, Shobha A. Waghmode	Natural cellulosic fiber as a Humidity Sensor	409
121	D. S. Sutrave, V. L. Mathe, P.S.Joshi, S. D. Gothe	Influence of Ruthenium doping on Structural Properties of MoO_3 Thin Films	413
122	Sunil D. Kumbhar, Sunil B. Patil, Mahesh G. Kukade, Anita J. Bodake	Green Synthesis of ZnO nanoparticles using plant extracts	416
123	M. M. Sutar, Birajdar, A.N. Patil	Magnetolectric Studies On Nanocrystalline BST-CNFMO Composites	419
124	Gaurav Lole, Krishna Daware, Manasi Kasture, Ramchandra Kalubarme, and Suresh Gosavi	Synthesis and Characterization of Ruthenium Decorated Reduced Graphene Oxide Nanosheets.	423
125	R.D.Mane, P.P. Chikode	Studies of Yttrium Telluride Electrodeposited Thin Films.	426
126	P.P. Padghan, P. P. Rathi and K.M. Alti	Effect of rotational Wiggling on speckle contrast	429
127	R.A.Lavate, S.S.Sathe, D.A.Kumbhar, G.D. Salunke, V.C. Mali, N.R.Bobade, M.B. Sajjan	Bryophytes As Source Of Silver Nanoparticles: A Review	431

Key Note Address

Recent Progress in Photocatalysis International Research Center

Chiaki Terashima

Photocatalysis International Research Center, Tokyo University of Science

2641 Yamazaki, Noda, Chiba 278-8510, JAPAN

E-mail: terashima@rs.tus.ac.jp

Conversion of solar to chemical energy has been an emerging field of research since its discovery in 1972 by Fujishima et al. using a TiO₂ photoanode¹. Solar energy conversion and storage in terms of chemical energy attract immense attention and has plenty of scopes. This is due to the fact that the energy demand of the globe increases day by day and a major portion of energy consumption is supplied from fossil fuel. Therefore, solar energy conversion or storage is one of the important future energy sources which could be utilized for mankind. Solar water splitting on a semiconductor surface to produce hydrogen is an art example of conversion and storage of solar energy to chemical energy. Hydrogen can easily be converted into heat energy or mechanical or electrical energy. In addition, it has very high energy density, zero carbon emission and as well easy transportation makes it to be a potential candidate for chemical energy source in the future energy field. Therefore, semiconductor photocatalysis has been engaging for solar to chemical energy conversion for a long time for practical applications. The present status of semiconductor photocatalysis deals with utilization of visible light and improvement of the efficiency to make it up to the benchmark efficiency of 10% solar to chemical energy conversion. Still various materials manipulation and strategies in photochemical or photoelectrochemical experimental conditions have been taking consideration for reliable applications.

Semiconductor photocatalysis is not only limited to the hydrogen production, but also utilized for other chemical conversions. Photocatalytic CO₂

Vision of future society using photocatalysis

References:

1. A. Fujishima and K. Honda, Electrochemical photolysis of water at a semiconductor electrode. *Nature* **238**, 37–38 (1972).
2. N. Roy, Y. Hirano, H. Kuriyama, P. Sudhagar, N. Suzuki, K. Katsumata, K. Nakata, T. Kondo, M. Yuasa, I. Serizawa, T. Takayama, A. Kudo, A. Fujishima and C. Terashima, Boron-doped diamond semiconductor electrodes: Efficient photoelectrochemical CO₂ reduction through surface modification. *Sci. Rep.* **6**, 38010 (2016).

reduction is one of them as atmospheric CO₂ concentration has increased a lot in last 50 years. Therefore, mimicking of natural photosynthesis and practical applications through semiconductor photocatalysis is considered to be a potential challenge for the scientific community. We recently succeeded in the high selectivity and recyclability for photoelectrochemical CO₂ reduction by using of Ag nanoparticle modified diamond semiconductor, which was synthesized as lightly boron-doped diamond². This material was effectively utilized as a semiconductor electron source to accelerate CO₂ reduction rate while Ag nanoparticles were decorated on diamond surface.

Semiconductor photocatalysis involving TiO₂ has further extended to environment remediation, water purification, and antibacterial activity. This is owing to that TiO₂ has very high photooxidation activity. Superhydrophilicity of TiO₂ is another potential property which has changed the direction of its use. This property of TiO₂ led it being utilized as self-cleaning agent, as anti-fogging material, as photocatalyst paint and so forth. The high photooxidation and superhydrophilic properties of TiO₂ have resulted in engaging a vast amount of research in automobile industries, construction plans, as deodorization and interior design. The high stability in ambient condition, low cost, easy fabrication methods and biocompatibility are the additional factors that have made TiO₂ is one of the most studies and versatile semiconductors for the above-mentioned applications which include energy conversion, water purification, health care, and environment remediation



Invited talks

Emergence of Perovskite solar cells

Prof. (Dr.) Pramod S. Patil

Founder Co-ordinator, School of nanoscience and Technology

Department of Physics,

Shivaji University, Kolhapur -416 004, India

Abstract

The photovoltaic solar cells are attracting great deal of interest from across the globe due to their potential of producing electrical energy by harvesting photon energy, available on the earth, which is abundant and available free of cost. However, the cost of electricity production and the efficiency with which it is produced are important attributes. Subsequently, several solar cell generations have been emerged in order to chase the low cost-high efficiency race. The initial solar cells, first generation, based on crystalline silicon exhibited high efficiency but it became practically impossible to bring down their cost, hence their utilization was limited to the extra-terrestrial applications. Afterwards, several other interesting inorganic materials in the form of thin films, second generation, were investigated for the fabrication of low cost-high efficiency solar cell devices that includes CuInS_2 , CuInSe_2 , CIGS, amorphous Si and CdTe. The market penetration of these devices were marginal due to the limited resources and cost of the elements like indium, gallium and toxicity of Cd. Further research is focused on low cost nanomaterials including configuration like dye sensitized solar cells, quantum dot sensitized solar cells and organic solar cells. However their performance is yet to be explored fully before arriving at any conclusion. Much efforts are still required in this direction to exploit their full potential.

Organometal trihalide organic-inorganic hybrid perovskites with general formula ABX_3 , where the "A" site is an organic-molecule cation, were first discovered in 1978. The structural understanding, solution-processing, and properties of this remarkable family of materials were further developed in the 1990s, but their use in solar cells in 2009 has sparked tremendous interest in these hybrid organic-inorganic materials for photovoltaics and also other applications. In this talk, a systematic approach of development in third generation solar cells will be highlighted. Further, a novel in-situ processed gold nanoparticle-embedded TiO_2 nanofibers, enabling plasmonic perovskite solar cells with power conversion efficiency exceeding 14%, will also be discussed.



Prof. P.B. Joshi Memorial Lecture

Recent results in some nanocrystalline ferrite thin film systems

N. Venkataramani

Metallurgical Engineering and Materials Science Department,
Indian Institute of Technology Bombay, Mumbai 400076

PERSONAL NEWS

Pradeep Baburao Joshi (1957–2016)

Prof. P. B. Joshi, former Director of the School of Physical Sciences, Solapur University, passed away on 10 February 2016 in Pune.

Joshi was born in Miraj, Maharashtra and had his early education there. He graduated from Willingdon College, Sangli with physics as the major subject. He then obtained his postgraduate degree from Shivaji University, Kolhapur. In 1987, Joshi completed his doctoral work in the Indian Institute of Technology Bombay, under the guidance of S. N. Bhatiya. For his doctoral thesis, he worked in low temperature physics. Joshi joined Shivaji University in 1989 at the Postgraduate Teaching Centre at Solapur as lecturer. Later he became reader and Director of the sub-center. He then became professor of physics and also shouldered the responsibility of the Management Council of Shivaji University as a member for five years. Joshi taught power electronics, digital electronics, computer programming, microprocessors and microcontrollers to postgraduate students.

His research interest was image instrumentation and development of prototypic sensors. Along with this, he



synthesized many materials with ferro- and anti-ferroelectric properties. He has made good contributions in the field of ferroelectric and dielectric materials. In 2008, he was felicitated for his contributions to ferroelectric and dielectric materials by Delhi University. The

Government of Maharashtra felicitated him with the Best Teacher Award in 2010. He was a elected Fellow of INSA, New Delhi. Joshi successfully guided many students for doctoral and M Phil degree. He completed many research projects sanctioned by UGC, DRDO, DST, etc. He was Director of the Board of College and University Development for a long time. Many a times he also took up the responsibilities of the Registrar as well as Finance and Account Officer of the University.

Joshi was known to be a walking encyclopaedia of statutes and ordinances of the Maharashtra University Act, UGC guidelines and rules. His demise is a great loss to the scientific community in general and the physics community in particular.

SHRIKANT R. KOKARE

*Department of Physics,
RajeRamrao College, Jath,
Sangli 416 404, India
e-mail: kshirikant@yahoo.com*

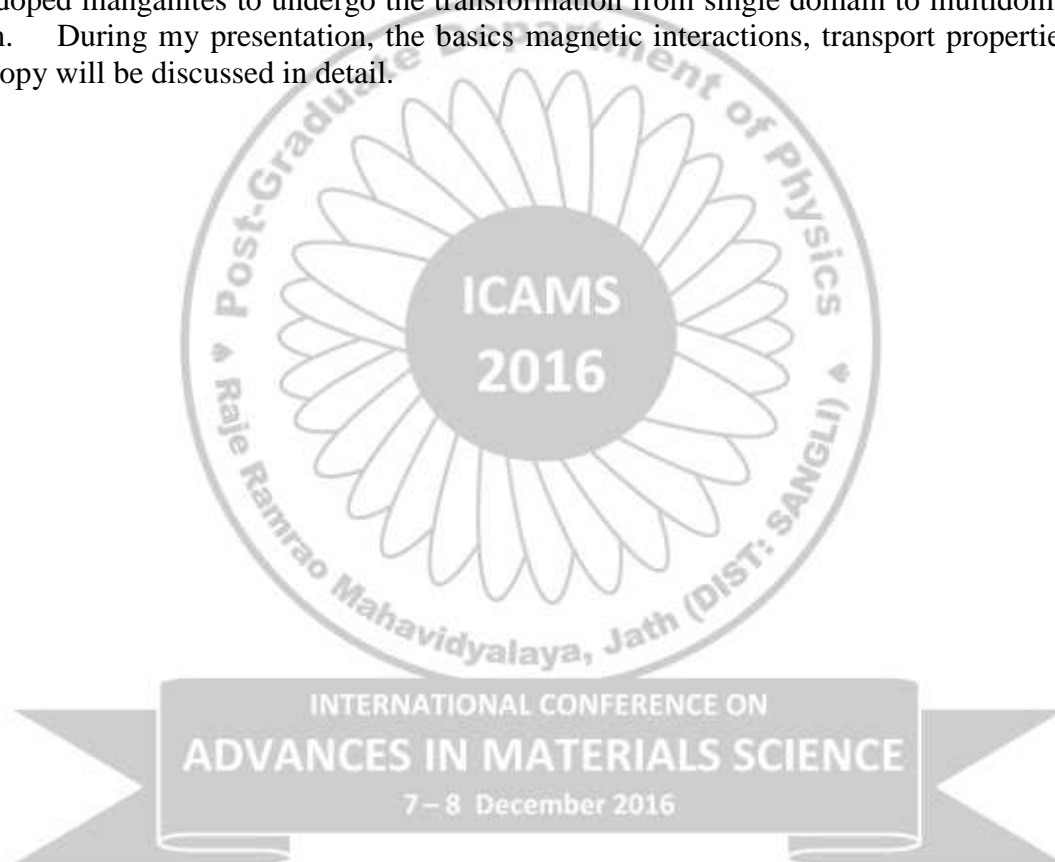
Ferrite systems comprise of spinels, hexaferrites, orthoferrites and garnets. Each of this system has found useful application in the bulk due to their magnetic properties. Due to planarization of most devices, experimental studies have been taken up in the case of ferrites as well, depositing them in the thin film form. There is an on-going effort to exploit these systems in the thin film form for sensors, magnetoelectric composites, high frequency components and few novel areas like spintronics and magnonics. We have been studying ferrite systems for over two decades by PVD processes. The deposited thin films are nanocrystalline in nature and develop very interesting magnetic properties, distinctly different from their bulk counterparts. In this talk I will discuss few interesting results from our recent studies on Zn ferrite, Co ferrite, substituted Zn ferrites and YIG.

Crystallographic Magnetic and Electrical properties of Hole doped manganites

S. I. Patil

Dept. of Physics, Savitribai Phule Pune University, Pune – 411007

The polycrystalline sample of $\text{La}_{0.7}\text{Sr}_{0.3}\text{MnO}_3$ with perovskite (Orthorhombic) crystalline structure was synthesized by soft chemical route. Samples were sintered at different temperature to vary the grain size of the crystallites. Phase formation and grain was estimated by XRD and SEM studies respectively. Magnetic parameters were observed by SQUID magnetometer and the valence band spectra were recorded with 56 eV photon energy at RRCAT Indore. The grain size increases with increase in sintering temperature and magnetic moment was found to be increase with increase in grain size. The critical size for the hole doped manganites to undergo the transformation from single domain to multidomain was found to be 23 nm. During my presentation, the basics magnetic interactions, transport properties, Valance band spectroscopy will be discussed in detail.



Electrochemical Properties of Spray Pyrolysed Metal Oxide Thin Films – A Supercapacitor Approach

Dr. B. J. Lokhande

Supercapacitive Studies Laboratory, School of Physical Sciences,
Solapur University, Solapur – 413 255, M.S. India

Abstract:

High performance electrical energy storage technologies are urgently needed in today's mobile, information-rich and energy-conscious society. Among the various energy storage systems, supercapacitor is one of the new emerging device which can deliver electrical energy at high charging/discharging rates, have high power density, long cycle life, large efficiency, low ESR and safety for operation. The major issue concerned with these devices is the low energy density. Hence, the recent studies in the field of supercapacitor has a great attention on preparing the high energy density electrode/ electrode materials. Transition metal oxides and conducting polymers serves the purpose well to provide the larger energy density, through the faradic reactions during the charge storage operation.

Present talk deals with the preparation of metal oxide thin film electrodes by using the spray pyrolysis technique and their supercapacitive properties. This will be followed by the structural, morphological, compositional etc. characterizations of the prepared electrodes. Supercapacitive characterizations like cyclic voltammetry, chronopotentiometry, stability study of the prepared metal oxide thin film electrodes has been systematically analyzed in depth and will be presented in detail.



Development of Functionalized Nanocomposite based VOCs (Volatile Organic Compounds) Profiler: An Aid on Early Diagnosis of Cancer

Suresh Gosavi

Centre for Advanced Studies in Material Science and Solid State Physics, Department of Physics, Savitribai Phule Pune University, (Formerly University of Pune) Ganeshkhind, Pune - 411007, INDIA

Email: swg@physics.unipune.ac.in

World cancer report 2014, states that, cancer is a major threat that caused 8.2 million deaths worldwide in 2012. [1] WHO estimated that cancer related death keep on increasing worldwide and will reach to approximately to 11 million by 2030. [2] It has been observed that early detection of cancer can reduce its fatality. Currently, cancer detection is achieved by conventional technique such as CT, MRI, etc., which are invasive and time consuming methods.

It has been evident that ancient Greek physicians from Hippocrates (460-370 BC) era noted the relevant typical odor of breath with physiological conditions of patients. In 1782–1783, Lavoisier proved that CO₂ is a product of metabolic reactions [3]. In this scenario “ohmics” (genomics, proteomics and metabolomics) approach for detection and profiling of VOC cancer markers seems to be a promising approach [4]. It is very important that VOCs based disease diagnosis enables real time monitoring with a non invasive way, as VOCs could be collected from any kind of biological specimen (blood, exhaled breath, urine, faeces, and sweat) [5-7]. An attempt is also made for detection of VOCs using GC, GC-MS etc. However, presently these methods are time consuming and may have major risk of contamination with solvent procedures and sample loss. In order to use the biosensors for clinical early diagnosis, the technology must be cost effective. The use of functional materials may increase the sensitivity of a biosensor and generate high accuracy and precision. Moreover, nano-sized devices generally allow faster response because electron transport occurs over smaller distances.

Nanomaterials are securing high impact on development of electrochemical biosensor field in the nano-sized semiconductor and the nanoscale should also results as cost effective due to the small quantities of material required. Metal nanoparticles demonstrated an ability to direct electron transfer between the electroactive molecules and electrode surface.

Dimethyl Disulfide (DMDS) is one of the VOCs found in cancer patients and can be subjected as a target molecule. Sulfur atoms from the CdS NPs might efficiently break disulfide bond which further leads to formation of CdS @ Methyl Disulfide bonds and extraction of elemental sulfur from VOC samples. Quantitative detection of formed trisulfide compound linkage can be carried out by using UV - Vis Spectroscopy.

Photochromic molecules are also well known probes to detect VOCs molecules. Depending on the chemical properties of the photochromic molecules, detection of specific bio-marker is possible. The photochromic molecule doped PDMS films are activated using UV exposure and then used for detection of VOCs in urine samples.

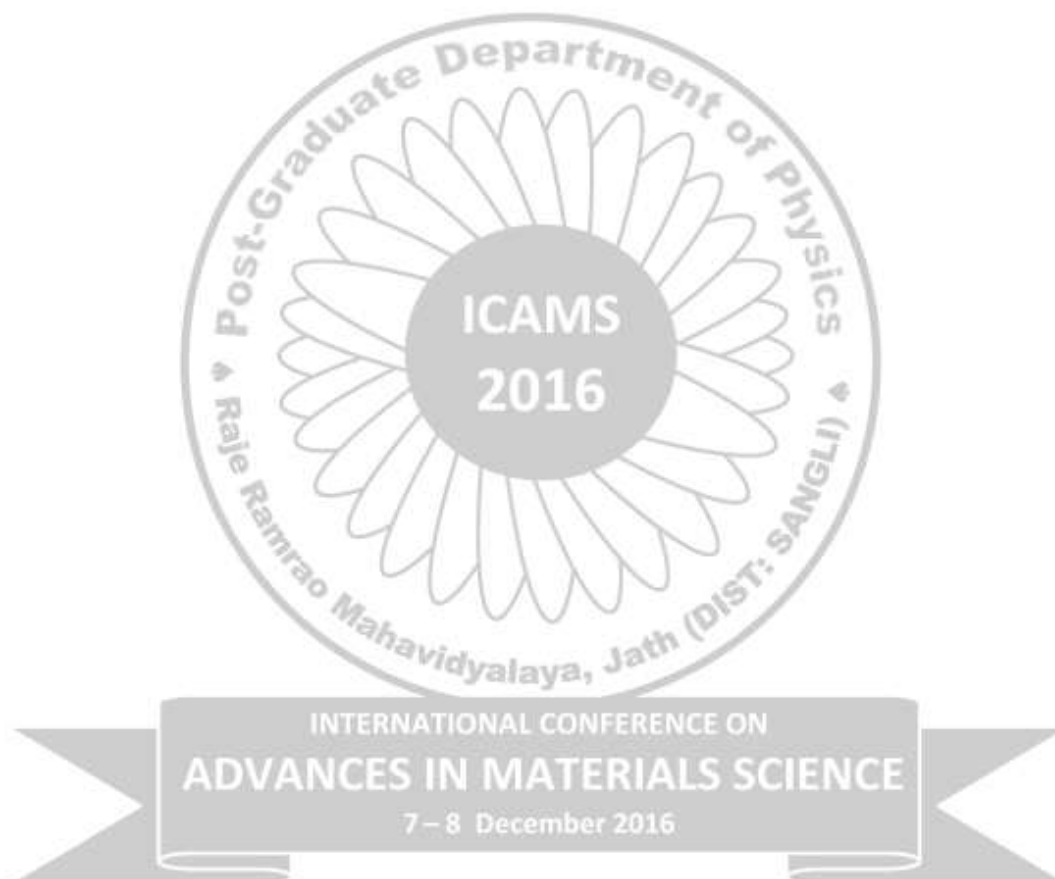
Some results on advanced graphene application for detection of biological activity will be presented. The SnO₂-RGO nanocomposites are found to be most sensitive towards various alcohols, phenols, toluene which are listed as biomarkers for cancer. The present material shows less response towards ammonia which is one of the interfering analyte while studying the urine samples of cancer patients.

Apart from this Yolk-shell nanoconjugates tend to mimic peroxidase enzyme activity when

reacted with TMB and H₂O₂ in presence with acidic pH condition, as well as produces chromogenic product where the sample turns greenish blue, proving their use as an alternative technique to ELISA.

References:

1. World cancer report 2014.
2. S. Suresh, ActaMaterialia 2007, 55, 3989.
3. Francesco, F. D., et al. , Microchemical Journal, 2005, 79, 405.
4. M. Philips et. al. J. Chromatogr. B. Biomed. Sci. Appl. 1999, 729, 75
5. L. Pauling, et.al. Proc. of the National Academy of Sciences of the USA, 1971, 68, No.10, 2374.
6. C. Deng et.al. Rapid Communications in Mass Spectrometry, 2004, 18, No. 15, 1715.
7. I. Ahmed, et.al. PLoS ONE, 2013, 8, no. 3, Article ID e58204, 2013



Tuning the structural, dielectric and ferroelectric properties of lead free Ca-modified BaTiO₃ ceramics

Bhavna C Keswani, S. I. Patil and Y. D. Kolekar*

Department of Physics, Savitribai Phule Pune University, Pune, Maharashtra-411007

Corresponding author email: ydk@physics.unipune.ac.in, banukeswani1990@gmail.com

Abstract:

Barium titanate (BaTiO₃) based materials are one of the lead-free ferroelectric which has high stability, high dielectric constant, higher Curie temperature ($T_c \sim 120^\circ\text{C}$), low losses, etc. Therefore, in the present case, Pb-free ferroelectrics, $\text{Ba}_{(1-x)}\text{Ca}_x\text{TiO}_3$ ($x=0, 0.08, 0.3$), were chosen and synthesized by solid state reaction method. The purity and phase confirmation of the samples were confirmed by X-ray diffraction (XRD) followed by Rietveld refinement. XRD results reveal the tetragonal crystal symmetry with $P4mm$ space group for all the synthesized samples and the structure is also confirmed from the presence of Raman shift around 720 cm^{-1} corresponding to $A_1(\text{LO})/E(\text{LO})$ mode which indicates the signature of tetragonal phase. It is observed that the unit cell volume of BaTiO₃ decreases with Ca^{2+} substitutions for Ba^{2+} due to smaller ionic size of Ca^{2+} as compared to Ba^{2+} . The microstructural study was made using scanning electron microscope (SEM) which reveals the formation of micron sized grains for all the compositions. All the samples exhibit the typical polarization-electric field (P-E) hysteresis loops which confirm the ferroelectric nature and show the increase of coercivity with Ca content. Temperature dependent dielectric measurements for all the samples show the presence of dielectric maxima (Curie temperature, T_c) in the range of $(120-140)^\circ\text{C}$ with maximum dielectric constant ~ 5100 for 8% Ca substitution. Hence, the Ca-modified BT system can be useful for capacitor, switching devices, permanent ferroelectric memory, etc. applications depending upon the Ca content in BT.

1. Introduction

Ferroelectric materials are widely used in variety of applications such as high dielectric capacitors, transducers, optoelectronic devices, memory devices, etc [1, 2, 3]. Among the different ferroelectric materials available, lead and lead based materials such as $\text{Pb}(\text{Zr}, \text{Ti})\text{O}_3$ (PZT) are the most widely used ferroelectrics due to their superior properties such as high dielectric constant ($>20,000$ at Curie temperature), high piezoelectric coefficient ($d_{33} \approx 580\text{ pC/N}$), high Curie temperature ($T_c > 390^\circ\text{C}$) [4]. But in 2006, RoHS (Restriction on Hazardous Substances) made a restriction on the use of environmental hazardous materials such as lead, cadmium, mercury, etc. based materials due to their toxic nature. Moreover, it is reported that the lead can injure the nervous connections and it accumulates in the bones over time, which can cause knee pain, neurological symptoms, hypertension, anemia, etc [5, 6]. Hence, these materials are banned by many European countries. Therefore, at present many researchers are focusing towards the search and development of lead-free ferroelectrics with comparable properties as that of the lead based ferroelectrics. Among the known lead-free materials such as $(\text{K}_{0.5}\text{Na}_{0.5})\text{NbO}_3$, $(\text{Bi}_{0.5}\text{Na}_{0.5})\text{TiO}_3$, BaTiO_3 , etc. and their compositions, BaTiO_3 (BT) based materials are

widely used ferroelectric materials due to their excellent properties such as relatively high chemical stability and can be easily sintered with maintaining good chemical stoichiometry [6], which makes them one of the important lead free ferroelectric material. However, BT has some practical limitations such as low range of tetragonal stability i.e. tetragonal structure of BT is stable only in the range from 5°C to 120°C , which hinders its practical applications compared to PZT. Doping and/or substitution in the ferroelectrics are one of the effective ways to improve the material performance [7]. Depending upon the applications, BaTiO_3 has been doped/substituted with various ions such as Ca^{2+} , Sr^{2+} , etc for Ba^{2+} and Zr^{4+} , Sn^{4+} , etc for Ti^{4+} to modify and improve their basic properties [8,9,10,11]. Among these, Ca^{2+} substituted BaTiO_3 materials have received a great attention as one of the lead free ferroelectric materials and has been chosen specifically for multilayer ceramic capacitor applications and in various other applications [8]. It is reported that the partial substitution of Ba^{2+} by Ca^{2+} in BaTiO_3 can slightly change the Curie temperature while remarkably lowers the orthorhombic to tetragonal phase transition which leads to increase in the tetragonal range stability [12]. Therefore, in the present case, the partial substitution of Ba^{2+} by Ca^{2+} i.e. $\text{Ba}_{(1-x)}\text{Ca}_x\text{TiO}_3$ ($x=0, 0.08, 0.3$) is chosen,

in which $x = 0.08$ is within the solubility limit and $x = 0.30$ is above the solubility limit in BaTiO_3 [13,14,15].

2. Experimental

A conventional solid state reaction method was used for the synthesis of $\text{Ba}_{(1-x)}\text{Ca}_x\text{TiO}_3$ ($x = 0, 0.08, 0.3$) i.e. BT, BCT8 and BCT30 respectively, by using high purity (>99%) precursors viz., BaCO_3 , TiO_2 and CaCO_3 (all are from Sigma-Aldrich). All the precursor powders were weighed with their stoichiometric proportions and grinded in an agate mortar for 3-4 hrs in an ethanol medium. Then the powders were calcined at 850 °C and at 1050 °C for 10 hrs, separately, in an ambient atmosphere with intermediate grindings. After calcination, the powders were grounded and pressed into pellets (diameter ~10mm) using hydraulic press by adding polyvinyl alcohol (PVA) as a binder and sintered finally at 1250 °C for 5 hrs. The pellets obtained after sintering at 1250 °C for BT and BCT8 were dense while for BCT30 samples were not dense. Therefore, BCT30 sample was sintered at higher temperature 1400 °C for 5 hrs.

The phase formation and crystal structure of the ceramics were confirmed by using Bruker D8 Advance X-ray diffractometer (XRD) ($\text{Cu } k_\alpha$ having $\lambda = 1.5406 \text{ \AA}$). For more detailed structural analysis, Raman spectra were obtained using Renishaw Invia Raman spectroscopy system LEICA DM 2500 M having 532 nm Ar ion laser excitation source while morphology of the samples were studied with the help of scanning electron microscope (SEM) (JEOL JSM 6360). For the ferroelectric and dielectric measurements, pellets were polished and then electroded on both sides of polished surface using silver paste and heated at 100 °C for overnight to cure the silver paste. The electroded samples were then used for polarization versus electric field (P-E) hysteresis loop measurements using P-E loop tracer (Marine India limited) and dielectric measurements by using HIOKI 3532-50 LCR HiTESTER.

3. Results and discussion

The XRD patterns of $\text{Ba}_{(1-x)}\text{Ca}_x\text{TiO}_3$ ($x=0, 0.08, 0.3$) reveals that all the ceramics exhibit polycrystalline perovskite structure without any trace of impurity phase. The peak positions were matched well with

ICSD (Inorganic Crystal Structure Database) collection code 34637 having tetragonal structure with P4mm space group. Further, Rietveld analysis of all the samples was performed using Fullprof software. Figure 1 shows the Rietveld fitted XRD patterns for all the samples. It is observed from the fig.1 that all the samples were fitted very well with the tetragonal structure having space group P4mm. The resulting parameters obtained from Rietveld analysis are tabulated in Table 1 and Table 2. The lower values of chi squared (χ^2) and goodness of fit factor (GofF) indicates the good agreement between the calculated and observed patterns. The crystallite size (t) was calculated by using Scherrer formula,

$$t = \frac{0.9\lambda}{\beta \cos \theta_B} \quad (1)$$

where, λ is wavelength of $\text{Cu } (K_\alpha) = 1.5406 \text{ \AA}$, β is full width at half maxima (FWHM), θ_B Bragg's angle.

The splitting of (200) peak into (002) and (200) peak near 45° in all the samples confirm the tetragonal phase formation. Though, the solubility limit of Ca in $\text{Ba}_{(1-x)}\text{Ca}_x\text{TiO}_3$ is $x = 0.23$ as reported in the literature [15] but in the present work, BCT30 sample also exhibits pure tetragonal structure without any impurity phase which may be due to some amount of Ca substitution at Ti site in BaTiO_3 as suggested by Krishna et al. [16]. It is observed from Table 1 that the lattice parameter a and c decreases with increasing Ca substitution due to the Ba^{2+} as the larger cation (radii $\approx 1.64 \text{ \AA}$) compared to Ca^{2+} (radii $\approx 1.34 \text{ \AA}$) [17]. The crystallite size calculated using Scherrer formula was found in the range of 42 nm to 48 nm. The X-ray density was observed to decrease with Ca substitution and remarkably decreased for BCT30 which may be due to the increase in grain size. The ion-ion distance i.e. bond length between different ions in the unit cell was also calculated from Rietveld refinement. The calculated values of bond length between Ti-O, Ba-O, Ba-Ti, Ba-Ba and the

number of bonds present in the unit cell are tabulated in table 2. From the values of bond length between different ions, more significant change in the bond lengths for BCT30 was observed as compared BT. From the values of Ti-

O bond lengths, it is observed that in TiO_6 octahedron, the bond length between Ti-O in the horizontal plane decrease with increase in Ca content and Ti-O bond lengths along vertical c-

axis, changes significantly which shows increase in the Ti off-centering with Ca substitution while Ba-O, Ba-Ti and Ba-Ba gets strained with Ca substitution [18].

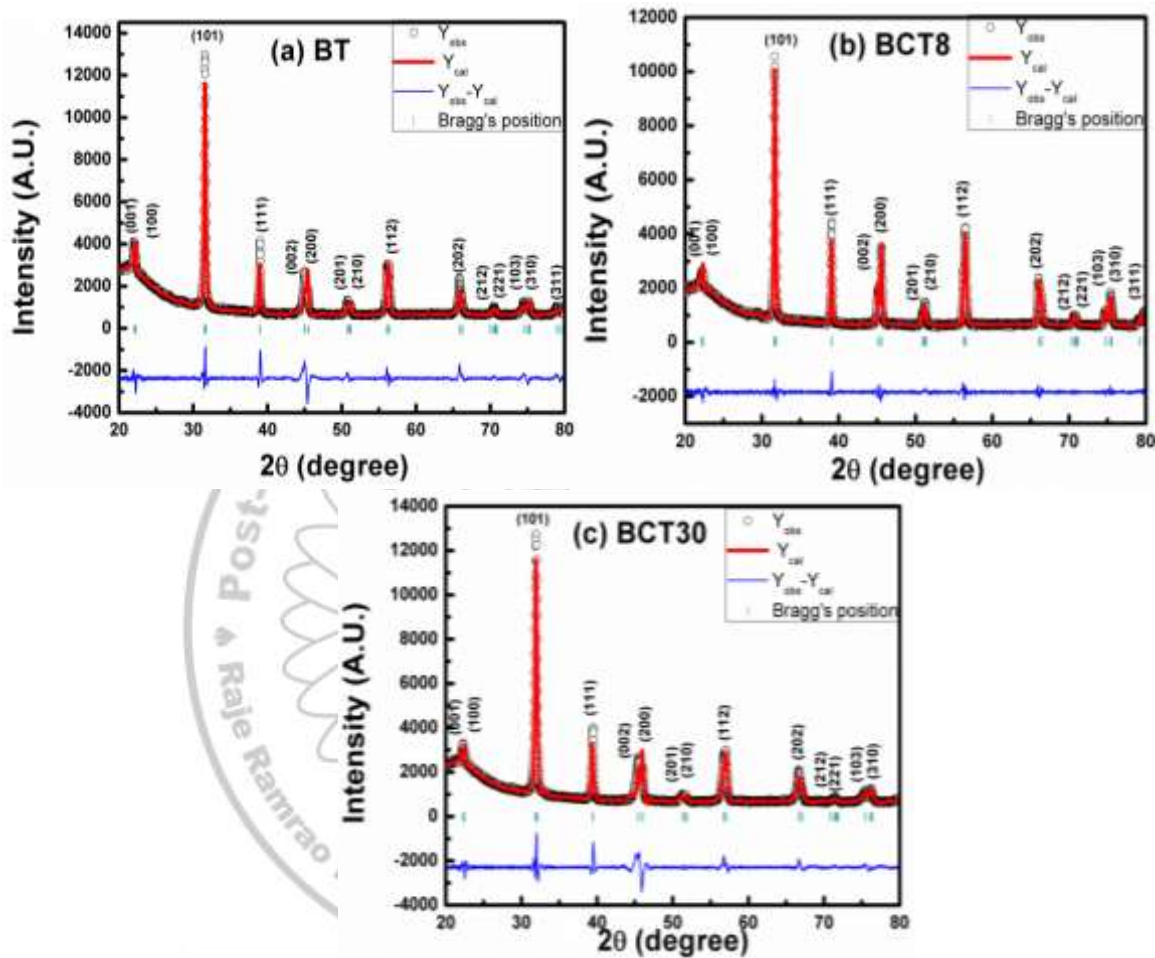


Fig.1: Rietveld fitted XRD patterns of (a) BT, (b) BCT8 and (c) BCT30

Table 1: The values of lattice parameter (a & c), x-ray density (ρ), chi square (χ^2), Goodness of fit factor ($GofF$), crystalline size (t), grain size for BT, BCT8 and BCT30

Composition	a (Å)	c (Å)	ρ (g/cm ³)	χ^2	$GofF$ ($\frac{R_{wp}}{R_{exp}}$)	t (nm)	Average Grain size (µm)
BT	3.9933	4.0307	6.024	9.68	3.10	46	2-3
BCT8	3.9814	4.0175	5.889	2.24	1.49	47	1.5-2
BCT30	3.9467	3.9921	5.4369	8.12	2.85	42	5-6

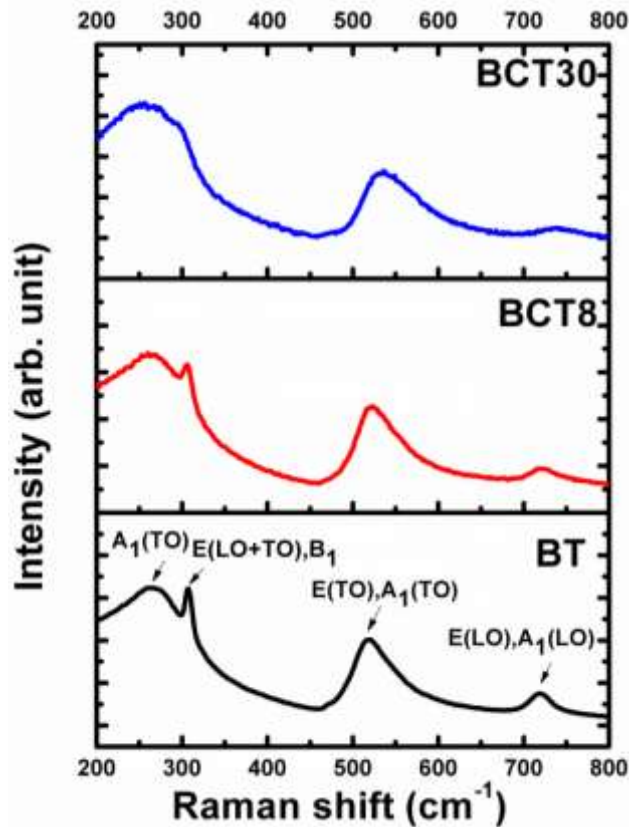
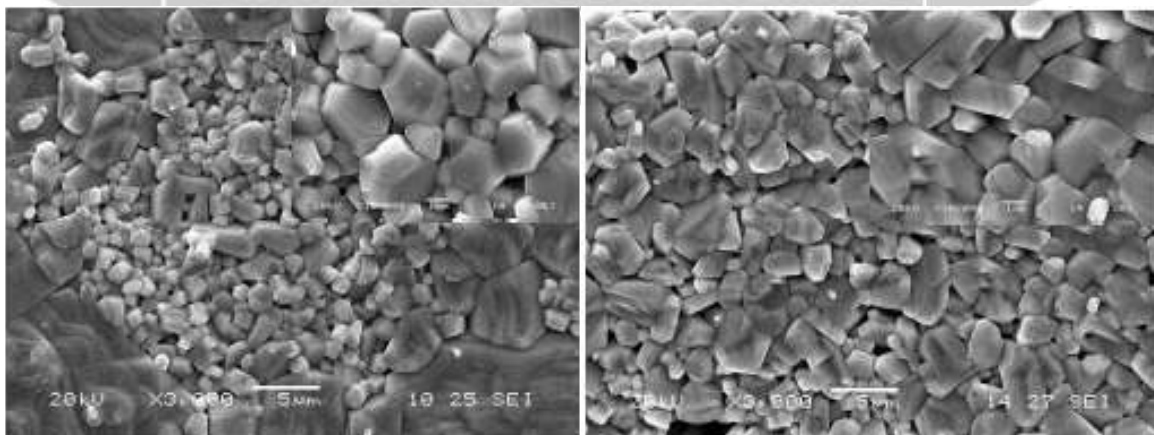


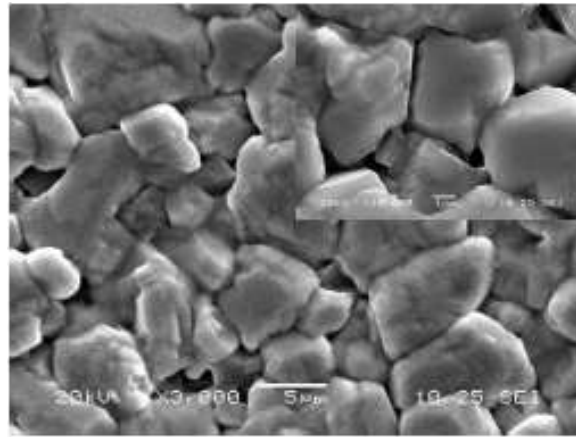
Fig.2: Raman spectra for BT, BCT8 and BCT30. In order to get more detailed information about the structural characterization, Raman spectra was recorded for all the samples which is very sensitive tool for structural characterization and complementary to XRD. According to crystallography, there are $4E(TO+LO) + 3A_1(TO+LO) + B_1(TO+LO)$ Raman active modes for tetragonal $BaTiO_3$ ($P4mm$) [19], whereas the

optical modes for cubic $BaTiO_3$ are Raman inactive. Room temperature Raman spectra for all the samples is as shown in fig. 2. The observed four distinct Raman peaks $A_1(TO)$, $E(TO+LO)/B_1$, $E(TO)/A_1(TO)$ and $E(LO)/A_1(LO)$ at 264 cm^{-1} , 307 cm^{-1} , 519 cm^{-1} and 719 cm^{-1} , respectively corresponds to tetragonal $BaTiO_3$ crystal structure [20]. With increase of Ca content, $A_1(TO)$ phonon peak shifts to lower frequency while sharp phonon peaks $E(LO+TO)$ and B_1 remains nearly at the same frequency and gradually weakens. $E(LO+TO)$ and B_1 modes become almost negligible for BCT30 samples which may be due to the substitution of some amount of Ca at Ti site [16]. The presence of $E(LO)/A_1(LO)$ mode around 720 cm^{-1} for all the samples is the signature of tetragonal phase present in the crystallographic structure which becomes broader and broader with increase in Ca content and become almost negligible for BCT30 samples. This indicated that the crystal structure gets distorted i.e. tetragonality decreases which is in agreement with the results obtained from XRD analysis. The increase in broadness of peaks suggests the decrease in structural coherence [21]. Moreover, the sharp drop in the peak intensity of $E(LO+TO)/B_1$ around 307 cm^{-1} and increase in the peak width of $E(LO)/A_1(LO)$ around 720 cm^{-1} with increase in Ca substitution also indicates the diffuse phase transition behavior for Ca substituted samples [21].



(a)

(b)



(c)

Fig.3: SEM images of (a) BT, (b) BCT8 and (c) BCT30

Table 2: Number of bonds and bond lengths values of Ti-O, Ba-O, Ba-Ti and Ba-Ba bonds for BT, BCT8 and BCT30 obtained from Rietveld analysis

SEM micro structural images for BT, BCT8 and

Name of the bond	No. of bonds	Bond length (Å)		
		BT	BCT8	BCT30
Ti-O	1	2.0362	2.1682	2.1545
	4	1.9969	1.9935	1.9762
	1	1.9946	1.8493	1.8376
Ba-O	4	2.8256	2.8171	2.7926
	4	2.8020	2.7932	2.7721
	4	2.8724	2.8634	2.8420
Ba-Ti	4	3.4222	3.4256	3.3984
	4	3.5174	3.4919	3.4644
Ba-Ba	4	3.9933	3.9814	3.9467
	2	4.0308	4.0175	3.9921

BCT30 are as shown in figure 3. All the samples show clearly visible grains with average grain size in the range of 1 to 6 μm . All the micro structural images show the uniform and non-porous grains with the presence of minimum number of voids, which indicates dense micro structure for all the samples and may be attributed to due to the effective sintering of the ceramics. Moreover, higher grain growth is observed in case of BCT30 samples which may be due to the higher sintering temperature of 1400 $^{\circ}\text{C}$ as compared to BT and BCT8 samples sintered at 1250 $^{\circ}\text{C}$.

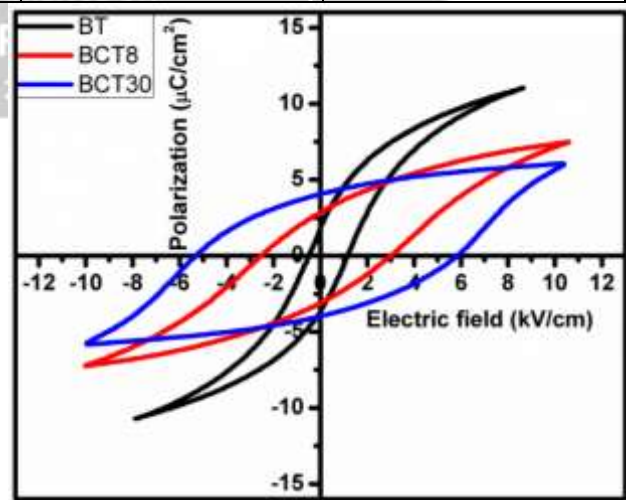
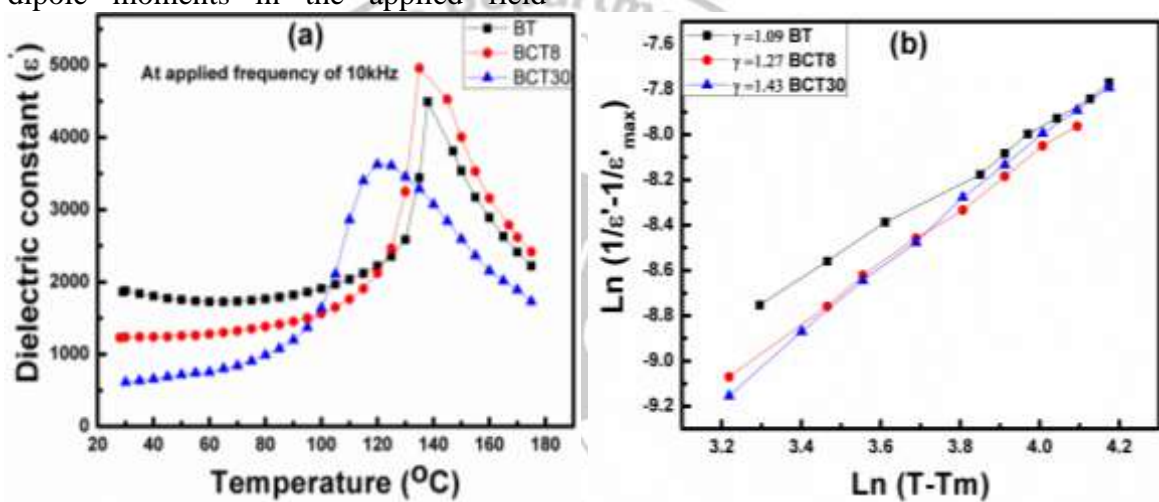


Fig.4: P-E hysteresis loops of (a) BT, (b) BCT8 and (c) BCT30

Fig. 4 shows the presence of polarization versus electric field (P-E) hysteresis loops for all the samples at an applied electric field 7 kV/cm which confirms the ferroelectric nature for all the samples. The values obtained for coercive field (E_c), remanent polarization (P_r) and maximum polarization (P_{max}) from fig. 4 are tabulated in table 3. It is observed that an E_c and P_r increases drastically and becomes almost double while P_{max} decreases with increase in Ca substitution. Higher values of E_c in BCT30 sample is due to its larger grain size (5-6 μm) as can be seen in figure 3 (c), hence it requires higher electric field to align its electric dipole moments in the applied field

direction compared to BT and BCT8. Thus, such high coercive field of Ca doped BT implies that the sample becomes “hard” with respect to the electric field and can be used for (permanent ferroelectric memories) ferroelectric memory storage devices. While the higher values of P_r in case of BCT8 and BCT30 samples may be due to the low defect density, compositional homogeneity, etc [22]. The observed decrease in P_{max} values with increasing Ca content is due to decrease in the tetragonality with Ca content as observed from XRD and Raman analysis.



**Figure 5: (a) Variation of dielectric constant (ϵ') with temperature at 10 kHz
(b) Variation of $\ln(1/\epsilon' - 1/\epsilon'_{max})$ vs. $\ln(T - T_m)$ for all the samples at 10 kHz**

Figure 5 (a) shows the variation of dielectric constant (ϵ') with temperature at an applied frequency of 10 kHz for BT, BCT8 and BCT30. It is observed from figure 5(a) that the BT sample shows sharp transition while BCT8 and BCT30 samples shows broadening of transition which is the characteristic of diffused phase transition from tetragonal (ferroelectric phase) to cubic (paraelectric phase). The Curie temperature (T_c) i.e. transition temperature is found to be in the range of 120 $^{\circ}C$ to 140 $^{\circ}C$. Also, ϵ' increases for BCT8 and further decreases for BCT30, which is in well agreement with the reported values. The change in T_c for BCT8 is almost negligible compared to BT [12] while for BCT30 sample, T_c decreases which may be due to the structural distortion and some amount of Ca substituted at Ti

site in BaTiO₃. The general expression for diffused phase transition (DPT) is given by equation (2),

$$\frac{1}{\epsilon'} = \frac{1}{\epsilon'_{max}} + \frac{(T - T_m)^{\gamma}}{C} \quad (2)$$

where, ϵ' , ϵ'_{max} , T , T_m , γ , C are the real part of dielectric constant, maximum value of dielectric constant, temperature, temperature corresponding to ϵ'_{max} , diffusivity factor, Curie constant, respectively. To confirm the diffused phase transition behaviour, we have plotted $\ln(1/\epsilon' - 1/\epsilon'_{max})$ versus $\ln(T - T_m)$ graph. Figure 5(b) shows the variation of $\ln(1/\epsilon' - 1/\epsilon'_{max})$ versus $\ln(T - T_m)$ for BT, BCT8 and BCT30 samples and from its slope, the diffusivity factor γ is calculated. With Ca substitution, it is observed that the diffusivity factor γ increases from 1.09 for BT to 1.43 for BCT30, which indicates that the sharp phase transition is transformed into partial diffused phase transition with diffusivity factor greater than 1 [23]. The

observed diffused phase kind of behaviour may be due to the cation disorder i.e. composition fluctuations of the different polar micro regions where different ions try to occupy same

crystallographic position in ABO_3 perovskite which causes microscopic heterogeneity in the compounds and gives different local Curie points [24,25].

Conclusions

In summary, the ferroelectric BT, BCT8 and BCT30 were synthesized by solid state reaction method. All the synthesized samples exhibited tetragonal structure with space group $P4mm$ without any impurity phases as confirmed from XRD studies. However, the tetragonal structure gets distorted with Ca substitution in BT as confirmed from XRD and Raman spectra analysis. The grain size for BT and BCT8 samples almost remains same while it increases for BCT30 samples due to the higher sintering temperature as compared to BT and BCT8 samples. Presence of typical P-E hysteresis loop for all the samples confirm the ferroelectric nature. The higher values of coercive field for Ca substituted samples indicates that the material becomes “hard” and can be used for permanent ferroelectric memory. The negligible shift in Curie temperature and increase in dielectric constant for BCT8 sample were observed while for BCT30 both the Curie temperature and dielectric constant decreases which may be due to the substitution of some amount of Ti^{4+} by Ca^{2+} . Also, the sharp phase transition has been transformed into diffused phase transition with Ca substitution. Thus, one can tune the structural, ferroelectric and dielectric properties of BT with different amount of Ca substitutions depending upon its applications such as capacitor, switching devices, permanent ferroelectric memory.

Table 3: Coercive field (E_c), remanent polarization (P_r), maximum polarization (P_{max}), Curie temperature (T_c) and dielectric constant (ϵ') at Curie temperature and diffusivity factor (γ) for BT, BCT8 and BCT30

Composition	E_c (kV/cm)	P_r ($\mu C/cm^2$)	P_{max} ($\mu C/cm^2$)	T_c ($^{\circ}C$)	ϵ' at T_c	Diffusivity factor (γ)
BT	0.83	2.78	10.88	138	4496	1.09
BCT8	2.77	2.99	7.35	135	4960	1.27
BCT30	5.56	3.98	5.91	120	4040	1.43

Acknowledgement

Authors are thankful to Department of Science and Technology, New Delhi for providing financial assistance (Ref. SR/FTP/PS-040/2010) to carry out the research work. One of the author, Bhavna Chander Keswani is thankful to University Grants Commission (UGC) for providing Research fellowship under BSR scheme.

References:

1. K. Uchino, Ferroelectric Devices, Marcel Dekkar, New York (2006)
2. B. Jaffe, W. R. Cook and H. Jaffe, Piezoelectric Ceramics, Academic Press, London (1971)
3. T. R. Shrout and S. J. Zhang, J. Electroceram. 19, 111 (2007)
4. C. A. Randall, N. Kim, J. Kucera, W. Cao and T. R. Shrout, J. Am. Ceram. Soc. 3,677 (1998)
5. J. N. Gordan, A. Taylor and P. N. Bennet, J. Clin. Pharmacol. 53, 451 (2002)
6. P. K. Panda, J. Mater. Sci. 44,5049 (2009)
7. G. H. Haertling, J. Am. Ceram. Soc. 84, 797 (1999)
8. S. Yun, J. Shi and X. Qian, Mater. Chem. and Phys. 133, 487 (2012)
9. X. Cheng and M. Sen, Solid State Communications. 141, 587 (2007)
10. Z. Yu, C. Ang, R. Guo and A. S. Bhalla, J. Appl. Phys. 92, 1489 (2002)
11. S. K. Upadhyay, V. R. Reddy, P. Bag, R. Rawat, S. M. Gupta and A. Gupta, Appl. Phys. Lett. 105, 112907 (2014)
12. T. Mitsui and W. B. Weshphal, Phys. Rev. 124, 5 (1961)
13. V. S. Puli, D. K. Pradhan, B. C. Riggs, D. B. Chirsey and R. S. Katiyar, J. Alloys and Compounds. 584, 396 (2014)
14. C. X. Li, B. Yang, S. T. Zhang and W. W. Cao, Ceramics International. 39, 2967 (2013)
15. X. Wang, H. Yamada and C. N. Xu, Appl. Phys. Lett. 86, 022905 (2005)
16. P. S. R. Krishna, D. Pandey, V. S. Tiwari, R. Chakravarthy and B. A. Dasannacharya, Appl. Phys. Lett. 62, 231 (1993)
17. V. D. Araujo, F. V. Motta, A. P. A. Marques, C. A. Paskocimas, M. R. D. Bomio, E. Longo and J. A. Varela, J. Mater. Sci. 49, 2875 (2014)
18. I. Levin, V. Krayzman and J. C. Woicik, Appl. Phys. Lett. 102, 162906 (2013)
19. U. D. Venkateswaran, V. M. Naik and R. Naik, Phy. Rev. B. 58, 21 (1998)
20. C. H. Perry and D. B. Hall, Phys. Rev. Lett. 15, 17 (1965)
21. M. B. Smith, K. Page, T. Siegrist, P. L. Redmond, E. C. Walter, R. Seshadri, L. E. Brus and M. L. Steigerwald, J. Am. Chem. Soc. 130, 6955 (2008)
22. J. P. Praveen, K. Kumar, A. R. James, T. Karthik, S. Asthana and D. Das, Current Applied Physics. 14, 396 (2014)
23. V. S. Puli, D. K. Pradhan, B. C. Riggs, S. Ahireddy, R. S. Katiyar and D. B. Chirsey, J. Adv. Dielect. 4, 1450014 (2014)
24. I. Coondoo, N. Panwar, H. Amor, M. Alguero and A. L. Kholkin, J. Appl. Phys. 113, 214107 (2013)
25. P. Mishra, Sonia and P. Kumar, J. Alloys and Compounds. 545, 210 (2012)

Research Papers

Rapid synthesis of boron-doped diamond by using in-liquid plasma

^{1,2}Yusei Sakurai, ^{1,2,3}Yohei Harada ²Chiaki Terashima, ^{2,3}Hiroshi Uetsuka, ²Norihiro Suzuki, ^{1,2}Kazuya Nakata, ²Ken-ichi Katsumata, ^{1,2}Takeshi Kondo, ^{1,2}Makoto Yuasa, ²Akira Fujishima

¹Faculty of Science and Technology, Tokyo University of Science, Japan

²Photocatalysis International Research Center, Tokyo University of Science, Japan

³Asahi Diamond Industrial Co., Ltd.

1. Introduction

Boron-doped diamond (BDD) is expected for yields of sensing and electrolysis because of its high stability and wide potential window¹. Microwave plasma chemical vapor deposition (MPCVD) method has been used for synthesis of diamond. However, it is still unable to provide sufficient growth rates.

In-liquid plasma process is a new method for efficient synthesis in solution using radio frequency or microwave. Since a liquid has high molecular density, the submerged plasma generates active reaction field². Thus, this research aimed to high speed synthesis of BDD by in-liquid plasma.

2. Methods

Fig.1 shows MPCVD equipment with ethanol-methanol solution (1:9.v/v) at the reactor part. The boron source, B₂O₃, was dissolved in the solution with a B/C atomic ratio of 10000 ppm.

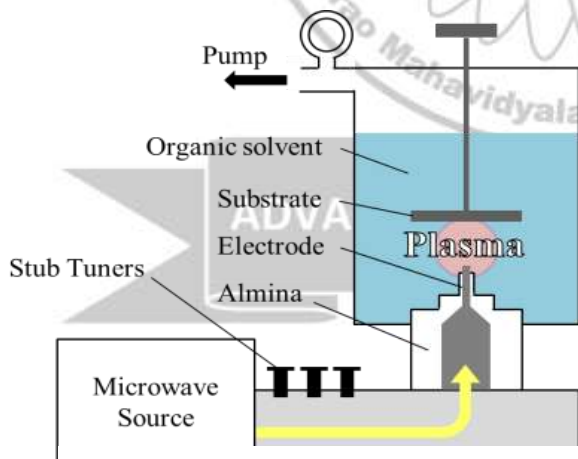


Fig. 1 In-liquid MPCVD equipment

Single crystalline Si is used as substrate. The microwave power was adjusted to 500 W. The pressure in the reactor was set to 60 kPa. The distance between Si substrate and electrode was set to 1.0 mm. Under these condition, it took 3 minutes for deposition.

3. Results and discussion

The surface was examined with a Laser Microscopy (Fig.2). It showed polycrystalline diamond structure and the growth rate was ca. 170 μm/h. Raman spectrums indicated a sharp peak at 1332 cm⁻¹ that was feature of diamond (Fig.3). The electrochemical behavior of BDD film in 0.1 M H₂SO₄ by using cyclic voltammetry showed a wide potential window. In-liquid plasma process enabled to synthesize a BDD film with high growth rate. From these results, it can be said that this technique is useful for synthesis of diamond electrode.

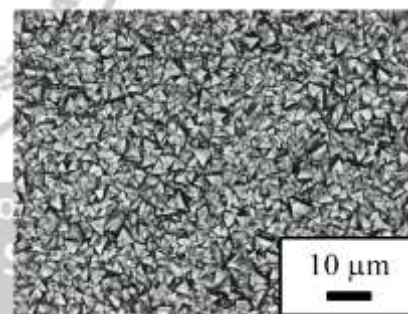


Fig.2 Laser microscopy image of diamond

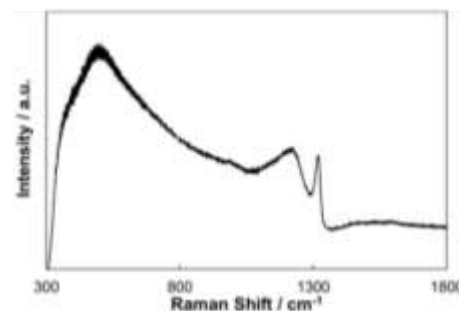


Fig. 3 Raman spectrum of diamond film

References

1. K. Nakata, T. Ozaki, C. Terashima, A. Fujishima, Y. Einaga, *Angew Chem. Int. Ed.*, 126 (2014) 890-893.
2. S. Nomura, *J. Plasma Fusion Res.*, vol.89, no. 4 (2013) 199-205.

Direct synthesis of ozone mist using boron-doped diamond electrode

Aiga Hara^{1,2}, Chiaki Terashima², Norihiro Suzuki², Kazuya Nakata²,
Ken-ichi Katsumata², Takeshi Kondo^{1,2}, Makoto Yuasa^{1,2}, Akira Fujishima²

¹ Faculty of Science and Technology, Tokyo University of Science

² Photocatalysis International Research Center, Tokyo University of Science

1. Introduction

Boron-doped diamond (BDD) electrode has excellent chemical and physical stability with high ozone generation efficiency. Also, ozone has attracted much attention in the fields of sterilization, deodorization and decolorization due to its high oxidation power and low persistence. Furthermore, in the case of ozone mist, it is reported that the function of sterilization and deodorization is faster than ozone, because it produces active species such as hydroxyl radicals.

In the previous report, ozone mist was synthesized using the zero-gap type electrolytic cell constructed by sandwiching a solid electrolyte membrane such as Nafion film between BDD mesh electrodes. However, this method using ultrasonic treatment was difficult to synthesize high concentration of ozone mist. This is because a lot of ozone is decomposed by ultrasonic treatment^{1,2}. Thus, to synthesise high concentration of ozone mist while ozone decomposition is prevented, this research aimed at directly synthesis of ozone mist from moisture in the air.

2. Experimental section

Fabrication of zero-gap cell. The BDD mesh electrode which was used as working electrode was obtained by the microwave plasma chemical vapor deposition (MPCVD) method. The raw material solution was prepared by adding boron oxide to a solution of acetone and methanol (Acetone : Methanol = 9 : 1, v/v. B/C, 10000 ppm). BDD was deposited on Ta mesh substrate by MPCVD method. As the counter electrode, Nb mesh with plated Pt was used. The zero-gap type cell was constructed by sandwiching the Nafion film between BDD mesh electrode and Pt mesh electrode.

Synthesis of ozone mist. BDD electrode was used as anode material and ozone mist was synthesized. The ozone mist was synthesized by constant current electrolysis and also its ozone generation was compared with Pt electrode.

3. Results and discussion

Evaluation of the BDD mesh electrode. As the

result of the surface observation with the laser microscope, several tens micrometers of polycrystalline diamond was confirmed. As the result of the Raman measurement, peaks related to diamond structure and boron doping were confirmed. Also, peak related to amorphous carbon as an impurity was not observed, so it was found that high purity BDD can be formed on Ta mesh substrate (Fig.2). Furthermore, as the result of the potential window measurement of the fabricated BDD mesh electrode in 0.5 M sulfuric acid solution, the characteristic wide potential

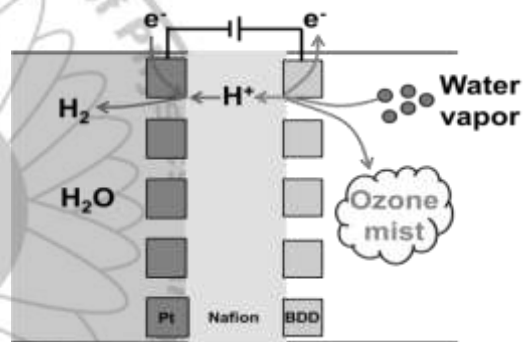


Fig.1 The cross section of this system

window of the diamond electrode was confirmed (from -0.8 to $+2.0$ V vs. Ag/AgCl). From the above results, it was suggested that the fabricated BDD mesh electrode is work as the diamond electrode.

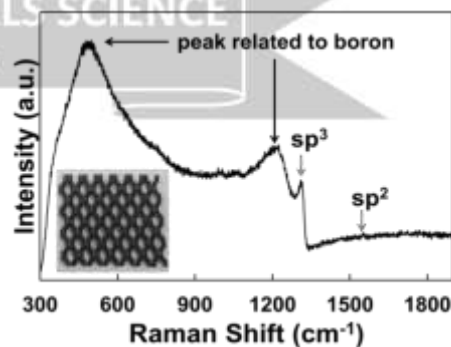


Fig.2 Raman Spectra

Quantitative of ozone mist. Figure 3 shows the quantitative amount of ozone mist related to any current value. It was found that the amount of ozone using BDD electrode is approximately 400 times higher than using Pt electrode at 50 mA. Therefore, it was confirmed that BDD is suitable

for ozone mist synthesis. Because BDD electrode can efficiently produce hydroxyl radical used for generating ozone as intermediate, it seems that this result was obtained³⁾. And, in the case of BDD electrode, the amount of ozone increases depending on current value, so it is easy to control the ozone mist concentration.

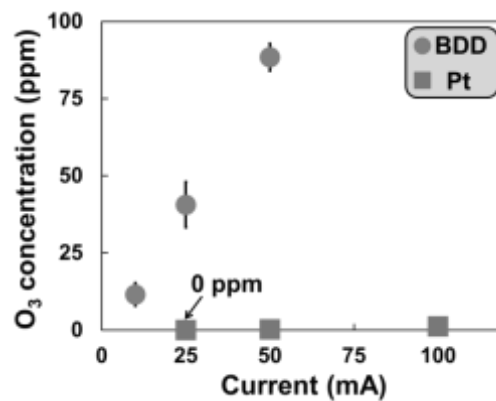


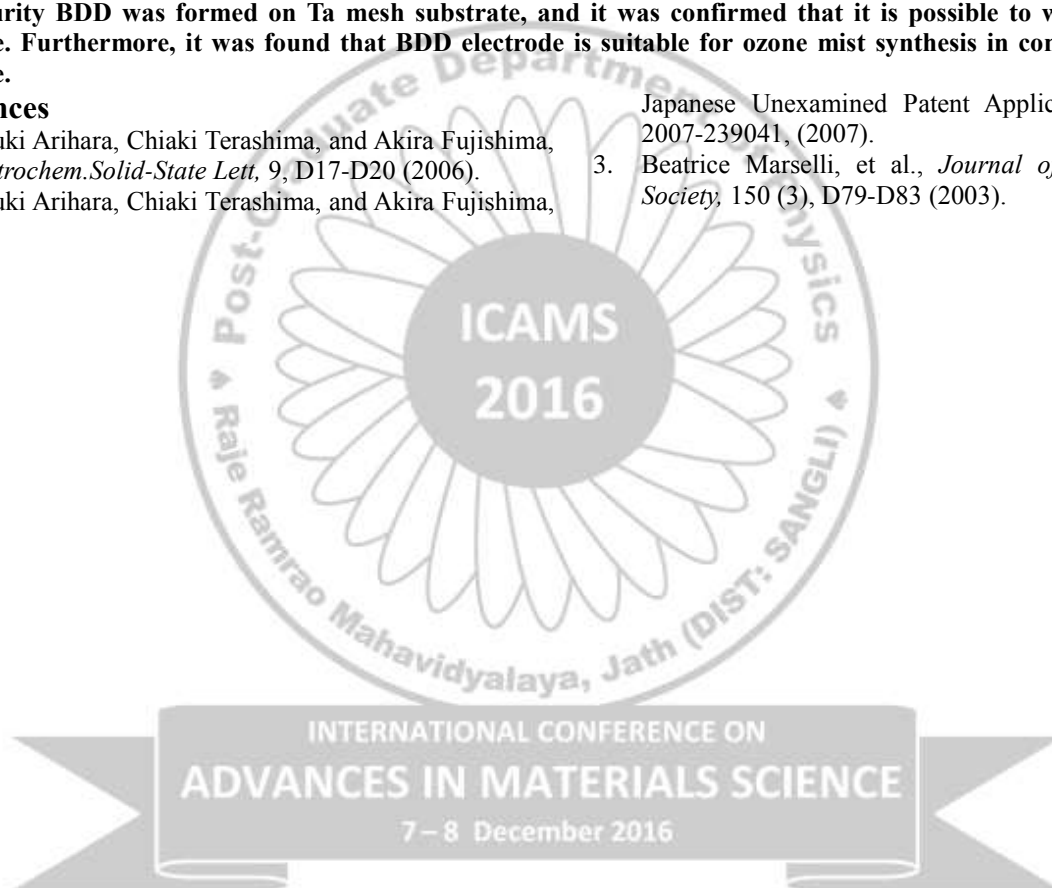
Fig.3 Generation amount of ozone (n=4)

4. Conclusion

High purity BDD was formed on Ta mesh substrate, and it was confirmed that it is possible to work as diamond electrode. Furthermore, it was found that BDD electrode is suitable for ozone mist synthesis in comparison with Pt electrode.

References

1. Kazuki Arihara, Chiaki Terashima, and Akira Fujishima, *Electrochem.Solid-State Lett*, 9, D17-D20 (2006).
2. Kazuki Arihara, Chiaki Terashima, and Akira Fujishima, Japanese Unexamined Patent Application Publication 2007-239041, (2007).
3. Beatrice Marselli, et al., *Journal of Electrochemical Society*, 150 (3), D79-D83 (2003).



Superhydrophobic Coatings developed using Modified Alumina Nanoparticles for Self-Cleaning Applications

Sanjay S. Latthe *

Self-cleaning Research Laboratory, Department of Physics, Raje Ramrao College, Jath 416 404, Maharashtra, India. E-mail ID: latthes@gmail.com

Abstract

Solid surfaces on which water drop achieves contact angle more than 150° and roll off at less than 10° are famously known as superhydrophobic surfaces. While rolling down on superhydrophobic surfaces, water drops effortlessly collect the dust particles performing self-cleaning effect. To prepare superhydrophobic coatings, the coating should be rough enough and its surface energy should be lowest as possible. The commercially available alumina nanoparticles were modified using sol-gel processing of (Heptadecafluoro-tetrahydrodecyl)trimethoxysilane (17FTMS). The modified hydrophobic alumina nanoparticles were spin coated on glass substrate and numbers of spin layers were thoroughly adjusted to achieve superhydrophobic wetting properties.

Keywords: Alumina nanoparticles, Lotus effect, Self-cleaning, Superhydrophobic, Contact angle.

1. Introduction

Self-cleaning superhydrophobic coatings are attracting tremendous attention of many researchers due to its potential industrial applications. The self-cleaning behavior observed in nature (Lotus leaves) can be mimicked, which can find potential industrial application for self-cleaning door and window glasses, windshields of automobiles, roadside mirrors, glassware, sport equipment's, solar panels, apparels and many [1-3]. Some of the problems in development of superhydrophobic coating are optical transparency and mechanical durability. The surface roughness is very important parameter in achieving highly water repellent (non-wettable) surface, however the high surface roughness can be get damaged by mechanical brushing and it also responsible for light scattering eventually and so it look opaque in nature [4]. The continuous efforts are devoted to overcome these problems since last two decades.

Abundant physical and chemical processes and deposition techniques are introduced to develop durable, transparent and self-cleaning superhydrophobic coatings [5]. Sol-gel processing of organosilanes is attracting much attention in preparation of superhydrophobic coatings. The hydrolysis and co-condensation of one or more organosilanes compounds in sol-gel system can alone achieve superhydrophobicity in a single step without post surface chemical modification. Yang Li et al [6] adopted layer-by-layer (LBL) coating procedure where porous silica layer was subsequently coated with hydrophobic silica nanoparticle and FAS layer to develop extremely transparent superhydrophobic coatings. P. N. Manoudis et al have dispersed hydrophilic silica nanoparticles in poly(methyl methacrylate) (PMMA) and poly(alkyl siloxane) and sprayed

their suspensions on various substrates to achieve superhydrophobic coatings [7]. Lin and researchers revealed a low-cost and large-scale way of producing superhydrophobic octadecylamine (ODA)-functionalized graphite oxide (GO) films. ODA was chemically grafted on GO sheets by the nucleophilic substitution reaction of amine groups with epoxy groups [8].

Herein, the sol-gel processed superhydrophobic silica-alumina coatings are prepared in a single-step for self-cleaning applications. Organosilane compound holding hydrophobic end group is used in sol-gel synthesis and by using alumina nanoparticles, rough microstructure on the coating surface was achieved to gain superhydrophobicity.

2. Experimental

2.1 Materials

Aluminum oxide nanoparticles (Al_2O_3 , dispersion of < 50 nm particle size) and (Heptadecafluoro-tetrahydrodecyl)trimethoxysilane (17FTMS) were purchased from Sigma Aldrich, USA. Methanol was bought from Loba Chemie Pvt. Ltd. Mumbai (India). Glass substrates were purchased from Polar Industrial Corporation Mumbai (India).

2.2 Preparation of Alumina Superhydrophobic Coating

A (Heptadecafluoro-tetrahydrodecyl) trimethoxysilane (17FTMS) (2 ml) was added dropwise in a mixture of deionized water (5 ml) and methanol (20 ml) under stirring and magnetically stirred for next 24 h. In 10 ml of above solution, the suspension of aluminum oxide nanoparticles (Al_2O_3 , dispersion of < 50 nm particle size) were ultrasonically dispersed in different volumes (1 to 5 v/v), separately. The coatings were prepared by spin coating with spin speed of 700 rpm for 15 sec, 1500 rpm for 45 sec, and 1000 rpm for 15 sec. The spin depositions

were made for 1, 2, and 3 layers. The superhydrophobic behavior of coating was observed after 3 layer spin deposition.

2.3 Characterization

The surface morphology and surface roughness of the coatings were obtained from field emission scanning electron microscope (FE-SEM) (Hitachi, S-4800) and laser microscopy (KEYENCE, VK-X200 series), respectively. The photographs of coatings were taken by Canon digital camera (G 15 series). The static and dynamic water contact angle values were obtained by using contact angle meter (Ramehart Instrument Co., USA). A water drop (~ 5 μ l) was gently dropped on the coating surface and the contact angle value was recorded after the drop acquired its equilibrium state. After placing water drop (~ 5 μ l), the coated substrate was slowly tilted (0.5°/sec) to obtain sliding angle values. All the wettability measurements were carried out on 5 different locations on the sample and average was taken as a final value.

3. Results and Discussion

3.1 Surface morphology and surface roughness

The coatings prepared with 4 v/v aluminum oxide nanoparticles in 20 ml of 17FTMS final solution revealed superhydrophobic wetting properties after spin deposition. These coatings are labelled as superhydrophobic alumina coating (SAC). **Fig. 1** depicts the scanning electron microscope images (~ 1 μ m magnification) of SAC samples prepared by 1, 2 and 3 spin layers. The SAC sample prepared with 1 spin layer shows less coverage of modified alumina particles on glass substrates resulting non-uniform coating, whereas the visible gaps found in single layer coating was partly filled by second layer coating and the coatings are nearly uniform. The rough and porous morphology was formed by modified alumina nanoparticles after three spin deposition layers which is favorable for superhydrophobicity. The morphology was changed from non-uniform to uniform after increasing the number of spin deposition layers. On contrary, the optical transparency was diminished with increasing spin deposition layers.



Fig. 1: FE-SEM images of SAC samples prepared by 1, 2 and 3 spin deposition layers.

The rms surface roughness was also enhanced due to increasing the layers of coating. **Fig. 2** shows the LASER microscopy images of SAC samples prepared by 1, 2 and 3 spin deposition layers. The rms surface roughness values for 1, 2 and 3 spin layer coated SAC samples are nearly 76, 154 and

232 nm, respectively. The LASER microscopy images are in good agreement with FE-SEM images where the surface coverage by coating material with increasing spin deposition layers is clearly observed.

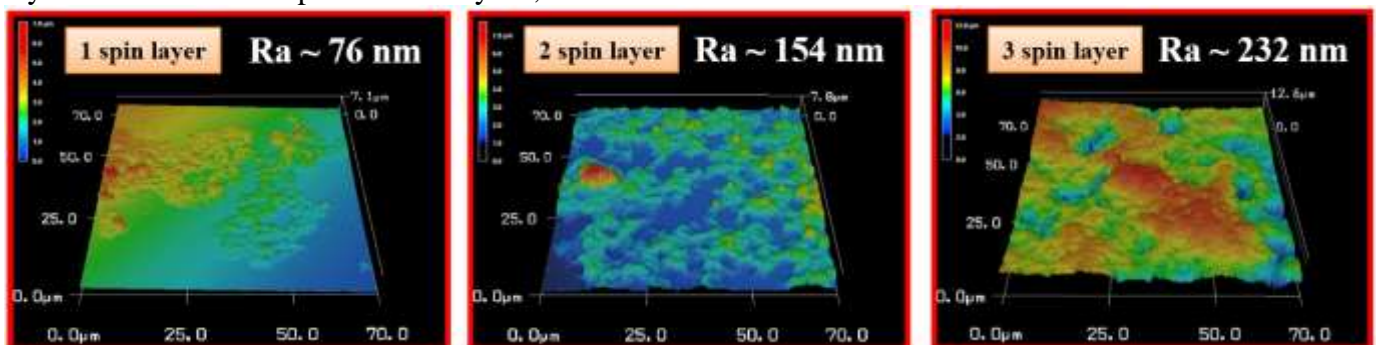


Fig. 2: LASER Microscopy images of SAC samples prepared by 1, 2 and 3 spin deposition layers.

3.2 Wetting Properties of Alumina Superhydrophobic Coating

The wetting properties of prepared alumina coatings were studied by water contact angle (WCA, static) and sliding angle (SA, dynamic) measurements. A 1 layer coated SAC samples showed a WCA of $\sim 95^\circ$ whereas the sliding angle was very high of $\sim 75^\circ$. This high wettability towards the coating surface is due to non-uniform surface morphology of the coating surface. The improved WCA $\sim 130^\circ$ and sliding angle $\sim 20^\circ$ was observed for 2 layer coated SAC samples. The superhydrophobicity with static and dynamic water contact angle of 155° and 9° , was observed for the coating prepared with 3 spin layers. **Fig. 3** shows the spherical transparent and blue coloured water drops on the 3 spin layer deposited SAC

sample. The spherical water drops prone to roll off eventually after small shaking the platform. The self-cleaning ability of the superhydrophobic coating was also confirmed. **Fig. 3** shows the self-cleaning characteristics of the superhydrophobic coating. The whole surface of 3 spin layer deposited SAC sample was fully covered by black carbon particles as a dust particles. The water drops were gently placed on this contaminated superhydrophobic coating and rolled to collect the dust particles. The spherical water drops quickly collected the dust particles and rolled off the surface by eventually cleaning the surface. This self-cleaning effect is appreciable in industry. Such self-cleaning coatings can find potential applications in day-to-day life.



Fig. 3: Spherical water drops, self-cleaning property and water jet impact test on 3 spin layer deposited SAC sample.

The mechanical durability of the coating was also checked by water jet impact test (**Fig. 3**). The water jet was produced using syringe and impacted on the superhydrophobic coating surface. The water jet was rebounded without sticking towards the surface or without damaging the surface. It confirms that the prepared alumina superhydrophobic coating is durable enough.

4. Conclusion

Alumina superhydrophobic coatings with rough and porous structure were prepared by spin coating technique. A water drop acquires a spherical shape on the coating surface exhibiting a water contact angle of $\sim 155^\circ$. A water drop immediately rolled off the coating surface at sliding angle of less than 9° . A $10 \mu\text{l}$ of water drop could individually collect the dirt particles along the way while rolling off. The superhydrophobicity of the coatings was stable under the impact of water jet. The coatings

maintained its excellent superhydrophobicity even after 6 months storage under normal conditions in air.

Acknowledgement

This work is financially supported by DST-INSPIRE Faculty Scheme, Department of Science and Technology (DST), Government of India. [DST/INSPIRE/04/2015/000281].

References

1. Q. Xie et al, Adv. Mater., 2004, 16 (4), 302-305.
2. [2] L. Zhang et al, Chem. Mater. 2007, 19, 948-953.
3. H. S. Lim et al, J. AM. CHEM. SOC. 2006, 128, 14458-14459.
4. J. Bravo et al, Langmuir 2007, 23, 7293-7298.
5. P. Ragesh et al, J. Mater. Chem. A, 2014, 2, 14773-14797
6. Yang Li et al, Chem. Commun., 2009, 2730-2732.
7. P. N. Manoudis et al, Langmuir, 2008, 24, 11225-11232.
8. Z. Lin et al, Langmuir 2010, 26(20), 16110 – 16114.

Influence of PVP concentrations on the microstructural characteristics of SrTiO₃ and BaTiO₃ nanoparticles: A comparative study

Uzma K.H. Bangi^{1*}, Hyung-Ho Park²

¹School of Physical Sciences, Solapur University, Solapur - Pune National Highway, Kegaon, Solapur- 413 255, Maharashtra, India

²Department of Material Science and Engineering, Yonsei University, Seoul 120-749, Republic of Korea

*Corresponding author, E-mail: uzma.phys@gmail.com

Abstract

Recently, the nanoparticles of perovskite family are of vast interest owing to their outstanding ferroelectric and thermoelectric properties. Particularly, strontium titanate (SrTiO₃) and barium titanate (BaTiO₃) nanoparticles have potential applications in the size dependent optoelectronic devices. The concentration of capping ligand used during synthesis has profound effect on the structure and surface morphology of the obtained nanoparticles, the present work is an outcome of such studies. The precipitation based synthesis of SrTiO₃ and BaTiO₃ nanoparticles was carried out using various concentrations of capping ligand namely polyvinylpyrrolidone (PVP) (typically from 0.001M to 0.008 M). And the influence of varying concentration of PVP on the structural and morphological characteristics of SrTiO₃ and BaTiO₃ were studied using the X-ray diffraction and Field emission scanning electron microscopy techniques respectively.

Keywords: PVP, SrTiO₃, BaTiO₃, XRD, FESEM

1. Introduction

Nanoparticles of inorganic high-k metal oxides like PbO, HfO₂, SrTiO₃, BaTiO₃, etc. are of current interest in size dependent optoelectronic devices such as complementary metal oxide semiconductors and field effect transistors [1]. Amongst these, strontium titanate (SrTiO₃) and barium titanate (BaTiO₃) are the promising materials having an exceptional property of very high dielectric constant (>300). SrTiO₃ and BaTiO₃ exist in different polymorphic forms, i.e. orthorhombic, tetragonal, and cubic etc. For the synthesis of nanoparticles, wet-chemistry techniques such as sol-gel [2], solvothermal [3] and precipitation [4] etc. are being used. Amongst all these techniques, precipitation is a simple and cost-effective technique involving the synthesis at low pressure. It was observed that the chemistry of capping ligand in particular their concentrations play a key role in controlling the materials characteristics. Therefore, in the present study, SrTiO₃ and BaTiO₃ nanoparticles were synthesized via a simple and cost-effective method of precipitation employing polyvinyl pyrrolidone (PVP) as capping ligand by varying its concentration from 0.001 to 0.008 M.

2. Experimental

For the synthesis of SrTiO₃ and BaTiO₃ nanoparticles, strontium nitrate, barium nitrate [99.9%] and potassium titanate oxalate [PTOX or K₂TiO(C₂O₄)₂, 99%] were used as starting materials while PVP (mol. wt. 40,000 g) as capping ligand. Deionised (DI) water and ethanol (EtOH) were used for precipitate formation and

washing purpose. The experimental procedure for the synthesis of SrTiO₃ and BaTiO₃ nanoparticles was followed as reported elsewhere [5, 6] and is presented in Fig. 1.

The products were cooled to R.T. and grinded in agate mortar for the characterisation purpose. The effects of varying concentrations of PVP (0.001–0.008 M) on the structural and morphological characteristics of SrTiO₃ and BaTiO₃ were studied. The structure of SrTiO₃ and BaTiO₃ were analysed using XRD (Ultima model, Rigaku, Japan) with Cu K α radiation of wavelength 1.541 Å at 2 θ values ranging from 20° to 80°. The morphological studies of the SrTiO₃ and BaTiO₃ samples were performed using field emission scanning electron microscopy (FESEM, JSM-600F, JEOL, Japan).

3. Results and discussion

The size and shape of nanoparticles can be controlled using capping ligand which forms a protective layer around the particles' surface during the growth process. Ligand consists of a head group and a tail group (alkyl chain). The head group anchors the surface of particle and tail group floats away from the surface in the dilute medium. The broad area of head and the long alkyl chain of tail of the ligand sterically affect the size of nanoparticles. Polyvinyl pyrrolidone (PVP) was used as capping ligand for the synthesis of SrTiO₃ and BaTiO₃ nanoparticles. The influence of varying concentrations of PVP (typically 0.001, 0.005, and 0.008 M) on the structure and surface

morphology of SrTiO₃ and BaTiO₃ particles was studied. SrTiO₃ and BaTiO₃ samples were prepared by keeping the concentrations of precursors fixed to 0.05 M and volume ratio of metal nitrate:PTOX:PVP to 1:1:0.05.

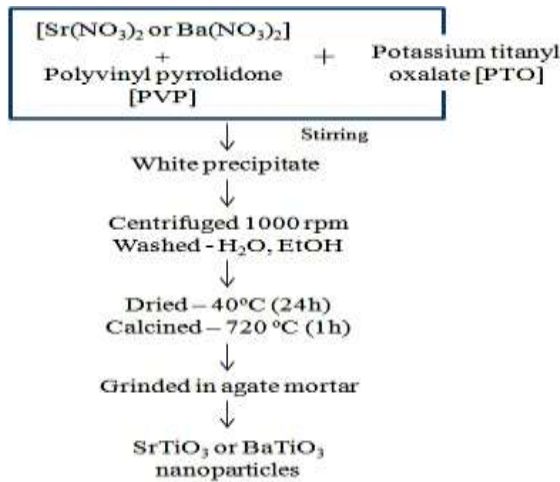


Fig. 1 Schematic flowchart for the synthesis

XRD diffractograms of the typical SrTiO₃ and BaTiO₃ samples prepared using PVP (0.005 M) are shown in fig. 2. From Fig. 2 it is obvious that SrTiO₃ sample has cubic crystal structure matching with the JCPDS data card number PDF#350734 while BaTiO₃ sample exhibit tetragonal crystal structure with the JCPDS data card number PDF#050626. The diffractograms of SrTiO₃ and BaTiO₃ exhibit sharper and stronger peak of (110) and (101) indicating phase orientation along <110> and <101> respectively. The average crystallite size, strain induced and dislocation density of these samples were determined using the formulae reported elsewhere [6]. Table 1 shows the average crystallite size, strain induced and dislocation density of the SrTiO₃ and BaTiO₃ samples prepared using PVP (0.005 M). From Table 1 it is clear that the average crystallite size determined for PVP capped SrTiO₃ sample is nearly 14 nm which is smaller than PVP capped BaTiO₃ (18 nm).

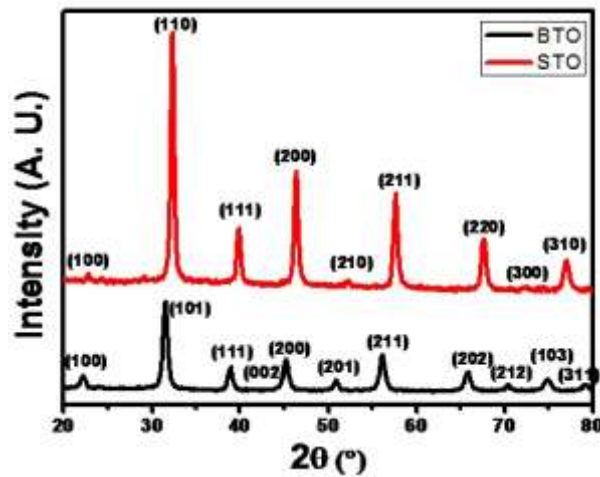


Fig. 2 XRD diffractograms of SrTiO₃ and BaTiO₃ samples synthesized using PVP (0.005M)

The morphological studies of SrTiO₃ and BaTiO₃ samples was carried out using FESEM as shown in figs. 3 & 4 respectively. As seen from figs. 3a & 4a, the FESEM images of pristine SrTiO₃ and BaTiO₃ samples exhibit the coalescence of particles with larger size and non-uniform shapes.

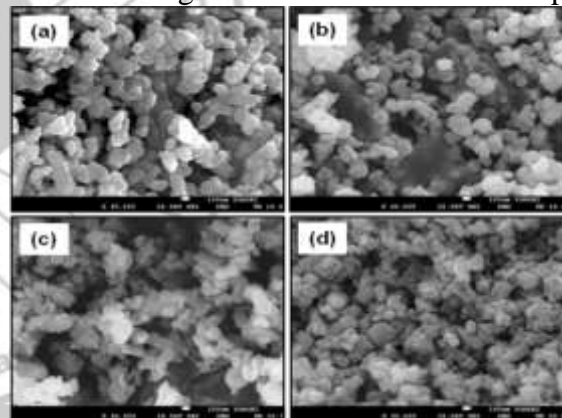


Fig. 3 FESEM images of SrTiO₃ samples with varying concentration of PVP (a) pristine (b) 0.001M, (c) 0.005M, (d) 0.008M

Table 1. Average crystallite size, strain and dislocation density of SrTiO₃ and BaTiO₃ samples synthesized using PVP (0.005M).

Sample identity	STO	BTO
Average crystallite size (nm)	13.43	17.33
Strain (ϵ)	2.69×10^{-3}	2.08×10^{-3}
Dislocation density (δ) (m^{-3})	5.54×10^{15}	3.33×10^{15}

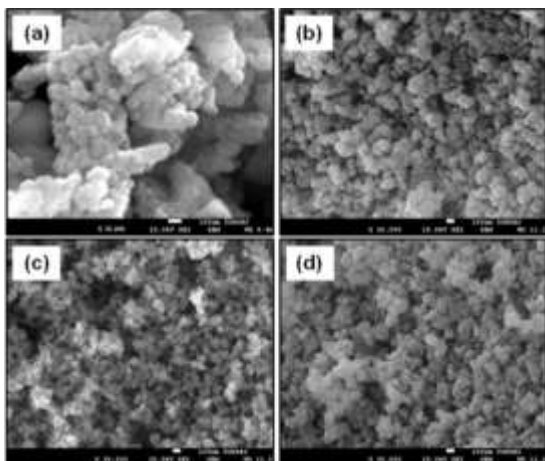


Fig. 4 FESEM images of BaTiO₃ samples with varying concentration of PVP (a) pristine (b) 0.001M, (c) 0.005M, (d) 0.008M

Further, it is seen that the grain size of the SrTiO₃ and BaTiO₃ samples reduced with increase in PVP concentration to 0.005 M (fig. 3c & 4c) which

increase further with the concentration of PVP to 0.008M (fig. 3d & 4d). The larger grain size of SrTiO₃ and BaTiO₃ samples at low concentration of PVP may be due to the incomplete capping of PVP to the surface of primary particles causing primary particles to permeate through the capping layer so as to deposit new atoms to the surface [7]. Moreover, at high concentration of PVP (>0.005 M) the presence of more ligand molecules form a double layer (with inverted polarity) around the surface of particle which attracts another particle causing agglomeration grains [8]. Thus 0.005M PVP solution leads to a smaller average SrTiO₃ and BaTiO₃ particle size by forming a size limiting layer around them reducing agglomeration.

Conclusions

The influence of varying concentrations of PVP on the structural and morphological characteristics of SrTiO₃ and BaTiO₃ was studied. SrTiO₃ and BaTiO₃ nanoparticles can be synthesised using cost-effective method of precipitation. SrTiO₃ and BaTiO₃ nanoparticles with average crystallite sizes of nearly 14 nm and 18 nm were synthesised as determined from the XRD. FESEM images revealed the decrease in particle size of SrTiO₃ and BaTiO₃ with increase in the PVP concentrations which further increased with PVP concentration.

Acknowledgments

This study was financially supported by the Department of Science and Technology – Science & Engineering Research Board (DST-SERB), New Delhi, India, through a major research project on ‘aerogels’ (no. SB/FTP/PS-030/2014). One of the authors, Uzma K. H. Bangi, is very grateful to the DST-SERB for Young Scientist Fellowship under fast-track scheme.

References

1. J. Robertson, Eur Phys J Appl Phys. 28(3) (2004) 265–291
2. G. A. Tompsett, W. C. Conner, K. S. Yngvesson, Chem. Phys. Chem. 7 (2006) 296-319
3. Y. Mao, S. Mao, Z.-G. Ye, Z. Xie, L. Zheng, Mater. Chem. & Phys. 124 (2010) 1232–1238
4. X. Chen, G. Wang, Y. Duan, S. Liu, J. Phys. D: Appl. Phys., 40 (2007) 1827-1830
5. U. K.H. Bangi, V. M. Prakshale, W. Han, H. H Park, N. N. Maldar, L. P. Deshmukh, Micro & Nano Letters, 2016, pp. 1-4, doi: 10.1049/mnl.2015.0531
6. U.K.H. Bangi, L. P. Deshmukh, H. H Park, N. N. Maldar, Proceedings of the 2015 2nd International Symposium on Physics and Technology of Sensors, 8-10th March, 2015, Pune, India, pp. 6-10, 978-1-4673-8018-8/15©2015 IEEE 6
7. T. Morris, T. Zubkov, Colloids Surf. A Physicochem. Eng. Aspects 443 (2014) 439–449
8. U.K.H. Bangi, W. Han, B. Yoo, H. H. Park, J. Nanopart. Res.15 (2013) 2070–2077

Supercapacitive performance of spray deposited Co_3O_4 thin film

U.J. Chavan¹, A.A. Yadav^{2*}

¹Thin Film Physics Laboratory, Department of Physics, Electronics and Photonics,

²Rajarshi Shahu Mahavidyalaya, (Autonomous) Latur, (M.S.) 413512 India

*Corresponding author email: aay_physics@yahoo.co.in

Abstract

Cobalt oxide thin films have been successfully deposited by spray pyrolysis at substrate temperature of 350°C. XRD study reveals formation of cubic Co_3O_4 . SEM shows porous structure with fine spherical grains. Maximum specific capacitance of 342 Fg^{-1} at scan rate of 10 mVs^{-1} has been observed.

Keywords: Co_3O_4 thin film, spray pyrolysis, super capacitor.

1. Introduction

The increasing demand of energy, depletion of fossil fuels, rise in global warming and environmental pollution suggests urgent need to find alternative sources for clean and efficient energy storage systems [1]. Electrochemical supercapacitors, secondary batteries and fuel cells are the main storage systems. Supercapacitor is the most promising energy storage device which fills the gap between secondary batteries and conventional capacitors in terms of energy and power density [2]. Carbon based materials; conducting polymers and transition metal oxides are widely studied materials for supercapacitor applications [3]. Nanostructured transition metal oxide thin films have their unique properties including electrical, optical, and electrochemical properties [4]. Amongst the different transition metal oxides, cobalt oxide is one of the most studied materials due to its low cost, low toxicity and environmental friendliness. It has many applications, such as solar selective absorber, pigment for glasses and ceramics, catalyst for oxygen evolution and oxygen reduction reaction, electrochromic material, sensors, electrochemical anodes in supercapacitors, negative electrodes in lithium-ion batteries [5-6].

Many methods have been employed to synthesize nanostructured cobalt oxide films [7-11] including R-F sputtering, electro deposition, SILAR, chemical vapor deposition, sol-gel process, chemical bath deposition and spray pyrolysis. Spray pyrolysis is simple, inexpensive, capability for preparing porous and nanostructure thin films and convenient for large area deposition [11]. In this report we discuss spray deposition of Co_3O_4 thin films for supercapacitor applications.

2. Experimental

The AR grade 0.05M cobaltous chloride ($\text{CoCl}_2 \cdot 6\text{H}_2\text{O}$) was used as precursor. Films are deposited with a typical spray pyrolysis system, using a glass spray nozzle of 0.5 mm diameter.

The substrate to nozzle distance was kept at 30cm. The films are prepared by spraying 30ml solution on preheated glass substrates at 350°C. Air was used as carrier gas. The spray rate employed was 3 mlmin^{-1} . Crystal structure of Co_3O_4 thin film is determined by Bruker D8 Advance X-ray diffractometer. Scanning electron microscopy technique is used to observe surface morphology. Supercapacitive performance is tested by cyclic voltammetry and electrochemical impedance spectroscopy.

3. Results and discussion

3.1 X-ray diffraction

Fig. 1 shows the XRD pattern of Co_3O_4 thin films spray deposited at 350°C. The peaks are observed at 19.3° , 31.5° , 37.1° , 45.1° , 59.7° and 65.3° representing the (111), (220), (311), (400), (511) and (440) reflections respectively. The matching of calculated and standard 'd' values confirms cubic phase of Co_3O_4 (JCPDS data card 76-1802). Film shows preferred (311) orientation. The lattice parameter was observed to be $a=b=c=8.016 \text{ \AA}$.

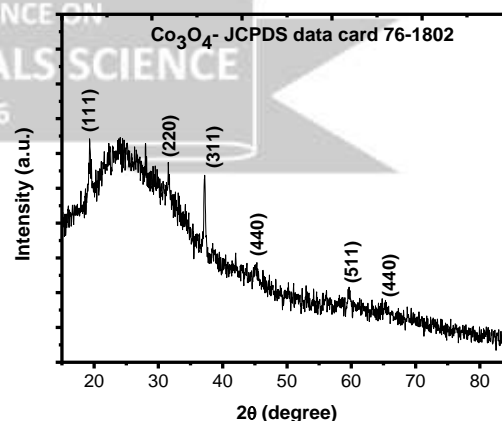


Fig. 1 XRD pattern of spray deposited Co_3O_4 thin film

3.2 Surface morphology

Fig. 2 shows the SEM images of Co_3O_4 thin films. The surface of cobalt oxide shows porous structure with fine spherical grains. The

agglomerated particles having small grain size less than 0.1 μm .

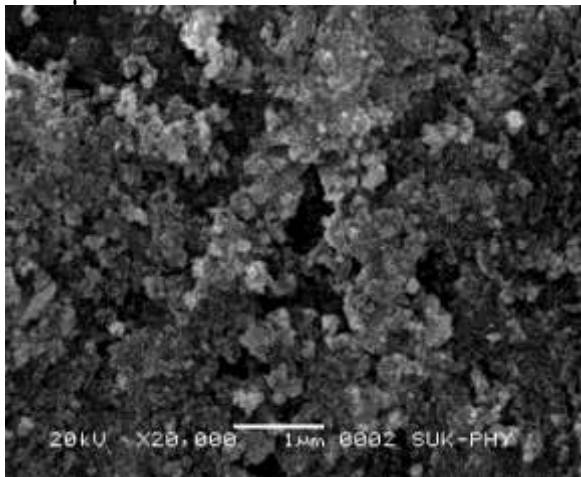


Fig. 2 SEM image of spray deposited Co₃O₄ thin film

3.3 Cyclic voltammetry

Supercapacitive performance of Co₃O₄ is studied with the help cyclic voltammetry (CV) technique in 2M aqueous KOH electrolyte. Fig. 3 shows the CV curves of Co₃O₄ electrode at different scan rates.

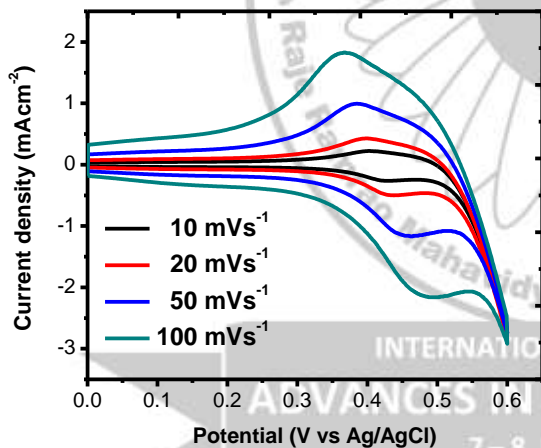


Fig.3 CV curves of spray deposited Co₃O₄ thin film at various scan rates

Specific capacitance (Cs) is calculated by using the relation;

$$C_s = \frac{1}{mv(V_a - V_b)} \int_{V_a}^{V_b} I dv \quad (1)$$

where 'I' is the average current in ampere, 'v' is the scan rate in mV/s, (V_a-V_b) is the high and low potential limits and m is the mass of active material dipped in electrolyte. It can be seen that all CV curves has same nature. Redox peaks are observed in both charging and discharging side. These peaks are shifted towards higher and lower

potentials for charging and discharging curves respectively as scan rate decreases from 100mVs⁻¹ to 10mVs⁻¹. Area under the curve increases as scan rate increases and specific capacitance decreases with increase in scan rate due to the presence of inner active sites, which cannot complete redox transition fully at higher scan rates. At lower scan rates the OH⁻ has more time to transfer, which means more charge can be stored resulting in high specific capacitance [12]. The maximum specific capacitance is found to be 342 Fg⁻¹ at 10mVs⁻¹ scan rate.

3.4 Electrochemical impedance spectroscopy

Fig. 4 shows Nyquist plot of Co₃O₄ electrode. The semicircle at high frequency region is associated with charge transfer resistance. First intercept of semicircle on real axis gives the electrolyte resistance. The straight line at low frequency region is attributed to diffusion resistance. Co₃O₄ electrode shows low electrolyte resistance 0.39 Ω and charge transfer resistance 13.95 Ωcm^{-2} . These result indicates that the cobalt oxide electrode provide easily access for intercalation and de-intercalation of charges.

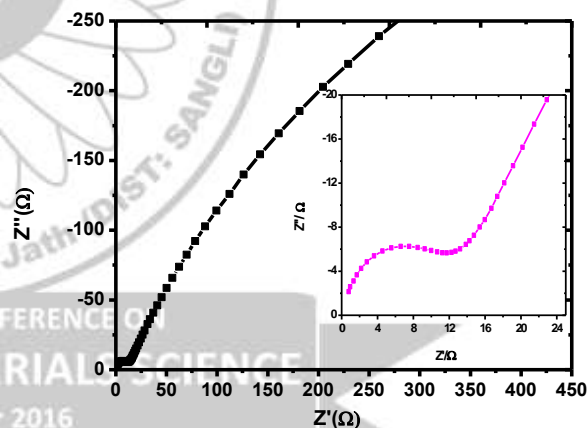


Fig. 4 Nyquist plot for Co₃O₄ thin films (Inset is the enlarged view of the plot)

Acknowledgements

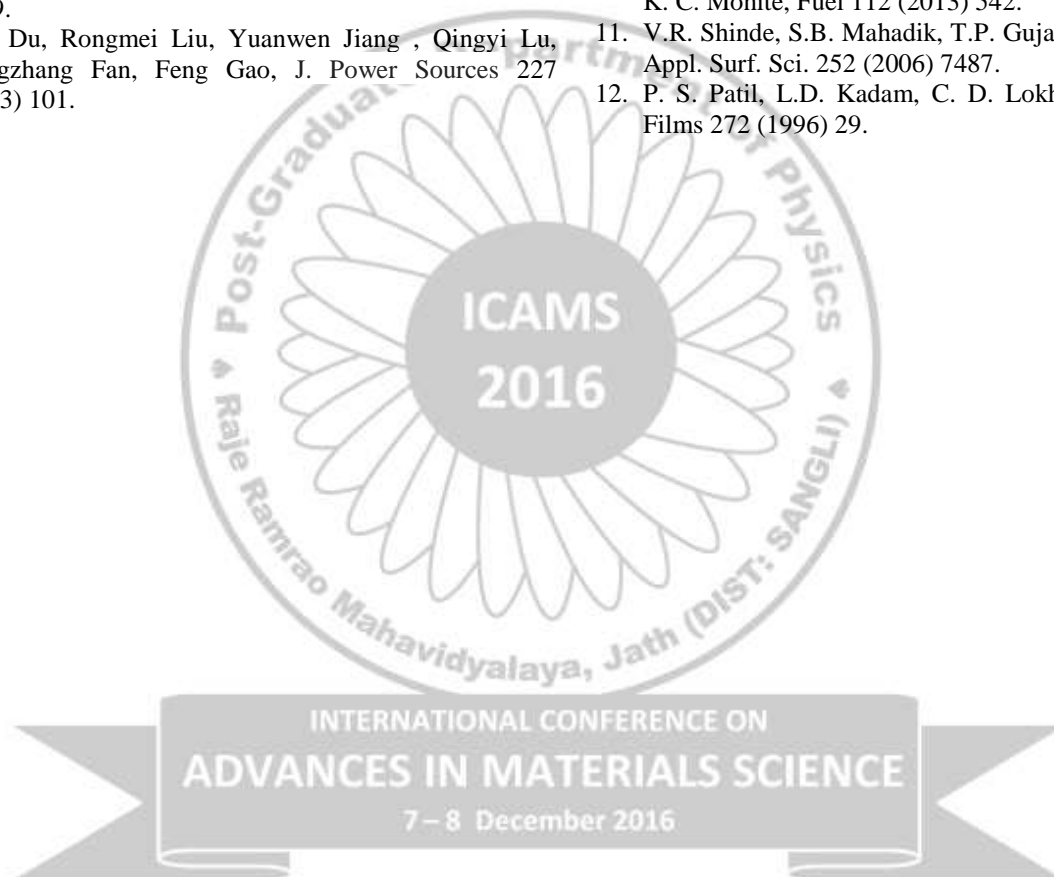
Dr. A. A. Yadav is grateful to the SERB, Department of Science and Technology, New Delhi, India for the financial assistance through the Project under SERC Fast Track Scheme for Young Scientist No. SB/FTP/PS-068/2013

4. Conclusions

Co₃O₄ thin films are successfully deposited by spray pyrolysis. The as deposited films are polycrystalline with cubic phase. Porous morphology has been observed from SEM. The maximum specific capacitance of 342 Fg⁻¹ has been observed at 10 mVs⁻¹.

References

1. Yufeng Zhao, Xuejiao Zhang, Jing He, Long Zhang, Meirong Xia, Faming Gao, *Electrochim. Acta* 174 (2015) 51.
2. L. Li, Y.Q. Zhang, X.Y. Liu, S.J. Shi, X.Y. Zhao, H. Zhang, X. Ge, G.F. Cai, C.D. Gu, X.L. Wang, J.P. Tu, *Electrochim. Acta* 116 (2014) 467.
3. Shen-Ming Chen¹, Rasu Ramachandran, Veerappan Mani¹, Ramiah Saraswathi, *Int. J. Electrochem. Sci.* 9 (2014) 4072.
4. H. Heli, H. Yadegari, *Electrochim. Acta* 55 (2010) 2139.
5. Wei Du, Rongmei Liu, Yuanwen Jiang, Qingyi Lu, Yongzhang Fan, Feng Gao, *J. Power Sources* 227 (2013) 101.
6. A. Louardi, A. Rmili, F. Ouachtari, A. Bouaoud, B. Elidrissi, H. Erguig, *J. Alloys Comp.* 509 (2011) 9183.
7. H.K. Kim, T.Y. Seong, J.H. Lim, W.I. Cho, Y.S. Yoon, *J. Power Sources* 102 (2001) 167.
8. S.G. Kandalkar, D.S. Dhawale, C.K. Kim, C.D. Lokhande, *Synth. Met.* 160 (2010) 1299.
9. C.U. Mordi, M.A. Eleruja, B.A. Taleatu, G.O. Egharevba, A.V. Adedeji, *J. Mater. Sci. Technol.* 25 (2009) 85.
10. P. N. Shelke, Y. B. Kholam, R. R. Hawaldar, S. D. Gunjal, R. R. Udawant, M. T. Sarode, M. G. Takwale, K. C. Mohite, *Fuel* 112 (2013) 542.
11. V.R. Shinde, S.B. Mahadik, T.P. Gujar, C.D. Lokhande, *Appl. Surf. Sci.* 252 (2006) 7487.
12. P. S. Patil, L.D. Kadam, C. D. Lokhande, *Thin Solid Films* 272 (1996) 29.



Preparation, optical and structural properties of ZnO thin films by SILAR method

S. G. Deshmukh^{a,*}, A. M. More^b

^aDepartment of Engineering Physics, SKN Sinhgad College of Engineering, Korti, Pandharpur-413304, Maharashtra, India.

^bDepartment of Physics, K. N. Bhise Arts, Commerce College, Kurduwadi, 413208, Maharashtra, India.* Corresponding author: samseeraj2009@gmail.com

Abstract

In this paper, we explore the preparation of nanocrystalline zinc oxide (ZnO) thin film by successive ionic layer adsorption and reaction (SILAR) method. The optical absorption studies revealed that the ZnO exhibit the optical band gap of 3.43 eV. The structural properties studied using X-ray diffraction showed that the prepared ZnO thin film exhibit hexagonal wurtzite structure with strong c-axis orientation. The crystallite size for ZnO was found to be 29 nm along (002) plane.

Keywords: ZnO, SILAR, Optical, XRD

1. Introduction

Semiconductor thin films are always essential in material science due to their excellent optical and electrical properties, which are useful in optoelectronic devices, photovoltaic and sensor applications [1]. Zinc oxide (ZnO) is one of the versatile and technologically important semiconducting material because of its typical properties such as transparency in the visible region, direct band gap (3.37 eV), abundance in nature, etc. [2]. ZnO thin films have been deposited by different methods such as chemical vapor deposition [3], hydrothermal method [4], spray pyrolysis [5] chemical bath deposition [6], successive ionic layer adsorption and reaction (SILAR) [7], sol-gel [8], electro-deposition [9] etc. Among all these various techniques for the deposition of ZnO, SILAR was successfully employed to obtain ZnO thin films due to its low cost, large area deposition and simplicity. However, M. Ristov [10] reported the first report on the preparation of ZnO film by SILAR in 1987. In this paper, we report our results of ZnO thin film deposited on a glass substrate by SILAR method and their characterization, making special importance on the optical and structural properties of the film.

2. Experimental

All the chemicals used for the preparation of ZnO were analytical grade (AR). ZnO thin films were grown on the glass substrate by alternatively dipping into Zn²⁺ source kept at room temperature and hot distilled water maintained at 60 °C. Prior to the deposition, glass substrates were cleaned with liquid soap, chromic acid followed by a distilled water rinse and ultrasonic cleaning with distilled water followed by acetone vapor. The 0.1M ZnCl₂ solution was used as a source of Zn ions and to make it alkaline, aqueous

ammonia solution was added with constant stirring. To deposit ZnO, one SILAR cycle involves the three steps: (1) immersing the glass substrate in the alkaline zinc chloride solution for 10 sec. so as to get zinc complex [Zn(NH₃)₄]²⁺ adsorbed on the substrate; (2) immersing immediately the withdrawn substrates in the hot water (60 °C) for 10 sec. to form ZnO layer; (3) rinsing the substrate in a distilled water for 10 sec. to remove loosely bounded ZnO particles. Such 40 immersions yield a uniform, white and well-adherent ZnO thin film.

The ZnO thin film thickness measurement was made by a weight-difference method in which area, mass and density of the material were considered. The optical absorption and transmission spectra was investigated within the wavelength range 350-650 nm using a Varian Carry 50 UV-VIS spectrophotometer (Varian, Switzerland) equipped with a thermostated cell compartment at room temperature. For the study of structural property of ZnO thin film, X-ray diffraction (XRD) pattern was obtained from Bruker axe D8 Advance diffractometer with CuK_α ($\lambda = 0.15406$ nm) target.

3. Results and discussion

3.1 Film thickness

The thickness of the ZnO thin film was measured by using a weight-difference method. i.e. the relation $t = m/(\rho \times A)$, where 'm' is the mass of the ZnO deposited on the substrate in 'g', 'A' is the surface area of the film in cm² and ρ is the density of the ZnO. For bulk ZnO, $\rho = 5670$ kg/m³ [11]. The thickness of the ZnO thin film was found to be 514 nm.

3.2 Optical studies

The variation of absorbance (αt) and transmission (T) with wavelength (λ) in the range 350-650 nm of ZnO thin film is shown in Fig.1. From the Fig.1, the absorbance at the higher wavelengths in the visible region is low, which is the characteristics of ZnO. In the transmission graph, it can be seen that there is a high transmission region with a sharply defined absorption edge at 361nm. The energy band gap of ZnO can be determined by using the equation, $E_g = 1240/\lambda$ and it is found to be 3.43 eV. The assessed band gap value is in good agreement with the literature [7].

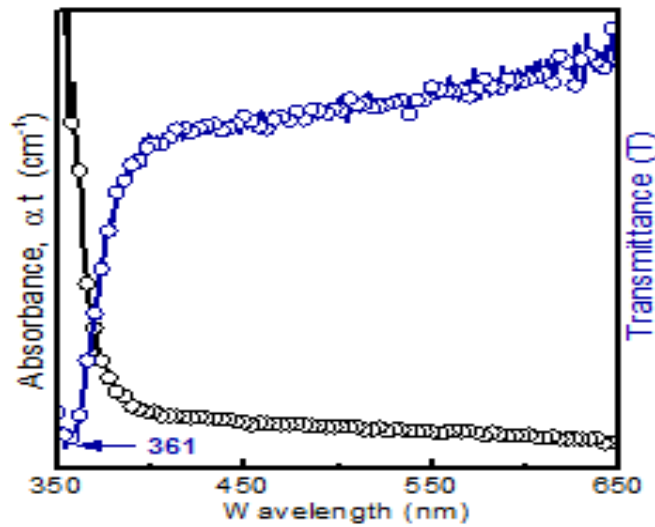


Fig.1. Variation of absorbance (αt) and transmission (T) with wavelength (nm) of ZnO thin film

3.3 Structural studies

Figure 2 shows the XRD profile of the ZnO thin film. The XRD profile of ZnO thin film indicates diffraction peaks of (100), (002), (101), (102), (110), (103) and (112) planes at angles 31.80° , 34.48° , 36.28° , 47.63° , 56.71° , 62.86° and 67.94° respectively of hexagonal structure of ZnO. These peaks are in good agreement with the JCPDF card number 79-2205 with lattice constant $a=3.250 \text{ \AA}$ and $c=5.207 \text{ \AA}$. The ZnO thin film is preferentially oriented with the c-axis perpendicular to the plane of the glass substrate resulting in relatively high intensity for (002)

reflection.

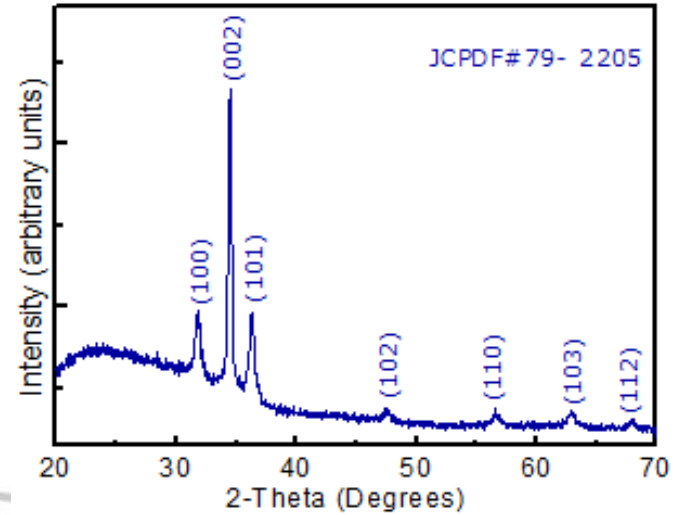


Fig. 2 X-ray diffraction profile of the ZnO thin film

The crystallite size was determined by using the Debye-Scherrer's formula, $D = 0.9\lambda/\beta \cdot \cos\theta$. [7], in which D is the crystallite size, λ is the X-ray wavelength used ($\lambda=0.15406 \text{ nm}$), β is the FWHM in radian and θ is Bragg's angle. The crystallite size was found to be 18.31, 29.00 and 18.63 nm for (100), (002) and (101) peak respectively. For the more information on the amount of defects in the film, the dislocation density (δ) and micro strain (ϵ) was calculated by using formula, $\delta=1/D^2$ [12], where D is the crystallite size and $\epsilon = \beta \cos\theta/4$ [13] respectively. The structural parameters such as observed 'd' values, FWHM (β), crystallite size (D), dislocation density (δ) and micro strain (ϵ) for ZnO thin film was summarized in Table 1.

Table 1: Summary of standard and observed 'd' values, FWHM (β), crystallite size (D), dislocation density (δ) and micro strain (ϵ) of ZnO thin film for (100), (002) and (101).

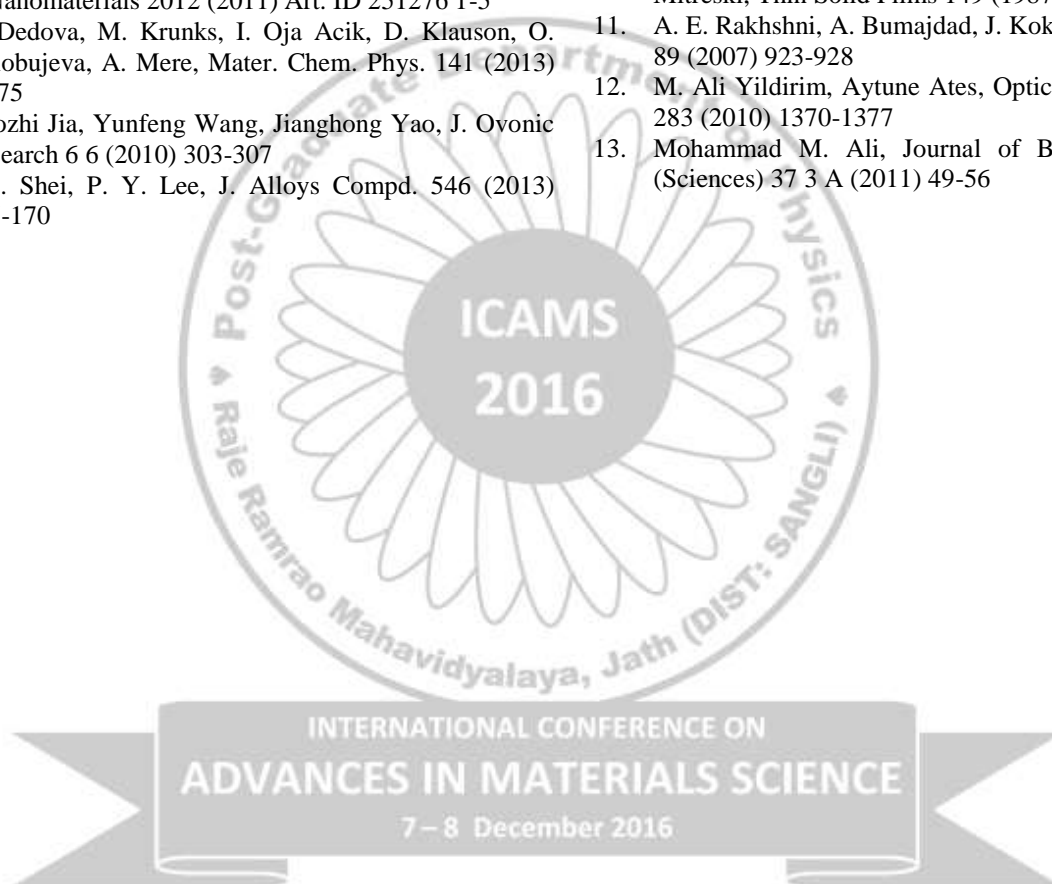
Parameter → Planes ↓	Standard 'd' (Å)	Observed 'd' (Å)	FWHM M (β)	D (nm)	δ in (nm) ⁻² (x10 ⁻³)	ϵ (x10 ⁻³)
(100)	2.8146	2.8131	0.4512	18.31	2.981	1.893
(002)	2.6035	2.6004	0.2869	29.00	1.189	1.195
(101)	2.4760	2.4754	0.4489	18.63	2.881	1.861

4. Conclusion

In this paper, we presented the preparation of ZnO thin film by successive ionic layer adsorption and reaction method. The band gap of obtained ZnO thin film was found to be 3.43 eV. The XRD shows the formation of a polycrystalline ZnO thin film with hexagonal phase. The deposited ZnO thin film exhibits strong c-axis orientation. The work will continue to increase the number of SILAR cycles.

References

1. R. K. Gupta, K. Ghosh, P. K. Kahol, Physica E 41 (2009) 617-620
2. A. E. Ajuba, S. C. Ezugwu, P. U. Asogwa, F. I. Ezema, Chalcogenide Lett. 7 10 (2010) 573-579
3. Ning Zhang, Ran Yi, Rongrong Shi, Guanhua Gao, Gen Chen, Xiaohe Liu, Materials Lett. 63 (2009) 496-499
4. Zhiwei Dong, Bing Han, Shixiong Qian, Deying Chen, J. Nanomaterials 2012 (2011) Art. ID 251276 1-5
5. T. Dedova, M. Krunks, I. Oja Acik, D. Klauson, O. Volobujeva, A. Mere, Mater. Chem. Phys. 141 (2013) 69-75
6. Guozhi Jia, Yunfeng Wang, Jianghong Yao, J. Ovonic Research 6 6 (2010) 303-307
7. S.C. Shei, P. Y. Lee, J. Alloys Compd. 546 (2013) 165-170
8. J. N. Hasnidawani, H. N. Azlina, H. Norita, N. N. Bonnia, S. Ratim, E. S. Ali, Procedia Chemistry 19 (2016) 211-216
9. Fabien Tsin, Amelie Venerosy, Julien Vidal, Stephane Collin, Johnny Clatot, Laurent Lombez, Myriam Paire, Stephan Borensztajn, Cedric Broussillous, Pierre Philippe Grand, Salvador Jaime, Daniel Lincot, Jean Rousset, Scientific reports 5 (2015) 8961
10. M. Ristov, Gj. Sinadinovski, I. Grozdanov, M. Mitreski, Thin Solid Films 149 (1987) 65-71
11. A. E. Rakhshni, A. Bumajdad, J. Kokaj, Appl. Phys. A 89 (2007) 923-928
12. M. Ali Yildirim, Aytune Ates, Optics communications 283 (2010) 1370-1377
13. Mohammad M. Ali, Journal of Basrah Researches (Sciences) 37 3 A (2011) 49-56



Diversity of Fleshy Mushroom in Dry Deciduous Forest in Sangli District, Maharashtra (India)

R. R. Tembhurne¹, S. P. Nanir², R. G. Pawar³

^{1,3}Sangola College, Sangola, Solapur (MS) 413307

²Former Director Govt. Institute of Science, Aurangabad (MS) 431004

Abstract

During the floristic study of the mushroom of this region author come across a number of mushroom species. In this study five species of mushroom are being discussed. 1. *Coprinus radians* (Desm.: Fr.) Fr., 2. *Morchella esculenta* Fr., 3. *Tricholoma sejunctum* Michel Kuo, 4. *Tricholoma sulphureum* (Bull. ex Fr.) P.Kumm. and 5. *Ganoderma tsugae* Murrill are being discussed with different five genus and species. All the different genus and species are being reported for the first time from this region.

Key words: Mushroom.

1. Introduction

The soil is one of the most important and interesting factor and is the most characteristics feature of terrestrial environment in which study of soil increase knowledge and helpful in practice of Agriculture, Horticulture and Forestry. The soil is the earthy material in which plants grow. The science deal with study soil is called as soil science. The soil is thin covering over the land consisting of mixture of minerals, organic materials, living organisms, air and water that together support the growth of plant life. Soil is the mixture weathered rock material and organic detritus both of which are formed through the physical, chemical and biological processes occurring slowly and slowly for a long periods at earth surface.

On the soil consists number of microorganisms like bacteria, viruses, fungus, protozoa and algae nutrients released in detritus are decomposed by various soil microbes like bacteria, algae, fungi and protozoa etc. bound in or on soil particles and taken back into plants through their root system. Soil (mud) also main source of nutrients for all aquatic plants. In addition soil is the means of support for all terrestrial organisms. Fungi plays very important role in decay and decomposition of plants and animal particles and also decomposed dead bodies of plants, animals and their waste.

Our paper focuses on the macromycetes fungi. This large group includes a majority of the species of the class basidiomycetes. Macromycetes constitute a large part of Sangali fungal reserve and are important components of its natural ecosystem. They create a secondary product beneficial to both animals and people in the form of fruiting bodies the yields of which the forests may reach over a ton of fresh weight per hectare. Macromycetes or mushrooms

tremendously valuable food products. Mushroom is technically confined to members of a fungi with gills of thousands of species of mushrooms know throughout the world. A few species produce death or serious illness when eaten.

The number of poisonous fungus species is probably more than 200 many mushrooms formerly considered doubtful or poisonous have been found to be edible. Fungal species are especially important components of biodiversity in tropical forest. Mushrooms are unique they are neither animal nor plant. Some people consider them plants for various reasons but they differ from plants in plants in that they lack the green chlorophyll that plants use to manufacture their own food and energy for this reason they are placed in a kingdom of their own the kingdom of fungi. The above described mushrooms are called saprophytic fungi due to their feeding habits.

Fungi are beneficial organisms we have derived number of useful antibiotics from them, including the wonder drugs penicillin. Fungi are play important role in industrial fermentation they contains various types of enzymes, vitamins, folic acid and vitamin B-12 absents in other foods are present in mushrooms. Due to low starch /sugar content mushrooms are ideal food for diabetic patient. Fat content of mushroom is rich in linoleic acid an essential fatty acid since they do not produce cholesterol there are good for heart patients. Due to their alkaline ash high potassium, sodium ratio and high fiber content mushroom are ideal food for those sufferings.

Organic acid fungi are cause pathogen and fungi perform great role in medicine as a source antibiotic. This paper introduced from Sangli district of three different regions that have been grown naturally on various types of natural biological media. Terrestrial mushroom are included. Many workers reported fungi from

decaying log, humus, dung, rhizosphere (Alexopoulos and Mims 1979, Alexopoulos 1962, Lincoff G. and Mitchel D.H. 1977, Lincoff Garry H. 1981, Ainsworth G.G., Sparrow F.K. and Sussman 1973, Miller O.K. 1975, 1977, Smith A.H. 1947, 1968, 1971, 1973, 1979, Snail 1970, 1971 Peter Jordan 1995, 1996 and 2000, Augusto Rinaldi Vassali Tyndalo 1985, Jacob E. Lange and Morten Lange 1961).

2. Material and Method:

All the samples were collected from different areas of Sangli district. The three regions were taken into consideration. These were Sagareshwar from Kadegaon taluka, Vita ghat from Vita taluka and Sukarachri from Atapadi taluka. From each three region sample were collected from different localities. Total 48 fleshy mushroom samples were collected.

All the fleshy mushroom samples were grown on natural media. The source of natural media on which fleshy mushrooms grown are humus, deadwood debris, decaying logs, wood decomposing fungi, dung, dying tree roots, roots of living plants, exterior and interior humus contain soil, lawn and garden, health forest and landscape, dead plant material, living plant material, bark of trees, living and non-living host of plants biomass, topsoil.

The entire fleshy mushroom collected from wild area of Vita, Sagareshwar and Sukarachari during month of September 2007 from the different localities and material deposited in the formalin and photographed it, listed it according to index of preservation and studied. Identification of all mushrooms is carried out with the help of movable suiting, stopper photographs, preserve material and following mushrooms to taking a reference of Simon and Schusters Guide to mushroom by Giovanni Pacioni, U.S. editor: Gary Lincoff., The mushroom guide and identifier by Peter Jordan, Augusto Rinaldi, Vassili Tyndalo-The complete book of mushrooms, Mushroom of the great lakes region by Verne Ovid Graham, Collins Guide to mushrooms and Toadstools by Morten Lange and F. Bayard Hora. This is the important method used for the identification of fleshy mushrooms.

3. Result And Discussions:

3.1. *Coprinus radians* (Desm.: Fr.) Fr.

Collection Examined: RRT/111, Sept.-2007, Vita, Dist.-Sangli. On moist soil.

Distribution: India: M. S. (Tem, 2007).

The etymology from the Latin radiating because of the mycelium at the base of stipe; Description cap 2-3.5 cm, gray to blackish brownish white in color, ovate, campanulate finally expanded with small mica-like scale, granular at the centre, sulcate, straight line arises from on upper surface of the cap, mouth of the cap open below side of the cap it is just cup like, stipe arise at the top of the portion of the inside of the cap just back region of the cap and mouth of the cap is lower side, inner portion of the cap is white, outer portion of the cap gray with arise lines; Stipe white, fleshy, smooth, fibrous, solid, near about 2-5 X 0.3-0.9 cm, broad at the base, narrow at the apex which arise from the soil; Flesh thin ochre; Odor and flavor negligible; Spores blackish, fusiform, elliptical, smooth 8-9 X 3-4 microns; Edibility not edible; Habitat on moist soil; Season rainy; Note this is easily identifiable lignicolous species even with carpophores, because of the bright orange brown white mycelium at the base of fruiting body.

3.2. *Morchella esculenta* Fr.

Collection Examined: RRT/112, Sept.-2007, Vita, Dist.-Sangli, on soil of plant debris.

Distribution: India: M. S. (Tem, 2007).

Morchella esculenta is also known as synonym *Morchella rotunda*, the common name of this species is Morel, etymology from Latin 'edible'; Corpophore near about 11-21 cm high or more, head normally rounded, wavy, curly hairs like gills arise from the apex of stipe, smooth, sometimes conical ochreous yellow, brown in colour with large alveoli, irregularly rounded, slightly venose, separated by sterile paler rib, hollow; stipe white, long, fibrous, smooth, hollow, strong, pale barely furfuraceous, enlarge and sulcate at the base, near about 6-15 x 1.2-2 cm, sometimes up to 4.5 cm at the base; flesh thick, tender white. Strong mushroomy odor, sweetish flavor; spore white, elliptical, smooth, 19-22.3 x 11.5-12.3 microns; edibility excellent also good for drying; habitat of this species on soil of plant debris, sandy or clayey sandy ground, in open places especially near tulip polar, ash and dead elm and in and old apple orchards; season spring, rainy; particular note of this species is variable in shape, size and color.

3.3. *Tricholoma sejunctum* Michel Kuo

Collection Examined: RRT/113, Sept.-2007, Vita, Dist.-Sangli. On moist soil of plant debris.

Distribution: India: M. S. (Tem, 2007).

This species also known as earth colored; cap white, sometimes grayish or brownish, depressed at the apex, smooth, campanulate or conical, fairly umbonate, often cracked, covered with small silken scales, cuticle detachable, tough, whitish then pale ash colored, fairly distant, long, large, equal, worn near stipe, fragile, margin denticulate; stipe long, white, smooth, packed, cylindrical, solid then subfistulose, fragile whitish shade with pale ash gray, grayish veil fairly conspicuous quite long lasting, near about 0.7-1 cm or 0.7-1 cm. Flesh grayish white, thin, fragile, mild sweetish flavor, somewhat bitter when mature or old; spore white, elliptical, smooth, 5.3-8 x 4.5-5 microns; very good edibility when young particularly; on moist soil of plant debris, groups, almost tuftlike or in rings in woods especially beneath conifers, season is rainy, summer and early winter.

3.4. *Tricholoma sulphureum* (Bull. ex Fr.) P.Kumm.

Collection Examined: RRT /114, Sept.–2007, Vita, Dist.-Sangli. On moist soil.

Distribution : India : M. S. (Tem. 2007).

In latin this species is called as sulfur colored; the cap sulfur yellow color, depressed at apex, white, often brownish at the centre, convex, flat, silky, glabrous at the apex, involute, near about 2.9-9 cm; Gills sulfur yellow, quite distant, many are small and large in shape, smooth, thick, lobed, fleshy, worn near the stipe; Stipe long, cylindrical, white at the below, ring like appearance, solid, sulfur yellow color, enlarge towards the base, striate lengthwise, fibrous, fleshy; Spores fibrous, odor of acetylene or coal gas, flavor mild, white, elliptical, smooth, 7-10 x 4.9-6 microns; Edibility suspected of having caused cases of mild poisoning; Habitat in moist soil, in broadleaf and coniferous woods; Late summer to late autumn, rainy season; In rare cases the gills may be pinkish or lilac color.

3.5. *Ganoderma tsugae* Murrill

Collection Examined: RRT/115, Sept.–2007, Vita, Dist.-Sangli. On moist wood.

Distribution: India : M. S. (Tem. 2007).

The corpophore 3.9-20 cm, fan or kidney shaped, surface glabrous, unequal, concentrically sulcate, appeared warnished, vermilion yellow red to red black, ochraceous, margin acute, bright yellow, finally cap colored and radially sulcate, often undulate or fairly lobate; Tubes 0.4-0.7 cm long brown, not detachable, pores circular or

polygonal, from white to light cinnamon colored; Stipe sessile, sometimes very small, lateral, cylindrical, often forked, similar in color and surface formation to cap; Flesh suberose, almost ligneous, fibrous, white or whitish beneath bark, hornlike appearance; Spores ochraceous brown, ovoid, warty, 9-11 x 6-8 microns; Edibility edible and tender when it first forms in the spring but soon become encrusted; Habitat on moist wood, on trunk and stumps of eastern hemlock and other conifers; Season rainy, an annual species which grows in summer and autumn, fairly persistent; The stipe may be fairly well developed and may be either on the same level as the cap or perpendicular to it and erect; Other species include *G. lucidum*, common on broadleaf trees, especially maple and *G. oregonense*, a northwest species that is larger and has a darker brownish, less shiny cap.

References

1. P.D.Sharma (1991, 1987), The fungi, 1st edition m/s Rastogi and co. merrut. P.N.-279.
2. Bressa G.L., L. Cima, and P.Costa. 1988. Bioaccumulation of Hg in the mushroom *Pleurotus ostreatus*. *Ecotoxicology and Environmental Safety* 16(2):85-89.
3. Fox, F.M. 1983. Role of Basidiospores as inocula for mycorrhizal fungi of birch. In: *Tree Root Systems and Their Mycorrhizas*, The Hague.
4. Stijve, T. 1992. Certain mushrooms do accumulate heavy metals. *Mushroom, the Journal of wilds Mushrooming* 38(1):9-14.
5. Stijve, T.R. Funbaux, and B. Philipposian. 1986. Agaritine, a p-hydroxymethylphenylhydrazine derivative in cultivated mushrooms (*Agaricus bisporus*), and in some of its wild growing relatives. *Deutsche Lebensmittel-Rundschau* 82:243-248
6. Stijve, T. and R. Roschnik. 1974. Mercuroly and methyl mercury content of different species of fungi. *Trav. chim. alimen. Hyg.* 65:209-220.
7. Augusto Rinaldi, Vassili Tyndalo, The complete book of mushroom. 1st edition "Variaa Grandi Opere" September 1972.
8. Verne Ovid Grahon, "Mushroom of the Great lakes mushroom. Plate-I to Plate-49
9. Morten Lange, F. Bayard Hora. Collins, 1963. Guide to Mushrooms and Toadstools.
10. Peter Jordan, The mushroom guide and Identifier, Anness publishing limited 1995, 1996, 2000.
11. Simon and Schuster's, Guide to mushroom By Giovanni Pacioni, U.S. Editor: Garry Lincoff fiveside Book published by Simon and Schuster Inc. New York, London, Toronto, Sydney and Tokyo.
12. David Arora's Mushrooms Demystified (1986).
13. M. Catherina Aime 2, 3, 4, Rytas Vilgalys 4 and Orson K. Miller Jr, THE Crepidotaceae (Basidiomycota, Agaricales), Phylogeny and taxonomy of the genera and revision of the family based on molecular evidence March 18, 2004 to September 21, 2004.

14. Maria Drumeva- Dimcheva and Melania Gyosheva- Bogoeva Section One: Bulgaria's Biiological Diversity, The macromyctes fungui of Bulgaria.
15. Michael Kuo. identifying mushroom-Retrieved from the mushroom Expert.Nov.2006.
16. Paul Stamets.The Overstory =//= 86, The Role of mushroom in nature. The overstory agroforestry ejournal.
17. Alexopoulos C.J. and C.W. Mims. Introduction mycology.Third edition P.N.359-387,429-445,446-469.
18. Lincoff, Gary H. and Parioni Giovannied, Simon and Schuster's Guide to mushroom (New York 1981).



1. *Coprinus radians*



2. *Morchella esculenta*



3. *Tricholoma sejunctum*



4. *Tricholoma sulphureum*



5. *Ganoderma tsugae*

Comparison of Electrowetting on Hydrophobic and Super Hydrophobic Surfaces

Kalyani Mitkari, Palak Shroff and Kamlesh Altı*

Department of Physics, Sant Gadge Baba Amravati University, Amravati-444602 Maharashtra

*Corresponding author email: kamleshalti@srbau.ac.in

Abstract

Commercially available 'Never wet spray' is used for preparing a super hydrophobic surface. Electrowetting has been observed on this surface. Results were compared with Electrowetting on hydrophobic (Teflon) surface. Lower voltages were required in case of super hydrophobic surface for decreasing the contact angle as compared to that on hydrophobic surface.

Keywords: Electrowetting, Super hydrophobic surface, contact angle.

1. Introduction

Wetting is one of the most important properties of solid surface. It is used in the fundamental material research to characterize a surface. The contact angle has been commonly used to represent the surface wettability. Surface roughness has profound influence on the wetting properties of a material. This fact is especially true with respect to wetting of superhydrophobic surface. For a solid surface, when the contact angle of water on it is larger than 150° then it is called as superhydrophobic. Superhydrophobic state of the surface means it is extremely repellent for water and other liquids. In 1875, the basics of the modern electrowetting were first described by Gabriel Lippmann. Later on Altti Torkkeli *et.al.* works on electrostatic transportation of water droplet on superhydrophobic alkylketene dimer and Teflon surfaces [1]. In 2002 M.G.Pollack *et. al.* gives an alternating approach to microfluidics based upon the micromanipulation of discrete droplet of aqueous electrolyte by electrowetting [2]. J.S.Kuo *et.al.* describes the electrowetting by induced movement of droplet in an immiscible medium [3]. In 2007 Yong Chae Jung and Bharat Bhushan proposed a criterion that the transition from Cassie-Baxter regime to the Wenzel regime occurs when the droplet droop is greater than depth of cavity [4]. Latest development in this field leads different techniques by which superhydrophobic surfaces can be produced easily and inexpensively. Recently in 2013 K. D. Esmeryan *et al.* works on manipulated wettability of a superhydrophobic quartz crystal microbalance through electrowetting [5].

In present paper we compare the Electrowetting effect on hydrophobic as well as superhydrophobic surfaces. Commercially available Teflon tape and 'Never wet spray' is used for getting hydrophobic and superhydrophobic surfaces. Results include the

variation of contact angle with applied voltage on both types of surfaces.

2. Experimental setup

Electrowetting is a phenomenon that relates changes in surface interfacial energy with the presence of an electric field. The basic experimental setup for realizing the electrowetting effect is as shown in Figure 1. The experimental setup consists of variable DC power supply of range up to 1 KV. The experimental set up uses two metal electrodes. One is metallic plate coated by insulating hydrophobic or superhydrophobic layer on which the water drop sits and other is thin wire of copper dipped into the drop. The voltage was applied across these electrodes. Hydrophobic surface is formed using a Teflon tape and its contact angle with water is 116° . Teflon tape is a polytetrafluoroethylene film generally used for sealing pipe threads.

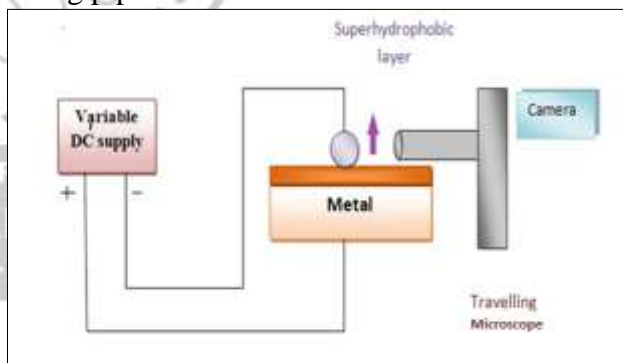


Fig. 1. Experimental setup for observing electrowetting on superhydrophobic surface

The superhydrophobic surface is made by using "Never Wet Spray". Never Wet is two step kit. In step first base coat is applied on the surface by spraying it approximately 6-12 inches from the surface and let it dry for about 30 minutes. Same procedure is used for application of top coat. Base coat contains methyl isobutyl ketone, butyl acetate and mineral spirits while top coat contains acetone. Both the base coat and top coat must be used to ensure superhydrophobic properties. The

superhydrophobic surfaces can give rise to contact angle as great as 165° .

Electrowetting was observed on both the surfaces after application of electric field. To observe enlarge image of droplet travelling microscope was used. A digital camera was attached to travelling microscope for capturing images of the droplet. Contact angle is determined by analyzing images of the droplet using 'ImageJ' software.

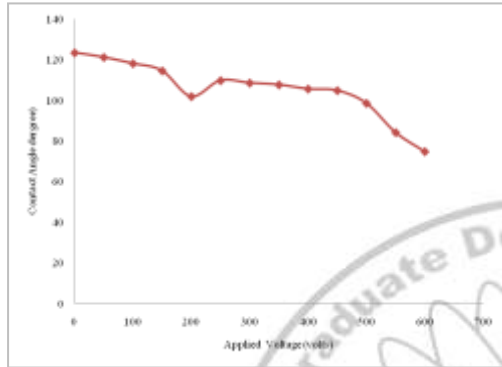


Fig 2: Variation of contact angle with applied voltage for hydrophobic surface

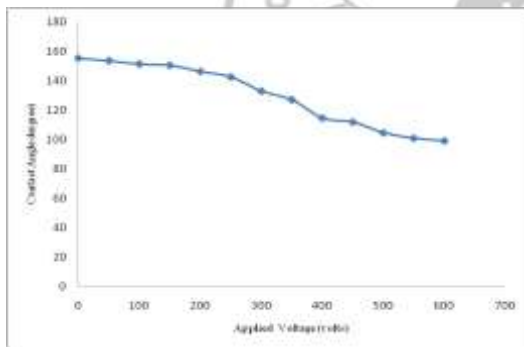


Fig. 3: Variation of contact angle with applied voltage for superhydrophobic surface

3. Result and discussion

The voltage across the droplet was increased in a stepwise fashion from 0V to 600V. Contact angle was determined at each voltage by capturing the image of the droplet. Figure 2 and Figure 3 shows the graph between applied voltage and the measured contact angle on the hydrophobic and superhydrophobic surface respectively. The highest contact angle measured on hydrophobic surface was 123.32 degrees and the lowest contact angle measured was 74.71 degrees. Similarly, the highest contact angle measured on superhydrophobic surface was 155.12 degrees and the lowest contact angle measured was 99.1 degrees on the same surface.

The graph shows the comparison between the variation in contact angle of hydrophobic and superhydrophobic surface. After linear fitting, the slope of graphs representing hydrophobic and superhydrophobic surface was found to be -0.0636 and -0.1077 respectively. So the variation of contact angle with same amount of applied voltage for superhydrophobic surface is found to be greater than that for hydrophobic surface.

4. Conclusion

Result clearly showed that for same amount of applied voltage the water droplet on hydrophobic surface shows less change in contact angle than that for superhydrophobic surface which was made using a commercially available spary. Further probing is required to know the fundamental physics of the observed effect.

Acknowledgement

Authors are very much thankful to Head of physics department, Sant Gadge Baba Amravati University, Amravati for providing us necessary facilities.

References

1. A. Torkkeli, J. Saarilahti and A. Haara "Electrostatic transportation of water droplet on superhydrophobic surfaces" Institute of Electrical and Electronics Engineers 1 (2001).
2. M. G. Pollack, A. D. Shenderovb and R. B. Fair "Electrowetting-based actuation of droplets for integrated microfluidics" Lab Chip 2, p.96-101 (2002).
3. J. S. Kuo, P. S. Mihalic, I. Rodriguez, and D.T.Chiu "Electrowetting-induced droplet movement in an immiscible medium" Langmuir 19, p. 250-255 (2003).
4. E. Bormashenko, T.Stein, G. Whyman, Y.Bormasheno, and R. Pogreb "Wetting Properties of the Multiscaled Nanostructured Polymer and Metallic Superhydrophobic Surfaces" Langmuir 22, p.9982-9985 (2006).
5. Y.P. Zhao and Y. Wang "Fundamentals and Applications of Electrowetting: A Critical Review" Rev. Adhesion Adhesives 1, p.114-174 (2013).

Studies on Complex Impedance of $\text{BaNd}_{2-x}\text{La}_x\text{Ti}_3\text{O}_{10}$ and $\text{BaNd}_{2-x}\text{La}_x\text{Ti}_4\text{O}_{12}$ Ceramic

P.B. Abhange^a, V.C. Malvade^a, S. Chandralingam^b, S.R. Kokare^{a*}

^a Department of Physics, Rajee Ramrao Mahavidyalaya, Jath (Sangli), Maharashtra State, India

^b Jawaharlal Nehru Technological University, Hyderabad, India

*Email: kshirikant@yahoo.com

Abstract

The ceramic materials have great research attention due to their good electric and magnetic properties. The electrical properties of electronic ceramic material contain various like grain, grain boundary and electrode contributions. We have to separate out these contributions to have the control over the properties like charge displacement, dipole reorientation and space charge formation. For separating out these contributions the complex impedance measurement and its analysis has become the powerful tool. The complex impedance curves observed for synthesized $\text{BaNd}_{2-x}\text{La}_x\text{Ti}_3\text{O}_{10}$ and $\text{BaNd}_{2-x}\text{La}_x\text{Ti}_4\text{O}_{12}$ (for $x=0.02, 0.04, 0.06$ and 0.08) consists of two hemispheres indicating the separate contribution of grain and grain boundaries. To resolve these contributions properly the studies are extended over the temperature. It was observed that the increase in temperature gives the more resolution of grain and grain boundary contribution. As the A.C. impedance measurements are very sensitive to the electrical fluctuations, its fitting gives a systematic correlation of the contributions.

Keywords: Ceramic material, complex impedance, charge displacement, grain and grain boundaries

1. Introduction: In recent years, discoveries on ferroelectric with perovskite-type structures have proved that these ferroelectric materials are the most important electronic materials for the technological progress and success. Now days, the use of ferroelectric materials for nonvolatile, high speed random access memories and dynamic random access memories is increased [1]. Also, the ferroelectric materials with high permittivity are having great demand in microwave applications and are extensively used for piezoelectric transducers, multilayer capacitors, ferroelectric thin film memories etc. [2, 3]. At the same time the research publications on hot topic of environment friendly ferro and piezoelectric materials are increased in last decade. The materials like $\text{Ba}_{2-x}\text{Sr}_x\text{NaNb}_5\text{O}_{15}$ were synthesized for narrow band filters. The increased research in lead-free material synthesis and its characterization motivated us to synthesize the proposed system. The high quality factor, high dielectric constant, low dielectric loss and small temperature coefficient of resonant frequency are the most desirable characteristics of the microwave materials [4,5]. The high temperature vibration transducer was developed by using the materials like $\text{Bi}_4\text{MTi}_4\text{O}_{15}$ ($M=\text{Ca, Sr, Ba}$) [6]. It is reported that the compounds present in Ba-Nd-Ti-O systems possess excellent temperature stability and dielectric properties [7,8]. The Ba-Nd-Ti-O system is composed of the mixed compounds like $\text{BaNd}_2\text{Ti}_3\text{O}_{10}$ (BNT), $\text{BaNd}_2\text{Ti}_4\text{O}_{12}$ and $\text{BaNd}_2\text{Ti}_5\text{O}_{14}$ [9]. The reported study on microwave dielectric properties of $\text{BaNd}_2\text{Ti}_5\text{O}_{14}$ shows that it is good for resonator application

[10]. It is also reported that the BNT has relatively high dielectric constant, good thermal stability and low loss in the low frequency region [11].

The present paper reports the synthesis and characterization of $\text{BaNd}_{2-x}\text{La}_x\text{Ti}_3\text{O}_{10}$ and $\text{BaNd}_{2-x}\text{La}_x\text{Ti}_4\text{O}_{12}$ system with $x=0.2, 0.4, 0.6, 0.8$ using solid state reaction method.

2. Materials and Method: The samples of compositions, $\text{BaNd}_{2-x}\text{La}_x\text{Ti}_3\text{O}_{10}$ and $\text{BaNd}_{2-x}\text{La}_x\text{Ti}_4\text{O}_{12}$ were prepared using solid state reaction method. The starting materials were weighed and mixed in stoichiometric proportion with an acetone to grind for 2 hours with agate mortar. Parent materials were BaCO_3 , Nd_2O_5 , TiO_2 and La_2O_5 (more than 99.9 % pure). After grinding, the powders were pre-sintered at 1050°C for five hours. The pre-sintered powders were again grinded in an agate mortar for 1 hour and used for pelletization. Poly-vinyl acetate (PVA) was used as an organic binder. The pressure of 5 ton/cm^2 was applied for pellet formation of sintered $\text{BaNd}_{2-x}\text{La}_x\text{Ti}_3\text{O}_{10}$ and $\text{BaNd}_{2-x}\text{La}_x\text{Ti}_4\text{O}_{12}$ ceramics. The $\text{BaNd}_{2-x}\text{La}_x\text{Ti}_3\text{O}_{10}$ and $\text{BaNd}_{2-x}\text{La}_x\text{Ti}_4\text{O}_{12}$ pellets were sintered in an aluminum crucible at 1150°C for seven hours. Sintered $\text{BaNd}_{2-x}\text{La}_x\text{Ti}_3\text{O}_{10}$ and $\text{BaNd}_{2-x}\text{La}_x\text{Ti}_4\text{O}_{12}$ samples were allowed to anneal at the rate of 2°C/min up to 400°C . Further $\text{BaNd}_{2-x}\text{La}_x\text{Ti}_3\text{O}_{10}$ and $\text{BaNd}_{2-x}\text{La}_x\text{Ti}_4\text{O}_{12}$ samples were brought to room temperature by natural cooling.

The synthesized samples were characterized by X-ray diffraction, Scanning electron microscopy, resistivity measurement and impedance analysis for their structural, morphological and electrical study.

3. Results and discussion:

3.1 XRD and SEM: The XRD patterns of the synthesized sample confirms the single phase material formation with few exceptional pyrochlore phases. The scanning electron microscopy reveals the information of surface morphology and it gives the confirmation of dense material. The average particle size observed from SEM micrographs is about 2 μ m.

3.2 Complex Impedance Measurement: The complex impedance measurement is necessary for complete understand of the electrical properties of the electro-ceramic materials [12]. The electrical properties of electro-ceramics are a result of different contributions of various components and processes present in the materials. In general the overall dielectric properties arise due to intra-grain, inter-grain and electrode processes. The motion of charges could take place in any fashion viz. charge displacement, dipole reorientation, space charges formation etc.[13] in order to achieve reproducibility and to have control over the properties, these so called grain, grain-boundary and electrode contributions must be separated out.

For separating out these contributions, the method of complex impedance analysis [13] has emerged as very powerful tool. In this method the imaginary part Z'' of the total complex impedance ($Z^* = Z' - jZ''$) of the sample is plotted as function of the corresponding real part, Z' at different frequencies. This plot shows different features depending upon various relative contributions. For example for an electronic ceramic having well separated relaxation times for grain-grain boundary and electrode contributions, three distinct semicircular arcs are obtained and for two contributions, two arcs are obtained [13-16]. The analysis is carried out further by representing and visualizing these contributions processes by simple components are determined by finding the intercepts on the Z axis [13] or by using the method of complex non-linear squares [13,17]. A general problem encountered here is the choice of a simple circuit that could represent the experimental data best. Before receiving at any particular systematic to fit the complex impedance curves, we shall define a few preliminary concepts and parameters.

The ac response of material can be expressed in any of four basic formalisms [13].

These are conventionally expressed as complex impedance (Y^*), complex permittivity (E^*) and complex modulus $M^* = (E^*)^{-1}$. The interrelationship among these can be explained with the help of lossy dielectric, which can be expressed as a RC circuit. The four functions broadly called emittance functions [12] are given by

$$Z^* = Z' - jZ''$$

$$Y^* = (Z^*)^{-1} = Y' + jY''$$

$$E^* = (j\omega C_0 Z^*)^{-1} = E' - jE''$$

$$M^* = (E^*)^{-1} = M' + jM''$$

Where ω is the frequency of the ac excitation and C_0 the capacitance of the empty cell used to house the material and it depends on the geometry. The study of E^* as a function of frequency has been widely used since the pioneering work of Cole and Cole [18] and it is mostly suited for dielectric materials having very low or vanishing conductivity [13]. Being a very low loss as observed in all the samples (>1) and very high resistivity (<20 M Ω), the above method of analyzing the complex impedance is best suitable tool.

It is observed that the complex impedance curves are composed of two hemispheres indicating separate contribution for the grain and grain boundaries. At room temperature, these contributions of grain and grain boundaries are not properly resolved; however, the temperature variation helps to resolve the grain and grain boundary contributions. To resolve these contributions with more appropriate values of series and parallel resistances and to arrive at any systematic variation of the grain and grain boundary contributions, the complex impedance studies are extended over the temperature.

Fig. 1 gives the Cole-Cole plot of modified BaNd₂Ti₃O₁₀. Table 1 to 8 gives the estimated values of resistance and capacitance due to grain and grain boundaries. The increase in temperature observes that the resistance due to grain and grain boundaries are decreasing and it is expected to decrease, because of higher mobility of charges in higher temperature. As A. C. measurement with low frequency is a critical experimentation. This may involve multiple sources of errors. To reduce these errors, one has to obtain the repeatability of data and finalize. Another important method to validate the data is curve fitting. If we fit the data by assuming few models, then one may arrive at

particular conclusion.

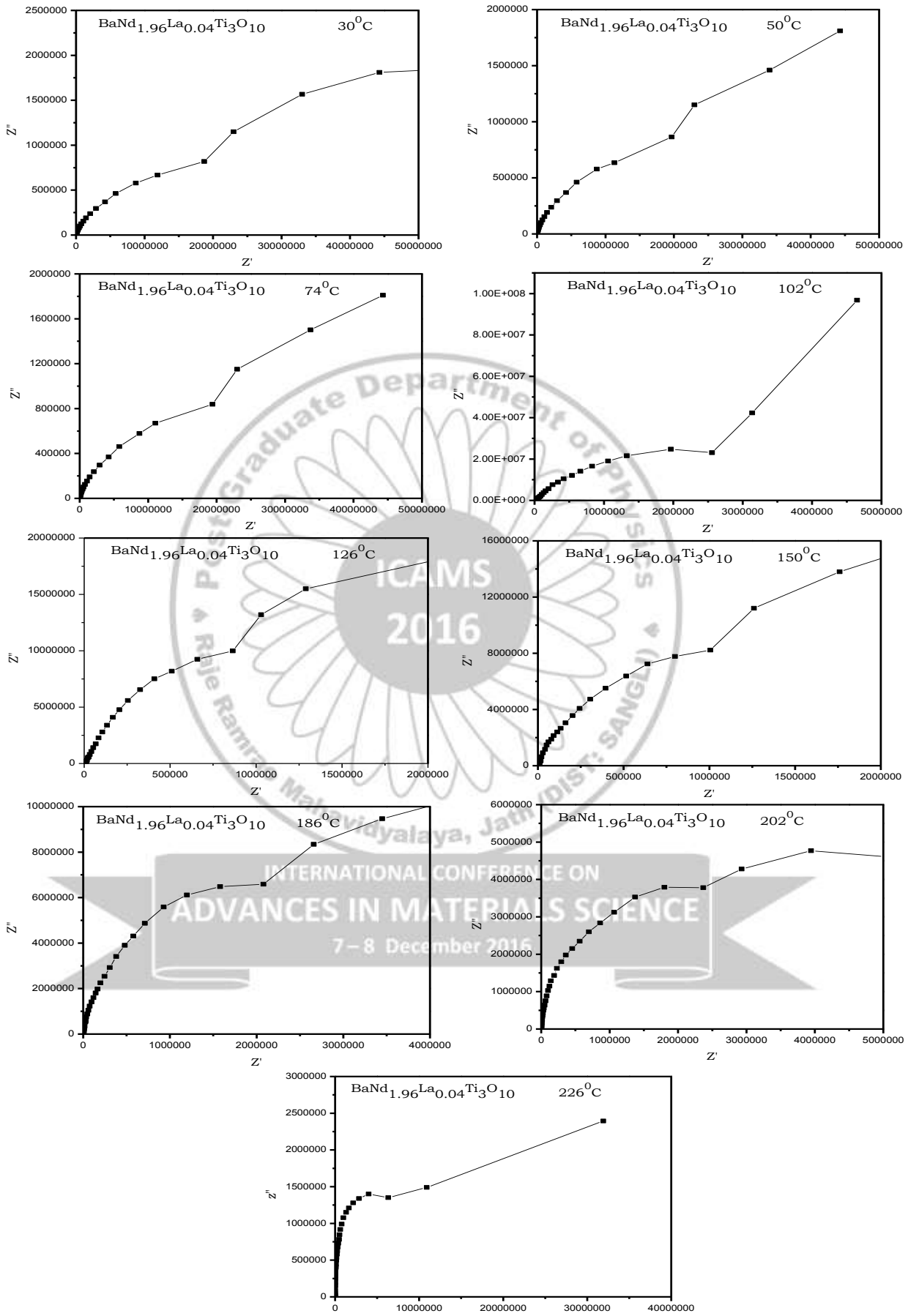


Fig.1 Cole-Cole plots for $\text{BaNd}_{1.96}\text{La}_{0.04}\text{Ti}_3\text{O}_{10}$

Table 1: Calculation of R_g , R_{gb} , C_g and C_{gb} for $BaNd_{1.98}La_{0.02}Ti_3O_{10}$

Temp.	30 ⁰ C	56 ⁰ C	75 ⁰ C	100 ⁰ C	130 ⁰ C	154 ⁰ C	202 ⁰ C	230 ⁰ C	250 ⁰ C
$R_g(M\Omega)$	25	11	30	22	15	12	14	4	2
$R_{gb}(M\Omega)$	50	24	45	60	30	40	35	6	5
C_g (nF)	92	328	196	39	30	35	68	129	198
C_{gb} (nF)	221	461	326	75	94	69	110	352	594

Table 2: Calculation of R_g , R_{gb} , C_g and C_{gb} for $BaNd_{1.96}La_{0.04}Ti_3O_{10}$

Temp.	30 ⁰ C	56 ⁰ C	75 ⁰ C	100 ⁰ C	130 ⁰ C	154 ⁰ C	202 ⁰ C	230 ⁰ C	186 ⁰ C
R_g (M Ω)	32	37	37	3	2	1.6	4	20	4
R_{gb} M Ω)	70	80	90	9	3	4	8	50	7
C_g (nF)	314	291	291	43	72	99	145	658	174
C_{gb} (nF)	841	813	763	43	120	132	372	1100	341

Table 3: Calculation of R_g , R_{gb} , C_g and C_{gb} for $BaNd_{1.94}La_{0.06}Ti_3O_{10}$

Temp.	30 ⁰ C	56 ⁰ C	75 ⁰ C	100 ⁰ C	130 ⁰ C	154 ⁰ C	202 ⁰ C	174 ⁰ C
R_g (M Ω)	2	45	1	3	1	4	5	11
R_{gb} M Ω)	5	100	2	6	3	8	14	30
C_g (nF)	38	222	34	73	140	195	746	528
C_{gb} (nF)	146	663	125	152	235	254	909	796

Table 4: Calculation of R_g , R_{gb} , C_g and C_{gb} for $BaNd_{1.92}La_{0.08}Ti_3O_{10}$

Temp.	30 ⁰ C	56 ⁰ C	75 ⁰ C	100 ⁰ C	130 ⁰ C	154 ⁰ C	202 ⁰ C	174 ⁰ C
R_g (M Ω)	4	2	5	4	3	5	2	3
R_{gb} M Ω)	10	5	13	9	7	14	3	7
C_g (nF)	174	349	285	440	720	470	833	1110
C_{gb} (nF)	338	309	279	498	676	919	1590	1030

Table 5: Calculation of R_g , R_{gb} , C_g and C_{gb} for $BaNd_{1.98}La_{0.02}Ti_4O_{12}$

Temp.	30 ⁰ C	56 ⁰ C	75 ⁰ C	100 ⁰ C	130 ⁰ C	154 ⁰ C	202 ⁰ C	230 ⁰ C	250 ⁰ C
$R_g(M\Omega)$	30	140	120	22	10	110	2	1	1
$R_{gb}(M\Omega)$	80	320	350	65	300	350	7	4	3
C_g (nF)	18	307	435	687	779	215	22	31	88
C_{gb} (nF)	28	730	1030	1630	557	389	44	88	300

Table 6: Calculation of R_g , R_{gb} , C_g and C_{gb} for $BaNd_{1.96}La_{0.04}Ti_4O_{12}$

Temp.	30 ⁰ C	56 ⁰ C	75 ⁰ C	100 ⁰ C	130 ⁰ C	154 ⁰ C	202 ⁰ C	230 ⁰ C	250 ⁰ C	174 ⁰ C
R_g (M Ω)	26	2	1	270	180	20	1	7	13	6
$R_{gb}(M\Omega)$	80	4	3	700	650	55	2.0	25	27	21
C_g (nF)	277	154	22	215	137	877	123	134	359	475

C_{gb} (nF)	909	171	113	742	332	1740	199	156	516	4000
---------------	-----	-----	-----	-----	-----	------	-----	-----	-----	------

Table 7: Calculation of R_g , R_{gb} , C_g and C_{gb} for $BaNd_{1.94}La_{0.06}Ti_4O_{12}$

Temp.	30 ⁰ C	56 ⁰ C	100 ⁰ C	130 ⁰ C	154 ⁰ C	202 ⁰ C	230 ⁰ C	250 ⁰ C	174 ⁰ C
R_g (M Ω)	1	11	40	6	300	4	2	1	30
R_{gb} (M Ω)	3	35	150	17	1100	12	6	2	130
C_g (nF)	54	310	919	642	150	1520	1900	636	760
C_{gb} (nF)	447	1880	2120	2810	557	3940	3980	557	1880

Table 8: Calculation of R_g , R_{gb} , C_g and C_{gb} for $BaNd_{1.92}La_{0.08}Ti_4O_{12}$

Temp.	56 ⁰ C	75 ⁰ C	100 ⁰ C	130 ⁰ C	154 ⁰ C	202 ⁰ C	230 ⁰ C	250 ⁰ C	174 ⁰ C
R_g (M Ω)	3	30	120	10	15	1	0.22	6	25
R_{gb} (M Ω)	8	105	450	25	55	1	0.60	16	65
C_g (nF)	877	1740	487	1400	860	220	225	220	769
C_{gb} (nF)	4780	1760	704	4470	2350	257	478	287	1440

We had not fitted this data to any particular model. However the nature of graphs and rough estimation of grain and grain boundary contribution suggests that there is no significant

contribution due to electrode, as the third hemisphere is not observed. But the contribution of grain and grain boundaries may be analyzed further after fitting the data.

4. Conclusion

The $BaNd_2Ti_3O_{10}$ and $BaNd_2Ti_4O_{12}$ systems are synthesized by doping Lanthanum with varying concentration from 2-8 % in the place of Neodymium using standard solid state ceramic route. The sintering temperature was used at 1150⁰C to form the single phase material. Though the material appears to be porous from the SEM image, the average grain size is slightly less than 2 μ m. The dielectric constant at room temperature is observed to be independent of doping concentration and the very low dielectric loss. Thus the discussion above indicates that the synthesized material is a good candidate for microwave dielectric resonators. The Cole-Cole plot gives the temperature dependence of grain and grain boundary contributions. The detailed curve fitting of Cole-Cole plot and measurement at microwave region is further necessary requirement.

Reference

- M. P. McNeal, S.J. Jang, and R. E. Newnham, "The effect of grain and particle size on the microwave properties of barium titanate ($BaTiO_3$)", *Journal of Applied Physics*, 83(6), 3288-97(1998).
- T. Ramoska, J. Banys, R. Sobiestianskas, M. V. Petrovic, J. Bobic, B. Stojanovic, "Dielectric investigations of La-doped barium titanate", *Processing and Application of Ceramics*, 4[3], 193-198 (2010).
- F. Wan, J. G. Han, Z. Y. Zhu, "Dielectric response in ferroelectric $BaTiO_3$ ", *Phys. Lett. A*, 372, 2137-40 (2008).
- D. Kajfez, P. Guillon, "Dielectric Resonators", Artech House, Norwood, MA, (1986).
- E. A. Nenasheva, N. F. Kartenko, "High dielectric constant microwave ceramics", *J. Eur.Ceram.Soc.*, 21, 2697 (2001).
- Y. -Q. Lu and Y. -X. Li, "A review on lead-free piezoelectric ceramics studied in china", *Journal of Advanced Dielectrics*, 1[3], 269-88 (2011).
- H. Ohsato, S. Nishigaki, T. Okuda, "Superlattice and dielectric properties of $BaO-R_2O_3-TiO_2$ ($R=La, Nd$ and Sm) microwave dielectric compounds", *Jap. J. Appl.Phys.*, 31, 3136 (1992).
- J. H. Choi, J. H. Kim, B. T. Lee, Y. M. Kim, J. H. Moon, "Microwave dielectric properties of Ba-Nd-Ti-O system doped with metal oxide", *Mater. Lett.*, 44, 29 (2000).
- A. Yamada, Y. Utsumi, H. Watarai, "The Effect of Mn Addition on Dielectric Properties and Microstructure of $BaO-Nd_2O_3-TiO_2$ ceramics", *Jap. J. Appl. Phys.*, 30, 2350 (1991).
- R. Ratheesh, H. Sreemoolanadhan, M. T. Sebastian and P. Mohanan, "Preparation, characterization and dielectric properties of ceramics in the $BaO-Nd_2O_3-TiO_2$ system", *Ferroelectrics*, 211,1-8 (1998).
- D. Kolar, S. Gabersecek, B. Volavsek, H. S. Parker and R. S. Roth, "Synthesis and Crystal Chemistry of $BaNd_2Ti_3O_{10}$, $BaNd_2Ti_5O_{14}$, and $Nd_4Ti_9O_{24}$ ", *J. Solid State Chem.*, 38,158 (1981).
- M. A. Ali, M. N. I. Khan, F.-U.-Z. Chowdhury, S. Akhter, M. M. Uddin, "Structural properties, Impedance spectroscopy and Dielectric spin relaxation of Ni-Zn Ferrite synthesized by double sintering technique", *J. Sci. Res.*, 7(3), 65-75 (2015).
- J. Macdonald, *Impedance Spectroscopy*, John Wiley & Sons, New York (1987).
- R. Gerhardt, A.S. Nowick. Grain-Boundary Effect in Ceria Doped with Trivalent Cations: I, Electrical Measurements. *J. Amer. Ceram. Soc.*, 69, 641-46 (1986).
- A. Hooper. A study of the electrical properties of single-crystal and polycrystalline β -alumina using complex plane analysis. *J. Phys. D. Appl. Phys.*, 10, 1487(1977).
- I. M. Hodge, M. D. Ingram, A.R.West. Impedance and modulus spectroscopy of polycrystalline solid electrolytes. *J. Electro. Chem.*, 74, 125-143(1976).
- Panday et al, Discussion meeting on ferroelectric ceramics, (1992).
- Von Hippel, *Dielectrics and Waves*, John Wiley and Sons, New York, (1954).

Dielectric and Ferroelectric Properties of $\text{Ba}_{0.99}\text{Ca}_{0.01}\text{Ti}_{0.99}\text{Sn}_{0.01}\text{O}_3$ Lead-Free Piezoceramic

Pravin S. Kadhane, B.G.Baraskar, T.C.Darvade, Y.D.Kolekar and R.C.Kambale*
Department of Physics, Savitribai Phule Pune University, Pune 411007, Maharashtra, India

*Email: rckambale@gmail.com

Abstract

Lead-free ($\text{Ba}_{0.99}\text{Ca}_{0.01}\text{Ti}_{0.99}\text{Sn}_{0.01}$) O_3 (BCTS) ceramic was synthesized by solid state reaction method and investigated their dielectric and ferroelectric properties. Room temperature x-ray diffraction reveals the tetragonal lattice symmetry for ($\text{Ba}_{0.99}\text{Ca}_{0.01}\text{Ti}_{0.99}\text{Sn}_{0.01}$) O_3 without any secondary phase suggests the formation of perovskite BaTiO_3 - CaTiO_3 - BaSnO_3 solid solution. The microstructural observation reveals the dense microstructure with an average grain size $\sim 11.32 \mu\text{m}$ having the relative density $\sim 96.83\%$. The temperature dependent dielectric study reveals the dielectric anomaly at Curie temperature ($T_c=121^\circ\text{C}$ is $\epsilon_r \sim 11670$). The electric field induced polarization-electric field (P - E) hysteresis confirms the ferroelectric nature having $\text{Pr} \sim 4.35 \mu\text{C}/\text{cm}^2$ and $E_c \sim 1.7 \text{ kV}/\text{cm}^2$. The piezoelectric charge coefficient (d_{33}) was found to be $287 \text{ pC}/\text{N}$. Thus, with this observed moderate dielectric constant and d_{33} values the ($\text{Ba}_{0.99}\text{Ca}_{0.01}\text{Ti}_{0.99}\text{Sn}_{0.01}$) O_3 composition may be useful for lead-free piezoelectric device applications.

1. Introduction

The lead zirconium titanate (PbZrTi) O_3 piezoelectric ceramics plays an important role in variety of applications viz. actuator, sensor, capacitors, etc. due to their high piezoelectric, dielectric and ferroelectric properties [1-6]. Nowadays, European Union (EU) has restricted the use of Pb and PbO based materials in electronic industries due to toxicity of lead and banned the PZT ceramics under restriction of hazardous substances (RoHS) legislations concerning to the environment and human health protection [1-2]. Therefore, there is an urgent need to invent and develop the new lead-free piezoelectric materials having comparable properties as that of PZT and transfer them into applications. In this view, different families of lead free piezoelectric ceramics were studied thoroughly which includes BaTiO_3 (BT), BaNaTiO_3 (BNT), NaKNbO_3 (KNN) ceramics. However, till date there is no reliable lead-free piezoelectric ceramic who can compete with PZT, because of some major issues such as low Curie temperature (T_c) and poor densification for BaTiO_3 and KNN based ceramics respectively. Among the different lead-free piezoelectric ceramics, the BaTiO_3 ceramics exhibits the stable piezoelectric and ferroelectric properties having proper densification. Therefore, there is a scope to develop the BaTiO_3 based lead-free ceramics with suitable substitution at A and B site of the ABO_3 perovskite structure in order to increase the T_c as well as ferroelectric/ piezoelectric properties. Hence, in the present work an attempt is made to investigate the dielectric, ferroelectric and piezoelectric properties of Ca^{2+} and Sn^{4+}

substituted BaTiO_3 ceramics at A and B site respectively and discussed the observed results.

2. Experimental Details

$\text{Ba}_{0.99}\text{Ca}_{0.01}\text{Ti}_{0.99}\text{Sn}_{0.01}\text{O}_3$ (BCTS) ceramic was prepared by solid state reaction method. Barium carbonates (BaCO_3), calcium carbonate (CaCO_3), tin Oxide (SnO_2), titanium dioxide (TiO_2) (all with purity $\geq 99\%$ received from Sigma-Aldrich) were used as raw materials. These materials were weighed in their stoichiometry proportion and ball milled for 24 hours in ethanol medium. Then the mixture was dried at 80°C for 6 hours and grounded for 1 hour. The dried powder of BCTS ceramic is pre-sintered at 1200°C for 10 hours. The pre-sintered powder is grounded further and ball milled for 24 hours then dried at 80°C for 6 hours. Then pre-sintered dried powder was pressed into 10 mm-diameter pellets using 5 wt% polyvinyl alcohol as binder. The prepared pellets of BCTS ceramic were sintered at 1300°C for 10 hours.

The sintered ceramic was characterized by x-ray powder diffraction analysis (XRD) using a $\text{CuK}\alpha$ radiation ($\lambda = 1.54178 \text{ \AA}$) (D8 Advanced, Bruker Inc., Germany). Density of sample was determined by the Archimedes principle using xylene medium. The microstructure of sintered sample was observed by scanning electron microscope (JEOL-JSM 6306A). The temperature dependent dielectric properties were examined using programmable furnace with LCR meter (HIOKI 3532-50) at 1 kHz, 10 kHz and 100 kHz in the temperature range of 30°C - 200°C . Ferroelectric hysteresis loop was measured using ferroelectric hysteresis loop tracer at 50 Hz (Marine India Elect., New Delhi, India). The electric polling was carried out at room

temperature to an applied DC voltage of 1 kV. The piezoelectric charge coefficient (d_{33}) of pooled sample was measured using YE2730A d33 meter (APC International Ltd.).

3. Results and Discussion

Figure 1 shows the x-ray diffraction pattern of BCTS ceramic sintered at 1300°C . All the observed XRD reflections are in good agreement with that of standard JCPDS (PDF 05-0626) data. Hence, confirms the formation of pure BCTS ceramic without any secondary phase as well as reveals the tetragonal lattice symmetry at room temperature. The doublet was observed at $2\theta = 44.8^{\circ}$ corresponding to (002)-(200) peaks which evidences the formation tetragonal crystal structure of BCTS ceramics having axial ratio $\sim c/a$ 1.02 with space group $P4mm$ [1, 3, 7]. The theoretical density and experimental density was found to be 6.01 gm/cm^3 and 5.82 gm/cm^3 respectively having porosity 3.16 % and density 96.83 % [6].

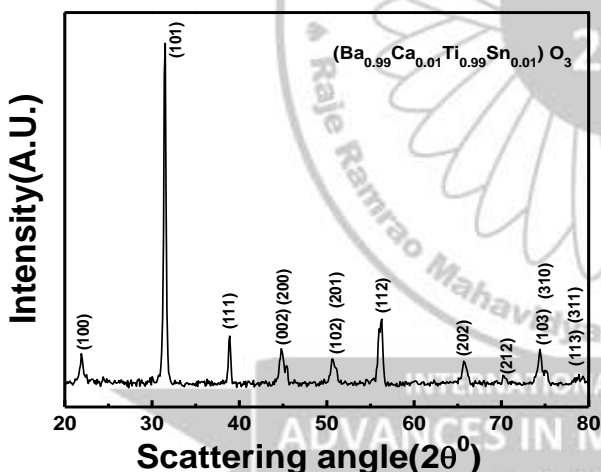


Fig.1. X-Ray diffraction pattern of BCTS sintered at 1300°C .

The microstructure of BCTS ceramics sintered at 1300°C for 10 hours is shown in the figure 2. The dense microstructure with inhomogeneous distribution of grains was observed in accordance with density measurements. The average grain size was calculated by using line intercept method is $11.32\mu\text{m}$. The observed dense microstructure with large grain size is good for piezoelectric and ferroelectric properties. The temperature dependant dielectric study of BCTS ceramics at different frequencies 1 kHz, 10 kHz, and

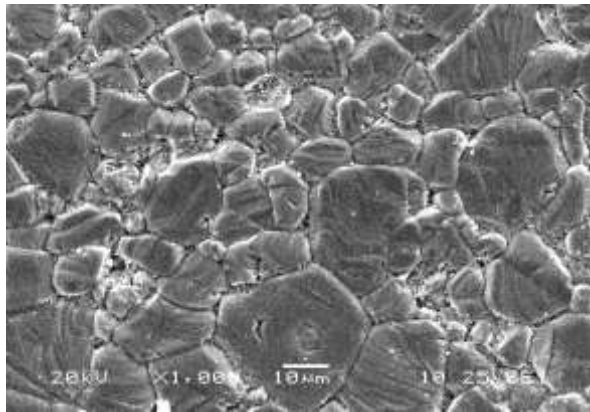
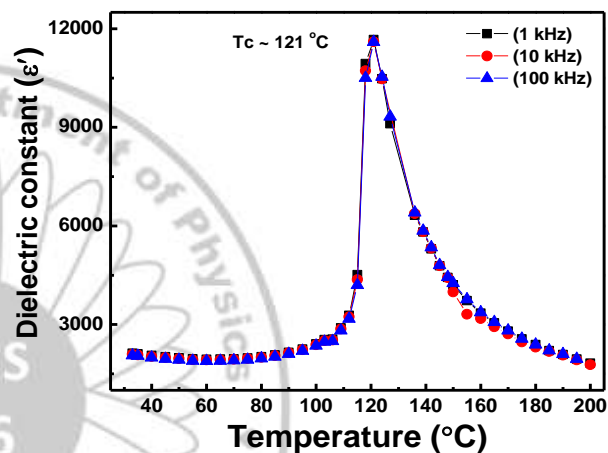


Fig.2. SEM microstructure of BCTS sintered at



1300°C for 10 hours

Fig.3. Temperature dependent properties of BCTS ceramic at 1 kHz, 10 kHz, and 100 kHz.

100 kHz is shown in the figure 3. The phase transition of BCTS from tetragonal to cubic occurs at Curie temperature 120°C . The observed Curie temperature 121°C is well matches with the reported values [1]. The observed values of dielectric constant for all frequencies 1 kHz, 10 kHz, 100 kHz are 11670, 11604, and 11594 respectively. Here, it should be noted that the observed high dielectric constant value of Ca^{2+} and Sn^{4+} modified BaTiO_3 ceramics due to proper stoichiometric control as well as densification.

Figure 4 shows the P-E hysteresis loop of BCTS ceramic measured at frequency 50 Hz and electric field 8.5 kV/cm . The observed remnant polarization (P_r) and the coercive electric field (E_c) values are $4.352\mu\text{C/cm}^2$ and 1.699kV/cm respectively. As sample shows higher relative density therefore reduces leakage current and effective increase in polarization value. DC polling of sample is carried out at 1 KV/cm for half hour for measurement of piezoelectric coefficient. The DC polled BCTS ceramics shows the value of

piezoelectric charge coefficient is 287 pC/N at 0.250N.

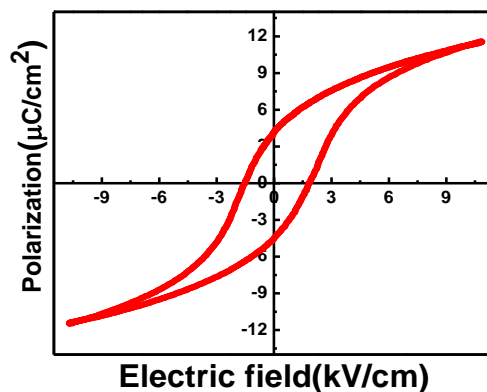


Fig.4. P-E hysteresis loop for BCTS ceramic

4. Conclusion

Dense microstructured lead free piezoelectric $\text{Ba}_{0.99}\text{Ca}_{0.01}\text{Ti}_{0.99}\text{Sn}_{0.01}\text{O}_3$ ceramic was successfully prepared by solid state reaction method. The tetragonal lattice symmetry was observed at room temperature with axial ratio $c/a \sim 1.02$. The temperature dependent dielectric measurements reveal the dielectric maxima at the Curie temperature of 121°C with $\epsilon_r \sim 11670$ at 1 kHz. The ferroelectric nature was evidenced by measuring the electric field induced polarization hysteresis loop having $P_r = 4.352 \mu\text{C}/\text{cm}^2$ and coercive field, $E_c = 1.699 \text{ kV}/\text{cm}$. Thus, with this observed moderate dielectric constant and d_{33} values the $(\text{Ba}_{0.99}\text{Ca}_{0.01}\text{Ti}_{0.99}\text{Sn}_{0.01})\text{O}_3$ composition may be useful for lead-free piezoelectric device applications.

Acknowledgments

RCK thankfully acknowledge the ISRO-UoP Space Technology Cell, Government of India (Grant No. GOI A (337) B (137)) and BCUD Savitribai Phule Pune University (RG-31) for providing Research grant.

References

1. L. F. Zhu, B. Zhang, X-K. Zhao, L. Zhao, P-F. Zhou, "Enhanced Piezoelectric properties of $(\text{Ba}_{1-x}\text{Ca}_x)(\text{Ti}_{0.92}\text{Sn}_{0.08})\text{O}_3$ Lead free ceramics," J. Am. Ceram. Soc., 96, 241-245 (2013).
2. W. L. Z. Xu, R. Chu, P. Fu, G. Zang. "Piezoelectric and Dielectric properties of $(\text{Ba}_{1-x}\text{Ca}_x)(\text{Ti}_{0.95}\text{Zr}_{0.05})\text{O}_3$ Lead free ceramics," J. Am. Ceram. Soc., 93 [10] 2942-2944 (2010).
3. W. L. Z. Xu, R. Chu, P. Fu, G. Zang. "Large Piezoelectric coefficient in $(\text{Ba}_{1-x}\text{Ca}_x)(\text{Ti}_{0.96}\text{Sn}_{0.04})\text{O}_3$ Lead free ceramics," J. Am. Ceram. Soc., 94 [12] 4131-4133 (2010).
4. S. Shao, J. Zhang, Z. Zhang, P. Zheng, M. Zhao, J. Li, C. Wang. "High piezoelectric properties and domain configuration in BaTiO_3 ceramics obtained through the solid-state reaction route," J. Phys. D: Appl. Phys. 42 (2009) 189801
5. C. Miclea, C. T. Asoiu, C. F. miclea, Gheorghiu. "Microstructure and Properties of Barium Titanate Ceramics Prepared by Mechanochemical Synthesis," RJST 10, 4, 335-345, 2007.
6. P. Zheng, J.L. Zhang, Y.Q. Tan, C.L. Wang. Grain-size effects on dielectric and piezoelectric properties of poled BaTiO_3 ceramics," Acta Materialia 60, 5022-5030 (2012).
7. W. Li, Z. Xu, R. Chu, P. Fu, G. Zang, "Structural and dielectric properties in the $(\text{Ba}_{1-x}\text{Ca}_x)(\text{Ti}_{0.95}\text{Zr}_{0.05})\text{O}_3$ ceramics," Current Applied Physics 12 748-751 (2012).

Electrodeposition of low cost Cu₂O thin films for electrochemical sensor application

Pavan K. Pagare and A. P. Torane*

Solid State Physics Laboratory, Department of Physics, Yashwantrao Chavan Institute of Science, Satara, 415001, Maharashtra, India

Email Address appasahebtorane@yahoo.in, pavanpagare25@gmail.com

Abstract

Cuprous oxide (Cu₂O) thin films have been deposited on stainless steel substrates via electrodeposition method. The structure and morphology of these films were characterized by X-ray diffraction (XRD) and Scanning electron microscopy (SEM) technique. The optical properties of thin films were analyzed by using UV-Visible spectroscopy. The band gap of electrodeposited Cu₂O thin films found to be 2.12 eV. The electrochemical sensing property of Cu₂O thin films investigated in an electrolyte containing 0.5 M NaOH at different concentration of glucose. The current of Cu₂O thin films changes with scan rate and concentration of glucose. The results shows electrochemical sensitivity of Cu₂O thin films increases with concentration of glucose at room temperature.

Keywords Electrodeposition, Thin films, Cu₂O, Band gap, Electrochemical sensing.

1. Introduction:

Nowadays electrochemical sensors is a better application in medical field because of its low cost and high stability. There are various materials are used for electrochemical sensors such as, boron doped diamond electrode (BDDE), reduced graphene oxide (RGO), titanium dioxide (TiO₂) and etc. From the above materials some materials have high band gap, high cost and less stable, because of these reason number of researchers attracted towards cuprous oxide material. Cuprous oxide (Cu₂O) is first known semiconducting material with low cost, non-toxic, abundant, environment friendly [1, 2] for various applications such as solar cell [3-8], gas sensor [9], photodiode [10], glucose sensor [11, 12] and supercapacitor [13]. The direct band gap of Cu₂O thin films has found to be 2.1 eV [14]. Cu₂O has been actively studied for energy conversion and sensor applications. The theoretical efficiency of Cu₂O solar cell is 20% and it has high absorption coefficient [15, 16]. The orientation variation of Cu₂O obtained under different bath temperatures, deposition potentials, pH and deposition conditions have been studied [17]. The Cu₂O is deposited using various deposition techniques such as electrodeposition [18-23], spin coating [24], thermal evaporation [25], rf-magnetron sputtering [26] and impregnation-reduction [27]. The low cost, simple and cheap electrodeposition method has been used for control of thickness and morphology of Cu₂O thin films.

In this work, we report the synthesis of Cu₂O thin films on stainless steel substrates via electrodeposition method. The XRD pattern shows single phase Cu₂O material with absence of Cu and CuO impurities. From SEM images truncated pyramidal morphology of Cu₂O thin films have

been observed. Finally cyclic voltammetry measurement shows Cu₂O is best material for electrochemical sensor because of its high stability, repeatability of sensing, reproducibility of electrode and high electrochemical sensing at room temperature.

2. Experimental:

2.1 Preparation of Cu₂O thin films

Cuprous oxide (Cu₂O) thin films were electrodeposited on stainless steel substrates using electrodeposition method. The stainless steel substrates were polished by zero grade polish paper, washed with distilled and cleaned in an ultrasonic cleaner. The three electrode system was used for electrosynthesis. The graphite rod was used as counter electrode. The stainless steel substrates were used as working electrode and Ag/AgCl was used as reference electrode. The electrolyte containing all analytical reagent chemicals such as 1M CuSO₄.5H₂O and 1M C₃H₆O₃ (lactic acid) were used. The cathodic potential was kept at -1.0 V/Ag/AgCl for 1h. The deposition time was varied to obtain well adherent and uniform Cu₂O thin films. It was observed that variation of deposition time gives different colour coatings on substrates. The electrodeposited Cu₂O thin films were washed with double distilled and dried using hair dryer. The cyclic voltammograms of Cu₂O thin films was carried out by using 0.5M NaOH electrolyte in presence of glucose and also in absence of glucose in three electrode system.

Characterizations

The crystal structure of electrodeposited Cu₂O thin films were determined by x-ray diffraction (XRD) technique using model Bruker D8 Advance with Cu K α radiation ($\lambda=1.54\text{\AA}$) in the range (2θ) of 20° - 80° for structural studies. The surface morphology were observed by using scanning electron microscope (SEM) of model

JEOL JSM-6360 with operating bias voltage 20kV. Optical absorption studies within the wavelength range 485-800 nm were carried out using UV-visible spectrophotometer SYSTRONICS 119. The cyclic voltammograms and current time response were carried out by using Autolab PGSTAT 101 instrument with Nova 1.11 software.

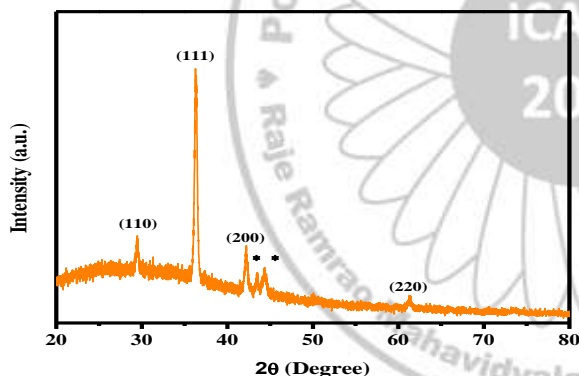
3. Results and discussion:

3.1 Structural and morphological study

The phenomenon of X-ray diffraction can be considered as reflection of X-rays from the crystallographic planes of the material and is governed by the Bragg's diffraction law.

$$2d\sin\theta = n\lambda \quad (1)$$

Where 'd' is lattice spacing, λ is the wavelength of the monochromatic X-ray, 'n' is order of diffraction and θ is diffraction angle. The XRD patterns of electrodeposited Cu_2O thin films are shown in Fig.1. The XRD pattern is found to be polycrystalline in nature. The symbol * detects



peaks of stainless steel substrate. The electrodeposited Cu_2O thin films results matches with standard JCPDS card no. 05-667. The XRD pattern shows more intensive (111) plane of Cu_2O material with other (110), (200) and (220) planes are also observed. There is no other impurity peaks such as Cu and CuO are observed in XRD pattern.

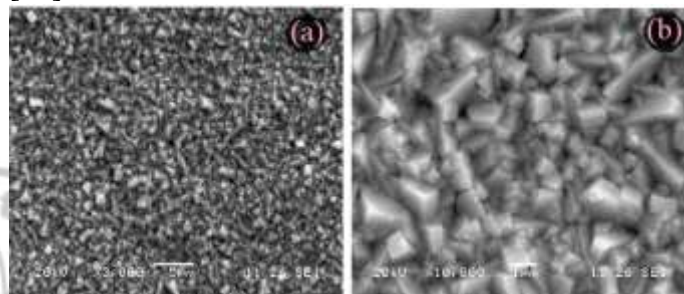
The crystallite size of the electrodeposited Cu_2O thin films are estimated by full width at half maximum (FWHM) for the intensive peaks by Debye- Scharrer's formula:

$$D = K\lambda / \beta \cos\theta \quad (2)$$

Where D is crystallite size, λ is wavelength of X-ray used, θ is the Bragg's angle, β is full width at half maximum of the peak in radian and K is a constant whose value varies from 0.89 to 1.39. For

more intensive (111) plane, the crystallite size was found to be 14.18 nm.

The surface morphology of Cu_2O thin films on stainless steel substrates by electrodeposition method is as shown in Fig.2. The micrographs at the magnifications (a) X3000 and (b) X10000 shows triangular pyramidal morphology. The SEM results of electrodeposited Cu_2O thin films are slightly different than reported earlier methods [21].

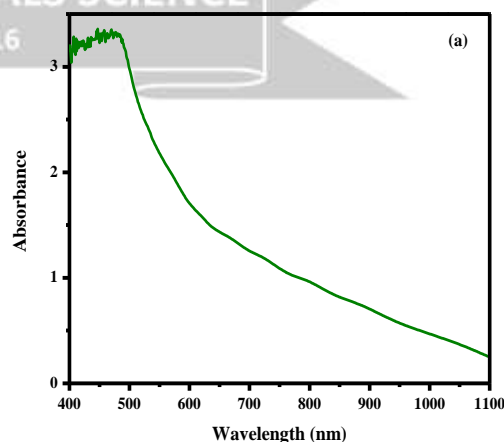


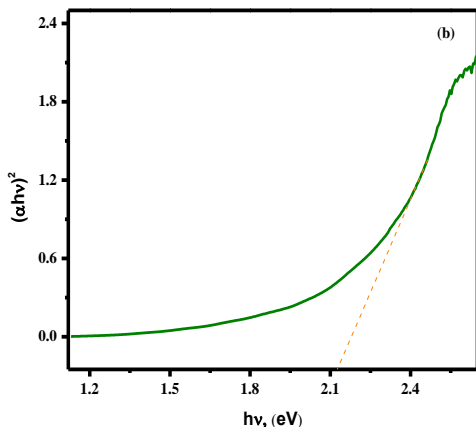
3.2 Optical measurement

The optical absorption edge at a certain incident photon energy, which can be attributed to the electrons excitation from valance to conduction band separated by energy equal to the band gap energy (E_g). The optical absorption spectrum is in the range of 400-1100 nm wavelength. The optical band gap (E_g) for Cu_2O thin films is determined by the equation [28].

$$(\alpha h\nu) = A (E_g - h\nu)^n \quad (4)$$

Where E_g band gap, $h\nu$ incident photon energy, A constant, α coefficient of absorption and n determines the electronic transition causing absorption, which is 1/2 (direct allowed), 3/2 (direct forbidden), 2 (indirect allowed), and 3 (indirect forbidden) transitions, respectively.



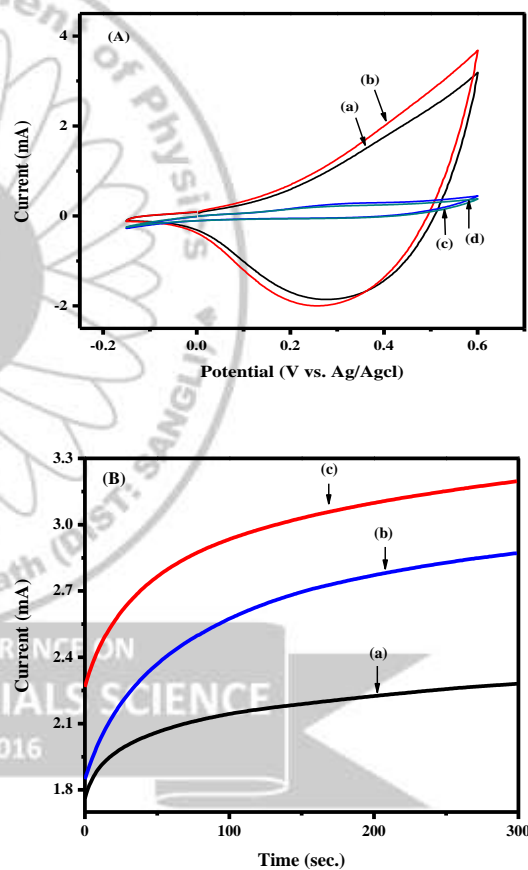


The UV-visible absorption spectrum is shown in Fig.3 (a). The absorption takes place at wavelength 610 nm. The direct band gap energy of Cu₂O thin film is found to be 2.12 eV shown in (Fig.3.b) which is slightly more than the reported value [14].

3.3 Electrochemical properties of Cu₂O thin films.

The cyclic-voltammograms of the Cu₂O thin films measured at different scan rates are shown in Fig.4 (A). The electrolyte 0.5M NaOH in presence of 1mM glucose was used in (a) and (b) cycles having scan rates 10 mV/s and 20 mV/s respectively while (c) and (d) cycles in absence of glucose for 10 mV/s and 20 mV/s scan rates are studied. The three electrode system was used for this investigation. The graphite was used as counter electrode and saturated calomel electrode (SCE) used as reference electrode at room temperature in the potential range - 0.20V to 0.60V. P. K. Pagare et al. [28] deposited Cu₂O thin films onto FTO substrates and reported more electrochemical sensing than these reported values. The same current response was detected in both anodic and cathodic directions. In existence of glucose, rise in current is noticed around + 0.60 V which displays that change in electrocatalytic capacity of Cu₂O near glucose oxidation. The current-time measurement curve in

Fig.4 (B) shows difference of current with time. The concentration of glucose (a) 1 mM, (b) 2 mM and (c) 3 mM in 0.5 M NaOH was used for current time measurement. The time was varied from 0 to 300s. It was observed that the current rises with increase in concentration of glucose. The current sensing measurement of Cu₂O thin films in presence of glucose are 2.28 mA, 2.87 mA and 3.20 mA for 1 mM, 2 mM and 3 mM glucose concentration respectively. M. Liu et al. reports different results than these reported values [29]. The high electrocatalytic presentation of Cu₂O thin films act as good electrochemical sensing for current time response of glucose.



4. Conclusions

In summary, we successfully deposited Cu₂O thin films using electrodeposition technique. The electrodeposited Cu₂O thin films shows (111) high intensity orientation at constant potential. The Cu₂O thin films shows triangular pyramidal morphology. The band gap of electrodeposited Cu₂O thin films is found to be 2.12 eV. The cyclic-voltammograms curves shows maximum sensing of current 3.20 mA/mM having 3 mM glucose concentration. The result displays rise of scan rate with increase in current. The current-time response of Cu₂O in presence of glucose changes with variation in concentration of glucose. The above result shows that Cu₂O is one of promising material for electrochemical sensing.

References:

1. A. Subramanian, J.D. Perkins, R.P. O'Hayre, S. Lany, V. Stevanovic, D.S. Ginley, Zakutayev, APL Materials 2 (2014) 022105.
2. L. Assaud, V. Heresanu, M. Hanb'u'cken, L. Santinacci, C. R. Chimie 16 (2013) 89.
3. A.R. Zainun, S. Tomoya, U.M. Noor, M. Rusop, I. Masaya, Mater. Lett. 66 (2012) 254.
4. K. Cheng, Q. Li, J. Meng, X. Han, Y. Wu, S. Wang, Sol. Energy Mater. Sol. Cells 116 (2013) 120.
5. M. Ichimura, Y. Kato, Mater. Sci. in Semiconductor Processing 16 (2013) 1538.
6. T. Minami, T. Miyata, Y. Nishi, Thin Solid Films 559 (2014) 105.
7. T. Minami, Y. Nishi, T. Miyata, J. Nomoto, Appl. Phys. Express 4 (2011) 062301.
8. T. Dimopoulos, A. Peic', S. Abermann, M. Postl, E.J.W. List-Kratochvil, R. Resel, EPJ Photovoltaics 5 (2014) 50301.
9. T. Jiang, T. Xie, W. Yang, H. Fan, D. Wang, J. Colloid and Interface Sci. 405 (2013) 242.
10. T.Y. Tsai, S.J. Chang, T.J. Hsueh, H.T. Hsueh, W.Y. Weng, C.L. Hsu, B.T. Dai, Nanoscale Res. Lett. 6 (2011) 575.
11. H. Yao, X. Zeng, D. Zhang, L. Liu, B. Yuan, Int. J. Electrochem. Sci. 8 (2013) 12184.
12. Y.H. Won, L.A. Stanciu, Sensors 12 (2012) 13019.
13. V.D. Patake, S.S. Joshi, C.D. Lokhande, O.S. Joo, Mater. Chem. Phys. 114 (2009) 6.
14. Y. Luo, L. Wang, Y. Zou, X. Sheng, L. Chang, D. Yang, Electrochem. Solid-State Lett. 15 (2012) H34.
15. L.K. Tsui, G. Zangari, Electrochim. Acta 128 (2014) 341.
16. P. Lv, L. Lin, W. Zheng, M. Zheng, F.Lai, Optik 124 (2013) 2654.
17. S. Joseph, P.V. Kamath, J. Electrochem. Society, 154 (2007) E102.
18. R. Oommen, U. Rajalakshmi, Sanjeeviraja, Int. J. Electrochem. Sci. 7 (2012) 8288.
19. C. Iida, M. Sato, M. Nakayama, A. Sanada, Int. J. Electrochem. Sci. 6 (2011) 4730.
20. M.C. Huang, T.H. Wang, W.S. Chang, J.C. Lin, C.C. Wu, I.C. Chen, K.C. Peng, S.W. Lee, Appl. Surface Sci. 301 (2014) 369.
21. P.E.D. Jongh, D. Vanmaekelbergh, J.J. Kelly, Chem. Mater. 11 (1999) 3512.
22. T. Mahalingam, J.S.P. Chitra, J.P. Chu, S. Velumani, P.J. Sebastian, Sol. Energy Mater. Sol. Cells 88 (2005) 209.
23. J. Cui, U.J. Gibson, J. Phys. Chem. C 114 (2010) 6408.
24. T. Oku, T. Yamada, K. Fujimoto, T. Akiyama, Coatings 4 (2014) 203.
25. P. Samarasekara, GESJ: Physics, 4 (2010) 2.
26. 'O'. Polat, T. Aytug, A.R. Lupini, P.M. Paranthaman, M. Ertugrul, D.F. Bogorin, H.M. Meyer, W. Wang, S. J. Pennycook, D.K. Cheisten, Mater. Res. Bull. 48 (2013) 352.
27. Z. Li, J. Liu, D. Wang, Y. Gao, J. Shen, Int. J. Hydrogen Energy 37 (2012) 6431.
28. P. K. Pagare, A. P. Torane, Microchim Acta 183 (2016) 2983
29. M Liu, R Liu, W Chen, Biosens Bioelectron 45 (2013) 206.

INTERNATIONAL CONFERENCE ON
ADVANCES IN MATERIALS SCIENCE
7 – 8 December 2016

Novel approach for the synthesis of CdZn(SSe)₂ thin films and its photoelectrochemical application

Sandip K. Jagadale¹, Popatrao N. Bhosale*¹, Raghunath K. Mane¹

¹Smt. K.R.P. Kanya Mahavidyalaya, Islampur-415 409, Tal-Walwa, Dist. Sangli,
E-mail: rmane.1970@gmail.com

*¹Materials Research Laboratory, Department of Chemistry, Shivaji University, Kolhapur-416004, E-mail: p_n_bhosale@rediffmail.com

Abstract:

Thin films of CdZn(SSe)₂ semiconductor were prepared on clean glass and FTO substrate using simple, cost effective arrested precipitation technique (APT). Preparative conditions were optimized during initial stage of experimentation to obtain good quality CdZn(SSe)₂ thin films. As deposited films were studied for its structural, morphological, optical, and compositional analysis by XRD, SEM, UV-Vis-NIR spectro-photometer and EDS analysis techniques respectively. XRD study revealed that the films are in polycrystalline nature and exhibit hexagonal crystal structure. The SEM micrograph shows the formation of spherical surface morphology. EDS results confirms the presence of Cd, Zn, S and Se elements in the synthesized thin film. The band gap value of thin film was calculated from the absorption spectra which is found to be 1.8 eV. From J-V measurements, photo-conversion efficiency is found to be 0.07 %.

1. Introduction:

The II-VI semiconducting compounds, especially the cadmium chalcogenides, have been extensively studied owing to their potential applications in solar cells [1] and opto-electronic devices [2]. The variety of techniques presently used for the synthesis of cadmium and zinc chalcogenide semiconductor thin films [3-4]. From all these methods, an attempt is made here to fabricate these films by a simple, inexpensive modified APT developed in our laboratory and set for its various deposition conditions [5-7]. In the present investigation, we proposed synthesis, growth mechanism, optostructural, morphological, compositional and photoelectrical properties of quaternary CdZn(SSe)₂ thin film.

2. Experimental Details

The CdZn(SSe)₂ thin films were obtained onto the optically plane amorphous glass and FTO slides. For the deposition, cadmium sulfate hydrate (CdSO₄.3H₂O), zinc sulfate hydrate (ZnSO₄.7H₂O), thiourea (NH₂-CS-NH₂) and sodium selenosulfite (Na₂SeSO₃), were used as precursors for Cd²⁺, Zn²⁺, S²⁻, Se²⁻ ions respectively. Ammonia is used to maintain pH of reaction bath and triethanolamine (TEA) was used as complexing agent. For measuring the PEC performance, sulfide/polysulfide redox electrolyte is used. The solution of sodium selenosulfite was prepared by refluxing selenium metal powder with Na₂SO₃ at 90°C for 9 h. Glass and FTO coated glass slides were mounted on a specially designed substrate holder and rotated with constant speed in mixture so as to achieve uniform churning of the reaction mixture for thin film deposition. To obtain good

quality films, the preparative parameters such as pH of reaction bath, precursor concentrations and temperature were optimized initially to 10.8±0.2, 0.1M and 55±2°C respectively.

The optical absorbance of as deposited films were measured using UV-Visible NIR-spectrophotometer (Hitachi model 330, Japan) in the wavelength range 300-1100 nm. The structural analysis is done by X-ray diffraction (XRD) analysis [Brukers AXS Analytical Instruments. Model D2 PHASER] with Cu K α target for the 2 θ ranging from 10° to 100°. The compositional analysis of deposited thin film was determined using energy dispersive X-ray analysis (EDS) attached to scanning electron microscope (SEM). (JEOL-JSM- 6360A). J-V measurements (PEC) were recorded on semiconductor characterization instrument (SCS-4200 Keithley, Germany) using a two electrode configuration.

3. Results And Discussion

The reaction mechanism for CdZn(SSe)₂ thin film formation were described in Ref.[5-7]. Thin films at different deposition time were deposited under the same experimental conditions within experimental accuracy. The optical absorption spectra was measured at room temperature for the CdZn(SSe)₂ thin films in the wavelength range of 300-1100 nm. The optical absorption plot having linear nature confirms the direct allowed transition as shown in fig.1a.

The Fig.1b. shows X-ray diffraction pattern of CdZn(SSe)₂ thin film. Four peaks observed at diffraction angle of 24.92 (100), 26.20 (100), 41.92 (110), and 71.87 (105) corresponding to 3.568, 3.396, 2.149 and 1.312 'd' values respectively.

These values are matched with standard JCPDS data (card No. 80-006, 35-1469 and 77-2307). XRD data demonstrate polycrystalline phase and a hexagonal crystal structure of CdZn(SSe)₂ thin film. The crystallite size is calculated by using Debye Scherer formula. The calculated crystallite size is 20 nm.

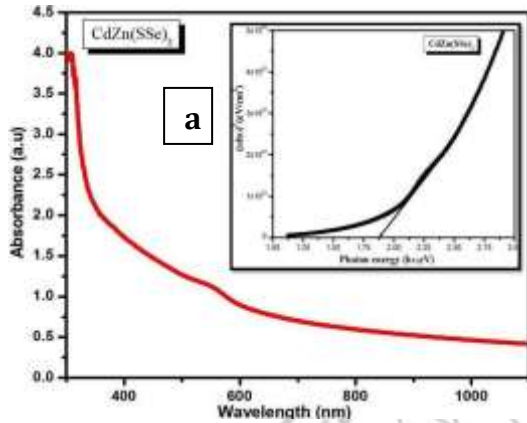


Fig. 1a) Optical absorption plot and **Inset:** band gap energy plot of synthesized thin film,

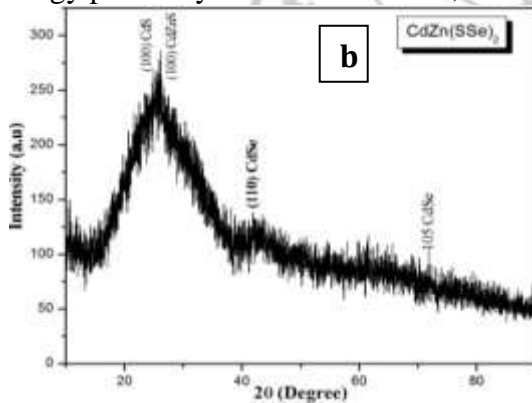


Fig. b) X-ray diffraction pattern of CdZn(SSe)₂ thin film

Fig.2 shows SEM micrograph of surface morphology of CdZn(SSe)₂ thin film which exhibits well adherent, smooth and uniform distribution of nanosphere, which cover all the substrate surface. The average grain size is calculated by standard scale bar method and is found to be 120 nm range. The EDS spectrum for CdZn(SSe)₂ film is shown in Fig.. The EDS spectrum indicates the present peaks for the Cd, Zn, S and Se elements in the synthesized thin film. Also spectrum shows peak for platinum, which is used for coating the sample during analysis.

The PEC performance of deposited CdZn(SSe)₂ thin film was checked with standard two electrode configuration, both in dark and under light illumination of a 500 W tungsten filament lamp having a light intensity of 30 mW cm⁻², in sulphide/polysulphide redox electrolyte. The

current density–voltage (J–V) characteristics of glass/FTO/CdZn(SSe)₂ / electrolyte / graphite were measured. J–V characteristic curve of CdZn(SSe)₂ thin film in dark display diode-like rectifying characteristics. Upon light illumination, the magnitude of the open circuit voltage (V_{oc}) increases with negative polarity towards the CdZn(SSe)₂ electrode, indicating cathodic behavior and which confirms that CdZn(SSe)₂ thin film is p-type. The output parameters of the PEC solar cell, i.e. light conversion efficiency (η %) and fill factor (FF), were calculated from eqn. (8) and (9), respectively.

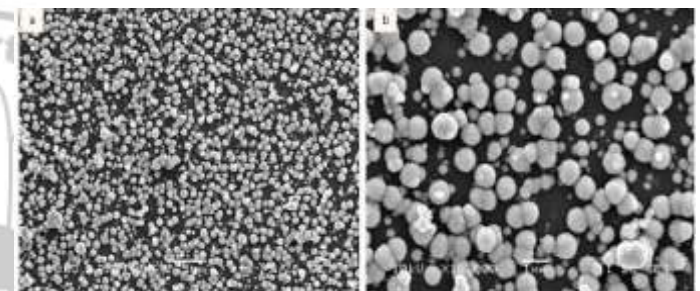


Fig.2. SEM micrographs of CdZn(SSe)₂ thin film-

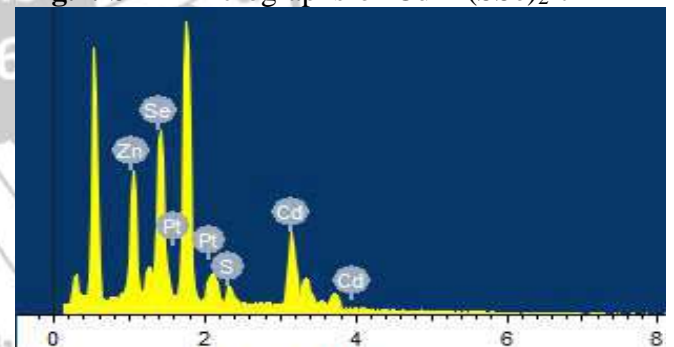


Fig. 3. EDS spectrum of CdZn(SSe)₂ thin film.

$$FF = \left(\frac{J_{max} \times V_{max}}{J_{sc} \times V_{oc}} \right) \quad (13)$$

$$\eta\% = \left(\frac{J_{sc} \times V_{oc}}{P_{in}} \times FF \times 100 \right) \quad (14)$$

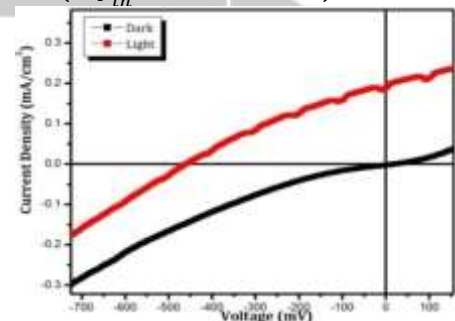


Fig.4. J-V measurement curve of CdZn(SSe)₂ thin films

Where J_{sc} is the short-circuit current density and V_{oc} is the open circuit voltage. J_{max} and V_{max} are the maximum current density and the maximum

voltage, and P_{in} is the input light intensity (30 mW cm^{-2} , 457.2 mV and 0.27 respectively. The cm^{-2}). From the J–V measurements, the obtained resultant conversion efficiency of the synthesized values of J_{sc} , V_{oc} and FF for the sample is 0.1917 thin film is 0.07% .

4. CONCLUSIONS

Deposition of CdZn(SSe)_2 thin films over a considerable range is made possible with a simple arrested precipitation technique. Optical band gap energy value was found to be 1.87 eV . The XRD study revealed the polycrystalline nature with pure hexagonal crystal structure of the CdZn(SSe)_2 thin film. The SEM micrograph shows, the presence of spherical grain structure of surface without any pinholes. EDS results confirms the presence of Cd, Zn, S and Se elemental in synthesized thin film. The J-V measurement curve shows the efficiency of CdZn(SSe)_2 film was found to be 0.07% . It reveals that CdZn(SSe)_2 thin films deposited by APT technique, show potential candidate for solar cell application.

References:

1. Wynands H, Cocivera M, J. Electrochem Soc.,139 (1992) 2052.
2. Pathan, H.M., Lokhande, C.D., Bull. Mater. Sci., 27, (2004) 85–111.
3. Chandramohan R., Mahalingam T., Chu J. P., Sebastian P. J., Solar Ene. Mater. And Sol. Cells, 81, (2004) 371.
4. Chavhan, S.D., Senthilarasu, S., Lee, S.H., App. Surf. Sci., 254, (2008) 45439-4545.
5. Jagadale S. K., Mane R. M., Bhosale P. N., Mane R. K., IEEE, (2013) (1) 567-569.
6. Jagadale S. K., Shinde D. B., R. M. Mane, Khot K. V., Ghanwat V. B., Bhosale P. N., Mane
7. R. K., Nanosystems: Phys., Chem., Mathem., 7(3), (2016) 523.
8. Jagadale S. K., Bhosale P. N., Mane R. K., Int. J. Sci. Research,5(10), (2016) 419
9. Bagade, C.S., Mali, S.S., Ghanwat, V. B., Khot, K. V., Patil, P.B., Kharade, S. D., Mane, R.M., Desai, N.D., Hong, C.K. Patil, P.S., Bhosale, P.N., RSC Adv., 5, 55658, 2015.
10. Khot, K. V., Mali, S.S., Pawar, N.B., Kharade, R.R., Mane, R.M., Kondalkar, V.V., Patil, P.B., Patil, P.S., Hong, C.K., Kim, J.H., Heo J., Bhosale, P.N., New J.Chem., 38, (2014)5964



Preparation of Nanoparticles of Bioactive Compounds for Enhanced Anti-angiogenesis Activity

Prakash Bansode^a, Gajanan Rashinkar^{a*}

^aDepartment of Chemistry, Shivaji University, Kolhapur, 416004, M.S., India.

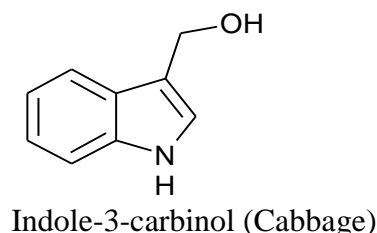
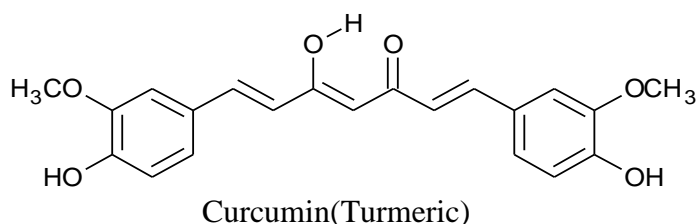
E-mail: gsr_chem@unishivaji.ac.in

Plant kingdom has been a rich source of bioactive and precursor compounds since a long time back. Many chemical constituents of plants are highly potent, nontoxic, bioactive agents found in dietary vegetables, fruits, spices and has been known for centuries as a household remedy to many ailments. There has been growing interest in cancer prevention by food plants and their products. Although several plant parts have potentials for chemoprevention and therapeutic use, some dietary plants and their phytoconstituents have modulating abilities on several signalling pathways including the inflammatory and apoptosis ones, which may be targeted for cancer therapy. (Khushnud and Mousa, 2013) Turmeric (curcumin), tea and coffee (quercetin), cabbage (Indole-3-carbinol) and the basic skeletal components of many plant pigments like vanillin, flavone, xanthone and anthraquinone have promising potential for developing as multitargeting anticancer agents.

Angiogenesis is a physiological process involving the growth of new blood vessels from pre-existing vessels. The process of angiogenesis is controlled by the balance between proangiogenic and angiogenic molecules. Angiogenesis is essential for embryonic development, organ formation and tissue regeneration and remodelling. It also contributes to the development and progression of a variety of pathological conditions including tumour growth and metastasis, cardiovascular diseases, diabetic retinopathy, rheumatoid arthritis and psoriasis. Angiogenesis plays an important role in many physiological processes like wound healing, corpus luteum formation and embryonic development. It is also important in pathological processes such as cancer, ischemic diseases and

chronic inflammation including artherosclerosis (Griffioen and Molema, 2000).

The aim of the present work is to study the angiogenesis activity of several such bioactive components from various natural products. The only disadvantage that these compounds suffer is of low aqueous solubility, poor bioavailability hindering their therapeutic applications. In the present investigation we report the preparation of nanoparticles of seven bioactive phytochemicals such as curcumin, quercetin, Indole-3-carbinol, vanillin, flavone, xanthone and anthraquinone with a view to improve their aqueous-phase solubility and examine the effect on their anti-angiogenic properties. Nanoparticles of bioactive compounds were prepared by controlled reprecipitation technique and were found to have a narrow particle size distribution in the range of 50-100 nm. The synthesized nanoparticles were characterized by UV-Visible spectroscopy, FTIR spectroscopy, NMR spectroscopy XRD, FESEM and TEM techniques. Unlike original bioactive compounds, nanoparticles were found to be freely dispersible in water in the absence of any surfactants. The chemical structures of the compounds were the same as that of curcumin, and there was no modification during nanoparticle preparation. This has been confirmed on the basis of TLC and NMR spectroscopy. *In vivo* anti-angiogenic potential of nanoparticles of bioactive compounds was evaluated using Chick Allantonic Membrane (CAM) assay and was compared to that of original compound. It was found that the aqueous dispersion of nanoparticles exhibit much more pronounced anti-angiogenic activity than the original compounds. Anti-angiogenic activity of nanoparticles was found to be markedly improved by particle size reduction up to the nano range.



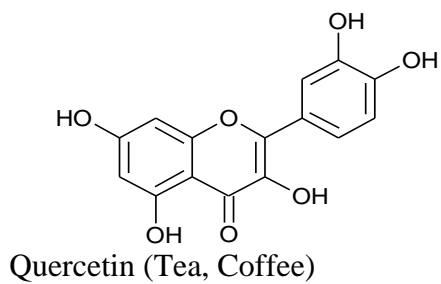
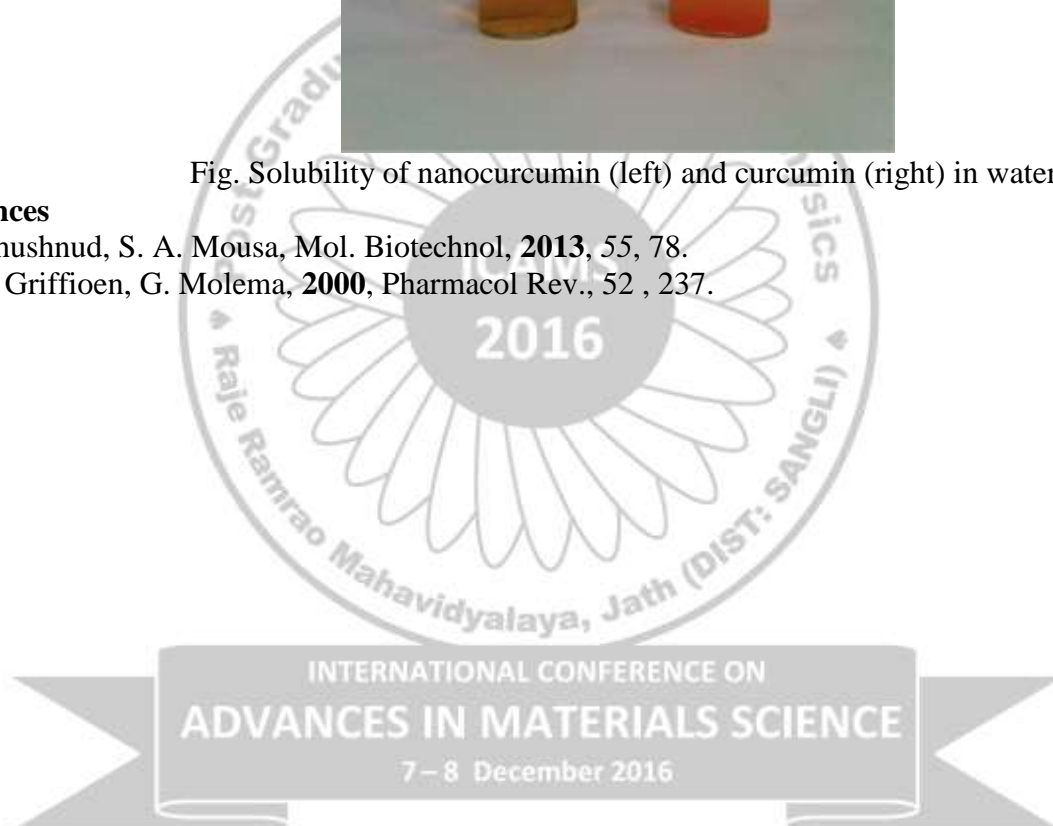


Fig. Solubility of nanocurcumin (left) and curcumin (right) in water.

References

- 1) T. Khushnud, S. A. Mousa, *Mol. Biotechnol*, **2013**, 55, 78.
- 2) AW. Griffioen, G. Molema, **2000**, *Pharmacol Rev.*, 52 , 237.



Structural and Morphological Study of LSM Thin Films as Cathode for SOFC

¹B. S. Kamble, ²V.J. Fulari, ³R. K. Nimat.

¹Department of Physics, D.B.J.College, Chiplun-415605, India

²Department of Physics, Shivaji University, Kolhapur-416004, India.

³Department of Physics, Balasaheb Desai College, Patan-415206, India.

Corresponding Author*: E-mail:- dr_rknimat@yahoo.com

Abstract

The Lanthanum strontium manganite is a mixed metal oxide ceramic material with the general formula $\text{La}_{1-x}\text{Sr}_x\text{MnO}_{3-\delta}$, where, 'x' gives doping percentage. The LSM thin film with 0.1, 0.2 and 0.3 mol % strontium were synthesized on alumina substrate by Chemical Spray Pyrolysis technique. The Structural and morphological properties of LSM thin films samples of The LSM have been studied using X-ray diffraction (XRD) and field emission scanning electron microscope. The XRD result indicated that sample have rhombohedral structure.

Keywords: Spray Pyrolysis, Cathode, LSM, SOFC.

1. Introduction

The Solid Oxide Fuel Cell has great importance as a green and an efficient device for power generation [1-4]. SOFCs are especially interesting because of their advantages respect to the other types of fuel cells: theoretical efficiency of 80-90 %, lower cost a better stability with time; although the operation temperature is still too high between 800°C – 1000°C for practical application [5]. A solid oxide fuel cell (SOFC) is a device that converts the chemical energy of fuels directly into electrical energy by an electrochemical reaction of the fuels with an oxidant. SOFCs need large quantities of strontium-doped lanthanum manganite (LSM) as cathode material in modern high capacity cell units. For each kilo-watt of power generation about 4.5 Kg of LSM is required [6]. Lanthanum strontium manganite (LSM) is considered as a classic cathode material for solid oxide fuel cells (SOFC) on account of its good electronic conductivity, mechanical and chemical stability [7]. Hence the attempts made that to form LSM thin film as possibly to reduce the operating temperature. Different methods tried out by various researchers for production of LSM are Pechni method, freeze-drying, sol-gel, glycine-nitrate, spray pyrolysis method. In the present work LSM thin films are prepared by low cost effective spray pyrolysis technique to get possibly adherent thin films.

2. Experimental:

The Lanthanum Strontium Manganite ($\text{La}_{1-x}\text{Sr}_x\text{MnO}_3$) thin films are deposited on alumina substrate by using Chemical Spray Pyrolysis technique. The basic principle used in chemical spray pyrolysis technique is that, a smallest droplet of the precursor solution sprayed from nozzle, reaches to the hot substrate leads to the pyrolytic decomposition of the solution which

forms the adherent thin films in the presence of air as neutral gas [8].

The Stoichiometric amounts of precursor Lanthanum Nitrate Hexahydrate $\text{La}(\text{NO}_3)_3 \cdot 6\text{H}_2\text{O}$, Strontium Nitrate $\text{Sr}(\text{NO}_3)_2$, Manganese Nitrate Tetrahydrate $\text{Mn}(\text{NO}_3)_2 \cdot 4\text{H}_2\text{O}$ were dissolved in double distilled water and stirred with magnetic stirrer for 10 minutes. This precursor solution is used to deposit LSM thin films on glass substrate at deposition temperature of 200°C, this further leads to pyrolytic decomposition of these metallic salts [9] and formation of Lanthanum Strontium Manganite thin film. The precursor flow rate is maintained as 10 ml/min, the nozzle to substrate distance is kept 20 cm and adherent thin films were obtained. The post deposition annealing conditions were chosen to be 2 hours at 1000°C in air. The deposited LSM thin film was used for structural and morphological characterization.

3. Result And Discussion:

The Structural and morphological characterization were done for the confirmation of the phase formation, the XRD study had done by Bruker X-Ray Powder diffractometer and the Morphological imaging had also done by Field effect Scanning Electron Microscope.

A) Structural Characterization:

The XRD patterns of the samples are shown in fig1. The XRD data is analyzed and it is found that the samples are polycrystalline with the rhombohedral structure with R-3c space group. The estimated average lattice parameters are $a=b=5.533\text{\AA}$ and $c=13.35\text{\AA}$ which are found close agreement with reported value (Shinde et.al.2011).

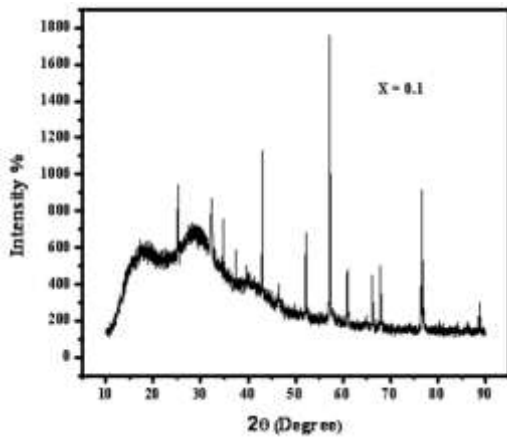


Fig. 1 .a) XRD of LSM thin films $x=0.1$ sintered at 1000°C

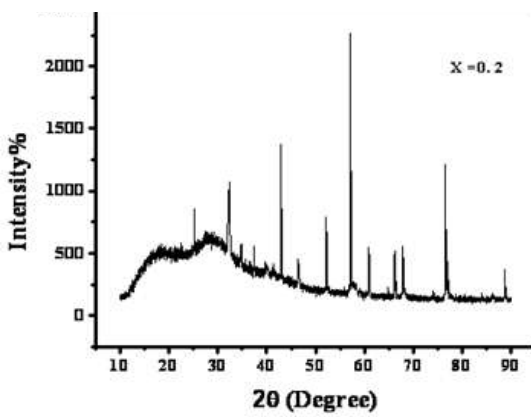


Fig.1 b) XRD of LSM thin films $x=0.2$ sintered at 1000°C

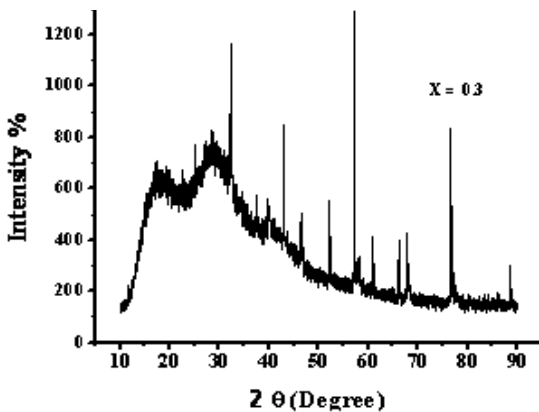


Fig.1 c) XRD of LSM thin films $x=0.3$ sintered at 1000°C

images show porous morphology, spongy aspect and good size distribution and particle separation which is applicable as cathode for solid oxide fuel cell as it is necessary in order to pass oxygen ions at cathode-electrolyte interface. The phase formation takes place after annealing at 750°C for 2 hours in air as compared to before annealing the LSM thin film.

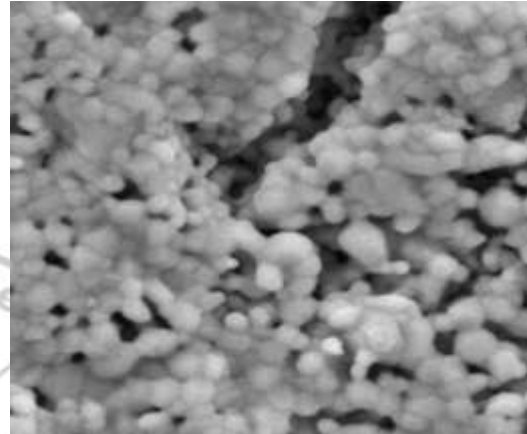


Fig.2 a) FESEM images of LSM thin films $x=0.1$ sintered at 1000°C

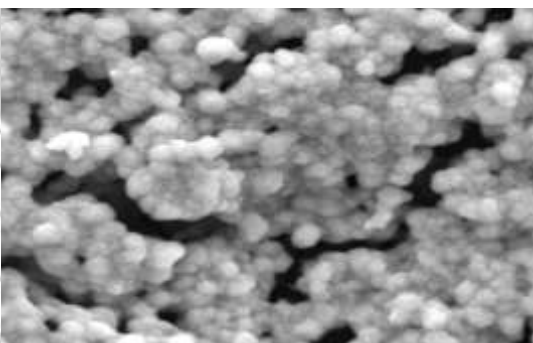


Fig.2 b) FESEM images of LSM thin films $x=0.2$ sintered at 1000°C

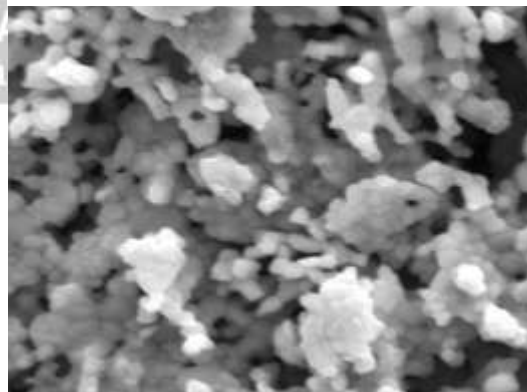


Fig.2 c) FESEM images of LSM thin films $x=0.3$ sintered at 1000°C

B) Morphological Characterization:

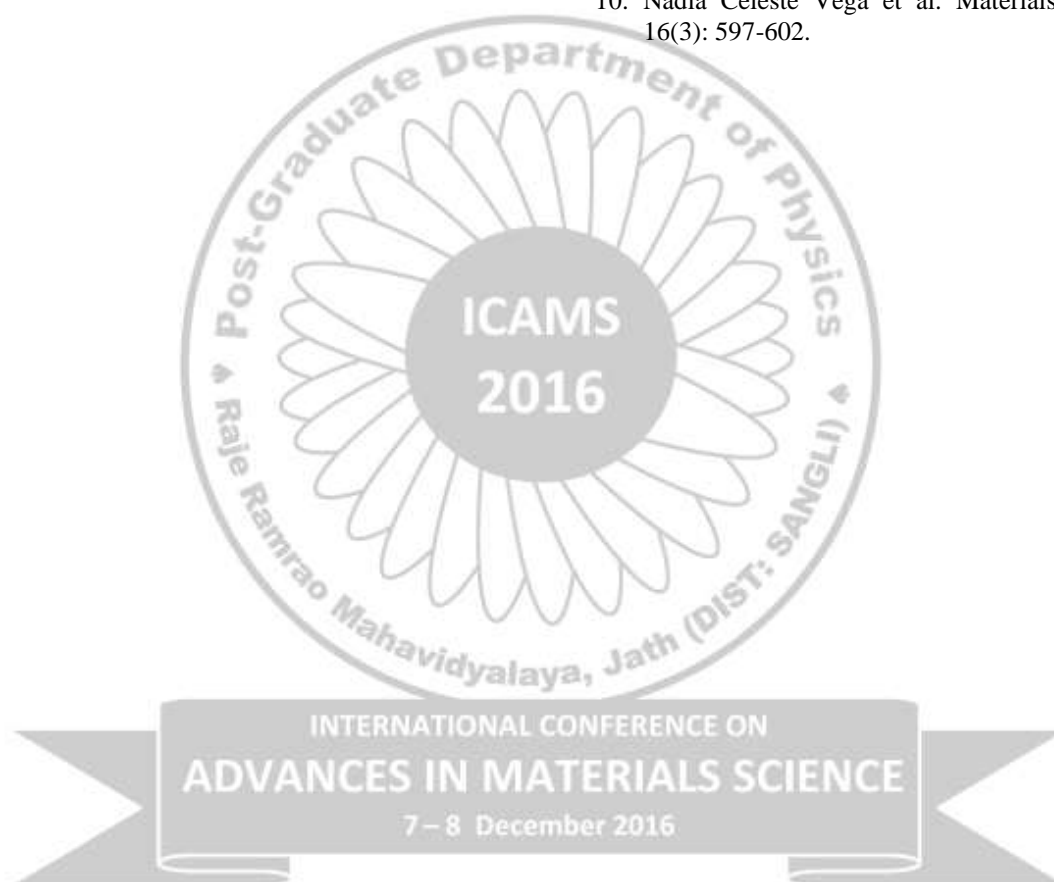
The morphology study of LSM thin film made by Field effect Scanning Electron Microscope. Fig.2. shows porous morphology. The porosity composed due to crystallites of Lanthanum Strontium Manganite^[10]. The FESEM

4. Conclusion

Continuous homogenous and crack-free, porous LSM nanosized thin films samples could be synthesized successfully by spray pyrolysis technique. Thin film porosity and thickness management is an advance for further SOFC applications because they induce polarization resistance at the air/cathode/electrolyte interface by optimizing the triple phase boundary lines. The performance and durability of SOFCs depend strongly on the microstructure and morphology of cell component.

Reference

1. R.K. Nimat, C.A. Betty, S.H.Pawar, Applied Surface Science 253 (2006) 2702-2707.
2. A.B. Stambouli, E. Traversa, Renewable and Sustainable Energy Reviews 6(2002) 433-455.
3. P.Charpentier, P. Fragnaud, D. M.Schleich, E. Gehain, solid state ionics 135 (2000) 373-380.
4. S.C.Singhal, Solid state ionics 135 (2000) 305-313.
5. R.Moriche, D. Marrero-Lopez, F.J. Gotor, M,J.Sayages, Journal of power sources 252 (2014) 43-50
6. S.Saha, S.J.Ghanawat, R.D. Purohit, J. Matter. Sci.41 (2006) 1939-1943.
7. Deepu J. Babu, Azad J. Darbandi, Jens Suffner, S.S. Bhattacharya and Horst Hann, Transactions of Indian Institute of metals, vol. 64. Issues 1&2 February- April 2011. pp. 181-184.
8. P.S. Patil, Materials Chemistry and Physics 59 (1999) 185-198.
9. R.Thiagarajan et al., Journal of American Science 2009; 5(6):51-56.
10. Nadia Celeste Vega et al. Materials Research. 2013; 16(3): 597-602.



CoFe₂O₄@SiO₂ core shell magnetic nanoparticles as a novel adsorbent for aqueous heavy metal removal

Shivaji V Bhosale[†], S.V.Bhoraskar⁺, and V.L.Mathe⁺

[†]Sir Parashurambhau College, Department of Physics, Pune-411030

⁺Savitribai Phule Pune University, Department of Physics, Pune, 411007

Presenting author: bhosale3399@gmail.com

Abstract

Heavy metals in aquatic system pose a severe threat to the public health and ecological systems. For the effective removal of these heavy metals a novel CoFe₂O₄@SiO₂ core-shell magnetic nanomaterial was developed. Here the CoFe₂O₄ nanoparticles were synthesized by dc thermal plasma arc at 500 Torr and 6 kW of dc power. Moreover the SiO₂ coating was carried out on these nanoparticles and was characterized by X-ray diffraction method and Fourier Transform Infrared spectroscopy (FTIR). The CoFe₂O₄@SiO₂ exhibited high adsorption affinity for Cu(II) ions. Findings of the present work highlight the potential use of CoFe₂O₄@SiO₂ magnetic nanoparticles as an effective and recyclable adsorbent for the removal of heavy metal ions in water and waste water treatment.

1. Introduction

Industrial wastes often causes serious water, air and soil pollution. Heavy metals are frequently found in wastewaters originating from chemical manufacturing, painting and coating, mining, extractive metallurgy, nuclear and other industries [1,2]. Copper is considered to be one of the most toxic metals in the waste water. A number of approaches, such as reduction, precipitation, ion exchange, reverse osmosis, adsorption and coagulation have been suggested for the removal of copper from industry effluents. Among these methods, selective adsorption deserves particular attention, because the sorbent materials can be made highly efficient and easy to handle.

Magnetic separation provides a convenient method for separation of solid particles in a multiphase suspension [3]. To further facilitate the adsorption affinity, surface modification, including physical coating and covalent binding has often been explored to enable specific metal complexation. Unfortunately, the most commonly used magnetic sorbents are based on iron oxides which are susceptible to leaching under acidic conditions.

Cabnas et al. reported the adsorption of metal ions on the metal oxide particles by formation of two surface complexes. The -XOCO⁺ and -(XO)₂Co is formed between the Co²⁺ and -XOH sites of magnetite [4]. Therefore, the present study aims at understanding the adsorption mechanism between Cu(II) ions and cobalt ferrite coated SiO₂ nanoparticles.

Griginova et al. reported the removal of heavy metals by using SiO₂ coated Fe₃O₄ nanoparticles [5]. The inorganic shell not only provides stability to the nanoparticles by

preventing their oxidation but also helps in selective uptake of ions. SiO₂ is stable under acidic conditions and inert to redox reactions as compared with the organic coating materials and hence functions as an ideal shell composite to protect the inner magnetite core. Silanation has been the most promising avenue for the adsorption of heavy metals.

2. Experimental

The nanoparticles of cobalt ferrite were synthesized by gas phase condensation method using dc thermal plasma arc reactor. During synthesis the pressure inside the chamber was maintained at 500Torr and power at 6kW. The micron sized powder of Co and Fe was mixed in the molar ratio of 1:2 to prepare the required pellets. The plasma plume of argon gas was made to strike on the pellets which cause its evaporation. These evaporated metal ions further reacts with ambient oxygen ions present in the chamber. The steep temperature gradient results in constraining the growth of particles.

Silica coating of CoFe₂O₄ magnetic nanoparticles synthesized by dc thermal plasma arc was carried out by alkaline hydrolysis of TEOS. Here, 100mg of CoFe₂O₄ nanoparticles were dispersed in 100ml ethanol. The suspension was thoroughly sonicated for 15min. Consequently, ammonia solution (10ml) and TEOS (200ml) were added and the suspension was further sonicated for 2 hrs. Finally the particles were washed thoroughly with initially with ethanol and finally with distilled water.

2.1 Adsorption of Cu(II) ions

The 20 mg of as-synthesized CoFe₂O₄@SiO₂ nanoparticles (adsorbent) were added in 100 ml of Cu²⁺ solution. The Cu(NO₃)₂ salt was added in 100ml of water to prepare the

requisite Cu(II) solution. The external parameters which affect the adsorption were kept constant. The effect of Cu(II) concentration was studied by changing the concentration in the range from 25mg/L to 200mg/L. The amount of Cu(II) adsorbed on the CoFe₂O₄@SiO₂ nanoparticles (q_e) was calculated by using mass balance equation.

$$q_e = (C_i - C_f)V/m \quad (1)$$

where, C_i is initial concentration, C_f is final concentration, V is total volume of the solution and m is total mass of the CoFe₂O₄@SiO₂ nanoparticles added into the solution. The concentration C_i and C_f were calculated by using atomic absorption spectroscopy (AAS).

3. Results

Fig. 1 shows the XRD pattern for CoFe₂O₄@SiO₂. The peaks observed agree with the standard pattern of CoFe₂O₄ phase in both the cases. The average crystallite size calculated from the scherrers equation is approximately 24 nm. The same characteristic peaks observed is found in CoFe₂O₄@SiO₂ suggests that the crystallite structure does not change after the surface modification.

The shoulder at 1078 cm⁻¹ present in the FTIR spectrum of this sample is composed of contributions from Si-O-H stretching and Fe-O vibrations. As no substantial shifts are observed when coated and non coated spectra are compared the formation of Fe-O-Si bonds may not be evoked (3).

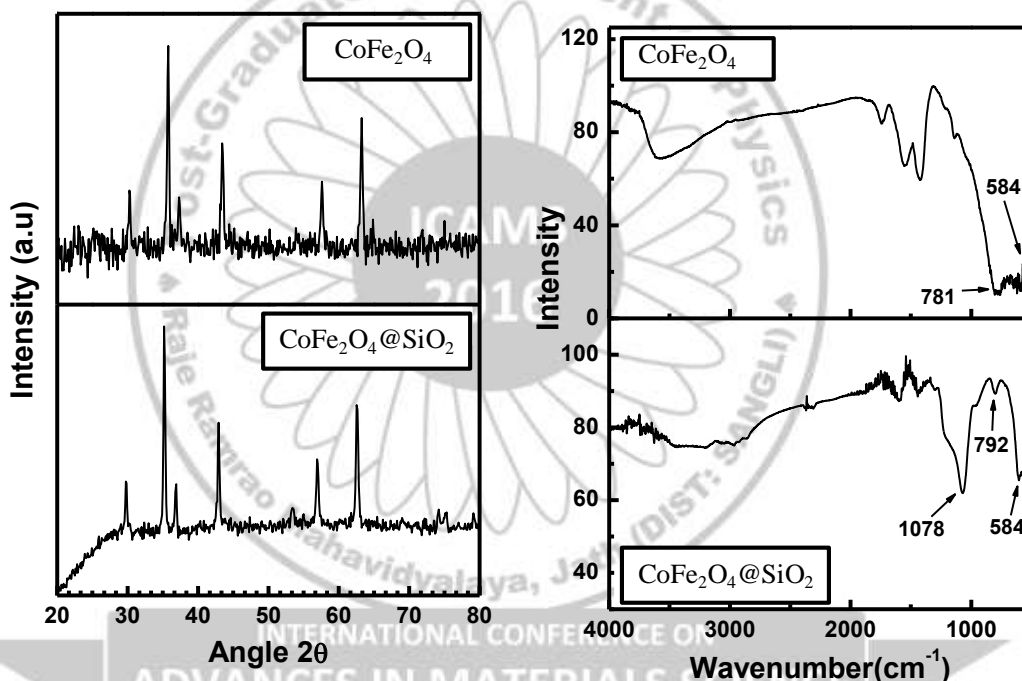


Fig. 1. (a) XRD spectra of CoFe₂O₄ and SiO₂ coated CoFe₂O₄ nanoparticles (b) FTIR Spectra of bare CoFe₂O₄ and SiO₂ coated CoFe₂O₄ nanoparticles.

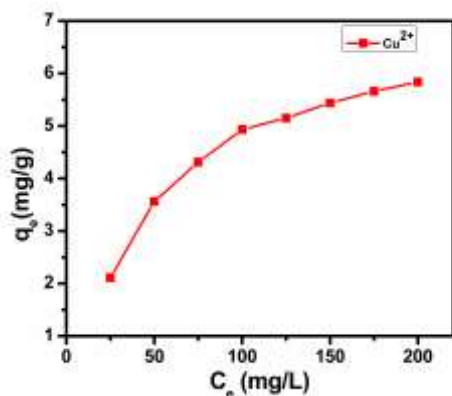


Fig. 2. Effect of concentration on the adsorption of Cu(II) ions from the solution.

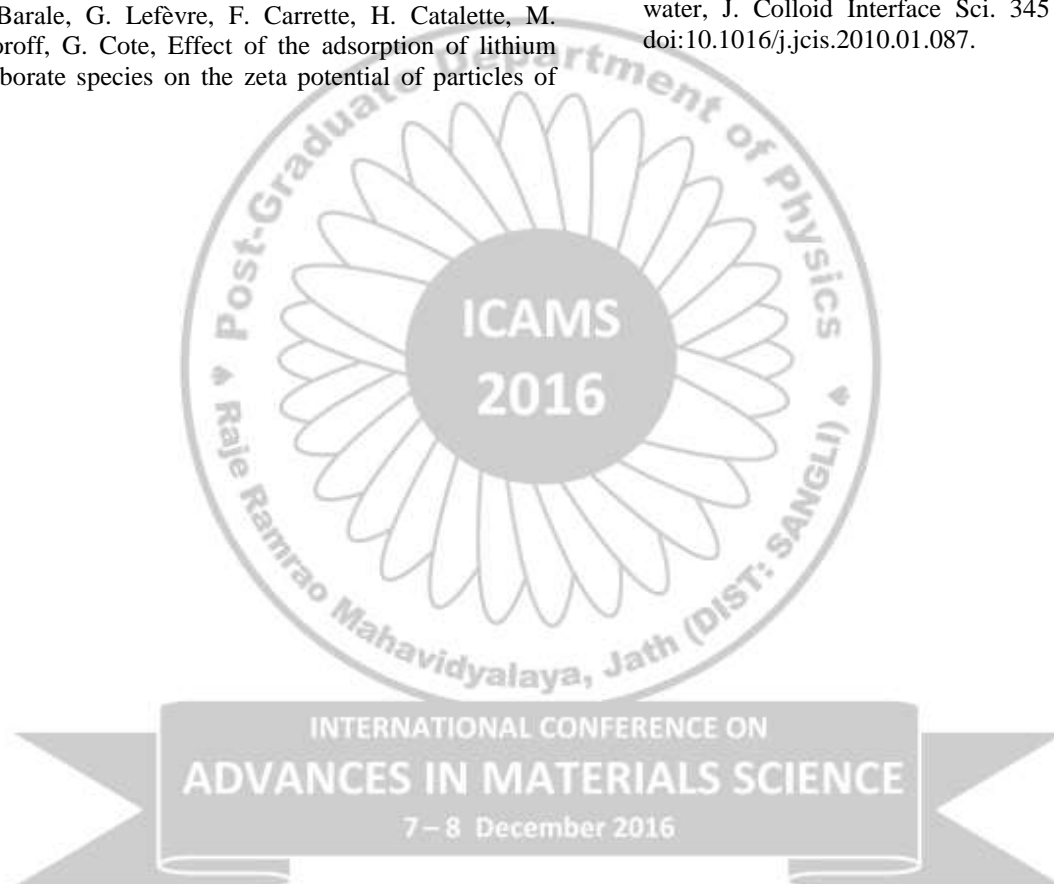
From Fig. 2 it can be observed that the amount of adsorption of Cu²⁺ increases with increase in concentration of Cu²⁺ ions. However, after 100mg/L the adsorption seems to have attained equilibrium. This phenomenon is observed due to increase in the Cu²⁺ concentration gradient initially but later on this gradient is ineffective in forcing the adsorption because of increase in the repulsion caused by already adsorbed Cu²⁺ ions. The observed adsorption phenomenon is possibly due to electrostatic interaction between the particles and the ions.

4. Conclusion

The dc thermal plasma can be used to synthesize highly crystalline cobalt ferrite magnetic nanoparticles for the magnetic separation purpose. The Cobalt Ferrite coated SiO₂ magnetic nanoparticles are effectively used for the removal of heavy metals from the aqueous solution. The high adsorption capacity observed for Cu²⁺ ions is due to electrostatic interaction between the particle surface and ions.

References

1. J. Song, H. Kong, J. Jang, Adsorption of heavy metal ions from aqueous solution by polyrhodanine-encapsulated magnetic nanoparticles, *J. Colloid Interface Sci.* 359 (2011) 05–511. doi:10.1016/j.jcis.2011.04.034.
2. T. Tuutijärvi, J. Lu, M. Sillanpää, G. Chen, As(V) adsorption on maghemite nanoparticles, *J. Hazard. Mater.* 166 (2009) 1415–1420. doi:10.1016/j.jhazmat.2008.12.069.
3. M. Barale, G. Lefèvre, F. Carrette, H. Catalette, M. Fédoroff, G. Cote, Effect of the adsorption of lithium and borate species on the zeta potential of particles of cobalt ferrite, nickel ferrite, and magnetite, *J. Colloid Interface Sci.* 328 (2008) 34–40. doi:10.1016/j.jcis.2008.09.007.
4. B. Martin Cabañas, S. Leclercq, P. Barboux, M. Fédoroff, G. Lefèvre, Sorption of nickel and cobalt ions onto cobalt and nickel ferrites., *J. Colloid Interface Sci.* 360 (2011) 695–700. doi:10.1016/j.jcis.2011.04.082.
5. P.I. Girginova, A.L. Daniel-da-Silva, C.B. Lopes, P. Figueira, M. Otero, V.S. Amaral, et al., Silica coated magnetite particles for magnetic removal of Hg²⁺ from water, *J. Colloid Interface Sci.* 345 (2010) 234–240. doi:10.1016/j.jcis.2010.01.087.



Optimized thermal treatment for hydrothermally grown stabilized nanostructured WO₃ thin films in electrochromic applications

A. V. Kadam, N.Y. Bhosale

D. Y. Patil College of Engineering & Technology, Kasaba Bawada, Kolhapur, Maharashtra (India) – 416006, E-mail: anamikasonavane@rediff.com

Abstract:

This research article consist of the hydrothermal synthesis of nanostructured tungsten oxide (WO₃) embedded with propylene glycol and its electrochromic (EC) performance. In this article, we developed a facile seed –layer -free hydrothermal approach for preparing WO₃ thin films with improved EC performance at optimized thermal treatment. Structural and morphological properties were studied using X-ray diffraction and scanning electron microscopy. The electrochemical stability of the propylene glycol (PG) assisted nanostructured WO₃ film was examined in lithium per chlorate-propylene carbonate (LiClO₄-PC) electrolyte for prolonged color/bleach cycles. The results showed an improvement in electrochemical stability with fast response time.

Keywords: Hydrothermal synthesis, tungsten oxide, smart window, electrochemical stability

1. Introduction:

Inorganic materials, such as WO₃, have received wide attention because of their potential applications. Among its diverse applications, the electrochemical properties of WO₃ have been extensively studied for several years [1], wherein most results concluded that the blue color was due to the reduction of WO₃ by atomic hydrogen. Recent research investigated various WO₃ nanostructures [2, 3-6] with various crystal structures that have crucial applications in a smart window. In particular, the nanoscale architecture of WO₃ improves the surface to volume ratio, thereby producing quantum confinement effect [7]. Significantly, monodispersed nanoparticles with control over size and morphology are essential, and this control strongly depends on the method of preparation.

Among various methods, hydrothermal synthesis offers promising advantages over the conventional methods of synthesis, such as producing low-temperature polymorphs, low reaction time, rapid growth rates due to the rapid diffusion processes, including simplicity, low cost, high product purity, and the ability to control the particle size [8]. Various hydrothermal methods have been developed for preparing WO₃ nanostructures, by adding different inorganic materials as capping agents. Particularly, two methodologies are common in the previous studies on WO₃ smart windows, with or without a seed layer.

Most of the reports reveals the synthesis of WO₃ by hydrothermal treatment is a facile, inexpensive, and green technique, which can be used to produce WO₃ or WO₃.nH₂O of different nanomorphologies by using tungstic acid or sodium tungstate (H₂WO₄ or Na₂WO₄) as a

precursor [9, 10]. However, residual sodium (Na) is a persistent contaminant in the products, which may affect the performances of materials negatively [11, 12]. In addition, ethylene glycol is toxic and its alternatives are required.

Previous studies on hydrothermal synthesis of WO₃ thin films for EC application reveals that WO₃ films can be prepared on a seed-layer coated conducting glass substrate [2, 13-14]. Although, significant results were achieved, the EC performance of hydrothermally grown WO₃ films could be improved. In the present research, we demonstrated seed-layer free synthesis of nanostructured WO₃ films directly on indium tin oxide (ITO)-coated glass substrates assisted by PG using the hydrothermal method. Subsequently, an annealing effect on the structural, morphological and EC performances of the film was examined.

2. Experimental section

All the analytical reagent grade chemicals sodium tungstate (98% Na₂WO₄.2H₂O), propylene glycol (99.5% C₃H₈O₂), lithium perchlorate trihydrate (99% LiClO₄.3H₂O), propylene carbonate (99% C₄H₆O₃), hydrogen peroxide (H₂O₂) and hydrochloric acid (HCl) were purchased from Loba Chem chemicals reagent company and used without further purification. All the aqueous solutions were prepared using double distilled water (DDW). ITO glass plates (10 Ω cm⁻², 3.5×1.0 cm²) were used as substrates that were previously cleaned with aqueous detergent, ultrasonicated in acetone, and ethanol followed by rinsing with DDW.

The procedure for preparing the precursor solution is discussed in earlier article [15]. The as-deposited film is represented as A-WO₃. Subsequently, A-WO₃ film was annealed at 400 °C

for 2h represented as B-WO₃ and was used for further characterization.

The morphologies of A-WO₃ and B-WO₃ films were characterized using scanning electron microscopy (SEM, Hitachi S-4700 II, 25 kV). X-ray diffraction (XRD, Thermo ARLSCINTAG X'TRA with copper K α irradiation, $\lambda = 0.154056$ nm) was used to analyze the crystallinity. The electrochemical and EC studies were performed using a three-electrode system (CH instruments, electrochemical analyzer, model-608) with LiClO₄ as the electrolyte, graphite as the counter electrode, and standard calomel electrode (SCE) as the reference electrode.

3. Results and discussions

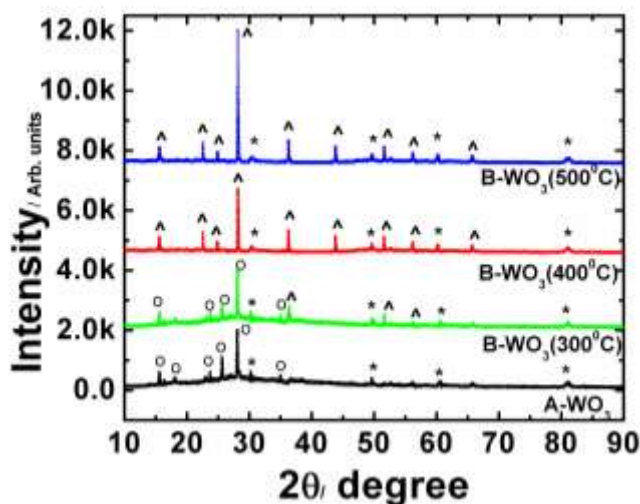


Fig. 1 X-ray diffraction patterns for (a) A-WO₃, and (b) B-WO₃ samples where asterisk specifies the peaks of ITO. The standard JCPDS data (54-1012) for A-WO₃ and JCPDS No. 00-033-1387 for B-WO₃ is indicated as sample peaks.

Figure 1 Shows the XRD patterns of the samples A-WO₃ and B-WO₃ films annealed at 300°C, 400°C and 500°C. The XRD spectra for A-WO₃ film revealed that the as-prepared film was of WO₃ hydrate, and all diffraction peaks can be indexed to the orthorhombic ($a \neq b \neq c$; $\alpha = \beta = \gamma = 90^\circ$) phase of WO₃·0.33H₂O (JCPDS Card no. 54-1012) represented as □ in figure. Peaks indicated by asterisk (*) are the diffraction peaks of ITO [16]. XRD pattern of B-WO₃ (300°C) film shows the mixed phase of orthorhombic and hexagonal structures. Above 400°C, the crystallinity of WO₃ changes to hexagonal phase ($a = b \neq c$; $\alpha = \beta = 90^\circ$, $\gamma = 120^\circ$) represented as □ wherein all the observed diffraction peaks are well indexed with h-WO₃ [JCPDS No. 00-033-1387]. Annealing may relieve the strain due to lattice

mismatch and also modify the surface morphology with the formation of specific structural phases. Consequently, the nucleation and growth of the crystals occur almost entirely on the surface developing a thick coating. The hygroscopic features of PG might be responsible for the small increase in the porosity [17-18].

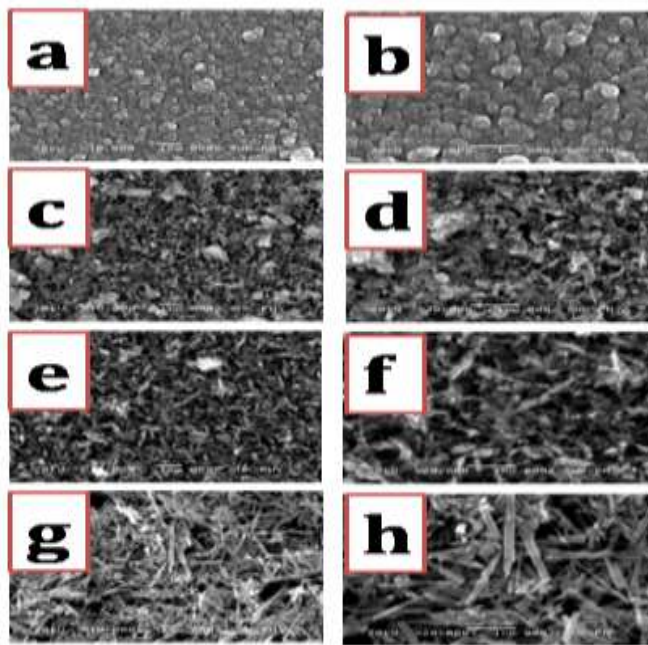


Fig. 2 Scanning electron microscopy for (a,b) WO₃ before annealing (A-WO₃), (c,d) WO₃ annealed at 300°C, (e,f) WO₃ annealed at 400°C (B-WO₃) and (g,h) WO₃ annealed at 500°C, deposited onto ITO coated conducting glass substrates. All the films are recorded at $\times 10,000$ and $\times 20,000$ magnifications.

The morphologies of A-WO₃ and B-WO₃ samples without seed layer are shown in Figure 2. The SEM images (Figure 2a, 2b) for A-WO₃ sample show that there is a collection of grains clumped together that may be due to absorption of water. The size of grains in this sample was in the range of 200-400 nm. A B-WO₃ sample (Figure 2c-2h) demonstrated hatched grains with increased porosity, having a pore size of 100-500 nm. This may be due to the hygroscopic properties of PG [17] that is the holding capacity of water in grains which hatch the grain during annealing. The morphological study indicates nucleation and growth of WO₃ nanoparticles changes from nanograins to nanorod with increase in temperature.

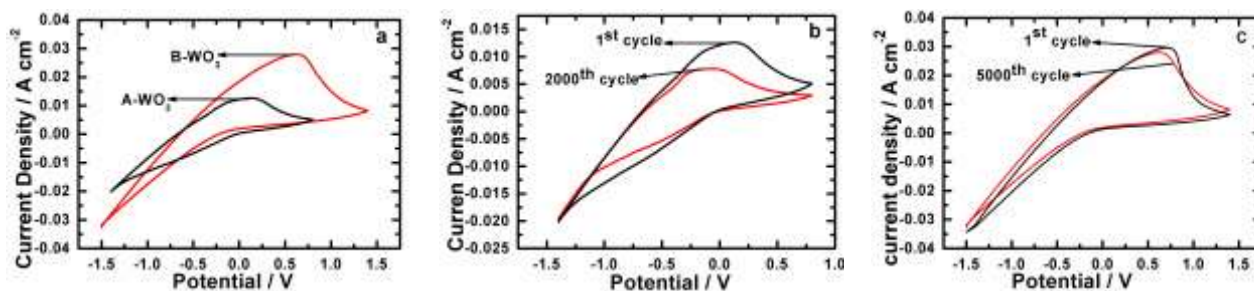


Fig. 3 (a) CV recorded in 0.5 M LiClO₄-PC electrolyte for A-WO₃, and B-WO₃ (b) stability of A-WO₃ film for 1st and 2000th cycle and (c) stability of B-WO₃ (400°C) film for 1st and 5000th cycle. The potential is swept from -1.4 to +0.75 V (vs SCE) for A-WO₃ and -1.5 to +1.5 V (vs SCE) for B-WO₃ at the scan rate of 20 mV s⁻¹.

Cyclic voltammogram (CV) curves were recorded to inspect the cause of the moderately good EC aspect for A-WO₃ and B-WO₃ films at room temperature using the three-electrode configuration system between -1.4 to +0.75 V and -1.5 to +1.5 V (vs SCE) respectively shown in Figure 3a. During each scan, the films changed color reversibly from blue to colorless.

The B-WO₃ film at 400°C displayed higher current density and faster Li⁺ intercalation/deintercalation mechanisms over an equal time duration than those of the A-WO₃ and B-WO₃ film annealed at 300 and 500°C. This may be due to the formation of pores among the nanostructures of B-WO₃ (400°C) film that could increase the interface between the anode and electrolyte, facilitating the hole transfer efficiently

[19]. Here PG plays a significant role of plasticizer increasing the intermolecular separation between molecules [20].

Electrochemical stability is another essential parameter for EC materials. To examine the stability of ion intercalation/deintercalation, CVs were recorded between -1.4 V and +0.75 V for the 1st and 2000th cycles (Figure 3b) for A-WO₃ film at room temperature. A large change was observed in the current densities and shape of CV curves after 2000 cycles. However, B-WO₃ (400°C) film showed excellent cyclic stability (Figure 3c) approximately 5000 c/b cycles with a very small amendment in the shape of CV curve. This indicates the high stability of the B-WO₃ film compared with that of the A-WO₃ film and with earlier reports [2, 13].

4. Conclusion

In this paper, we proposed an optimized temperature to develop electrochemically stabilized hydrothermally grown WO₃ thin films. In conclusion, large quantity WO₃ nanorods have been synthesized through a hydrothermal method. Structural characterizations by XRD and SEM revealed that WO₃ nanorods possess hexagonal phase. EC study showed improved electrochromic cycling stability (5000 c/b cycle). Thus, a seed layer free synthesis of WO₃ nonporous structures can speed up the electron carrier to the ITO glass and increases the ion intercalation/deintercalation efficiency compared with the thin films prepared using a seed layer.

Acknowledgement

The authors would like to express gratitude to the Department of Science & Technology (DST), Science & Engineering Research Board (SERB), New Delhi, India for full financial support (SERB Sanction Order No and date: SB/FTP/PS-030/2013, Date: 21.02.2014).

References

- Kobosev NI, Nekrasov NZ (1930) *Electrochem.* 36:529-544
- Jiao Z, Sun XW, Wang J, Ke L, Demir HV (2010) *J Phys D: Appl Phys* 43:285501-285506
- Zhang J, Tu JP, Xia XH, Wang XL, Gu CD (2011) *J Mater Chem* 21:5492-5498
- Li H, Shi G, Wang H, Zhang Q, Li Y (2014) *J Mater Chem A*, 2:11305-11310
- Song X, Zhao Y, Zheng Y (2006) *Mater Letters* 60:3405-3408
- Zheng F, Zhang M, Guo M (2013) *Thin Solid Films* 534:45-53
- Houweling ZS, Harks PPRML, Kuang Y, van derWerf CHM, Geus JW, Schropp REI (2015) *Thin Solid Films* 575:76-83
- A.T. Chien (1998) *Hydrothermal Epitaxy of Perovskite Thin Films*, Doctor of Philosophy, University of California
- Zhao ZG, Miyauchi M (2008) *Angewandte Chemie International Edition* 47:7051-7055
- Rajagopal DN, Mangalaraj D, Djaoued Y, Robichaud J, Khyzhun OY (2009) *Nanoscale Research Letters* 4:8-14
- Huang K, Pan Q, Yang F, Ni S, Wei X, He D (2008) *J of Physics D: Applied Physics* 41:155417-155420
- Stoycheva T, Vallejos S, Blackman C, Moniz SJA, Calderer J, Correia X (2012) *Sensors and Actuators B: Chemical* 161:406-413
- Jiao Z, Wang J, Ke L, Liu X, Demir HV, Yang MF, Sun X W (2012) *Electrochim. Acta* 63:153-160
- Jiao Z, Wang X, Wang J, Ke L, Demir HV, Koh TW, Sun XW (2012) *Chem Commun* 48:365-367
- Kadam AV (2016) *Journal of Applied Electrochemistry*, 46:1-8.
- Kumar VB, Mohanta D (2011) *Bull Mater Sci* 34:435-442
- Karimi M, Sahraian B, Naghipour F, Sheikholeslami Z, Davoodi MG (2013) *International Journal of Agriculture and Crop Sciences* 5(11):1209-1213
- Pourfarzad A, Khodaparast MHH, Karimi M, Mortazavi SA, Davoodi MG, Sourki AH, Jahromi SHR (2011) *Journal of food process engineering* 34:1435-1448
- Jiao Z, Wang J, Ke L, Sun XW, Demir HV (2011) *ACS Appl Mater Interfaces* 3:229-236
- Snejdrova E, Dittrich M (2012) *Pharmaceutically Used Plasticizers, Recent Advances in Plasticizers: Luqman M (Ed.), InTech, Europe, pp 45-68*

Photoluminescence Properties of ZnO thin films prepared by spray CVD technique

S. C. Yadav¹, M. D. Uplane^{2*}

¹Head & asst. Prof., Dept. of Physics, Miraj Mahavidyalaya, Miraj; Dist: Sangli; Maharashtra-416410;

²Head & Professor, Dept. of Instrumentation Science, Savitribai Phule Pune University-411007

Email: scyadav12@gmail.com, mduplane@gmail.com.

Abstract

Thin films of ZnO have been synthesized for varying substrate temperature in the range of 190°C to 220°C in steps of 30°C on a glass substrate by a novel, newly fabricated, homemade spray CVD technique. Structural analysis of as deposited thin films has been investigated by X-ray diffraction (XRD) technique. It is observed that, substrate temperature 220°C offers maximum crystallite size for undoped ZnO thin film. This increase in crystallite size shows predominant role of temperature on crystal growth kinetics. The surface morphology and topography of these films have been characterized by FESEM and AFM techniques. FESEM morphology reveals pyramidal shaped enlarged grains of length ~ 2µm and somewhat periodic arrangement of grains. Optical transmittance measured using a double-beam spectrophotometer reveals that the average optical transmittance of films increases with increasing substrate temperature showing maximum transparency at 220°C. The transmittance curve indicates interference fringe pattern between the wave fronts generated at the two interfaces (air and substrate). The extinction coefficient of the films is nearly equal to zero which suggests there is no absorption of light at grain boundary. To examine the luminescence spectra of undoped ZnO thin film fabricated at various substrate temperatures the photoluminescence measurements were carried out at room temperature with an excitation wavelength of 325 nm. It reveals strong near band edge UV emission for substrate temperature 220°C

Keywords: Transparent, CVD Technique, X-Ray Diffraction, FE-SEM, AFM

1. Introduction:

Applications of thin films range from micrometre dots in microelectronics to the coatings of several square meters on window glasses. Hence, thin film physics and technology is a keystone in modern applied physics. It is the prime need of this informative, global society, to develop technology at nanoscale level which is also a fascinating research. This enables researchers to create thin film systems. In view of this aspect we have done an innovative attempt to develop thin films by a novel, newly fabricated, homemade spray CVD technique.

Due to the increased need of society for solid state light sources and detectors in the blue, violet and UV spectral ranges [1, 2] all wide bandgap semiconductors such as GaN, ZnS, InO have been extensively studied. With binary semiconductors such as GaN and alloys light emitting diodes and laser diodes were developed in the visible spectral range (460 nm). However, among all these semiconductors, ZnO is considered to be more favourable for creating UV light emitting diodes and laser diodes, since the binding energy of excitons in it is considerably higher (60 meV) than in GaN (25 meV) [2]. It is one of the promising materials in the field of thin film technology. It allows efficient excitonic emission at room temperature [2]. It opens the prospect of fabricating semiconductor lasers in uv spectral region. It has the unique optical and electrical properties which can be used in variety of applications, such as high transmittance

conductive coating oxides for solar cell [3], SAW devices[4], gas sensors[5], UV photo detectors, laser diodes [6,7]. Information storage device, heat mirrors, transparent electrodes [8]. Zinc oxide has been used in medical treatment for quite number of years in China. The objective of this work was to synthesize ZnO thin films for the study of optical and luminescence properties

2. Experimental Technique:

Thin film of ZnO had been deposited by using 0.075M solution of Zinc acetate dihydrate in methanol, at 200 ml. Compressed air having constant flow rate of 10 lpm was used as a carrier gas with constant solution flow rate of 6ml/min. Preheated glass substrates kept at low temperature offers initial nucleation growth for deposition of thin film. During deposition the substrate temperature had been varied in the range of 190°C to 220°C in steps of 30°C by keeping the reaction chamber temperature constant. The crystallinity of as deposited thin films was investigated by using a Bruker AXS X-ray diffractometer. A double-beam spectrophotometer (Shimadzu UV-1800model), with an uncoated substrate in the reference path of the beam was used for optical measurement of thin films in the spectral range of 290–1100 nm. Photoluminescence spectra of the samples were recorded with a spectrofluorimeter JASCO, model –F.P.-750, Japan using a 325nm line of an ultraviolet lamp as an excitation source.

3. Results and Discussion

3.1a Structural Properties

The crystal structure and orientation of the ZnO thin films were investigated by X-ray diffraction (XRD) patterns. The XRD spectra for ZnO thin films with variation of substrate temperature from 190⁰C to 250⁰C in steps of 30⁰c are as shown in fig. 1. It shows three well-defined peaks, identified as the (100), (002), and (101) diffraction planes of ZnO, along with less intense peaks (102), (110), (103), (200), (112) indicating the polycrystalline wurzite structure of ZnO. The d values of thin films were in good agreement with those reported in the PDF for ZnO (JCPDS card file no: 80-0075, a = 3:24982 and c = 5.20661 Å). All the samples show enhanced intensities for the peak corresponding to (002) plane, indicating preferential orientation along the c-axis. B. J. Lokhande et al [9] have already reported the synthesis of highly oriented ZnO thin films along the (002) direction.

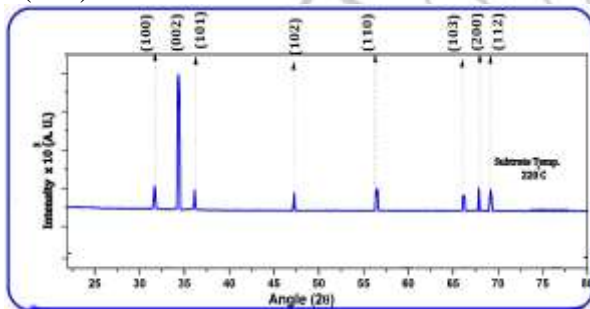


Fig. 1 A typical XRD patterns of ZnO thin films for substrate temperature 220°C

3.1b. Topographical Characterization

Figure 2 shows 3D topography (for 220⁰C substrate temperatures) of pure ZnO thin films synthesized by spray CVD technique.

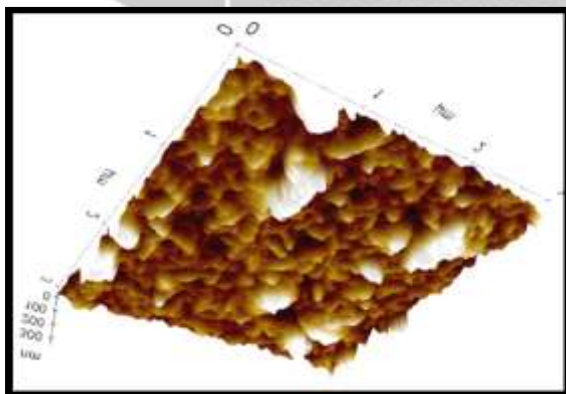


Fig. 2 (3D) Topography of ZnO thin film for a typical 220⁰C substrate temperature

The 3D topography of the typical sample shows large height of triangular shaped pyramids which confirms vertically aligned growth of crystal

structure (along c-axis perpendicular to substrate) as observed with X ray diffraction technique.

3.3 Optical Absorption Studies

The room temperature transmittance spectrum of ZnO thin films grown at various substrate temperatures is as shown in Figure 3. It reveals interference phenomena between the wave fronts generated at the two interfaces (air and substrate) which causes the sinusoidal behaviour of the curves. These films exhibited good transparency in the visible and infrared region which is higher than 83% with a sharp fundamental absorption edge. It reveals that the increased crystallinity with increase in substrate temperature may affect transparency of thin films.

The Photoluminescence measurements were carried out at room temperature with an excitation wavelength of 325 nm. It shows a strong peak at 375nm (3.26eV). The broad and intense PL band is associated with the electron transition from the level of interstitial Zn to the valence band, (10, 11, 12).

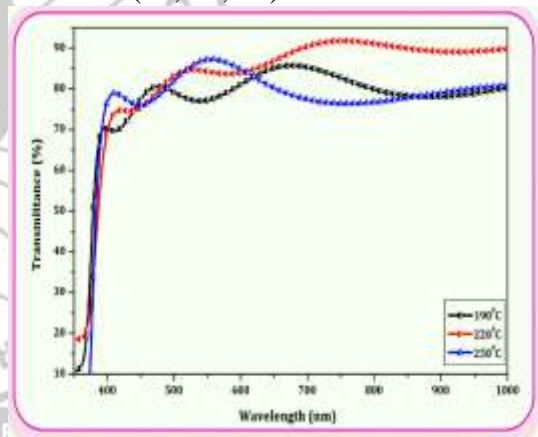


Fig. 3. Transmittance spectra

3.4 Photoluminescence Spectra:-

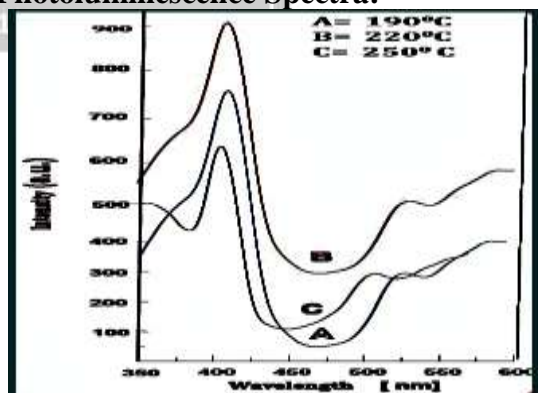


Fig. 4. Photoluminescence Spectra of ZnO thin films

The narrower and higher energy near band edge emission UV peak indicate that the undoped ZnO thin films synthesized by spray CVD

technique exhibits higher crystalline quality for substrate temperature 220°C. In addition, a weak blue green emission peak is present at the wavelength 470nm. It corresponds to the electron

transition from the level of interstitial Zn (Zn_i) to the Zinc vacancy (V_{Zn}).

Conclusion:

Thin films of ZnO had been successively synthesized by using newly assembled spray CVD technique for different substrate temperatures. The structural analysis reveals that all films exhibits orientation along c-axis perpendicular to substrate. From the optical study it is found that, transmittance increases with increase in substrate temperature. The photoluminescence measurements show that the near band edge UV emission is enhanced at substrate temperature 220°C. The narrower and higher energy near band edge emission UV peak indicate that the undoped ZnO thin films synthesized by spray CVD technique exhibits improved crystalline at substrate temperature 220°C.

Acknowledgement: One of the author is grateful to University Grant Commission, New Delhi, for providing Teacher Fellowship under XIIth plan.

Reference

1. K.L. Chopra, Thin Film Phenomena, Mc Graw- Hill Book Company, 1, (1969)
2. Z. L. Wang, J. Phys. Condense matter 303 , (2004) R829
3. H. H. Afifty, S. H. EL-Hefnawi, A.Y. Eliwa, M. M. Abdel-Naby and N.M. Ahmed, Egypt. J. Solids, Vol. (28), No. (2), (2005)
4. G. Epurescu, N. D. Scarisoreanu, D.G. Matei, G. Dinescu, C. Ghica, L. C. Nistor, M. Dinescu, Romanian reports in Physics, Vol. (60), No. (3), (2008), 807-814
5. Maldonado, S. Tirado-Guerra, J. M. Cázares, M. de La L. Olvera, Thin Solid Films 518 (2010) 1815–1820
6. S. Y. Lee, E. S.S him, H. S. Kang, S. S. Pang, J. S. Kang, Thin Solid Films 473 (2005) 31.
7. M. H. Huang, S. Mao, H. Feick, H. Yan, Y. Wu, H. Kind, E. Weber, R. Russo, P. Yang, Science 292 (2001) 1897
8. Huiyong Liu, V. Avrutin, N. Izyumskaya, Ü.Özgür, H. Morkoç, Superlattices and Microstructures 48 (2010) 458–484
9. B.J. Lokhande, M. D. Uplane, Applied Surface Science 167 (2000) 243–246
10. Hsin-Ming Cheng, Hsu-Cheng Hsu, Shiow-Lian Chen, Wen-Ti Wu, Chih-Chun Kaob, Li-Jiaun Lin, Wen-Feng Hsie, Journal of Crystal Growth 277 (2005) 192–199
11. Jin Hyung Jun, Hojun Seong, Kyoungah Cho, Byung-Moo Moon, Sangsig Kim, Ceramics International 35 (2009) 2797–2801
12. Jun-Liang Zhao, Xiao-Min Li , Ji-Ming Bian, Wei-Dong Yu, Can-Yun Zhang , Thin Solid Films 515 (2006) 1763 – 1766



Effect of Pyrochlore Phase on Structural and Dielectric Properties of 0.75PMN-0.25PT

A.N. Tarale, V.L. Mathe*

Savitribai Phule Pune University, Pune, India-411007

*email- vikasamathe@gmail.com

Abstract

The paper reports synthesis of 0.75PMN-0.25PT ferroelectric solid solution by chemical route. The PMN-PT composition is sintered at 1250 °C for 2 hr, 4 hr and 6 hr. Formation of phase is confirmed by X-ray Diffractometer (XRD). It is observed that single phase is obtained for sintering time 2hr, while for 4 and 6 hr sintering time XRD shows the pyrochlore phase. Further paper discusses the effect of pyrochlore phase on the dielectric and ferroelectric properties of 0.75PMN-0.25PT.

Keywords: Dielectric constant, XRD, ferroelectrics

1. Introduction

Lead based relaxor ferroelectrics are characterized by their high value of dielectric constant with diffused phase transition. In general, lead based relaxors have formula $Pb(B'B'')O_3$, where B' is low valence cation like Mg^{2+} , Ni^{2+} , Zn^{2+} , Fe^{3+} , Sc^{3+} and B'' is high valence cation like Nb^{5+} , W^{5+} , Ta^{5+} and so forth. The resulting lead niobate compositions are $Pb(Mg_{1/3}Nb_{2/3})O_3$ (PMN), $Pb(Zn_{1/3}Nb_{2/3})O_3$ (PZN), $Pb(Ni_{1/3}Nb_{2/3})O_3$, $Pb(Fe_{1/2}Nb_{1/2})O_3$ (PFN), $Pb(Sc_{1/2}Nb_{1/2})O_3$ (PSN) etc [1,2]. Out of these Lead magnesium niobate $Pb(Mg_{1/3}Nb_{2/3})O_3$ (PMN), a well known relaxor ferroelectric material, demonstrates a quite high maximum dielectric constant around -10 to -5°C, with a diffuse phase transition [1-2].

On the other hand, ABO₃ type normal ferroelectrics compound of lead titanate $PbTiO_3$ (PT) shows a sharp phase transition in the vicinity of 490 °C with maximum value of dielectric constant [1]. It is reported that the dielectric properties of PMN can be enhanced by the addition of $PbTiO_3$ (PT) [1]. The (1-x)PMN-(x) PT system has shown interesting ferroelectric and piezoelectric properties at its morphotropic phase boundary (MPB) [1-2]. However in addition to MPB system, 0.75PMN-0.25PT composition has shown excellent relaxor behavior with very high value of maximum dielectric constant ϵ_{max} [2], maximum polarization P_{max} and piezoelectric coefficient d_{33} . It is well known that single-phase (1-x)PMN-xPT with perovskite structure is very difficult to prepare via the conventional solid-state method. Main obstacle to synthesis single phase (1-x)PMN-xPT is formation of pyrochlore phase in initial stage of the reaction process. The presence of pyrochlore phase reduces the piezoelectric and dielectric properties of PMN-PT. Therefore, resulting material is scientifically and technologically less important [3].

Aim of the present work is to investigate the effect of pyrochlore phase on dielectric properties of 0.75PMN-0.25PT ferroelectric solid solution.

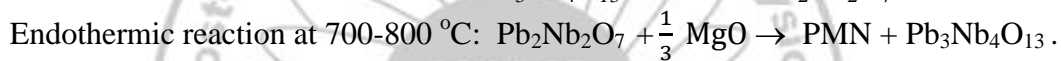
2. Experimental

The 0.75PMN-0.25PT has been synthesized by hydroxide co-precipitation method. Precursors used were $Pb(CH_3COO)_2 \cdot 3H_2O$ (Loba Chemie Make) and $Mg(NO_3)_2 \cdot 6H_2O$ (Loba Chemie Make), $NbCl_5$ (Sigma Aldrich) and titanium isopropoxide $C_{12}H_{28}O_4Ti$ (Sigma Aldrich) with purity > 99%. The chemical synthesis method is used as previously reported by our group [4]. The stoichiometric amount of $NbCl_5$ was dissolved in 10 ml of HCl (36.5%) with constant stirring at room temperature for 15 min. $Mg(NO_3)_2 \cdot 6H_2O$ was then added slowly to the clear solution of $NbCl_5$ with constant stirring for 15 min, followed by slow addition of $C_{12}H_{28}O_4Ti$ at 90 °C to obtain Nb-Mg-Ti precursor solution. The $Pb(CH_3COO)_2 \cdot 3H_2O$ was separately dissolved in the acetic acid with constant stirring for 20 min, and then added, drop by drop, to the Nb-Mg-Ti solution with constant stirring at 90 °C. Finally, white turbid solution containing all the elements was obtained. This solution was precipitated with NaOH solution having pH 12 at 90 °C with constant stirring. The white coloured precipitate so obtained was washed several times using double distilled water and filtered until the pH of the filtrate became neutral. Obtained precipitate was dried at 150 °C for 4 hr followed by grinding for 2hr in agate mortar and pestle using acetone as a medium. The powder was calcined at 870 °C for 4 hr. The calcined powder was milled for 2 hr in agate mortar and pestle using acetone as a medium. Then the powder was pressed into the pellet having diameter of 10 mm and thickness of nearly 1mm. These pellets were finally sintered at 2, 4 and 6 hr, in Pb rich environment. The silver (Ag) electrode on both side of the pellet was used for electrical characterization.

The Bruker D8 advance X-ray diffractometer was used to record X-ray diffraction pattern useful for structural analysis, while HIOKI IM 3523 LCR meter was used for the measurement of dielectric constant ϵ and loss tangent $\tan \delta$ at as a function of temperature at 1 kHz. The P-E loop tracer of Marin India Make was used for ferroelectric hysteresis loop measurement.

3. Result and discussion

Figure 1 shows X-ray diffraction pattern of 0.75PMN-0.25PT composition sintered for a) 2hr, b)4 hr and c) 6hr at 1250 °C. From the Fig. 2, it is seen that a pure pervoskite phase formed at sintering temperature of 1250 °C for 2 hr of sintering time. However a dominant pyrochlore phase is observed when the sintering time was increased to 4 and 6 hr. In Fig.1 the reflections indicated by ‘*’ correspond to Pb and Mg deficient pyrochlore phases $Pb_3Nb_4O_{13}$, while the reflections correspond to pure pervoskite phase are



In the present study, the observation of pyrochlore phase with increasing sintering time is attributed to Pb evaporation to significant extent and hence leads to formation of Pb deficient $Pb_3Nb_4O_{13}$ pyrochlore phase.

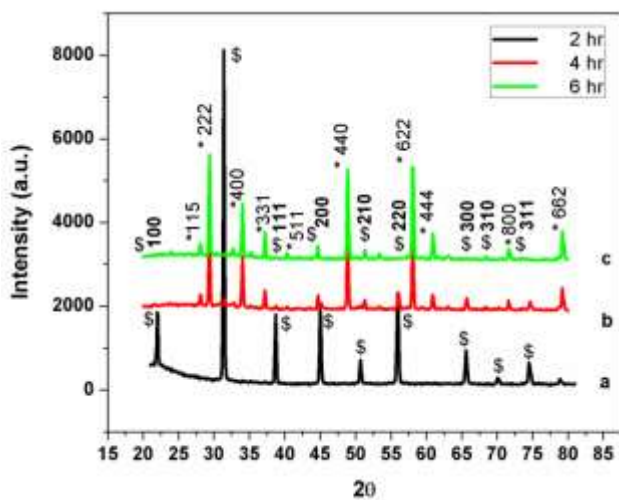


Fig. 1 X-ray diffraction pattern of 0.75PMN-0.25PT compositions sintered at 1250 °C for different duration : a) 2 hr, b) 4hr and c) 6 hr. ‘\$’ indicates the reflections are related to pervoskite phase and ‘*’ indicates the reflections are related to pyrochlore phase.

Figure 2 shows the variation of dielectric constant ϵ as a function of temperature at frequency $f = 1\text{kHz}$ for the 0.75PMN0.25PT composition sintered at 1250 °C for sintering duration of 2, 4 and 6 hr respectively. The transition temperature T_m is observed

indicated by ‘\$’. The reflections correspond to pyrochlore phase $Pb_3Nb_4O_{13}$ match well with JCPDS card no. 230352. It is reported that the $Pb_3Nb_4O_{13}$, $Pb_2Nb_2O_7$ and $Pb_3Nb_2O_8$ are the possible pyrochlore phases formed during synthesis of PMN and PMN-PT [5,6]. Formation of pyrochlore phase is related to the Pb or Mg deficiency in the composition. During synthesis process, once the pyrochlore phase is formed it is difficult to convert it to pervoskite phase. The reason is that, compared with the pervoskite phase, $Pb_3Nb_4O_{13}$ is B-site rich and it is difficult to enter Mg into the B-site to form pervoskite structure [5,6]. Rhombohedral $Pb_2Nb_2O_7$ and cubic $Pb_3Nb_4O_{13}$ are lead deficient pyrochlore phases, while $Pb_3Nb_2O_8$ is Pb rich cubic pyrochlore phase [5]. H.M. Jang et al. have reported following reactions which show the formation of pyrochlore and pervoskite phase of PMN during sintering process [7].

at 114 °C for 2 and 6 hr sintering samples, while it is 96 °C for sample sintered for 4 hr. It is seen from Fig. 2 that the value of dielectric constant of samples sintered for 4 and 6 hr decreases drastically compare to value of ϵ of sample sintered for 2 hr. From the fig.2, it is seen that the values of ϵ_{max} for samples sintered for 4 and 6 hr approximately seems to be almost equal but these are only 14% to that of the values of ϵ_{max} for pure pervoskite phase. The low value of dielectric constant is attributed to presence of pyrochlore phase as evidenced from the XRD data. It is reported that in the literature that the pyrochlore phase reduces the dielectric, piezoelectric and ferroelectric properties the of the material and hence device fabrication is not recommended using pyrochlore materials. S. Yu et al. have also reported effect of pyrochlore phase on dielectric properties of 0.65PMN-0.35PT composition [6]. Therefore, for further studies we have concentrated on the pyrochlore phase free PMN-PT samples.

Figure 3 shows the variation of loss tangent $\tan \delta$ as a function of temperature at 1 kHz for 0.75PMN-0.25PT ceramic composition sintered at 1250 oC for 2hr, 4h and 6hr respectively. The $\tan \delta$ data passes through a peak just below temperature T_m , which appears to be a common behavior for ferroelectric systems. The effect of pyrochlore phase is not significant on $\tan \delta$.

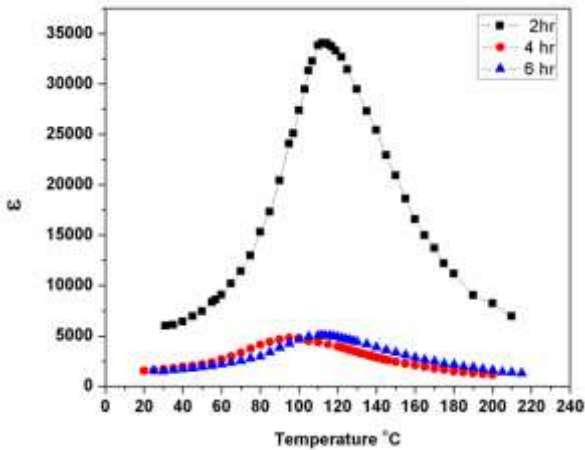


Fig. 2 The variation of dielectric constant ϵ as a function of temperature at frequency $f = 1\text{kHz}$ for the 0.75PMN0.25PT composition sintered at $1250\text{ }^\circ\text{C}$ for sintering duration of 2, 4 and 6 hr respectively.

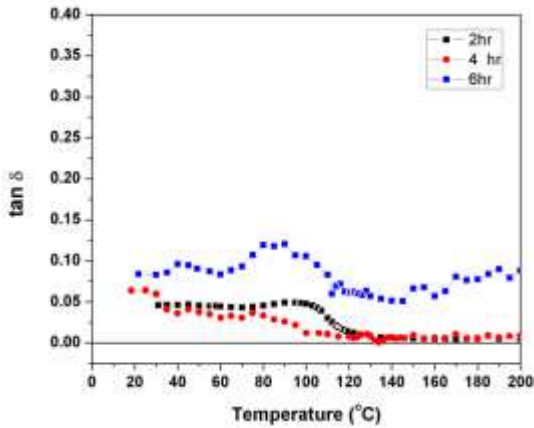


Fig. 3 The variation of loss tangent $\tan \delta$ as a function of temperature at frequency $f = 1\text{kHz}$ for the 0.75PMN0.25PT composition sintered at $1250\text{ }^\circ\text{C}$ for sintering duration of 2, 4 and 6 hr respectively.

Acknowledgments

Dr. A. N. Tarale would like to acknowledge the UGC, New Delhi, India for the financial support under the scheme of Dr. D.S. Kothari postdoctoral fellowship (No.F4-2/2006(BSR)/PH/13-14/0087, dt08/08/2014)

References

1. J.Kelly, M. Leonard, C. Tantigate, and A. Safari, J. Am. Ceram. Soc. 80 (4): 957–64,(1997) .
2. D.H.Suh, D.H. Lee, N.K. Kim, J. of the European Ceramic Society 22: 219-223,(2002).
3. A. Mergen & W.E. Lee, J of the European Ceramic Society 17, 1033-1047, (1997).
4. A.D. Sheikh, H.H. Kumar, V.L. Mathe. Solid State Sciences, 12:1534-1539, (2010).

Figure 4 shows the variation of polarization P with applied electric field E for 0.75PMN-0.25PT composition sintered at $1250\text{ }^\circ\text{C}$ for 2 hr, 4 hr and 6 hr respectively. The observed values of maximum polarization P_{max} , remnant polarization P_r , and coercive field E_c are given in Table 1. The maximum values of P_{max} and P_r are 35 and $26\text{ }\mu\text{C}/\text{cm}^2$ respectively at $1250\text{ }^\circ\text{C}$ (2hr sintering time), which is Useful for ferroelectric memory applications. It is seen that values P_{max} and P_r decreases with increase in sintering duration for 4 and 6 hr, which is attributed to presence of pyrochlore phases.

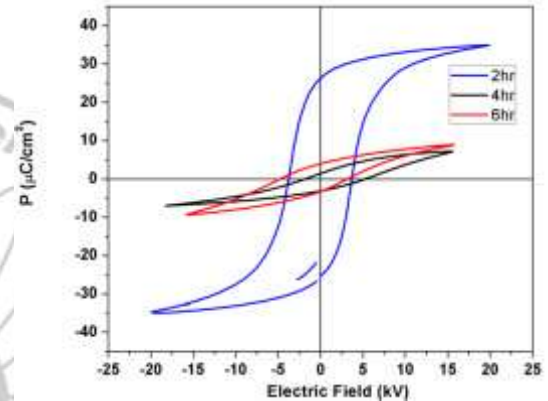


Fig. 4 The PE loops of the 0.75PMN0.25PT composition sintered at $1250\text{ }^\circ\text{C}$ for sintering duration of 2, 4 and 6 hr respectively.

The 0.75PMN-0.25PT synthesized by chemical route and sintered for 2 hrs at $1250\text{ }^\circ\text{C}$ shows good ferroelectric and dielectric properties. However presence of pyrochlore phase (Pb reach or Pb deficient) leads to decrease the martial properties.

An investigation of the electrochromic and optical transmittance of copper and copper oxide thin films prepared by vacuum evaporation technique

B. B. Dhale¹, S. H. Mujawar² and P. S. Patil³

¹Gogate Jogalekar College, Ratnagiri (M.S), India

²Mahatma Phule Mahavidhyalaya, Pimpri, Pune (M.S), India

³Thin Film Materials Laboratory, Department of Physics, Shivaji University, Kolhapur (M.S.) India

Abstract

Copper thin films were synthesized by vacuum evaporation technique on both glass and F.T.O. substrate. In order to make oxide of Cu, the deposited films were further annealing. In this work we present the electrochromic properties and optical transmittance of copper and copper oxide thin films. EC oxide films operating via lithium ion insertion are well known. The present investigation deals with the copper metallic materials converted to semiconductors that is its switching from the as deposited mirror state to transparent state achieved by addition or removed of lithium ions. Structural characterization of the film was carried out using X-ray diffraction technique and A Raman scattering spectra. Electrochemical characterizations were carried out using cyclic-voltammetry, chronoamperometry and chronocoulometry.

Keywords: Electrochromism; Copper Oxide; Thin films; Cyclic-voltammetry; Chronoamperometry; Coloration Efficiency.

1. Introduction

Electrochromism is the process by which a material can exhibit a reversible and persistent colour change with applied appropriate electric current or external field [1]. Then electrochromic materials switch from uncoloured state to coloured state. It was discovered by Deb [2] in 1969. Despite of more than three decades intense studies, the physical mechanism of this color change is still not fully understood. Transmittance modulation in the films is believed to be directly related to electrically controlling the oxidation/reduction states of an electrochromic electrode and a counter electrode when ions are intercalated or deintercalated due to an applied voltage, and electrons are injected or ejected correspondingly. As the ionic transport, and thus the change in optical properties is reversible. That is why electrochromic coating, when incorporated in electrochromic devices (ECD) offer dynamic reflection / transmission modulation of radiant energy. As a result, electrochromic devices have fascinating possibilities to be used as solar control windows modulating transmission and contributing significantly to save energy in buildings [3, 4]. By allowing the electrical control of light transmission and reflection, electrochromic windows, usually called "smart windows", can increase comfort, optimize illumination and reduce energy consumption in buildings. Electrochromic devices can be used in automotive mirrors to prevent glare during night driving, and in large area information displays [5]. Electrochromic displays have good visibility in a variety of conditions and viewing angles, without constantly drawing power [6]. Very recently, a

strong interest has been focused on satellite thermal control [7, 8]. NASA thinks that electrochromic devices working over a wide infrared range could advantageously replace the louver-type radiator on small low earth orbit (LEO) satellites [8]. A large number of transition metal oxides such as WO_3 , TiO_2 , NiO_x , V_2O_5 , etc. have been investigated as EC materials. Recently, electrochromic behaviour of copper (I) oxide thin films [10] and lithium intercalation of Cu_xO films have been reported [11–13]]. Because copper oxide is inexpensive, non-toxic material which could be prepared using simple techniques, it has been investigated in context of solar photovoltaic conversion. Cuprous oxide (Cu_2O) thin films have been subject of numerous studies as for a candidate for solar cell application [14–16]. It has been recently found that the cuprous oxide thin films exhibit cathode electrochromism [17–20], i.e. they are transparent for visible light in their oxidized state, and almost black when switched in their reduced state. Nevertheless, the electrochromic properties of these films have not been investigated extensively. So far, there is very limited number of scientific publication on this matter. In our research, electrochromic properties of copper and copper oxide thin films prepared by the simple and inexpensive vacuum deposition technique are discussed.

2. Experimental

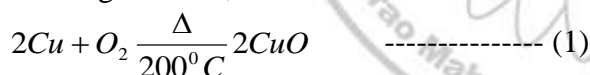
Copper thin films on FTO coated glass substrates were deposited using vacuum deposition system HIND HIVAC India, by resistive heating method. During depositions the order of pressure was maintained between 10⁻⁵ to 10⁻⁶ mbar. Tungsten helical wire and Cu foil [0.1

mm thick] were used as resistive heating source and starting material respectively. The distance between the source and substrate was maintained at 25 cm. The thickness of the films measured using profilometer was found to be ~250nm, which is in agreement with the value obtained through quartz crystal monitor mounted in the evaporation unit. Deposited copper thin films were brownish with reflecting surface. Optimized deposition parameters of copper films on FTO by vacuum evaporation technique are as shown in table.

Preparative Parameters	Optimized value
Deposition rate	20 Å/sec
Pressure	10-5 mbar
Thickness	0.25 μm.
Growth substrate temperature	Room Temperature

The as deposited copper films were post-annealed at 300°C in ambient air for 5h. The thickness of the as-deposited films increased slightly to ~28 nm upon annealing. The increase in film thickness upon annealing has also been reported earlier by V. Figueiredo et al. [35].

Annealing of the Cu films leads to the conversion of Cu into CuO This is because as oxygen diffuses into the films, Cu starts reacting with oxygen and forms CuO according to following reaction,



The post annealed films were further used for characterization. The structural properties of the films were studied from X-ray diffraction (XRD) patterns recorded using an X-ray diffractometer (Philips, PW 3710, Almelo, Holland) operated at 25 kV, 20 mA with CuKα radiation (λ = 1.5406 Å). The surface morphology of the films was examined by analyzing the scanning electron microscopy (SEM) images recorded using a scanning electron microscope (Model JEOL-JSM-6360, Japan), operated at 20 kV. The optical transmittance was measured using a UV-Vis spectrophotometer (Systronics, model 119, Bangalore, India) in the wavelength range of 350–1000 nm. The cyclic voltammetry (CV) experiments were conducted at a scan rate of 20mVs-1 using a versa stat-II (EG and G) potentiostat/galvanostat, computer-controlled by M270 software and the potential was swept between anodic (+1.4V) to cathodic (-0.4V) cycle

with respect to SCE. For electrochemical characterizations of CuO the standard three-electrode chemical cell of following configuration was used.

Glass/ FTO /CuO / 0.1M LiClO4 PC / C / SCE where CuO thin film acts as a working electrode, 0.1M LiClO4 in propylene carbonate (PC) is an electrolyte for Li+ ion source. Saturated calomel electrode (SCE) was used as a reference electrode to which all measured were referred; C is the graphite electrode which acts as a counter electrode. The cyclic voltammetry (CV) and chronoamperometry (CA) experiments for electrochemical injection or extraction of electrons and Li+ ions were conducted at the scan rate of 20 mV/s using a VersaStat-II (EG&G Make PAR 362), computer-controlled by M270 software. The potential was swept between anodic (+1.4 V) and cathodic (-0.4 V) cycle with respect to SCE.

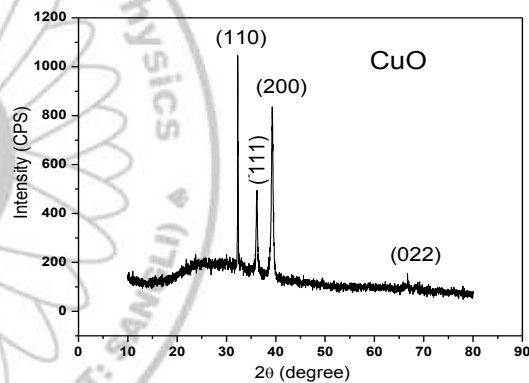


Fig. 1

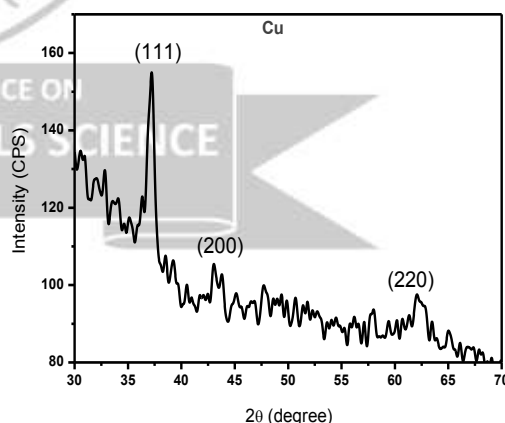


Fig. 2

3. Results and discussion

Fig (1 and 2) shows the XRD spectra of films as-deposited, annealed at 200 and 300°C respectively. As deposited Cu sample exhibit phase pure Cu with (111) crystal structure. The peaks at 2θ angle 37.21, 42.76 and 61.96 with d_{hkl}

correspond to diffraction from planes (111),(200) and (220).

Also a Raman spectrum of same sample is shown in fig (3). The peak of Cu sampled occurs at 561 and 646 cm^{-1} indicates phase of C

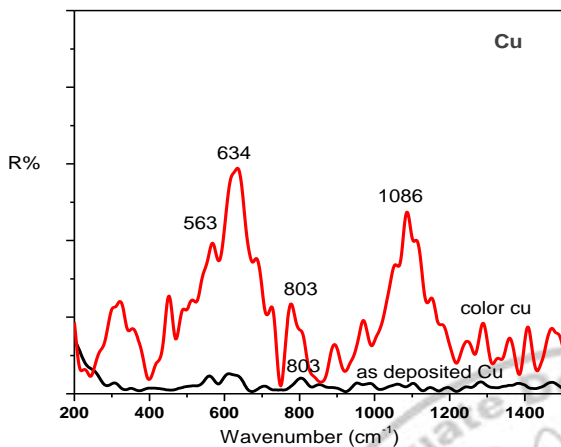


Fig 3

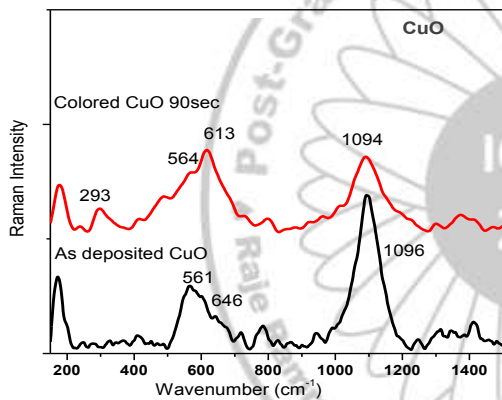


Fig 4

The sample annealed at 300°C exhibit phase pure CuO with cubic crystal structure. The peaks at 2θ angle 37.21, 42.76 and 61.96 with d_{hkl} correspond to diffraction from planes (111),(200) and (220). Also a Raman spectrum of same sample is shown in fig (4). The peak of Cu_2O sampled occurs at 561 and 646 cm^{-1} indicates phase of Cu_2O . The peak at about 1096 cm^{-1} was assigned to multiphonon transition.

The sample annealed at 300⁰ C exhibit phase pure CuO with monoclinic crystal structure. The peaks at 2θ angle 32.47, 36.21 39.16 and 66.79 with d_{hkl} correspond to diffraction from planes (110), (111),(200) and (022) respectively. Also a Raman spectrum of same sample is shown in fig (3). The peak of CuO sampled occurs at 243, 308 and 620 cm^{-1} indicates phase of CuO.

Electrochemical characterization:

For electrochemical characterizations of Cu and CuO the standard three-electrode chemical cell of following configuration where used.

Glass/ FTO | Cu | 0.1M PC- LiCl_4 | C | SCE, and Glass/ FTO | CuO | 0.1M PC- LiCl_4 | C | SCE

Where Cu and CuO thin films acts as a working electrode 0.1M PC- LiCl_4 is an electrolyte for Li^+ ion source. Saturated calomel electrode (SCE) was used as a reference electrode to which all measured were referred; C is the graphite electrode which acts as a counter electrode.

Fig (5) shows the CV spectrum (1st cycle) recorded for the Cu thin film in scanning potential range -0.3 to +0.5 V at 20 mV/sec. During the anodic potential scan simultaneous intercalation of electrons and Li^+ ions into the Cu film cause the oxidation to higher valence state, Cu^{1+} and hence the film gets coloured. In its oxidation state the film appears brownish and transparent may be due to the formation of CuO. During cathodic potential scan deintercalation of Li^+ ions causes the bleaching of the film.

Fig (6) shows the CV spectra recorded for Cu thin film for its 1st, 100th, 500th and 1000th cycles. The area of CV decreased as increase in cycles indicates that the film is not stable for long time.

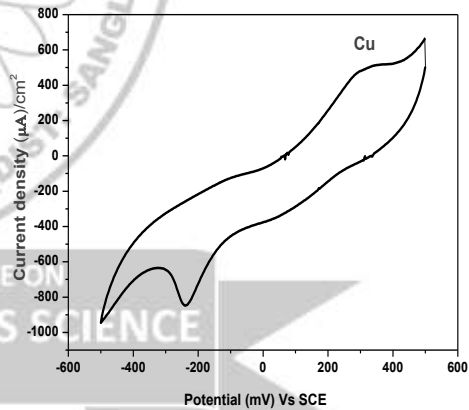


Fig.5

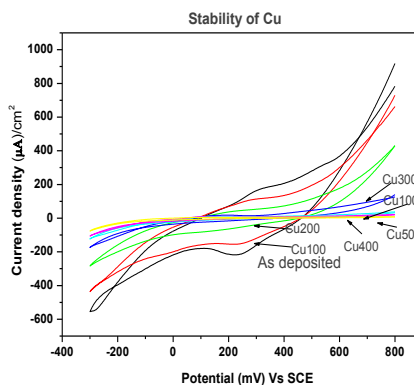


Fig. 6

The transmittance spectra of the Cu sample in the colored and bleached state were recorded in the wavelength range of 350-1600 nm, at room temperature. Coloration and bleaching processes were carried out at +0.5 and -0.5 V Vs SCE for a different coloration time that is for 30, 60, 90 sec and bleaching time is 30 sec and its transmittance spectra is shown in fig (7). From this fig we revealed that the optical transmittance of Cu sample changes after coloration and bleaching. Fig (8) shows the transmittance spectra for Cu sample in their colored (Tc) and bleached (Tb) states.

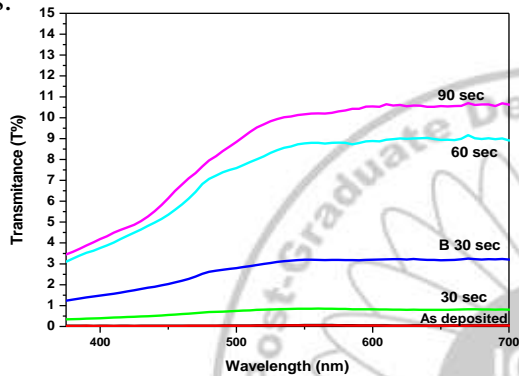


Fig.7

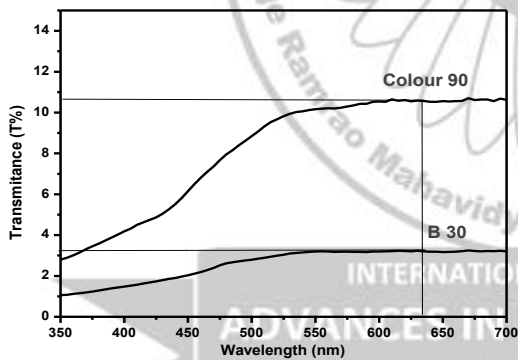


Fig. 8

The change in optical transmittance at 630 nm (OD) was calculated using relation (2). The value of optical transmittance and coloration efficiency are as shown in table (1).

$$\Delta OD = Ln \left(\frac{T_b}{T_c} \right) \quad \text{----- (2)}$$

Where, Tb is the transmittance of bleached state and Tc is transmittance of colored state.

Coloration efficiency (CE) was calculated using the relation 3

$$(CE)_{\lambda=630nm} = \frac{(\Delta OD)_{630nm}}{Q_i} \quad \text{----- (3)}$$

Where Qi is the amount of charges intercalated in the sample, which was estimated by integrating the area under the current of current density Vs time. The copper to copper oxide transition reveals anodically coloring, electrochromic system which combines a highly reflecting metallic state with highly transparent semiconducting state. At the colored state the Cu sample oxide into CuO, it is confirmed by FT-Raman as shown in fig (3). The peak 634 and 563cm⁻¹ corresponds to the CuO phase. But it shows very low reversibility (45.98%) that is it is very low cathodic features prior to CuO reduction to Cu it may be due to the low conductivity of CuO. The nucleation and distinct growth of Cu from the oxide may also account for the occurrence of the metallic copper film relating to the original copper film. Fig (9) shows the CV (1st cycle) recorded for the Cu₂O films in the scanning potential range (-0.4 to 1.4V) at 20 mV/sec. The Cu₂O film exhibit cathodic electrochromism that is they are transparent for visible light in their oxide state and almost black when switched in their reduced state.

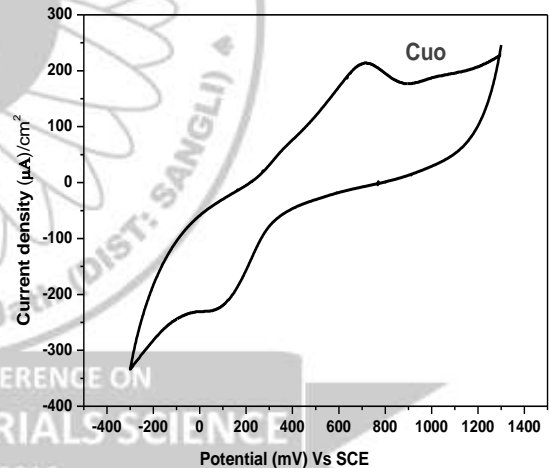
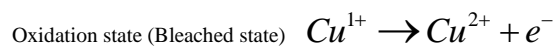
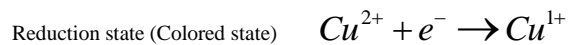


Fig. 9

Following reaction can be take place during oxidized and reduced state.



From cyclic voltagram we revealed that the cathode and anode peaks corresponding to the reversible red-ox conversion of CuO into Cu.

Fig (10) shows CV spectra recorded for CuO thin film for its 1st, 50th, 500th and 100th cycles. From the figure, it was observed that with an increase in number of cycles flattening of anodic peak and decrease in its area indicates that the rate of bleaching kinetics decreases and leads to residual coloration in the Cu₂O thin film.

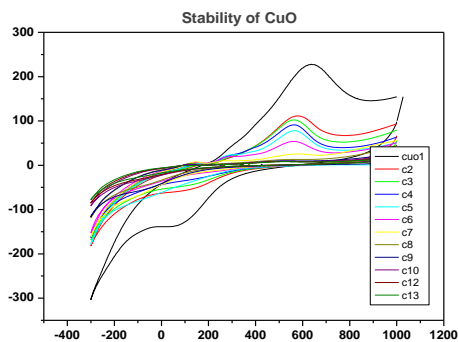


Fig.10

The transmittance spectra of the CuO sample in the colored and bleached state were recorded in the wavelength range of 350-1600nm, at room temperature. Coloration and bleaching processes were carried out at +0.5 and -0.5 V Vs SCE for a different coloration time that is for 30, 60, 90 sec and bleaching time is 30 sec as shown in fig(19), from this fig we revealed that the optical transmittance of CuO sample changes after

Table 1. Various electrochromic parameters calculated from electromical and iono-optical studies of Cu and CuO thin films.

Sample name	Response time		Q_i (mC/cm ²)	Q_{di} (mC/cm ²)	Reversibility (%)	ΔOD	Coloration efficiency (cm ² /C)
	t_c (sec)	t_b (sec)					
Cu	10.8	3.3	5.35	2.46	45.98	0.50	22
CuO	20	20	10	10	1	1	-

4. Conclusions

Copper thin films were successfully synthesized by vacuum evaporation technique. In order to make oxide of copper, the deposited films were further annealed at 300°C. The copper-to-copper oxide transition reveals anodically coloring, electrochromic system which switches from a highly reflecting metallic state to transparent semiconducting state. Here also we present the electrochromic properties of cupric oxide (CuO) thin films but transmittance at 630nm does not occurs, hence CuO phase does not exhibit electrochromic properties however it shows IR modulation.

References

- C. G. Granqvist, Handbook of Inorganic Electrochromic Materials, Elsevier, Amsterdam, 1995.
- S. K. Deb, Appl. Opt. Suppl. 3 (1969) 192.
- C. M. Lampert, Solar Energy Mater 11 (1984) .
- C. G. Granqvist, in "Materials Science for Solar Energy Conversion Systems", Pergamon, Oxford, (1991), 106.
- S. A. Agnihotry, S. Chandra, Ind J Mater Sci & Eng 1 (1994) 320.
- C. G. Granqvist, Sol. Energy Mater. Sol. Cells 60 (200) 201-262.
- A. L. Larsson, G. Niklasson, L. Stenmark, Proc. SPIE 3738, 486 (1999) .
- J. S. Hale, J. A. Woollam, Thin Solid Films 339, 174 (1999) .
- H. Bach, d. Krause, Thin Films on glass, Springer-Verlag, Berlin,1997.
- T.J. Richardson, J.L. Slack, M.D. Rubin, Electrochim. Acta 46(2000) 2281
- N. Ozer, F. Tepehan, Sol. Energy Mater. Sol. Cells 30 (1993) 13.
- H. Demiryont, US Patent 4, 830, 471.
- F. I. Brown, S. C. Schulz, US Patent 5, 585, 959.
- A.E. Rakhshani, J. Appl. Phys. 62 (1987) 1528.
- A.E. Rakhshani, A.A. Al-Jassar, J.Varghese, Thin Solid Films 148 (1987) 191.
- A.E. Rakhshani, J. Appl. Phys. 69 (1991) 2365.
- N. Ozer, F. Tepehan, Sol. Energy Mater. Sol. Cells 30 (1993) 13.
- H. Demiryont, US Patent No. 4830471, 16 May 1989.
- F.I. Brown, S.C. Schulz, US Patent No. 5585959, 17 Dec. 1996.
- T.J. Richardson, J.L. Slack, M.R. Rubin, Electrochim. Acta 46 (2001) 2281.
- A. Roos, T. Chibuye, B. Karlsson, Sol. Energy Mater. 7 (1983) 453.
- M.E. Abu-Zeid, A.E. Rakhshani, A.A. Al-Jassar, Y.A. Youssef, Phys. Status Solidi, A 93 (1986) 613.
- V. Georgieva, M. Ristov, Sol. Energy Mater. Sol. Cells 73 (2002) 67.
- S.C. Ray, Sol. Energy Mater. Sol. Cells 68 (2001) 307.
- W.M. Sears, E. Fortin, Sol. Energy Mater. 10 (1984) 93.
- E. Fortin, D. Masson, Solid-State Electron. 25 (1982) 281.

coloration and bleaching. Fig (11) shows the transmittance spectra for Cu₂O sample in their colored for 90 sec (Tc) and bleached for 30sec (Tb) states. The change in optical transmittance at 630 nm (OD) was calculated using relation (2). The value of optical transmittance and coloration efficiency are as shown in table (1)

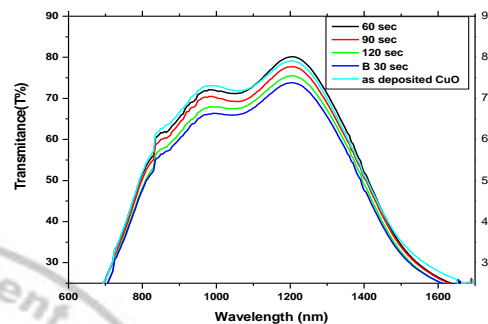


Fig.11

DC Electrical Resistivity of Ni-Zn Ferrite Thick Films

S. P. Dalawai^{1*}, T. J. Shinde², A. B. Gadkari³, P. N. Vasambekar¹

¹Department of Electronics, Shivaji University, Kolhapur - 416 004, (MS) India.

²Department of Physics, KRP Kanya Mahavidyalaya Islampur- 416 409, (MS) India.

³Department of Physics, GKG College, Kolhapur- 416 012, (MS) India.

* Correspondence author email: sanjeevdalawai@gmail.com, MobileNo.9890253825.

Abstract

The nano-sized ferrite powders with composition of $\text{Ni}_x\text{Zn}_{1-x}\text{Fe}_2\text{O}_4$ ($x = 0, 0.2, 0.4, 0.6, 0.8, 1.0$) were prepared by oxalate co-precipitation method. The ferrite thick films (FTFs) were prepared by screen printing technique. X-ray diffraction (XRD), Fourier transforms infrared spectroscopy (FTIR) and scanning electron microscopy (SEM) techniques were used for characterization of samples. The DC electrical resistivity study shows, the semiconducting behavior of FTFs. Room temperature resistivity of FTFs was found to decrease with increasing Ni^{2+} content up to $x = 0.6$ and thereafter increases for the compositions $x \geq 0.8$. Ni-Zn ferrite samples have higher values of resistivity and it has higher values of activation energies and vice versa respectively.

Keywords: Ni-Zn ferrite; Thick Films; DC resistivity; Semiconductor behavior.

1. Introduction.

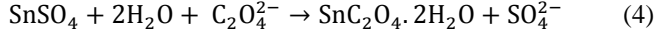
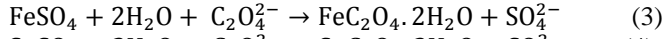
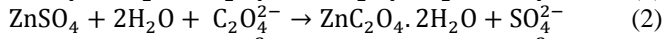
The ferrite materials are mostly used in the different technological applications such as microwave [1], magneto optical recording [2], multilayer chip inductors [3], magnetic fluids [4], spintronics [5], soft magnetic materials [6], magneto-optics [7], electro-magnetic compatibility [8], biomedical [9] environmental [10], radio and TV [11], gas sensors [12] etc. From the last two decades, different types of ferrite materials such as Co [2], Ni-Cu-Zn [3], Mn-Zn [4, 6], Ni [5], Mn [9-10], Ni-Zn [13], ferrite have good properties for various applications. After few years, researchers concentrated on the these ferrite materials by adding with different rare earth ions like Sm^{3+} , Gd^{3+} and Dy^{3+} [14] and different valency like Zn^{2+} [15], Nd^{3+} [16], Sn^{4+} [17-19], Ti^{4+} [18], $\text{Sn}^{4+}/\text{Nb}^{5+}$ [20] ions to improvement of its structural, electrical and magnetic properties. The many investigators study the structural and electrical properties are improved in case of pellet, thin and thick films. Shinde *et al.* [13] reported that the Ni-Zn ferrites were prepared by the oxalate precipitation method and to study the resistivity of each sample. Further observed that the nickel-zinc ferrites resistivity higher for co-precipitation method than that prepared by ceramic and citrate precursor method. Inbanathan *et al.* [14] reported that the electrical resistivity is improved due to the structural changes induced by the substitution of R^{3+} ($\text{R} = \text{Sm}, \text{Gd}$ and Dy) ions for Fe^{3+} ions at the B-sites and the formation of small amounts of RFeO_3 phase is present. Varshney *et al.* [15] reported that the Sn^{4+} and Zn^{2+} substituted nickel ferrite was prepared by ceramic method and studied for saturation magnetization, Curie temperature, magnetocrystalline anisotropy, initial permeability and magnetic losses. Balaji *et al.* [17]

reported that the Sn^{4+} substituted NiFe_2O_4 were prepared by novel combustion synthetic method. They also studied the structural and electrical properties of these ferrites and the DC electrical conductivity of the Sn^{4+} substituted Ni ferrite found to be increased with increasing temperature. Rao *et al.* [18] reported that the $\text{Sn}^{4+}/\text{Nb}^{5+}$ substituted Mn-Zn ferrites for magnetic and micro-structural properties. They also studied for the variation of DC resistivity with $\text{Sn}^{4+}/\text{Nb}^{5+}$ substituted ferrites are influenced by formation vacancy, valency fluctuations and electron hopping mechanism. Tewari *et al.* [19] reported that the $\text{Ni}_{0.6+x}\text{Zn}_{0.4}\text{Sn}_x\text{Fe}_{2-2x}\text{O}_4$ ($x = 0$ to 0.04) samples were prepared by solution route technique, studied for structural and magnetic properties. Vaithyanathan *et al.* [20] reported that the Ti and Sn doped cobalt ferrite materials were solid state chemical reaction method and studied for structural and magnetic properties. Hemeda *et al.* [21] reported that the nano Zn-Ni ferrites were prepared by using combustion techniques. The decrease of activation energy may be due to the creation of smaller number of oxygen vacancies and also due to the decrease in resistivity with increasing Ni concentration. Islam *et al.* [22] reported that the DC electrical resistivity and thermo-electric power confirms that the in Ni-Zn ferrites, the conduction mechanism is due to hopping of small polarons. Ajmal *et al.* [23] reported that the influence of zinc substitution on $\text{Ni}_{1-x}\text{Zn}_x\text{Fe}_2\text{O}_4$ ferrites and studied their structural and electrical properties. Recently, we have reported that the structural and gas sensing properties of Ni-Zn FTFs [24]. In this present communication, we report the DC Electrical resistivity of Ni-Zn ferrite thick films.

2. Experimental

2.1 . Ni-Zn FTFs preparation

The nano-sized $Ni_xZn_{1-x}Fe_2O_4$ ($x = 0, 0.2, 0.4, 0.6, 0.8, 1.0$) was prepared by oxalate co-precipitation method. The detailed experimental procedure is explained in elsewhere [24]. The ferrite precipitation reaction is chemically written as



The prepared ferrite powders were pre-sintered at 200°C for 1h and finally sintered at 450°C for 2h. The Ni-Zn FTFs were prepared by using the screen printing technique. The FTFs were sintered at 300°C for removal of organic and inorganic binders.

2.2. Characterization of FTFs

Ni-Zn ferrites were characterized by using XRD pattern recorded on Bruker D2 phaser desktop X-ray powder diffractometer with Cu-K α radiation. The FT-IR spectra of Ni-Zn-Sn ferrite powders were recorded using Perkin Elmer spectrum one spectrometer by KBr pellet technique in the range of 300-800cm⁻¹. The surface morphology of the FTF was studied with the help of FE-SEM on Hitachi S-4700, Japan.

2.3. Measurement of DC resistivity of FTFs

The DC resistivity of the FTF was measured by using two probe methods in the range of room temperature to 300°C. The current was measured by using picometer (Model:DPM-111) by applying a constant potential of 5.8V. The FTFs resistivity is given by [25],

$$\rho = \frac{RA}{L} = \frac{R \times b \times t}{L} \quad (5)$$

Where ρ - resistivity of thick films (FTs); (ohm/m), R - resistance of TFs (ohm/cm), A - cross sectional area of TFs [(A= $b \times t$), cm²], b - bread of FTs(cm), t - thickness of TFs (cm), L - length of TFs (cm). The FTFs thickness measured by using surface profiler Ambios Tech. XP-1 and was found to be 15-20 μ m. The area of the FTF was 10x10mm. The activation energy (ΔE) is calculated by using Arrhenius relation [26],

$$\rho = \rho_0 \exp \left[\frac{\Delta E}{KT} \right] \quad (6)$$

Where ρ_0 - the pre-exponential factor with dimensions in $\Omega \cdot cm$, K - Boltzmann constant, ΔE - the activation energy, T - the absolute temperature.

3. Results and discussion

3.1 Structural properties

The typical XRD pattern of $Ni_{0.6}Zn_{0.4}Fe_2O_4$ is presented in Fig. 1. From this figure, it is shown that face centered cubic spinel structure of ferrite [24]. The typical FE-SEM of $Ni_{0.6}Zn_{0.4}Fe_2O_4$ is presented in Fig. 2. The grain size of the samples was increases with increasing nickel content. The grain size of Sn⁴⁺ substituted Ni-Zn FTFs lies in the range 25-60 μ m [24]. The FT-IR spectrum of $Ni_{0.6}Zn_{0.4}Fe_2O_4$ is presented in Fig. 3, shows two major absorption bands in the range of 400cm⁻¹ in octahedral and 600cm⁻¹ in tetrahedral sites respectively [24]. The structural and gas sensing properties of Ni-Zn FTFs are already reported [24]. The structural properties of Ni-Zn ferrite thick films is already published [24]

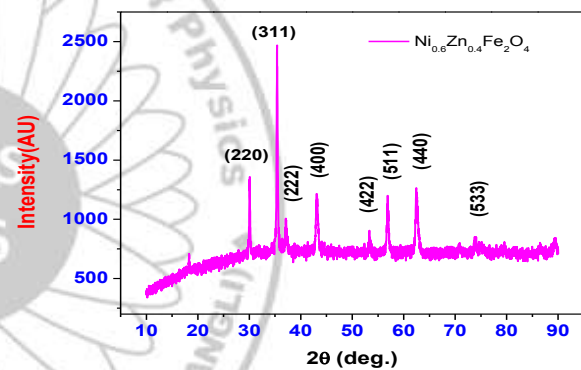


Fig. 1. Typical XRD pattern of $Ni_{0.6}Zn_{0.4}Fe_2O_4$ FTFs

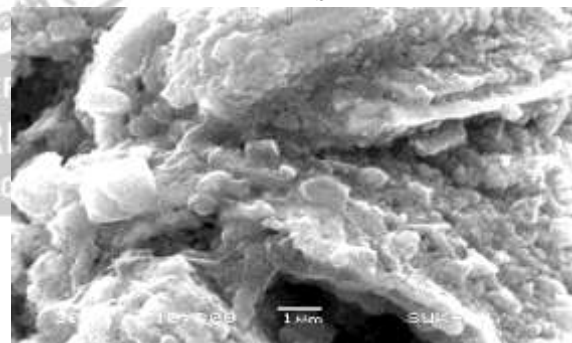


Fig. 2. Typical SEM image of $Ni_{0.6}Zn_{0.4}Fe_2O_4$ FTFs

3.2. DC electrical resistivity of FTFs

The DC resistivity of nano-sized of $Ni_xZn_{1-x}Fe_2O_4$ ($x = 0, 0.2, 0.4, 0.6, 0.8, 1.0$) FTFs measured by using two probe methods are presented in Fig. 4. From these figures, it is noticed that the DC resistivity of FTFs is decreasing with increasing in temperature and it shows the semiconductor nature of the FTFs. The DC resistivity decreased with increase in Ni²⁺ content up to sample x= 0.6 under

investigation. This is due to the decrement of grain size of the sample.

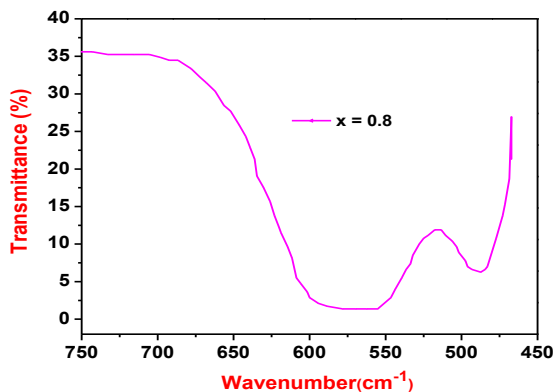


Fig. 3. Typical FT-IR spectrum of $Ni_{0.6}Zn_{0.4}Fe_2O_4$ FTFs

Further, increment of DC resistivity with an increase in nickel content. This is due to the Fe^{2+} and Fe^{3+} conduction mechanism in the Ni-Zn FTFs. The observed DC resistivity prepared under the screen printing technology is higher than reported values of resistivity of ferrite prepared by ceramic method, co-precipitation and citrate precursor method. The greater value of resistivity is due to the greater homogeneity and smaller grain size [13]. The conduction in ferrites is due to hopping of electrons between Fe^{2+} and Fe^{3+} ions.

The room temperature of DC resistivity of Ni-Zn FTFs was presented in the **Fig. 5**. From this figure, it is noticed that the room temperature DC resistivity was decreased with increase in nickel content up to sample $x = 0.6$. Further, increment of DC resistivity with an increase in nickel content for sample $x = 0.8$ and $x = 1.0$. This is due to room temperature DC resistivity increases by increasing Ni content. Similar results are reported by Ghazanfar *et al.*[28] in case of Ni-Zn ferrites. This attributed due to the decrement of the grain size of the samples. The room temperature DC resistivity lies in the range of 8.0×10^9 to $8.5 \times 10^9 \Omega cm$. This higher values of bulk sample reported by Shinde *et al.* [16] which shows that the room temperature DC resistivity of Nd^{3+} substituted zinc ferrite is 10^2 times larger than the pure zinc ferrite. The decrease in resistivity might be understood as due to the formation of grain growth and decrease of grain size.

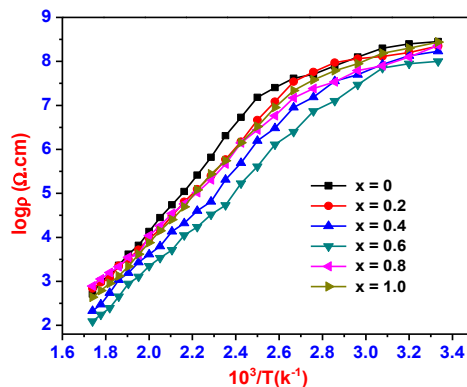


Fig. 4. Variation of $\log \rho$ with temperature of $Ni_xZn_{1-x}Fe_2O_4$ ($x = 0, 0.2, 0.4, 0.6, 0.8, 1.0$)

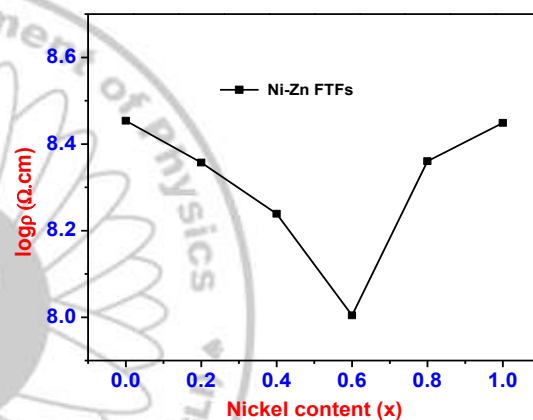


Fig. 5. Room temperature DC resistivity of $Ni_xZn_{1-x}Fe_2O_4$ ($x = 0, 0.2, 0.4, 0.6, 0.8, 1.0$)

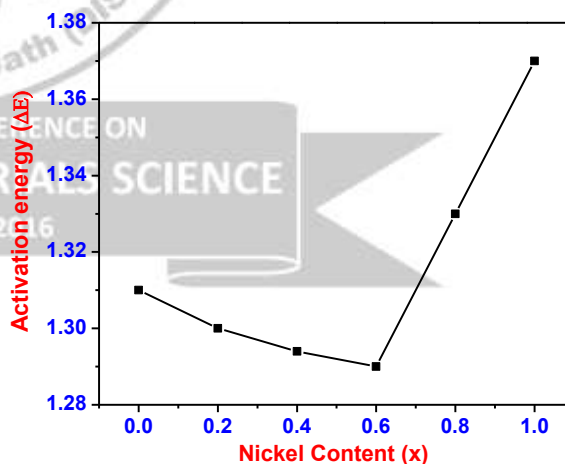


Fig. 6. The activation energy (ΔE) of $Ni_xZn_{1-x}Fe_2O_4$ ($x = 0, 0.2, 0.4, 0.6, 0.8, 1.0$)

The activation energy of ferromagnetic region is calculated by using Arrhenius relation and plot of $\log \rho$ versus $1/T$. The ferromagnetic region of activation energy is presented in the **Fig. 6**. From this figure, the activation energy of decreases with increasing nickel content up to $x =$

0.6. The decrease of activation energy in the ferromagnetic region is associated with the effect of spin disordering. It is responsible for the electrical conduction in the Ni-Zn ferrites are for the electron and hole hopping between the Ni^{3+}/Ni^{2+} , Zn^{3+} and Zn^{2+}/Fe^{3+} and Fe^{2+} ions [29].

For the sample $x=0.8$ and 1.0 the activation energy increase with increasing nickel content. This is because of the Ni-Zn ferrite samples having higher values of resistivity and it has higher values of activation energies and vice versa [28].

4. Conclusion

The nano-size powders of $Ni_xZn_{1-x}Fe_2O_4$ ($x=0, 0.2, 0.4, 0.6, 0.8, 1.0$) were prepared by oxalate co-precipitation method and screen printing technique was used to prepare the ferrite thick films (FTF). The typical ferrite sample was characterized by XRD, FTIR and FE-SEM. The DC electrical resistivity study shows, the semiconducting behavior of FTFs. Room temperature resistivity of FTFs was found to decrease with increasing Ni^{2+} content up to $x=0.6$ and thereafter increases for the compositions $x \geq 0.8$. Ni-Zn ferrite samples have higher values of resistivity and it has higher values of activation energies and vice versa respectively.

Reference

- Harris VG, *et al.* Recent advances in processing and applications of microwave ferrites, *J. Magn. Magn. Mater.* 2009;321:2035-2047.
- Martens J, Voermans A, Cobalt ferrite thin films for magneto-optical recording, *Magnetics, IEEE Trans.* 1984;20:1007-1012.
- Krishnaveni T, Kanth BR, Raju VSR, Murthy SR, Fabrication of multilayer chip inductors using Ni-Cu-Zn ferrites, *J. alloy. Comp.* 2006;414:282-286.
- Lin M, Huang J, Sha M. Recent advances in nanosized Mn-Zn ferrite magnetic fluid hyperthermia for cancer treatment. *J. Nanosci. Nanotechnol.* 2014;14(1):792-802.
- Luders BU, Barthelemy A, Bibes M, Bouzouhane K, Fusil S, Jacquet E, Contour JP, Bobo JF, Fontcuberta J, Fert A, $NiFe_2O_4$: A versatile spinel material brings new opportunities for spintronics, *Adv. Mater.* 2006;18:1733-1736.
- Zaspalis V, Tsakaloudi V, Papazoglou E, Kolenbrander M, Guenther R, Valk PV, Development of a new Mn-Zn ferrite soft magnetic material for high temperature power applications, *J. Electroceramic.* 2004;13:585-591
- Wettling W, Magneto-optics of ferrites, *J. Magn. Magn. Mater.* 1976; 3:147-160.
- Subramani AK, Kondo K, Tada M, Abe M, Yoshimura M, Matsushita N, High resistive ferrite films by a solution process for electromagnetic compatible (EMC) devices, *J. Magn. Magn. Mater.* 2009;321:3979-3983
- Peng E, Choo ESG, Chandrasekharan P, Yang CT, Ding J, Chuang KH, Xue JM, Synthesis of manganese ferrite/Graphene oxide nanocomposites for biomedical applications, *Small* 2012;8:3620-3630.
- Suite M, Muntean C, Militaru B, Fine $MnFe_2O_4$ nanoparticles for potential environmental applications, *J. Therm. Anal. Calorim.* 2015; 121:1003-1010.
- Goldman A, Ferrites for entertainment applications-Radio and TV, *Modern Ferrite Technology*, 2006, pp 291-306.
- Gadkari AB, Shinde TJ, Vasambekar PN, Effect of rare earth ion (Sm^{3+}) on gas sensing properties of $Mg_{1-x}Cd_xFe_2O_4$ system, *Sensors and Actuators B Chem.* 2013;178(1),34-39.
- Shinde TJ, Gadkari AB, Vasambekar PN, DC resistivity of Ni-Zn ferrites prepared by the oxalate precipitation method, *Mater. Chem. Phys.* 2008;111:87-91.
- Inbanathan SSR, Vaithyanathan V, Chelvane JA, Markandeyulu G, Bharathi KK Mossbauer studies and enhanced electrical properties of R (R = Sm, Gd and Dy) doped Ni ferrite, *J. Magn. Magn. Mater.* 2014;353:41-46.
- Varshney U, Puri RK. The effect of substitutions of Sn^{4+} and Zn^{2+} ions on the magnetic properties of nickel ferrites, *IEEE Tran. Magn.* 1989; 25:3109-3116.
- Shinde TJ, Gadkari AB, Vasambekar PN, Effect of Nd^{3+} substitution on structural and electrical properties of nanocrystalline zinc ferrite, *J. Magn. Magn. Mater.* 2010;322:2777-2781.
- Balaji S, Selvan RK, Berchmans LJ, Angappan S, Subramanian K, Augustin CO, Combustion synthesis and characterization of Sn^{4+} substituted nanocrystalline $NiFe_2O_4$, *Mater. Sci. Eng. B.* 2005;119:119-124.
- Rao ADP, Ramesh B, Rao PRM, Raju SB, Magnetic and microstructural properties of Sn/Nb substituted Mn-Zn ferrites, *J. Alloy. Comp.* 1999;282: 268-273.
- Tewari BS, Dhyani A, Joshi SK, Dubey S, Pandey K, Study of magnetic property of Sn doped Ni-Zn-Fe nanoparticles, Hindawi Publishing Corporation, Conference Papers in Science, Volume 2014, Article ID 816970, 4 pages.
- Vaithyanathan V, Ugendar K, Chelvane JA, Bharathi KK, Inbanathan SSR, Structural and magnetic properties of Sn and Ti doped Co ferrite, *J. Magn. Magn. Mater.* 2015;382: 88-92.
- Hemeda OM, Mostafa NY, AbdElkader OH, Hemeda DM, Tawfik A, Mostafa M, Electrical and morphological properties of magnetocaloric nano Zn-Ni ferrite, *J. Magn. Magn. Mater.* 2015;394:96-104.
- Islam MU, Abbas T, Niazi SB, Ahmad Z, Sabeen S, Chaudhry MA, Electrical behaviour of fine particle co-precipitation prepared Ni-Zn ferrites, *Mater. Sci. Eng. B* 2007;139:164-170.
- Ajmal M, Maqsood A, Influence of zinc substitution on structural and electrical properties of $Ni_{1-x}Zn_xFe_2O_4$ ferrites, *Mater. Sci. Eng. B.* 2007;139:164-170
- Dalawai SP, Shinde TJ, Gadkari AB, Vasambekar PN, Ni-Zn ferrite thick film gas sensors, *Mater. Sci. Mater. Elect.* 10.1007/s10854-015-3585-z
- Wargo C. Characterization of conductors for printed electronics. PChem Associates. 3599 Marshall Lane. Bensalem, PA 19020. (215) 244-4603.
- W. Chen, W. Zhu, Deposition of $CoFe_2O_4$ Composite Thick Films and Their Magnetic, Electrical Properties Characterizations, INTECH Open Access Publisher, 2011, ISBN- 9533073322.
- Rao ADP, Ramesh B, Rao PRM, Raju S.B, Influence of Sn/Nb on the resistivity of Mn-Zn ferrites, *Ind. Pure. Appl. Phys.* 1999;37:51-56.
- Ghazanfar U, Siddiqi SA, Abbas G, Study of room temperature DC resistivity in comparison with activation energy and drift mobility of Ni-Zn ferrites, *Mater. Sci. Eng. B.* 2005;118:132-134.
- Lee JY, Lee GH, Kim HS, Lee SH, Lee DH, Yo CH, Kim KH, Ahn K, Electrical and magnetic properties of the Sn^{4+} substituted spinel ferrite, $ZnSn_xFe_{2-4x/3}O_4$ ($0.00 \leq x \leq 0.30$). *Mater. Chem. Phys.* 1998; 52:267-271.

Self-cleaning Superhydrophobic Silica Coatings Modified by Polystyrene

Rajaram S. Sutar¹, A. K. Bhosale², S. P. Dharigouda³ and Sanjay S. Latthe^{1*}

¹ Self-cleaning Research Laboratory, Department of Physics, Raje Ramrao College, Jath 416 404, Maharashtra, India.

² Department of Physics, Raje Ramrao College, Jath 416 404, Maharashtra, India.

³ Department of Statistics, Raje Ramrao College, Jath 416 404, Maharashtra, India.

Corresponding author*: latthes@gmail.com

Abstract

Here we report a facile way to prepare a superhydrophobic silica coating modified by polystyrene (PS) using simple dip coating method. A commercially available silica nanoparticles were dip-coated on glass substrate and the stability of the coating was improved by applying a layer of PS. A superhydrophobic coating with a water contact angle (WCA) greater than 160° was achieved by a simple dip-coating method. A sliding angle (SA) less 5° indicated the self-cleaning properties of the superhydrophobic surface. This coated substrate mimics the self-cleaning property of superhydrophobic lotus leaves. The mechanical stability of the prepared superhydrophobic coatings was confirmed by adhesive tape test. The WCA before and after adhesive tape test was measured and the coating prepared with 4 mg/ml and dipping time in PS for 4 min revealed good mechanical stability with small decrease in WCA of ~ 140°. A dip-coating technique can be applied to glass substrate to make them superhydrophobic, self-cleaning and adherent which can be applicable for windows glass, solar cell module, vehicle glass, metals, fabrics and many.

Keywords: Superhydrophobic, Contact angle, Wettability, Self-cleaning, Lotus effect.

1. Introduction

Glass is a common and essential material in daily life and adherent and self-cleaning superhydrophobic coating on it might have an important industrial application. The surface structure of Lotus leaf has two levels of roughness (on the micro and nano scale) that enable the trapping of air under water droplets, thereby contributing to the rolling water droplet effect that is characteristic of a well-designed superhydrophobic surface. Self-cleaning Lotus leaf is a well-known superhydrophobic surface in nature which is composed of micro and nanometer-scaled patches coated with a few nanometer thick hydrophobic layer [1, 2]. The roughness of the patches enables trapping of air below the water droplet, thus helping the rolling of water droplets easily, resulting in superhydrophobic surface. A surface with micro- or nano sized roughness was created by lithography technique or by deposition of a micro or nano-materials [3]. Subsequently, molecules with a low surface energy were deposited to provide water-repelling properties [4]. The low cost amorphous polystyrene (PS) was dissolved in solvent and casted under ambient atmosphere, the resultant coating was almost smooth provided some micro-scale holes appeared in the coating [5]. A rough film consisting of micro-bead and nano-fiber mixed structures was formed by spraying a PS solution onto a large area and any type of substrates [6].

Bravo and his research group reported a development of transparent superhydrophobic

films from layer-by-layer assembled silica nanoparticle, the nanoporous nature of the Silica nanoparticle layer gives rise to antireflection properties however not reported self-cleaning property and adhesion [7-11]. Superhydrophobic surface was prepared by increasing roughness of surface using silica nanoparticles via dip-coating [9]. Here we report a simple method to prepare a superhydrophobic coating by silica nanoparticle deposition on glass substrate and applying a layer of PS by dip coating method with varying concentration of silica nanoparticle and deposition time. Dip coating method is low-cost, simple and can be applied over a large area. Water droplets easily roll-off from the surface at around 5° tilting indicating good water repellency [8-10]. Superhydrophobic coating can be prepared by using cheapest polymer and simple dip coating method in low cost on large area. It is applicable for windows glass, solar cell panel, vehicle glass, metals, apparels and so on.

2. Experimental Section

2.1 Material and Chemicals

Glass slides (75 mm long X 25 mm wide) was purchased from Polar Industrial Corporation Mumbai (India). Silica nanoparticles (RX-300-5, Hydrophobic fumed silica treated with HMDS) was purchased from NIPPON AEROSIL Co. Ltd., JAPAN. Hexane was purchased from Spectrochem Pvt. Ltd. Mumbai (India). Polystyrene (average Mw ~ 192,000) was purchased from SIGMA-ALDRICH Co. (USA). Toluene (99.5%) was purchased from Loba Chemie Pvt. Ltd. Mumbai (India).

2.2 Preparation of Silica Nanoparticles (SN) coated glass substrate

A coating solution was prepared by adding silica nanoparticles in hexane with different concentrations (2, 4, 6, 8 and 10 mg/ml) and ultrasonicated for 10 min before use. The cleaned glass substrate was dipped and taken out and then dried at room temperature.

2.3 Preparation of Superhydrophobic Coating

A polystyrene solution was prepared by dissolving PS in toluene with different

concentrations (4 and 6 mg/ml) and it was ultrasonicated for 30 min. Silica Nanoparticle coated glass substrate was dipped into this polymer solution for different dipping time and take out. The dipping time was varied for 4 and 6 min. This PS layer coated silica film was annealed at temperature 100 °C for 1 h. Experimental scheme as shown in **Fig.1**.

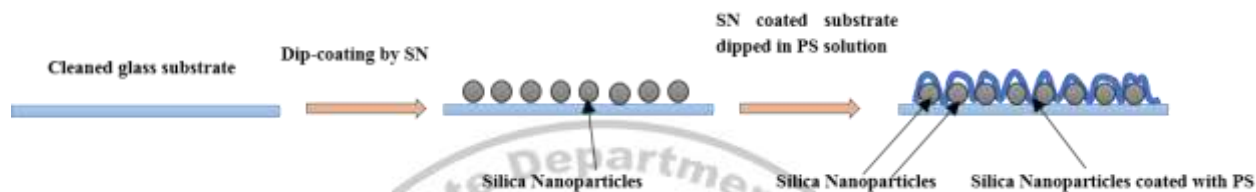


Fig.1: Preparation of superhydrophobic coating using silica nanoparticles and post-polymer modification.

2.4 Characterizations

Water droplet was placed on superhydrophobic coating by syringe and captured a digital image of water droplet placed on superhydrophobic coating. A tangent was drawn at three phase solid-liquid-air contact and contact angle was measured using goniometer. Water droplets were gently placed on the coating surface by syringe and roll-off angle was measured by slowly tilting the surface. This tilting (sliding angle) was measured by simple goniometer. To check the mechanical stability of the coating, adhesive tape test was performed. An adhesive tape was applied on the coating surface and pressed gently to make good contact between tape and superhydrophobic coating and followed by peeling off. WCA was measured after this adhesive tape test. Carbon dust particles were sprayed randomly on superhydrophobic coating. The water drops were dropped on superhydrophobic coating having dust particles, water droplets roll-off with absorbing dust particles and cleaned the surface.

3. Results and Discussion

3.1 Measurement of WCA and SA

Table I. and Table II summarizes water contact angle (WCA) and sliding angle (SA) of superhydrophobic coating. At first, the coatings were prepared from different concentrations of the SNPs namely from 2, 4, 6, 8 and 10 mg/ml and dried at room temperature for 30 min. The coatings prepared with 2 to 10 mg/ml showed very less WCA in the range of 80 to 90°. At the same

time, the coating was easily wiped out by gentle finger touch, which confirms weak mechanical stability. To improve the mechanical stability of the prepared coating from SNPs, we modified the coating by polymer (PS). Two polystyrene solutions in toluene was prepared with concentrations of 4 and 6 mg/ml and the prepared SNPs coatings were dipped in these solutions separately for different dipping times. The dipping times were varied from 4 and 6 min for both the PS solution.

As shown in Table I and II, a PS modification for the coating prepared with 2 mg/ml SNPs showed improved water contact angle of nearly 143 ° and sliding angle of 8°. A superhydrophobicity was achieved for the coating prepared with 4 mg/ml SNPs modified with 4 and 6 mg/ml PS solution and for dipping time of 4 min. This is critical PS concentration and dipping time to achieve superhydrophobicity. However for the higher concentrations of SNPs coating and higher concentrations of PS solution, the WCA was decreased due to decrease in surface roughness. For higher concentrations of PS, the roughness achieved by SNPs was ruined by the PS and the coatings are smooth in nature which is not a good sign for superhydrophobicity. So it was possible to achieve critical surface roughness where the 4 mg/ml SNPs coating modified with 4 and 6 mg/ml PS solution with dipping time ~ 4 min showed superhydrophobicity as shown in **Fig. 2**.

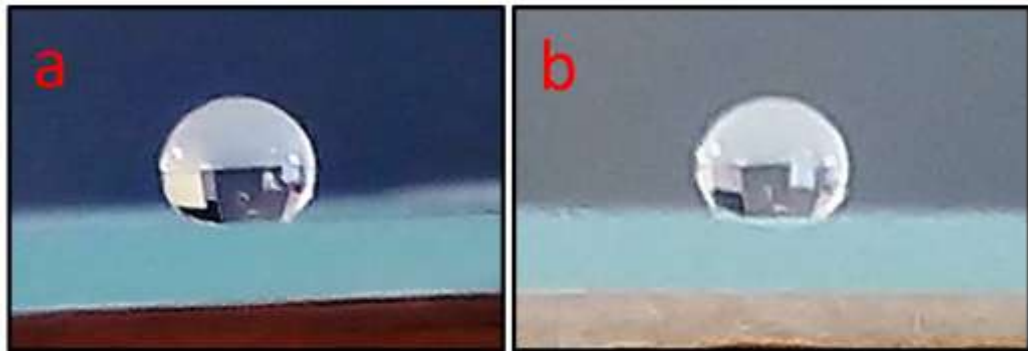


Fig.2: a) 4 mg/ml SNPs coated substrate dipped in 4mg/ml PS solution for 4 min having CA~(160±3°) and SA~(5±1°) b) 4mg/ml SNPs coated substrate dipped in 6mg/ml PS solution for 4 min having CA~(155±3°) and SA~(5±1°).

Table I: WCA for different concentration of SNPs and PS solutions for different dipping time.

Silica nanoparticles solution	Sliding angle in degree			
	4 mg/ml PS solution		6 mg/ml PS solution	
	4 min	6 min	4 min	6 min
2 mg/ml	8±1	17±1	17±2	17±2
4 mg/ml	5±1	8±1	5±1	8±1
6 mg/ml	17±2	17±2	17±2	17±2
8 mg/ml	17±2	17±2	17±2	17±2

Table II: SA for different concentration of SNPs and PS solutions for different dipping time

Silica nanoparticles solution	Contact angle in degree			
	4 mg/ml PS solution		6 mg/ml PS solution	
	4 min	6min	4min	6min
2 mg/ml	143±3	135±2	130±2	130±3
4 mg/ml	160±2	142±3	155±3	124±2
6 mg/ml	140±2	140±2	140±4	140±4
8 mg/ml	146±3	145±3	144±2	148±3

Table III: WCA for different concentration of SNPs and PS solutions for different dipping time after Adhesive Tape test

Silica nanoparticles solution	Contact angle in degree			
	4 mg/ml PS solution		6 mg/ml PS solution	
	4 min	6 min	4 min	6 min
2 mg/ml	100±2	100±2	100±3	105±2
4 mg/ml	140±3	125±2	140±3	130±3
6 mg/ml	125±2	115±3	115±2	120±3
8 mg/ml	120±2	105±3	110±2	120±2

3.2. Self-cleaning test

The superhydrophobic coatings are well-known for their self-cleaning performance. The Carbon particles (candle soot carbon particles) were sprayed randomly on to prepared superhydrophobic coating. At first, superhydrophobic coating was kept tilted for ~ 5° with hand-made tilting and then water droplets were dropped onto this film using a syringe. We

observed that the water droplet absorbed carbon particles and rolled off eventually cleaning the superhydrophobic surface. The superhydrophobic self-cleaning process as shown in **Fig.3**.



Fig.3: Super hydrophobic coating shows Self-cleaning property.

3.3. Adhesive Tape test

In adhesive tape test, a pressure was applied to make good contact between the tape and silica nanoparticle coating modified by PS and the tape was gently lifted from superhydrophobic film (Fig.4). The superhydrophobic surface examined by measuring contact angle before and after adhesive tape test. The **Table I and III** shows difference between contact angle before and after adhesive tape test. This test shows adhesion between coating and glass was strong. It indicates that prepared coating is mechanically stable.

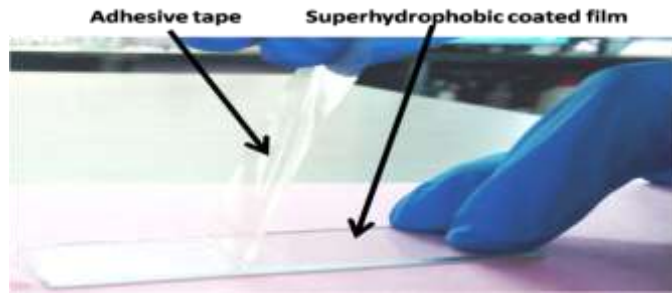


Fig.4: Lifting the tape from superhydrophobic film

Wettability of water droplet on different place of superhydrophobic coating was shown in Fig.5. On clean glass, wettability is high and on superhydrophobic coating it is low. After adhesive tape test, the coating was partly removed by the tape so that the WCA was lowered.

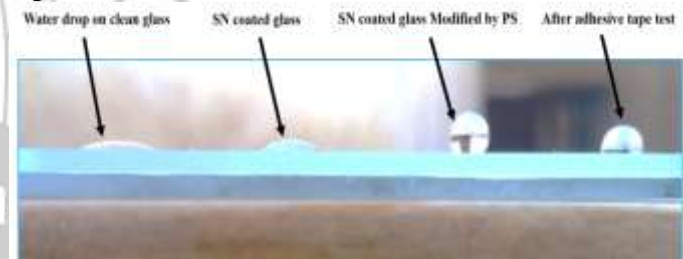


Fig.5: Shape of water drops on different places on the coated glass substrate.

4. Conclusion:

We achieved high contact angle (160°) and low sliding angle (5°) by using simple dip coating method on glass substrate. In this work, only at critical concentration of silica nanoparticle (4 mg/ml) with dipping time (4 min) at concentration of PS (4 mg/ml and 6 mg/ml) showed superhydrophobic nature with self-cleaning property and good adhesion. The critical surface roughness was achieved by thoroughly changing the silica nanoparticle and PS concentration. This technique has high potential to applicable for windows glass, solar cell panel, vehicle and so on.

Acknowledgment

This work is financially supported by DST-INSPIRE Faculty Scheme, Department of Science and Technology (DST), Government of India. [DST/INSPIRE/04/2015/000281].

References

1. Xu, Q. F.; Wang, J. N.; Sanderson, K. D. *ACS Nano* 2010, 4, 2201.
2. Li, X. M.; Reinhoudt, D.; Crego-Calama, M. *Chem. Soc. Rev.* 2007, 36, 1350.
3. Tserepi, A. D.; Vlachopoulou, M. E.; Gogolides, E. *Nanotechnology* 2006, 17, 3977.
4. Jeong-Ho Kong, Tae-Hyun Kim, Ji Hoon Kim, Jong-Kweon Park, Deug-Woo Lee, Soo-Hyung Kimac and Jong-Man Kim. *Nanoscale*, 2014, 6, 1453
5. Shuaixia Tan , Qiongdan Xie , Xiaoying Lu , Ning Zhao , Xiaoli Zhang , Jian Xu *Journal of Colloid and Interface Science* 322 (2008) 1–5
6. Cheng-Wei Tu, Chia-Hua Tsai, Chih-Feng Wang, Shiao-Wei Kuo, Feng-Chih Chang *Macromol. Rapid Commun.* 2007, 28, 2262–2266 2007 WILEY-VCH Verlag GmbH & Co.KGaa, Weinheim
7. Javier Bravo, Lei Zhai, Zhizhong Wu, Robert E. Cohen, and Michael F. Rubner, *Langmuir* 2007, 23, 7293-7298
8. Adem Yildirim, Tural Khudiyev, Bihter Daglar, Hulya Budunoglu, Ali K. Okyay, Mehmet Bayindir *ACS Appl. Mater. Interfaces* 2013, 5, 853–860
9. Lebo Xu, Raghuraman G. Karunakaran, Jia Guo, and Shu Yang *ACS Appl. Mater. Interfaces* 2012, 4, 1118–1125
10. Xing Yi Ling, In Yee Phang, G. Julius Vancso, Jurriaan Huskens, and David N. Reinhoudt. *Langmuir* 2009, 25, 3260-3263
11. Jing Lin, Cheng Zheng, WenJin Ye, HuaQuan Wang, DanYan Feng, QiaoYi Li, BoWei Huan J. *APPL. POLYM. SCI.* 2015, DOI: 10.1002/APP.41458

Selected Plants from Arid Zone Conditions as a Source of Novel Biomaterials

Kulkarni N.A., Dangat B.D., Teli P.B., Andoji Y.S.

P.D.V.P.Mahavidyalaya, Tasgaon 416 312 (M.S), Email : nakul24in@yahoo.com

Abstract

Since from ancient times man has used the plants to cure various diseases and relieving physical suffering. It is found that in the modern days also plant based medicines are more preferred as allopathic medicines are showing detrimental side effects. Plant based medicines are proved to be more effective, cheap and easily available in the nature. The studies on medicinal uses of flowering plants of Jat Tehsil of Sangli district of Maharashtra state (17° 00" N to 17° 07" N and 75° 03" E to 75° 09" E) revealed that some of the medicinal plants are also found in the drought prone areas also with so much adverse conditions. The approx. area of the tehsil is 45 sq.km with small hills, ravines and bare plateaus of several km. with xeric habitat. Most of the plants show xerophytic adaptations to withstand extreme conditions of water and temperature. Besides all these adverse conditions some of the rare and unique species with medicinal uses show their appearance which need to be detected and understand. The study was focused for documentation of traditional knowledge of local people about use of native medicinal plants as ethno medicines. The ethno medicinal data on 74 plant species were recorded during field trips from remote villages of the area. The check list and ethno medicinal inventory was developed by botanical name, followed by local name, family, part used and biomaterials. This study will help scientific community to undertake further investigations on plants of this region.

Key words: Plants, Biomaterials, Maharashtra

1. Introduction

The arid tropical regions have all the adverse conditions for the plants. Besides all these adverse conditions some of the rare and unique species show their appearance, which need to be detected and understand. Some of families like *Capparidaceae* show their frequent occurrence. The species like *Elophia*, *Tinospora* which are declared as rare and endangered at the recent FRLHT workshop are found in the area. Some of the important medicinal plants like *Asparagus*, *Alangium*, *Morinda* are found in the wild.

The present study aims to analyze the diversity of plants of Jat tehsil in general and surrounding in particular for the use of these plants as a source of biomaterials . Attempts will be made to conserve the germplasm of these plants, which will be useful to the users. The seasonal collection will be made from time to time.

2. Material and Methods

Present study was confined to the identification of useful flora of Jat tehsil. Frequent field visits were arranged in order to collect the information about the medicinal plants used traditionally due to their unique medicinal properties. Plants are then identified with the help of available literature. Ethno medicinal Inventory was developed consisting botanical name followed by their local name, family part used and source of biomaterials.

3. Results and Discussions

In India number of publications are devoted for medicinal plants (Kirtikar and Basu 1935, Chopra and Chopra 1956, Kapoor and Mitra 1979, Satyavati et.al. 1976 – 87, Agarwal and Ghosh

1985, Warriar, 1996). There is also vast information on medicinal properties and uses of plants unknown to scientific community. During the last few decades, attempts were made to gather information on plants of our country (Jain 1981, 1991, Shivanranjan and Indira, De, Philips 1991 and several others.) Some of the information about the ethno medical importance of the plants has been compiled and published under the title ethno botany (Naik 1998, Agharkar 1953, Agarwal et.al. 1985.) In recent times much of the work on these aspects has been carried out by Yadav et.al. 2004, Hebbar et.al. 2004, Sahu et.al. 2004, Mahajan et.al. 2004.)The ayurvedic applications and formulations of drugs has been studied and applied since from ancient times as like Charak- Samhita. On the same lines the accounts has been attempted by (Sharma 1966, Bhanduri 1990, Summy- Dommen et.al. 2000, Ram et.al. 1993, Thakur et.al. 1989, Mathew 1983, Malhotra 1966, Shivanranjan 1994.)

Forty three plants are selected and studied for their biomaterial properties and are listed in the Table – I. During the study it is found that the plants are used singly or in combination with some other plants or plant parts. Some of the plants are claimed to be quite effective remedies for coetaneous affection of the head, snakebite, diarrhea, malaria, cough and cold, and stomach troubles etc. Since the uses of these plants are based on empirical knowledge, the scientific study of all these herbal drugs is highly desirable to establish their efficacy for safe use. The details of these plants and their importance are given in the Table: I. Various parts of the plant are used

incurring different ailments. Regularly chemical screening of medicinal plant and their useful parts collected from the fields in different seasons should be done.

4. Summary and Conclusion

The study conclude that the further work in these lines should formulized on base line of indigenous studies because there are still some diseases like Cancer and Aids for which there are no identified cures. So ethno directed studies can help in these research works. It was concluded from this study that a nationwide survey of medicinal flora should be conducted to investigate and update the inventory of existing natural plants resources of the area. It is suggested to establish small scale processing units for the valued drugs.

References

1. Kirtikar, K.R. and B.D. Basu, *Indian Medicinal Plants* Vol : 1-4 Lalit Mohan Basu., Allahabad. 1935.
2. Chopra, R.N., S.L. Nayar and I.C. Chopra, *Glossary Of Indian Medicinal Plants* C.S.I.R., New Delhi. 1956.
3. Kapoor S.L. and R.Mitra. *Herbal Drugs In Indian Pharmaceuticals Industry*. Lucknow. 1979.
4. Satyavati , G.V. and A.K. Gupta. *Medicinal Plants Of India: 1-2* I.C.M.R., New Delhi. 1976-1987.
5. Agarwal, V.S.and Barin Ghosh. *Drug Plants of India*. Root Drugs. Kalyani Publishers, New Delhi. 1985.
6. Warriar, P.K. et.al. *Indian Medicinal Plants a compendium of 500 species* Vol.1-5. Indcom press Madras. 1996.
7. Jain, S. K. (ed.) *Glimpses of Indian Ethnobotany*, Oxford and IBM Publishing Co., New Delhi. 1981.
8. Jain, S. K. (ed.) *Contribution to Indian Ethnobotany*, Scientific Publisher. Jodhpur 1991a.
9. Shivarajan and Indira, *Medicinal plants of India*. 1991.
10. De, Philips et.al. *Medicinal plants*, 1991.
11. Naik, V.N. Vanaushadhi, Amrut Prakashan, Aurangabad. 1998.
12. Agharkar, S.P. *Medicinal Plants of Bombay State Gaz.Se. A. Pt.I*.1953.
13. Yadav S.R., et.al. *Bull. Bot. Surv. India*, Vol.46, Nos. 1-4., 2004.
14. Hebbar, S.S., et.al. *Bull. Bot. Surv. India*, Vol.46, Nos. 1-4., 2004.
15. Sahu, B. et.al. *Bull. Bot. Surv. India*, Vol.46, Nos. 1-4., 2004.
16. Mahajan, S.K., et.al. *Bull. Bot. Surv. India*, Vol.46, Nos. 1-4., 2004.
17. Sharma, P.V., *Classical uses of medicinal plants*, Chowkhamba, Visvabharati, Varanasi. 1966.
18. Bhandari, M.M., *Flora of Indian deserts*, MPS Repros, Jodhpur, 1990.
19. Summy- Dommen and et.al., *Tropical Indian Medicinal Plants*, Propagation methods, FRLHT, Banglore,2000.
20. Ram, P., and et.al., *Compendium of Indian Medicinal Plants*, 1993.
21. Thakur, R.S., and et.al., *Major Medicinal Plants Of India*, 1989.
22. Charak- Samhita. Mathew, K.M., *The Flora Of Tamil Nadu Carnatic*, Vol,1-3, 1983.
23. FRLHT, A Database on Distribution Of Medicinal Plants.
24. Malhotra, S. C., *Pharmacological Investigations*, 1966.
25. Shivarajan, V.V., and et.al., *Ayurvedic Drugs and Their Plant Resources*, 1994.

Table: I List of plants with their biomaterials

Sr. No.	Botanical Name	Family	Parts used	Medicinal Uses	Potential Biomaterials
1	<i>Tribulus terrestris</i>	Zygophyllaceae	Leaves, seeds	Cough, urinary stones, impotency, raktapitta.	Kaempferol, Quercetin, Harnine, Harmol
2	<i>Calotropis gigantea</i> (L) R.Br. <i>C.Procera</i> (Ait) R.Br.	Asclepiadaceae	Leaf, stem, roots, latex	Piles, asthma, filaria, earache, boils, abortifacient, antitussive	B-Sitosterol, Triterpene, Giganteol, B-Amyrin, Sigmasterol, Calotropeols, Akundarin, Cardenolides, Uscharin
3	<i>Pongamia pinnata</i> Linn.	Papilionaceae	Root, leaf, seeds.	Skin diseases, eczema, leucoderma	Furoflavanes, Kaaranjin, Pongapin, Pinnatin, Glabrol, Kaempferol
4	<i>Solanum xanthocarpum</i> Schrad. Wendi. <i>S. vargineatum</i>	Solanaceae	Whole plant	Piles, carminative, laxative, cough, asthma, facial paralysis, abdominal pain, urinary disorders, earache, anti abortive	Tigonenin, Uttronins, Steroidal, Glycosides, Quercetin
5	<i>Solanum indicum</i> Linn.	Solanaceae	Whole plant	Anti-alopecia, digestive disorders, piles, eye problems.	Tigonenin, Uttronins, Steroidal, Glycosides, Quercetin
6	<i>Solanum nigrum</i> Linn.	Solanaceae	Whole plant	Eye disorders, rat poisoning, skin disorders, oedema, cough, conception, strength, ulcer	Tigonenin, Uttronins, Steroidal, Glycosides, Quercetin
7	<i>Andrographis paniculata</i> Burn F. syn. <i>Swertia chirata</i> Roxb.	Acanthaceae	Whole plant	Abortifacient, Anti bacterial, Hepatotoxic, Anti Fertility, Anti ulcer.	Andrographine, Andrographidine, Panicolin, Apigenin, Carvacrol, Eugenol, Kalmeghin
8	<i>Balanites aegyptica</i> (L.) Delile <i>B. roxburghii</i> Planch (L.)	Balanitaceae	Whole plant	Cosmetic, ulcer, liver spleen problems, malaria, snake poison, sperm deficiency, diabetes.	Balabyptin, Sapoginins, Balanitin, Bergapten, Cholestadiant
9	<i>Citrullus colocynthis</i> (Linn.) <i>Trichosanthes bracteata</i> lam. <i>Cucumis trigonus</i> Roxb	Cucurbitaceae	Root, Fruits	Jaundice, warts, alopecia, hair problems, arthritis, abortion, amenorrhoea	Balabyptin, Sapoginins, Balanitin, Bergapten, Cholestadiant
10	<i>Abrus precatorius</i> Linn.	Fabaceae	Root, stem, leaves	Dental caries, dandruff, scalp, cardiac problems, anti fertility	Abrine, Abrectonin, Abrasine,
11	<i>Tinospora cordifolia</i> (willd.) Hook.	Menispermaceae	Stem, leaves	Fever, Kustha, jaundice, headache, anti-toxic, antipyretic.	Furanoditerpenes, Columbine, Tinosporaside, Jatrrrhizine, Palmatine, Berberine, Tembeterine, Sesquiterpene, Glucoside, Tinocordifoliside, A & B-Choline, Tinosporal
12	<i>Aloe vera</i> Linn. <i>A. barbadensis</i> Mill.	Liliaceae	Leaf, root	Splenomegaly, jaundice, breast, pain, fever, headache, epilepsy, palpitation in heart	Aloe emodin, Aloin, Chrysophanic acid, Uronic acid, Anthrone
13	<i>Ricinus communis</i> Linn.	Euphorbiaceae	Seeds, roots, leaves	Seed oil medicinal, vatvyadhi, fever, constipation, diarrhea, piles, cough, chest pain heart pain, stomach ache, digestive problems	Ricinin, Kaempferol, Ricinolic acid,
14	<i>Leucas aspera</i> (Willd) Spreng <i>L. cephalotes</i> L.	Lamiaceae	Whole plant	Jaundice, Fever, eye-disorders, anti venom, psoriasis.	Glucoside, Triterpenes, Ursolic acid, Antivenin

	<i>plukenetil</i>				
15	<i>Cassia tora</i> Linn.	Caesalpiniaceae	Seeds, roots, leaf.	Skin diseases, rheumatism, leprosy, delivery problems.	Flavonol glycosides, Anthraquinone, Emodin, Chrysophanic acid,
16	<i>Cassia auriculata</i> Linn.	Caesalpiniaceae	Leaves flowers	Diabetes, skin disorders, stomatitis, eye disorders.	Flavonol glycosides, Anthraquinone, Emodin, Chrysophanic acid,
17	<i>Bacopa monnieri</i> (L.) Pennell. <i>Centela asiatica</i> Linn.	Scrophulariaceae Apiaceae	Whole plant	Mental disorders, insanity, epilepsy, promote intellect.	Alkaloids(brahmine and herpestine), saponins (d-mannitol and hersaponin, acid A, and monnieriin), flavonoids (luteolin and apigenin), betulinic acid, stigmaterol, beta-sitosterol, and bacopasaponins (bacosides A, bacosides B, bacopaside II, bacopaside I, bacopaside X, bacopasaponin C, bacopaside N2). The minor components include bacopasaponin F, bacopasaponin E, bacopaside N1, bacopaside III, bacopaside IV, and bacopaside
18	<i>Phyllanthus amarus</i> Schum. <i>P. urinaria</i> Linn. <i>P. niruri</i> Linn.	Euphorbiaceae	All parts	Jaundice, dysentery, dyspepsia, cough, indigestion, diabetes, urinary problems, skin problem, ulcer, swelling.	Lignans, tannins, polyphenols, alkaloids, flavonoids, terpenoids and steroids
19	<i>Eclipta alba</i> Hassk. Linn.	Asteraceae	Whole plant	Hair problems, muscle relaxant, spasmolytic, anti hypocholesterol.	Coumestros, Wadelolactone, Dimethylactone, Thiophene, Ecliptene, Nicotine, Apigenin
20	<i>Zizypus mauritiana</i> Lam. <i>Z. hummularia</i> Weight. <i>Z. vulgaris</i> Lam.	Rhamnaceae	Leaf, root, bark, seed	Burning sensation, diarrhea, cough, voice, headache, obesity, piles	Peptide alkaloids, Mauritines, A-F, Frangulofoline, Amphibines, Jubanines, Mucronine, Triterpenes, Spinisin
21	<i>Acacia nilotica</i> (L.) Willd <i>A. arabica</i> Del..	Mimoseae	Leaves, Fruit, bark	Diarrhoea, excessive perspiration, lacrimation, pain relief, abdominal disorders. Diuretic, blood purifier, haemostatic, skin disorders, arthritic, acidity, burning sensation	Resins
22	<i>Melia azedarach</i> Linn. <i>M. composita</i> willd.	Meliaceae	Leaf, root, bark	Skin disorders, arthritis, acidity, burning sensation	Azadirachtin
23	<i>Withania somnifera</i> (Linn.) Dunal.	Solanaceae	Root, leaf, seeds	Antibiotic, analgesic, anti malarial, respiration stimulant, anti spermato genic, muscle relaxant, ulcer, tumor	Nicotine, Somnoferine, Withanin, Isopelleterine, Tropine, Choline, Anaferine, Withanolides, Withanone, Sominone
24	<i>Achyranthes aspera</i> Linn.	Amaranthaceae	Root, leaf,	Excessive hunger, piles, calculi, wound, difficult labour, eye disorders, dog bite.	Betanine, Achyranthine, saponins A & B, Ecdysone, Ecdysterone, Inokosterone, Olenolic acid, Glycosides
25	<i>Alangium salvifolium</i> (Linn.) F. Wang.	Alangiaceae	Root bark, seeds, seed oil	Diarrhoea, jaundice, abdominal disorders, animal poisoning, rabies, bronchial asthma	Allangenine
26	<i>Clerodendrum Flomoides</i> Linn. F. <i>C. multiflorum</i> Linn.	Verbenaceae	Bark, leaf, leaves	Malarial fever, liver and rheumatism, abortifacient, hypoglycemic activity, hypotensive, muscle relaxant, uterine stimulant, diabetes.	Triterpenes, Daucosterol, Luteolin,

27	<i>Trichodesma indica</i> R. Br.	Boraginaceae	Whole plant	Leprosy, skin disorders	Triterpenes, Daucosterol, Luteolin, Nellionol, Premenol, Premnazole, Beta- setosterol
28	<i>Susbania grandiflora</i> (L.) Poiret.	Fabaceae	Leaves, flowers	Fever, night blindness, cough, epilepsy, astringent, small pox, ulcer, muscle relaxant	Ascorbic acid, Alpha carotene, cyanin, Kaempferol 3-7-diglucoside, Leucocyanidin, Alkanes, Alkanols, triterpenes, Beta-sitosterol, Stigmasterol
29	<i>Capparis decidua</i> Forsk.	Capparidaceae	Leaves, roots, fruits, Bark.	Bleeding piles, dry piles, oedema, blood purifier, eye sight problem, laxative.	Glycosides, Anthocyanins, Flavonoids, Steroids, Beta-sitosterol, Daucosterol, Terpenes
30	<i>C. aphylla</i> Forsk.	Capparidaceae	Leaves, roots, fruits, Bark.	Jaundice, swelling, fracture.	Flavonoids, Steroids, Beta-sitosterol, Daucosterol, Terpenes
31	<i>C. divaricata</i> Forsk.	Capparidaceae	Leaves, roots, fruits, Bark.	Jaundice, swelling, fracture.	Steroids, Beta-sitosterol, Daucosterol, Terpenes
32	<i>C. zeylanica</i> Forsk.	Capparidaceae	Leaves, roots, fruits, Bark.	Jaundice, swelling, fracture.	Beta-sitosterol, Daucosterol, Terpenes
33	<i>C. Floribunda</i> Forsk.	Capparidaceae	Leaves, roots, fruits, Bark.	Jaundice, swelling, fracture.	Daucosterol, Terpenes
34	<i>C. rotundifolia</i> Forsk.	Capparidaceae	Leaves, roots, fruits, Bark.	Jaundice, swelling, fracture.	Anthocyanins, Flavonoids, Steroids, Beta-sitosterol, Daucosterol,
35	<i>Cadaba indica</i> Forsk.	Capparidaceae	Leaves, roots, fruits, Bark.	Jaundice, swelling, fracture.	Steroids, Beta-sitosterol, Daucosterol,
36	<i>Gynandropsis gynandra</i> L. <i>G. pentaphylla</i> L. Briquet.	Capparidaceae	Leaves, roots, fruits, Bark.	Jaundice, swelling, fracture.	Daucosterol, Terpenes
37	<i>Cleome viscosa</i> Linn. <i>C. Gynanadra</i> Linn.	Capparidaceae	Leaves, roots, fruits, Bark.	Jaundice, swelling, fracture.	Glycosides, Anthocyanins, Flavonoids, Steroids, Beta-sitosterol, Daucosterol, Terpenes
38	<i>Saccharum spontaneum</i> Linn.	Poaceae	Whole plant	Whole plant epilepsy, dysuria, diuretic, aphrodisiac	Triterpenes
39	<i>Lawsonia inermis</i> L.	Lythraceae	Leaves	Diabetes, haemorrhage, skin disorders, hair problems	Lawson, Laxanthone II, Luteolin, B- sitosterol, mannitol, Lawsoniaside, Lalioid, Gallic acid, Napthaquinone
40	<i>Gymnema sylvestre</i> (Retz). R. Br. Ex. Syn. <i>Pergularia daemia</i> (Forsk.)	Asclepiadaceae	Leaves	Inflammation of glands, enlargement of spleen, indigestion, constipation, jaundice, piles, sinusitis, cough, respiratory problems, urinary stone, fever, diabetes	Alkaloids, cardiac glycoside, Oils- copadiene, rotundone, cypertone, epoxyguaiene, Benzoquinone
41	<i>Cyperus rotundus</i> Linn.	Cyperaceae	Whole plant	Digestive, disorders, diarrhea, arthritis, quick healing	Alkaloids, cardiac glycoside, Oils- copadiene, rotundone, cypertone, epoxyguaiene, Benzoquinone
42	<i>Vernonia cinerea</i> Less.	Asteraceae	Roots	Eruptive boils, fever, filaria, leucorrhoea	Diterpene abieta, Acerosin, Vitexin, Wogonin, Artemetin, Agnuside, Cadinol, Camphene, Gardenin, luteolon, Orientin
43	<i>Morinda pubescens</i> J.E. Smith. <i>M. tomentosa</i> Hook. <i>F. M. tictoria</i> Roxb.	Rubiaceae	Fruit, root, leaves	Energetic, anti-oxidant, disease resistant, blood disorders	Diterpene abieta, Acerosin, Vitexin, Wogonin, Artemetin, Agnuside, Cadinol, Camphene, Gardenin, luteolon, Orientin

Protection of lacquer materials from UV irradiation using the TiO₂/SiO₂ photocatalyst

Takahiro Adachi^{*}, Chiaki Terashima^{**}, Kazuya Nakata^{**}, Ken-ichi Katsumata^{**}, Norihiro Suzuki^{**}, Takeshi Kondo^{*,**}, Makoto Yuasa^{*,**}, Akira Fujishima^{**}

^{*} Department of Pure and Applied Chemistry, Faculty of Science and Technology, Tokyo University of Science, Tokyo, Japan

^{**} Photocatalysis International Research Center, Tokyo, Japan

TiO₂ is photocatalyst material, which shows super-hydrophilic and oxidative decomposition properties by UV irradiation. Water spreads out by forming a thin layer on TiO₂ and carries away dust particles from surface. In addition, organic compounds are decomposed by strong oxidation power. Lacquer is natural paint based on urushiol gathered from a lacquer tree. Due to its superior durability (acid, base, and water-resistance) and high adhesion, the lacquer has been applied to various substrates including tableware for a long time.

water contact angle, and lacquer deterioration was evaluated by IR spectrum under UV irradiation as well as was observed its surface morphology by laser microscope.

TiO₂/SiO₂ composite film was coated by dip coating or spray coating with SiO₂ slurry and TiO₂/SiO₂ slurry sequentially on lacquer substrates which were pretreated by ozone. Samples were dried 100 °C for 1 h after coating. The decrement of water contact angle was confirmed after 1 h UV irradiation from aging changes of water contact angle. This was due to the photo-induced hydrophilicity of TiO₂ by UV irradiation. Fig.1 shows the change of IR spectrum with UV irradiation time, a peak around 1700 cm⁻¹ increased and a peak around 1050 cm⁻¹ changed by keeping UV irradiation. This was because C=O bond increased, and also changed into ester bond of primary alcohol. Laser microscope observation revealed that the lacquer surface became rougher after UV irradiation due to the degradation. As the surface became rough, the diffused reflectance light increased, causing the decrease of the luster of the lacquer surface. Therefore, coating of TiO₂/SiO₂ composite film is needed to more absorb UV irradiation and to protect the lacquer surface from UV light by photocatalytic effects.

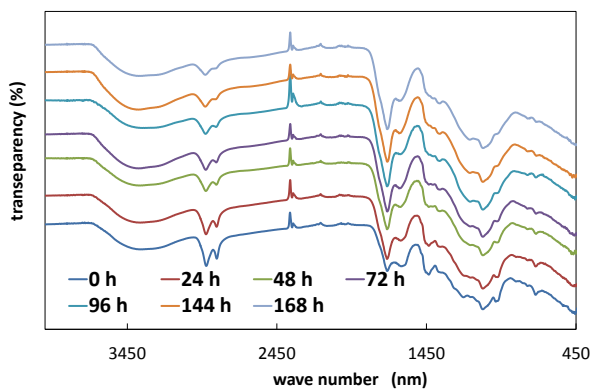


Fig. IR spectrum of Ti₂ on Lacquer

However, the lacquer deteriorates and decreases in luster by UV irradiation¹⁾. In this work, the coating of TiO₂/SiO₂ composite film on lacquer was conducted in order to absorb UV light, aiming to prevent deterioration and give the self-cleaning properties. Self-cleaning effects was evaluated by

References

1. Ogawa T, Urushi-no-Kgaku (Science of Lacquer) (in Japanese)

Structural Optimization and Improved Activity of Photoelectrochemical Glutathione Sensor by Electrochemical Impedance Spectroscopy

Kensuke Katagishi^{*,**}, Asako Kuragano^{*,**}, Chiaki Terashima^{**}, Norihiro Suzuki^{**}, Kazuya Nakata^{*,**}, Ken-ichi Katsumata^{**}, Yoshinao Hoshi^{*}, Isao Shitanda^{*,**}, Takeshi Kondo^{*,**}, Makoto Yuasa^{*,**}, Masayuki Itagaki^{*} and Akira Fujishima^{**}

^{*}Tokyo University of Science (2641, Yamazaki, Noda, Chiba 278-8510, Japan)

^{**}PIRC, E-mail address: 7216621@ed.tus.ac.jp

Human blood contains a high concentration of glutathione (GSH), which is an antioxidant component. The higher the concentration of the in-vivo GSH, the higher a risk of cancer. Therefore, it is important to detect the GSH concentration of the high density region. Photoelectrochemical sensors using photocatalyst can be kept low applied potential from becoming a source of energy from light and electricity. Therefore, high sensitivity sensing can be expected. According to the previous report, it was confirmed that a hybrid Au-TiO₂ photocatalyst material can detect GSH. In this study, deeper studies were carried out in order to design a smarter and more sensitive GSH

The physical properties of prepared film were evaluated by X-ray diffraction (XRD) and diffuse reflectance spectrum analysis. XRD was let found to be the titanium oxide of anatase type. In addition, the diffuse reflection showed an increase in the peak of gold due to the increased amount of gold (about 570 - 580 nm).

The morphology of TiO₂ is found to be fiber structure in our study. To reproducibly deposit titanium oxide film of the fiber is required to have humidity control, and it was possible to produce fiber membranes by increasing the humidity. This is because the hydrolysis tends to occur by high humidity.

This study was performed on the impedance measurement using an electrolyte prepared by , which was further confirmed by Mott-Schottky plot. Therefore, recombination of exited electrons of TiO₂ can be suppressed by modifying with Au nanoparticles.

Furthermore, we measured chronoamperometry

sensor.

This is the method for manufacturing the electrode of the present study. Au-TiO₂ thin film was prepared by two steps method. First, a mixture of titanium (IV) bis (ethyl acetoacetato) diisopropoxide and 1-butanol was spin-coated on FTO glass. Second, the coated FTO glass was calcined at 450 °C for 1 h. After cooling to room temperature, a solution of gold chloride dissolved in PVP, ethanol, and acetic acid was deposited on the TiO₂-modified FTO glass using electrospinning (ES) method, and heated at 500 °C for 2 h.

adding 0.5mM of GSH in phosphate buffered saline (PBS). In this research, reference electrode is Ag/AgCl, counter electrode is platinum and the light source is a solar simulator (1 SUN).

By changing the ES method, different samples of Au-TiO₂ on FTO was prepared and electrochemical properties were measured. Equivalent circuit was designed in this experimental system. Charge transfer resistance and space charge layer capacitance between electrolyte interface with Au-TiO₂ electrode were studied and fitted to the experimental results. The measurement results, loading of Au nanoparticles was decreased charge transfer resistance and increased space charge layer capacity (Fig.1). This indicates that carrier density in TiO₂ would increase in order to know the concentration range that can be put to practical use as a sensor. GSH was then detected by the electrode (Au 0.1 g) and detection level is found to be in the range of 1 - 5 mM (Fig.2).

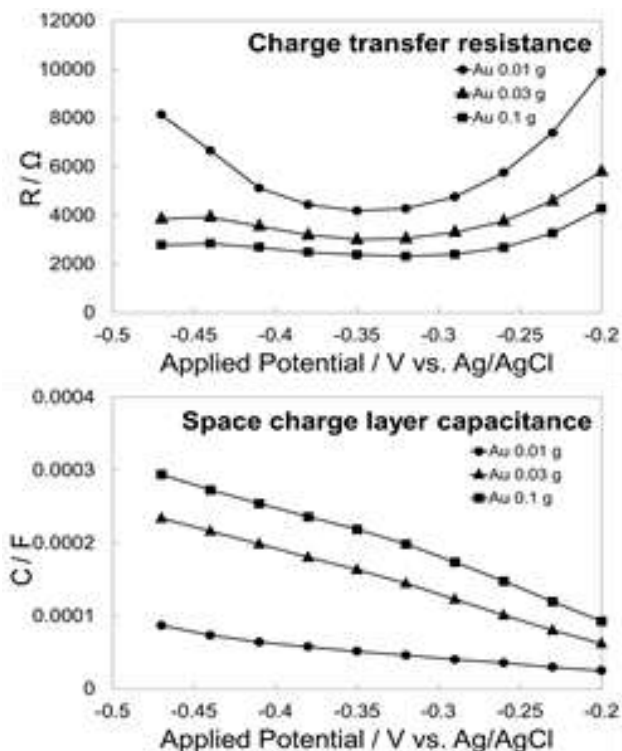


Fig.1. When changing the amount of gold (A) charge transfer resistance and (B) space-charge layer capacity
 From the above result, the fiber morphology as well as the loading of Au nanoparticles enable

high-sensitivity sensing by using an electrode of Au 0.1 g, leading to the determination at a high concentration range.

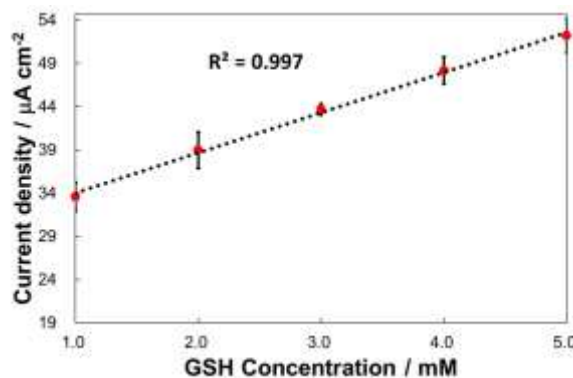
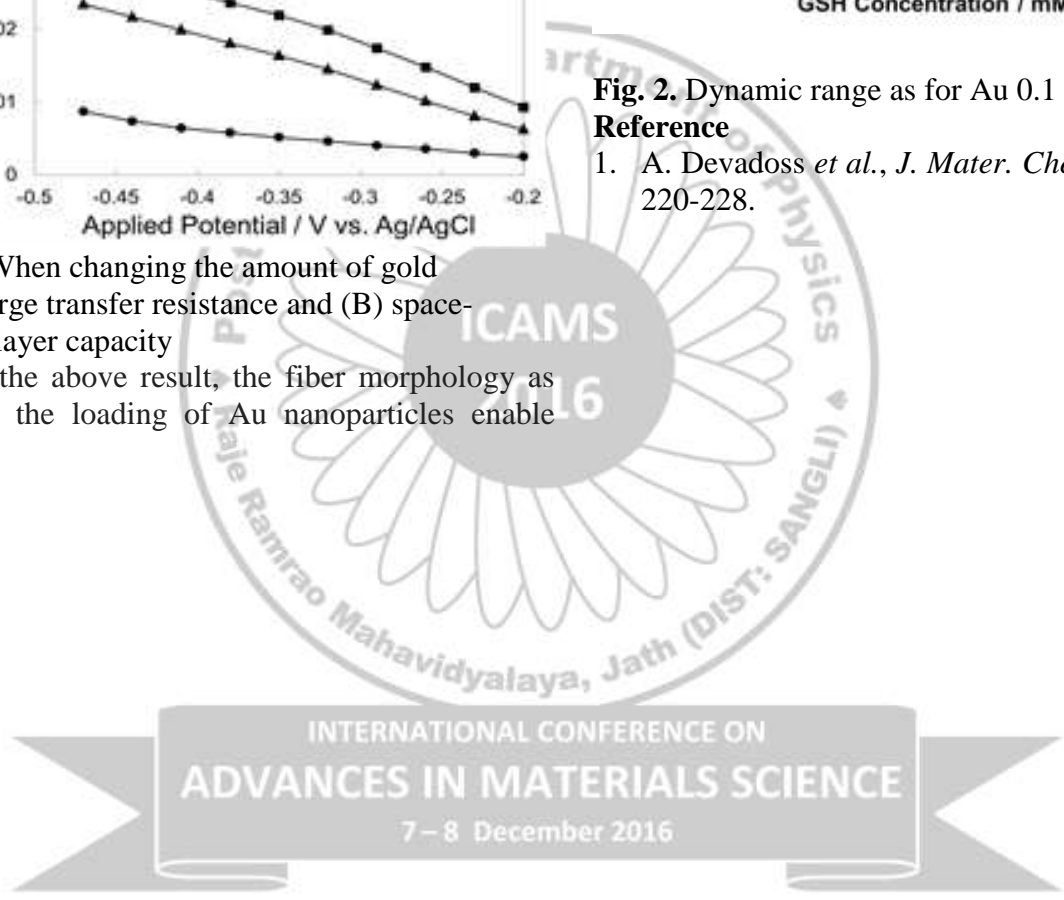


Fig. 2. Dynamic range as for Au 0.1 g electrode
Reference

1. A. Devadoss *et al.*, *J. Mater. Chem B*, 2016, 4, 220-228.



INTERNATIONAL CONFERENCE ON
ADVANCES IN MATERIALS SCIENCE
 7 – 8 December 2016

Influence of solvent on diamond synthesis by microwave in-liquid plasma method

Kazuya Miyasaka¹, Yusei Sakurai¹, Yohei Harada^{1,2}, Chiaki Terashima³,
Hiroshi Uetsuka^{2,3}, Norihiro Suzuki³, Kazuya Nakata^{1,3}, Ken-ichi Katsumata³, Takeshi Kondo^{1,3},
Makoto Yuasa^{1,3}, Akira Fujishima³

¹Department of Science and Technology, Tokyo University of Science,

²Asahi Diamond Industrial Co., Ltd.,

³Photocatalysis International Research Center, Tokyo University of Science

1. Introduction

Diamond has outstanding properties, such as high chemical and physical stability. This material exhibits for a wide range of applications, such as a cutting tool and an electrode and so on. Microwave plasma chemical vapor deposition method used for synthesis diamond. However, this method has low growth rate due to low plasma density. In the microwave assisted plasma in-liquid method, it is possible to synthesis diamond rapidly. This research is aimed to investigate the effect of solution on diamond synthesis by using microwave assisted plasma in-liquid method.

2. Experimental

Fig. 1 shows the schematic image of microwave assisted plasma in-liquid method. A mixture of methanol (M) and ethanol (E) added with tetrahydrofuran (THF) or methyl acetate (MA) was poured into the reactor. 2.45 GHz microwave of (440 W) was irradiated from the generator, and conducted into the reactor via the waveguide and the electrode. The mixture was adjusted so that the ratio of C: H: O is nearly 17.2: 66.6: 16.1. A tungsten rod of 3 mm in diameter is used for the electrode. The substrate was monocrystalline silicon, and the distance between the tip of the electrode and the substrate was set to 1.0 mm. The time for synthesis diamond was 5 minutes under 60 kPa.

3. Result and discussion

Fig. 2 shows the laser microscope image and the Raman spectrum. As a result of synthesis, diamond was obtained in all conditions because the Raman spectra showed a characteristic peak of diamond at 1332 cm^{-1} . However, when solvent was M : E : MA = 399.6: 35: 0.4 mL, the film was not synthesized uniformly. On the other hand, the film was synthesized uniformly when solvent was M : E = 360: 40 mL and M: E : THF = 396: 25: 4 mL. Furthermore, when the mixture of M: E : THF = 396: 25: 4 mL was used as a solvent, a sharper

peak was obtained in raman spectra compared with M : E = 360: 40 mL. And then, raman spectra showed that the decreased sp^2 component.

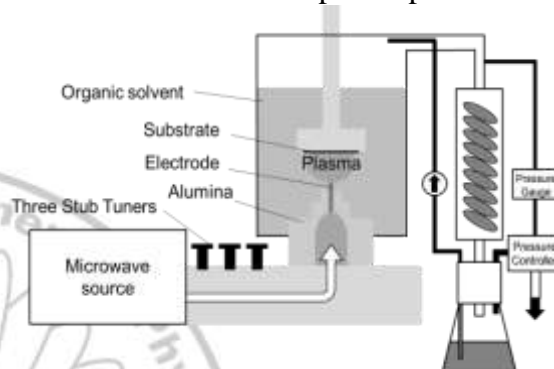


Fig. 1. In liquid MPCVD equipment

When THF was added to the solution, the infrared region in the emission spectrum was more stable than THF was not added. This resultsuggests that THF enable the substrate temperature to be more stable. Therefore, the crystallinity was improved by adding THF. In the future, it is necessary to investigate the mechanisms why the crystallinity was improved by adding THF.

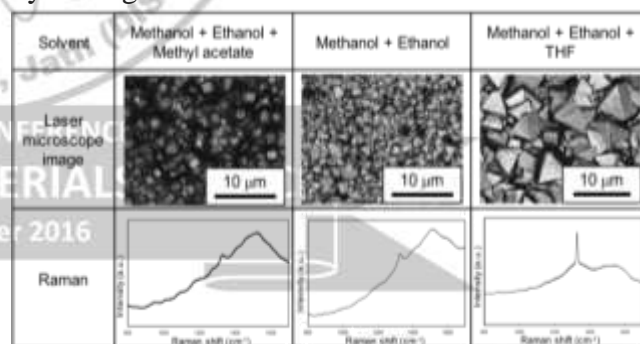


Fig. 2 Laser microscope image and Raman spectrum

References

1. H. Toyota, S. Nomura, Y. Takahashi, S. Mukasa, *Diamond Relat. Mater.* 17 (2008) 1902.
2. Y. Harada, R. Hishinuma, C. Terashima, H. Uetsuka, K. Nakata, T. Kondo, M. Yuasa, A. Fujishima, *Diamond Relat. Mater.* 63 (2016) 12

Effect of Additives on the Structural and Magnetic Properties of Nano crystalline Spinel Ferrites

A.D. Patil¹ and S. M. Patange*²

1- Department of Physics D.A.B. N. Arts and Science College, Chikhali.MS. India

²* Material Science Research Laboratory. S.K.M Gunjoti. Osmanabad. MS. 413613 India

Abstract

As reported by many researchers, it is seen that electromagnetic properties of Spinel Ferrites mainly depends on two factors such as density and microstructure. By addition of most widely used sintering additives like B_2O_3 , V_2O_5 , MoO_3 , Bi_2O_3 , Nb_2O_5 improved the electromagnetic properties. Also, mixed additives such as $CaCO_3$, SiO_2 , V_2O_5 , and SnO_2 have been used and seen that these have more influence on ferrites properties as compared to individual additives. An extensive review of the literature it is found that the mixed additives like V_2O_5 , MoO_3 , B_2O_3 and Bi_2O_3 can be used to find its effect on electromagnetic properties.

Keywords – Additives, ferrite preparation, sinter aids.

1. Introduction -

Field of magnetic materials has been identified as one of the primary fields where processing improvements and more advanced products can be anticipated. Most of the industrialized countries of the world have invested heavily in the manufacturing (processing) of new magnetic materials; this has led to the production of lower priced ceramics with better properties. Due to the large variety of structural, chemical, electrical and magnetic properties that magnetic materials presently exhibit, there is almost no social and industrial application without magnetic materials.

Among the available magnetic nanoparticles, spinel families are interesting and popular family as these crystal structure oxides can be half metallic (Fe_3O_4) [1], ferrimagnetic insulators (like most spinel ferrites) [2], transparent conductors (as Cd_2SnO_4) [3], and superconductors ($LiTi_2O_4$) [4]. Furthermore spinel is a complex crystal structure with many degrees of freedom available to engineer physical properties. Spinel ferrite is an important class of mixed-metal oxides in spinel families, which has the general chemical formula AB_2O_4 (A site = divalent cations and B site = trivalent Fe cations). One unit cell consists of eight formula units $[MFe_2O_4]_8$. In spinel ferrite, the lattice consists of 32 divalent oxygen ions that are in direct contact to one another forming a closed-pack face-centred cubic structure with 8 tetrahedral (A-sites) and 16 octahedral (B-sites) sites, occupied by the metal cations. The local symmetry of the cation sites is cubic in the case of tetrahedral (A) site and trigonal in the case of octahedral (B) site. According to the site occupancy of metal ions, the spinel ferrites are classified into three categories: (a) normal spinel, where the tetrahedral sites are occupied by divalent metal ions, (b) inverse spinel, where all the divalent ions are present in the octahedral sites and

(c) mixed spinels, where divalent ions are present both in tetrahedral and octahedral sites [5]. Nanosized ferrite particles exhibit unusual magnetic properties which are not observed in the bulk material, e.g. single domain behavior, superparamagnetism, and reduced Curie temperature and magnetization [6-8]. The spatial confinement at nanoscale enhances the role of surface atoms with reduced symmetry and the consequent larger number of broken exchange bonds can result in surface anisotropy, frustration and spin disorder [9].

Ferrite is a magnetic material of two types one is soft ferrite and second is the hard ferrite. Soft ferrite is class of magnetic material used as transformer core mainly for television, telecommunication computer, medical and other industrial electronic system. Hard ferrites are used for permanent magnets mainly in loud speakers, micro motors. Ferrite is a ferromagnetic material also ferrite is an inverse spinel taken to be collinear ferrimagnet. The low loss polycrystalline ferrites should be used in a high frequency range. For the good performance in application and classified by the initial permeability, for the low and high frequency applications, the most important technological properties are saturation magnetization (M_s), coercive force (H_C) initial permeability (μ_i) and losses. It is not possible generally to obtain the best combination of these properties for any specific application. By varying the compositions or adding additives or by varying the preparation technique, one can, to a large extent control most parameters for any particular applications.

A small amount of an additive in a host material can drastically change the nature and concentration of defects, which can influence the kinetics of grain boundary motion, pore mobility and pore removal [10]. Such an additive generally lowers the sintering temperature, i.e., promotes the

densification at lower temperatures. The presence of liquid phase between particles during sintering facilitates the rearrangement of particles and improves mass transport mechanisms due to the capillary forces between particles. It can induce a transition from normal to anomalous grain growth and change the composition and vacancy concentration at the grain boundaries, which may degrade the magnetic permeability.

Some oxides of transition elements such as B_2O_3 , Bi_2O_3 , V_2O_5 , or MoO_3 , melt around $700^\circ C$ and form liquid phases [11, 12]. Additives can be divided into three categories. The first group consists of additives that segregates to the grain boundaries and affect the grain-boundary resistivity. The second group consists of additives that affect microstructure development. The third group consists of additives that are dissolved into the grains and alter the magnetic properties

The relation between the structure and properties of oxide materials and their applications are of great importance. With expanded applications of soft magnetic materials expected in the future, it is appropriate to study the influence of various additives on the magnetic properties and microstructure of nano crystalline ferrite materials. In this paper a review of influence of different additives on properties of Spinel ferrites are presented.

2. Literature Survey

2.1 Different methods of ferrite preparation-

There are various methods of ferrite preparation such as solid state reaction method [13,14,16,17,22] conventional ceramic process [15,20,21] conventional powder method [18,19], sol gel auto combustion[23] etc.

The solid state reaction method [13, 14, 16, 17, and 22] is most widely used method by the investigators in which different metal oxides are mixed by ball mill. The dried powers were calcinated up to $800^\circ C$. In calcinated powder different amounts of B_2O_3 [13, 16], B_2O_3 - MoO_3 , V_2O_5 , Bi_2O_3 were added and mixture was milled further for more than one hour. The granulated powders pressed into pellets and toroidal form with polyvinyl alcohol [PVA, 10 wt. %].

Conventional ceramic process was used to prepare Mn -Zn ferrites [15, 20, and 21] with $CaCO_3$ - SiO_2 , V_2O_5 - SnO_2 , Bi_2O_3 , V_2O_5 and Nb_2O_5 additives. O. Mirzaee et. al. [18] reported effect of V_2O_5 on the magnetic properties and

microstructure development of $Ni_{0.64}Zn_{0.36}Fe_2O_4$ soft ferrite and also Ni-Zn ferrites [19] with V_2O_5 and MoO_3 additives by conventional powder method.

These ferrite preparation methods also have few disadvantages such as multiple step path ways, time consuming and are highly pH sensitive.

Sol gel auto combustion method has some advantages such as excellent composition control, low temperature process, low production cost and better results. In sol gel auto combustion method metal nitrate salts can be used as reactant and citric acid as a fuel. This process has been proved to be a simple and economic way to prepare nano-scale ferrite powders.

2.2 Enhancing micro structural, electrical and magnetic properties of spinel ferrites by using additives-

The spinel ferrites magnetic and electrical properties are influenced due to addition of small quantity of additives which forms a liquid phase at sintering temperature. At lower temperatures additives promote the densification. The major additives used by several researchers are B_2O_3 , V_2O_5 , MoO_3 , Bi_2O_3 , and Nb_2O_5 etc.

Wei-Shen et.al [13] observed the effect of doped with B_2O_3 on low temperature fired Ni-Cu-Zn ferrites. The author added B_2O_3 by 0.05 wt. % resulted into improved sinterability, remanent flux density, permeability, saturation flux density & reduced the coercive field strength. With further addition of B_2O_3 greater than 0.05 wt. % leads to increase in porosity and appearance of liquid phase causes deterioration of magnetic properties.

Haikui Zhu et. al [14] used B_2O_3 – MoO_3 additive and studied its influence on low temperature fired Ni-Cu-Zn ferrites. It is seen that by addition of these additives densification of specimens are improved due to liquid phase formation and promoted grain growth. The proper B_2O_3 and MoO_3 additions can increase the initial permeability, saturation flux density but decreased remanent flux density and coercive field strength.

Kaiqi-Jiang et.al [15] studied the effect of multi-additives on the high permeability Mn-Zn ferrite. For additive $CaCO_3/SiO_2$ frequency stability of initial permeability significantly improved. Proper addition of additives such as Bi_2O_3 , SnO_2 and V_2O_5 affects grain growth, porosity, and initial permeability of ferrites at different concentrations.

M. Kavanlou et al. [16] also presented effect of B_2O_3 as sintering aids on Li-Zn ferrite. The result showed that low melting point ($960^\circ C$) B_2O_3 oxide forms a liquid phase during sintering. This affects properties of ferrites such as densification and grain growth. The doped sample with 1 wt % B_2O_3 sintered at $1000^\circ C$ had the highest density and magnetic induction in comparison with undoped samples. It also showed highest permeability and the lowest magnetic loss with highest grain size.

The V_2O_5 is widely used additive by many authors. Shireen Akther et al. [17] Experimentally studied influence of V_2O_5 addition on properties of iron deficient ferrite with composition $Ni_{0.65}Zn_{0.35}Fe_{1.94}O_4 + x V_2O_5$. For samples of V_2O_5 up to 0.004 wt% sintered density, Curie temperature, saturation magnetization, and dc resistivity increases and then decreases. O. Mirzee et al investigated effect of V_2O_5 , MoO_3 and V_2O_5 co-doping on properties of $Ni_{0.65}Zn_{0.35}Fe_2O_4$ ferrites [18] and Ni-Zn ferrites [19] respectively. The results of V_2O_5 addition showed initially increase in permeability, relative density and grain size with addition up to 1.6 wt. % of V_2O_5 and then decreased with further addition. The peak values of Curie temperature and saturation magnetization are reported at 0.8 wt. % and 1.2 wt. % of V_2O_5 respectively. The result with addition of 0.05 wt. % of MoO_3 and 0.2 wt. % of V_2O_5 at frequency above 1MHz observed noticeable increase in magnetic permeability and saturation magnetization and decrease in power

loss. It is also seen that with MoO_3 and V_2O_5 addition there is increase in grain size and sintered density.

Zhong Yu et. al. [20] had used Bi_2O_3 as a sintering additive. The effect of Bi_2O_3 addition on microstructure and magnetic properties of Mn-Zn ferrites were presented. This additive mainly segregates and concentrates in the grain boundary regions. It promotes solid state reaction and grain growth which enhances density but reduces porosity. With optimum addition of Bi_2O_3 increased the permeability and saturation magnetic induction.

S.H.Chen. et. al. [21] investigated improvement on magnetic power loss of Mn-Zn ferrite material by V_2O_5 and Nb_2O_5 co doping. It was found that sintered density of materials increases with sintering temperature. It is found that magnetic power loss mainly depends on the grain size. The power loss is low for fine grain size.

Chengyong Liu et. al. [22] reported the effect of sintering temperature and Bi_2O_3 content on properties of Ln-Zn ferrite. The addition of Bi_2O_3 results into improvement in densification behavior and grain growth rates. The Bi_2O_3 is present at grain boundaries as a reaction centre at low temperature. The samples of Bi_2O_3 with 1.00 wt % additive sintered at $1100^\circ C$ showed highest squareness ratio, saturation magnetization, low coercive force and minimum ferromagnetic resonance line width.

3. Conclusion

The above meticulous literature survey can be concluded in following points. The ferrites such as Ni-Cu-Zn, Ni-Zn, Li-Zn, Mn-Zn have been studied thoroughly for different additives doping. The major influence is observed on the structural, electrical and magnetic properties of ferrites. The widely used additives are B_2O_3 , V_2O_5 , MoO_3 , Bi_2O_3 , and Nb_2O_5 etc. The maximum wt% addition of additives is about 1.6 % and further increase declines the desirable properties of the ferrites.

References

- Xiaohan Chai, Chunsheng Shi, Enzuo Liu, Jiajun Li, Naiqin Zhao, Chunnian He, Applied Surface Science, 347,(2015)178
- V.A.M. Brabers, in: K.H.J. Buschew (Ed.), Handbook of Magnetic Materials, vol. 8, North-Holland Publishing, 1982.
- S.B. Jhang, S.H. Wei, Appl. Phys. Lett. 80 (2002) 1376.
- Huan Duan, Jia Li, Sum Wai Chiang, Hongda Du, Wenhui Duan, Computation. Materials Science, 96, (2015)263
- A. N. Birgani, M. Niyafar, A. Hasanpour, Journal of Magnetism and Magnetic Materials, 374,(2015)179
- C. Breschignag, P. Houdy, M. Lahmani (Eds.), Nanomaterials and Nanochemistry, Springer-Verlag, 2006 (Chapter 5).
- J.P. Chen, C.M. Sorensen, K.J. Klabunde, G.C. Hadjipanayis, E. Devlin, A. Kostikas, Phys. Rev. B 54 (1996) 9288.
- K. Maaz, A. Mumtaz, S.K. Hasanain, M.F. Bertino, J. Magn. Mater. 322 (2010) 2199–2202.
- R.H. Kodama, A.E. Berkowitz, E.J. McNiff, S. Goner, Phys. Rev. Lett. 77 (1996) 394.
- D.W. Ready, J. Am. Ceram. Soc. 49 (1966) 366
- J. Lopez-Martinez, A. Romero-Serrano, A. Hernandez-Ramirez, B. Zeifert, C. Gomez-Yañez, M. Hallen-Lopez, Journal of the European Ceramic Society, 34,(2014)3729.
- Ru-Yuan Yang, Min-Hang Weng, Hon Kuan, Ceramics international, 35,(2009)39.
- Wei Shen Haikui Zhu, Yu Jin, Hong qing Zhou, Zhiming Xu, J. Ceramic international, 40 [2014] 9205-9209.
- Haikui Zhu, Wei Shen, Haiou Zhu, Yu Jin, Hong qing Zhou, J. Ceramic international, 40 (2014) 10985 to 10989.
- Kalqi Jiang, Kangkang Li, Changhong Peng, Yun Zhu, J. Alloys and Compounds, 541 (2012) 472-476.
- M. Kavanlou, B. Hashemi, J. material and Design, 32 (2011) 4257-4261.
- Shireen Akther, MD. Amanillah Choudhury, Jalalur Rahman, J. Bangladesh Academy of Sciences, 2[2009] 145-149.
- O. Mirzaee, M.A. Golozar, A. Shafyei, J. materials characterization, 59 (2008) 638-641.
- O. Mirzaee, A. Shafyei, M.A. Golozar, H. Shokrollahi, J. Alloys and compounds, 461 (2008) 312 to 315.
- Zhong Yu, Ke Sun, Lezhong Li, Yuntei, Liu, Zhongwen Lan, Huaiwu, Zhaohg, J. magnetism and magnetic materials, 320 (2008) 919-923.
- S.H. Chen, S.C. Chang, C.Y. Tsay, K.S. Liu, J.N. Lin, J. European Ceramic society, 21 (2001) 1931-1935.
- Chenyong Liu, Zhongwon Lan, Xiaona Jiang, Zhong Yu, Ke Sun, Lezhong Li, Peiyuanliu, J. magnetism and magnetic material, 320 (2008) 1335-1339.
- Sagar E. Shirsath, R. H. Kadam, S. M. Patange, M. L. Mane, Ali Ghasemi, Akimitsu Morisako, Appl. Phys. Lett. 100(2012)042407.

Sol-gel Synthesis of Crystalline SnO₂ Nanopowder: Advantage of Sonochemical Method over Conventional Method

Bharat Govind Pawar

Assistant Professor, Department of Chemistry, Sangola College Sangola, Kadlas Road Sangola, Dist-Solapur, Pin 413307 INDIA. *Email: pawarbg12@gmail.com, Mobile-+91- 9881661376

Abstract

In the present study, nano-sized tin oxide (SnO₂) powders were prepared using conventional and sonochemically assisted sol-gel method, with citric acid as complexing agent, using tin chloride. The synthesized tin oxide powders were characterized by XRD, TGA and SEM to determine crystallite size, % crystallinity, and thermal weight loss and shape respectively. It was found that the crystallite size obtained in both the synthesis methods were below 50 nm. There was also a significant reduction in the reaction duration.

Keywords: Tin oxide (SnO₂), Nanomaterial, Sonochemical method

1. Introduction

Advances in nanostructured materials have been led by the development of new synthetic methods that provide control over size, shape, and nano/microstructure. The high intensity ultrasound offers a facile, recent tool for nanostructured materials that are often unavailable by conventional methods [1]. Tin dioxide, SnO₂, as an environmentally friendly semiconductor with band gap of 3.6 eV at room temperature, has attracted much attention due to its unique optical and electrical properties and potential applications as the anode material in lithium-ion batteries [2,3], gas sensors [4], and so on. Several methods, such as thermal evaporation [5], chemical vapor deposition [6], the sol-gel technique [7] and the sonochemical route [8] have been used to synthesize SnO₂ based materials.

The sonochemical method has been proved to be a useful method to obtain novel materials [9-10]. The chemical effects of ultrasonic irradiation arise from acoustic cavitation, in other words, the formation, growth and implosive collapse of bubbles in a liquid medium, which results in an instantaneously high temperature and pressure pulse [11-12]. These special conditions of high temperature, pressure and local intense micromixing attained during acoustic cavitation lead to many unique properties in the irradiated solution and particles suspended in the same [13].

In this paper, tin oxide nanopowder was synthesized using conventional (NUS) and sonochemical (US) assisted sol-gel method. The effect of ultrasound on % crystallinity, crystallite size, % weight loss and morphology of the synthesized SnO₂ has been studied to understand the advantage of ultrasound in the synthesis of SnO₂.

2. Materials and methods

Materials

Tin chloride dihydrate (95%) precursor and complexing agent citric acid (99.5%) was obtained from Merck Ltd, Mumbai, India. *Ultrasound Set-up* Ultrasound for sonochemical synthesis is generated with the help of ultrasonic instrument set up (horn type). The specification and details of the set-up, processing parameters used during the experiments are: Make: Ace, USA, Operating frequency: 22 kHz, Rated output power: 750 W, Diameter of stainless steel tip of horn: 1.3×10^{-2} m Surface area of ultrasound irradiating face: 1.32×10^{-4} m², Expected ultrasound intensity: 3.4×10^5 W/m² Sol-gel Synthesis of SnO₂ by conventional method (NUS) is prepared as reported earlier[14] Synthesis of SnO₂ by sonochemical method (US)

The SnO₂ sols were prepared by dissolving 1.5 g tin chloride dihydrate (95% SnCl₂. 2H₂O Merck) and 5 g citric acid (99.5% C₆H₈O₇.H₂O Merck) in 8mol⁻¹ HNO₃ in flask until a clear solution was obtained. Aqueous ammonia (25%) was added drop wise into the solution with stirring, until pH value of 9 was reached. The sol prepared was found to be transparent and stable with no precipitate or turbidity. The sol solution kept under sonication using an Ultrasonic Horn (ACE 22 KHz) at 40% amplitude for 3 minutes with a 5 second pulse and 5 second relaxation cycle at time t= 0 hours., the solution was again exposed to acoustic cavitation (by using ultrasonic horn) for further 10 minutes, by keeping all sonication parameters constant (same as that was used during mixing), to carry out the complete reaction. gel was separated by decantation, washed several times with double distilled water and ethanol to remove impurities. After drying at 373K for 5h in hot air oven, for TGA analysis the dried gel power was ground in a mortar, and finally calcinated in muffle furnace at 600⁰C, for 2h. and characterized by XRD and SEM analysis.

3. Characterizations

The dried SnO₂ samples (powder form) were first characterized by studying their X-Ray Diffraction patterns on a Rigaku Mini-Flex X-Ray Diffractometer. XRD patterns were recorded at angles between 2° and 80°, with a scan rate of 2°/min. Particle sizes were determined using the Debye-Scherrer equation. Thermogravimetric analysis (TGA) studies were performed using Thermal Analyser (TA Instruments, USA). The sample was heated in ambient air atmosphere in alumina crucible at the rate of 20 K/min. Sample preparation for Scanning Electron Microscopy (SEM) includes the deposition of platinum on SnO₂ powder. Scanning Electron Microscopy of the samples was carried out on a JOEL JSM 680LA 15 KV SEM to estimate the surface characteristics of the sample. Together, the XRD and SEM methods are expected to provide exact knowledge regarding the particle size and crystalline characteristics of the synthesized SnO₂.

4. Results

4.1 Crystallinity and Crystallite Size of SnO₂

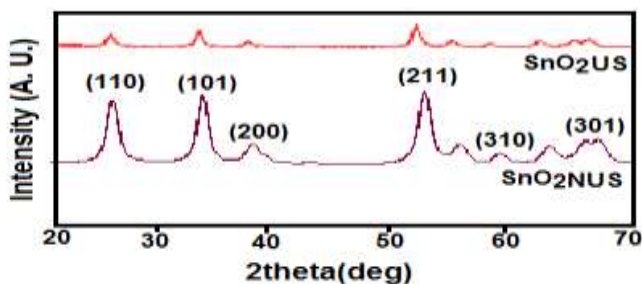


Fig. 1 XRD pattern of the conventionally (NUS) and sonochemical (US) synthesized SnO₂

Table 1: % crystallinity and crystallite size of the conventionally (NUS) and sonochemically (US) synthesized SnO₂

Method	Crystallinity		Crystallite size (nm)	
	Average	± variation	Average	± variation
Conventional	43.18	1.52	14	2
Sonochemical	37.13	2.15	8	1

For the NUS and US synthesized SnO₂ samples, the XRD, shows the observed reflection peaks were compared with JCPDS (41-1445), and confirmed the presence of pure crystalline SnO₂. No peaks corresponding to tin metal or any other phase as impurity peaks were identified in both cases NUS and US. From the XRD patterns (Fig. 1. All the computed results including %

crystallinity and crystallite size have been tabulated in Table 1. XRD pattern of synthesized SnO₂ for both NUS and US process exactly matches with the XRD pattern of SnO₂. Also the peaks at different crystal planes of US synthesized SnO₂ matches exactly with that of NUS synthesized SnO₂ indicating essentially no difference with respect to the type of crystalline phase in the two products. The crystallinity of all the samples is still substantial because of the inherent characteristics of the sonically assisted process. It was found that NUS synthesized SnO₂ shows more crystallinity than US synthesized SnO₂. This may be because of adverse environments created during sonication and facilitating faster reaction, not allowing the nucleation and crystal growth to occur fully. The peak broadening in the XRD pattern (for both samples) clearly indicates that very small nanocrystals are present in the samples. It could also be due to the reduction in crystallinity. As the crystallinity of metal oxide reduces, its crystallite size is also known to reduce.

4.2 Thermogravimetric Analysis (TGA)

Fig. 2: TGA graph of the conventionally (NUS) and sonochemically (US) synthesized SnO₂. The thermo gravimetric (TGA) analysis (Fig.2) shows the weight loss of synthesized SnO₂ sample. It has been observed that continuous weight loss was occurred for both the samples (NUS and US synthesized SnO₂). At 50 °C, it has been observed that weight for NUS and US synthesized SnO₂ are 3.64 % and 2.8 %, respectively.

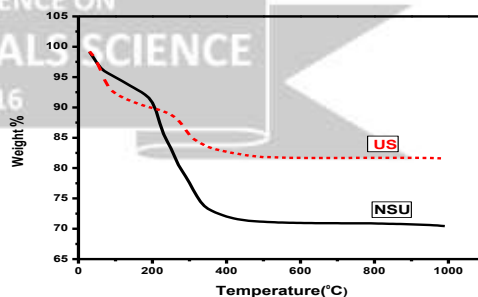


Fig. 2. TGA graph of the conventionally (NUS) and sonochemically (US) synthesized CeO₂

As the both samples get heated at 200 °C, again notable weight loss was found. It is 4.8% for NUS synthesized SnO₂ and 8.03 % for US synthesized SnO₂, when the water molecules (H₂O) start to disassociate themselves from Sn(OH)₃. It has been found that at 500 °C, total weight loss for NUS and US synthesized SnO₂

was 20.26% and 7.17% respectively. Uses of ultrasound to the reaction mixture are changing their crystallography. Here, by observing results obtained in terms of % crystallinity, crystallite size and % weight loss for both the samples (NUS and US synthesized SnO₂), we feel that as the crystallinity of the metal oxide decreases, its size is also found to be lowered and increased weight loss. Another possible reason behind the higher weight loss observed in case of US synthesized SnO₂ may be attributed to the formation of agglomeration due to high energy

These bonds are created by ultrasound enhanced high intensity collisions occurring

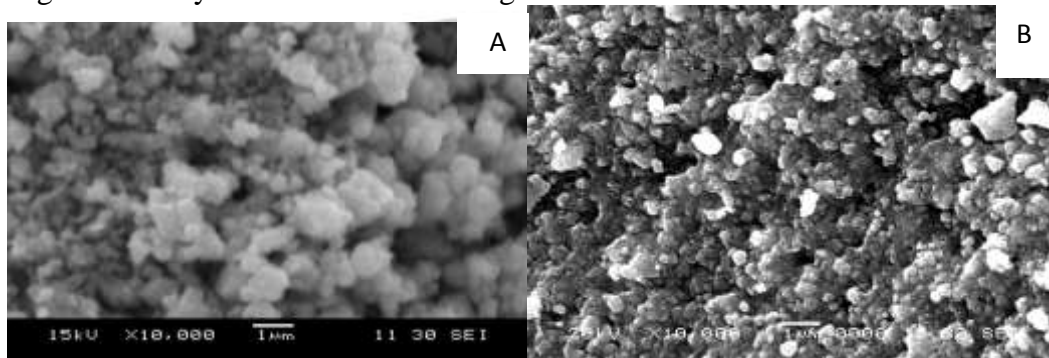


Fig. 3: SEM Micrograph of synthesized SnO₂. The US synthesized SnO₂ shows not only comparatively smaller particle size but also considerably less agglomeration. Here, we have interestingly observed that structure of NUS synthesized SnO₂ consists of small particles aggregated with larger particles but this is not observed for US synthesized SnO₂ material. These particles are smooth and sharp cuts (US synthesized) as compared to NUS synthesized particles. This may be due to active surface charge

between these particles in solution. The above mentioned observation of higher weight loss in the case of US synthesized sample could be due to this phenomenon.

4.2 Scanning Electron Microscopy (SEM)

From the SEM micrographs (Fig. 3 A and B) of the US and NUS synthesized SnO₂ samples some observations have been made, that supported the results observed from the XRD patterns. We have compared the SEM image results of the SnO₂ for NUS (Fig. 3 B) and US (Fig. 3 A) at the same magnification.

5. Conclusions

Nanostructured SnO₂ particles were successfully synthesized, by conventional (NUS) and sonochemical method (US). The sonochemical synthesis method has saved substantial time for the synthesis of SnO₂. Thus, the sonochemical synthesis technique is fast, simple, convenient, time saving, economical, and environmentally benign. We believe that this method promises us a future large-scale synthesis for many applications in nanotechnology field.

References

1. By Jin Ho Bang and Kenneth S. Suslick. Adv. Mater. 2010, 22, 1039–1059.
2. Wang Y, Zeng H C and Lee J Y 2006 Adv. Mater. 18 645–9
3. Lou X W, Wang Y, Yuan C L, Lee J Y and Archer L A 2006 Adv. Mater. 18 2325–9
4. Fang G J, Liu Z L, Ji X D, Wang H Z and Yao K L 1999 J. Mater. Sci. Lett. 18 639–41
5. Schosser V and Wind G 1998 Proc. 8th EC Photo Voltaic Solar Energy Conf. (Italy, Florence) p 998
6. Tarey R D and Raju T A 1985 Thin Solid Films 128 181–9
7. Shek C H, Lai J K L and Lin G M 1999 Nanostruct. Mater. 11 887–93
8. Zhu J J, Lu Z H, Aruna S T, Aurbach D and Gedanken A 2000 Chem. Mater. 12 2557–66
9. B. Aiken, W.P. Hsu, E. Matijevic, Preparation and Properties of Monodispersed Colloidal Particles of Lanthanide Compounds: III, Yttrium(III) and Mixed Yttrium(III)/Cerium(III) Systems, J. Am. Ceram. Soc. 71 (1988) 845 – 853.
10. P.L. Chen, I.W. Chen, Reactive Cerium(IV) Oxide Powders by the Homogeneous Precipitation Method, J. Am. Ceram. Soc. 76 (1993) 1577 – 1583.
11. Joon-Sung Lee, Jin-Seok Lee, Sung-Churl Choi, Synthesis of nano-sized ceria powders by two-emulsion method using sodium hydroxide, Mater. Lett. 59 (2005) 395– 398.
12. Huey-Ing Chen, Hung-Yi Chang, Homogeneous precipitation of cerium dioxide nanoparticles in alcohol/water mixed solvents, Colloids and Surfaces A: Physicochem. Eng. Aspects 242 (2004) 61–69.
13. Emanuel Kockrick, Christian Schrage, Anett Grigas, Dorin Geiger, Stefan Kaskel, Synthesis and catalytic properties of microemulsion-derived cerium oxide nanoparticles, J. Solid State Chem. 181 (2008) 1614–162.
14. Bharat G. Pawar, Dipak V. Pinjari, Sanjay S. Kolekar, Aniruddha B. Pandit, and Sung H. Han, Effect of Sintering Temperatures on the Synthesis of SnO₂ Nanospheres ISRN Chemical Engineering Volume 2012 (2012) 7.

Studies on New Perovskite Material for Pyroelectric Sensor Application

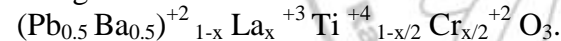
N.T. Padal¹, Sarika M. Salunkhe²

¹Willingdon College, Sangli,

² Bharti Vidyapeet Deemed University College of Engineering Pune.

1. Introduction

As generalized observations the Curie point is suppressed due to substitution except for the substitution of Ba by Sr or Ca by Pb (1). Our interest was to maintain the Curie point in the vicinity of 280°C and therefore we have opted for the systems based on $Pb_{0.5}Ba_{0.5}TiO_3$. Both $PbTiO_3$ and $BaTiO_3$ possess substantial value of spontaneous polarisation P_s . Further PLT ($Pb_{1-x}La_xTiO_3$) systems have proved to be important for the device applications (2). Additionally the substitution of $LaFeO_3$, $AlFeO_3$, $BiFeO_3$, $LaMnO_3$ matrices have shown relaxation effects (3) The relaxation effects in these compositions are attributed to the valence Fluctuations of Fe, Co or Mn ions. Additionally the substitution of La is expected to improved resistivity of the material also. Therefore, it was taugth to investigate this relaxation effect in combined PbBa system by substituting ($Pb_{0.5}Ba_{0.5}$) by La^{+3} with a simultaneous substitution of Ti by a Fe or Cr ion. The resulting system taken up for the investigation is as given below.



1. Experimental

The samples are prepared using standard ceramic synthesis route. A HP 4284 A impedance bridge is used to record the dielectric dispersion. The resistivity measurements are carried out using two

Table 1. Lattice parameter

x	C A.U.	a A.U.	c/a
0.00	4.06	3.96	1.025
0.01	4.05	3.94	1.027
0.02	4.04	3.95	1.022
0.03	4.06	3.95	1.027
0.04	4.05	3.96	1.023
0.06	4.04	3.96	1.020

Temperature dependence of dielectric constant and tan δ

The overall natures of the curves for other systems follow the similar nature Fig.1.

1. The ϵ_r is observed to pass through a maximum, the Curie point, and then decreases with an increase in the temperature (5) .

probe method in a custom designed setup and a tabular furnace for the temperature variation. The pyroelectric coefficient \emptyset is measured on the poled smaples using direct method proposed by Byer and Roundy.

2. Results and Discussion

3.1 Structural property

The lattice parameter 'a', 'c' and 'c/a' are independent of x at a=3.95, c=4.04 and c/a= 1.02. For x=006 and 0.1 the ratio 'c/a' slightly decreases to 1.015. The value of 'c/a' observed to be nearly equal to 1.02, which indicates that the crystal structure is tetragonal. For this system no significant change in the value of 'a', 'c' and 'c/a' is observed upto x=0.1. This feature could be attributed to the reduced percentage of Cr in the system

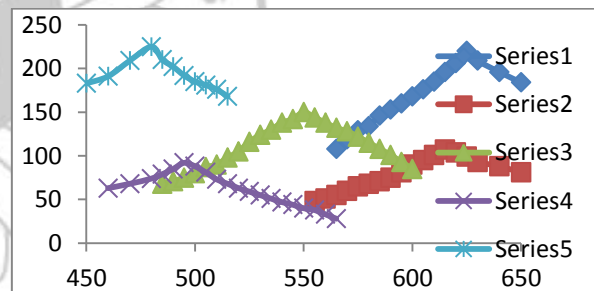


Fig.1. Variation of dielectric constant with temperature.

2. The Curie point (T_c) shifts towards lower temperature side as level of substitution (x) is increased.

3. For a given level of substitution (x) the Curie point does not change with frequency significantly.

4. In case of compositions where ϵ_{rmax} is maximum for a particular system, the ϵ_r in the vicinity of T_c shows an anomalous behavior. Hence the ϵ_r decreases with x for frequency upto 100 kHz and then increases again as frequency is increased. It appears that additive contribution of relax or and displacers in these composition may lead to such an anomaly.

5. Tan δ versus T behavior passes through a maximum for T slightly less than T_c . This

behavior is commonly observed for all the ferroelectric systems.

The ϵ_r versus T behavior is shown in the Fig.1, while the corresponding values of ϵ_r , ϵ_{rmas} , Q_r , T_c and γ are shown in Table 1. It is observed that as the level of substitution is increased the T_c decrease. ϵ_{rmas} goes on decreasing from 1359 to 201 for $x= 0.01$ to 0.04 for $x= 0.06$ the ϵ_{rmas} observed to be a little higher at 280. Table 1. Shows the values of γ . The γ always lies between 1 and 2 this may indicate a partial relax behavior or that it could be due to the effect of polycrystallinity also. To confirm this behavior we have determined the frequency dispersion of ϵ_r on this system. The frequency dispersion for $x= 0.02$ studied. In this case no significant change in T_c with f is observed. Neither any anomalous behavior in variation of ϵ_r with F is observed for any composition in this series.

Pyroelectric coefficient

From Fig. 2. The Φ become maximum where dPs/dT is maximum. In this case the material shows a diffused phase transition and therefore the peak in Φ versus T behavior is also sufficiently broad. This may result in a little mismatch in the Curie points determined from the ϵ_r , ϵ_r versus T behavior and those determined from the Φ versus T behavior. In the vicinity of T_c the value of Φ is observed to be maximum. The Φ_{max} is maximum for $x=0.01$ for the system, as x is increased the Φ_{max} is observed to decrease. From the present data no direct correlation between ϵ_{rmas} and Φ_{max} are observed.

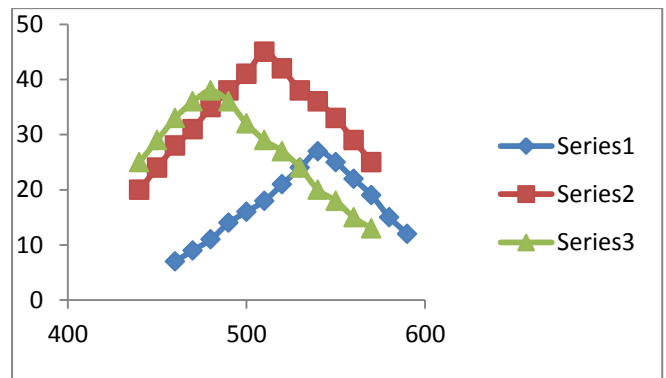


Fig. 2. Variation of pyroelectric coefficient with temperature

Acknowledgement: Author is thankful to Late Prof. P. B. Joshi, Solapur, for his mentoring. Also indebtedness to Dr. Shrikant Kokare of Raje Ramrao College, Jath, for his cooperation

References

1. Jaffe : Piezoelectric ceramics pp 91-97
2. Fedulov S.A. et al Bull. Acad. Sci U.S.S.R. 26,(361)1962
3. Havinga E. E. Philips Rese. Repo. 21(49), 1966
4. Shirane G and Suzuki J. Phys. Soc. Japan 6(274) 1951
5. Kokare et al Indian Jour. Sci.and Appl. Sci 6(317)2000
6. Prasad k. et al Bull. Mater. Sci. 3(305)1996

Table 2. Values off ϵ_r ($rmas$ T_c Q_r and γ for $(Pb_{0.5}Ba_{0.5})_{1-x}La_xTi_{(1-x/2)}Cr_x/2O_3$

X	Φ mC/Cm ²	Curie TempBy Φ .	Curie Temp. by ϵ_r
0	5000	610	604
0.01	7220	604	622
0.02	3701	600	615
0.03	27	542	550
0.04	45	507	496
0.06	36	471	485

Table 3. Pyroelectric coefficient of $(Pb_{0.5}Ba_{0.5})_{1-x}La_xTi_{(1-x/2)}Cr_x/2O_3$

x	ϵ_r at 10kHz	ϵ_r at 1MHz	ϵ_{rmas} at 10kHz	ϵ_{rmas} at 10MHz	Q_r at 10kHz	Q_r at 10MHz	T_c K	γ
0.00	165	160	2550	184	4.8	----	604	1.4
0.01	220	224	1359	1334	12		622	1.3
0.02	107	102	531	807	3	184	615	1.15
0.03	150	141	339	327	14	57	550	1.1
0.04	92	90	201	164	9		496	1.0
0.06	225	218	280	245	1.8	42	485	1.0

Microwave assisted green synthesis of 1H-Pyrazolo [1, 2-b] Phthalazine-5, 10-Dione Derivatives with 5%CTAB capped ZnO nanoparticles as catalyst

Kiran N. Patil¹, Dipak A. Kumbhar², Shrikrishna S. Karhale³, Vasant B. Helavi³

¹Department of Chemistry, Dr. Ghali College, Gadhinglaj, Maharashtra 416502, India

²Department of Chemistry, Raje Ramrao College, Jath, Maharashtra 416404, India

³Department of Chemistry, Rajaram College, Kolhapur, Maharashtra 416004, India

Abstract

5% CTAB capped ZnO nanoparticles have been used for a highly efficient synthesis of 1H-Pyrazolo [1, 2-b] Phthalazine-5, 10-Dione by the four component condensation reaction of phthalic anhydride, hydrazine monohydrate, aromatic aldehydes and ethyl cyanoacetate under microwave irradiation. The advantage of this method includes the use of green catalyst, short reaction time, easy work-up and excellent yields.

Keywords: Green approach, Nanoparticles, Microwave, Multicomponent reaction, Phthalazine derivative

1. Introduction

Multicomponent reactions (MCR) gain more importance for the rapid and highly efficient synthesis of diverse and complex heterocyclic molecules. Multi-component reactions constitute a very powerful tool to synthesize more classical drug-like, heterocyclic core structures [1]. Nitrogen-containing heterocyclic compounds are widespread in nature, and their applications to pharmaceuticals, agrochemicals, and functional materials are becoming more and more important. [2] Among a large variety of N-containing heterocyclic compounds, those containing an hydrazine moiety as a "fusion site" have received considerable attention because of their pharmacological properties and clinical applications [3]. Phthalazine derivatives have been reported to possess anticonvulsant, [4] cardiotonic, [5] vasorelaxant, [6] cytotoxic, [7] antimicrobial, [8] antifungal, [9] anticancer [10] and anti-inflammatory activities. [11] In addition, the titled compounds, pyrazolo[1,2-b] phthalazine-diones, were also found to have analgesic, antihypoxic, and anti-pyretic activities. [12]

In the research work of multicomponent reactions, herein we describe the preparation of functionalized 1H-pyrazolo[1,2-b]phthalazine-5,10-dione derivatives from four-component condensation reaction of hydrazine monohydrate, phthalic anhydride, malononitrile or ethyl cyanoacetate, and aromatic aldehydes in the presence of 5% CTAB capped ZnO nanoparticles as catalyst and which are irradiated by microwaves.

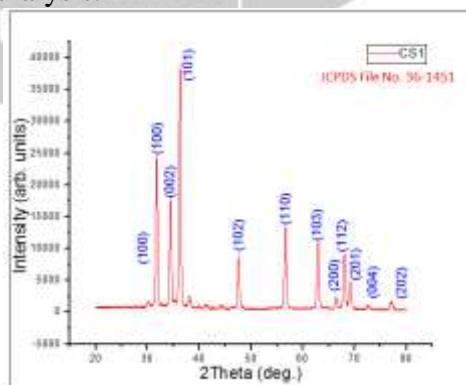
Nano-chemistry is an up growing research area due to their unique properties. [13] The usage of nanomaterials such as heterogeneous catalyst has gained significant role in organic synthesis due to simple work-up procedure, environmentally benign nature, reusability, low cost, and ease of

isolation. Zinc oxide nanoparticles (ZnO-NPs) are heterogeneous catalysts and widely used in cosmetics, paints, and fibers. It can also play a role of Lewis acid in various organic transformations. (14)

We have prepared ZnO nanoparticles capped with surfactant like cetyltrimethylammonium bromide (CTAB). CTAB-capped zinc oxide has smallest particle size, due to this fine particle size which provides large surface area and reaction proceeds faster and gives excellent yield in shorter time.

2. Results and Discussion:

The morphology and particle size of 5% CTAB capped ZnO nanoparticles, was investigated by scanning electron microscopy (SEM) Fig. 2. The SEM images show particles with diameters in the range of nanometers. The XRD pattern of the capped ZnO nanoparticles is shown in Fig. 1. The results show that spherical capped ZnO nanoparticles were obtained with an average diameter of 10–30 nm as confirmed by XRD analysis.



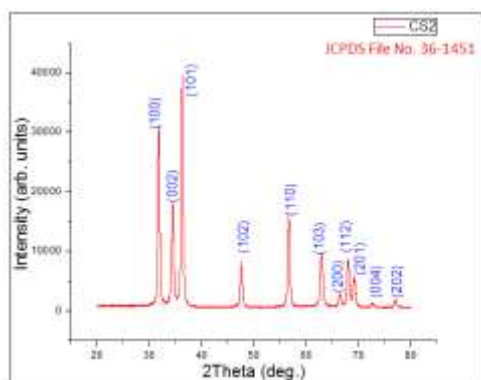


Fig. 1. X-ray diffraction (XRD) patterns of the prepared ZnO nanoparticles

The XRD of 5% CTAB Capped ZnO show the average particle size in the range of 10 to 30 nm and are in hexagonal phase and wurtzite in structure which also matches with JCPD File No. 36-1451.

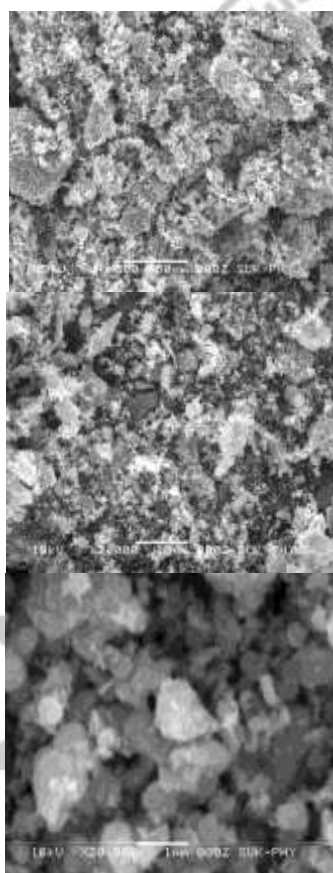
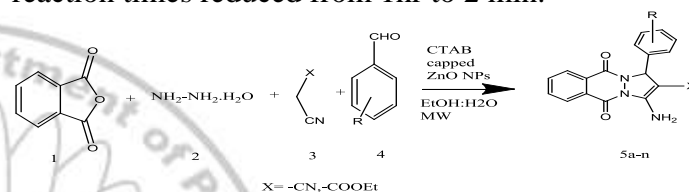


Fig. 2 SEM images of 5%CTAB capped ZnO NPs

A mixture of phthalic anhydride 1,hydrazine monohydrate 2,and catalytic amount of CTAB capped ZnO nanoparticles were irradiated in microwave synthesizer system at 560W(65C) for 60 sec then aromatic aldehyde 3, malononitrile or ethyl cyanoacetate 4 and ethyl alcohol :water(1:1) was added and further irradiated for 60 sec at 560 W. The results are compared with conventional heating in Table 1. The yields obtained using microwave heating are generally higher than conventional heating and reaction times reduced from 1hr to 2 min.



Scheme 1. Synthesis of 1H-pyrazolo [1, 2-b] phthalazine-5, 10-dione derivatives

In the absence of catalyst, reaction did not yield desired product which indicate crucial role of catalyst. 0.03g of 0.05 CTAB capped ZnO nanoparticles as catalyst is suitable to catalyze the reaction smoothly and results are given in Table 1.

Table 1 Comparison between classical and microwave heating for synthesis of 1H-pyrazolo [1, 2-b] phthalazine-5, 10-dione derivatives

mixture was recrystallized from MeOH to afford

Product	Aldehydes	X	M.P. C (Ref)	Classical Heating		Microwave Heating	
				Time /min	Yield / %	Time /sec	Yield /%
5a	4-Cl-C ₆ H ₅	-CN	270-272(15)	50	88	120	92
5b	4-NO ₂ -C ₆ H ₅	-CN	228-230(15)	50	90	120	94
5c	3-NO ₂ -C ₆ H ₅	-CN	268-270(15)	50	84	120	88
5d	4-OCH ₃ -C ₆ H ₅	-CN	120-122(15)	50	85	120	90
5e	4-Br-C ₆ H ₅	-CN	256-260(15)	50	86	120	90
5f	-C ₆ H ₅	-CN	275-277(15)	50	84	120	90
5g	4-Cl-C ₆ H ₅	-COOEt	166-168(15)	50	90	120	94
5h	4-NO ₂ -C ₆ H ₅	-COOEt	230-232(15)	50	88	120	92
5i	3-NO ₂ -C ₆ H ₅	-COOEt	236-238(15)	50	82	120	90
5j	4-OCH ₃ -C ₆ H ₅	-COOEt	146-148(15)	50	85	120	92
5k	4-Br-C ₆ H ₅	-COOEt	198-202(15)	50	85	120	90
5l	-C ₆ H ₅	-COOEt	112-116(15)	50	86	120	92

Experimental Section:

General Procedure

3. Preparation of 5% CTAB capped ZnO Nanoparticles: 0.02M capping agent cetyltrimethylammonium bromide(CTAB) was added into the 0.2M Zinc Acetate solution which was made in distilled water. The mixture was stirred for 30 min on magnetic stirrer, then aqueous ammonia (1:1) was added to maintain the pH in between 7 to 8 to get a gel. After 4 h continues stirring white gel was dried at 80°C for 6 h and the obtained dry product was calcinated at 400 °C for 3 h in a muffle furnace. The size and their perfect morphology were observed under XRD and SEM.

4. General procedure for the preparation of 1H-pyrazolo[1,2-b]phthalazine-5,10-dione

Derivatives:

a) **Thermal Method:** Hydrazine monohydrate (1 mmol), phthalic anhydride (1 mmol) and CTAB capped ZnO nanoparticles (0.03g) as catalyst was mixed at 70°C (15 min). Then, aromatic aldehydes (1 mmol), malononitrile or ethyl cyanoacetate (1 mmol) and ethyl alcohol: water (1:1), was added and stirred at 70°C for 50 min. After completion of the reaction, the reaction

the pure product.

b) Microwave Irradiation Method:

Hydrazine monohydrate (1 mmol), phthalic anhydride (1 mmol) and CTAB capped ZnO nanoparticles (0.03g) as catalyst was mixed and irradiated in microwave synthesizer system(CATA R) for 60 sec (560W) at 65°C . Then, aromatic aldehydes (1 mmol), malononitrile or ethyl cyanoacetate (1 mmol) and ethyl alcohol: water (1:1), was added and irradiated at 65°C for 60 sec (560W). After completion of the reaction, the reaction mixture was recrystallized from MeOH to afford the pure product. **Spectroscopic data of a representative sample**

3-amino-1-(4-chlorophenyl)-5,10-dioxo-5,10-dihydro-1H-pyrazolo[1,2-b]phthalazine-2-carbonitrile (5a): (92%), Pale Yellow powder, m.p. = 270 -272 °C; 1H NMR (400 MHz, DMSO-*d*₆) δ ppm: 8.15-7.730 (10H, m, H-Ar and NH₂), 6.15 (1H, s, CH). Ethyl-3-amino-1-(4-chlorophenyl)-5,10-dioxo-5,10-dihydro-1H-pyrazolo[1,2-b]phthalazine-2 carboxylate (5g): (94%), Pale Yellow powder, m. p. = 166-168 °C; 1H NMR (400 MHz, DMSO-*d*₆) δ ppm: 7.01-7.90 (10H, m, H-Ar and NH₂), 6.05 (1H, s, CH), 4.14-3.97 (2H, m, CH₂), 1.04 (3H, t, CH₃).

Conclusion

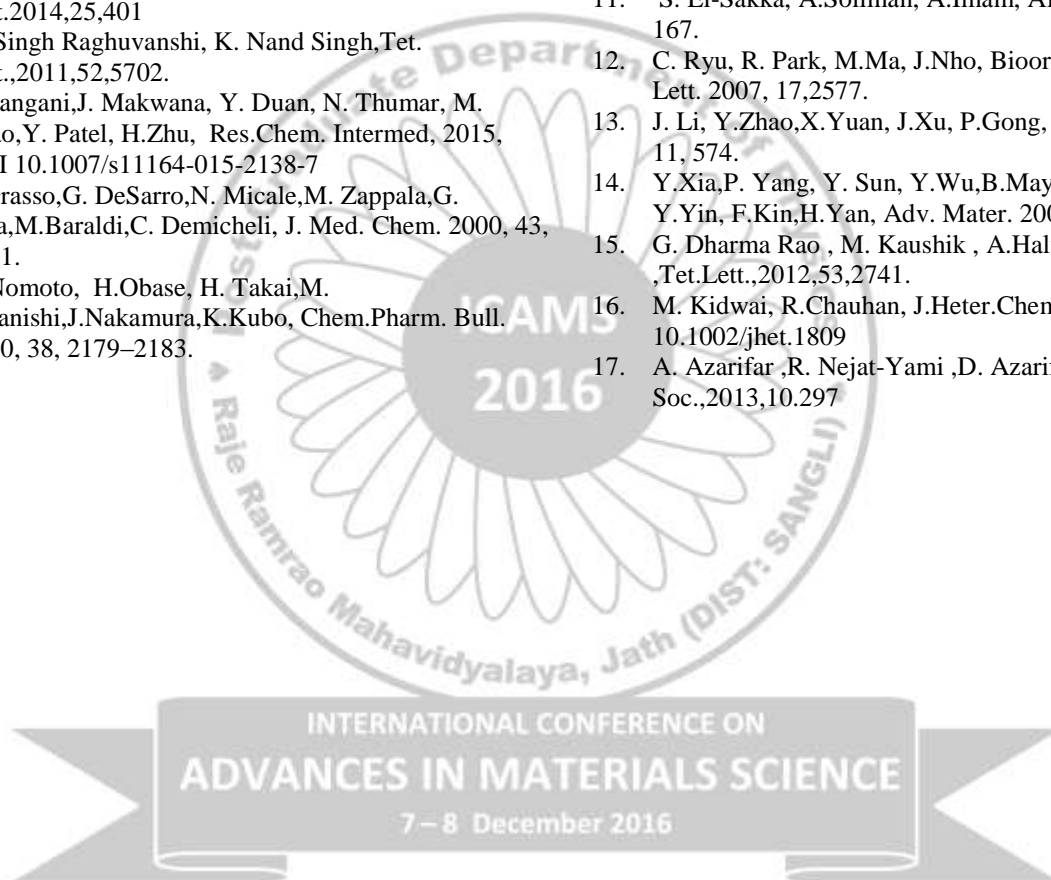
High surface area and recyclability of the nano-crystalline CTAB capped ZnO catalyst, easy preparation of the catalyst; low reaction times are the main advantages of this method. Satisfactory yields of products and easy workup make this a useful protocol for green synthesis of this class of compounds.

Acknowledgments

The author KNP is thankful to UGC for sanctioning Minor Research Project [File No. 47-1160/14(WRO) dated: 28th Dec. 2015] and Principal, Dr.Ghali college, Gadhinglaj for providing necessary facilities and encouragement during research work.

References:

1. J. Safaei-Ghomi , H. Shahbazi-Alavi, A. Ziarati, R. Teymuri, M. Reza Saberi, Chinese chem. Lett. 2014, 25, 401
2. D. Singh Raghuvanshi, K. Nand Singh, Tet. Lett., 2011, 52, 5702.
3. C. Sangani, J. Makwana, Y. Duan, N. Thumar, M. Zhao, Y. Patel, H. Zhu, Res. Chem. Intermed, 2015, DOI 10.1007/s11164-015-2138-7
4. S. Grasso, G. DeSarro, N. Micale, M. Zappala, G. Puia, M. Baraldi, C. Demicheli, J. Med. Chem. 2000, 43, 2851.
5. Y. Nomoto, H. Obase, H. Takai, M. Teranishi, J. Nakamura, K. Kubo, Chem. Pharm. Bull. 1990, 38, 2179–2183.
6. N. Watanabe, Y. Kabasawa, Y. Takase, M. Matsukura, K. Miyazaki, H. Ishihara,
7. K. Kodama, H. Adachi, J. Med. Chem. 1998, 41, 3367–3372.
8. V. Chebanov, E. Muravyova, S. Desenko, V. Musatov, I. Knyazeva, S. Shishkina, O. Shishkin, C. Kappe, J. Comb. Chem. 2006, 8, 427
9. J. Liu, J. Li, L. Zhang, L. Song, M. Zhang, W. Cao, S. Zhu, H. Deng, M. Shao, Tet. Lett. 2012, 53, 2469.
10. J. Kim, H. Rhee, H. Park, S. Lee, C. Lee, H. Park Choo, Bioorg. Med. Chem. 2008, 16, 4545.
11. S. El-Sakka, A. Soliman, A. Imam, Afinidad 2009, 66, 167.
12. C. Ryu, R. Park, M. Ma, J. Nho, Bioorg. Med. Chem. Lett. 2007, 17, 2577.
13. J. Li, Y. Zhao, X. Yuan, J. Xu, P. Gong, Molecules 2006, 11, 574.
14. Y. Xia, P. Yang, Y. Sun, Y. Wu, B. Mayers, B. Gates, Y. Yin, F. Kin, H. Yan, Adv. Mater. 2003, 15, 353
15. G. Dharma Rao, M. Kaushik, A. Halve, Tet. Lett., 2012, 53, 2741.
16. M. Kidwai, R. Chauhan, J. Heter. Chem., 2014, DOI 10.1002/jhet.1809
17. A. Azarifar, R. Nejat-Yami, D. Azarifar, J. Iran Chem Soc., 2013, 10, 297



INTERNATIONAL CONFERENCE ON
ADVANCES IN MATERIALS SCIENCE
7 – 8 December 2016

Synthesis and characterization of advance spray deposited Cu: CdO thin films and their LPG sensing performance

C. R. Bobade ^a, C. U. Mulik ^a and M. D. Uplane*^b

^aDepartment of Physics, Balwant College, Vita, Dist:Sangli -415 311 (MS) India

^bDepartment of Instrumentation Science, Savitribai Phule Pune University, Ganeshkhind, Pune-411 007 (MS) India

*Corresponding Author: Prof (Dr.) M. D. Uplane Email ID: mduplane@gmail.com, Tel : 020 25695195 /+919890902031

Abstract

Copper doped Cadmium Oxide (Cu: CdO) thin films were deposited onto glass substrate at low substrate temperature (210°C) using novel advanced spray pyrolysis (ASP) technique. For Cu doping cupric chloride di-hydrate (CuCl₂·2H₂O) was used in appropriate proportion with aqueous solution of Cadmium acetate dehydrate [Cd(CH₃COO)₂·2H₂O] and used as a precursor. The films were synthesized at preoptimized preparative parameters. Effect of Cu doping on the physical, morphological, optical and gas sensing properties of the films have been investigated. X-ray diffraction (XRD) studies show that films thus prepared are polycrystalline and have a cubic crystal structure with preferential orientation along (111) plane. Field Emission Scanning Electron Microscopy (FESEM) indicates that the films are granular and grains are ~126 nm in diameter. From optical properties studied by UV-VIS-NIR spectroscopy, the band gap of Cu: CdO films were found to vary between 2.51 to 2.63 eV. The LPG gas sensing properties were studied by in-house made gas sensor unit which reveals that 2% doped films show about 34% sensitivity to LPG gas at a temperature of 300°C.

Keywords: advanced spray pyrolysis, FESEM, EDAX, LPG response.

1. Introduction

LPG is widely used as fuel for domestic as well as industrial purpose. It is highly combustible and hazardous gas. For human safety it is necessary to detect it at its initial stages of leakage [1]. Recently thin films oxide semiconductors have received lot of attention because of their potential applications in the field of gas sensing and optoelectronics. The n-type transparent semiconducting oxide (n-TCOs) such as zinc oxide (ZnO), cadmium oxide (CdO), indium tin oxide (ITO), tin oxide (SnO₂) are the most popular members in the field of gas sensing also [2-5].

Till date, techniques such as chemical bath deposition (CBD) [6], thermal oxidation [7], sol-gel [8], pulsed laser deposition (PLD) [9,10] and spray pyrolysis (SP) etc. [4,11-13] have been developed to synthesize metal oxide thin films. Amongst these techniques, the spray pyrolysis (SP) method seems to be the most competent considering its simplicity, cost effectiveness and good reproducibility on a large scale compared to other techniques [14]. In spray pyrolysis process, a precursor solution is forced inside the reaction chamber of furnace using air or neutral gas to arrive at the preheated substrates in the form of very fine droplets. The ingredients undergo chemical reaction to form solid vapours and ultimately a chemical compound on top of the substrate. This makes the substrate temperature, as a key parameter in spray pyrolysis that

predominates the physical and chemical properties of the deposited oxide.

Till date, researchers have studied physical, optical and gas sensing properties of undoped and doped CdO thin films grown by spray pyrolysis, at high substrate temperatures > 400 °C [4,15]. However, the advanced spray pyrolysis technique helps to achieve good quality thin films at sufficiently low substrate temperature.

The present study reports on synthesis of good quality Cu: CdO thin films on to glass substrate via aqueous route. The films were synthesized by advanced spray pyrolysis technique (ASP) by using optimized preparative parameters. The structural, optical, morphological properties of these films were studied along with gas sensing applications.

3. Experimental

The advanced spray pyrolysis system, reported earlier [16] was used in the present experimentation. A 0.02 M aqueous solution (300 ml) of high purity cadmium acetate (Cd(CH₃COO)₂·2H₂O) (Thomas Baker, India) was used as a initial ingredient. Doping of 1 to 3 at. % of Cu cupric chloride (CuCl₂·2H₂O) (Thomas Baker, India) was used in appropriate volume. The solution thus prepared was atomized through a glass nozzle by using air as carrier gas. The sprayed solution undergoes pyrolytic decomposition inside the core and the desired

compound gets deposited on to the glass substrates kept at top of the chamber at 210 °C. The films deposited with 0, 1, 2 and 3 at.wt % are denoted by C₀, C₁, C₂, and C₃ respectively.

The crystalline structure and phase formation of the Cu:CdO films was characterized using X-ray diffractometer [Analytical instruments, Pvt. Ltd. Germany] in the scanning range of 20–80° at a step size of 0.1. The Cu K_α (λ = 1.5406 Å) radiation was used as incident radiation. Surface morphology and thickness of the films was studied by field emission scanning electron microscopy FESEM (Nova Nano SEM 200). The electrical resistivity (ρ) was examined by using home made two probe set up in the range 150 to 300 °C. Transmittance and absorbance was measured by using UV-VIS-NIR spectrophotometer (made by Shimadzu, Japan) in the range 300nm-1000nm.

Gas sensing performance of the films was studied by injecting a known concentration of liquefied petroleum gas (LPG) into the airtight steel chamber of volume 250 cm³. Variation in film resistance with time is measured by the “RIGOL DM3062” digital multimeter.

4. Results and Discussion

3.1.1. X-ray diffraction analysis

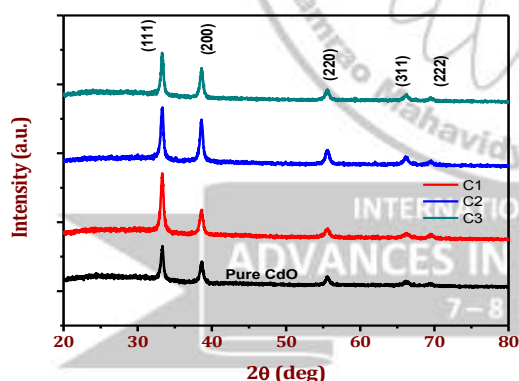


Fig.1. XRD patterns of Cu:CdO films.

The effect of doping concentration on the crystalline state of the films has been studied using X-ray diffraction (XRD). Fig.1. shows the XRD patterns of films grown at different doping concentrations. It is evident from figure that crystallographic property of the Cu: CdO films depend on level of doping. All the films were polycrystalline in nature indicating presence of (111), (200), (220), (311) and (222) planes with preferential orientation along (111) plane. The observed 'd' values are in good agreement with the reported values of the films (JCPDS card No.05-

0640) [17]. These results further reveal that the films are cubic in nature.

The crystallite size was calculated using Scherrer formula [18]. The calculated average crystallite size was ~27- 59 nm indicating that films were nanocrystalline in nature.

3.1.2. Surface morphological analysis

The FESEM micrographs of C₀, C₁, C₂ and C₃ samples are shown in the Fig. 2. It is seen that the surface of the films is uniform and granular in nature. It is clearly depicted from these micrographs that, the surface is granular in nature, which is uniformly covered over the entire substrate. Apart from this C₂ and C₃ sample films surface was observed to be of compact morphology as compared to pure CdO and C₁. Tiny crystallites have coalesced to form larger grains. The surface of C₀ and C₂ appears to be the same but grain boundaries are more prominent in C₂. Hence, the sample C₂ is tested for gas sensing properties by exposing it to LPG.

3.1.3. Optical Study

The direct band gap energy of pure CdO is found to be 2.35 eV and it is in good agreement with the value reported by other researchers [19]. Fig.3. shows that the band gap values for samples C₁, C₂ and C₃ as 2.54, 2.59 and 2.63 eV, respectively. As compared to pure CdO, the band gap is observed to increase with increase in quantity of copper in the doped samples.

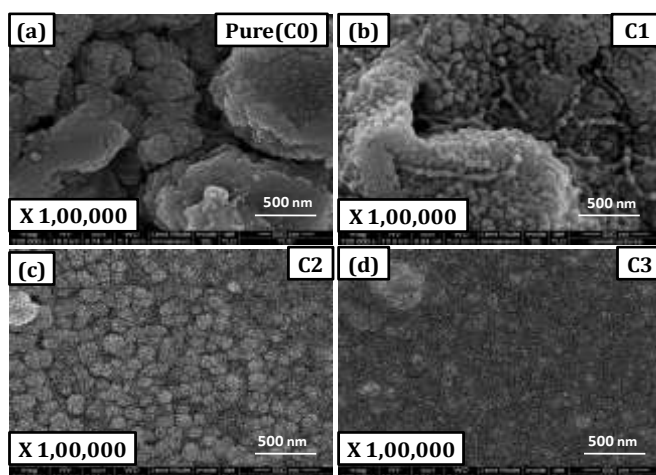


Fig.2. Plain view FESEM micrographs for a) pure CdO, C₀ b) sample C₁, c) sample C₂, & d) sample C₃.

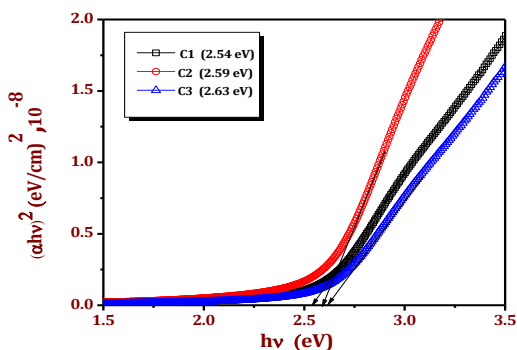


Fig. 3: Band gap energy plots for Cu doped CdO samples

3.1.4 LPG Sensing Study

The gas sensing measurements of Cu doped CdO films is studied for different gases. It is known that gas sensing performance depends on the physico-chemical properties of the films [20-22]. Some researchers have reported that different morphologies also affect the sensing performance of the sensors [23,24]. The reducing gas reacts with the adsorbed oxygen on the film surface as can be explained by the following reaction:



where R is the reducing gas [20]. This electron affects the charge neutrality of the surface. To regain neutrality, the electron is released back to the bulk. Consequently electron concentration increases thereby decreasing resistivity of the material [25]. It was observed that when the doped

5. Conclusions

Copper doped cadmium oxide (Cu: CdO) thin films were successfully synthesized at low substrate temperature (210°C) using advanced spray pyrolysis technique. The effect of Cu doping on structural properties of was studied by XRD and FESEM. XRD results shows that films are polycrystalline in nature with cubic crystal structure. The films deposited at 2 at% Cu doping (C₂) are highly oriented along (111) and (200) plane and exhibit good crystallinity. FESEM analysis of CdO films support the XRD analysis and confirm that the films are polycrystalline having granular morphology. Optical properties show that films are transparent to visible light, with a direct band gap ~2.54-2.63 eV. The gas sensing performance reveals that 2 at% doped films show about 34% sensitivity to LPG.

References

- L. D. Feng, X. J. Huang, Y. K. Choi, *Microchim. Acta* (2006).
- J. Tores, J.I. Cisseneros, G. Gordillo, F.Alvarez, *Thin Solid Films* 289 (1996) 238.
- K.L. Chopra, S. Major, D.K. Pandey, *Thin Solid Films* 102 (1983) 1.
- C. H. Bhosale, A.V. Kambale, A.V. Kokate, K.Y. Rajpure, *Materials Science and Engineering B* 122 (2005) 67-71.
- P. Cowache, D. Lincot, J. Vedd, *Electrochem. Soc.* 139 (1989) 67.
- R. R. Salunkhe, D. S. Dhawale, U. M.Patil, C. D.Lokhande, *Sensors and Actuators B: Chemical* 136 (2009) 39-44.
- C. Dantus, G. G. Rusu, m. Dobromir, M. Rusu, *Applied Surface Science* 255 (2008) 2665-2670.
- M. Benhaliliba, C.E. Benouis, A. Tiburcio-Silver, F. Yakuphanoglu, A. Avila-Garcia, a. Tavira, R. R. Trujillo, Z. Mouffak, *Journal of Luminescence* 132 (2012) 2653-2658.
- B. J. Zeng, J. S. Lian, L. Zhao, Q. Jiang, *Vacuum* 85 (2011) 861-865.
- R. K. Gupta, K. Ghosh, R. Patel, P.K. Kohol, *Applied Surface Science* 255 (2009) 6252-6255.
- R. Kumaravel, K. Ramamurthi, *Journal of Physics and Chemistry of Solids* (2010) 1545-1549.
- M. K. R. Khan, M. Azizar Rahman, M. Shahjahan, M. Mozibur Rahman,, M. A. Hakim, *Current Applied Physics* 10 (2010) 790-796.
- R. Ferro, J. A. Rodriguez, *Thin Solid Films* 347 (1999) 295-298.

samples were exposed to LPG at different operating temperatures from 200-300° C at intervals of 50°C and at different concentrations of LPG, the notable change in resistance of the film was observed. The % sensitivity was found to vary between 4.3-34%, the variation in sensitivity with operating temperature is shown in Fig.4. The maximum percentage sensitivity was observed to be ~ 34% for 2% copper doped cadmium oxide film at operating temperature of 300°C.

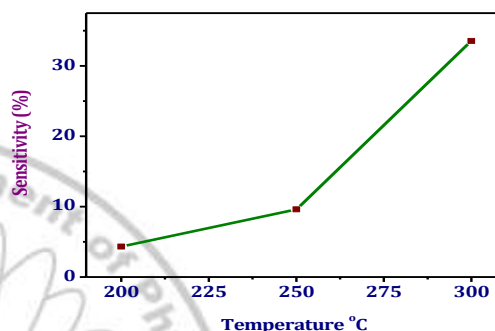


Fig. 4. LPG gas sensing performance

Acknowledgements

One of the authors C.R. Bobade is grateful to University Grants Commission (UGC), New Delhi, India for awarding Teacher Fellowship under FIP scheme.

- P. S. Patil, Versatility of chemical spray pyrolysis technique, *Mater. Chem. Phys.* 59 (1999) 185-198.
- R. J. Deokate, S. M. Pawar, A. V. Moholkar, V. S. Sawant, C. A. Pawar, C. H. Bhosale, K. Y. Rajpure, *Applied Surface Science* 254 (2008) 2187-2195.
- P. S. Shewale, S. I. Patil and M. D. Uplane, *Semiconductor Science and Technology*, 25 (2010) 115008 (6pp).
- JCPDS card no.05-0640.
- B. D. Cullity, *Elements of X-ray Diffraction*, Second ed., Addison-Wesley, Reading MA, (1978) 162.
- B. Saha, S. Das and K. K. Chattopadhyay, *Sol. Energy Mater. Sol. Cells*, 91 (2007) 1692.
- R. R. Salunkhe and C. D. Lokhande, *Sens. Actuators B* 129 (2008) 345.
- R. R. Salunkhe, V. R. Shinde and C. D. Lokhande, *Sens. Actuators B* 133 (2008) 296.
- R. Ferro, J. A. Rodríguez, I. Jiménez, A. Cirera, J. Cerdà, and J. R. Morante, *IEEE Sensors Journal*, 5 (2005) 48.
- M. Chen, Z. Wang, D. Han, F. Gu and G. Guo, *Sens. Actuators B* 157 (2011) 565.
- M. Yao, P. Hu, Y. Cao, W. Xiang, X. Zhang, F. Yuan and Y. Chen, *Sens. Actuators B* 177 (2013) 562.
- A. M. Farag, M. Cavas, F. Yakuphanoglu, *Mater. Chem. Phys.* 132 (2012) 550.

Bio-Polymer Entrapped Catalyst for Organic Transformations

Shital Shinde^a, Gajanan Rashinkar^a, Rajashri Salunkhe^{a*}

^aDepartment of Chemistry, Shivaji University, Kolhapur, 416004, M.S., India

E-mail: rss234@rediffmail.com

*Corresponding author: Tel.: +91 231 260 9169; fax: +91 231 2692333.

Abstract

A protocol has been developed for the efficient synthesis of structurally diverse tetrahydrobenzo[*b*]pyran via three-component reactions of dimedone, malanonitrile with various aldehydes and in the presence of bio-polymer entrapped NaOH as a catalyst.

Keywords: Bio-polymer Entrapped Base Catalyst, tetrahydrobenzo[*b*]pyran, multicomponent reaction (MCR), recyclability,

1. Introduction

Multicomponent reactions (MCRs) have attracted considerable attention owing to high synthetic efficiency, and, in many cases, the facile construction of novel molecular libraries. These methodologies are of particularly great utility when they lead to the formation of privileged medicinal scaffolds. Tetrahydrobenzo[*b*]pyrans are an important class of heterocyclic scaffolds in the field of drugs and pharmaceuticals. These compounds are widely used anti-coagulant, anti-cancer and anti-anginal agents.¹⁻⁴ In addition, they have been shown to act as cognitive enhancers, for the treatment of neurodegenerative disease, including Huntington's disease, amyotrophic lateral Sclerosis, Alzheimer's disease, AIDS associated dementia and Down's syndrome as well as for the treatment of Schizophrenia and myoclonus.^{5, 6} The polyfunctionalized benzopyrans are used as cosmetics, pigments and biodegradable agrochemicals.⁷ Other than their biological importance, some tetrahydrobenzo[*b*]pyrans have been widely used as photoactive materials.⁸ Looking at their importance from pharmacological and industrial point of view, several methods for the multi-component synthesis of tetrahydrobenzo[*b*]pyrans have been reported. These include both homogeneous as well as heterogeneous conditions, catalyzed by Na₂SeO₄, hexadecyldimethylbenzyl ammonium bromide,⁹ NaBr,¹⁰ tetra-methyl ammonium hydroxide (CH₃)₄N⁺OH,¹¹ TEBA,¹² KF-montmorillonite,¹³ KF-alumina,¹⁴ organocatalysts,¹⁵ acetic acid,¹⁶ diammonium hydrogen phosphate¹⁷ and hexadecyltrimethylammonium bromide.¹⁸ Microwaves¹⁹ and ultrasonic irradiation²⁰ have also been used to promote the reaction. Although the literature on synthesis of tetrahydrobenzo[*b*]pyrans enjoys a rich array of versatile methodologies, new efficient approaches

can be valuable additions to the contemporary arsenal of synthetic strategies.

The concept of gel entrapped base catalysts (GEBCs) combines the advantages of alkali and organic bases with those of heterogeneous supports.²¹ These catalysts are prepared by immobilization of alkali or organic bases by entrapping them in an aqueous gel matrix of agar-agar which is a polymer composed of repeating agarobiose units alternating between 3-linked β-D-galactopyranosyl (G) and 4-linked 3, 6-anhydro-α-L-galactopyranosyl (LA) units (Fig. 1).

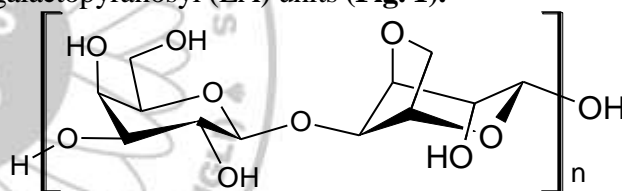


Fig.1: Structure of agarose



Fig. 2: Photograph of GENaOH

The use of GEBCs in organic transformations abates the amount of bases used and affords easy and efficient separation of products from the catalyst simply by filtration. Often, bases like alkalis absorb moisture when exposed to air and get spoiled. On the contrary, the GEBCs do not absorb moisture on exposure to air and remain intact. They also provide excellent opportunity of recyclability and reusability which is rarely possible using bases alone as catalyst. Further advantages of GEBCs

include their ease of handling and being less corrosive. However, despite of their well recognized advantages, there have been only limited and sporadic reports dealing with the use of GEBCs in organic synthesis.²²

In continuation to our research work devoted to the development of green methodologies for MCRs,²³ we report herein an efficient synthesis of tetrahydrobenzo[*b*]pyrans from dimedone, malanonitrile and aryl aldehydes in the presence of Gel entrapped NaOH as a catalyst.

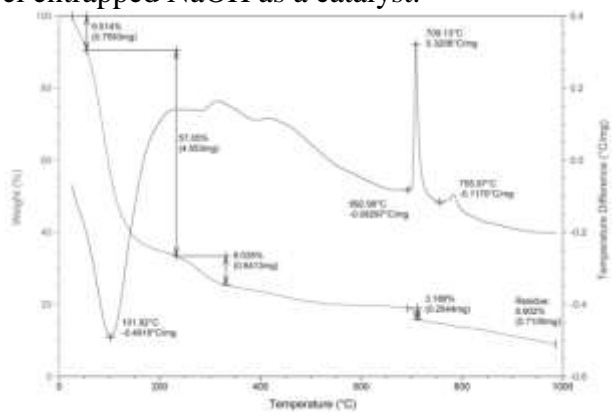


Fig.3: DSC-TGA graph of GENaOH

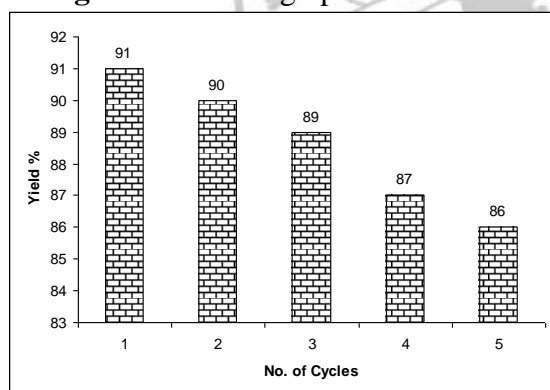


Fig. 4: Recyclic use of GENaOH tetrahydrobenzo[*b*]pyran synthesis

2. Results and Discussion

We focused our initial studies on synthesis of Gel entrapped NaOH (acronymed as GENaOH). A series of experiments were undertaken in which different concentrations of NaOH (5-25 %) were dissolved in a varying amount of agar-agar in water. After a considerable experimentation, we found that 20 % w/w of agar-agar aqua gel containing 10 % NaOH resulted in the formation of soft gel that served as GEBC in the present work. The GENaOH was light yellow jelly like substance that could be cut into pieces (Fig. 2). The changes in physical nature of GENaOH were studied in different solvents. The

GENaOH swelled in water and become soft. The nature of gel remained intact in organic solvents like ethanol, acetone, dichloromethane, toluene and isopropanol.

The TGA analysis of agar-agar and GENaOH are displayed in fig. The TGA profiles shows three different weight losses at different temperatures. The fourth weight loss which occurs below 150 °C for GENaOH as well as agar could be due to removal of physisorbed or occluded water. The second step of decomposition which is initial above 240 °C in both agar-agar as well as GENaOH differed in their amount of respective weight losses (GENaOH ~ 8%, agar-agar 63.5% could be assigned to thermal decomposition of agar polymer was agar-agar. The decomposition of remaining polymer matrix is accompanied with ~21 % weight loss. Third step in the temperature range of 440-480 °C. On the other hand the additional exothermic weight loss centered at 710 °C is observed and could be assigned the decomposition of carbonates frame if any. The entrapment of NaOH in gel matrix is evidenced by the comparatively large residual weight observed in the TGA profile of GENaOH than that of agar-agar.

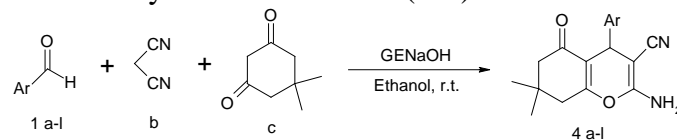
In order to assess the catalytic activity of GENaOH in the synthesis of tetrahydrobenzo[*b*]pyrans (Scheme 1), an equimolar mixture of dimedone, malanonitrile and benzaldehyde (5 mmol each) was stirred in the presence of 1 gm of GENaOH in ethanol at ambient temperature till the completion of reaction as monitored by thin layer chromatography. The reaction proceeded efficiently yielding the corresponding tetrahydrobenzo[*b*]pyran in 91% yield in just 5-15 minutes. In order to check the generality of this methodology, a series of tetrahydrobenzo[*b*]pyrans were prepared by reaction of dimedone, malanonitrile with various aryl aldehydes. The results are summarized in (Table 1). We were gratified to find that with both electron-poor and electron-rich benzaldehydes, the corresponding products were obtained in excellent yields. The reaction of the sterically hindered *o*-nitrobenzaldehyde even gave higher yields highlighting the general applicability of the protocol. The striking feature of all the reactions was the isolation of products. During the course of the reaction the product precipitates out and can be isolated simply by filtration. The product obtained after sufficient washing with water was found to be

practically pure. The identity of all the compounds was ascertained on the basis of IR, ¹H NMR, ¹³C NMR and mass spectroscopy data. The physical and spectroscopic data are in consistent with the proposed structures.

It has been well established that in case of the GEBs, the reagent trapped in the gel may leach into the solvent. To study the leaching of NaOH in solvent, 1 gm GENaOH was stirred in 5 mL of ethanol at room temperature. The GENaOH was filtered and water (3 mL) was added to the filtrate. The NaOH leached out was determined by titration with 0.1 N succinic acid solution using phenolphthalein as an indicator. The study revealed that only 3.91 % NaOH leached out from gel into ethanol. Using the amount of NaOH same as that leached out, the reaction between dimedone, malanonitrile and benzaldehyde did not gave quantitative yield of the corresponding product. This clearly demonstrated that catalysis was solely due to intact GENaOH rather than leached NaOH.

A proposed mechanism for the formation of tetrahydrobenzo[*b*]pyrans using GENaOH is depicted in (Fig. 5). The mechanism suggests that in step-1 Knoevenagel condensation takes place to form the α-cynocinnamonitrile derivative.

dimedone react with the electrophilic C=C double of α-cynocinnamonitrile giving the intermediate 6, which tautomerizes into 7. The latter is then cyclized by nucleophilic attack of the OH group on the cyano (CN) moiety, giving intermediate 8. Finally, the expected product 4 is afforded by tautomerization (8-4).

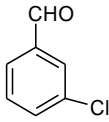
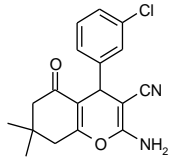
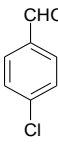
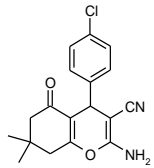
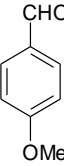
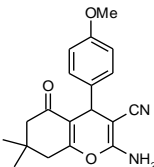
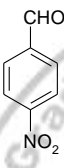
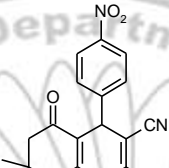
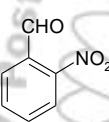
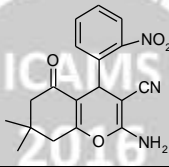
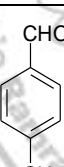
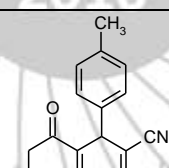
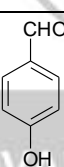
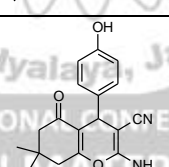
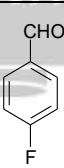
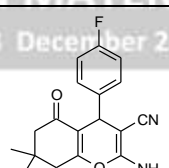


Scheme 1: GENaOH catalyzed multicomponent synthesis of tetrahydrobenzo[*b*]pyrans

The use of catalyst is especially interesting when it can be used several times. To investigate the possibility of catalyst recycling, the reaction of dimedone, malanonitrile with benzaldehyde using GENaOH in ethanol was carried out. After completion of the reaction, the GENaOH was recovered by simple filtration, washed with ethanol and reused in another reaction with identical substrates. The catalyst could be reused for five runs without noticeable drop in the yield of product (Fig. 4).

Table 1: Synthesis of tetrahydrobenzo[*b*]pyrans catalyzed by GENaOH

Entry	Aldehyde	Products	Time/ min	Yield ^b , %	M.P. ^c /°C
a			10	91	[226-228] ²⁴ 230
b			15	90	[229-231] ²⁵ 228
c			10	89	[198-200] ²⁴ 199
d			10	87	[217-218] ²⁴ 215

e			10	86	[235-237] ²⁴ 235
f			05	89	[209-211] ²⁴ 210
g			15	90	[199-201] ²⁴ 200
h			05	88	[177-178] ²⁴ 175
i			10	87	[215-217] ²⁴ 215
j			10	90	[214-216] ²⁵ 215
k			10	88	[208-210] ²⁶ 211
l			10	86	[176-178] ²⁴ 175

a) All products were characterized by IR, ¹H NMR, ¹³C NMR and mass spectrometry.

b) Isolated yields.

c) Literature values in parenthesis

3. Experimental

Infrared spectra were recorded on a Perkin-Elmer FTIR spectrometer. The samples were examined as KBr discs ~5% w/w. ¹H NMR and ¹³C NMR spectra were recorded on a Bruker Avon 300 MHz spectrometer using DMSO/CDCl₃ as solvent and TMS as internal reference. Mass

spectra were recorded on a Shimadzu QP2010 GCMS with an ion source temperature of 280 °C. The thermal gravimetric analysis (TGA) curves were obtained by using the instrument STA 1500 in the presence of static air at a linear heating rate of 10 °C/min from 25 ° to 1000 °C. Melting points were determined in an open capillary and are

uncorrected. All chemicals were obtained from local suppliers and used without further purification.

3.1 Preparation of gel entrapped NaOH

To a boiling mixture of agar-agar (20 Mg) in water (60 mL) was added a solution of NaOH (10 gm) in water (10 mL). The resultant solution was boiled with stirring for five minutes and cooled in ice bath to yield the desired GENaOH.

A mixture of dimedone (5 mmol), malanonitrile (5 mmol) and aryl aldehyde (5 mmol) was stirred in the presence of GENaOH (1 gm) in 5 mL of ethanol at ambient temperature till the completion of the reaction as monitored by TLC. The resulting crude product was filtered off, washed with water and recrystallized from ethanol to afford the desired product.

3.2 Spectral data of representative compounds

2-Amino-3-cyano-5,6,7,8-tetrahydro-7,7-dimethyl-5-oxo-4-phenyl-4H-benzopyra (4a): IR (KBr): ν

3396, 3323, 3213, 2961, 2199, 1976, 1660, 1371 cm^{-1} ; ^1H NMR (300 MHz, DMSO- d_6): δ 1.05 (s, 3H), 1.12 (s, 3H), 2.21 (d, 1H), 2.22 (d, 1H), 2.44 (s, 2H), 4.39 (s, 1H), 4.50 (s, 2H), 7.17-7.31 (m, 5H); ^{13}C NMR (75 MHz, DMSO- d_6): 27.39, 28.92, 32.13, 35.88, 50.52, 59.03, 113.36, 120.03, 126.92, 127.50, 128.57, 144.78, 158.91, 162.73, 196.05; MS (EI): $m/z = 294$ (M^+).

2-Amino-3-cyano-5,6,7,8-tetrahydro-7,7-dimethyl-4-(4'-hydroxy, 3-methoxy)-5-oxo-4H-benzopyran (4b): IR (KBr): ν 3497, 3323, 3215, 2192 cm^{-1} ; ^1H NMR (300 MHz, DMSO- d_6): δ 0.95 (s, 3H), 1.03(s, 3H), 2.03-2.17 (m, 2H), 2.40 (s, 2H), 3.73 (s, 3H), 4.07 (s, 1H), 6.29 (s, 2H), 6.46-6.64 (m, 3H); ^{13}C NMR (75 MHz, DMSO- d_6): 27.32, 28.19, 29.07, 31.88, 32.11, 35.33, 50.60, 55.88, 59.52, 111.69, 113.71, 115.60, 119.73, 135.96, 145.53, 147.49, 158.70, 162.12, 195.82; MS (EI): $m/z = 340$ (M^+).

Conclusion

We have described a general and highly efficient procedure for the preparation of multi-component synthesis of tetrahydrobenzo[b]pyrans from dimedone, malanonitrile and aryl aldehydes in the presence of gel entrapped NaOH. The method offers several significant advantages, such as high conversions, easy handling, clean reaction profile, no energy consumption, high conversions, cost effective short reaction time and green methodology which make it a useful and an attractive addition to the existing methodologies.

Acknowledgements

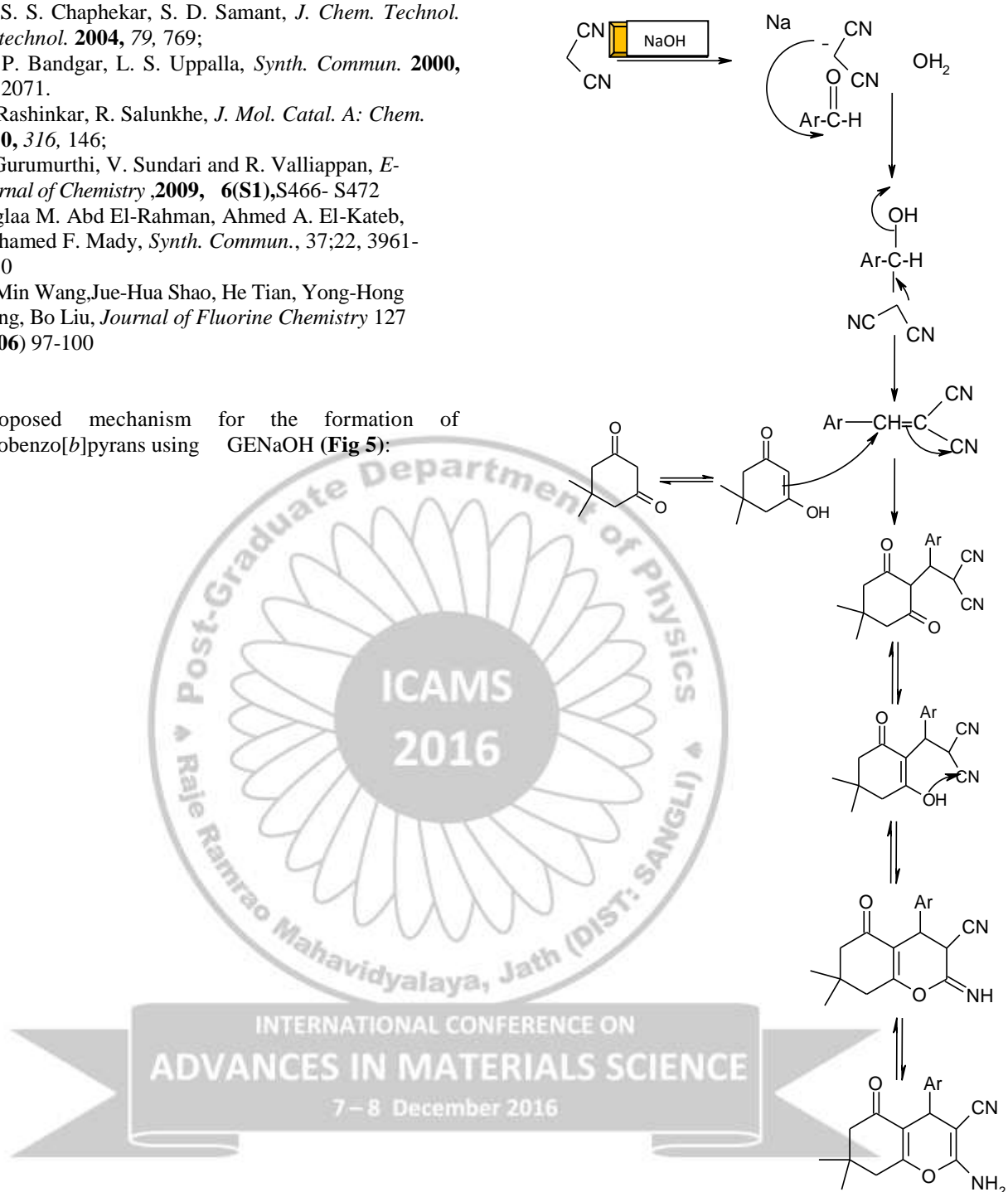
We gratefully acknowledge the financial support from the Department of Science Technology and University Grants Commission for FIST and SAP respectively.

References

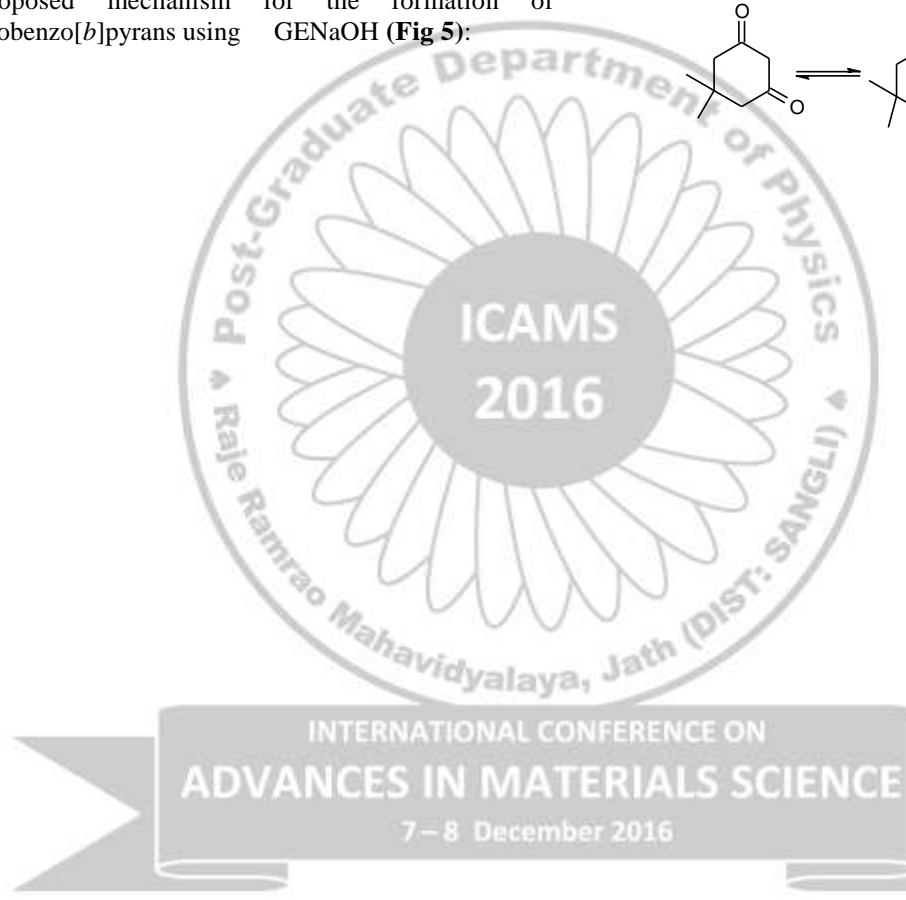
- Zhang Y L, Chen B Z, Zheng K Q, Xu M L, Zhang L Z and Lei X H, Yao Xue Xue Bao., **1982**, 17(1), 17-22.
- Zhang Y L, Chen B Z, Zheng K Q, Xu M L and Lei X H, *ChemAbstr.*, **1982**, 96, 135383e.
- Andreani L L and Lapi E, *Bull Chim Fr.*, **1960**, 99, 583.
- Witte E C, Neubert P and Roesch A, *ChemAbstr.*, **1986**, 104, 224915f.
- Konkoy C S, Fick D B, Cai S X, Lan N C and Keana J F W, PCT IntAppl WO, 00, 75 **2000**, 123.
- Konkoy S, Fick D B, Cai S X, Lan N C and Keana J F W, PCT IntAppl WO 0075123 *ChemAbstr.*, **2000**, 134, 29313a.
- (a) Hafez E AA, Elnagdi M H, Elagamey A G A and EL-Taweel F M AA, *Heterocycles*, **1987**, 26, 903; (b) Abdel Galil F M, Riad B Y, Sherif, S M and Elnagdi M H, *ChemLett.*, **1982**, 1123.
- Arnesto D, Horspool WM, Martin N, Ramos A, Seaone C (**1989**) *J Org Chem* 54:3069
- (a) Jin T S, Wang A Q, Shi F, Han L S, Liu, L B and Li T S, *ARKIVOC*, **2006**, (xiv), 78-86; (b) Wang X S, Shi D Q, Tu S J and Yao C S, *Synth Commun.*, **2003**, 33, 119.
- Devi I and Bhuyan P J, *Tetrahedron Lett.*, **2004**, 45, 8625-8627.
- Balalaie S, Sheikh-Ahmadi M and Bararjanian M, *CatalCommun.*, **2007**, 8, 1724-1728.
- Rong L, Li X, Wang H, Shi D, Tu S and Zhuang Q, *Synth Commun.*, **2006**, 36, 2363.
- Zhuang Q Y, Wu N, Shi D Q, Tu S J and Wang X S, *Chin J Org Chem.*, **2006**, 26, 1217.
- Wang X S, Shi D Q, Tu S J and Yao C S, *Synth Commun.*, **2003**, 33, 119-126.
- Lian X Z, Huang Y, Li Y Q and Zheng W J, *Monatshefte fur Chemie*, **2008**, 139, 129.
- Kamaljit S, Jasbir S and Harjit S, *Tetrahedron*, **1996**, 52, 14273.
- (a) Balalaie S, Bararjanian M, Sheikh-Ahmadi M, Hekmat S and Salehi P, *Synth Commun.*, **2007**, 37, 1097; (b) Balalaie S, Bararjanian M, Amani A M and Movassagh B, *Synlett.*, **2006**, 263-266.
- (a) Jin T S, Wang A Q, Wang X, Zhang J S and Li T S, *Synlett.*, **2004**, 871; (b) Wang L M, Shao J H, Tian H, Wang Y H and Liu B, *J Fluorine Chem.*, **2006**, 127, 97; (c) Seifi M and Sheibani H, *CatalLett.*, **2008**, 126, 275; (d) Gao S, Tsai C H, Tseng C and Yao C F, *Tetrahedron*, **2008**, 64, 9143.
- Devi I, Bhuyan P J, *Tetrahedron Lett.* **2004**, 45, 8625.
- Tu SJ, Jiang H, Zhuang QY, Miu CB, Shi DQ, Wang XS, Gao Y. *Chin. J. Org. Chem.* **2003**, 23(5), 488.
- R. S. Natekar, S. D. Samant, *Ind. J. Chem.* 35B (**1996**) 1347

22. (a) S. S. Chaphekar, S. D. Samant, *J. Chem. Technol. Biotechnol.* **2004**, *79*, 769;
 (b) P. Bandgar, L. S. Uppalla, *Synth. Commun.* **2000**, *30*, 2071.
23. G. Rashinkar, R. Salunkhe, *J. Mol. Catal. A: Chem.* **2010**, *316*, 146;
24. S. Gurumurthi, V. Sundari and R. Valliappan, *E-Journal of Chemistry*, **2009**, *6(S1)*, S466- S472
25. Naglaa M. Abd El-Rahman, Ahmed A. El-Kateb, Mohamed F. Mady, *Synth. Commun.*, *37*;22, 3961-3970
26. Li-Min Wang, Jue-Hua Shao, He Tian, Yong-Hong Wang, Bo Liu, *Journal of Fluorine Chemistry* *127* (2006) 97-100

The proposed mechanism for the formation of tetrahydrobenzo[*b*]pyrans using GENaOH (Fig 5):



General procedure for the multi-component synthesis of tetrahydrobenzo[*b*]pyrans



Electrical properties of gallium doped zinc oxide thin films by spray pyrolysis

A.R. Babar*

Materials Science and Thin film Laboratory, Department of Physics,
Shankarrao Mohite Mahavidyalaya, Akluj 413 101, India

Abstract

Gallium doped zinc oxide thin films have been deposited by spray pyrolysis method on glass substrates using zinc acetate and gallium nitrate. The effect of Ga doping on the electrical properties of sprayed ZnO thin films was investigated using Hall Effect techniques. The addition gallium induces a decrease in electrical resistivity of ZnO:Ga films up to 2 at% gallium doping. The observed lowest resistivity of the film was $1.5 \times 10^{-4} \Omega \text{ cm}$. The concentration increases, so does the mobility, until it reaches a maximum value for the film deposited with 2 at% gallium doping. The values of carrier concentration and mobility were $12 \times 10^{19} \text{ cm}^{-3}$ and $99 \text{ cm}^2/(\text{Vs})$ respectively.

Keywords: Zinc oxide, thin film, spray pyrolysis, electrical properties.

Corresponding author: Marked by *, E-mail: babarar2008@gmail.com

1. Introduction

Transparent conducting oxide (TCO) thin films have been extensively studied because of variety applications. Zinc oxide thin film form has generated renewable interest in science and technology due to wide application in opto-electronic and electronic devices [1-3]. Transparent conduction ZnO thin films are emerging as the most attractive alternative to ITO and various other TCOs [4]. ZnO is considerable attention for its possible applications in UV light emitters, spin functional devices, gas sensors, transparent electronics and surface acoustics and wave devices [5]. ZnO thin films have been deposited several techniques such as pulsed laser deposition [6], d.c. sputtering [7], sputtering [8], reactive evaporation [9], chemical vapor deposition [10], spray pyrolysis [11-12] and sol gel [13]. Among these chemical spray pyrolysis technique is simple, low cost and can be used effectively for the large area deposition and film properties can tailored by controlling spraying conditions.

2. Experimental

Zinc oxide (ZnO) thin films were deposited on ultrasonically cleaned preheated corning glass substrate using chemical spray pyrolysis technique. The concentration of sprayed solution was 0.2M. In order to dope Ga in ZnO thin films, for five different Gallium concentrations (0.5,1,1.5,2,2.5, and 3at% measured as atomic weight percentage) were selected. The electrical parameters such as electrical resistivity (ρ), carrier concentration (n) and Hall mobility (μ_H) were measured at room temperature by Hall effect set up, in Van der Pauw configuration, supplied by Scientific Instruments, Roorkee, India.

3. Results and discussion:

Electrical properties:

Figure 1 shows the variation of conductivity (σ) of ZnO:Ga films with the Ga doping at room temperature. Initially the conductivity increases with doping concentrations up to 2 at% and then decreases with further doping concentrations. The lowest value of resistivity calculated from conductivity is $1.5 \times 10^{-4} \Omega \text{ cm}$ for Ga content of 2 at%. As the Ga content further increases, the conductivity decreases at Ga content of 3 at%. Hall measurements show that all the films are n-type. The variation of the electric parameters Hall mobility (μ), carrier concentration (n) as a function of the Ga doping concentration is illustrated in Fig.2. The value of the carrier concentration reaches the maximum value $12 \times 10^{19} \text{ cm}^{-3}$ at the Ga content of 2 at%. The decrease of the mobility with Ga doping is a consequence of a rapid increase of the carrier concentration, which lowers the mobility due to more charge carrier scattering from ionized impurities.

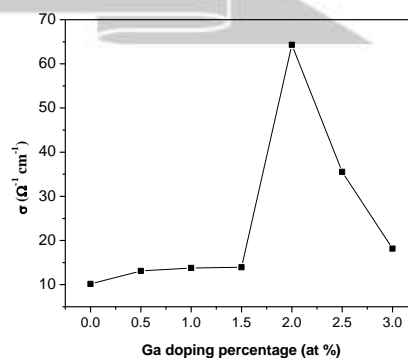


Fig.1. Variation of electrical conductivity with gallium doping concentration for sprayed ZnO:Ga thin films.

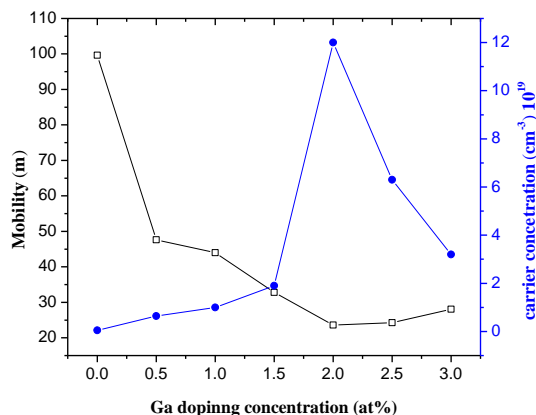


Fig.2. The dependence of carrier concentration and mobility of Ga: ZnO thin films with respect to doping concentration.

4. Conclusions

Zinc oxide and Gallium doped n type Zinc oxide thin films were prepared at 673 K substrate temperature using chemically spray pyrolysis technique and effect of gallium doping on some physical characteristic was studied. Gallium doping leads to considerable increase in electrical conductivity of Ga: ZnO thin films. The electrical resistivity value of $1.5 \times 10^{-4} \Omega \text{ cm}$ from Hall effect measurement performed at room temperature, electronic mobility $\sim 99 \text{ cm}^2 \text{ v}^{-1} \text{ s}^{-1}$ and carrier concentrations (n) of $12 \times 10^{19} \text{ cm}^3$ were obtained.

Acknowledgement:

The author is highly grateful to Mr. Jaysingh Mohite- Patil President Shikshan Prasark Mandal, Akluj for the inspiration and support. Also thankful to Secretary and all management of Shikshan Prasark Mandal. Author also acknowledge to Dr. A. L. Deshmukh, Principal, Shankarrao Mohite Mahavidyalaya, Akluj for his co-operation, encouragement, love and homely behavior given to me in every movement of this work.

References

1. A. Dutta, S.Basu, J. Mater. Sci.: Mater. El. 6 (1995) 415.
2. A.S.Riad, S.A.Mahmoud, A.A. Ibrahim, Physica B 296 (2001) 319
3. S.Tuxemen, Gong Xiong, J.Wikinson, Physica B 308 (2001) 1197.
4. Ozgur, Ya. I.Ailvot, C.Liu, A.Teke, M.A. Reshchikov, S. Dodan, V. Auruti .J. Cho, H. Morkoc, J. Appl. Phy.989 (2005).
5. S.J.Pearnton, D.P.Norton, K.Ip, Y.W. Heo, T.Steine, Prog.Mater. Sci.50 (2005) 293.
6. G.A. Hirata, J. McKittrick, T. Cheeks, J.M. Siqueiros, J.A. Diaz, O. Contreras, O.A. Lopez, Thin Solid Films 288 (1996) 29.
7. M.Br ett, R. McMahan, J. Affinito, S.Parson, J.Vac. Sci. Technol. A 1 (1984) 162.
8. P. K. Song, M.Watanabe,M. Kon, A. Mitsui, Thin Solid films 411 (2002) 82.
9. J.Zhao, L. Z. Hu, Z.Y. Wan, X.P. Liang, Appl. Surf. Sci. 229 (2004) 311.
10. J.Hu, R. G. Gordon, Sol. Energy 30 (1991) 437.
11. M.Krunks, E. Mellikov, Thin solid films 270 (1995) 33.
12. J. Rodriguez-Baez, A. Malsonado, L. Castaneda, G.Torres, Delgado, R. Castanedo. Perez, M. de la L. Olvera, Thin Solid films 515 (2007) 8689.
13. T. Schuler, M. A. Aegerter, Thin Solid films 531 (1999) 125.

Structural and Magnetic Properties of Lanthanum Substituted Mg –Zn Ferrite Nanoparticles Prepared By Co-Precipitation Method

R.A.Bugad^a, T.R. Mane^a, B.B.Navale^c, J. V. Thombare^c, A.R. Babar^b, B.R. Karche^b

^aSangola Mahavidyalaya, Sangola Dist: Solapur (M.S.) 413307

^bShankarrao Mohite Mahavidyalaya, Akhuj. Dist: Solapur (M.S.) 413101

^cVidnayan Mahavidyalaya, Sangola Dist: Solapur (M.S.) 413307

Abstract

Nanoparticles of Lanthanum substituted Magnesium Zinc ferrites with general formula $Mg_{0.6}Zn_{0.4}La_{2y}Fe_{2-2y}O_4$ (where $y = 0.0, 0.05, 0.1, 0.15, 0.20$ and 0.25) have been synthesized using co-precipitation method. The effects of La^{3+} on structural properties are studied. Phase formation was investigated using X-ray diffraction and Infrared absorption technique. Two prominent infrared absorption bands for all ferrite samples are observed; one at 412 cm^{-1} due to tetrahedral (A) interstitial voids and other at 524 cm^{-1} due to octahedral (B) interstitial voids is observed. The lattice parameter increased with increasing La^{3+} content. The effect of lanthanum substitution was observed on X-ray density, ionic radius and bond length. Magnetic properties of the samples are investigated by using Vibrating Sample Magnetometer (VSM). The effects of La^{3+} on both structural and magnetic properties are studied.

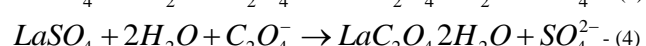
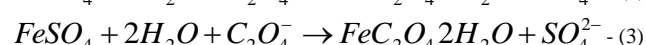
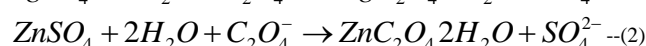
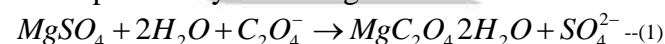
1. Introduction

Recently, many research groups have been focused on the preparation of variety of ferrites such as; Zn-Mn ferrite [1, 2], Ni-Zn ferrite [3], Mg ferrite [4], Mg-Cd ferrite [5] and Mg-Zn ferrite [6]. Among all these ferrites, Mg-Zn ferrite have been mostly studied thanks to their lower value of the magneto-striction constant and better magnetic properties of Mg-Zn ferrite materials [6]. Ferrites are the mixed metal oxide with iron oxide as main component [7]. Most of the ferrites have a spinel structure. The general formula of a spinel can be written as AB_2O_4 [8]. In the normal spinel structure, the A cations are in the tetrahedral sites and the B cations are in the octahedral site. Alternatively, half of the B cations and all the A cations are randomly distributed in octahedral sites, resulting in the inverse spinel structure [9]. The lanthanum substituted magnesium zinc ferrites are quite versatile from the point of view of their application. Rare earth substituted magnesium zinc ferrite have attracted considerable attention in the field of technological applications extending from microwave to radio frequency. The addition of rare earth metal ions like La^{3+} introduces changes in the structure and texture [10]. Magnetic properties of nanoparticles find wide technological applications such as high density recording, magnetic refrigeration, Spintronics and drug delivery etc. [11]. Ishtiaq Ahmad reported that lanthanum substituted magnesium zinc ferrite finds a wide number of applications in gas sensors [12]. Many researchers reported that, lanthanum substitution ferrite enhances magnetic properties such as saturation

magnetization, remenant magnetization and coercivity, as well as dielectric constant [13].

2. Experimental procedure

The $Mg_{0.6}Zn_{0.4}La_{2y}Fe_{2-2y}O_4$ (where $y=0.0, 0.05, 0.10, 0.15, 0.20$ & 0.25) were prepared by the oxalate co-precipitation method. The high purity starting materials $MgSO_4 \cdot 7H_2O$, $ZnSO_4 \cdot 7H_2O$, $LaSO_4 \cdot 7H_2O$ and $Fe_2SO_4 \cdot 7H_2O$ were used for preparation of samples. All chemicals are in AR grade. These chemicals were weighted in desired stoichiometric proportion and dissolved in distilled water. The pH of the solution was maintained at 4.8 by drop wise addition of concentrated H_2SO_4 . The resulting solution was heated at 80°C for 1 h in order to complete the ionization of metal sulfates [14]. The precipitating reagent was prepared in distilled water by adding required proportion of AR grade ammonium oxalate. The precipitating reagent was added by drop into metal sulfate solution with constant stirring until the process of precipitation was completed. The process of precipitation can be explained by following chemical reaction.



The resultant precipitation was the solid solution of magnesium oxalate, zinc oxalate, lanthanum oxalate and ferrous oxalate. The precipitate along with solution was digested on sand bath for 1h in order to settle down the precipitate at the bottom of the beaker. The precipitate was filtered by Whatman filter paper no.41 using suction flask operating with the

vacuum pump. The precipitate was thoroughly washed with distilled water in order to remove sulfate ions. The absence of sulfate ion in the filtrate was confirmed by barium chloride test. The co-precipitate product was dried and calcined at 450 °C for 5h in air. The calcined powder was milled in an agate mortar with AR grade acetone as a base. The powder was pre-sintered at 700 °C for 5h. The pre-sintered powder was pressed under hydraulic pressure of 5 tones /cm³ to form pellet using polyvinyl alcohol as binder. Then pellets were finally sintered at 900 °C for 12h; the temperature was raised and cooled at the rate of 100 °C per hours. The sintering process had cause the atom to move to its lattice completely.

3. Result and discussion

3.1 XRD studies

The X-ray diffraction patterns of Mg_{0.6}Zn_{0.4}La_{2y}Fe_{2-2y}O₄ (y = 0.0, 0.05, 0.10, 0.15, 0.20 & 0.25.) are presented in (fig.1). Powder X-ray diffractometer of the ferrite samples reveals the formation of single phase cubic structure of all samples. The lattice constants 'a' (Å) for all prepared samples was calculated by using prominent (311) XRD peak using the equation.

$$a = [d^2 (h^2 + K^2 + l^2)]^{1/2} \quad \text{----- (1)}$$

Where d is value of line spacing in XRD pattern, h k l are corresponding Miller indices to each line in pattern. The value of lattice constant was further used for determination of particular plane (h k l) for known angle. The calculated and observed values of interplaner distances (d) are in good agreement with each other. The average crystallite size for all the ferrite samples using (311) was determined by Debye Scherer formula.

$$D = \frac{0.94 \lambda}{\beta \cos \theta} \quad \text{----- (2)}$$

Where λ is the wavelength of radiation used for diffraction. 2θ is the angular position of a prominent peak (311) and β is full width of prominent peak at half maximum intensity. The average crystallite size t is presented in the Table 1. From this table it is observed that, the crystallite size of the sample lies in nano particle range 4.39 nm to 4.81 nm. The average crystallite size of all the samples is smaller than that prepared by ceramic method.

The X- ray density ρ_x of each sample was calculated using the relation [3].

$$\rho_x = \frac{z \times \text{mol. mass}}{V N_A} \quad \text{----- (3)}$$

Where, Z is the number of molecules per formula unit (Z = 8 for spinel system), Mol. mass is the molecular mass of the sample, V is the unit cell volume (V = a³), and N_A is the Avogadro's number.

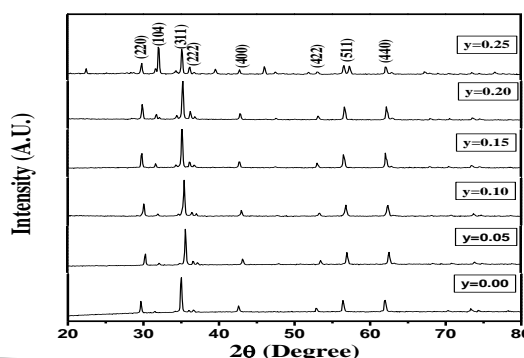


Fig. 1 XRD patterns of ferrite system Mg_{0.6}Zn_{0.4}La_{2y}Fe_{2-2y}O₄ (y = 0.0, 0.05, 0.1,0.15, 0.20 and 0.25)

The variation of X- ray density ρ_x with the La³⁺ content (y) is presented in table1. The X- ray density ρ_x for all composition of lanthanum substituted magnesium zinc ferrite increases with increase in La³⁺ content.

The metal oxygen bond length A-O on tetrahedral A site is calculated by equation (4)

$$A-O = \left(u - \frac{1}{4}\right) a (3)^{1/2} \quad \text{----- (4)}$$

The bond length B-O on octahedral B site is calculated by equation (5)

$$B-O = \left(\frac{5}{8} - u\right) a \quad \text{----- (5)}$$

Where, u is oxygen ion parameter.

The ionic radii on tetrahedral A site and octahedral B site is calculated by using equation (6) & (7)

$$r_A = \left(u - \frac{1}{4}\right) a (3)^{1/2} - r(O_2)^- \quad \text{----- (6)}$$

$$r_B = \left(\frac{5}{8} - u\right) a - r(O_2)^- \quad \text{----- (7)}$$

Where r(O₂)⁻ is the ionic radii of oxygen

3.2 FT-IR studies

The FT-IR spectra of Mg_{0.6}Zn_{0.4}La_{2y}Fe_{2-2y}O₄ ferrite system have been studied in the frequency range 400-4000cm⁻¹ and it is shown in Fig 2. The IR spectra of ferrite is found to exhibits two major bands in the range of 400-600 cm⁻¹ are attributed to the fundamental vibrations of the ions of the crystal lattice. This difference in the band position is expected because of the difference in the Fe³⁺ – O²⁻ distance for the octahedral and tetrahedral compounds. The Infrared absorption spectra shows two distinct absorption bands ν₁ due to tetrahedral interstitials in the range (400 -424) cm⁻¹ and ν₂ due to octahedral interstitials in the

range (492 – 537) cm^{-1} , the typical bands of spinel structure are attributed to the intrinsic stretching vibrations of the unit cell of spinel in the tetrahedral (A) site and the metal oxygen vibration in the octahedral site. This result is good agreement with previous report [15-16].

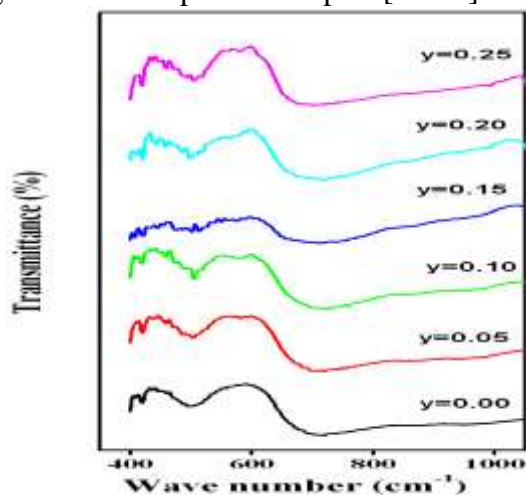


Fig. 2: FT-IR of $\text{Mg}_{0.6}\text{Zn}_{0.4}\text{La}_{2y}\text{Fe}_{2-2y}\text{O}_4$ ferrite system

3.3 Magnetic studies

The magnetic hysteresis loop of $\text{Mg}_{0.6}\text{Zn}_{0.4}\text{La}_{2y}\text{Fe}_{2-2y}\text{O}_4$ ferrite system (Where $y = 0.0, 0.05, 0.1, 0.15, 0.20$ and 0.25) were traced using a vibrating sample magnetometer in the range of 10000 Gauss at room temperature as shown in Fig.3. It is seen from the hysteresis loop that the all samples do not saturate completely even in the maximum applied field around 10,000 Gauss. It is observed that the saturation

magnetization decreases with the substitution of lanthanum. This decrease in trend can be explained on basis of site occupancy of the cations and modifications brought about in the exchange effect due to the substitution of La. The main contribution of magnetic properties derived from Fe^{3+} on B-site of cubic spinel. The lanthanum ion has high octahedral preference and hence occupies B-site at the expense of Fe^{3+} ion shifting to the A-site. La^{3+} has no unpaired electrons and is paramagnetic in nature having magnetic moment is $0 \mu_B$ as compared to Fe^{3+} ion have $5 \mu_B$. Thus the magnetization of B- sub lattice gets diluted resulting in the observed decrease in saturation magnetization for the lanthanum substitution ferrites [7].

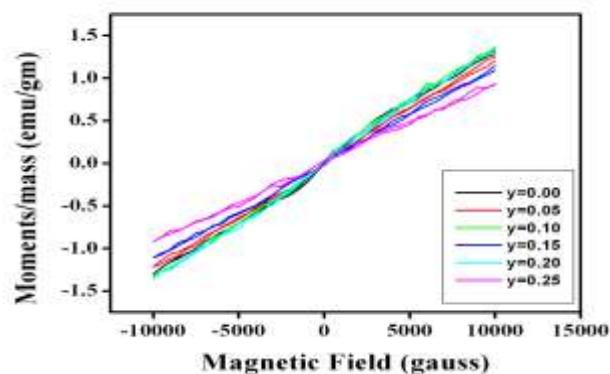


Fig. 3: Magnetic hysteresis loop of $\text{Mg}_{0.6}\text{Zn}_{0.4}\text{La}_{2y}\text{Fe}_{2-2y}\text{O}_4$ ferrite system

4. Conclusion

Lanthanum substituted magnesium zinc ferrite is cubic spinel ferrite. Nanocrystalline Lanthanum substituted magnesium zinc ferrite have been prepared by oxalate co-precipitation. The crystalline size and Lattice constant exhibit decreases as a function La concentration. Crystallites size of all samples is found in the range of 48 nm to 41 nm. The X-ray parameters, viz. Lattice constant, X-ray density, bulk density, ionic radius and bond length were determined affected by La^{3+} ion substitution. Bond length and ionic radii were decreases with La^{3+} content. X-ray density of samples goes on increasing with La^{3+} content and found in the range 4.76 gm/cc to 5.68 gm/cc. The absorption bands in FTIR spectra are found in the expected range of ferrites and this corroborates the spinel structure of the samples. The addition of La^{3+} has reduced the saturation magnetization values where the coercivity increases making the La doped ferrite more reliable for memory storage devices. Lanthanum alters the structural and magnetic properties of Mg-Zn ferrite.

References

- P.P. Hankare, R.P. Patil, U.B. Sankpal, S.D. Jadhav, K.M. Garadkar, S.N. Achary, Journal of Alloys and Compounds, 509 (2011) 276–280.
- N. M. Deraz, O. H. A. Elkader, Int. J. Electrochem. Sci., 10 (2015) 7138 – 7146.
- K. R. Krishna, K. V. Kumar, D. Ravinder, Advances in Materials Physics and Chemistry, 2(2012) 185-191.
- M. A. Khan, M.U. Islam, M. Ishaque, I.Z. Rahman, Ceramics International, 37 (2011) 2519–2526
- B.R. Karche, B.V. Khasbarder, A.S. Vaingankar, Journal of Magnetism and Magnetic Material, 168 (1997) 292.
- H. M. Zaki, S. A. Heniti, A. Umar, F. A. Marzouki, A. A. Daiem, T. A. Elmosalami, H. A. Dawoud, F. S. A. Hazmi, S. S. A. Allah, J. of Nanoscience and Nanotechnology, 13(2013) 4056–4065.
- G. kumar, M. Kanthwal, B.S. Chauhan & M. Singh. Indian J. pure & Appl. Phy. Vol. 44, (2006) 930-934.
- M. Kaur, B.S.Randhawa, J. Singh, D.Utreja, J. Ceramics Int. 39, (2013), 325-328.
- V. Raghavan, Material Science and Engineering, 5th ed. PHI Learning Pvt. Ltd. New Delhi, (2004).
- I. Ahmad, M.T. Farid, R. Kousar, S. B. Niazi. World Appl. Sci. J. 22(6): (2013) 796-801.
- P. C. Rajesh Varma et.al, J. Alloys.comp.453 (2008) 29.
- I. Ahmad, M.T. Farid, R. Kousar and S. B. Niazi. World Appl. Sci. J. 22(6):(2013) 796-801.
- Y.L. Liu, Z.M. Liu, Y. Yang, H.F. Yang, G.L. Shen and R.Q. Yu, Sensor and Actuators B; Chem. 107, (2005) 600-604.
- A. B. Gadkari, T. J. Shinde, P. N. Vasambekar, J. Mater Sci: Mater Electron 21 (2010) 96-103.
- R. D. Waldron, Phys. Rev; 99 (6) (1955) 1727.
- K. V. S. Badarinath, Phys. Stat. Solidi (a) 91 (1985) 19-23.
- R. U. Mullai, P. P. Pradeep, G. Chandrasekaran, International Journal of recent trends in Science and technology, 5, (2012) 78-85.

Calibration and testing of low cost optical phase shifter

P.P. Padghan[†] and K.M. Alti^{*}

Department of Physics, Sant Gadge Baba Amravati University, Amravati, Maharashtra, India

^{*}Author for Correspondence E-mail: kamleshalti@sgbau.ac.in

[†]Presenting author E-mail: pppadghan5@gmail.com

Abstract

In this research article, the process for calibration of the optical phase shifter fabricated in the laboratory is discussed on the basis of the intensity profile of phase shifted linear fringe patterns of Michelson's interferometer. A phase shift was introduced in consecutive fringe patterns by varying the voltage supplied to phase shifter. Finally wrapped phase map was obtained from fringe patterns having constant $\pi/2$ phase shift using Hariharan's algorithm.

Keywords: Optical phase shifter, Michelson's interferometer, phase shifting methods

1. Introduction

In recent years large numbers of optical methods based on electronic speckle pattern interferometers (ESPI) were developed to investigate properties of the object under the mechanical, thermal and acoustic loads [1, 2]. In order to measure the quantitative amount of deformations on objects, phase shifting methods[3], Fourier transform methods [4], Image processing algorithms [5], Time sequence phase shifting methods[6] are used. Phase-shifting methods among them are very straightforward and give a precise measurement of deformation. This method is also categorized into two groups: temporal phase shifting method and spatial phase shifting method [7]. In temporal phase shifting methods, phase of one of the interfering beam is shifted by using optical phase shifter and in spatial phase shifting methods phase of shifted light waves analyzed by two or more CMOS cameras. However optical phase shifter is commercially expensive. But we can fabricate optical phase shifter in the laboratory using cost effect piezoelectric disc by attaching mirror on it [8, 9]. Mirror attached to the piezoelectric disc is translated from its mean position with respect to applied voltage due to property of piezoelectric effect. Hence phase of the light wave reflected from translated mirror is shifted with respect to applied voltage. In this research article calibration of the fabricated phase shifter is demonstrated using the intensity profile of linear interference fringe patterns of Michelson's interferometer.

2. Experimental setup

The experimental setup of Michelson's interferometer is shown in the Fig.1, in which light wave of He-Ne laser source is divided into two light beams using beam splitter. One beam is incident on fixed mirror and other is incident on optical phase shifter or PZT mirror. If the voltage is supplied to PZT mirror then the mechanical extension occurs in the piezoelectric disc and the

mirror is translated from its means position. Light reflecting from the PZT is therefore also shifted in its phase due to the translation of mirror. Phase shift in fringe patterns of Michelson's interferometer is observed at different voltages and recorded by using CMOS camera.

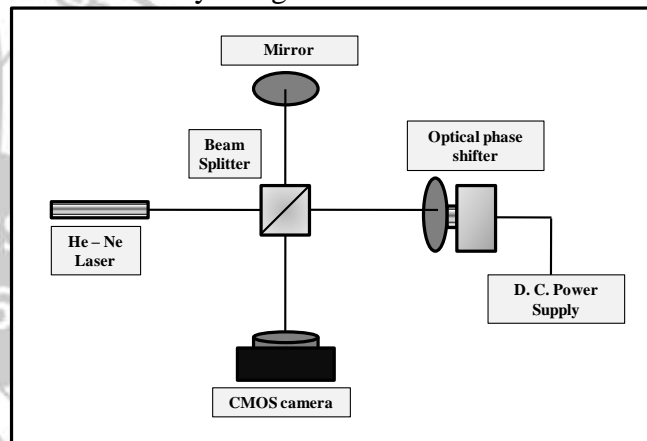


Fig. 1: Experimental setup of phase shifting Michelson's interferometer

3. Result and discussion

Fringe patterns resulting from Michelson interferometer were recorded and stored in the computer. Phase shift in fringe patterns can be analyzed from one-dimensional intensity profile of fringe pattern. Fig.2 shows the one-dimensional intensity profiles of linear fringe patterns which are having a $\pi/2$ phase shift between them at 0 V, 7 V, 18 V, 36 V and 50 V respectively. The Linear fringe pattern at 0 V is considered as a reference fringe pattern. The phase of reference fringe pattern is translated as voltage given to optical phase shifter.

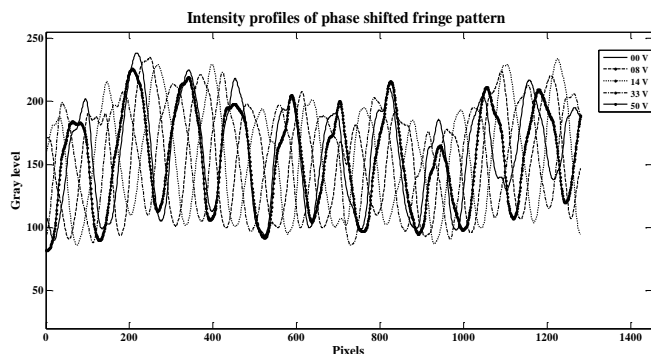


Fig.2: Intensity profiles phase shifted of fringe patterns. The linearity of phase shift with respect to applied voltage is verified from the plot between phase shifts against voltage supplied to the phase shifter. Fig. 3 shows the calibration curve between phase shifts versus voltage supplied to PZT mirror. R-square value for the linear fitting of phase shifted fringes was found that 0.95. This value is nearly closest to 1, which is clearly showing the linearity between phase shift and applied voltage.

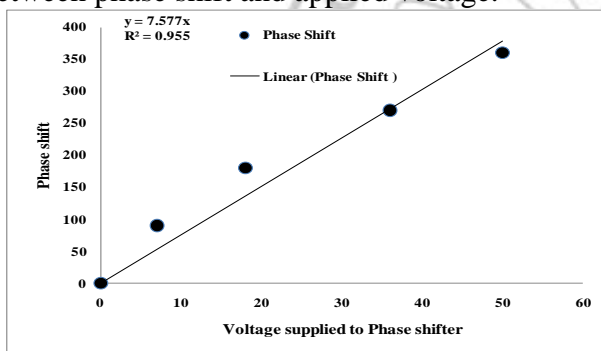


Fig. 3: Calibration curve of phase shifter.

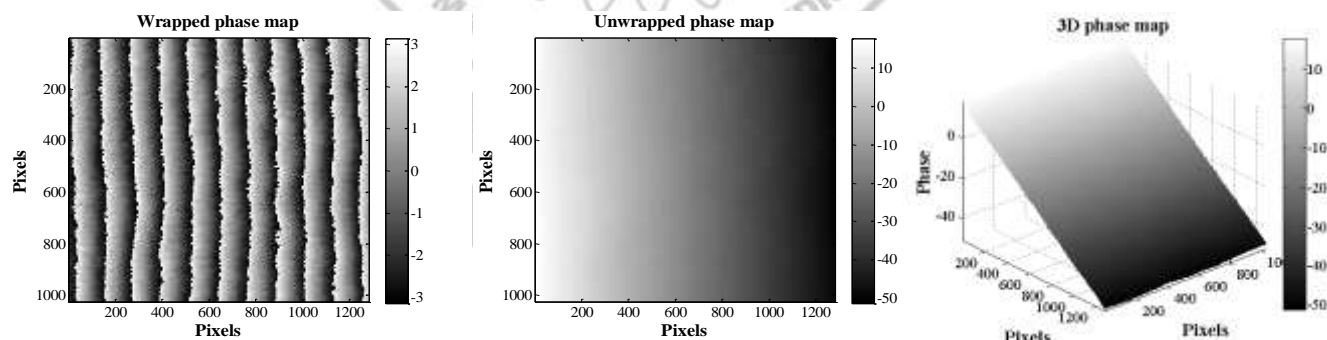


Fig. 4: Wrapped, unwrapped and 3D phase map obtained from Hariharan’s algorithm.

References

1. J.N. Petzing, J.R. Tyrer, The Journal of Strain Analysis for Engineering Design Recent developments and applications in electronic speckle pattern interferometry, (1998).
2. A. Kishen, V.M. Murukeshan, V. Krishnakumar, A. Asundi, Analysis on the nature of thermally induced deformation in human dentine by electronic speckle pattern interferometry (ESPI), J. Dent. 29 (2001) 5.
3. K. Creath, Phase-shifting speckle interferometry, 29th Annu. Tech. Symp. 24 (1985) 337–346.
4. T. Kreis, Digital holographic interference-phase measurement using the Fourier-transform method, J. Opt. Soc. Am. A. 3 (1986) 847. doi:10.1364/JOSAA.3.000847.
5. H.A. Vrooman, A.A. Maas, Image processing algorithms for the analysis of phase-shifted speckle interference patterns., Appl. Opt. 30 (1991) 1636–41.
6. X. Li, G. Tao, Y. Yang, Continual deformation analysis with scanning

Hence this optical phase shifter can be used in phase shifting methods to study various aspects. To examine the performance of optical phase shifter, Hariharan’s five step phase shifted algorithm is used[10],

$$\delta = \tan^{-1} \left[\frac{2 * I_4(x, y) - I_2(x, y)}{I_1(x, y) - 2 * I_3(x, y) + I_5(x, y)} \right] \dots\dots\dots(1)$$

Where $I_1(x, y)$, $I_2(x, y)$, $I_3(x, y)$, $I_4(x, y)$ and $I_5(x, y)$ be the intensities of five interference fringe patterns which has $\pi/2$ phase shift introduce by phase shifter and δ is the phase difference between five phase shifted fringe patterns. This algorithm gives the wrapped phase, which has phase discontinuity from $-\pi$ to and $+\pi$. Hence to remove this discontinuity from wrapped phase map 2D SNRP unwrapping algorithm[11] is used. Fig. 4 shows wrapped phase map, unwrapped phase map and 3D phase map.

4. Conclusion

We have proposed the calibration method for phase shift introduced in the Michelson’s interferometer experiment using cost effective optical phase shifter. The phase shift was introduced in the fringe patterns by supplying voltage to phase shifter. The calibration was tested from the 3D phase map obtained from Hariharan’s algorithm

Acknowledgement

Authors are very much thankful to Head of physics department, Sant Gadge Baba Amravati University, Amravati for providing us necessary facilities.

7. X. Xie, L. Yang, X. Chen, N. Xu, Y. Wang, Review and comparison of temporal- and spatial-phase shift speckle pattern interferometry for 3D deformation measurement, Proc. SPIE - Int. Soc. Opt. Eng. 8916 (2013) 89160D. doi:10.1117/12.2036603.
8. D. Tipton, R. May, R. Claus, Calibration of optical phase shifter using a Michelson interferometer, 2885 (n.d.) 220–227.
9. M. Asmad, G. Baldwin, H. Rabal, R. Arizaga, M. Trivi, Low cost piezoelectrical mirror for DSP!, 4419 (2001) 174–177.
10. P. Hariharan, B.F. Oreb, T. Eiju, Digital phase-shifting interferometry: a simple error-compensating phase calculation algorithm., Appl. Opt. 26 (1987) 2504–2506.
11. M.A. Herráez, D.R. Burton, M.J. Lalor, M. a Gdeisat, Fast two-dimensional phase-unwrapping algorithm based on sorting by reliability following a noncontinuous path., Appl. Opt. 41 (2002) 743.

Low density silica aerogel synthesized in less processing time via mechanical shaker

Sunetra Dhare

Shri. S. H. Kelkar College of Arts, Commerce & Science, Devgad

1. Introduction

Silica aerogels possess extremely low density ($< 0.500 \text{ g/cm}^3$) which can be characterized by low thermal conductivity (0.005 W/mK), high porosity ($\sim 99\%$) and large surface area ($\sim 1000 \text{ m}^2/\text{g}$) [1-4]. These properties lead silica aerogel a wide range of applications of monoliths and granules in variety of fields such as insulator, Cherenkov radiation detection etc. [4-6]. Light weight silica aerogel monoliths are prepared by supercritical drying process which is difficult to follow due to requirements of high temperature ($\sim 240 \text{ }^\circ\text{C}$), high pressure ($\sim 8 \text{ MPa}$), expensive instruments [7]. The ambient pressure drying (APD) or subcritical drying method can be assumed to be easy and inexpensive as compared to supercritical drying. The steps to follow to obtain silica aerogels are homogenization of precursor, hydrolysis and condensation reactions, and drying of wet gel. During drying of wet gel by APD, solvent exchange and silylation processes are carried out which prolong the processing time. In order to shorten the processing time we employed mechanical shaking during solvent exchange and silylation of alcogel thus the processing time was reduced considerably to ~ 27 hours.

2. Experimental

Chemicals used for silica aerogel synthesis were tetraethoxysilane (TEOS) as precursor, methanol (MeOH) as a solvent, oxalic acid, NH_4OH as catalysts, Hexane for solvent exchange and tetramethylchlorosilane (TMCS) as surface modifier. All the chemicals were used as received without further purification. Flow chart (fig. 1) gives the detailed process of silica aerogel synthesis followed in the present work. Here, the shaking time for solvent exchange was optimized by observing the density.

3. Characterizations

The obtained silica granules were characterized for density and contact angle and existence of silica network and effect of surface modification (silylation) was confirmed by Fourier transform infrared (FTIR) spectroscopy.

The time of solvent exchange (exchanging MeOH by low surface tension Hexane) with mechanical shaking employed was varied and the

density of samples was calculated. The bulk density of the aerogel was calculated by considering mass to volume ratio:

$$\rho = \frac{m}{V} \quad (1)$$

where, m = mass (gm) and V = volume occupied (cm^3) of the silica aerogel graduals.

The static contact angle measurement was done using the travelling microscope to measure the base and height of drop and high quality photographs of the water on the powdered silica aerogel spread on glass substrate were taken. Following formula to determine the contact angle (θ) was used:

$$\theta = 2 \tan^{-1} \left(\frac{2h}{b} \right) \quad (2)$$

where, h = height and b = base of the water drop.

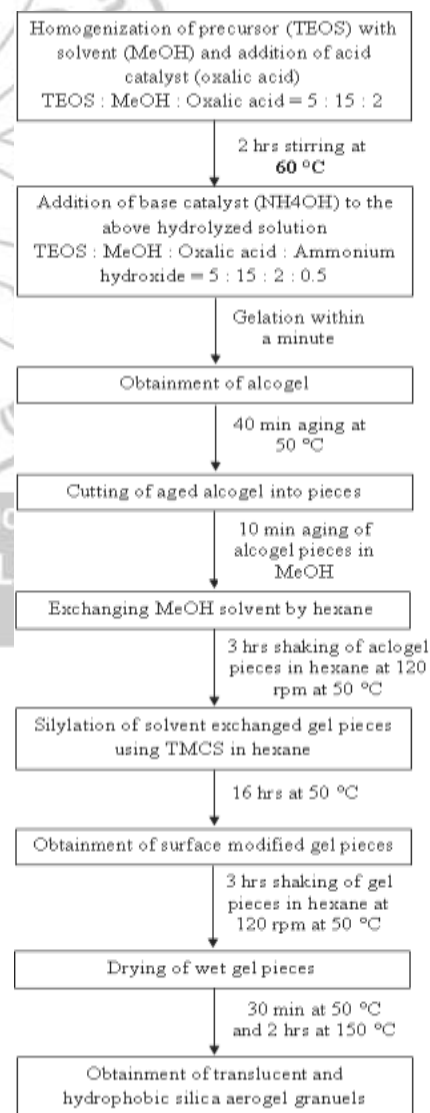


Fig. 1: Flow chart of steps involved in synthesis of silica aerogel

4. Results and discussion

The table 1 shows the variation in the density and contact angle with solvent exchange shaking time. For 3 hours of shaking in hexane for exchanging the solvent MeOH produced minimum density of 0.07 g/cm^3 indicating the large surface area and thus excellent thermal insulation. Based on the available reports and to best of our knowledge, we claim that it is the least preparation time reported for silica aerogel synthesis. The static water contact angle measurement image and Fourier transform infrared (FTIR) spectrum are shown in fig 2. All the samples exhibited appreciably high hydrophobic behavior but the sample III with 3 hours shaking time showed contact angle of 146° proving incorporation of hydrophobic character to a considerable extent. FTIR proves the silica network formation (absorption peak at 1074 cm^{-1}) [8] and the effective surface modification by TMCS (absorption peak at 1460 and 3000 cm^{-1}) [9].

As the density and contact angle for III Sample with 3 hours shaking time has minimum density (0.07 g/cm^3) and contact angle (146°), 3 hours can be considered as the optimum solvent exchange shaking time which results in good quality aerogels.

Table 1: Comparison of density and contact angle of samples with varied time of shaking at solvent exchange

Sample ID	I	II	III	IV	V	VI
Time of shaking at solvent exchange step (t) hr	1	2	3	4	5	6
Density (ρ) gm/cm^3	88.1	88.7	70.0	75.2	77.0	78.1
Contact angle (θ) degree	135	144	146	149	136	137

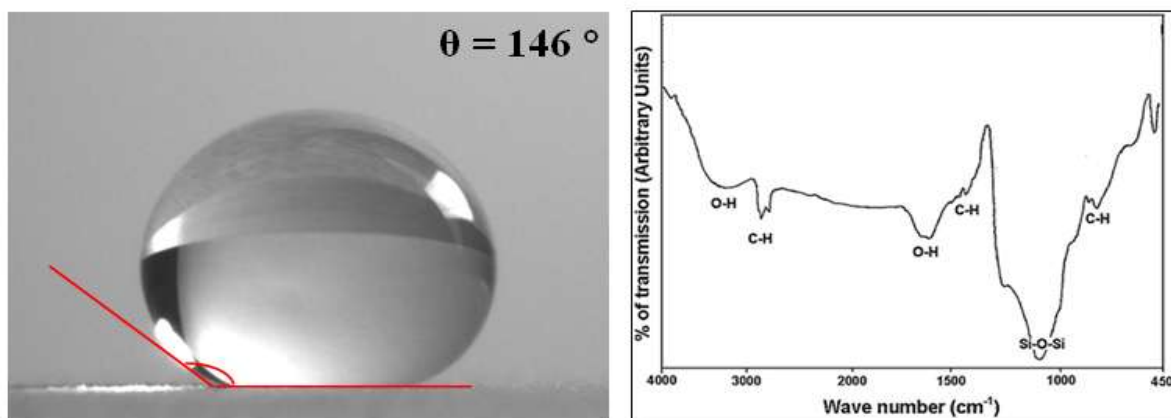


Fig. 2: shape of water drop on the silica aerogel powder and FTIR of the silica aerogel

5. Conclusion

Considering the properties of the TEOS based silica aerogel synthesized at ambient pressure drying employing mechanical shaking during solvent exchange, we conclude that we could obtain the silica aerogel in 27 hours and 10 minute which is the least time reported till date. The properties such as low density (70 mg/cm^3) and high contact angle (146°) have not been hampered due to reducing the processing time by use of mechanical shaker.

Acknowledgement

The author is thankful to the Principal and the Head of Department of Chemistry, S. H. Kelkar college, Devgad for extending the necessary facilities and allowing access to equipments to carry the experiments.

References:

- C. J. Brinker, G.W. Scherer, Sol-Gel Science, 1st edn. (Academic Press Inc., London, 1990), pp. 12-36,
- M. Reim, G. Reichenauer, W. Korner, J. Manara, M. Arduini Schuster, S. Korder, A. Beck, J. Fricke, J. Non Cryst. Solids 350 (2004) 358
- A. Soleimani Dorcheh, M. H. Abbasi, J. Mater. Process. Technol, 199 (1-3) (2008) 10
- R. Baetens, B-P. Jelle, A. Gustavsen, Energy and Buildings 43 (4) (2011) 761
- M. Reim, W. Korner, J. Manara, S. Korder, M. A. Schuster, H. P. Ebert, J. Fricke, Sol. Energy 78 (2005) 131
- J. L. Gurav, A. Venkateswara Rao, J. Sol-Gel Sci. Tech. 50 (2009) 275
- K. Tajiri, K. Igarashi, T. Nishio, J. Non-Cryst. Solids 186 (1995) 83
- J. K. Hong, H. R. Kim, H. H. Park, Thin Solid Films 332 (1998) 449
- N. Hering, K. Schriber, R. Riedel, O. Lichtenberger, J. Woltersdorf, Appl. Organomet. Chem. 15 (2001) 879

Literature Survey on Study of Toxicity of Nanomaterials

M. P. Yadav^a, A. A. Mane^{b,*}

^aRajarambapu Institute of Technology Diploma Wing (Second Shift), Rajaramnagar

^bThin Film Nanomaterials Laboratory, Department of Physics, Shivaji University, Kolhapur 416 004,

* Corresponding author: yadavmpmscphy@rediffmail.com

Abstract

Nanotechnology is emerging and promising field of material study. Due to large surface area and small size, it can be used effectively in different field like medicine, cosmetics, sensor, paints etc. But same property is responsible for toxicity of nonmaterial. Basically it is multidisciplinary field. But there is need of scientific clarification about health of worker and customer. Every study of nanomaterial should include medical aspect to user and worker. This Study include the a) Need of Study; b) Identification of risk; c) selection and implementation of controls; d) establishment of medical system ; and e) rules for production of nanomaterial inview of toxicologic and control research.

Keywords: Nanomaterials; toxicity

1. Introduction

Properties of material changes as its particle size decreases. Nanomaterial (10-100nm) shows extremely different properties than bulk. Much research is needed on generalized issues such as equity, privacy, security, environmental impact and application for human-machine interaction [1-3]. Presently No prper precaution and care has being taken to avoid diverse effect on health. Scientific knowledge of toxicity of nanomaterial is need of hour. No scientific theory can be considered to be wholly objective, but one theory may be more objective than another [4].

Framework for Ethical Assessment

Risk assessments are partly target oriented and partly politicized. Hence all risk projections are value laden. Hazard of each material is different hence no single methodology is applicable to all. Research shows that alternative assessments are needed to overcome obstacles in ethical and political values in policy frame working [5].

Current State of Knowledge about Nanotechnology Hazards and Risks

The present speed of development of nanotechnology is very high as compare to awareness of hazard of nanomaterial on human health and environment. The term "nanotechnology" is misleading, since it is not a single technology but a multidisciplinary grouping of physical, chemical, biological, engineering, and electronic processes, materials, applications, and concepts in which size is the defining haracteristic [6]. We can classify nanomaterial in engineering nanomaterial and Incidental nanomaterial. Engineering nanomaterial has specific sice and properties while Incidental nanoparticles (Natural and anthropogenic) are generated in relatively

uncontrolled manner and physically and chemically heterogeneous compared with engineered nanoparticles [7]. The unifying theme is that nanoparticles are smaller than their bulk counterparts but have a larger surface area and particle number per unit mass; these characteristics generally increase toxic potential as a result of increased potential for reactivity [6].

Knowledge about hazards and risks

Very less information available on hazards and risk of nanomaterial. Chronic decises developed in workers but they are not known real cause of it. The most of human exposure to ultra fine (<100nm) and fine (2500nm) particle. Such particle can easily assessed in epidemiologic air pollution studies and in studies of occupational cohorts exposed to mineral dusts, fibers, welding fumes, combustion products, and poorly soluble, low-toxicity particulates such as titanium dioxide and carbon black [8, 9]. Hazards of engineering nanomaterial also reported in animal study [10, 11]. A strong relationship exists between the surface area, oxidative stress, and proinflammatory effects of nanoparticles in the lung. The greater the oxidative stress, the more likely the risk of inflammation and cytotoxicity [9, 11]. Adverse effects include the development of fibrosis and other pulmonary effects after short term exposure to carbon nanotubes [11]. However, this effect is very low as compare to usefulness of nanomaterial and present scenario is developing of nanotechnology [6]. **Fig. 1** shows the interrelation of criteria for responsible development of nanotechnology

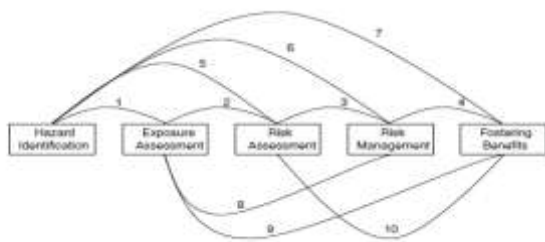


Fig. 1 Interrelation of criteria for responsible development of nanotechnology

HI hazard identification (anticipate, identify and track potentially hazardous nanomaterials in the workplace), EA exposure assessment (assess workers exposures to nanomaterial), RA risk assessment (assess and communicate hazards and risks to workers), RM risk management (manage occupational safety and health risks), FB foster benefits (foster the safe development of

nanotechnology and the realization of societal and commercial benefits).

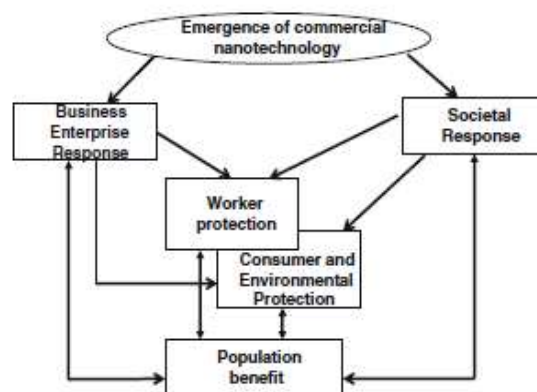


Fig. 2 Pathways for responsible development of nanotechnology

Conclusions

The ethical questions about nanotechnology in the workplace arise from the state of knowledge about the hazards of nanomaterials and the risks they may pose to workers. The lack of clarity on these issues requires an interim assessment of the hazards and risks that might exist in various situations. Workers will be able to exercise their autonomy only if the processes leading to hazard identification and risk assessment are transparent and understandable. Employers will conform to the principles of autonomy, beneficence, nonmaleficence, justice, privacy and respect for persons to the extent that they a) accurately portray hazards and risks, b) are precautionary in their approach to hazards, c) engage in communication and dialogue with workers, and d) take the necessary steps to control risks so that they appear reasonable and acceptable to workers.

Table 1 Relationship between occupational safety and health criteria for responsible development of nanotechnology

Link No. in Figure	Relationship	Implications
1	HI to EA	Provides priorities for exposure assessment
2	EA \$ RA	Component factor in risk assessment provides priorities for exposure assessment
3	RA \$ RM	Informs risk management
4	RM \$ FB	Minimizes worker risks and enhances societal acceptance
5	HI \$ RA	Component factor in risk assessment; provides priorities for toxicology study
6	HI \$ RM	Triggers risk management
7	HI \$ FB	Identifying worker hazards useful for identifying consumer and environmental hazards
8	EA \$ RM	Assessing exposures is critical in controlling them
9	EA \$ FB	Identifying risk of exposures to workers provides information needed for effective risk management
10	RA \$ FB	True depiction of risks and risk management decisions to minimize risk enhances societal acceptance

References

- Mnyusiwalla A, Daar AS, Singer PA. "Mind the Gap": science and ethics in nanotechnology. *Nanotechnology* 2003; 14:R9–R13.
- nanoscale from an ethical point of view. In: Baird D, Nordmann A, Schummer J, editors. *Discovering the Nanoscale*. Amsterdam: IOS Press; 2004. p. 301–310
- Singer P. *Nanotechnology Ethics. Designing Nanostructures - A Tutorial*. New York: New York Academy of Sciences; 2004. [accessed 16 Nov 2006]. Available from: <http://www.nyas.org/ebriefeps/splash.asp?intebriefID=321>
- Schrader-Frechette K. *Ethics of Scientific Research*. Lanham, MD: Ronan and Littlefield; 1994.
- Schrader-Frechette K. *Environmental Justice: Creating Equality, Reclaiming Democracy*. New York: Oxford University Press; 2002.
- Aitken RJ, Creely KS, Tran CL. *Nanoparticles: An Occupational Hygiene Review*. Health Safety Executive, Research Report 274. London: HSE Books; 2004.
- NIOSH. *Approaches to Safe Nanotechnology: An Information Exchange with NIOSH*. Cincinnati, OH: National Institute for Occupational Safety and Health; 2006. [accessed 11 Sept 2006]. Available from: <http://www.cdc.gov/niosh/topics/nanotech/safenano>
- Maynard AD, Kuempel ED. Airborne nanostructured particles and occupational health. *J Nanoparticles Res* 2005; 7:587–614.
- Nel A, Xia T, Mädler L, Li N. Toxic potential of materials at the nanolevel. *Science* 2006; 311:622–627.
- Donaldson K, Stone V, Tran CL, Kreyling W, Borm PJA. Nanotoxicology. *Occup Environ Med* 2004; 61:727–278.
- Oberdörster G, Oberdörster E, Oberdörster J. Nanotoxicology: an emerging discipline evolving from studies of ultrafine particles. *Environ Health Perspect* 2005; 113:823–837.

Optical, Structural and Spectroscopic Study of Metal Chalcogenide Doped Oxide Glasses: A Review

A. L. Patil¹ and U. B. Chanshetti²

¹Research Scholar, Dr. Babasaheb Ambedkar Marathawada University,
Aurangabad, MS, INDIA

²Department of Chemistry, Arts, Science and Commerce, College, Naldurg,
Dist. Osmanabad, MS, INDIA

Corresponding author: amitpatils24@gmail.com

Abstract

In this review photoluminescence (PL) and excitation spectra of Bi melt-doped oxide and chalcogenide glasses are very similar, indicating the same Bi center is present. When implanted with Bi, chalcogenide, phosphate and silica glasses, all display characteristically different PL spectra to when Bi is incorporated by melt-doping. This indicates that ion implantation is able to generate Bi centers which are not present in samples whose dopants are introduced during melting. The CdS quantum dots were grown in a special glass matrix, which involved a sequence of steps. The obtained glass was of uniformly bright yellow in color and the bulk glass was pulverized to a fine powder of micron size particles. The glass powder was characterized structurally and morphologically.

Keywords: Glass, bismuth sulfide, cadmium sulfide, doping, photoluminescence, chalcogenide

1. Introduction:

Bismuth-doped glasses can give rise to photoluminescence (PL) at wavelengths ranging from 400 nm^[1] to 2500 nm^[2], under variation of the pump wavelength and composition of the host glass. A wide variety of traditional glass hosts containing Bi have been investigated to date, mainly silicates^[3-5] and germanates^[6-8], but also phosphates^[9], borates^[10], chalcogenides^[11, 12] and chlorides^[2]. The origin of the infrared emission from Bi-doped glasses remains controversial, with convincing arguments being made for a variety of different emission centers, including Bi₊^[10], Bi₅₊^[13, 14], Bi metal clusters^[8], point defects^[15] and negatively charged Bi₂ dimers^[16, 17]. Pb doping has also been shown to have very similar absorption and PL behavior to that of Bi in glasses^[15]. Broadband Bi-doped fiber lasers operating at wavelengths between 1150 and 1550 nm^[18], with powers up to 20 W^[19] and slope efficiencies of up to 30%^[20], have been reported. A mode-locked Bi-doped fiber laser with 900 fs pulses has also been demonstrated^[21]. Consequently, linear and non-linear optical (NLO) properties arise in QDs, which give rise to their technological applications in telecommunications and optical switching devices^[22]. QDs of CdS in glass^[23] and SnO₂ in SiO₂^[22] have been studied for their optical properties in relation to their NLO characteristics.

2. Experimental

2.1 Synthesis

In this review a glass composition of 60 SiO₂, 6 Na₂O, 15 K₂O, 8 ZnO, 3 B₂O₃, 2 TiO₂, 6 BaO, (wt%) found optimal in a study of compositional

variation was adopted in the preparation of glass. In a typical procedure, the respective raw materials weighed as per this composition were ground in a pestle and mortar to obtain a homogeneous mixture. Cadmium sulfide powder (0.5 wt%) was added to this mixture and it was again ground well until homogeneity was realized. For simplicity the flow chart is given below (figure 1).

The entire mixture was then ball milled for 6 h for better homogeneity. It was melted in a recrystallized alumina crucible using an electrically heated muffle furnace (Thermolyne-U3200) at 1500–1600°C. The glass melt was homogenized at the same temperature for three hours. After refining, the glass melt was quenched in air on a hot brass plate and processed immediately for annealing. In the annealing process, the glass samples were heat-treated from 500 to 600°C, that covered its transition temperature (T_g = 570–580°C), for 72 h in several programmed heating cycles so as to ensure uniform nanocrystal growth of CdS throughout the glass matrix and were cooled down to room temperature to remove the stresses. Bright yellow colored bulk glass containing CdS quantum dots was thus obtained. It was then pulverized to a fine powder of 2–5 mm size particles (Q-CdS– glass powder). The glass powder was subjected to various physico-chemical characterizations and studied for its photocatalytic decomposition of hydrogen sulfide and production of H₂ under visible light.

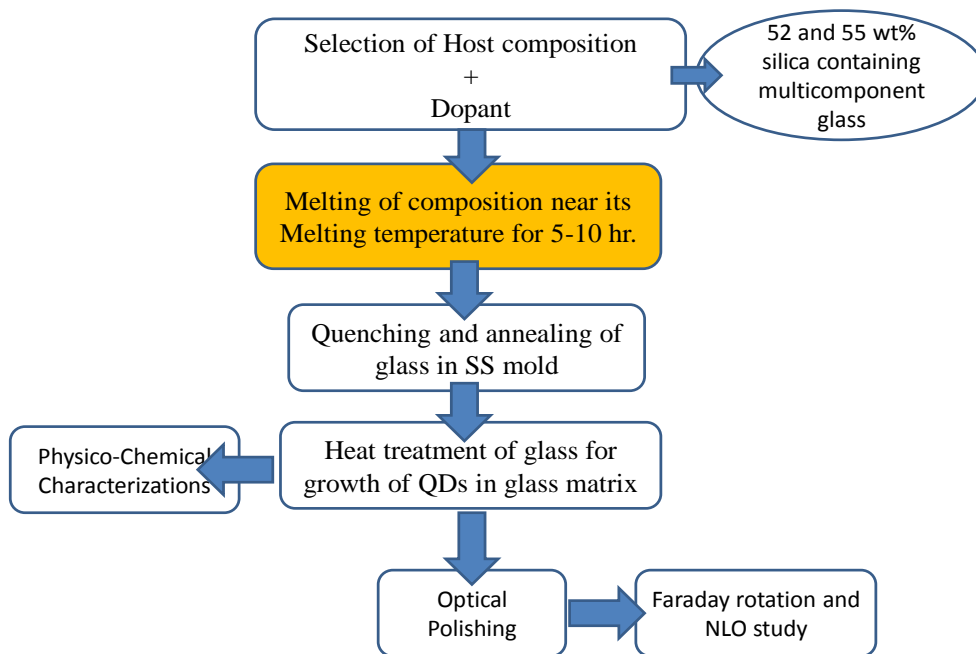


Fig.1 Flow chart of methodology of glass fabrication



Fig. 2. Muffle Furnace Set Up for Glass Preparation

2.2 Characterization

Powder X-ray diffraction (XRD) patterns were recorded with a Rigaku-D/MaX-2200 V Model X-ray Diffractometer with Cu K α radiation using a Ni filter. The surface morphology and particle size were determined using a Field Emission Scanning Electron Microscope (FESEM; JEOL-JSM Model 6700F) and Transmission Electron Microscope [TEM; Model 912 Omega, Carl Zeiss (LeO)]. Electron Diffraction (ED) for structural elucidation was performed with the TEM instrument. The spectroscopic study of the catalyst was carried out using a UV VIS (SHIMADZU

Model UV-2450 diffuse reflectance mode) spectrophotometer (UV VIS DRS).

3. Results and Discussion:

In the preparation of glass with CdS QDs *B. B. Kale et. al.*,^[24] studied different compositions comprising (1) variation in wt% of the main ingredients (given below), (2) addition/removal of the minor ingredients such as TiO₂, BaO and Li₂O and (3) variation in wt% of the guest material CdS (0.1–10.0), were tried and all the glass compositions were tested for their CdS up-taking ability within the matrix during the melting process, which is the key step in fabricating Q-CdS-glass entities. The optimum glass composition of 60 SiO₂, 6 Na₂O, 15 K₂O, 8 ZnO, 3 B₂O₃, 2 TiO₂, 6 BaO and 0.5 CdS (wt%) was arrived at only after intense research, where a uniform transparent yellow glass due to the homogeneous incorporation of CdS quantum dots (CdS nanocrystals of 2.5 nm size) was obtained. The PL spectra *M. A. Hughes et. al.*,^[25] of Bi-implanted GLSO films along with bulk phosphate and silica glass, and crystalline CaF₂ and BaF₂, excited at 782 nm. Damage-related optical centers are known to produce PL; however, when implanted with other species such as Ag and V, no PL was observed. This indicates that the observed PL is related to a Bi center, rather than damage caused by the implantation.

3.1 Spectroscopic study

The UV VIS diffuse absorption spectra of the host glass and the Q-CdS–glass powder, respectively, are done. They have absorption edges at 340 and 500 nm respectively that correspond to band gaps of 3.65 eV for the host glass and 2.48 eV for the Q-CdS–glass powder. The original UV absorption of the host glass shifts to the visible region due to the formation of CdS quantum dots throughout the glass matrix. The band gap obtained for Q-CdS–

glass (2.48 eV) is higher than that of bulk CdS (2.4 eV), which is attributable to the CdS QD particle formation. The steep, smooth and broad absorption of Q-CdS–glass reveals a uniform distribution of CdS QDs particles; also the absorption of CdS quantum dots (in glass powder) involves certainly a transition between the valence band and conduction band but not the transition of any impurity levels.

4. Conclusions

In this review a highly crystalline, homogeneous and monodispersed hexagonal CdS quantum dots (2.5 nm) were grown in a special glass matrix. Thus the present work has established a novel approach in augmentation of photostability of otherwise corrosive CdS QDs and for the first time employment of CdS QDs in photodecomposition of H₂S and solar H₂ production under visible light. The features of CdS QDs, i.e., the easy handling, stability and impressive catalytic function are industrially preferable from an economic point of view. Comparing contour plots of PL spectra at various excitation wavelengths of Bi-doped chalcogenide, Bi-doped germanate and Pb-doped germanate glasses, indicates that five absorption/PL bands are in approximately the same position. This suggests that very similar active centers are present in Bi- and Pb-doped oxide and chalcogenide glasses. NIR PL bands in Ge₂₃Ga₁₂S₆₄Bi₁ glass, which has a very similar composition to those in which carrier-type reversal has been observed. This suggests that very similar active centers are present in Bi- and Pb-doped oxide and chalcogenide glasses.

References:

- G. W. Chi, D. C. Zhou, Z. G. Song, and J. B. Qiu, *Opt. Mater.*, 31, 945-948 (2009).
- N. Romanov, Z. T. Fattakhova, A. A. Veber, O. V. Usovich, E. V. Haula, V. N. Korchak, V. B. Tsvetkov, L. A. Trusov, P. E. Kazin, and V. B. Sulimov, *Opt. Express*, 20, 7212-7220 (2012).
- M. Peng, D. Chen, J. Qiu, X. Jiang, and C. Zhu, *Opt. Mater.*, 29, 556-561 (2007).
- Y. Arai, T. Suzuki, Y. Ohishi, S. Morimoto, and S. Khonthon, *Appl. Phys. Lett.* 90, 261110.(2007).
- M. Peng, B. Wu, N. Da, C. Wang, D. Chen, C. Zhu, and J. Qiu, *J. Non-Cryst. Solids*, 354, 1221-1225 (2008).
- J. Ren, J. Qiu, B. Wu, and D. Chen, *J. Mater. Res.* 22, 1574-1577 (2007).
- M. Peng, J. Qiu, D. Chen, X. Meng, I. Yang, X. Jiang, and C. Zhu, *Opt. Lett.* 29, 1998-2000 (2004).
- M. Peng, J. Qiu, D. Chen, X. Meng, and C. Zhu, *Opt. Lett.* 30, 2433-2435 (2005).
- X. G. Meng, J. R. Qiu, M. Y. Peng, D. P. Chen, Q. Z. Zhao, X. W. Jiang, and C. S. Zhu, *Opt. Express*, 13, 1628-1634 (2005).
- X. G. Meng, J. R. Qiu, M. Y. Peng, D. P. Chen, Q. Z. Zhao, X. W. Jiang, and C. S. Zhu, *Opt. Express*, 13, 1635-1642 (2005).
- G. P. Dong, X. D. Xiao, J. J. Ren, J. Ruan, X. F. Liu, J. R. Qiu, C. G. Lin, H. Z. Tao, and X. J. Zhao, *Chin. Phys. Lett.* 25, 1891-1894 (2008).
- M. A. Hughes, T. Akada, T. Suzuki, Y. Ohishi, and D. W. Hewak, *Opt. Express*, 17, 19345-19355 (2009).
- Y. Fujimoto and M. Nakatsuka, *J. Appl. Phys. Part 2 Lett.* 40, L279-L281 (2001).
- X. Wang and H. Xia, *Opt. Commun.* 268, 75-78 (2006).
- M. Y. Sharonov, A. B. Bykov, V. Petricevic, and R. R. Alfano, *Opt. Lett.* 33, 2131-2133 (2008).
- S. Khonthon, S. Morimoto, Y. Arai, and Y. Ohishi, *J. Ceram. Soc. Jpn.* 115, 259-263 (2007).
- V. O. Sokolov, V. G. Plotnichenko, and E. M. Dianov, *Opt. Lett.* 33, 1488-1490 (2008).
- A. Bufetov and E. M. Dianov, *Laser Phys. Lett.* 6, 487-504 (2009).
- S. V. Firstov, A. V. Shubin, V. F. Khopin, M. A. Mel'kumov, I. A. Bufetov, O. I. Medvedkov, A. N. Guryanov, and E. M. Dianov, *Quantum Electron.* 41, 581 (2011).
- V. V. Dvoyrin, V. M. Mashinsky, and E. M. Dianov, *IEEE J. Quantum Elect.* 44, 834-840 (2008).
- S. Kivisto, J. Puustinen, M. Guina, O. G. Okhotnikov, and E. M. Dianov, *Electron. Lett.* 44, 1456-1458 (2008).
- N. Chiodini, A. Paleari, D. DiMartino and G. Spinolo, *Appl. Phys. Lett.*, 81, 1702, (2002).
- J. Allegre, G. Arnaud, H. Mathieu, P. Lefebvre, W. Granier and L. Boudes, *J. Cryst. Growth*, 138, 998, (1994).
- B. Kale, J. O. Baeg, S. K. Apte, R. S. Sonawane, S. D. Naik and K. R. Patil, *J. Mater. Chem.*, 17, 4297-4303, (2007).
- M. A. Hughes, Y. Federenko, T. H. Lee, J. Yao, B. Gholipour, R. M. Gwilliam, K. P. Homewood, D. W. Hewak, S. R. Elliott, and R. J. Curry, *Optical Components and Materials XI, Proc. of SPIE*, Vol. 8982, 898216, (2014).

An Eco-friendly Green Route for Synthesis of Magnetite Nanoparticles using *Bryophyllum pinnatum* Aqueous Leaf Extract

Pallavi Pawar^a, Swati Pawar^a, Shubhada More^a, Shubhangi Davale^a, Madhuri Varade^a, Prakash Patil^b, Raghunath Shinde^b, Bharat Pawar^b, Renukacharya Khanapure^b, Prakash Bansode^{b*}

^aUndergraduate students, Department of Chemistry, Sangola College Sangola, Dist.-Solapur-413307 (M.S.) India

^bAssistant Professor, Department of Chemistry, Sangola College Sangola, Dist.-Solapur-413307 (M.S.) India, Email: bansode.prakash4@gmail.com

Abstract

In the present investigation, a simple, rapid, and eco-friendly green method was successfully introduced to synthesize magnetite nanoparticles (Fe_3O_4 NPs). *Bryophyllum pinnatum* was employed as a green solvent, reducing and capping agents. The synthesized Fe_3O_4 NPs were characterized with Ultraviolet-Visible spectroscopy (UV-VIS), X-ray diffraction (XRD), Fourier Transform Infrared (FT-IR), Scanning Electron Microscopy (SEM) and Transmission Electron Microscopy (TEM) techniques. The X-ray diffraction planes at (220), (311), (400), (422), (511), (440), and (533) were corresponding to the standard Fe_3O_4 patterns, which showed the high purity and crystallinity of Fe_3O_4 NPs had been synthesized. Based on FT-IR analysis, two characteristic absorption peaks were observed at 556 and 423 cm^{-1} , which proved the existence of Fe_3O_4 in the prepared nanoparticles. TEM image displayed the synthesized Fe_3O_4 NPs were mostly in spherical shape with an average size of 14.5 nm.

Keywords: Green synthesis, Fe_3O_4 nanoparticles, *Bryophyllum pinnatum*, Transmission electron microscopy

1. Introduction

Nanoscience is an upcoming area of research interest in the field of materials chemistry. Optimization of the synthetic parameters to design nanomaterials in the size range of 1-100 nm and the investigation of different properties is the area covered under nanoscience. Nanoscale materials exhibit size dependent properties varying from the corresponding bulk materials. Recent research activities have been focused towards the synthesis of the nanoparticles by environmentally benign conditions. Nanocrystalline iron oxide particles have shown promising applications in diverse research areas such as biomedicine [1], catalyst [2], bimolecular detection [3], sensor [4], batteries [5] etc. In the last few years, various synthesis techniques have been developed to produce iron nanoparticles such as chemical reduction [6], laser pyrolysis technique [7], electrochemical synthesis [8] etc. Nowadays the main focus is to develop economical and environmentally clean synthesis methods to synthesize iron nanoparticles. Numerous eco-friendly materials have been used for synthesis of iron nanoparticles like plant extracts [9] etc. for the same. These eco-friendly techniques do not require high temperature, pressure or the use of corrosive chemical reagents and toxic solvents.

Bryophyllum pinnatum (Family-Crassulaceae) is a plant commonly found in India and China. It has been reported to be a rich source of bioactive chemicals like Saponins, flavonoids, terpenoids, alkaloids and phenols in our

earlier studies on the basis of detailed phyto-chemical analysis.[10] In the present study, an eco-friendly novel route for the synthesis of iron nanoparticles has been reported using the solutions of FeCl_3 and FeCl_2 by the aqueous extract of leaves of *Bryophyllum pinnatum*.



Fig. 1. *Bryophyllum pinnatum* plant

2. Materials And Methods

2.1 Collection of Plant material and preparation of extract

The leaves of *B.pinnatum* were collected from the local area of place Sangola (District Solapur) of Maharashtra state in the month of September 2016. The plant was authenticated by botanists. The 20 g. of fresh leaves were boiled with 100 ml of deionized water in Erlenmeyer's flask. The crude extract was thus obtained.

2.2 Chemicals

Ferric chloride hexahydrate ($\text{FeCl}_3 \cdot 6\text{H}_2\text{O}$) and Ferric chloride (FeCl_2) used for the synthesis were analytical grade (Merck). All the aqueous solutions were prepared with deionized water.

2.3 Synthesis of Iron oxide nanoparticles

Solution of 0.05 M FeCl_3 and 0.025 M FeCl_2 solution were prepared in deionized water. 5 ml of aqueous leaf extract of *Bryophyllum pinnatum* was mixed with 10 mL of 0.05 M FeCl_3 and 0.025 M FeCl_2 solution under the ultrasonication at a room temperature. The formation of yellow to dark green colour was observed indicating the formation of nanoparticles.



Fig.2. Synthesis of Iron oxide nanoparticles

T. T. A] 0.05 M FeCl_3 solution B] 0.025 M FeCl_2 solution C] B. pinnatum aq. Leaf extract D] Fe_3O_4 nanoparticles

3. Results and Discussions

a. UV-visible spectra

The UV-vis spectra of iron nanoparticles synthesized by using *Bryophyllum pinnatum* aqueous extract is shown in figure 3. An absorption peak observed at 415 nm [10]-[11]. After the addition of Ferric chloride (FeCl_3) and Ferrous chloride (FeCl_2) solution, the colour of the solution changes from faint yellow to green indicating the synthesis of iron oxide nanoparticles in the aqueous medium [12].

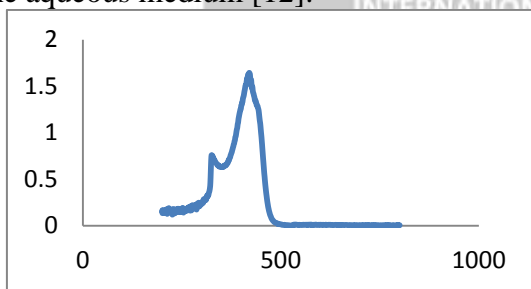


Fig. 3. UV-visible spectra of oxide nanoparticles

b. Fourier transform infrared spectroscopy (FTIR)

FTIR spectrum of Iron oxide nanoparticles with *Bryophyllum pinnatum* aqueous leaf extract showed the presence of bands at 468, 669, 803, 959, 1023, 1154, 1282, 1426, 1510, 1600, 1630, 2918 and 3402 cm^{-1} (figure 4). The bands at 1510 and 1282 cm^{-1} corresponded to C-C and C-N stretching respectively indicating the presence of ligands

similar to those found in biopolymers (proteins, carbohydrates) [13]. The region of $3600\text{-}3100\text{ cm}^{-1}$ showed a broad band is corresponding to $-\text{OH}$ stretching vibration due to phenolic compounds. C-H stretching vibration due to the presence of CH and CH_2 was observed at 2918 cm^{-1} . Anti-symmetrical deformation of C-O-C resulted in a peak at 1154 cm^{-1} [14]. Fe-O bond observed at 468 cm^{-1} [15].

c. X-ray diffraction

The formation of iron oxide nanoparticles using *Bryophyllum pinnatum* aqueous extract was further confirmed by X-ray diffraction (XRD) analysis. The observed peak at $(2\theta) 41.23^\circ$ was attributed to the 113 plane, which exhibited good crystallinity. A broad peak indicated the size in nano scale, which matches with standard (JCPDS number 87-1164) [16]-[17]. The particles size was determined using Scherrer's formula, $D = 0.9\lambda/\beta\cos\theta$ was estimated at 24nm. (figure 5)

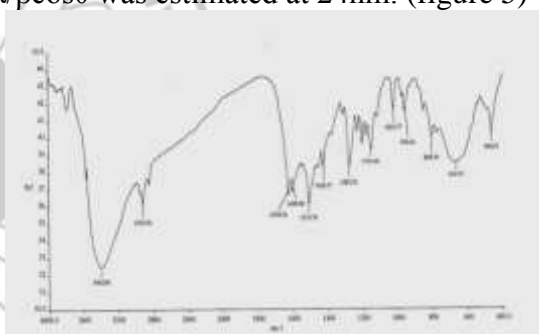


Fig. 4. FT-IR spectra of Iron oxide nanoparticles

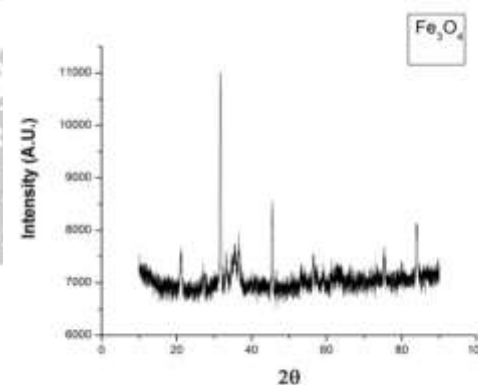


Fig. 5. XRD of Iron oxide nanoparticles

d. Field emission scanning electron microscopy (FE-SEM)

FE-SEM analysis results of iron nanoparticles were clearly distinguishable at different enlargements. Iron oxide nanoparticles in the *Bryophyllum pinnatum* aqueous extract (natural material) were found to be polydispersed (figure 6) and measured in size from 24 to 34 nm.



Fig. 6. FE-SEM of Iron oxide nanoparticles

3.5 Transmission electron microscopy (TEM)

Iron oxide nanoparticle size was found between 20 to 34 nm, which nearly matched with the TEM (figure 7) as well as XRD results. The selected area electron diffraction pattern (SAED) studies showed the nanocrystalline nature and

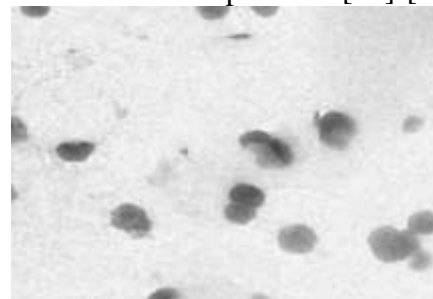


Fig. 7 TEM of Iron oxide nanoparticles

5. Conclusions

Iron oxide nanoparticles were synthesized successfully by using the *Bryophyllum pinnatum* aqueous extract. The Iron oxide nanoparticles were spherical as confirmed by TEM technique. The size of iron nanoparticles ranged from 24 to 34 nm. The method provides simple, rapid and environmentally safe protocol to synthesize iron oxide magnetic nanoparticles.

Acknowledgement

One of the authors (PAB) is thankful to IIT, Bombay for providing instrumentation for characterization of FE-SEM and TEM micrographs. The help provided by CFC Solapur University is also greatly acknowledged for the support in recording XRD, FTIR, UV-Visible spectra of the prepared sample.

References

1. C.C. Berry, A. S. Curtis, "Functionalisation of magnetic nanoparticles for applications in biomedicine," *Journal of physics D: Applied physics*, vol. 36, no.13, pp. 198-200, June 2003.
2. J.M. Yan, X.B. Zhang, S. Han, H. Shioyama, Q. Xu, "Iron-Nanoparticle-Catalyzed Hydrolytic Dehydrogenation of Ammonia Borane for Chemical Hydrogen Storage," *Angewandte Chemie International Edition*, vol.47, no.12, pp. 2287-2289, Feb. 2008.
3. D. J. Maxwell, J. R. Taylor, S. Nie, "Self-assembled nanoparticle probes for recognition and detection of biomolecules," *Journal of the American Chemical Society*, vol.124, no.32, pp. 9606-9612, July 2002.
4. B. Fang, G. Wang, W. Zhang, M. Li, X. Kan, "Fabrication of Fe₃O₄ nanoparticles modified electrode and its application for voltammetric sensing of dopamine," *Electroanalysis*, vol.17, no.9, pp. 744-748, April 2005.
5. B.Koo, H. Bonil, Koo, B., H. Xiong, M. D. Slater, V. B. Prakapenka, M. Balasubramanian, P. Podsiadlo, E. V. Shevchenko, "Hollow iron oxide nanoparticles for application in lithium ion batteries," *Nano letters*, vol. 12, no.5, pp. 2429-2435, April 2012.
6. K. C. Huang, S. H. Ehrman, "Synthesis of iron nanoparticles via chemical reduction with palladium ion seeds," *Langmuir*, vol.23, no.3, pp. 1419-1426, Dec. 2007.
7. O. Bomati-Miguel, L. Mazeina, A. Navrotsky, S. Veintemillas-Verdaguer, "Calorimetric study of maghemite nanoparticles synthesized by laser-induced pyrolysis," *Chemistry of Materials*, vol. 20, no.2, pp. 591-598, Jan. 2008.
8. C. Pascal, J. L. Pascal, F. Favier, M. L. Elidrissi Moubtassim, C. Payen, "Electrochemical synthesis for the control of γ -Fe₂O₃ nanoparticle size. Morphology, microstructure, and magnetic behavior," *Chemistry of materials*, vol.11, no.1, pp.141-147, Dec. 1999.
9. M. Pattanayak, P. L. Nayak, "Ecofriendly Green Synthesis of Iron Nanoparticles From Various Plants And Spices Extract," *International Journal of Plant, Animal and Environmental Sciences*, vol. 3, no.1, pp. 68-78, Dec. 2013.
10. (a) P. Bansode, P. Pawar, M. Babar, "British Journal of Pharmaceutical and Medical Research" Vol.01, Issue, 01, Pg.34-40, July-August 2016
(b) M. Mazur, A. Barras, V. Kuncser, A. Galatanu, V. Zaitzev, K. V. Turcheniuk, S. Szunerits, "Iron oxide magnetic nanoparticles with versatile surface functions based on dopamine anchors," *Nanoscale*, vol.5, no.7, pp. 2692-2702, Jan. 2013.
11. M. Mahdavi, F. Namvar, M. B. Ahmad, R. Mohamad, "Green biosynthesis and characterization of magnetic iron oxide (Fe₃O₄) nanoparticles using seaweed (*Sargassum muticum*) aqueous extract," *Molecules*, vol.18, no.5, pp.5954-5964, May 2013.
12. S. K. Kulkarni, *Nanotechnology: Principles and Practices*, Capital Publishing Company, ISBN-81-85589-29-1, pp. 264-265, 2009.
13. J. Cookson, "The preparation of palladium nanoparticles," *Platinum Metals Review*, vol.56, no.2, pp. 83-98, April 2012.
14. I. M. De Rosa, J. M. Kenny, D. Puglia, C. Santulli, F. Sarasini, "Morphological, thermal and mechanical characterization of okra (*Abelmoschus esculentus*) fibres as potential reinforcement in polymer composites," *Composites Science and Technology*, vol.70, no.1, pp. 116-122, Sept. 2010.
15. R. Palanivel, G. Velraj, "FTIR and FT-Raman spectroscopic studies of fired clay artifacts recently excavated in Tamilnadu, India," *Indian journal of pure and applied physics*, vol. 45, no.6, pp. 501-508, Jun. 2007.
16. S. Laurent, D. Forge, M. Port, A. Roch, C. Robic, L. Elst Vander, R. N. Muller, "Magnetic Iron oxide nanoparticles: synthesis, stabilization, vectorization, physicochemical characterization and biological application," *Chemical reviews*, vol. 108, no.6, pp. 2064-2110, April 2008.
17. M. Mikhaylova, D. K. Kim, C. C. Berry, A. Zagorodni, M. Toprak, A. S. Curtis, M. Muhammed, "BSA immobilization on amine-functionalized superparamagnetic iron oxide nanoparticles," *Chemical of materials*, vol.16, no.12, pp. 2344-2354, May 2004.
18. S. J. Park, S. Kim, S. Lee, Z. G. Khim, K. Char, T. Hyeon, "Synthesis and magnetic studies of uniform iron nanorods and nanospheres," *Journal of the American Chemical Society*, Vol.122, no.35, pp. 8581-8582, May 2000.
19. N. Aguiló-Aguayo, M. J. Inestrosa-Izuieta, J. Garcia-Cespedes, E. Bertran, "Morphological and magnetic properties of superparamagnetic carbon-coated Fe nanoparticles produced by arc discharge," *Journal of nanoscience and nanotechnology*, vol. 10, no.4, pp. 2646-2649, April 2010.
20. B. Kumar, K. Smita, L. Cumbal, A. Debut, "Biogenic synthesis of iron oxide nanoparticles for 2-arylbenzimidazole fabrication," *Journal of Saudi Chemical Society*, vol.18, no.4, pp. 364-369, Sept. 2014.
21. S. Bagheri, K. G. Chandrappa, S. B. A. Hamid, "Generation of Hematite Nanoparticles via Sol-Gel Method," *Research Journal of Chemical Sciences*, vol.3, no. 7, pp.62-68, July 2013.

Chemical Synthesis and Characterization of Nano-Sized $\text{Ni}_{0.75}\text{Co}_{0.25}\text{Al}_2\text{O}_4$

Prakash Patil^{a,b}, Bharat Pawar^c and Sunil Mirgane^{b,*}

^aDepartment of Chemistry, Sangola College Sangola, Kadlas Road Sangola, MS, India - 413307

^bDepartment of Chemistry, J E S College Jalana, MS, India- 416004

*Corresponding author, E-mail:mrprakashpatil1979@gmail.com Mobile- +91-9421717790

Abstract

Chemical synthesis of nano-sized $\text{Ni}_{0.75}\text{Co}_{0.25}\text{Al}_2\text{O}_4$ crystals has been successfully developed. The procedure involves wet chemical mixing of nickel nitrate, cobalt nitrate and aluminum nitrate and adding glycene with constant stirring where gel is formed. Resulting gel is heated on hot plate so that the combustion of gel takes place, which is heated in muffle furnace at 900 °C for 2 h. Thermal gravimetric analysis (TGA), is a method of thermal analysis in which changes in physical and chemical properties of materials are measured as a function of increasing temperature. The morphological, structural properties have been investigated using X-ray diffraction (XRD), scanning electron microscopy. The XRD study revealed the formation of crystalline porous $\text{Ni}_{0.75}\text{Co}_{0.25}\text{Al}_2\text{O}_4$ particles. These particles have possible applications in the field of nanotechnology.

Keywords: Gel-combustion, Wet Chemical, XRD, SEM

1. Introduction

Chemistry plays a major part in the science of nanomaterials. The three important classes of nanomaterials are zero-dimensional nanocrystals, one-dimensional nanotubes and nanowires. In addition, there are two-dimensional nanowalls and nanofilms. A variety of chemical methods have been employed for the synthesis of inorganic nanoparticles, nanotubes and nanowires. [1] Magnetic spinel ferrite nanoparticles are of interest in examining the relationships between magnetic properties and crystal chemistry and structure. Spinel ferrites have been investigated in recent years for their useful electrical and magnetic properties and applications in information storage systems, magnetic cores, magnetic fluids, microwave absorbers, and medical diagnostics. [2]. A variety of wet chemical methods (solgel, co-precipitation, hydrothermal, aerosol *etc.*) have been reported to generate nano-sized materials [3-6]. However, complex processes, expensive precursors, and low production rates are common problems [7]. In the past decade, a solution combustion method has been utilized to synthesize simple and mixed –metal oxides [8-13]. Organic compounds (*e.g.* glycine, urea, citric acid, alanine and carbohydrazide) have been mixed directly with metal nitrates to enhance the efficiency of combustion synthesis. The metal nitrates act as oxidants as well as as cation sources, and the organic compound is the fuel [14,15].

2. Experimental

The procedure involves wet chemical mixing of 3.425 g nickel nitrate, 1.818 g cobalt nitrate and 18.75 g aluminum nitrate by adding glycene with constant stirring where gel is formed. The resulting gel is heated on hot plate so that combustion of gel

takes place and char is formed which is heated in muffle furnace at 900 °C for 2 hr. Thermal gravimetric analysis (TGA) is a method of thermal analysis in which changes in physical and chemical properties of materials are measured as a function of increasing temperature. The structural, morphological properties have been investigated using X-ray diffraction (XRD), Scanning electron microscopy.

3. Result and discussion

Formation of spinel $\text{Ni}_{0.75}\text{Co}_{0.25}\text{Al}_2\text{O}_4$ compound, is same as reported in earlier work [16] XRD studies shows that formation of nanosized $\text{Ni}_{0.75}\text{Co}_{0.25}\text{Al}_2\text{O}_4$. In XRD studies small peak for Co appears due to less percentages of cobalt. Thermo gravimetric analysis (TGA) was used to measure the oxygen carrier's oxygen uptake and release and reaction rates during oxidation and reduction. The TGA continuously measures the weight of a sample during heating and while reacting with a gas stream. TGA studies shows that total 61 % weight loss in the whole process. As shown in(fig. 1) At temperature above 800 °C complete removal impurities takes place. In fig 2. Shows porous morphology of nanomaterial. At different magnifications.

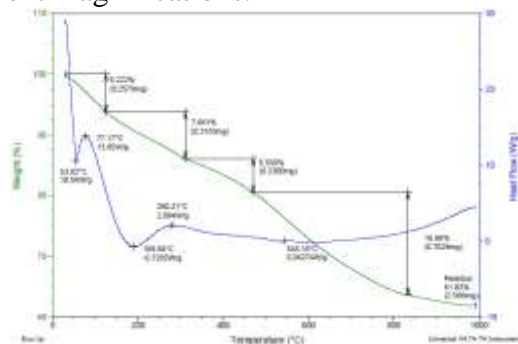


Fig.1. TGA study of $\text{Ni}_{0.75}\text{Co}_{0.25}\text{Al}_2\text{O}_4$

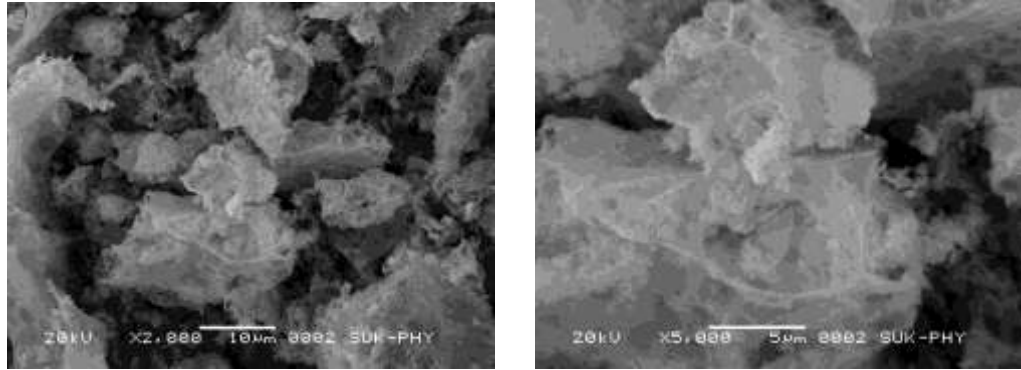


Fig.2.SEM study of $\text{Ni}_{0.75}\text{Co}_{0.25}\text{Al}_2\text{O}_4$

4. Conclusion

Glycine-assisted combustion route resulted in formation of $\text{Ni}_{0.75}\text{Co}_{0.25}\text{Al}_2\text{O}_4$ nano- particles. The powder XRD data obtained on $\text{Ni}_{0.75}\text{Co}_{0.25}\text{Al}_2\text{O}_4$ powder are in good agreement with the standard reported data. The SEM pictures show the presence of porous morphology found in the powder. The obtained samples have a homogenously distributed species in the whole mass prepared. This particle has possible application in the field of nanotechnology.

References

1. C. N. R. Rao, A. Govindaraj and S. R. C. Vivekchand, Annu. Rep. Prog. Chem., Sect. A, 2006, 102, 20–45.
2. Abdülhadi Baykal, Nermin Kasapoğlu, Yüksel Köseoğlu, Ali Cemil Başaran, Hüseyin Kavas, Muhammet S. Toprak, Cent. Eur. J. Chem. 6(1) 2008, 125-130.
3. T.A.S. Ferreira, J.C. Waerenborgh, M.H.R.M. Mendonça, M.R. Nunes and F.M. Costa; Sol. Stat. Sci.,15, 383 (2003)
4. X. He, G. Song and J. Zhu; Mater. Lett., 59, 1941 (2005)
5. P.S.A. Kumar, J.J. Shrotri and C.E.Deshpande; J. Appl. Phys., 81 (8), 4788 (1997)
6. S. Singhal, J. Singh, S.K. Barthwal and K. Chandra; J. Sol. Stat. Chem. 178, 3183 (2005)
7. Z. Yue, J.Zhou, L. Li, H.Zhang and Z.Gui; J. Magn. Mater., 208, 55 (2000)
8. T. Mimani and K.C. Patil; Mater. Phys. Mech.; 4, 134 (2001)
9. R.D. Purohit, S. Saha and A.K. Tyagi; J. Nucl. Mater., 288, 7 (2001)
10. Y.P. Fu and C.H. Lin; J. Magn. Mater., 251, 74 (2002)
11. A.C.F.M. Costa, E.Tortella, M.R. Morelli and R.H.G.A. Kiminami; J. Magn. Mater., 256,174 (2003)
12. Y.P. Fu, K.Y. Pan and C.H. Lin; Mater. Lett., 57, 291 (2002)
13. A.G. Merzhanov; Int. J. Self-Propag. High-Temp. Synth., 16, 119 (1997)
14. A.M. El Sayed; Ceram. Int., 28, 363 (2002)
15. N.Kasapoglu, A.Baykal, Y.Koseoglu and M.S. Toprak; Scripta Mater. 57, 441 (2007)
16. P. Patil, B. Pawar and S. Mirgane, World journal of pharmacy and pharmaceutical Science 5, Issue 8, 1047-1052 (2016)

INTERNATIONAL CONFERENCE ON
ADVANCES IN MATERIALS SCIENCE
7 – 8 December 2016

Spectroscopic Studies on M-TiO₂ (M = Mn, Ni and Fe) nanoparticles for degradation of malachite green dye

Ravi Kamble¹, Vijaya Puri², Smita Mahajan^{1*}

¹Department of Physics, Jaysingpur College, Jaysingpur-416101(M.S.) India

²Department of Physics, Shivaji University, Kolhapur-416004(M.S.) India

Abstract

Phase pure anatase TiO₂ and (M = Mn, Ni and Fe) doped TiO₂ nanoparticles have been prepared by simple hydrothermal method. The particles were characterized using X-ray diffraction analysis (XRD), UV-vis diffuse reflectance spectroscopy and Energy dispersive spectroscopy (EDS). The obtained samples were further studied for its photocatalytic activities using malachite green dye under UV and visible light.

Keywords: Hydrothermal synthesis; Mn-TiO₂, Ni-TiO₂, Fe-TiO₂; visible light Photocatalyst; Nanoparticles.

1. Introduction

Titanium dioxide (TiO₂) has attracted significant attention due to their broad spectrum and effective application particularly in photocatalysis, catalyst support, antibacterial, environmental remediation, air purification and water disinfection. This is due to its low cost, nontoxicity and eco-friendly nature [1]. The catalyst is the most important factor of any photocatalytic system as it would affect the reaction efficiency. TiO₂ and TiO₂-based catalyst have been studied worldwide [2]. Among various photocatalysis, titania, particularly anatase TiO₂ has been extensively used in photocatalytic applications. Especially, textile industries produce large amount of color dye effluents which are toxic and non-biodegradable. The photocatalysed degradation of dye in solution is initiated by illuminating the TiO₂ photocatalyst with light of energy higher than its band gap, electron excite from valence band to conduction band leaving holes in valence band. These photo excited electrons and holes oxidizes or deoxidizes adsorbates on the surface of catalyst [3]. Particularly anatase TiO₂ has a band gap 3.2 eV, thus its photocatalytic property can be activated under UV light ($\lambda < 400$ nm). But by doping with metals and nonmetals this band gap energy can be decreased. The doping with small amount of metal impurities like manganese, nickel, iron, copper, silver, gold etc. used to tune the absorption in visible region so as to decrease the band gap energy and to visible light active photocatalyst [4]. Various methods have been reported to synthesize TiO₂ nanoparticles like sol-gel, layer by layer deposition, self-assembly, solvent evaporation, solvothermal, hydrothermal, solvent extraction, chemical vapour deposition, physical vapour deposition etc [5]. In present study the change in characteristics properties by doping with 3 wt. %

Mn, Ni and Fe and its effect on photocatalytic properties has been studied. The M-doped TiO₂ nanoparticles were synthesized by stainless steel autoclave hydrothermal method. The obtained samples were characterized using X-ray diffractometer for its structural properties, UV-visible DRS for band gap studies, EDX for its compositional confirmation. Degradation of malachite green was studied under both UV and visible light using sample to evaluate effect of M-doping on TiO₂ photocatalyst.

2. Materials and Methods:

Pure TiO₂ and M-TiO₂ (M=Mn, Ni and Fe) nanoparticles were synthesized by stainless steel autoclave hydrothermal method. In the preparation, 5 mL glacial acetic acid was mixed with 5 ml TTIP with constant stirring to get clear solution. The stirring was continuous for 15 min followed by addition of 10 mL water. To achieve the desired concentration of Mn²⁺ ion as dopant (3 wt. %) in TiO₂ host lattice, required amount of Manganese sulphate was dissolved in 10 mL water. This dopant solution was added to the mixture and stirred vigorously to obtain clear solution. The obtained solution was transferred to Teflon lined stainless steel autoclave; it was sealed and heated at 120 °C for 5 hrs. After heating autoclave was allow to cool down in muffle furnace. The final product was washed with 30 mL of ethanol. The supernatant liquid was discarded and residue was taken out in a beaker. After drying at 60 °C, the residue was crushed to get TiO₂ nanoparticles. Obtained sample was annealed at 350 °C for 2 hrs. Similarly, experiment was carried out reaching the parameters same for nickel and iron dopant were prepared by same method. All the samples of M-TiO₂ powder were analysed using XRD, UV and EDX. The study was extended to investigate the effect on photocatalytic property of the TiO₂ in dye

degradation using malachite green as model dye. All the chemicals used during the experiment were of analytical grade and used without further purification. Double distilled water was used throughout the experiment.

The structural properties of M-TiO₂ powder were determined by X-ray diffractometer, BRUKER AXS using monochromatic copper radiation (Cu K α) at 40 kV, 25 mA over 2 θ range 20-80 $^{\circ}$. Elemental composition was determined from Energy Dispersive X-ray spectrometer (EDS) analysis, Model JEOL JSM 5600. The diffused reflectance spectra (DRS) were recorded in the range of 200-600 nm on UV-Visible NIR spectrophotometer JASCO, Model V-770 and photocatalytic properties of nano TiO₂ for dye degradation were carried out using JASCO V-670.

The photocatalytic degradation of malachite green in the M-TiO₂ suspension under UV and visible light was investigated in order to evaluate its photocatalytic activity. In this experiment 5.0 mg photocatalyst was added in photoreactor containing 50 mL of dye solution. Before the irradiation of light, the solution was stirred for 30 min to ensure adsorption-desorption equilibrium, then exposed to UV light. At a particular time interval aliquots were collected from photoreactor. The nanoparticles were separated out by centrifugation and further the solution was used to monitor the concentration of malachite green by recording the absorbance using UV-Visible double beam spectrophotometer (Lab India, Model-UV-3000⁺). Same experiment was performed for the degradation of malachite green dye under Visible light keeping the parameters same. The percentage of degradation at irradiated time intervals was calculated according to the equation

$$\text{Degradation Percentage} = [1 - A_t / A_0] \times 100$$

Where, A_t is absorbance after time 't' and A₀ is absorbance of dye solution before degradation.

3. Results and Discussion

The structural properties were determined from XRD patterns. Fig 1 shows the XRD patterns of a, b, c and d samples annealed at 350 $^{\circ}$ C. The diffraction peaks at 2 θ = 25.40 $^{\circ}$, 37.82 $^{\circ}$, 48.04 $^{\circ}$, 53.51 $^{\circ}$, 54.76 $^{\circ}$, 62.42 $^{\circ}$, 68.78 $^{\circ}$, 70.09 $^{\circ}$ and 75.12 $^{\circ}$

corresponds to (101), (004), (200), (105), (211), (204), (116), (220) and (215) respectively for plane of tetragonal anatase TiO₂ (JCPDS 21-1272). The major peak (101) of M-doped TiO₂ was found to be shifted to lower angle from 25.40 $^{\circ}$ to 25.28 $^{\circ}$, due to doping of M-doped TiO₂, which confirms that only one crystalline phase was formed during the synthesis process. No extra peak corresponds to rutile phase or oxide of the dopant metal ions was found. The crystallite size was calculated using Debye-Scherrer's formula [6].

$$D = \frac{0.9\lambda}{\beta \cos \theta} \quad (1)$$

The calculated crystallite sizes are 11.00 nm, 7.35 nm, 7.86 nm and 6.25 for TiO₂ (a), 1.90 wt. % Mn²⁺-TiO₂ (b), 1.60 wt. % Ni²⁺-TiO₂ (c) and 1.87 wt. % Fe³⁺-TiO₂ (d) respectively. It is observed that the crystallite size decreases can be correlated to increase in structural defects that prevent particle growth [7].

Fig 2 shows the UV-visible absorption spectra in the range of 200-600 nm for samples a, b, c and d respectively. The absorption spectra of these doped samples show a stronger visible light absorption indicating the band gap was decreased upon M-doping in TiO₂. Band gap values were calculated using E=h ν / λ [8]. The calculated band gap values are reported in table 1.

Fig 3 shows the composition of sample is determined by EDX and composition is reported in the table 1. The table shows the addition of M-doped TiO₂ was successfully done upto 3 wt. % which attributes to the decrease in band gap and visible active photocatalyst. Further these samples were explored for the degradation of malachite green dye. Fig 4 shows the photocatalytic activity of pure TiO₂ and M-TiO₂ samples under a) UV and b) visible light from fig it is observed that the TiO₂ sample is efficient in UV light irradiation while, degradation decreases with Mn²⁺, Ni²⁺ and Fe³⁺ concentration under visible light degradation increases with Mn²⁺, Ni²⁺ and Fe³⁺ concentration the prominent feature of synthesized catalyst is that, it is most efficient under visible light in which 1.87 wt. % Fe³⁺-TiO₂ sample degrades 85.88 % of malachite green dye in 180 min as compare to Mn²⁺-TiO₂ and Ni²⁺-TiO₂

4. Conclusion

The simple hydrothermal method was used to synthesize M-TiO₂ nanoparticles using stainless steel autoclave at 120 $^{\circ}$ C for 5 hrs. The crystallite size as well as band gap energy decreases. The obtained samples were explored for the photo degradation of malachite green dye under UV and visible light 1.87 wt. % Fe³⁺-TiO₂ sample shows most

efficiency (85.88 %) for the degradation of malachite green dye under visible light as compare to Mn^{2+} -TiO₂ and Ni^{2+} -TiO₂

Table 1: Obtained crystallite size, lattice constant, band gap values and composition of a, b, c and d samples

Sample	Crystallite size, D (nm)	Lattice constant		Band gap	Composition (wt. %)		
		a/b	c		Ti	O	Mn / Ni/ Fe
a	11.00	3.7754	9.5099	3.18	55.34	44.66	0.0
b	7.35	3.7805	9.5047	2.38	33.74	64.36	1.90
c	7.82	3.7836	9.4977	2.43	53.85	44.55	1.60
d	6.30	3.7542	9.5090	2.21	39.70	58.44	1.87

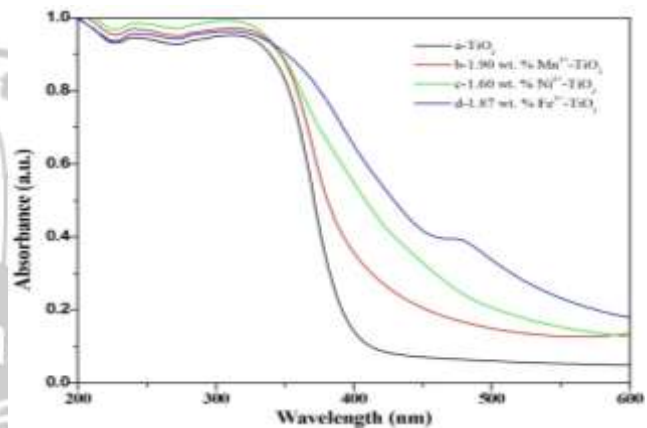
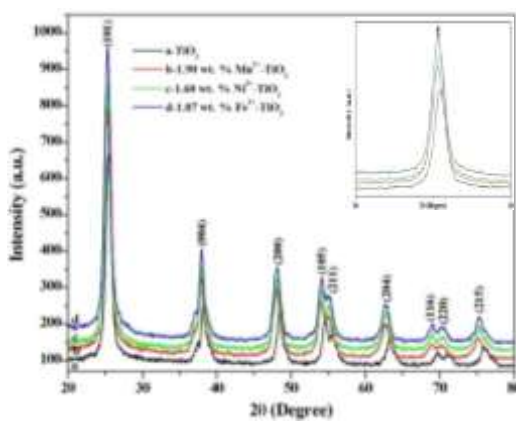


Fig. 1: X-ray diffraction patterns of obtained Titania samples

Fig. 2: UV-Vis. Absorbance spectra for obtained Titania samples

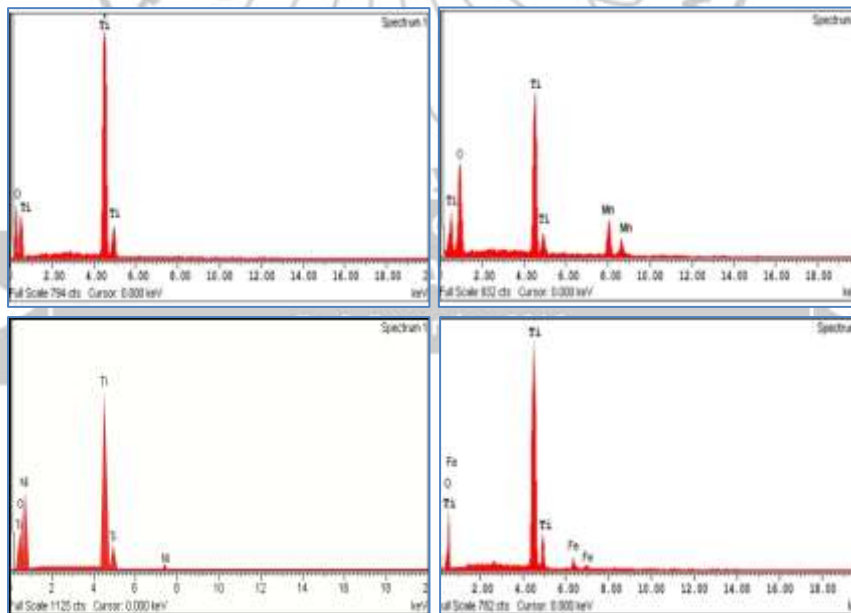


Fig. 3 EDX micrographs of obtained Titania samples

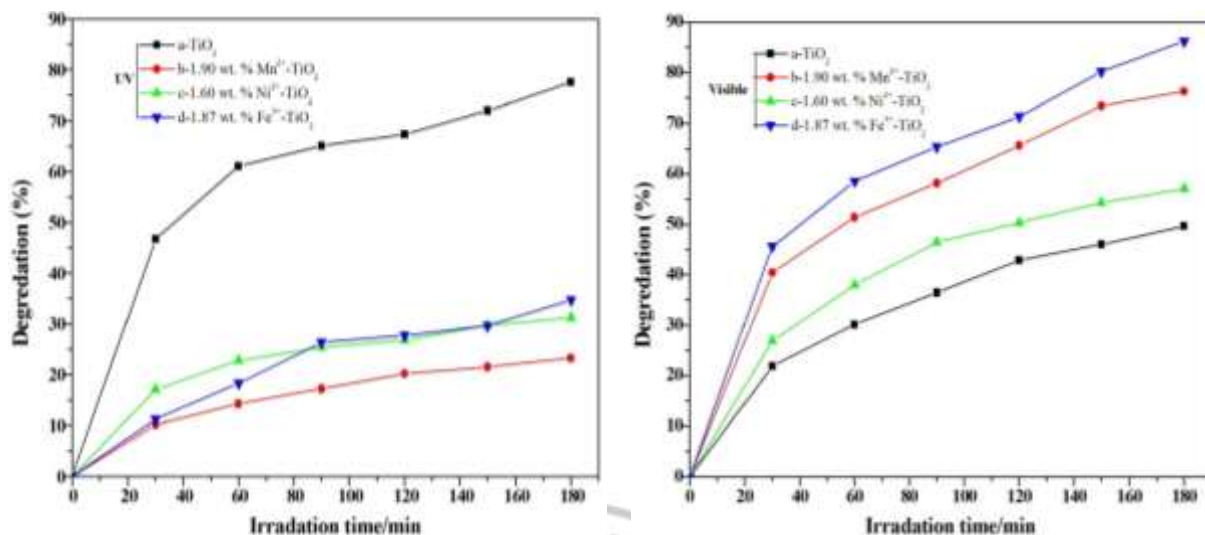


Fig. 4: Photocatalytic activity of TiO_2 , 1.90 wt. % Mn^{2+} - TiO_2 , 1.60 wt. % Ni^{2+} - TiO_2 and 1.87 wt % Fe^{3+} - TiO_2 under; UV and visible light for malachite green dye.

References

1. S. Chavan, R. Kamble, S. S. mahajan, G. Nikam and S. Sabale, Synthesis, Characterization and effect on photocatalytic property of Fe^{3+} - TiO_2 nanoparticles under U.V. light irradiation. IJRBT, (3) 2 (2015) 13-17.
2. B. Zhou, Xu. Zhao, H. Liu, J. Qu, C. P. Huang, Synthesis of visible-light M-BiVO₄ (M= Ag, Co, and Ni) for the photocatalytic degradation of organic pollutants. Separation and purification Technology 77 (2011) 275-282.
3. R. Kamble, S. Sabale, P. Chikode, V. Puri and S. Mahajan, Structural and photocatalytic studies of hydrothermally synthesized Mn^{2+} - TiO_2 nanoparticles under UV and visible light irradiation. Material Research Express 3 (2016) 115005.
4. N. A. Quiroz, D. J. Gutierrez, S. S. Martinez and C. L. Bahena, Degradation of gesaprim herbicide by heterogeneous photocatalysis using Fe-doped TiO_2 . International Journal of Geosciences (2) 669-675.
5. X. B. Chen, S. S. Mao, Titanium Dioxide Nanomaterials: Synthesis, Properties, Modifications, and Applications. Chem. Rev., 2007, 107 (7), 2891-2959
6. B. D. Cullity, Elements of X-ray Diffraction, Addison-wesley Publishing Co Inc, (1976) Ch 14.
7. B. Choudhury, A. Choudhury, Structural optical and ferromagnetic properties of Cr doped TiO_2 nanoparticles, Material Science Engineering B. 178 (2013) 794-800.
8. V. V. Jadhav, R. S. Dhabbe, S. R. Sabale, G. H. Nikam and B. V. Tamhankar, Degradation of dyes using high temperature stable anatase nanosphere TiO_2 photocatalyst. Universal Journal of Environmental Research Technology 3 (6) 667-676.

An overview on Advances in material science research

Vilas S. Hogade

Department of chemistry, Shrikrishna Mahavidyalaya, Gunjoti, Tq. Omerga Dist. Osmanabad

Abstract

Material science research is playing important role in the development. Different materials are prepared in the laboratory such as composites, ceramics, Nano materials, biomaterials etc. material is the term used to understand the processing, structure and property relationship of the concerned materials. The development of material science research has been observed since 8000 BC. The world of tomorrow will be much different than the present one. It is virtually impossible to predict future discoveries and inventions; what we can predict, however, are societal needs, which is responsible for the material science and engineering research community to respond.

Key words: Metals, polymers, ceramics, nanomaterial, composites, biomaterials.

1. Introduction

Discovery and design of new materials particularly solids in chemical science has emerged as interdisciplinary field covering chemistry, physics and engineering streams. Material science branch widely considered as a specific and distinct field of science and engineering. Materials science is a syncretic discipline hybridizing metallurgy, ceramics, solid-state physics, and chemistry [1]. Material paradigm is the term used to understand the processing, structure and property relationship of the materials. The paradigm is used to advance understanding in the research areas such as nanotechnology, biomaterials forensic science and metallurgy. A material is defined as a substance most often a solid, but other condensed phases can also be included that is intended to be used for certain applications or in brief it can be defined as, material science is the study of stuff [2].

Structural study is one of the most important components in the field of materials

science. In the process characterization is important tool for the understanding of the structure of a material. The characterization involves methods such as diffraction with X-rays, electrons, or neutrons, and various forms of spectroscopy and chemical analysis such as Raman spectroscopy, chromatography, thermal analysis, electron microscope analysis, etc. A primary application of materials science is matching the right material or combination of materials to the intended purpose and use of a specific product. In doing so, materials scientists must consider such things as the weight and strength of a certain material as well as its ability to conduct electricity or insulate the product from heat along with the material's chemical stability, corrosion resistance, and economy [2]. The development of material science in chronological order is given in the following table [2].

Development of Material Science Research In chronological order:

8000 BC Hammered copper	7000 BC Clay pottery
6000 BC Silk production	5000 BC Glass making
4000 BC Smelted copper	4000-3000 BC Bronze Age
3200 BC Linen cloth	2500 BC Wall plaster
2500 BC Papyrus	1000 BC Iron Age
300 AD Glass blowing	20 AD Brass alloy
105 AD Paper	600-900 AD Porcelain
1540 AD Foundry operation	late-1500s Magnetization of iron
1729 Electrical conductivity of metals	1774 Crude steel
1789 Discovery of titanium	1789 Identification of uranium
1800 Volta's electric pile (battery)	1824 Portland cement
1839 Vulcanization of rubber	1850 Porcelain insulators
1850s Reinforced concrete	1856 Bessemer steelmaking
1866 Microstructure of steel discovered	1866 Discovery of polymeric compounds
1868 Commercial steel alloy	1870 Celluloid
1871 Periodic table of the elements	1875 Open-hearth steelmaking
1880 Selenium photovoltaic cells	1884 Nitrocellulose (first man-made fiber)
1886 Electrolytic process for aluminum	1889 Nickel-steel alloy
1891 Silicon carbide (first artificial abrasive)	1896 Discovery of radioactivity
1906 Triode vacuum tube	1910 Electric furnace steelmaking

1913 Hydrogenation to liquefy coal	1914 X-ray diffraction introduced
1914 Chromium stainless steels	1923 Tungsten carbide cutting materials
1930 Beginnings of semiconductor theory	1930 Fiberglass
1934 Discovery of amorphous metallic alloys	1937 Nylon
1940s Synthetic polymers	1947 Germanium transistor
1950 Commercial production of titanium	1952 Oxygen furnace for steelmaking
1950s Silicon photovoltaic cells	1950s Transmission electron microscope
Mid-1950s Silicon transistor	1957 First supercritical U.S. coal plant
1958 Ruby-crystal laser	1959 Integrated circuit
1960 Production of amorphous metal alloy	1960 artificial diamond production
1960s Micro alloyed steels	1960s Scanning electron microscope
1966 Fiber optics	late-1970s Discovery of amorphous silicon
1984 Discovery of quasi-periodic crystals	1986 Discovery of high temp. superconductors
1989 Bucky balls (Buckminsterfullerene)	

Classification of Material:

In our day to day activities we come across with thousands of materials available for use from different disciplines. Most materials are classified into different classes that are based on the atomic bonding forces of a particular material. These three classifications are metals, ceramic, polymers, composites, semiconductors, biomaterials, advanced materials and materials of the future. Within each of these classifications, materials are often further organized into groups based on their chemical composition or certain physical or mechanical properties. Composite materials are often grouped by the types of materials combined or the way the materials are arranged together.

1. Metals:

Generally it is observed that metallic materials are combinations of metallic elements. These elements have large number of non-localized electrons, i.e. these electrons are not bound to particular atoms. Many properties of metals are accounted directly on these electrons. All metals are characterized by metallic properties such as luster, opacity, malleability, ductility and electrical conductivity etc. Metals account for about two thirds of all the elements and about 24% of the mass of the planet. From the periodic table, it can be seen that a large number of the elements are classified as being a metal. A few of the common metals and their typical uses are presented below [3].

- Iron/Steel - Steel alloys are used for strength critical applications.
- Aluminum - Aluminum and its alloys are used because they are easy to form, readily available, inexpensive, and recyclable.
- Copper - Copper and copper alloys have a number of properties that make them useful,

including high electrical and thermal conductivity, high ductility, and good corrosion resistance.

- Titanium - Titanium alloys are used for strength in higher temperature (~1000° F) application, when component weight is a concern, or when good corrosion resistance is required.
- Nickel - Nickel alloys are used for still higher temperatures (~1500-2000° F) applications or when good corrosion resistance is required. Refractory materials are used for the highest temperature (> 2000° F) applications.

2. Ceramics:

Ceramics are crystalline compounds that are placed between metallic and non-metallic elements. Oxides, nitrides and carbides are the important classes of ceramic compounds. In addition to these graphite is also categorized as ceramic compound. The wide range of these materials which constitutes the ceramic materials are clay minerals, cement and glass. Hardness, abrasion resistance, brittleness and chemical inertness are the important properties of ceramic compounds. They are typical insulate towards the passage of heat and electricity and are more resistant to high temperature and harsh environment.

3. Polymers:

Polymers are organic compounds that are derivatives of carbon and hydrogen. These include the plastic and rubber materials. They are differentiated into thermoplastic polymers, thermosetting polymers and elastomers that are generally called as rubbers. Most of the polymers are light weight and are soft compared to metals and have low densities. They are extremely flexible and are widely used as insulators for thermal and electrical purposes. Polyethylene,

polyesters, nylon, rubber etc. are the different examples of polymers.

4. Composites:

Composites are becoming an essential part of today's materials because they offer advantages such as low weight, corrosion resistance, high fatigue strength, faster assembly, etc. Composites are used as materials ranging from making aircraft structures to golf clubs, electronic packaging to medical equipment, and space vehicles to home building. Composites are generating curiosity and interest in students all over the world. They are seeing everyday applications of composite materials in the commercial market, and job opportunities are also increasing in this field [4].

Composites are the materials which constituents metals, ceramics and polymers wherein the properties of each constituents is observed. Wood, clad materials, fiber glass, plastics, cemented carbides etc. are some of the examples of composite materials. Fiber glass is a most familiar composite material, in which glass fibers are embedded within a polymeric materials. Composites materials are designed to display a combination of the best characteristics of each of the component materials. For ex- fiber glass acquires strength from the glass and the flexibility from the polymer materials. Now a day many of the recent developments of materials science have involved composite materials. Probably, the composites will be the steels of this century.

5. Semiconductors:

Semiconductors are the materials which are having electrical properties that are intermediate between electrical conductors and insulators. The electrical characteristics of semiconducting materials are extremely sensitive to the presence of minute concentrations of impure atoms. Silicon, Germanium and certain elements from group II, III, IV, V, VI and VII form the vast majority of semiconducting crystals. The semiconducting materials are used in a number of devices such as diodes, transistors, solar batteries, radiation detectors, thermistors and lasers. Semiconductor materials have complexly revolutionized the computer industries.

6. Biomaterials:

Biomaterials are the substances employed in components that are implanted into the human body for replacement of damaged part of the

body. In other words biomaterials are nonviable materials used in medical devices intended to interact with biological systems. Some important examples of biomaterial equipment's are intraocular lenses, vascular grafts, artificial hip joints and substitute heart valves etc. which are playing important role in medical science [5]. Metals, ceramics, polymers, composites, semiconductors etc. are used as biomaterials taking care that they should not produce any toxic effect in the body.

7. Nano materials:

Nano materials are the solids having microstructural feature in the range of 1-100 nm. Nano materials have outstanding mechanical and physical properties due to their extremely fine grain size and high grain boundary volume fraction. Nano-structured materials exhibit properties which are quite different from their bulk properties. These materials contain a controlled morphology with at least one Nano scale dimension. Nano crystals, Nano wires and Nano tubes of a large number of inorganic materials have been synthesized and characterized in recent years. The mixing of Nano-particles with polymers to form composite materials has been practiced for decades. For example, the clay reinforced resin known as Bakelite is the first mass-produced polymer-nanoparticle composites and fundamentally transformed the nature of practical household materials. Materials produced out of Nano particles have some special features, e.g. very high ductility, very high hardness ~4 to 5 times more than usual conventional materials, transparent ceramics achievable, manipulation of color, extremely high coercivity magnets and developing conducting inks and polymers.

Prospective view of material science research:

As Pearl S. Buck said so eloquently: "One faces the future with one's past;" hence it is interesting to go back and view the future in view of the past [6] as is overviewed previously, many advances in material science is due to research in material science and engineering. We have witnessed the re-shaping of our lives through revolutions that have taken place in medicine, telecommunications, and transportation industries. Looking beyond the through fifty years as future of material science and engineering research the world community to influence public policy and to make a difference by how we direct our efforts for

shaping the world of tomorrow [7]. The scientific community in the field is thinking about the energy resources and the energy storage materials, transportation industry, sustainable construction materials, packaging materials and their recycling and use of biomaterials in health issues. It is virtually impossible to predict future discoveries and inventions; what we can predict, however, are societal needs, which beckon the material science and engineering community to respond.

Recent Advances in material science Research:

Study shows particle collisions may explain overheated circuits, improve thermoelectric devices. In the coming years, as more transistors are packed into ever smaller areas within computer chips, MIT engineers say cellphones, laptops, and other electronic devices may face a higher risk of overheating, as a result of interactions between electrons and heat-carrying particles called phonons. The researchers have found that these previously underestimated interactions can play a significant role in preventing heat dissipation in microelectronic

devices. Their results are published today in the journal Nature Communications [8].

In transistors made from semiconductor materials such as silicon, and electrical cables made from metals, electrons are the main agents responsible for conducting electricity through a material. A main reason why such materials have a finite electrical resistance is the existence of certain roadblocks to electrons’ flow — namely, interactions with the heat-carrying phonons, which can collide with electrons, throwing them off their electricity-conducting paths. Scientists have long studied the effect of such electron-phonon interactions on electrons themselves, but how these same interactions affect phonons — and a material’s ability to conduct heat is explained in the present communication. Investigating the Relationship between Knitted Fabric Porosity and Light Permeability has been studied by Manoj Kumar et al [9]. A group of researchers has studied on modified Nano emulsions with iron oxide for magnetic resonance imaging has been reported [10].

Conclusion:

We are living in the society that is market driven. Material developments take far too long until its applications. As the material science branch has been developed with interdisciplinary approach, the societal needs are fulfilling by the recent outcome of the products. The materials like composites, polymers, semiconductors, biomaterials, Nano materials etc. have become the need of the hour. A novel discovery in nanomaterial’s for ex. Silver nanowire have been an attractive research subject due to their unique or improved electronic, catalytic, and optical properties. Materials scientists and engineers have to play important role as to design for everything from tennis racquets to space shuttles. And, increasingly, the disposal of used materials will require attention with emphasis on recycling these materials. “Environmentally friendly” materials that can be produced, used, and disposed of without harmful effects to the biosphere is a field of study just beginning to emerge. This will require much research in future perspective for the development of technology.

Acknowledgement:

Author is thankful to the principal, Shrikrishna Mahavidyalaya Gunjoti, for providing the infrastructural facility in the college.

References:

1. Eddy, Matthew Daniel 2008, the language of mineralogy: John Walker, Chemistry and The Edinburgh Medical School 1750-1800.
2. Material science and technology teacher’s handbook 1994, Pacific Northwest National Laboratory, Washington.
3. www.nde-ed.org.
4. Mechanics of composite materials, Autar K. Kaw, 2006, Second Edition, CRC Press Taylor & Francis Group
5. Biomaterial Science: An introduction to materials in medicine, Buddy D. Ratner, Allan S. Hoffmann, Friedric J. Schoen, Jack E. Lemons, 1996, Academic Press, New York.
6. <http://www.wisdomquotes.com>
7. Diran Apelian 2007, looking beyond the last 50 years: the future of material science and engineering, Journal of Materials, PP-65-73.
8. MIT News, Jennifer Chu, October 2016
9. Manoj kumar Imirith, Roshan Unmarand, Satyadev Rosunee 2016, Indian Journal of Materials Science, Volume 2016.
10. Yongyi Fan,Rui Guo,Xiangyang Shi,Steven Allen,Zhen gyi Cao,James R. Baker and Su He Wang 2016, Nano materials Vol. 6(12), 223.

Synthesis and Propertise Of (BSPT) Compositions Material

S.N. Tambe, S.G. Chavan, S.R. Kokare, Y. D. Kolekar, D. J. Salunkhe

Department of Physics, Nano- Composite Laboratory, Karmveer Bhaurao Patil Mahavidhyalaya, Pandharpur, 413 304, Maharashtra, India.

e-mail: salunkhedj@rediffmail.com

Abstract

The compositions $Ba_{0.8-x}Sr_xPb_{0.2}TiO_3$ (BSPTx), with $x = 0.2, 0.25, 0.3, 0.35$ and 0.4 are synthesized using ceramic route. From XRDs, it is observed that with increase in x the c/a ratio decreases. The investigations on the P-E hysteresis loop reveal that all the compositions possess useful values of maximum polarization (P_{max}) and remnant polarization (P_r) and it is seen that d_{33} is maximum for BSPT0.3 however for BSPT0.35 & BSPT0.4 magnitude of d_{33} is large and nearly equal. Thus for compositions BSPT0.3 and BSPT0.35, P_{max} and d_{33} are large. The present observations suggests that the BSPTx could be a useful ferroelectric / piezoelectric system.

Keywords: Synthesis, X-ray diffraction, P-E loop, d_{33} and Ferroelectricity.

1. Introduction:

$Ba_{(1-x)}Sr_xTiO_3$ (BSTx) is a well known ferroelectric material, which has a large number of applications for the devices like DRAM, FERAM, tunable filters, tunable resonators etc. It is observed that the dielectric properties of BST are dependent on the percentage of Sr i.e x . Here BST0.3 is known to possess a very large value of dielectric constant ϵ at T_m nearly equal to $35^\circ C$ [1-3].

The compositions above $(BaSrPb)TiO_3$ (BSPT) systems have also attracted enormous interest in past a few years [4,5]. Here it is observed that the properties of BSPT are critically dependent on the percentage of Pb, Ba and Sr. Here in BSPT compositions. The substitution of lead causes an increase in the curie temperature T_m of $BaTiO_3$ (BT) or $SrTiO_3$ (ST) compositions. It is reported that the substitution of Pb at 20% in $BaTiO_3$ (BT) increases the curie temperature of BT by nearly $75^\circ C$ [6]. Considering the discussion above it appears that the BSPT compositions with $(Pb_{0.2}Ba_{0.8-x}Sr_x)/TiO_3$, for $x=0.2, 0.25, 0.3, 0.35, 0.4$ may exhibit interesting electrical polarization and Piezoelectric Coefficient (d_{33}) for various BSPTx compositions. Thus the present paper reports synthesis and characterization of $Ba_{0.8-x}Sr_xPb_{0.2}TiO_3$ (BSPTx) for $x = 0.2, 0.25, 0.3, 0.35$ and 0.4 . The paper presents analysis of crystal structure, e ferroelectric hysteresis loops of the BSPTx system and Piezoelectric Coefficient (d_{33}) for various BSPTx compositions.

2. Experimental:

2.1 Synthesis of BSPTx compositions:

All the compositions in the series $Ba_{0.8-x}Sr_xPb_{0.2}TiO_3$ (BSPT) with $x = 0.2, 0.25, 0.3, 0.35$ and 0.4 were synthesized by using conventional ceramic synthesis route. Here $BaCO_3$, $SrCO_3$, Pb_3O_4 and TiO_2 of AR grade are used as starting

materials. All these starting carbonates/oxides were mixed together in the required stoichiometric ratio and were ground thoroughly and manually for 3 to 4 hours. After grinding thoroughly, powders were calcinated at $1000^\circ C$ for 12 hours. The calcinations was carried out in alumina crucibles closed with leads to avoid evaporation of PbO. The corresponding powders were then pelletized with diameter 1.2 cm and final sintering was carried out at $1180^\circ C$ for 12 hours [3]. During sintering, powder of the same material was sprinkled on the pellets and sintering was carried out in crucibles closed with leads This process ensures minimum evaporation of PbO. In the present case, silver paint was employed as an electrode for characterization, where it is observed that by using silver paint to form the electrodes, the electrode effect could be minimized [7].

To understand the crystal structure of the BSPTx, Bruker D8 advance X-ray diffractometer was used, while the P-E hysteresis loops are determined using an automatic P-E loop Tracer due to M/s Marine India, New Delhi. The linear piezoelectric coefficient (d_{33}) of all the BSPTx compositions has been measured

3. Results and discussions:

3.1 Crystal Structure and Microstructural Analysis:

Figure 1 show the X-ray diffractograms of the BSPTx for $x = 0.2, 0.25, 0.3, 0.35$ and 0.4 . It could be seen from the figure 1 that the XRD spectra are typical of the ABO_3 system and all the peaks could be indexed according to the standard JCPDs data of BST0. 23(card no.440093). It is also seen that no peak corresponding to any impurity is recorded in figure 1. However the X-ray diffractograms, for $x \geq 0.25$ show a slightly different feature than the X-ray diffractograms of BST0.2. Here, the closer observation of the peaks

corresponding to (002) and (200) show that the intensity of the peak corresponding to (002) is greater than the intensity of the peak corresponding to (200). However, this feature is not prominently seen from figure 1. This difference may occur because of evaporation of PbO and increasing content of Sr. During sintering. Further the cation redistribution may cause distortion of the crystal structure. However it is seen that the BSPT_x is formed as a single phase tetragonal composition except for BSPT_{0.2}. From figure 1 it could be seen that the peaks corresponding to (100) and (110) appear broad, but could not be separately resolved in two peaks. However, the peaks corresponding to (002), (200) and other peaks occurring in the vicinity of $2\theta = 53^\circ$ and 63° , could be separately resolved. From the observed X-ray diffractograms, the lattice parameters 'a', 'c' and the ratio 'c/a' has been determined. Here table 1 shows variation of 'a', 'c' and ratio 'c/a' for the BSPT_x system despite of a limited accuracy of average values of 'a' and 'c'. It is observed that except for small increase for $x = 0.25$, the 'c/a' ratio shows a decreasing trend as the x increases from 0.2 to 0.4. These

observations are consistent with the earlier reports on BSPT_x system [1,3].

Further, from the X-ray diffractograms, the crystallite size of the BSPT_x compositions are also determined shown in table 1. It could be seen that the crystallite size increases as the percentage of Sr in the composition of BSPT increases

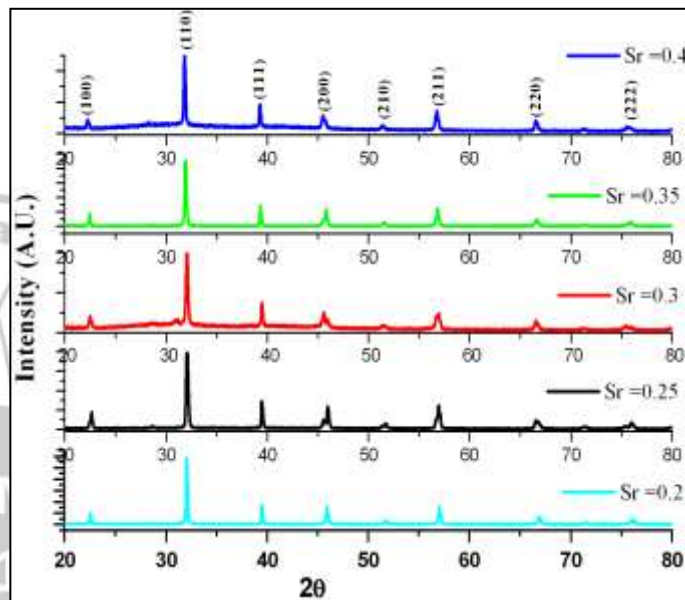


Figure 1: XRD of BSPT_x for x = 0.2, 0.25, 0.3, 0.35 and 0.4.

Table 1. Lattice parameters 'a', 'c' and ratio 'c/a' and densities for Ba_{0.8-x}Sr_xPb_{0.2}TiO₃ for different values of x.

X	'a' in A°	'c' in A°	'c/a'	Crystallite size (nm)	Densities (g/cc)
0.2	3.943	3.974	1.007	49	6.310
0.25	3.940	3.972	1.008	67	6.553
0.3	3.953	3.976	1.005	60	6.067
0.35	3.958	3.978	1.005	53	6.193
0.4	3.933	3.944	1.002	57	6.256

3.2 P-E Hysteresis loop of BSPT_x:

Figure 2 shows the P-E hysteresis loops for the BSPT_x compositions for $x = 0.2, 0.25, 0.3, 0.35$ and 0.4 , while table 2 shows variation of maximum polarization (P_{max}), remanent polarization (P_r), coercive field (E_c) and the ratio P_r/P_{max} for varying x. from table 2, It could be seen that the P_{max} increases with increasing x for

x up to 0.35. For further increasing x the P_{max} shows a decreasing trend with x. Further it could be seen that for $x = 0.25$ and 0.3 there occur certain exception. Similar behaviour is also recorded for BST_{0.25} and BST_{0.3} [2]. Additionally the P_r/P_{max} is also sufficiently high thus essentially substitution of Sr causes increase in P_{max} for x up to 0.35, for x greater than 0.35, P_{max} may reduce as the transition temperature T_m of BSPT_x approaches room temperature, for x greater than 0.4. The observations of increasing P_{max} could be correlated to the variation of c/a with increase of x. More is the c/a the be cations could be increasingly free to oscillate around its mean position. Therefore the P_{max} may follow a similar trend as observed for the c/a ratio.

3.3 Piezoelectric Coefficient (d_{33}):

The important parameters of a ferroelectric/ piezoelectric material is the linear piezoelectric coefficient (d_{33}), for this samples were poled using DC poling unit. Poling voltage was kept constant at 1 kV for 6 hours. Figure 3 show the variation of linear piezoelectric coefficient (d_{33}) as a function of x for Ba_{0.8-x}Sr_x

Pb_{0.2}TiO₃ (BSPT_x) for x = 0.2, 0.25, 0.3, 0.35 and 0.4 compositions. The linear piezoelectric coefficient (d₃₃) of all the BSPT_x compositions has been measured and it tabulated in table 3. From this it is seen that d₃₃ is maximum for BSPT0.3. However for BSPT0.35 & BSPT0.4 magnitude of d₃₃ is large and nearly equal. Thus for compositions BSPT0.3 and BSPT0.35, the ε, P_{max} and d₃₃ are large. In fact all these parameters indicate ferroelectric / piezoelectric performance of the materials.

Table 2: Values of Maximum polarization (P_{max}), remnant polarization (Pr), coercive field (Ec) and P_r/P_{max} of Ba_{0.8-x}Sr_xPb_{0.2}TiO₃ for different values of x.

Compos itions(x)	P _{max} (μC /cm ²)	P _r (μC/c m ²)	Ec(kV /cm)	P _r /P _{max}
0.2	2.2481	0.7567	2.6278	0.3365
0.25	4.2821	1.9548	3.2520	0.4565
0.3	3.8597	1.4960	2.8349	0.3876
0.35	6.4558	2.8080	1.9549	0.4349
0.4	6.2293	1.9187	1.3773	0.3080

Table 3. Piezoelectric Coefficient (d₃₃) for various BSPT_x compositions.

Compositions (x)	Piezoelectric Coefficient (d ₃₃) (pC/N)
BSPT0.2	70.33
BSPT0.25	108.63
BSPT0.3	137.49
BSPT0.35	84.83
BSPT0.4	84.83

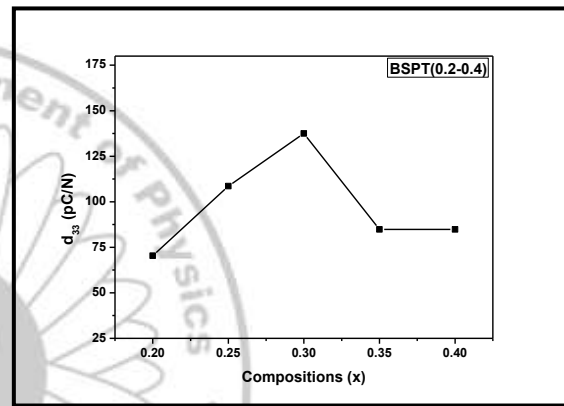


Fig.3: Variation of d₃₃ as a function of x for Ba_{0.8-x}Sr_xPb_{0.2}TiO₃ (BSPT_x) for x = 0.2, 0.25, 0.3, 0.35 and 0.4 compositions.

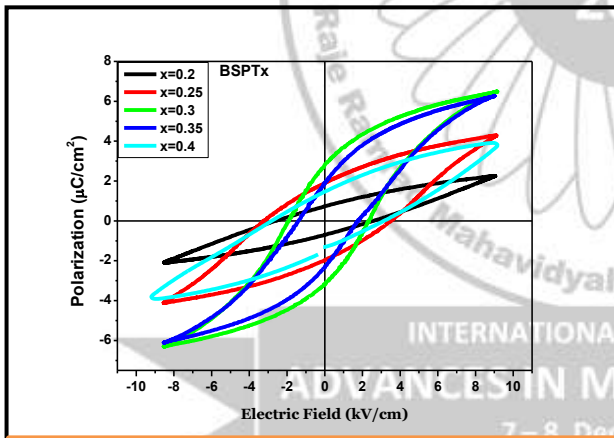


Fig.2: P–E hysteresis loops of Ba_{0.8-x}Sr_xPb_{0.2}TiO₃ for different values of x.

4. Conclusion:
The present observations show that the BSPT_x compositions exhibit a tetragonal crystal structure. However, certain distortions are seen in the crystal structure mainly because of evaporation of PbO during sintering. Further, it is observed that the agglomeration of crystallites increase as the x increases. All the compositions are observed to possess a significant value of P_r/P_{max}.

The present observations on BSPT_x system, for x = 0.2 to 0.4 show that the substitution of Pb at 20 atomic percent causes an increase in T_m, P_{max} and P_r as compared to the corresponding BST_x system. Therefore the BSPT compositions may become an alternative with improve performance over BST_x system the d₃₃ is maximum for BSPT0.3. In fact all these parameters indicate ferroelectric / piezoelectric performance of the materials.

Acknowledgements:

All Authors thankful DRDO-NRB for their financial support.

References

1. A Iansculescu, D Berger, L Mitoseriu, L P Curecheriu, N Dragan, D Crisan, *et al. Ferroelectrics* 369 (1) 22 (2008).
2. Lavinia Petronela Curecheriu, Liliana Mitoseriu, Aldelina Ianculescu *Journal of Alloys and Compound* 482 (2009) 1-4
3. M M Sutar, A N Tarale, S R Jigajeni, S B Kulkarni and P B Joshi *Appl. Nanosci.* 2 311 (2012).
4. Xiaohua Sun, Huiming Huang, Shengxiang Wang , Meiya Li, Xing-zhong Zhao. *Thin Solid Films* 516 (2008) 1308–1312
5. Wei Liu, Xiaohua Sun, Hongwei Han, Meiya Li, and Xing-Zhong Zhao *Applied Physics Letters* 89, 163122 (2006).
6. S M Salunkhe, S R Jigajeni, M M Sutar, A N Tarale, P B Joshi *Journal of Physics and Chemistry of Solids* 74 388 (2013).
7. S R Jigajeni, A N Tarale, D J Salunkhe, P B Joshi, S B Kulkarni *Ceramics International* 39 2331 (2013).

Effect of sintering temperature on structural and morphological analysis of $\text{Co}_{0.50}\text{Cu}_{0.5}\text{Fe}_2\text{O}_4$ synthesized by sol-gel method

S. P. Patil^a, K. R. Sanadi^b, K. K. Patankar^a, V. B. Helavi^a

^a Department of chemistry, Rajaram college, Kolhapur. (Maharashtra), India 416004

^b Department of chemistry, Doodhsakhar Mahavidyalaya, Bidri, Kolhapur. (Maharashtra), India 416208

Corresponding author: -Miss. S. P. Patil, Email: simspatil@gmail.com

Abstracts

Nanocrystalline cobalt copper ferrite powders were synthesized by simple sol-gel auto combustion method. After sintered at different temperature they were characterized by different technique. Structural analysis was carried out by X-ray diffraction technique (XRD) while morphological analysis by Scanning electron microscopy (SEM). XRD study shows formation of single cubic spinel phase while purity of the sample was analyzed by energy dispersive X-ray analysis.

Keywords: - Sol-gel chemistry, Cubic spinels, Semiconductors, Nanoparticles.

1. Introduction:-

Nano composites metal oxide containing transition metal becomes a centre of attraction because of its magnetic view due to their partially filled orbital, ability to form metal complex with variety of organic ligands [1, 2]. Nano material based catalyst having large surface area receiving active sites very familiar for its known heterogeneous and homogeneous catalysis. The different color shading in precious transition metal is by virtue of charge transfer phenomenon in between metal ligand and vice a versa [3]. Nano structured materials are employed for their scientific discipline and technical applications. The administration of these physico-chemical properties of metal oxide is current need in material science, nanoscience. The transition metal and rare earth metal ferrite or chromites having spinel construction are notable and substantial interest in different fields such as solar cells, magnetic devices, transformer, photocatalytic oxidation reduction systems etc[4]. Although the crystal parameters (chemistry) are considering for explaining their various properties[5,6]. The cation distribution in sub lattices of octahedral and tetrahedral geometry decides the disturbance of symmetry of compound called as Jahn Teller distortion, the molecule undergo degeneracy [7,8].

There are various methods used for synthesis of nano structured metal oxides such as co precipitation,[9,10] hydrothermal,[11] auto ignition(sol-gel)[4]. The various preparation methods have been developed to obtain high quality powders, which may lead to improvement in efficiency of catalytic activity. Moreover, sol-gel route is more favorable due to its inexpensiveness, simple procedure and cost effective.[12]

2. Experimental Procedure

2.1 Sample preparation:

Polycrystalline powder of $\text{Co}_{1-x}\text{Cu}_x\text{Fe}_2\text{O}_4$ was prepared by sol-gel auto combustion method. The A.R. Grade citric acid ($\text{C}_6\text{H}_8\text{O}_7 \cdot \text{H}_2\text{O}$), copper nitrate [$\text{Cu}(\text{NO}_3)_2 \cdot 5\text{H}_2\text{O}$] cadmium nitrate [$\text{Co}(\text{NO}_3)_2 \cdot 4\text{H}_2\text{O}$] and ferric nitrate [$\text{Fe}(\text{NO}_3)_3 \cdot 9\text{H}_2\text{O}$] were used as starting materials. The samples were prepared by sol-gel auto-combustion method as prepared in our previous work [4].

2.2 Characterization:

X-ray diffraction Philips PW1710 x-ray diffractometer with Cr $k\alpha$ radiation (2.2927\AA) was used to determine the phase, lattice parameter and average grain size. The morphology and size of particle were observed by scanning electron microscopy (SEM) while element contents were determined by using an energy dispersive x-ray spectroscopy (EDAX).

3 Result and discussion:-

3.1 Crystallographic study:

The effect of temperature on crystallographic data of $\text{Co}_{0.50}\text{Cu}_{0.50}\text{Fe}_2\text{O}_4$ was shown in Fig.1. Figure 1 shows the formation of single cubic spinel phase only. In this figure, (311) is the most intense peak. By using JCPDS data of this peak we can calculate lattice parameter, crystal size and physical density. Peak broadening clearly indicates increase in Lattice parameter, crystallite size and physical density with increase in temperature.

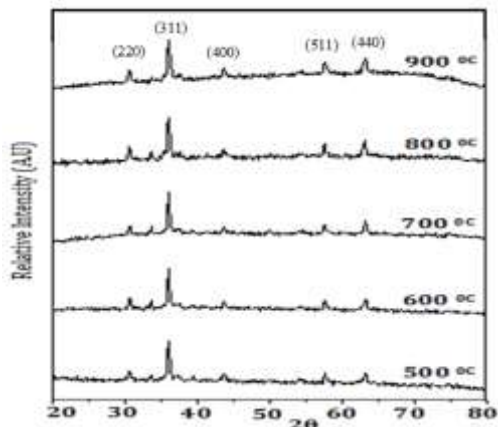


Fig.1. X-ray diffractograph of $\text{Co}_{0.50}\text{Cu}_{0.50}\text{Fe}_2\text{O}_4$

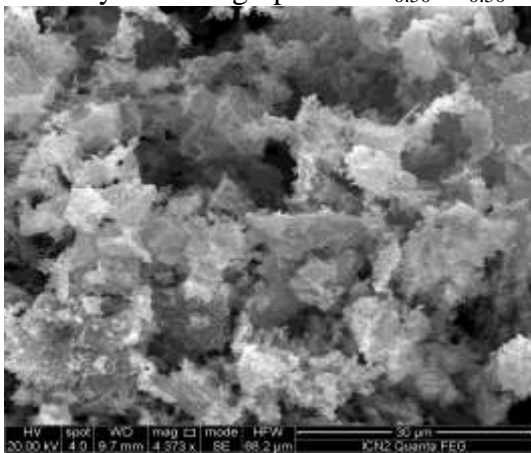


Fig.2. SEM micrograph images of $\text{Co}_{0.50}\text{Cu}_{0.50}\text{Fe}_2\text{O}_4$

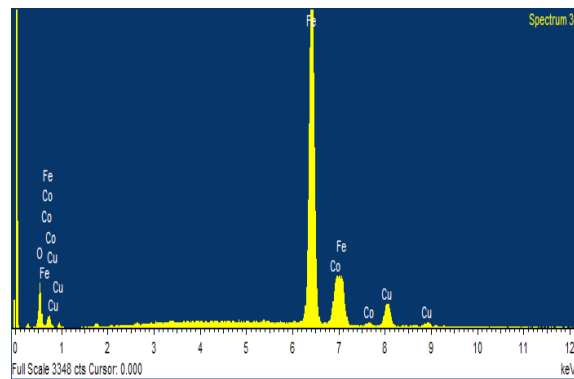


Fig.3 EDAX pattern of $\text{Co}_{0.50}\text{Cu}_{0.50}\text{Fe}_2\text{O}_4$

2) SEM analysis:-

The Scanning Electron Microscopy shows morphological character of the sample. The SEM micrograph of cobalt copper ferrite is as shown in figure. The grain size was calculated from Cottrell's method [12] which is 1.2 μm . This is due to the agglomeration of crystallites.

3) Elemental analysis:-

Figure.3 shows the EDAX pattern of $\text{Co}_{0.50}\text{Cu}_{0.50}\text{Fe}_2\text{O}_4$. The elemental studies indicate presence of all metals without any impurity which intern shows the removal of the entire precursor from the sample during sintering.

4. Conclusions:

Nanocrystalline cobalt copper ferrite powders were synthesized by simple sol-gel auto combustion method. XRD data reveals the formation of cubic single spinel phase only. SEM micrograph shows uniform distribution of grains throughout the surface.

References:-

- Hogan ,C. Michael (2010) "Heavy metal" in Encyclopedia of Earth. National Council for Science and the Environment. E. Monosson and C. Cleveland (eds.) Washington DC.
- B.N. Figgis, J. Lewis,R.G.Wilkins,eds.The Magnetochemistry of Complex Compounds.Modern coordination chemistry.New York Wiley Interscience. pp.400-454.
- P.J.Atkins, D.F.Shriver,(1999) inorganic chemistry(3rd ed.) New York :W.H.Freeman and CO.ISBN 0-7167-3524-1.
- P.P.Hankare,K.R.Sanadi,N.M.Patil,K.M.Garadkar,I.S.M ulla,J.Alloys and Compd.550 (2012)290-296.
- D.R.Modeshia,R.I.Waiton, Chem.Soc.Rev.39 (2010)4303-4325.
- E.Roduner,Chem.Soc.Rev.35(2006)583-592.
- N.A. Iavnov, V. Ya. Metrofanov,L.D.Falkovakaya, A.Y.Fishman.
- F.S.Ham, in electron paramagnetic resonance,eds.S.Geshwind(plenium new York and London 1972) p-4.
- M.F. Zawrah, H. Hamaad, S.Meky, Ceram. Int.33(2007)969.
- R.B. Jotania, P. A. Patel,Int.J.Eng. Res.Appl.2(2012)494.
- W.Zheng,W.Pang,G.Meng,D.Peng,J.Mater.Chem. 9(1999)2833-2836.
- O.G.Wells.;"Scanning Electron Microscopy"McGraw Hill Inc.(1974).

Synthesis and characterization of SnO₂ by CBD method for LPG gas sensor

K.S. Pakhare¹, R.D Tasgaonkar¹, B.D. Bhosale², S.N. Zende³, B.M. Sargar^{1*}

¹&* *DIST-FIST sponsored Material research laboratory, Jaysingpur College, Jaysingpur, Tal-Shirol, Dist- Kolhapur -416101*

² *Rajaram College, Kolhapur, Tal-Karvir, Dist Kolhapur-416004*

³ *DDdhsakhar Mahavidyalay, Bidri, Tal-Kagal Dist-Kolhapur-416216*

Abstract:

Tin oxide (SnO₂) thin film was synthesized by using CBD method at room temperature (25°C). The structural, morphological properties were investigated by using XRD, SEM spectroscopy respectively. The structural studies revealed that synthesized annealed films of SnO₂ showed tetragonal phase. SEM study of the annealed film depicts nano agglomerated spheres like morphology which grown over complete substrate. The annealed films have been successfully applied for LPG gas sensor at different operating temperatures and at different concentrations. The room temperature synthesized thin films of SnO₂ showed maximum LPG gas response 37.45% at operating temperature 325° and 10 ppm gas concentration

Keywords: SnO₂ thin Films, Chemical bath deposition, X-Ray Diffraction, Optical properties, Gas sensing.

1. Introduction:

Semiconductor gas sensor are used as domestic as well as other hazardous gas detector to produce alarm at a given gas concentration to avoid gas explosion hazards. Such sensor should have high sensitivity, selectivity and long term stability of the alarm threshold. It helps to escape accidental leakages and explosions of inflammable gases. The sensitivity to target LPG gas has been studied in terms of degree of lowering of resistance which outputs the results in to digital signals in gas sensor unit.

Many metal oxide semiconducting materials have been used for gas sensor but very few of them are appropriate for a good response to the LPG gas. ZnO, SnO₂ and In₂O₃ are very common metal oxides are commercially available semiconducting gas sensor and they are more sensitive to many combustible, oxidizing and reducing gases [1]. Although many different oxides have been investigated for their gas sensing properties, commercially available gas sensors are made mainly of SnO₂ in the form of thick films, porous pellets, or thin film [2]. Tin oxide is n-type semiconductor [3] and has wide ($E_g = 3.6-3.8$ eV) band gap energy [4]. In recent years, doping, film forming, heat treatment, structure and so on has caught wide attention. It can be synthesized by Hydrothermal, Sol-gel, pulsed laser deposition, Spray pyrolysis, Magnetron sputtering and Thermal evaporation [4-11] etc. but Chemical bath deposition method is suitable for the synthesis of tin oxide due to its easy working, cost effectiveness, and rapid results. G.L.M.P Aponso et.al. had reported effects of enhanced photovoltaic dye-sensitized solar cell for Tin oxide. Jieun Kim et.al had reported Photo catalytic activity of tin oxide and Gas sensor applications

[12-13]. In this work, Tin oxide thin film has been successfully achieved by using chemical bath deposition method at room temperature and synthesized tin oxide thin film characterized by XRD, SEM, UV-Visible, and Resistivity and applied for LPG gas sensing application.

2. Experimental:

2.1 Chemicals Used:

Chromic Acid [Mixture of Concentrated Hydrochloric Acid (HCl) + Potassium Dichromate (K₂Cr₂O₇)] Anhydrous Stannic Chloride (SnCl₄), Triethanolamine (C₆H₁₅NO₃), Sodium Hydroxide (NaOH) Chemicals were purchased by Alfa Acer and used without any further purification.

2.2 Experimental Procedure:

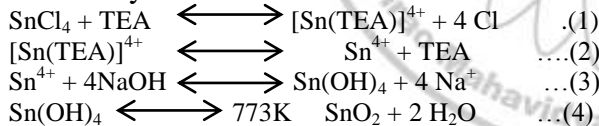
Synthesis of SnO₂ thin films was carried out by using CBD which is based on the stirring of alkaline bath of tin salt containing the substrates immersed in it. Initially, the glass micro-slides were cleaned with the soap solution and chromic acid and then subsequently washed with double distilled water followed by ultrasonically cleaning for 15 min. Afterward, 2.60 gm of anhydrous stannic Chloride was dissolved in Double distilled water to prepare 0.1M solution of Stannic Chloride. Then 1 ml Triethanolamine was added drop wise with continuous stirring for complex formation. Again, to this solution 2N Sodium hydroxide (NaOH) was added with constant stirring till the solution reaches to its superstation point. Finally this solution was kept at room temperature along with vertically inserted washed substrates for 48 hours without any disturbance. White colored deposition was obtained on glass substrates. These films were air dried for 2-3 hours and then subjected to annealing at temperature 600°C for 2 hours. To study the structural properties of annealed films, X-ray diffraction

patterns were obtained using X-ray diffractometer over 2θ (scanning angle range of 10° – 80° with Cu K α radiation). The surface morphological studies were carried out with scanning electron microscopy. Energy dispersive X-ray analysis (EDAX) was employed for the compositional studies. The gas sensing properties of synthesized films were studied.

2.3 Reaction Mechanism:

Nanoparticles growth involves two steps. In first step dissociation of Chloride salt of Tin was carried out in distilled water. Solutions of appropriate concentrations had been prepared and dissolved in distilled water with continuous stirring. After 5 min, stirred solutions were converted in to water soluble hydroxides of tin. Afterwards 1 ml Triethanolamine complexing agent was added with drop wise stirring. This results into the complex formation. Finally 2N NaOH solution was added to it. Initially, on addition of NaOH clear solution becomes converted into white viscous liquid but on addition of excess solution of NaOH solution turns to clear transparent solution. These reactions can be represented stepwise by following reaction mechanism in equation (1) to (4)

In second step, Nanoparticles so deposited on glass slide were annealed at 773K temperature to remove hydrated water containt.



3. Results and discussion

3.1. X-RD analysis

The structure and identification of phases of SnO₂ thin film obtained by CBD are investigated with the help of X-ray diffraction (XRD). Synthesized sample was characterized by Philips automated X-Ray diffractometer (PW-3710) equipped with crystal monochromator employing Cu-K α radiation of wavelength 1.5406 Å. The diffracting angle (2θ) is varied between 10° - 90° and the recorded XRD patterns for the thin films are shown in Fig.1 From Figure it is observed that the films deposited at room temperature has tetragonal phase in the major peaks appear at 2θ values are 26.9° , 34.3° , 38.9° , 52.1° , and 62.1° are corresponds the planes of (110), (101), (200) and (211) respectively. Average crystallite size is around 25 nm for the as-prepared glass deposited tin oxide. The obtained XRD

spectrum was confirmed by matching with the JCPDS file [No. No. 88-0287] . The average particle sizes were calculated from X-ray line broadening using the Scherer formula (5).

$$D = K\lambda/\beta\text{COS } \Theta \dots\dots\dots(5)$$

Where, K is constant called as the shape factor = 0.94, λ is the Wavelength, β is Full width at half maximum (FWHM) given in radian, Θ = It is the Bragg's angle, D = Nanoparticle size in nanometer Fig. 2 shows SEM micrographs of annealed SnO₂ thin films deposited at room temperature at various magnifications (a1) and (a2). The SEM micrograph films deposited at room temperature showed agglomerated spherical nanoparticle like morphology with interconnected clusters of particles were observed.

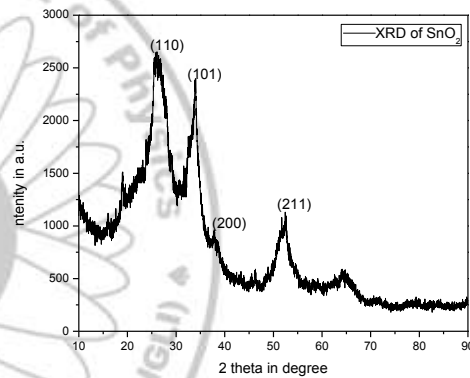


Fig.1: X-Ray Diffraction pattern of SnO₂ sample

3.2. SEM analysis



Fig.2: SEM images of SnO₂ with two different magnifications (a1) and (a2).

4. LPG gas sensor

4.1 Instrumentation

The gas sensing properties of synthesized films were studied using a “static gas-sensing system.” There were electrical feeds through the base plate. The heater was fixed below the base plate to heat the sample under test up to required operating temperatures. Al-Cr thermocouple was used to sense the operating temperature of the sensors. The output of the thermocouple was connected to digital temperature indicators. A gas inlet valve was provided at one port of the base plate. The required gas concentration inside the

static system was attained by injecting a known volume of test gas using a gas-injecting syringe. For electrical measurements, silver paste contacts were made on the sample of area 1 cm×1 cm. Initially, the I-V characteristics were studied within ±10V and it was found that in the above voltage range, the silver contacts showed ohmic behavior. The electrical resistance of films in air (Ra) and in the presence of test gas (Rg) was measured to evaluate the gas response, S, defined as follows(6)

$$S (\%) = \frac{Ra - Rg}{Ra} \times 100 \dots\dots\dots (6)$$

4.2 Effect of temperature

Before exposing to LPG gas, the SnO₂ films were allowed to be stable for electrical resistance for half an hour and the stabilized resistance was taken as Ra. Initially the gas response was studied as a function of operating temperature for annealed SnO₂ film. The temperature of the sensor surface is one of the most major parameters. The temperature affects the physical properties of the semiconductor such as charge carrier concentration, Debye length, work function etc. The optimum operating temperature for an effective sensor performance corresponds to that value at which material able to catalytically reduce or oxidize the target gas, simultaneously changing the electrical properties of the sensor material. Response of sensor depends on speed of chemical reaction on the surface and the diffusion of gas molecules to that surface.

These are activation processes, and the activation energy of chemical reactions is higher. At low temperature, the sensor response is restricted by the speed of chemical reaction while at higher temperature it is restricted by the speed of the diffusion of gas molecules to the surface. At some intermediate temperature, the speeds of two processes become equal, and at that point the sensor response reaches to its maximum [14]. According to this mechanism, for every gas, there is a certain temperature at which the sensor response reaches at its peak value. Above this maximum temperature, the gas response decreases due to desorption of the oxygen which are adsorbed on the surface of the sensor [14]. Another reason for the decrease in the gas response, could be the increase in the carrier concentration due to intrinsic thermal excitation which decreases the Debye length [16]. This length describes the size of the space-charge region next to the surface where the free carrier concentration may be affected by the surface species. In the present case we found that the sensor response reaches maximum 37.45% sensitivity at temperature 325° upon exposure of 10 ppm of LPG gas as shown in fig.3(a). Therefore, the temperature 325 was taken as an optimum operating temperature for further studies. Once the operating temperature was fixed the sensor response was studied at different gas concentrations.

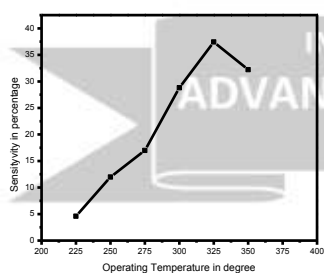


Fig 3 (a)

(a) Dynamic sensing transient of LPG gas at different operating temperature (b) Dynamic sensing transient of LPG gas response at different time. (c) Dynamic sensing transient of LPG for different concentration at temp. 325°C with respect to time.

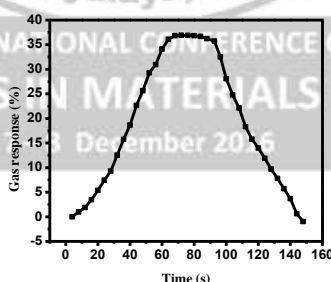


Fig 3 (b)

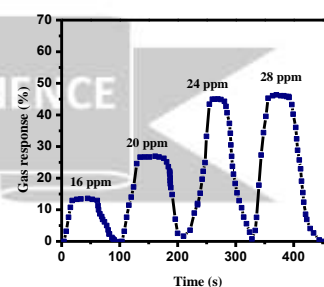


Fig 3 (c)

16 to 28 ppm at operating temperature 325°C. As the gas concentration increased from 16 to 28 ppm of LPG the response increased rapidly with concentration. However, at higher concentrations the increase in gas response value was steady and saturated. The response of a sensor mostly depends on the removal of adsorbed oxygen molecules by reaction with a target gas and generation of electrons. For a small concentration of gas, when gas exposed on a fixed surface area

4.3 Effect of ammonia gas concentration

The fig.4 reveals that the response increased from 12.5 to 59.7% for the sample with respect to LPG gas concentration increased from

of a sample there is a lower coverage of gas molecules on the surface hence, minor surface reaction takes place. Increases in surface reaction observed with increase in gas concentration due to a larger surface coverage. A further increase in

surface reaction will be gradual when the saturation point of the coverage of molecules is reached.

Conclusion

Tin oxide (SnO_2) thin film was synthesized by using CBD method at room temperature (25°C). The structural studies revealed that synthesized annealed films of SnO_2 showed tetragonal phase. SEM study of the annealed film depicts nano agglomerated spheres like morphology. The annealed films have been successfully applied for LPG gas sensor at different operating temperatures and at different LPG gas concentrations. Synthesized thin films of SnO_2 showed maximum LPG gas response 37.45% at operating temperature 325°C and 10 ppm gas concentration. It is also observed that the LPG gas concentration increases the sensitivity at constant temperature gradually increases till it reaches to its saturation point of concentration 28 ppm LPG gas.

References

1. C. Wang, "Metal Oxide Gas Sensors: Sensitivity and Influencing Factors," 2010, 2088.
2. K. Grossmann, *Semiconducting Metal Oxides Based Gas Sensors*, 2013, 88, 261–282.
3. S. Baco, "Study on Optical Properties of Tin Oxide Thin Film at Different Annealing Temperature."
4. Kiran Jain, *Synthesis and Controlling the Morphology of SnO_2 Nanocrystals via Hydrothermal Treatment*, ECS Transactions, 2006, 1 (21) 1-7
5. S.Gnanam, V.Rajendran "Luminescence Properties of EG-Assisted SnO_2 by Sol–Gel Process ", *Journal of Nanomaterials and Biostructures* 2010 (3), 699-704.
6. Adawiya J., A study of morphological, optical and gas sensing properties for pure and Ag doped SnO_2 prepared by pulsed laser deposition (PLD), *Science direct* 2013, 36 ,776.
7. F. De Estudios, S. Cuautitlán, C. De Ciencias, D. Tecnológico, U. Nacional, and A. De México, "Free-standing SnO_2 nanoparticles synthesized by hydrothermal route," 2008, 1, 741–743.
8. S. Mishra, C. Ghanshyam, N. Ram, and S. Singh, "Alcohol sensing of tin oxide thin film prepared by sol–gel process," 2002, 25, (3), 231–234.
9. M. A. Sánchez-garcía, "Characteristics of SnO_2 : F Thin Films Deposited by Ultrasonic Spray Pyrolysis : Effect of Water Content in Solution and Substrate Temperature," 2012, 2012, 690–696.
10. F. De Moure-flores, " SnO_2 : F thin films deposited by RF magnetron sputtering : effect of the SnF_2 amount in the target on the physical properties," 2013, 59, 335–338.
11. S. J. Ikhmayies, "Properties of Amorphous SnO_2 Thin Films , Prepared by Thermal Evaporation," 2012, 2, (4)173–177.
12. K. K. Khun, A. Mahajan, and R. K. Bedi, "Surfactant Assisted Growth of Nanostructured Tin oxide films for gas sensing applications," 2011, 7 (4) 303–308.
13. I. Hwang, "Gas sensing properties of SnO_2 nanowires on micro-heater," *Sensors Actuators B. Chem.*, 2009.
14. M. Gürbüz, *Applied Surface Science*, 2014, 318, 334–340.
15. C. Suryanarayan, 'X-Ray Diffraction: A Practical Approach', 1998 Plenum Press, New York.
16. P. Singh , *J Alloys and Compounds* 2009, 471, 11.



Studies on Nanosized Molybdenum Trioxide (α -MoO₃) Thin Films

S. A. Khalate, R. S. Kate and R. J. Deokate*

Vidya Pratishthan's Arts, Science and Commerce College, Baramati-413 133 (MS), India

*Corresponding Author's Mail-ID: rjdeokate@gmail.com, Tel.: +91- 02112- 243832, Fax: +91-02112-243488.

Abstract

The molybdenum trioxide (α -MoO₃) thin films of single orthorhombic phase have been deposited by using spray pyrolysis technique on the glass substrates. α -MoO₃ thin films were characterized for structural, morphological and optical measurements. XRD results shows that α -MoO₃ thin films are polycrystalline, crystallizes in orthorhombic structure crystalline quality improved with substrate temperature. Surface morphological study shows the conversion of grains into nanorod like structure with increasing substrate temperature. The value of optical band gap shows 2.72 eV at the substrate temperature 400 °C.

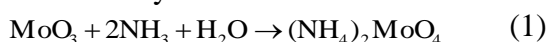
Keywords: Thin film, orthorhombic phase, optical properties

1. Introduction

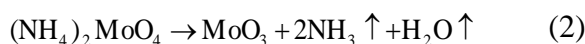
Metal oxide semiconductor films have great importance and demand because of their special physical-chemical properties and stability. Literature survey shows, the effect of temperature on the delocalization of electrons and different phases among the multi-valance states in MoO₃ thin films are present [1]. These phases are stable orthorhombic α -MoO₃, meta-stable monoclinic β -MoO₃ and hexagonal γ -MoO₃. The thermodynamically stable α -MoO₃ has α -MoO₆ octahedral base in its unit cell, and all of the α -MoO₃ compounds share edges and corners forming zigzag chain, layered structure stacked along (0 *k* 0) direction [2]. The physical properties of the films depend on certain parameters such as substrate temperature, heat treatment, substrate material and the preparation method itself. Keeping in view all these aspects an attempt has been made to deposit α -MoO₃ thin films at different substrate temperatures by spray pyrolysis. The influence of it on the microstructural, morphological and optical properties of molybdenum trioxide reported.

2. Experimental

0.1 M molybdenum trioxide powder dissolved in ammonia solution forming ammonium molybdate.



The solution was sprayed onto the glass substrates at various temperatures within 350-450 °C. The pyrolytic decomposition of (NH₄)₂MoO₄ on the surface of the substrates results in the formation of α -MoO₃ thin films according to the following equation:



The structural properties of α -MoO₃ thin films were carried out by X-Ray Diffractometer (XRD Bruker AXS D8 Advance Model) with the

radiation source Cu-K α ($\lambda=1.5406$ Å) in the 2θ range 20° to 80°. Surface morphology of the deposited α -MoO₃ thin films was studied with field emission scanning electron microscope (FE-SEM SU8000 Hitachi). The optical parameters were studied at room temperature in the wavelength range 400-900 nm through Uv-Visible spectroscopy (Perkin Elemer Lambda 1050 Uv-Vis-NIR Spectrophotometer).

3. Results and Discissions

i) X-Ray Diffraction Study

The substrate temperature change will improve the crystallinity, stoichiometry and other structure related parameters of thin films. Fig. 1(a) shows the typical X-ray diffraction pattern of α -MoO₃ thin films deposited at various substrate temperatures (350-450 °C). All these observed peaks correspond to stable orthorhombic α -MoO₃ phase according to the standard JCPDS data card: 01-0706 [3]. From XRD patterns integrated intensities of the diffraction peaks suggests that α -MoO₃ films grow in the preferential orientation (0 *k* 0) direction where, *k*=4, 6. The average crystallite size (*D*) of the prepared films was calculated by the Scherrer relation [4]. It was initially increases with substrate temperature, reaches maximum 34.83 nm at 400 °C and decreases for higher temperature. Increase in the crystallinity and crystallite size is due to the optimum rate of supply of thermal energy for recrystallization [5].

ii) Morphological Study

Fig. 1(b) show surface morphology of α -MoO₃ thin films prepared at 400 °C substrate temperature. As temperature increases to 400 °C, multilayered plates with nanorods and large pores are observed. The nanorods are about 1 μ m long and 200 nm thick. They are agglomerated in reticulated oblate structured grains. Porous

structure confirmed due to random arrangement of the nanorods.

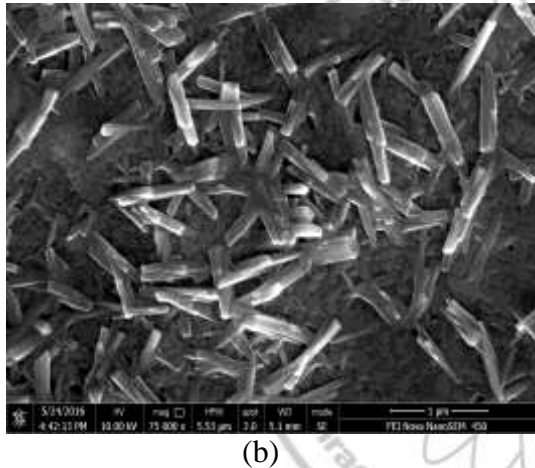
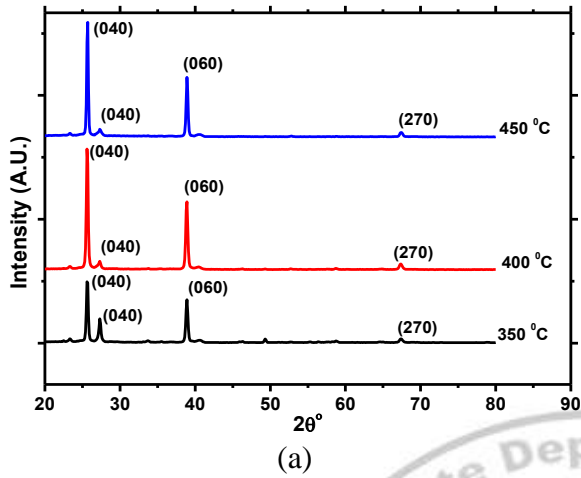


Fig. 1. (a) X-ray diffraction patterns at various substrate temperatures and (b) Surface FE-SEM

images of α -MoO₃ thin film deposited at 400 °C substrate temperature.

iii) Optical Study

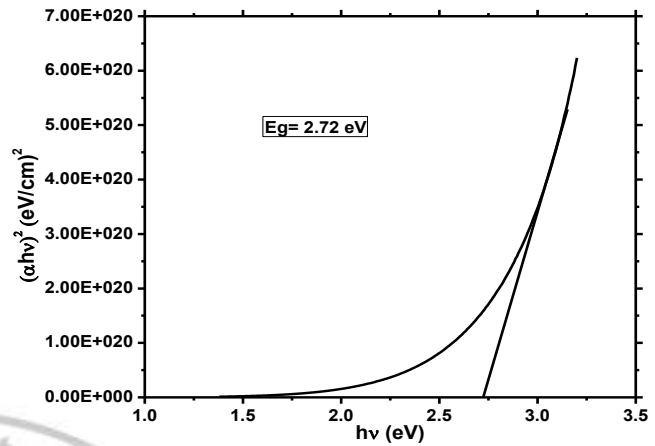


Fig.2. Plot of $(\alpha hv)^2$ versus the photon energy (hv) of α -MoO₃ thin films for 400 °C substrate temperature.

The optical band gap energy E_g can be determined from the experimental values of absorption coefficient as a function of photon energy $h\nu$, using the equation [6]. The plot of $(\alpha h\nu)^2$ versus $(h\nu)$ is shown in Fig. 2 which is linear at absorption edge, indicating a direct allowed transition. The value of absorption coefficient is found to be of the order of 10^4 cm^{-1} . The band energy is found to be 2.72 eV at 400 °C substrate temperature.

Conclusions

The effect of substrate temperature on the structural, morphological and optical properties of α -MoO₃ thin films prepared by spray pyrolysis was investigated. XRD results reveal that the as prepared films shows single orthorhombic phase for all substrate temperatures. The nanorod like structures were observed at 400 °C agglomerated in reticulated oblate structured grains. Optical absorption study revealed direct band gap nature with band gap energy 2.72 eV at 400 °C.

Acknowledgement

Authors wish to acknowledge the SERB (DST), New Delhi (India) for the financial support through young scientist scheme (SB/FTP/PS-079/2014).

References

1. Liang Zhou, Lichun Yang, Pei Yuan, Jin Zou, Yuping Wu, Chengzhong Yu, α -MoO₃ Nanobelts: A High Performance Cathode Material for Lithium Ion Batteries, J. Phys. Chem. C. 114 (2010) 21868-21872.
2. Alexander Gavriluk, Ulf Tritthart, Wolfgang Gey,

- The nature of the photochromism arising in the nanosized MoO₃ films, Sol. Energy Mater. Sol. Cells 95 (2011)1846-1851.
3. JCPDS data card: 01-0706.
4. P. Scherrer, Gottinger Nachrichten 2 (1918) 98-100.
5. H. Buckley, Crystal Growth, John Wiley & Sons, New York, 1951.
6. P. Kireev, La Physique des semiconducteurs, Mir, Moscou, 1975.

Influence of Cd substitution on structural and photocatalytic activity of copper ferrites synthesized by sol-gel auto-combustion method

K. R. Sanadi^a, S. P. Patil^b, H. D. Dhayagude^a, G. S. Kamble^c

^aDepartment of chemistry, Doodhsakhar Mahavidyalaya, Bidri, Kolhapur. (Maharashtra), India 416208

^bDepartment of chemistry, Rajaram college, Kolhapur. (Maharashtra), India 416004

^cDepartment of chemistry, KIT college, Kolhapur. (Maharashtra), India 416004

Corresponding author: - Dr. Sanadi. K. R, Email: sanadikishor@gmail.com

Abstract:

Nanocrystalline cadmium substituted copper ferrites ($\text{Cu}_{1-x}\text{Cd}_x\text{Fe}_2\text{O}_4$, where, $x = 0.0, 0.25, 0.50, 0.75, 1.0$) were synthesized by simple, cost effective, sol-gel auto-combustion method. The entire samples were characterized by different techniques. The phase composition of Cu-Cd ferrites powder was characterized by x-ray powder diffraction analysis (XRD). The crystallite size varies in between 14 to 24nm. The photocatalytic activity of $\text{Cu}_{1-x}\text{Cd}_x\text{Fe}_2\text{O}_4$ was studied in presence of ultra violet light. After 240min CuFe_2O_4 shows good photocatalytic performance for degradation of Rhodamine B dye. But better photocatalytic performance was occurs at 0.10g Pd loaded CuFe_2O_4 catalyst varying from 0.020g to 0.10g at natural pH (7) with 10ppm Rhodamine B solution.

Keywords: - Sol-gel chemistry, Cubic spinels, Semiconductors, Nanoparticles, Photoactivity.

1. Introduction:

Spinel types of ferrites having general formula AFe_2O_4 (A = Ni, Cu, Cd, Fe, Co etc.) are technologically important class of metal oxides because of their varying oxidation state, high electric resistivity and overlap of their optical absorption spectrum with UV radiation [1-2]. These properties are controlled by the nature of their ions, their charge and site distribution amongst tetrahedral and octahedral sites. A literature survey indicates that considerable work has been on zinc chromium ferrite, manganese chromium ferrite and nickel chromium ferrite [3]. The structural and electrical properties of ferrites are found to be sensitive to their composition and microstructure, which in turn are dependent on their processing conditions [4]. In mixed ferrites, the conductivity is found to be dependent on the availability of $\text{Fe}^{2+} / \text{Fe}^{3+}$ ions and $\text{M}^{2+}/\text{M}^{3+}$ pairs in octahedral sites. Thus, cation distributions along with their characteristic oxidation states play a dominant role in the conduction process.

Textile dyes containing organic moieties and having low biodegradability have become major water environmental pollutant. These organic pollutants during dying lose their identity and get mixed with water streams in many industrial areas. So, to solve this eco-problem, photocatalytic degradation of these dyes using inorganic nano-semiconductor is a current need. Therefore, decomposition of organic dyes using various nanocomposites under irradiation of UV light is now emerging out as a new research area [5].

In the present paper, we have reported the structural and photocatalytic properties of cadmium substituted copper ferrites synthesized by sol-gel method.

2. Experimental Procedure

2.1 Sample preparation:

Polycrystalline powder of $\text{Cu}_{1-x}\text{Cd}_x\text{Fe}_2\text{O}_4$ was prepared by sol-gel auto combustion method. The A.R. Grade citric acid ($\text{C}_6\text{H}_8\text{O}_7 \cdot \text{H}_2\text{O}$), copper nitrate [$\text{Cu}(\text{NO}_3)_2 \cdot 5\text{H}_2\text{O}$] cadmium nitrate [$\text{Cd}(\text{NO}_3)_2 \cdot 4\text{H}_2\text{O}$] and ferric nitrate [$\text{Fe}(\text{NO}_3)_3 \cdot 9\text{H}_2\text{O}$] were used as starting materials. The samples were prepared by sol-gel autocombustion method as prepared in our previous work [6].

Table 1. Lattice constant, Crystallite size, X-ray (where $x = 0.0, 0.25, 0.50, 0.75, 1.0$) density, Physical density of the system $\text{Cu}_{1-x}\text{Cd}_x\text{Fe}_2\text{O}_4$

Compos ition	Lattice Constant s (Å)	Crystallite Size (nm)	X-ray density, (d_x) (gm/cm^3)	Physical density (d_B)
X = 0.0	8.3565	14.17	5.4841	4.9843
X = 0.25	8.4819	14.59	5.7641	5.0683
X = 0.50	8.5575	22.00	6.0440	5.2440
X = 0.75	8.6505	22.12	6.3471	5.4580
X = 1.0	8.7127	24.21	6.6042	5.8126

2.2 Preparation of Pd doped CuF_2O_4 :

To a suspension of CuF_2O_4 (1.0 g) in absolute ethanol (100 ml), $[\text{PdCl}_2]$ wg ($w = 0.020$,

0.040, 0.060, 0.080, 0.10 g) was added separately. The olive green slurry was stirred for 7 h at room temperature. The solvent was then evaporated under reduced pressure on rotatory evaporator. The Pd impregnated solid was dried in oven at 200 °C for 6 h to give a dark grayish green powder.

2.3 Characterization:

X-ray diffraction Philips PW1710 x-ray diffractometer with Cr $K\alpha$ radiation (2.2927 Å) was used to determine the phase, lattice parameter and average grain size. The morphology and size of particle were observed by scanning electron microscopy (SEM) while element contents were determined by using an energy dispersive x-ray spectroscopy (EDAX). The degradation experiment was conducted in a semi-batch photocatalytic reactor with initial concentration of Rhodamine B 10 mg/L.

3. Results and discussion:

3.1 X-ray diffraction (XRD) studies:

The structural characterization of the ferrite powders as prepared was carried out using x-ray diffractometer. The average crystallites size D was calculated using most intense peak (311) employing the Scherer formula [7].

$$D = 0.9\lambda / \beta \cos\theta$$

Where β is the FWHM of the most intense peak (311) and θ is the Bragg's angle for the actual peak. Fig.1 shows the x-ray diffractograms of $Cu_{1-x}Cd_xFe_2O_4$ ($x = 0.0; 0.25; 0.50; 0.75; 1.0$) samples. The XRD patterns clearly indicate that the prepared sample contain cubic spinel structure only. The close examinations of XRD patterns reveal that the diffraction peaks become shorter with increasing cadmium content x . The sizes of crystallites in the sample were evaluated by using Scherer formula. The results are shown in **Table no.1**.

3.2 Elemental and Morphological analysis:

The typical EDAX pattern for the sample $Cu_{1-x}Cd_xFe_2O_4$ ($x = 0.0; 0.50; 1.0$) were studied which gives the elemental composition in the sample. The compound shows the presence of Cu, Cd, Fe, and O without any impurities. Thus the result indicates that most of the undesired precursor materials have been completely removed from the product.

Morphological studies of the samples were carried out by using scanning electron microscope (SEM). The grain size of the sample was calculated by using Cottrell's method [8], which

was lie in between 0.71 μm to 0.90 μm . The SEM micrograph further reveals that the grains are uniformly distributed throughout the surface.

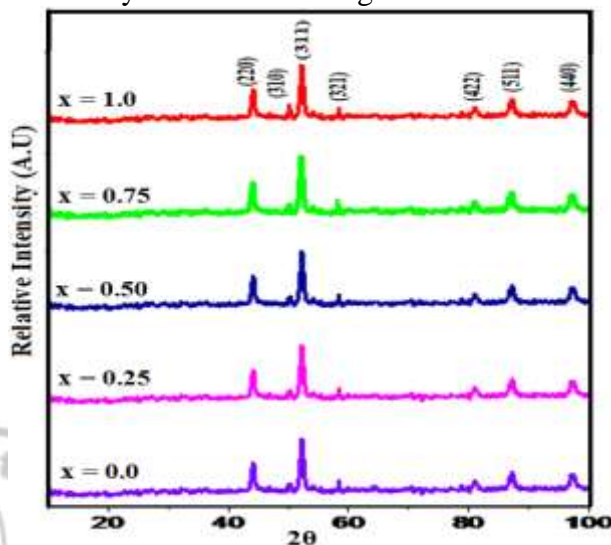


Fig.1. XRD patterns of the system $Cu_{1-x}Cd_xFe_2O_4$

3.3 Photocatalytic Activity:

Photocatalytic degradation of Rhodamine B was carried out in a semi-batch photocatalytic reactor with initial concentration of RB 10mg/L. In the present investigation it is observed that as the irradiation time increases the absorption of the solution decreases which was shown in Fig.2 (b). Mineralization efficiency of RB by $CuFe_2O_4$ is maximum i.e 67 % while that of $CdFe_2O_4$ is lower i.e. 52 % in UV light after 240 min. So $CuFe_2O_4$ has been considered as an optimized catalyst for palladium loading for degradation of RB Dye. Different concentrations of Pd were loaded on $CuFe_2O_4$ catalyst varying from 0.020g/L to 0.10g/L at natural pH 8 which was shown in Fig 2(b). Maximum 94 % Mineralization has been observed at 0.10 g/L and 89% at 0.020 g/L in UV light after 40 min. The enhancement of the degradation is due to the increase in the amount of catalyst which increases the number of active sites available on the catalyst surface for the reaction.

4. Conclusions

A series of cadmium substituted copper ferrite were synthesized by the pH controlled sol-gel auto combustion method. XRD data reveals the formation of cubic single spinel phase only. The copper ferrite loaded with palladium was observed to have an excellent photo mineralization of water on reduced time scale.

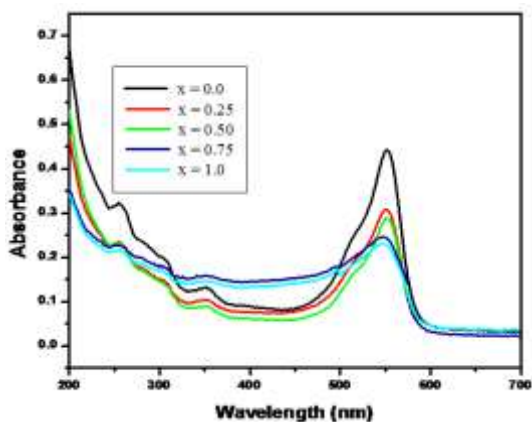


Fig.2 (a) photocatalytic degradation of Rhodamine B by $Cu_{1-x}Cd_xFe_2O_4$ ($0 \leq X \leq 1$)

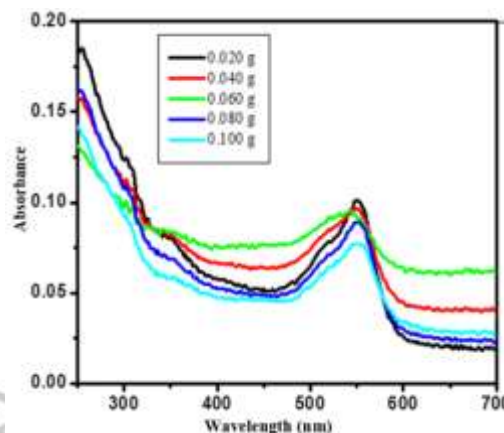


Fig.2 (b) photocatalytic degradation of Rhodamine B by Pd loaded $CuFe_2O$

References

1. C. Suchomski, C. Reitz, K. Brezesinski, C.T. Desouse, M. Rchnke, K. Limura, J.P.E. deAraujo, and T. Brezesinski, *Chem. Mater.* 24 (2012) 155-165.
2. D. Fino, N. Russo, G. Saraceo, V.J. Specchia, *Catal.* 242 (2006) 36-47.
3. D.C. Kim, S.K. Ihm, *Environ. Sci. Technol.* 35 (2001) 222-226.
4. S. Wang, K. Huang, C. Hou, L. Yuan, X. Wu and Dayong, *Roy. Socie. Chem, Dalton. Trans.* 44 (2015) 17201-17208.
5. M. H. Habibi, S. Tangestananejad, B. Yadollahi, *Appl. Catal. B: Environ.* 33 (2001) 57.
6. P. P. Hankare, K. R. Sanadi, N. M. Patil, K. M. Garadkar, I. S. Mulla, *J. Alloys Comps* 540 (2012) 290.
7. Raghavendar A.T, Pajic Zadro, Milekovic D.K, Venkateshwar Rao T.P, Jadhav K.M. Ravindar D, *J. Mag. mag. mater.* 2007, 316: 1
8. A. H. Cottrell, "An Introduction to Metallurgy" Edward Arnold Publishers Ltd. London, (1967) 172.

Infrared and Dielectric Study of Ti-Ni-Zn Ferrites

J. S. Ghodake^{*a}, T. J. Shinde^b, M. M. Sutar^c, P. K. Maskar^a

^aDepartment of Physics, P.D.V.P. College, Tasgaon, MH, India

^bSmt. K. R. P. Mahavidyalaya, Islampur, MH, India

^cShikshanmaharshi Dr. BapujiSalunkhe, Mahavidyalaya, Miraj, MH, India

*Email ID:jeevan.ghodake@rediffmail.com, Tel:91-02346-250665,Fax:91-02346-250665

Abstract

TiNiZn ferrites have been synthesized by a standard ceramic method. The Fourier transform infrared spectra of sintered powder at 1200°C were recorded in the range 800 cm⁻¹ – 400 cm⁻¹. The infrared spectra show two absorption bands which were attributed to tetrahedral (A) and octahedral (B) sites of the spinel lattice. The force constants for tetrahedral (k_t) and octahedral (k_o) sites have been determined. The real dielectric constant (ε'), complex dielectric constant (ε'') and resistivity were investigated at room temperature as a function of frequency by using Hioki LCR-Q meter. The plot of dielectric constant with frequency shows a normal dielectric behavior of spinel ferrites. The results show a usual dielectric dispersion due to the Maxwell – Wagner type of interfacial polarization.

Keywords: Ferrite, Infrared, Dielectric constant, Ceramic method

1. Introduction

Ferrites have good dielectric properties and a large number of applications from microwave to radio frequencies. The study of dielectric properties produces valuable information on the behavior of localized electric charge carriers leading to greater understanding of the mechanism of dielectric polarization in the ferrite samples. Dielectric properties of ferrite are stable at higher frequency; hence they can be used for relevant applications. Therefore it is important to study the dielectric properties of ferrites as a function of temperature and frequency [1]. Ni-Zn ferrite has unique high dielectric properties which makes them useful in designing electronic devices. High frequency applications of Ni-Zn ferrites include large number of microwave components such as circulators, isolators, gyrators, phase shifters, and switches for microwave integrated circuits [2].

Dielectric and magnetic behavior of ferrites depends upon the structural and mechanical properties such as X-ray diffraction, Scanning electron microscopy and infrared spectroscopy. Also these behavior depends upon type of ions, their charge distribution between tetrahedral (A) and octahedral (B) sites, microstructure and preparation method. Infrared spectroscopy is powerful analytical techniques used for analysis of different cations present on tetrahedral (A) and octahedral (B) sites of the spinel lattice. It is used to investigate various vibrational and rotational modes in organic and inorganic molecules which are used to study structure of molecules and nature of bonds. Waldron [3] attributed the high frequency band ν_1 to tetrahedral complexes and low frequency band ν_2 to octahedral complexes. The detailed analysis of IR spectra helps to determine elastic moduli,

Debye temperature, molecular heat capacity, longitudinal and shear velocity [4]. Elastic constants closely related to many physical properties of solids like Debye temperature, internal stress, acoustic-phonon frequencies [5-7].

Ghatage et al [8] studied electrical conduction in Ti substituted Ni – Zn ferrite. They have found that the increase in resistivity with composition is attributed to increase in Ti concentration in the system. Patil et al [9] studied the frequency dependent dielectric properties of Ni-Mg-Zn-Co ferrites. He pointed out that dielectric constant with frequency show a normal dielectric behavior of spinel ferrites. Nasir et al [10] investigate structural, electrical and magnetic properties of Ni – Zn ferrites prepared by sol-gel and co-precipitation methods. They have show that low dielectric constant materials are required for high frequency applications to reduce dielectric losses and the skin effect. Ghatage et al [11] reported electrical resistivity and thermoelectric power as a function of temperature of Ti substituted Ni – Zn ferrite. The aim of the present work is to study infrared spectral properties and dielectric properties of Ni_{0.55}Zn_{0.45}Ti_xFe_{2-x}O₄(x=0, 0.005) compositions were prepared by a standard ceramic method sintered at 1200°C.

2. Experimental details

The compositions Ni_{0.55}Zn_{0.45}Ti_xFe_{2-x}O₄(x=0, 0.005) prepared by standard ceramic method using pure metal oxides of NiO, ZnO, TiO₂ and Fe₂O₃. These oxides were weighed in the required mole proportions using single pan balance having least count 0.001gm and mixed thoroughly in the agatemortar in acetone for about 2hrs. The mixture of each composition was presintered in platinum crucible at 750°C to

achieve homogenization of end products. The pre sintered samples were then ground by agate mortar in acetone medium and fine powder was collected.

The presintered powder was mixed with small amount of polyvinyl alcohol and uniaxially pressed at 6 tones/inch to form pellet shaped sample with diameter 1cm and thickness 3mm and then sintered at 1200⁰C. The Perkin – Elmer infrared spectrometer was employed to study the absorption spectra of Ni_{0.55}Zn_{0.45}Ti_xFe_{2-x}O₄(x=0, 0.005) ferrite powder sintered at 1200⁰C. Fourier transform infrared spectra of the powders were recorded using the KBr pellet method in the spectral range 800 cm⁻¹ – 400 cm⁻¹. The dielectric measurements were made using the two-probe method. The pellets with silver paste on both sides of 1cm diameter and 3mm thickness were used for the dielectric measurements which were carried out at room temperature. The real dielectric constant (ε'), complex dielectric constant (ε''), and electrical resistivity (ρ) were measured with frequency by using Hioki (3532-50) LCR-Q meter. The dielectric constant (ε') of the ferrites sample was calculated by using the relation [12],

$$\epsilon' = \frac{C_p \times d}{\epsilon A}$$

where, ε₀ = free space permittivity (8.854X10⁻² pF/cm), C_p = capacitance of the specimen in pF, d = thickness of the specimen in cm and A= area of the specimen in cm².

The complex dielectric constant (ε'') of the ferrite samples is given by

ε''= ε' tanδ, from the value of resistance resistivity was calculated using relation.

$$\rho = \frac{\pi r^2}{d} R \quad \text{where } r \text{ is the radius of pellet.}$$

3. Result and discussion

3.1 Fourier transforms infrared spectral analysis

The infrared of a sample is recorded by passing a beam of infrared light through the sample. When frequency of the infrared is same as the vibrational frequency of a bond, absorption occurs. The Fourier transform infrared absorption spectra of the compositions Ni_{0.55}Zn_{0.45}Ti_xFe_{2-x}O₄(x=0, 0.005)sintered at 1200⁰C in the range 800 cm⁻¹ – 400 cm⁻¹ are shown in figure 1.

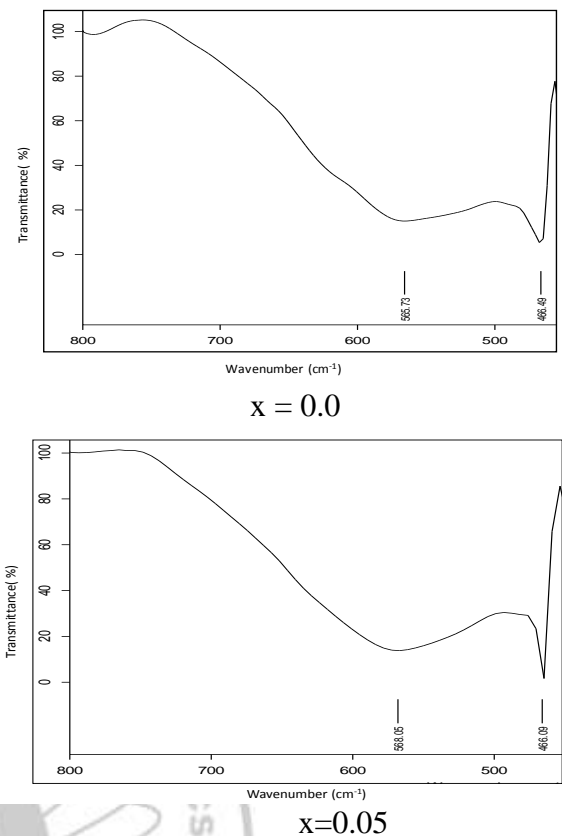


Fig. 1 Fourier transforms infrared absorption spectra of Ni_{0.55}Zn_{0.45}Ti_xFe_{2-x}O₄(x=0, 0.005)

Infrared absorption spectra indicate the presence of two absorption bands which is a common behavior of the spinels. The first band observed at frequency of 588 cm⁻¹ to 566 cm⁻¹ (ν₁) is attributed to the stretching vibration of tetrahedral group Fe³⁺- O²⁻ and second band observed at frequency of 466cm⁻¹ (ν₂) is attributed to the stretching vibration of octahedral group Fe³⁺-O²⁻. The existence of two bands ν₁ and ν₂ shows that samples are single phase spinel ferrites. The force constant for tetrahedral site (k_t) and octahedral site (k_o) were calculated from the method suggested by Waldron [3]. Table 1 shows data on the values of the force constant for tetrahedral site (k_t) and octahedral site (k_o).

Table1. Spectral analysis data for Ni_{0.55}Zn_{0.45}Ti_xFe_{2-x}O₄ (x = 0, 0.005)

x	ν ₁ cm ⁻¹	ν ₂ cm ⁻¹	k _t x 10 ² N/m	k _o x 10 ² N/m
0.0	588.05	466.09	1.56	1.07
0.005	565.73	466.49	1.44	1.07

3.2 Dielectric Properties

The dielectric properties of ferrites sensitively depend on method of preparation, the sintering temperature, the sintering atmosphere

and the amount and type of substitution. The polycrystalline ferrites have high dielectric constant at low frequencies which decrease to a low value at high frequencies. The dispersion in the dielectric properties of the polycrystalline ferrites has been attributed to the inhomogeneous nature of these materials as suggested by Maxwell and Wagner Phenomenological theory. Kuanar et al[13] have reported dispersion in electrical properties of titanium substituted lithium ferrites.

They observed decrease a conductivity, loss tangent, and dielectric constant on addition of titanium. The observed values of dielectric data for $Ni_{0.55}Zn_{0.45}Ti_xFe_{2-x}O_4$ ($x=0.0, 0.005$) at sintering temperature $1200^{\circ}C$ for 10 KHz and 1MHz are summarized in Table 2.

The frequency variation of real dielectric constant (ϵ'), complex dielectric constant (ϵ'') and resistivity of $Ni_{0.55}Zn_{0.45}Ti_xFe_{2-x}O_4$ ($x=0, 0.005$) compositions are shown in fig. 2,3 and 4.

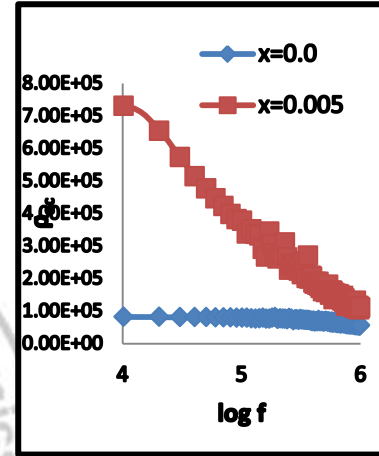
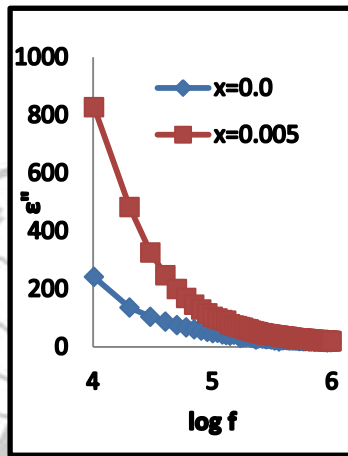
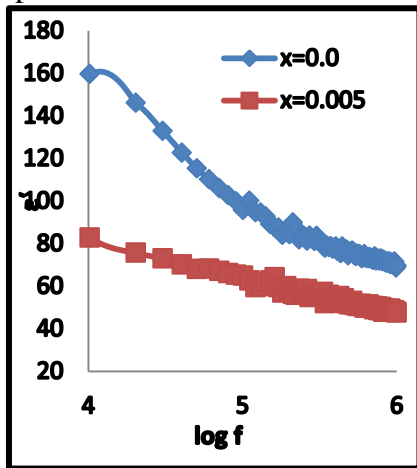


Fig.2 Frequency variation of ϵ' Fig.3 Frequency variation of ϵ'' Fig.4 Frequency variation of ρ

Table 2 Dielectric data for $Ni_{0.55}Zn_{0.45}Ti_xFe_{2-x}O_4$ ($x=0.0, 0.005$)

x	Dielectric constant (ϵ')		Dielectric constant (ϵ'')		$\rho_{ac} \times 10^5 \text{ Ohm/m}$	
	10kHz	1MHz	10kHz	1MHz	10kHz	1MHz
0.0	160	70	241	16	0.82	0.56
0.05	83	48	827	19	7.3	1.1

It is observed that the dielectric constant decreases with increasing frequency and then at higher frequency becomes almost steady. The observed variation of dielectric constant is explained on the basis of space charge polarization due to the inhomogeneous dielectric structure discussed by Maxwell and Wanger. The polarization process takes place through the mechanism similar to the conduction process [14]. The Dielectric polarization in ferrites is depends on electron exchange between Fe^{2+} and Fe^{3+} ions. The variation in dielectric constant at lower frequencies can be well explained with the Maxwell- Wagner interfacial polarization effect, in agreement with the koops phenomenological theory [15].

The frequency variation of resistivity of $Ni_{0.55}Zn_{0.45}Ti_xFe_{2-x}O_4$ ($x=0, 0.005$) compositions

are shown in fig.4. Resistivity of spinel ferrites depends on sintering temperature, chemical composition, grain size etc. The ac resistivity of ferrites is explained by electron hopping mechanism occurring between multivalent ions at different sites as well as microstructure. The observed values of resistivity at sintering temperature $1200^{\circ}C$ are summarized in Table 2. It is seen that with the addition of titanium in Ni-Zn ferrite the dielectric constant decreases while the resistivity increases. It is clearly evident that nickel has strong preference for B-sites, while zinc has strong preference for A-site and Fe^{3+} ions get distributed over A and B sites. Increase of titanium concentration has an effect of reducing the net Fe ion concentration.

4. Conclusions

$\text{Ni}_{0.55}\text{Zn}_{0.45}\text{Ti}_x\text{Fe}_{2-x}\text{O}_4$ ($x=0, 0.005$) composition were successfully prepared by a standard ceramic method. The Fourier transform infrared spectra of sintered powder at 1200°C were recorded in the range $800\text{ cm}^{-1} - 400\text{ cm}^{-1}$. The infrared spectra show two absorption bands which were attributed to tetrahedral (A) and octahedral (B) sites of the spinel lattice. The first band observed at frequency of 588 to 566 cm^{-1} (ν_1) and second band observed at frequency of 466 cm^{-1} (ν_2). The variation of dielectric constant with frequency shows a normal dielectric behavior of spinel ferrites. It is observed that dielectric constant decreases with increase of frequency and then at higher frequency becomes almost steady. The observed variation of dielectric constant can be explained on the basis of space charge polarization as discussed by Maxwell and Wanger theory. The substitution of titanium plays an important role in changing electrical properties of ferrites.

References

1. Ravinder, A. Chandrashekar Reddy, Mater. Lett. 57(2003)2855.
2. Santosh s Jadhav, Sagar E. Shirsath, B. G. Toksha, D. R. Shengule, K. M. Jadhav, Journal of optoelectronics and Advanced Materials, Vol. No. 10, October 2008, p 2644.
3. Waldron R. D., Phys Review, 99, No. 6 (1955) 1727.
4. Modi K B, Gajera J D, Pandya M P, Vora H G, Joshi H H, Pramana Journal of Physics, Vol. 62, No. 5 (2004) 1173.
5. Sihan Lin, Yusheng He, Chongde Wei, Zhaohui Shen, Supercond. Sci. Technol. 2(1989) 145.
6. Lakhani V K, Modi K B, Solid State Sci. 12 (2010) 2134.
7. Reddy P Venugopal, Rao T Seshagiri, Solid State Commun. 56 (1985) 985.
8. Ghatage A. K, Kolekar Y. D., Patankar K. K. and Patil S. A., Proceeding of the solid state physics symposium 41 (1998).
9. Patil S. B., Patil R. P., J. S. Ghodake, B. K. Chougule, Journal of Magnetism and Magnetic Materials 350 (2014) 179-182.
10. Nasir S. and M Anis-ur-Rehman Phys. Scr. 84 (2011) 025603 (7pp)
11. Ghatage A. K, Tamboli S. H., Patil R. N., Patil R. A., Archives of Physics Research, 2011, 2(1):1-5
12. Ghodake J S, Kambale R C, Kulkarni S D, Sawant S R, and Suryavanshi S S, Smart Mater. Struct. 18 (2009).
13. Kuanar B.K.G.P. Srivastava and PranKishan Proceedings of International conference on ferrites -5 227,(1989)
14. Gul I H, Amin F, Abbasi A Z, Anis-ur-Rehman M Maqsood A 2007 Scr. Mater. 56 497.
15. A. Sutka, K A Gross, G. Mezinskis, G Bebris M KnitePhys. Scr. 83 (2011)025601 (6pp)



INTERNATIONAL CONFERENCE ON
ADVANCES IN MATERIALS SCIENCE
 7 – 8 December 2016

Synthesis of High Dielectric Constant and Low Loss Lead Zirconate Titanate for By-Pass Capacitor in Microelectronics and Energy Storage Devices

C.M. Kanamadi^{a*}, A.A.Wali^a, V.P. Kothavale^b

^aDepartment of Physics, Devchand College, Arjunnagar, Dist:Kolhapur - 591237

^bDepartment of Physics, Bhogavati College, Kurukali, Dist: Kolhapur – 416001

*Author for correspondence: cmkanamadi@gmail.com

Abstract:

Low loss and high dielectric constant lead zirconate titanate $\text{PbZr}_{0.52}\text{Ti}_{0.48}\text{O}_3$ (PZT) was synthesized by double sintering solid state reaction method. The crystal structure and homogeneity of the sample was characterized by X – ray diffraction and field emission scanning electron microscope (FESEM). The dependence of dielectric constant on frequency and temperature was investigated. The dielectric constant measured by an impedance analyzer HP 4194 A is 6316 at 1 MHz, which is higher than the dielectric constant obtained in other ferroelectrics. This ceramic is the best candidate for by pass capacitor in microelectronics and energy storage devices due to its high dielectric constant.

1. Introduction

Lead zirconium titanate $\text{PbZr}_{0.52}\text{Ti}_{0.48}\text{O}_3$ (PZT) ceramics with high dielectric constant are widely required for applications such as bypass capacitors in microelectronics and energy storage devices. These materials have also great interest since they offer promising ferroelectric and piezoelectric properties and the ability of tailoring their properties either by changing their composition or by doping them with different ions. These ceramics can be widely used as an ultrasonic transducer for medical diagnostic applications [1 - 4]. Recently, the application of PZT ceramics for piezoelectric transformers was vigorously investigated for lighting liquid crystal display (LCD) backlights [5 – 6]. The spontaneous polarization of this type of material can be used to produce small actuator components, ultrasonic transducers, hydrophones, speakers, sensors, electrical resonators and other devices for microelectronics [7]. Ferroelectric properties, crystal structure and microstructure of PZT are greatly affected by the compositional fluctuations near the morphotropic phase boundary (MPB). The best piezoelectric and ferroelectric properties can be obtained near the MPB. The MPB of ABO₃ perovskite type $\text{PbZr}_{1-x}\text{Ti}_x\text{O}_3$ solid solution have been attributed to a mixture of ferroelectric tetragonal and rhombohedral phases for

composition $x = 0.48$. The high dielectric constant and low loss tangent at MPB make PZT-based compounds as one of the most prominent and useful electroceramics [8].

It is well known that the dielectric permittivity of the materials has a crucial influence on deciding its piezoelectric property. High dielectric permittivity and large remnant polarization of these ferroelectrics make them useful in the synthesis of dynamic random access memories and non-volatile random access memories. These materials have also practical importance because of low operating voltage, leakage current and their dielectric permittivity [9]. So far various different methods have been used to synthesize such materials. Among them, solid state reaction method is most widely used because of their cost effectiveness, ease of fabrication and better control of their process parameters [10]. By this method, it is possible to control the stoichiometric ratio of Zr and Ti near the MPB.

2. Synthesis and characterization

Commercially available PbO , ZrO_2 and TiO_2 powders were used as the starting materials to synthesize PZT. The appropriate amount of the powders for the designated PZT ceramic was ball milled for 12 h with zirconia balls as the grinding media and deionized water as the solvent. After milling, the slurry was dried at 150 °C in oven. The mixture powder was calcined at 1050 °C for 2 h to achieve the PZT powder. The calcined powder was crushed into fine powder in agate mortar and then mixed with 4 wt % PVA liquid. The mixed powder was pressed into pellets of diameter 15 mm and thickness of 1-2 mm at 300 KgF/cm^2 using the hydraulic press. The pellets were finally sintered at 1250 °C for 2 h in air. All the pellets were placed in a covered alumina crucible containing PZT powder to compensate the lead evaporation during sintering of PZT at the elevated temperatures. X-ray diffraction analysis of the powder was performed using Philips X'Pert-MPD type diffractometer with $\text{CuK}\alpha$ radiation. A Field Emission Scanning Electron Microscope

(FESEM - EDS, JEOL JSM 6700F) with an energy dispersive spectroscope was used to investigate the microstructure and composition. All the sintered samples were then polished and covered with silver paste as the electrode for electrical and dielectric measurement. The dielectric constant and dielectric loss as a function of frequency and temperature were measured using an impedance analyzer HP 4194A. Ferroelectric hysteresis (P-E) loop was observed using Sawyer – Tower circuit.

3. Results and discussion

The phase formation and microstructure of the PZT is shown in Fig. 1. From XRD pattern (Fig.1a), it is found that pure single phase

perovskite structure was exhibited and no second phase was found. The diffraction peaks are matched and indexed based on JCPDS data (card No.33 – 0784). The lattice constants for tetragonal PZT are $a = 4.064 \text{ \AA}$, $c = 4.100$ and $c/a = 1.008$. The FESEM image of the sample is shown in Figure 1b. The average grain size was calculated by Cottrell’s method and is near about $1.1 \mu\text{m}$. It is reported that Pb can evaporate during final sintering at high temperature. Keeping this factor in mind, we sintered the pelletized sample in PZT atmosphere. The compositional analysis of the sintered PZT was confirmed by energy dispersive spectroscope and shown in figure 1c.

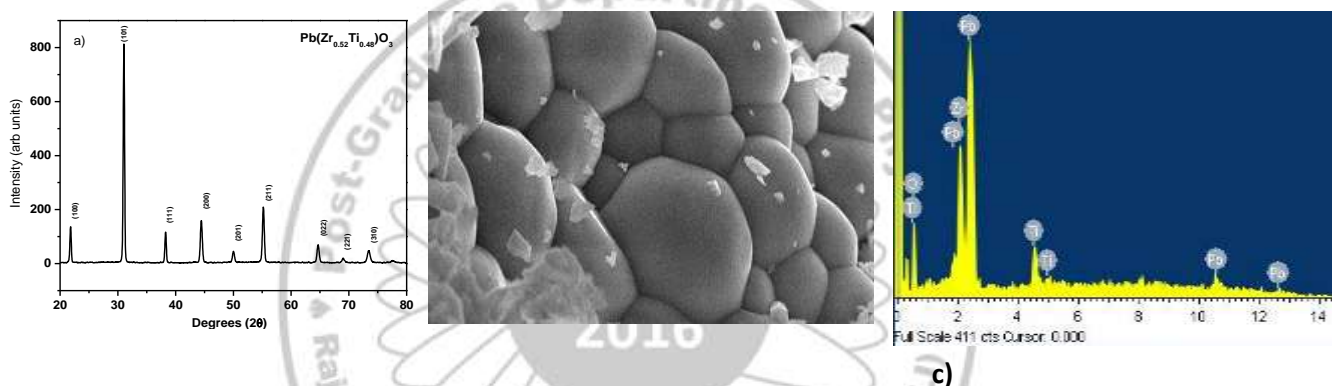


Fig.1. a) X-ray diffraction pattern, b) Field emission scanning electron microscope image and c) EDS (energy dispersive spectroscope) pattern of PZT ceramic.

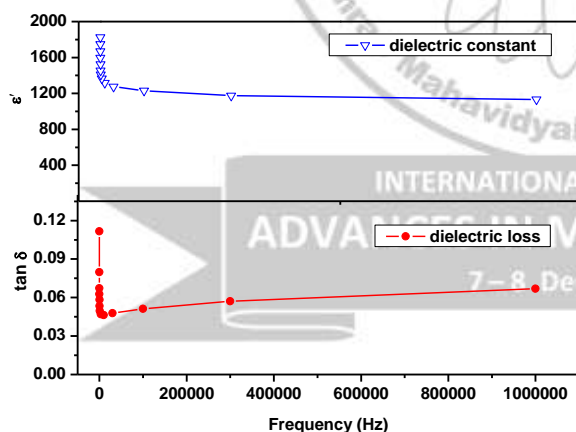


Fig.2 Frequency dependence of dielectric constant and dielectric loss at room temperature

The dielectric constant decreased gradually with increasing frequency. At higher frequencies the dielectric constant remains independent of frequency due to inability of electric dipoles to follow the alternating applied electric field. Since an assembly of space charge carriers in the dielectric structure requires finite time to line up their axes parallel to an alternating electric field,

the dielectric constant naturally decreases, if the frequency of the reversal field increases [11].

The dielectric constant is found to be depending on the variation of temperature and frequency. Fig. 2 shows the frequency dependence of the dielectric constant (ϵ') and dielectric loss ($\tan \delta$) at room temperature. The figure depicts the dielectric dispersion of PZT. The dielectric constant at 100 Hz and 1 MHz is 1524 and 1132 respectively, which is higher than the dielectric constant of other reported ferroelectric ceramics at room temperature.

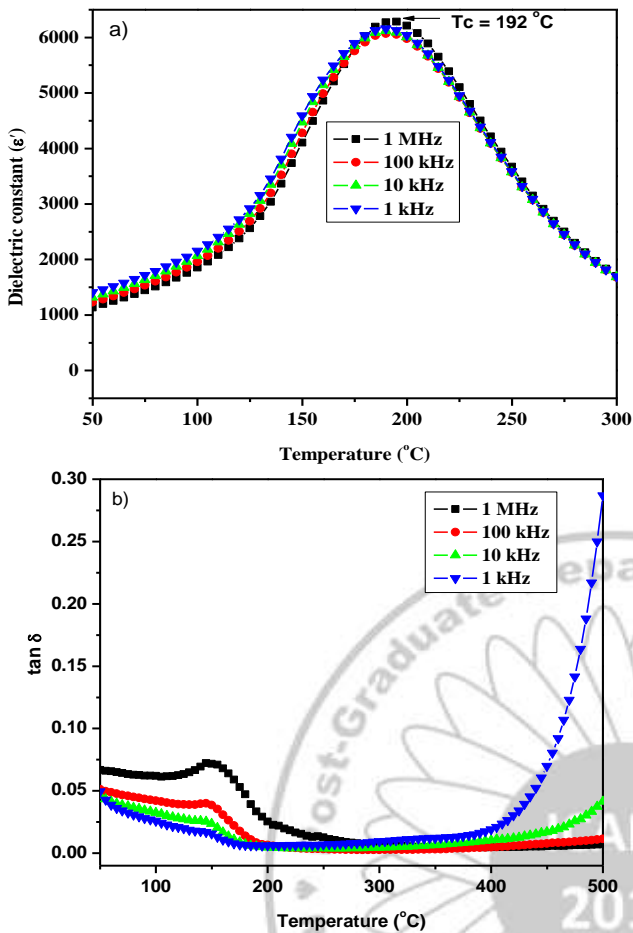


Fig. 3. Variation of dielectric constant and dielectric loss with temperature

Figure 3 show the temperature dependence of the dielectric constant and dielectric loss measured at 1 kHz, 10 kHz, 100 kHz and 1 MHz. Clearly, the dielectric constant reaches its maxima at 195 °C, which is the transition temperature (T_c) between the ferroelectric and paraelectric phases of PZT. The increase in dielectric constant with temperature is attributed to the dipole polarization process in PZT ceramics, which is according to the frequency change of AC field. The dielectric constant of PZT changes significantly with temperature but is nearly independent of applied

frequency, except in the vicinity of transition temperature. This clearly seen from figure that the dielectric constant is nearly same for frequencies 1 kHz to 1 MHz but the transition temperature slightly changes from 189 °C for 1 kHz to 195 °C for 1 MHz. This is normally an expected behaviour that has been observed in all reported ferroelectric ceramics. The dielectric constant reported here reaches to 6316 at 1 MHz, is higher than the dielectric constant obtained in other ferroelectrics. More interestingly, besides a higher dielectric constant, a lower dielectric loss is obtained in the PZT at T_c (Fig. 3b).

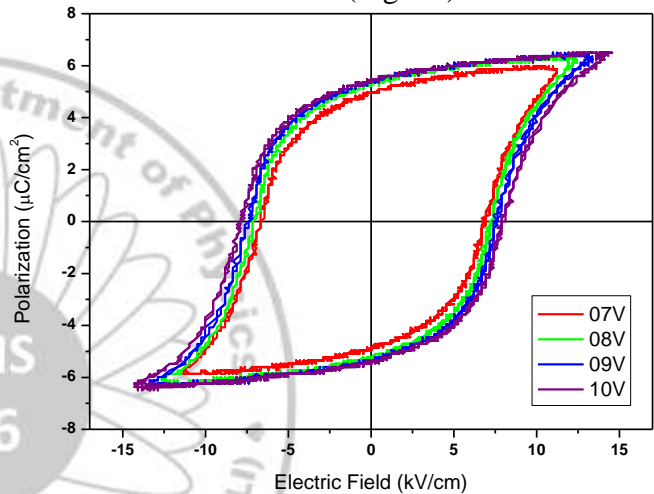


Fig. 4 Ferroelectric hysteresis (P-E) loop of PZT ceramic at room temperature.

Figure 4 shows the well saturated ferroelectric (P – E) hysteresis loop measured at room temperature. At an applied field of 15 kV/cm, the remnant polarization ($2P_r$) and coercive field ($2E_c$) of the PZT ceramics were 11 $\mu\text{C}/\text{cm}^2$ and 16 kV/cm respectively.

4. Conclusion

In summary, the enhanced dielectric and ferroelectric properties of PZT was successfully synthesized by solid state reaction method. This ceramic is the best candidate for by pass capacitor in microelectronics and energy storage devices due to its high dielectric constant

References

1. Z.M. Dang, Y. H. Lin and C. W. Nan, Novel Ferroelectric Polymer Composites with High Dielectric Constants *Adv. Mater.* 15(9) (2003) 1625
2. M. Arabatti, X. Shan and Z. Cheng, *Adv. Mater.* 19 (2007) 1369
3. R. Mani, S.N. Achary, K. R. Chakraborty, S.K. Deshapande, J.E. Joy, A. Nag, J.G. Gopalakrishnan and A.K. Tyagi, *Adv. Mater.* 20 (2008) 1348
4. L. Dong, C. Xiong, H. Quan and G. Zhao, *Scripta Mater.* 55 (2006) 835
5. C.S. Kim, S.K. Kim and S.Y. Lee, *Mater.Lett.* 77 (2003) 2233
6. Y. Fuda, K. Kumasaka, M. Katsuno, H. Sato and Y. Ino, *Jpn.J.Appl.Phys.* 36(1997) 3050
7. Z.M. Dang, D. Xie, Y.F. Yu, H.P. Xu and Y. D. Hou, *Mater.Chem.Phys.*109 (2008) 1
8. N. Vittayakorn and T. Tunkasiri, *Phys. Scr.* T129 (2007) 199
9. T. Zeng, X. Dong, H.Yang, C. Mao, H. Chen, *Scripta Mater.* 55 (2006) 923
10. C.M. Kanamadi and B.K. Chougule, *J.Magn.Magn.Mater.* 295 (2005) 139
11. B. Parvatheeswara Rao, K.H. Rao, K. Trinadh and O.F. Calfun, *J. Optoelect. and Adv.Mater.* 6(3) (2004) 951

Extraction of ion-pair complex of mercury(II) and N-n-octylcyclohexylamine from hydrochloric acid : analysis of real samples

Arjun Kokare^a, Sunil Zanje^a, Vishal Suryavanshi^a, Ganesh Kamble^a, Balasaheb kokare^a, Mansing Anuse^{a*}

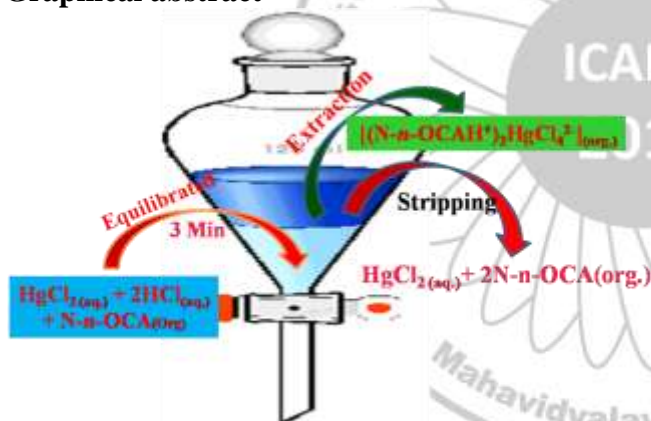
^aAnalytical Chemistry Laboratory, Department of Chemistry, Shivaji University, Kolhapur, 416004

Abstract

N-n-octylcyclohexylamine (N-n-OCA) is used as analytical extractant for the extraction, separation and determination of Hg(II). N-n-OCA was employed as a ion-pair forming a neutral $[(N-n-OCAH^+)_2 HgCl_4^{2-}]$ complex from hydrochloric acid (0.3 to 0.7 M) medium. The maximum extraction of Hg(II) was observed with N-n-OCA in the range 0.03 to 0.07 M dichloromethane and xylene. The extracted ion-pair complex of Hg(II) and N-n-OCA was back stripped with 4M NH₃ and determined by spectrophotometrically with PAN method. The quantitative extraction of Hg(II) found in DCM : xylene ratio 1:4 as a solvent mixture. The optimum extraction conditions were determined from a critical study of effect of acid, concentration of N-n-OCA, equilibrium time, solvent study, loading capacity, stripping study. On the basis of slope analysis method stoichiometry of extracted ion-pair complex was determined and it was found to be 1: 4: 2 (Metal: Acid: Extractant). The method has been extended to separate and to estimate Hg(II) in the presence of diverse ions, binary mixture of associated metal ions, multicomponent mixture, ayurvedic sample and water samples by using N-n-OCA and Hg(II) was determined with the PAN and results of analysis were confirmed by ICP-OES.

Keywords: Liquid-liquid extraction; Hg(II); N-n-octylcyclohexylamine; Real samples analysis

Graphical abstract



1. Introduction

Mercury is one of the abounded elements with highest environmental risk and it is considered a global pollutant. Mercury in environmental, biological, industrial and food samples are monitored very carefully as far as its toxicity is concern. Generally its toxicity depends on the concentration and its chemical form [1]. Organic mercury (alloy compound of mercury metal Hg⁺) is more toxic than inorganic mercury because of its high solubility of organic mercury in lipids and low elimination rate from the organism which causes bioaccumulation. Consumption of contaminated fish and other seafood that bioaccumalate organic mercury [2]. Mercury poisoning leads to minamata diseases which causes mental disturbance, hearing difficulty, coma and finally death [3]. Short term exposure to high concentration of mercury

vapours causes dangerous effect on the nervous, digestive, respiratory systems and the kidneys [4].

The commonly different extractant are used for separation of Hg(II) and determined by different methods like spectrophotometry, inductively coupled plasma atomic absorption spectroscopy and other methods. The extractant are 3-nitro benzaldehyde thiosemicarbazone (3-NBT) [5]. The developed method is an effective extraction and removal of mercury(II) from associated metal ions with hydrochloric acid medium by using N-n-OCA. The method was optimizing various parameters like effect of acid, concentration of extractant (N-n-OCA), equilibrium time, effect of solvent, strippant study, loading capacity of the extractant, effect of aqueous to organic volume ratio and stoichiometry of formed HgCl₄²⁻ species. The utility was checked by extraction of mercury(II) from diverse ions, binary mixture of associated metal ions, multicomponent mixture and ayurvedic samples.

2. Experimental

2.2 Reagents

2.2.1 Standard mercury(II) solution (1 mg/mL)

A stock solution of mercury(II) was prepared by dissolving 6.765 g of A. R. grade (BDH) mercuric chloride in 1000 mL of water containing 5 mL concentrated hydrochloric acid. The solution was standardized complexometrically [6].

2.2.2 N-n-octylcyclohexylamine (N-n-OCA) (0.05 M)

N-n-OCA was synthesized by acetonitril method [7] and its 0.05 M solution was prepared by dissolving 1.05 g N-n-OCA in a mixture of dichloromethane (DCM) and xylene (1:4) diluted to 100 mL, with xylene.

3. General extraction and determination procedure of mercury(II)

To an aliquot of solution containing 100 µg of mercury(II) was taken and acidity was adjusted to 0.4 M by hydrochloric acid in a 25 mL aqueous phase and transferred in to 125 ml separating funnel, 10 mL of 0.05 M N-n-OCA in xylene was added. The aqueous and organic phase was equilibrated for 3 min. Mercury(II) was back extracted from the organic phase by shaking with 4 M ammonia solution (3x10 mL). The aqueous phase was evaporated to remove ammonia to moist dryness and mercury(II) was determined by 1-(2-pyridylazo)-2-naphthol (PAN) method spectrophotometrically [8].

4. Results and Discussion

4.1 Effect of Acid concentration

The extraction of mercury(II) was carried out by using various mineral as well as weak organic acid medium with 10 mL 0.05 M N-n-OCA in xylene. It was observed that, the extraction of mercury(II) was quantitative from hydrochloric acid medium in the range of 0.3 to 0.7 M while the extraction of mercury(II) in other acid like nitric acid, perchloric acid, sulfuric acid and acetic acid showed incomplete extraction (Fig-1). However 0.4 M hydrochloric acid was recommended for further extraction.

4.2 Effect of shaking time

The extraction of mercury(II) was carried out from 0.4 M hydrochloric acid with 0.05 M N-n-OCA in xylene with various values of shaking time 30 s to 30 min. It showed that extraction starts at 30 s and became quantitative at 2.5 min and remains constant upto 8 min. There was decreased in extraction above 8 min shaking time, this may be due to dissociation of ion-pair complex [fig 2(A)]. Therefore 3 min shaking time was chosen in order ensure the complete extraction of mercury(II).

4.3 Effect of N-n-octylcyclohexylamine (N-n-OCA) concentration

The concentration of mercury(II) was studied in the concentration range of 0.001 M to

0.2 M of N-n-OCA from 0.4 M hydrochloric acid. The extraction starts at 0.001 M N-n-OCA and became quantitative in the range of 0.025 M to 0.07 M, further increase in the concentration of extractant the extraction was found to be decreased. The decrease the extraction above 0.07 M due to formation stable species was $[N-n-OCAH^+Cl^-]$. Therefore 0.05 M N-n-OCA recommended for extraction study [fig 2(B)].

4.4 Study of stripping agents

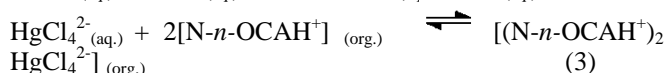
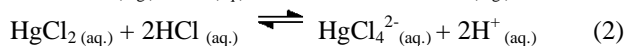
If the organic phase containing coloured ion-pair complex it is measured directly by spectrophotometrically but when ion-pair complex colorless, then mercury(II) from the organic phase was stripped with suitable electrolyte.

Stripping is the reverse of extraction. If the extraction took place in acidic medium, generally the higher acidic strippant or basic strippant become more efficient and vice versa. The various stripping agents were employed to back extract the mercury(II) from N-n-OCA laden organic phase such as ammonia, water, hydrochloric acid, acetic acid, acetate buffer, water and various electrolyte solution in the range 0.1 M to 10 M (Table 1). The successfully stripping of mercury(II) from organic phase was possible with ammonia while other strippant showed incomplete recovery of mercury(II). Therefore 4 M (3x10 mL) ammonia was used as strippant for the further extraction procedure. The advantage of ammonia as a stripping agent that it can be removed very easily by evaporation.

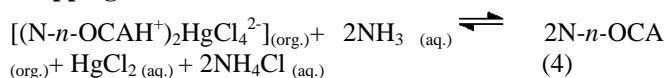
4.5 Composition of the extracted species by slope analysis method

Log-Log plot of distribution ratio of mercury(II) versus N-n-OCA and chloride concentration were used to determine stoichiometry of the extracted species. The graph of $\text{Log}D_{[Hg(II)]}$ vs $\text{Log}C_{[N-n-OCA]}$ having straight line with slope values 1.61 and 1.58, (Fig 3) at 0.1 M and 0.2 M hydrochloric acid respectively. The graph of $\text{Log}D_{[Hg(II)]}$ vs $\text{Log}C_{[HCl]}$ at 0.01 M and 0.02 M N-n-OCA give straight line graph with slope values 3.72 and 3.75, respectively. The stoichiometry of mercury(II): N-n-OCA was found to be 1:2 and mercury(II): HCl was found to be 1:4. Hence the overall stoichiometry of the extracted species was 1:4:2 (metal: acid: extractant). The extraction proceed via ion-pair formation of cationic species $[N-n-OCAH^+]$ and anionic species $[HgCl_4^{2-}]$.

The possible extraction mechanism



Stripping mechanism



5 Applications

5.1 Effect of diverse ions

The most important factors in the solvent extraction of metals is the selectivity of the extractant towards the specified metal ion to be recovered. The effect of various ions (cations and anions) was studied for the selectivity of the proposed method by using 0.05 M N-n-OCA as an extractant. Initially the foreign ion was added to the mercury(II) solution in large excess; 100 mg for anions and 25 mg for cations. When interference was found to be intensive, the test was repeated with successively smaller amounts of foreign ion. The tolerance limit was fixed as the maximum amount of an ion causing an error not greater than ± 2 in the extraction (Table 2). It was found that almost all of the cations and anions were tolerated at high ratio. The metal ions such as Ni(II), Pb(II), Ru(III), Bi(III) and Cr(VI) whose tolerance limit was low were masked by suitable masking agent like 25 mg EDTA, 25 mg tartrate, 25 mg citrate and 25 mg iodide to enhance the tolerance limit.

5.2 Separation of mercury(II) from binary mixture

The validity of proposed method was tested by applying it to the separation and determination of Hg(II) from a various associated metal ions. Separation of Hg(II) from binary mixture of Cd(II), Co(II), Ni(II), Cu(II), Zn(II), Fe(III), Cr(VI), Cr(III), Bi(III), Ru(III), Se(IV), Te(IV), Pb(II), Mn(VII) was carried out and determination after separation takes place (Table 3). Lead was determined by PAR method, Cr(VI) by diphenyl carbazide method, Cd(II) by PAR method, Co(II) by 2',4'-dinitro APTPT method, Ni(II) by Dimethylglyoxime (DMG) method, Cu(II) by 4'-Chloro PTPT method, Zn(II) by PAR method, Fe(III) by Potassium thiocyanate method,

Table 1. Study of different stripping agents

Molarity, (M)	HCl % R	CH ₃ COOH % R	NH ₃ % R	KOH % R	NaOH % R
0.1	29.4	18.2	46.7	25.9	23.7

Cr(III) by EDTA method, Bi(III) by Potassium Iodide method, Ru(III) by Thiourea method, Se(IV) by 4'-Bromo PTPT method, Te(IV) by 4'-Bromo PTPT method [9-15]. The organic phase containing Hg(II) was stripped with 4 M NH₃ (3x10 mL) was determined by PAN method and results of analysis were confirmed by ICP-OES.

5.4 Analysis of mercury(II) from ayurvedic samples

To determine amount of mercury present in real samples like ayurvedic as well as pharmaceutical samples and to examine the validity of developed method. The analysis of mercury(II) in vasant kusumkar rasa, arogyavardhini (Dabar), mahawat vidhvans rasa(ayurveda rasashala) smruti sagar rasa was carried out.

The ayurvedic sample was dried, weighed and dissolved in minimum amount *aqua-regia*. The solution was heated to moist dryness and the procedure was repeated thrice, 30 mL water was added and the solution was heated, filtered the solution to remove residue if any and washed with water. The filtrate was diluted to 100 mL with water. The sample was taken for analysis by the proposed method and the results were in close agreement with those of the values obtained by ICP-OES (Table 4).

6. Conclusion

The importance feature of develop method are:

- I. The low concentration of extractant (N-n-OCA 0.05 M) was used for extraction of mercury(II) with hydrochloric acid medium.
- II. The extraction of ion-pair complex $[(N-n-OCAH^+)_2 HgCl_4^{2-}]$ was carried out at room temperature and required one step for quantitative extraction of mercury(II). The 4M ammonia (3x10 mL) was used as strippant for mercury(II).
- III. The developed method has been extended to separate and to estimate mercury(II) from diverse ions, binary mixtures, multicomponent mixture and ayurvedic samples.
- IV. The method is simple, easy for operation, good accuracy and precision, low cost and a good enrichment factor.

0.5	41.6	20.6	49.8	26.2	25.6
1.0	68.4	27.4	59.8	26.6	28.3
2.0	79.2	29.8	82.9	29.5	31.2
2.5	81.8	34.4	94.3	35.7	34.5
3.0	86.5	36.5	99.5	48.1	37.9
3.5	91.7	42.9	99.6	-	-
4.0*	93.7	45.7	99.7*	-	-
4.5	99.8	51.1	99.1	-	-
5.0	99.2	55.0	99.3	-	-
6.0	99.5	46.8	99.4	-	-
7.0	90.2	46.0	99.8	-	-
8.0	71.9	44.3	80.2	-	-
9.0	71.4	40.8	71.9	-	-
10.0	67.4	40.0	68.3	-	-

* Recommended as strippant for extraction procedure, % R= Percentage recovery

Hg(II) = 100 µg, Hydrochloric acid = 0.4 M, N-n-OCA = 0.05 M in xylene, Equilibrium time= 3 min, Aqueous: organic ratio = 2.5:1, Solvent = xylene

Table 2. Effect of diverse ions

Metal ion	Added as	Tolerance limit, mg	Metal ion	Added as	Tolerance limit, mg
Nitrate	Sodium nitrate	20	Zn(II)	ZnSO ₄ .7H ₂ O	10
Fluoride	Sodium fluoride	15	Ni(II) ^a	NiCl ₂ .H ₂ O	5
Acetate	Sodium acetate	10	Mn(VII)	MnCl ₂ .6H ₂ O	15
Oxalate	Oxalic acid	15	Pb(II) ^a	Pb(NO ₃) ₂	5
Nitrite	Sodium nitrite	25	Cu(II)	CuSO ₄ .5H ₂ O	10
Malonate	Sodium malonate	15	Co(II)	CoCl ₂ .6H ₂ O	2
Succinate	Sodium succinate	10	In(III)	InCl ₃ .4H ₂ O	5
Sulphate	Sodium sulphate	50	Os(VIII)	OsO ₄	10
Thiosulphate	Sodium thiosulphate	15	Te(VI)	Na ₂ TeO ₃	10
Ascorbate	Ascorbic acid	5	Al(III)	AlCl ₃ .6H ₂ O	5
Tartarate	Sodium tartarate	15	Ru(III) ^b	RuCl ₃	2
Iodide	Potassium iodide	10	Th(IV)	Th(NO ₃) ₄	5
Salicylate	Sodium salicylate	15	Se(IV)	SeO ₂	10
Pt(IV)	Platinum chloride	3	Bi(III) ^c	Bi(NO ₃) ₃ .5H ₂ O	3
Na ₂ EDTA	EDTA	25	Sn(II)	SnCl ₂	5
Au(III)	HAuCl ₄ .4H ₂ O	5	Pd(II)	PdCl ₂	3
Ag(I)	AgNO ₃	3	Cr(VI) ^b	K ₂ CrO ₄	10
V(V)	NH ₄ VO ₃ .H ₂ O	10	Fe(III)	FeCl ₃	5
Rh(III)	RhCl ₃	5	U(VI)	UO ₂ (NO ₃) ₂ .6H ₂ O	10
Ir(III)	IrCl ₃	10	Cd(II) ^d	CdCl ₂	3

^a Masked with 25 mg EDTA, ^b Masked with 25 mg tartarate.

^c Masked with 25 mg citrate. ^d Masked with 25mg Iodide,

Hg(II) = 100 µg, Hydrochloric acid = 0.4 M, N-n-OCA = 0.05 M in xylene, Equilibrium time= 3 min, Strippant = 4 M NH₃ (3x10 mL) Aqueous: organic ratio = 2.5:1

Table 3. Separation of Hg(II) from binary mixture

Metal ions	Amount taken in (µg)	Average recovery* (%)	ICP-OES % recovery*	Chromogenic Reagent
Hg(II)	100	99.7	99.6	
Cd(II) ^a	100	99.4	99.8	PAR

Hg(II)	100	99.6	99.8	
Co(II)	400	99.5	99.6	2',4'-dinitro APTPT
Hg(II)	100	99.4	99.7	
Ni(II)	500	99.6	99.7	Dimethylglyoxime (DMG)
Hg(II)	100	99.6	99.8	
Cu(II)	400	99.2	99.8	4'-Chloro PTPT
Hg(II)	100	99.4	99.7	
Zn(II)	60	99.3	99.6	PAR
Hg(II)	100	99.5	99.5	
Fe(III)	300	99.4	99.8	Potassium thiocyanate
Hg(II)	100	99.7	99.7	
Cr(VI) ^b	50	99.6	99.6	Diphenyl Carbazide
Hg(II)	100	99.6	99.7	
Cr(III)	100	99.3	99.8	EDTA
Hg(II)	100	99.4	99.9	
Bi(III)	300	99.5	99.6	Potassium Iodide
Hg(II)	100	99.5	99.6	
Ru(III)	200	99.4	99.4	Thiourea
Hg(II)	100	99.7	99.8	
Se(IV)	100	99.6	99.6	4'-Bromo PTPT
Hg(II)	100	99.6	99.7	
Te(IV)	100	99.5	99.3	4'-Bromo PTPT
Hg(II)	100	99.4	99.6	
Pb(II) ^c	100	99.3	99.4	PAR

^a Masked with 25mg Iodide

^b Masked with 25 mg tartarate.

^c-Masked by 25mg EDTA

Hg(II) = 100 µg, Hydrochloric acid = 0.4 M, N-n-OCA = 0.05 M in xylene, Equilibrium time= 3 min, Strippant = 4 M NH₃ (3x10 mL) Aqueous: organic ratio = 2.5:1

Table 4. Analysis of Hg(II) from ayurvedic samples

Ayurvedic samples	Hg(II) found by Proposed Method* µg/gm	Hg(II) found by ICP-OES µg/gm	Recovery (%)	R.S.D, (%)
Smruti Sagar Rasa	236.80	237.0	99.6	0.4
Arogyavardhini (Dabar)	32.44	33.61	99.5	0.5
Mahawat Vidhvans Rasa (Ayurveda Rasashala)	132.81	133.52	99.7	0.3
Vasant kusumkar Rasa (Sandu)	81.67	82.73	99.4	0.6

^a-masked by 10mg EDTA

Hg(II) = 100 µg, Hydrochloric acid = 0.4 M, N-n-OCA = 0.05 M in xylene, Equilibrium time= 3 min, Strippant = 4 M NH₃ (3x10 mL) Aqueous: organic ratio = 2.5:1

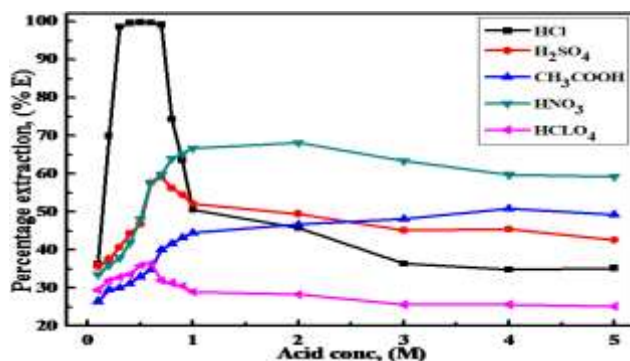


Figure 1. Effect of Acids

Hg(II) = 100 μ g, N-n-OCA = 0.05 M in xylene, Solvent = xylene, Equilibrium time = 3 min, Aqueous: organic ratio = 2.5:1, Strippant = 4 M NH₃ (3x10 mL)

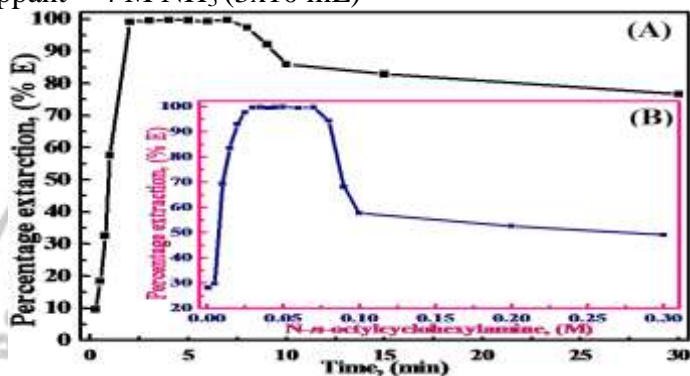


Figure 2.

(A) Effect of shaking time

Hg(II) = 100 μ g, N-n-OCA = 0.05 M in xylene, Solvent= Xylene, Aqueous: organic ratio = 2.5:1, Strippant = 4 M NH₃ (3x10 mL), Hydrochloric acid = 0.4 M

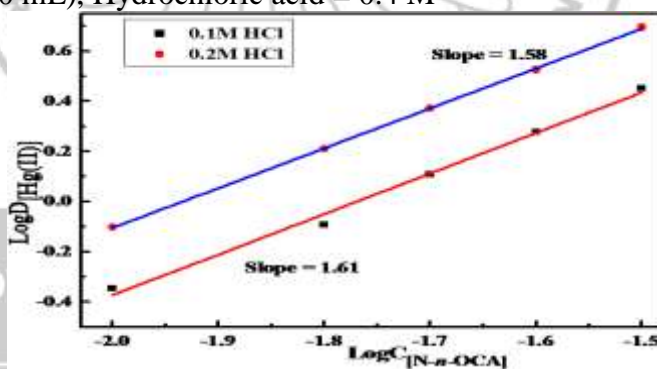


Figure 3. Composition of the extracted species by slope analysis method LogC_[N-n-OCA] vs LogD_[Hg(II)]

Hg(II) = 100 μ g, Solvent = xylene, Equilibrium time = 3 min, Aqueous: organic ratio = 2.5:1, Strippant = 4 M NH₃ (3x10 mL), Hydrochloric acid = 0.4 M.

References

- Atlanta, G. A. Agency for Toxic Substance and Disease Registry ATSDR, Toxicology profile for mercury, Public Health Service. 1999.
- Shah, A.; Kazi, T.; Baig, J.; Afridi, H.; Kandhro, G.; Arain, M.; Kolachi N.; Wadhwa, S. *Food Chem. Toxi.* 2010, 48, 65–69.
- Klaassen, C.; Casarete and Doull's, *Toxicology*, McGraw-Hill. New York. 2001, 834.
- Rajesh, N; Gurulakshmanan, G, *Spectro. Acta Part A.* 2008. 69. 391–395.
- Shoae, H.; Roshdi, M.; Khanlarzadeh, N.; Beiraghi, A. *Spectro. Acta. Part A, Mole. & Biomole. Spect.* 2012, 98, 70–75.
- Li, Z.; Wei, Q.; Yuan, R.; Zhou, X.; Liu, H.; Shan, H.; Song, Q. *Talanta.* 2007. 71. 68–72.
- Welchar, F. J.; Van, D. *Nostrand Company Inc., New York.* 1958.
- Moore, L.; Stephen, M.; Taylor.; Vandim, A. *Arkivoc.* 2005, 6. 287–292.
- Flaschka, H. A.; Bernard, A. J. *Chelates in Analytical Chemistry*, A collection of monographs, Marcel Dekkar, Inc. New York, 1972, 164. 4. 79.
- Kamble, G. S.; Ghare, A. A.; Kolekar, S. S.; Sung H. Han.; Anuse, M. A. *Spectro. Acta Part A*, 2011, 84. 117–124.
- Marczenko, Z. *Spectrophotometric Determination of Elements*, Ellis Harwood Limited Chinchester, 1976, 363. 372-373. 2173. 219. 153.
- Anuse, M. A.; Kuchekar, S. R.; Chavan, M. B. *Ind. J. Chem.* 1986, 25. 1041.
- Sandell, E. B. *Colorimetric determination of trace metals*, third edition, Interscience New York, 1965, 783.
- Kolekar, G. B.; Anuse, M. A. *Research, J. Chem. Environ.*, 1998, 2. 9.
- Kolekar, G. B.; Anuse, M. A. *Chem. Soc. Japan*, 1998, 71. 859.

Transparent Nanocrystalline Zinc Oxide Thin Films by Double Pulse Method

Anand Sawant^{1*}, Rajaram S. Sutar²

¹New English School, Khanderajuri, Tal: Miraj, Dist: Sangli, 416410, Maharashtra, India

²Department of Physics, Raje Ramrao College, Jath 416 404, Maharashtra, India

*Corresponding Author: anandsawant83.as@gmail.com

Abstract

The attempt has been made to fabricate nanocrystalline zinc oxide thin films by using double pulse potentiostatic deposition technique in oxygen saturated zinc acetate bath onto FTO coated conducting glass substrates. The influence of pulse parameters like nucleation pulse potential (E_1) and growth pulse potential (E_2) of a potentiostatic double-pulse on the size distribution of zinc oxide thin films is investigated. The structural, morphological and opticle properties of zinc oxide thin films were investigated. Hexagonal wurtzitr phase of ZnO along (101) orientation has been confirmed by using x-ray diffraction technique. The ZnO particles with diameter 120 to 200 nm has been fabricated by varying nucleation pulse potential (1200 to 900 mV) and the particle with size 100 to 250 nm has been obtained by varying growth pulse potential (600 to 750 mV). The results obtained showed how to create nanoparticles with respect to size, monodispersity and density of the deposit. By using double pulse technique one fabricate oxide nanoparticles in oxygen saturated zinc acetate bath by optimizing pulse parameters. The size effect on optical band gap energies has been extensively studied for the ZnO nanocrystalline thin films.

1. Introduction

Electrochemical deposition technique is a convenient and fast method to deposit metals on large scale onto the conducting substrate. The conventional electrochemical technique is not so successful in case of homogeneity and particle size or it requires templates, nanotemplates and catalysts to overcome this disadvantage, According to W. Plieth [1] to decrease dispersion in particle size during electrocrystallization, two important principles should be taken into account. Firstly, the crystal seed formation has to occur spontaneously, thus preventing progressive nucleation. Secondly, the crystal growth has to be conducted at a slow rate, i.e. at low overvoltage. Silver [2], gold [3], platinum [4] and cadmium [5] nanoparticles have been successfully synthesized by Penner et al. by elucidating this fundamental principal. Double pulse is the ideal method for the controlling electrodeposition of nanoparticles which favors monodispersity in experimental procedure. This method invented by Scheludko and Todorova [6] is based on an extremely short nucleation pulse of high cathodic potential followed by a much longer growth pulse at low cathodic overvoltage [7]. In this technique nucleation only occurs within the first pulse and exclusive particle growth in the second pulse. The high cathodic potential of the first pulse is necessary in order to initiate nucleation. With this method, the conflict between both optimal condition for nucleation and growth is partially difused. This is due to the amount of small seed additionally nucleated at the higher polarization and resolved as soon as the potential is switched

over to the lower polarization of the growth pulse [1].

Previously we have successfully deposited zinc oxide thin films by using conventional electrodeposition technique [8, 9]. In the present work we have applied our previous experience and the attempt has been made to deposit zinc oxide nancrystalline thin films by using double pulse technique. In our article, it is invented that the use of the electrochemical double-pulse method is a convenient, fast and easy way to produce nanocrystalline zinc oxide thin films in single step. This work focused on the development of non-template, electrochemical routes to dimensionally uniform zinc oxide nanostructures by using double pulse electrodeposition. To demonstrate how to tailor nanoparticles structures with respect to size, density and monodispersity of the particle.

2. Experimental

A three electrode electrochemical cell was used for electrochemical deposition of nanocrystalline ZnO thin film on to FTO coated conducting glass substrate. FTO coated conducting glass substrate of 3 cm² area are used as a working electrode, a graphite plate as a counter electrode and saturated electrode (SCE) as a reference electrode (SCE $E_0 = 0.244$ V Vs SHE, the saturated hydrogen electrode). The electrodes were placed parallel to each other separated by a distance 2 cm. A aqueous electrolyte of 50 mM zinc acetate (Thomas baker, 99.5%), with 0.1 M KCL as supporting electrolyte was used. Oxygen bubbling was maintained during the deposition in electrolyte. Prior to the film deposition, the substrate were cleaned with detergent in distilled

water and under ultrasonic cleaner, for 5 min in acetone, 5 min in alcohol and 5 min in deionized water. EG and G versastat-II model PAR-362 was used for the deposition of nanocrystalline zinc oxide thin films in potentiostatic mode. After preparation electrodes were rinsed into distilled water, naturally dried and used for further analysis. The schematic for the double pulse deposition is shown in Fig 1 [1]. The pulse parameters are chosen as follows,

Nucleation pulse: $E_{1max} = -1200$ mV, $E_{1min} = -900$ mV, $t_1 = 50$ ms, $t_2 = 360$ s

Growth pulse: $E_{2max} = -750$ mV, $E_{2min} = -600$ mV, $t_1 = 50$ ms, $t_2 = 360$ s

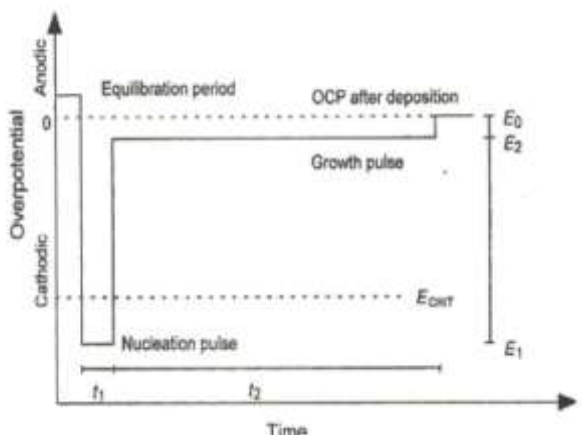


Fig.1: The schematic for the double pulse deposition

In this study the nucleation pulse was varied by keeping constant potential of growth pulse constant for above mentioned duration. In second part the potential of growth pulse was varied by keeping constant potential of nucleation pulse for the same duration. The surface morphology of sample was observed using the JEOL-JSM 6360 scanning electron microscope (SEM). X-ray diffraction (XRD) spectra of the films were recorded on an X-ray diffractometer (Philips PW-3710) with Cu-K α radiation of 1.5418 Å wavelength. The optical transmittance and absorption were measured by using Scimatzu make US-VIS 3600 spectrometer.

3. Results and Discussion

The linear sweep voltammogram of an FTO coated conducting glass electrode in 50 mM oxygen saturated zinc acetate bath with 0.1 M KCL supporting electrolyte is shown in Fig.2 (a). The potential scan was started at 0.2 V vs SCE reversed at -1.5 V vs SCE and terminated at 0.2 V vs SCE. Arrow indicate scan direction. The

EQCM measurements were recorded at the same time for the oxygen saturated zinc acetate bath with scan rate of 10 mV/s vs SCE. Fig 2 (b) shows plots of delta mass (μ g) vs potential (V) deposited onto pt Electrode. During the cathodic scan a rise in cathodic current, is observed at the potential of -0.75 V vs SCE Fig 2 (b) associated with the reduction reaction is accompanied by a concurrent shift in the frequency of the coated quartz crystal electrode with applied voltage. According to EQCM theory [10], such a shift is proportional to an increase of mass on the electrode surface as shown in figure. A small increment of mass starts around -0.6 V vs SCE, while a much greater accumulation is noted beyond -0.8 V (Fig.2 (b)). The data presented in Fig. 2 (a-b) reveals the potential ranges at which nucleation and growth pulse occur. The rate of mass accumulation onto electrode surface is faster beyond the potential of -0.9 V vs SCE (Region-I), due to faster rate of mass accumulation on electrode surface this potential is considered as critical nucleation potential for the ZnO. At the potential greater than -1.2 V vs SCE, hydrogen takes place in aqueous zinc acetate bath. Region-II is considered as growth pulse (Fig. 2b) because according to theory of double pulse growth pulse is more positive than critical potential. The double pulse procedure is an efficient way to control the particle size distributions of depositions. The first pulse, more negative than E_{CRIT} , is used to initiate the formation of nuclei and the second pulse, more positive than E_{CRIT} , is used to control the growth of the nuclei formed during the first pulse. The original distribution of stable nuclei formed during the first pulse should be preserved in second pulse.

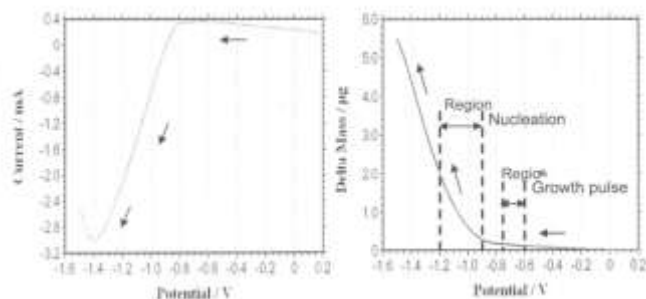


Fig.2.(a-b): a) Linear sweep voltammogram recorded in oxygen saturated zinc acetate solution on to FTO coated conducting glass substrate, b) Delta mass Vs Potential (V).

Fig. 3 shows the X-ray diffraction patterns of the films deposited at $E_1 = -1200$ (nucleation pulse potential) and $E_2 = -650$ mV (growth pulse

potential) V vs SCE in zinc acetate solution for the fixed time interval. The angle of diffraction, 2θ , was varied over 20-100°. The sample exhibit phase pure ZnO phase with hexagonal wurtzite structure (JCPDS card No. 36-1533) having preferred orientation along (100). The substrate peaks are indicated by star. In addition to this one minor peak of (102) orientation at 47° is observed. From the XRD analysis it is concluded that pure and orientated zinc oxide thin films could deposit using novel double pulse technique.

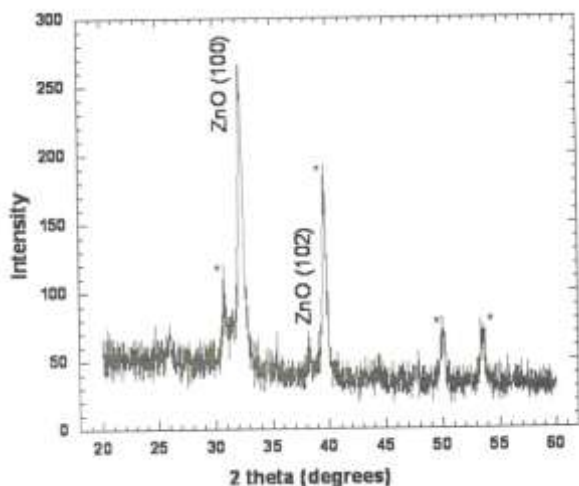


Fig.3: XRD pattern for the film deposited by using double pulse

Fig. 4 shows the SEM images for the zinc oxide thin films deposited at various nucleation pulse potential ranging from $E_{1MAX}=-1200$ mV to $E_{1min}=-900$ mV and $E_2= -650$ for the fixed time of t_1 50 ms, $t_2= 360$ s. SEM images shows variation in particle size depending on nucleation pulse potential (E_1).

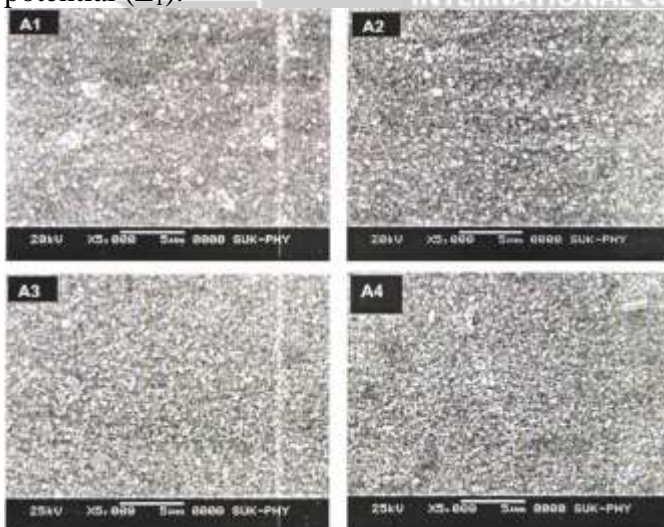


Fig.4: Scanning electron micrographs for the films deposited at A1) $E_1=-1200$ mV A2) $E_1=-1100$ mV

A3) $E_1=-1000$ mV A4) $E_1=-900$ mV nucleation pulse.

The increase in nucleation pulse potential (E_1) means increase in nucleation rate leading to increments in particle density (**Fig. 4**). It means that $E_{1min}=-900$ mV is the critical potential (E_{CRIT}) for the nanostructured nuclei formation. Bellow this critical potential there is no successful deposition. At this critical nucleation potential homogeneous, uniform and granular films with about 200 nm grain size are obtained (Fig. 4 A4). With increase in nucleation pulse potential a decrement in particle size from 200 to 120 nm is observed (Fig. 4 (A4 to A1)). For the higher nucleation pulse potential (above $E_1=-1000$ mV) the nucleation rate was faster than the critical nuclei formation leads to increase in particle density and a slight decrease size. Similarly M. Ueda et.al [1] stated that on increasing the nucleation pulse potential the nucleation becomes more spontaneous and the interdependent particle growth due to overlapping of diffusion zones increases.

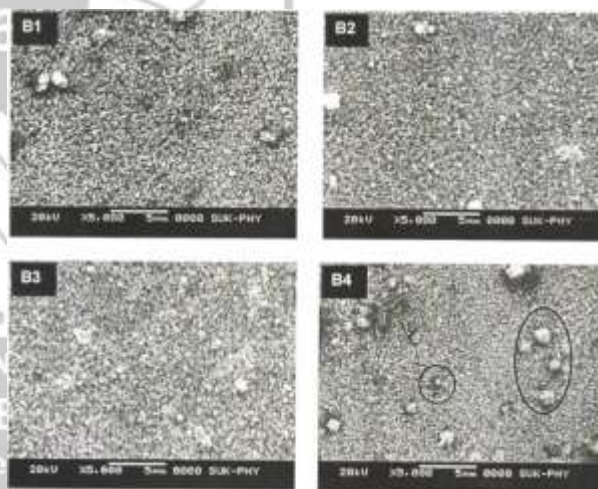


Fig.5: Scanning electron micrographs for the films deposited at B1) $E_2=-750$ mV B2) $E_2=-700$ mV B3) $E_2=-650$ mV B4) $E_2=-600$ mV growth pulse.

In the second part we have varied growth pulse potential from $E_{2max}= -750$ mV to $E_{2min}= -600$ mV with fixed time of $t_1=50$ ms, $t_2=360$ s. The SEM images for the films deposited at different growth pulse potentials are shown in fig. 5.

From SEM images it is observed that the size of particles born in the nucleation pulse is remains constant at the growth pulse potential of $E_2=-650$ mV (Fig.5 b3). The homogeneous and uniform films with the grain size of 120 nm were

obtained at this growth pulse potential. Below this critical growth pulse potential (at $E_2 = -600$ mV) the uniform film were obtained (Fig.5 B4). The overgrown particles and undeposited surfaces are indicated by circles in Fig.5 B4. With increase in growth pulse potential above $E_2 = -650$ mV the particle size increases up to 250 nm (Fig.5 B2, B1). Cluster aggregation rises when the growth pulse potential was increased, finally leading to cluster formation (of about 700 nm) at $E_2 = -750$ mV. From the above discussion it is concluded that the, $E_2 = -650$ mV is critical growth pulse potential for the uniform and nanocrystalline zinc oxide thin films deposition. Overall we can say that, one can deposit nanocrystalline zinc oxide thin film keeping $E_1 = -1200$ mV nucleation pulse potential and $E_2 = -650$ mV growth pulse potential by double pulse deposition technique.

The optical properties of thin films are strongly related to their morphologies. The optical absorption and transmittance spectra of the ZnO thin films were recorded in the wavelength range of 300-800 nm range. Fig. 6 shows the optical transmittance spectra of ZnO film deposited at -1200 mV (vs SCE) nucleation pulse potential onto FTO coated conducting glass substrate from oxygen saturated zinc acetate bath. The films were almost 85 % transparent in non absorbing region and absorbed strongly at the band gap.

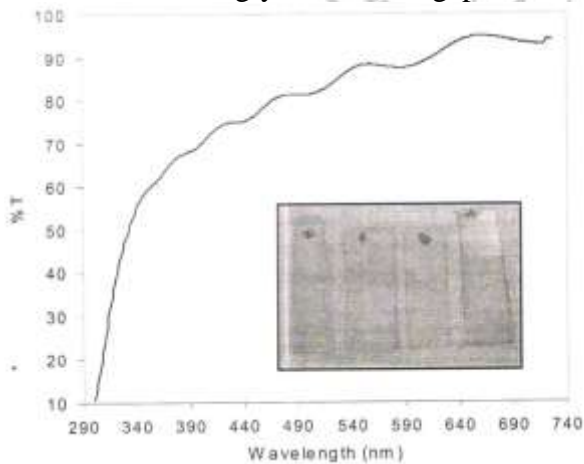


Fig.6: Transmittance spectra for the film deposited by double pulse electrodeposition.

Fig. 7 shows the absorbance of the films deposited at various nucleation pulse potential as -1200, -1100, 1000 and -900 mV. From the figure the sharp absorbance edge is observed in 330-370 nm range. The analysis of the edge can be performed by plotting $(ah\nu)^2$ versus $h\nu$, with $h\nu$ the energy of the incident light. Inset of Fig. 7 displays the band gap energy determination at zero

absorption coefficients. The band gap energy for the A1-A4 films were found in the range 3.8-3.85 eV with increase in nucleation pulse potential from -900 to -1200 mV respectively.

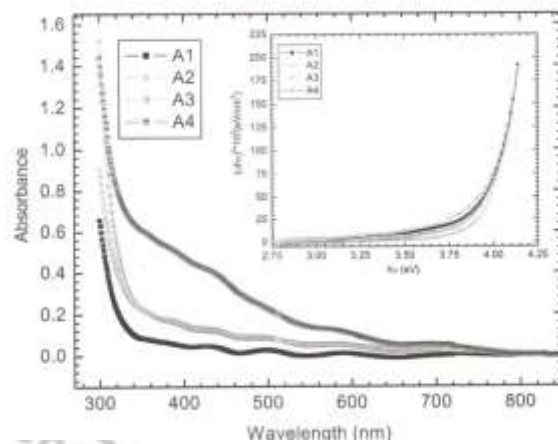


Fig. 7: Optical absorption spectra for the films deposited at A1) $E_1 = -1200$ mV A2) $E_1 = -1100$ mV A3) $E_1 = -1000$ mV A4) $E_1 = -900$ mV nucleation pulse.

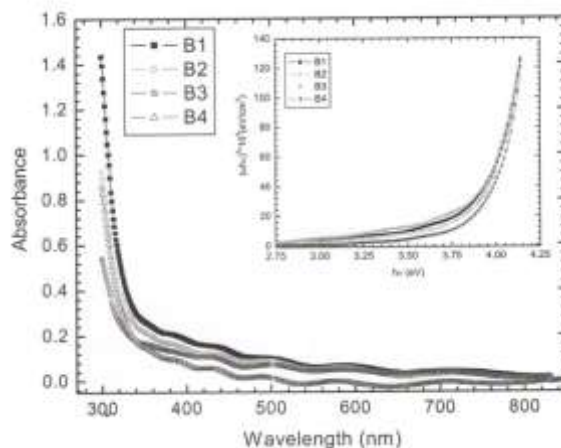


Fig. 8: Optical absorption spectra for the films deposited at B1) $E_2 = -750$ mV B2) $E_2 = -700$ mV B3) $E_2 = -650$ mV B4) $E_2 = -600$ mV growth pulse.

Similarly the absorbance for the films deposited at various at growth pulse potentials are shown in Fig. 8 (B1-B4). The inset of fig. 8 displays the band gap energy determination for the films deposited at various growth pulse potentials. The band gap energy found in the range of 3.8-3.9 eV. Band gap energy for the ZnO thin films have been reported from 3.3 to 3.57 eV for electrodeposited films [10,11]. The blue shift in the band gap energy is observed for double pulse deposited ZZnO nanocrystalline thin films. Possible reason for the band widening is the the decrement in particle size with change in nucleation and growth pulse potentials. The

widening in band gap energy as much as 1 eV is reported when going from the bulk to approximate 3 nm particle size [12, 13]. Green and Hussain et al reported that the quantum confinement contributes to the widening of band gap at small grain size [14], According to Moss rule [15],

$$n^4 E_g = 95 \text{ eV} \quad (1)$$

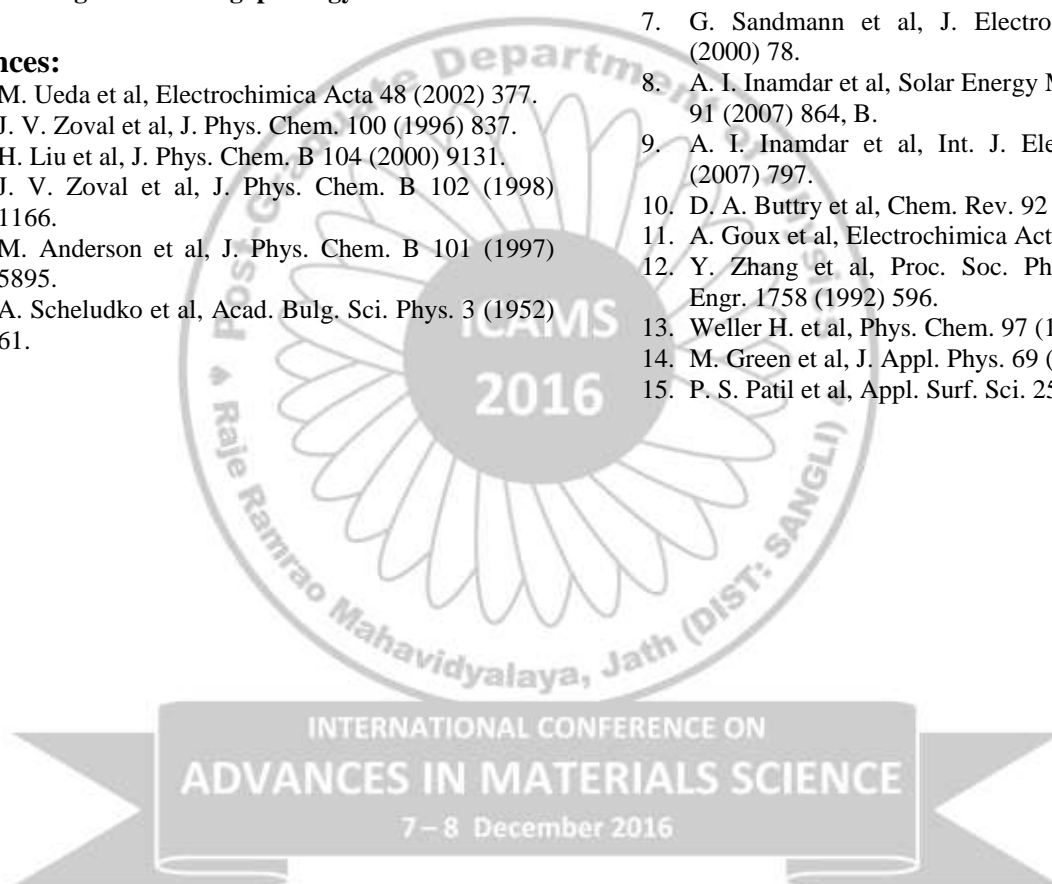
where n is the refractive index of the film and E_g is the band gap of the material; as the film becomes more dense, angle of refraction ($\sin r$) increases, leading to decrement in the refractive index of the film and increment in the band gap energy.

4. Conclusions

Nanocrystalline zinc oxide thin films has been successfully deposited by using double pulse method in oxygen saturated zinc acetate by this technique are optically transparent, adherent and smooth. Mean particle size of the deposit can be controlled by controlling the pulse parameters. With this technique, nanocrystalline zinc oxide thin films preparation is possible on a time scale of minutes. The ZnO particles with diameter 120 to 200 nm has been fabricated by varying nucleation pulse potential and the particle with size 100 to 250 nm has been obtained by varying growth pulse potential. One can generalize this technique to fabricate nanocrystalline oxide thin films. The effect of size on widening in the band gap energy is observed for all the films.

References:

1. M. Ueda et al, *Electrochimica Acta* 48 (2002) 377.
2. J. V. Zoval et al, *J. Phys. Chem.* 100 (1996) 837.
3. H. Liu et al, *J. Phys. Chem. B* 104 (2000) 9131.
4. J. V. Zoval et al, *J. Phys. Chem. B* 102 (1998) 1166.
5. M. Anderson et al, *J. Phys. Chem. B* 101 (1997) 5895.
6. A. Scheludko et al, *Acad. Bulg. Sci. Phys.* 3 (1952) 61.
7. G. Sandmann et al, *J. Electroanal. Chem.* 491 (2000) 78.
8. A. I. Inamdar et al, *Solar Energy Mater. Solar Cells*, 91 (2007) 864, B.
9. A. I. Inamdar et al, *Int. J. Electrochem. Sci.* 2 (2007) 797.
10. D. A. Buttry et al, *Chem. Rev.* 92 (1992) 1355.
11. A. Goux et al, *Electrochimica Acta* 50 (2005) 2239.
12. Y. Zhang et al, *Proc. Soc. Photo-Opt. Instrum. Engr.* 1758 (1992) 596.
13. Weller H. et al, *Phys. Chem.* 97 (1993) 630.
14. M. Green et al, *J. Appl. Phys.* 69 (1991) 7788.
15. P. S. Patil et al, *Appl. Surf. Sci.* 252 (2005) 1643.



Preparation of $\text{Ni}_x\text{Zn}_{1-x}\text{Fe}_2\text{O}_4$ thin films by spray pyrolysis method and to study their structural and electrical properties

S. S. Kumbhar¹, C. R. Bobade¹, S. T. Salunkhe¹, C. H. Bhosale^{2*}

¹Department of Physics, Balwant College Vita.

²Department of Physics, Shivaji University Kolhapur.

Abstract

The $\text{Ni}_x\text{Zn}_{1-x}\text{Fe}_2\text{O}_4$ thin films have been prepared using a simple spray pyrolysis method. The X-ray diffraction studies reveal that, the films are polycrystalline with spinel structure. The lattice parameters vary in the range of 8.35–8.48 Å with composition (x) obeying Vegard's rule. AFM studies show that the surface of the films exhibit a smooth, compact and a pin hole free morphology. X-ray photoelectron spectroscopy is used for chemical and structural analysis. As temperature increases the resistivity decreases which is attributed to the semiconducting behavior of the films.

Keywords: $\text{Ni}_x\text{Zn}_{1-x}\text{Fe}_2\text{O}_4$ thin films; Rietveld Analysis; XPS; Resistivity; etc.

*Corresponding author Tel.: +91 231 2609223, E-mail: bhosale_ch@yahoo.com

1. Introduction

Ferrites are an integral part of the modern industrial society because of their wide range of applications [1]. The recent technological advances in electronics needs more compact ferrite core for using it at higher frequencies. Among the different ferrites, $\text{NiZnFe}_2\text{O}_4$ are one of the most important magnetic materials used in high frequency applications [2]. $\text{NiZnFe}_2\text{O}_4$ possesses the advantages such as high Curie temperature, high resistivity, low temperature coefficient and excellent properties at high frequency. It is found that the bulk Ni-Zn ferrite components cannot be compatible with the rapid development of electronic applications which stares towards multifunction, lightweight and downsizing [3]. Hence, the current research on $\text{NiZnFe}_2\text{O}_4$ has focused to make nano-sized ferrite particles to reduce energy losses [4]. In order to readily integrate ferrite materials into electronics devices, it is desirable to obtain them in thin-film form. The trends for downsizing electronic equipments and the potential applications of ferrite materials have led to the fabrication of ferrite thin films [5]. It is found that, the thin films of ferrite with spinel crystal structure are of great importance for microwave control components in Ga-As microwave monolithic integrated circuits (MMIC) [6]. The recent discoveries of giant magneto resistance (GMR) and macroscopic quantum tunneling have attracted additional attention to these materials regarding to their potential use in magnetic recording and magneto-optic device [7]. Ferrite nanomaterials have been fabricated by a number of methods such as citrate-route [8], wet chemical [9], spin-coating [10], mechanical alloying method and combustion method etc. [11, 12]. In comparison with other

chemical deposition methods, spray pyrolysis has several advantages such as high purity, excellent control of chemical uniformity and stoichiometry in multi-component system. The other advantage of the spray pyrolysis method is that it can be adapted easily for production of large-area films [13]. The present study aims to prepare $\text{Ni}_x\text{Zn}_{1-x}\text{Fe}_2\text{O}_4$ (where $x = 0.0, 0.2, 0.4, 0.6, 0.8, 1.0$) thin films by spray pyrolysis method. The deposition conditions of ferrite thin films by using a spray pyrolysis method are also optimized. The effect of deposition temperature and annealing temperature on $\text{Ni}_x\text{Zn}_{1-x}\text{Fe}_2\text{O}_4$ is studied. Also, the effect of Ni substitution in $\text{Zn}_{1-x}\text{Fe}_2\text{O}_4$ is studied by XRD, XPS, AFM, Resistivity, etc.

2. Experimental

The $\text{Ni}_x\text{Zn}_{1-x}\text{Fe}_2\text{O}_4$ (where $x = 0.0, 0.2, 0.4, 0.6, 0.8, 1.0$) thin films were deposited onto the ultrasonically cleaned quartz substrates using simple and inexpensive chemical spray pyrolysis method. The nickel nitrate, zinc acetate and ferric nitrate were used as starting materials. These starting materials were dissolved separately in double distilled water and stock solution was prepared by mixing appropriate amounts of these solutions. The resulting 30 cc (0.1 M) stock solution was sprayed onto preheated substrates. The compressed air was used as a carrier gas. In order to optimize the deposition temperature for $\text{Ni}_x\text{Zn}_{1-x}\text{Fe}_2\text{O}_4$ ferrite thin films, $\text{Ni}_x\text{Zn}_{1-x}\text{Fe}_2\text{O}_4$ (where $x = 0.0$, i.e., ZnFe_2O_4) thin films were deposited onto the quartz substrates at various substrate temperatures between 350 and 500 °C in the step of 50 °C. The prepared films were characterized for structural, morphological properties. The structural properties of $\text{Ni}_x\text{Zn}_{1-x}\text{Fe}_2\text{O}_4$ (where $x = 0.0, 0.2, 0.4, 0.6, 0.8, 1.0$) thin films were studied by using Bruker D2: Phaser X-

ray diffractometer using Cu-Ka radiation. The images of film surface topography were taken by means of atomic force microscopy (AFM, Bruker instrument, Innova 1B3BE) operated at room temperature.

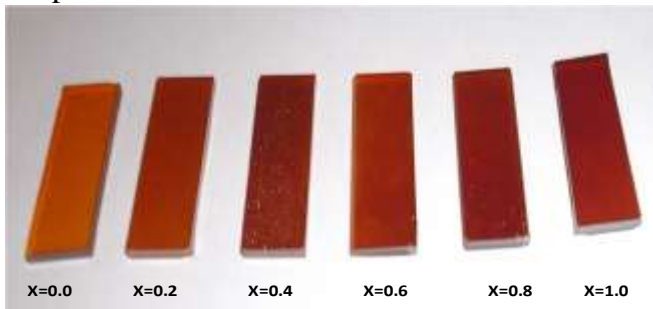


Fig. 1

3. Results and discussion

3.1 XRD and Rietveld Analysis

Fig. 2 shows X-ray diffraction patterns of annealed $Ni_xZn_{1-x}Fe_2O_4$ thin films deposited at the 400 °C onto the quartz substrate by varying x (x = 0.0, 0.2, 0.4, 0.6, 0.8, 1.0) value. All these deposited films are polycrystalline in nature and exhibit spinel cubic crystal structure.

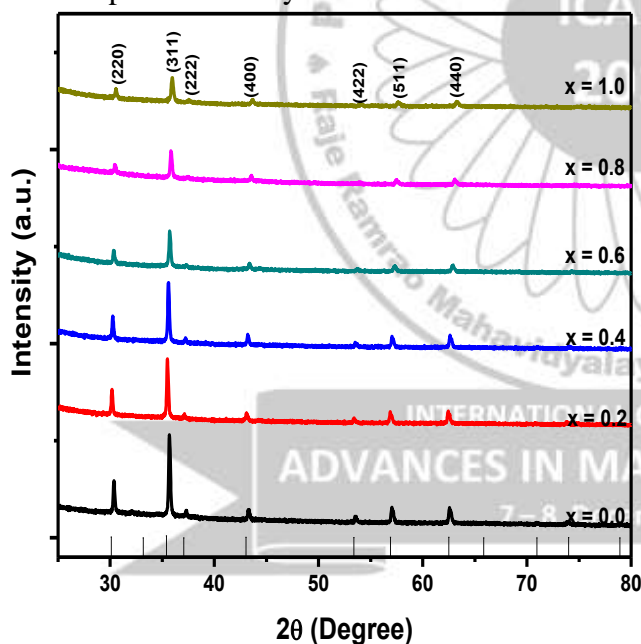


Fig.2

The comparison of observed and standard ‘d’ values have been made using JCPDS card No.08-0234 confirms the spinel cubic structure. The planes (220), (311), (222), (400), (422), (511) and (440) are also observed with smaller intensity. The Crystallite size calculated by Debye Scherrer's formula,

$$D = \frac{0.9\lambda}{\beta \cos \theta} \tag{1}$$

Crystallite size varies in between 35.8-26.5 nm. X-ray diffraction patterns show the intensity of peaks is increased and the peaks are slightly shifted due to the influence of nickel content. The lattice parameter of the crystalline material ‘a’ is calculated by using the following formula,

$$d = \frac{a}{\sqrt{h^2 + k^2 + l^2}} \tag{2}$$

The value of lattice parameter is also decreased from 8.48 to 8.35 Å with x and obeys Vegards rule.

The Rietveld fitting output of X-ray powder diffraction patterns of $Ni_xZn_{1-x}Fe_2O_4$ thin films is shown in Fig. 3. Reflection positions are marked at the bottom of the plot along with residues of the fittings. For $Ni_xZn_{1-x}Fe_2O_4$ thin films, the (cubic) space group is taken as Fd-3m (227) with various atoms in special Wyckoff positions. The various R factors and microstructure parameters of Reitveld profile fitting are specified in Table 1. A low value of χ^2 (goodness of fit- GoF) have been observed which supports good agreement between the observed and calculated intensities. Lattice parameter decreases with the addition of Ni content possibly due to replacement of larger Zn^{2+} (Ionic radius ~ 0.83Å) ions by relatively smaller Ni^{2+} (Ionic radius ~ 0.74Å) ions [14, 15]. This result is in good agreement with results obtained from XRD. Relative peak intensities decreased with composition (x). Observed small misfits of a calculated profile of the x = 0.2 and x = 0.4 samples is due to the slight FWHM mismatch [16]. The peak shape is assumed to be a pseudo-Voigt function with asymmetry. To account for an instrumental broadening correction, a Si standard sample is used. The particle size of the thin films decreases with composition possibly due to decrease in lattice constant with composition (x). The lattice strain is found to be isotropic with respect to composition for x = 0.2. Relatively higher value of the r.m.s. strain for x = 0 thin film sample is due to the lesser crystallite size of this composition.

3.2 Atomic Force Microscopy (AFM)

The Fig. 4 shows the 3D AFM images of annealed $Ni_{0.4}Zn_{0.6}Fe_2O_4$ thin films deposited onto quartz substrate at 400 °C. Surface topography of thin films at the nanoscale is analyzed using the AFM. AFM images are collected in contact mode using a silicon nitride

cantilever. From these AFM images it is seen that the films are crack-free and having densely packed

microstructure.

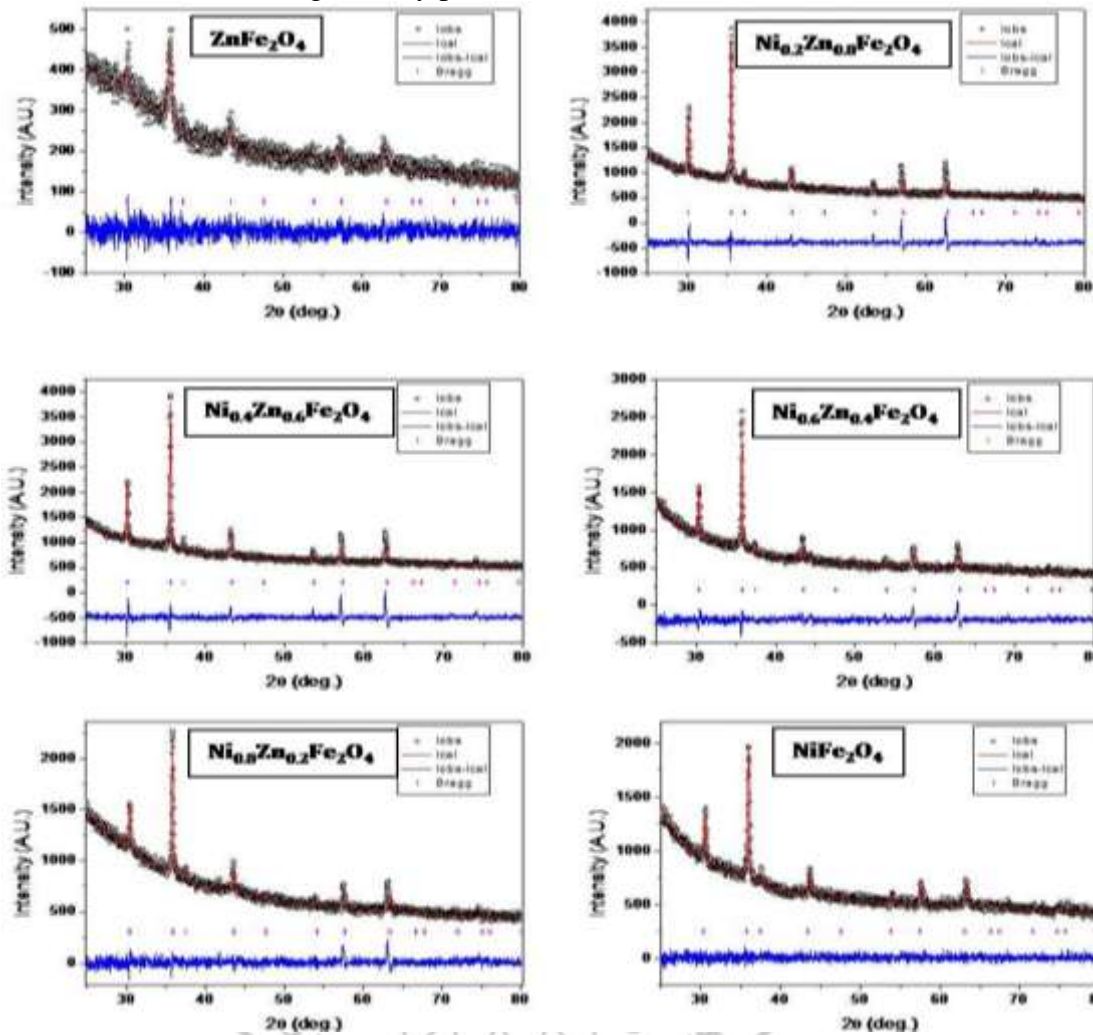


Fig. 3

Table 1 Data on Rietveld agreement factors and lattice constant of $Ni_xZn_{1-x}Fe_2O_4$ thin films

Rietveld factors	Composition (x)					
	x = 0	x = 0.2	x = 0.4	x = 0.6	x = 0.8	x = 1
χ^2	0.99	1.59	1.55	1.23	1.17	0.98
R_{wp} (%)	7.02	6.12	5.85	5.09	4.59	4.07
R_b (%)	5.42	5.66	4.89	6.69	5.27	3.01
R_{exp} (%)	7.09	3.86	3.78	4.14	3.93	4.17
Lattice constant (Å)	8.4183	8.3837	8.3626	8.3348	8.3068	8.2961
Cell volume (Å ³)	596.59	589.26	584.82	579.01	573.19	570.98
Crystallite size (Å)	807	1648	1555	1352	1198	778
Microstrain, 10^{-4}	48.19	11.72	9.96	11.99	14.54	7.88

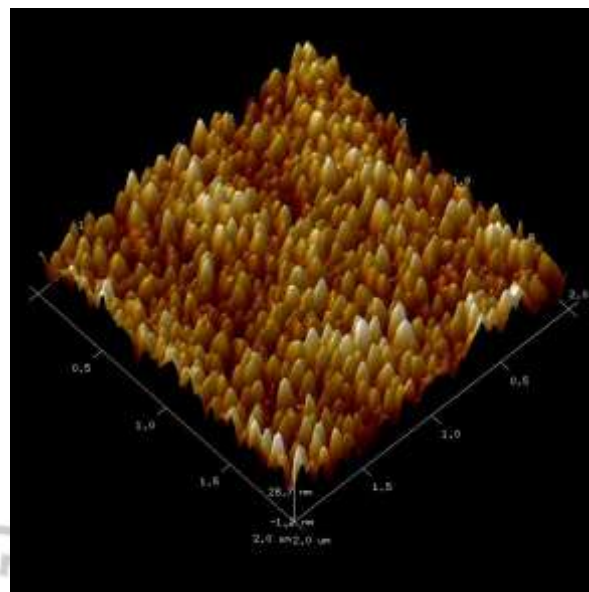
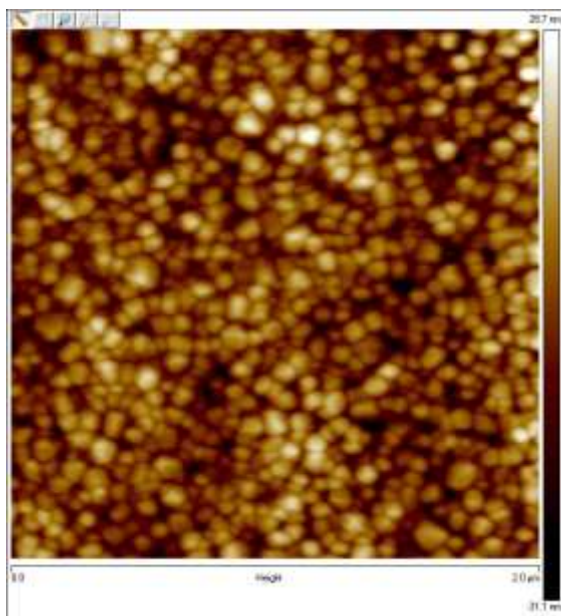


Fig. 4

3.3 X-ray photoelectron spectroscopy (XPS)

X-ray photoelectron spectroscopy is used for chemical and structural analysis and it is an effective tool for analyzing elements for their corresponding valence state [20, 21]. Fig. 5 shows the survey scan spectrum of $Ni_{0.4}Zn_{0.6}Fe_2O_4$ thin films deposited onto the quartz substrates at substrate temperature $400\text{ }^{\circ}\text{C}$. It is clearly seen that the material is mainly composed of Fe, Ni, Zn, C, O and N. The two peaks at 975.90 eV and 783.82 eV , correspond to the binding energies of Zn_{2p} and Ni_{2p} .

3.4 DC Resistivity measurement

Resistivity measurement of the $Ni_xZn_{1-x}Fe_2O_4$ (where $x = 0.0, 0.2, 0.4, 0.6, 0.8, 1.0$) films is carried out by two probe method. The temperature dependent DC resistivity of $Ni_xZn_{1-x}Fe_2O_4$ (where $x = 0.0, 0.2, 0.4, 0.6, 0.8, 1.0$) films is shown in Fig. 6. As temperature increases the resistivity decreases which is attributed to the semiconducting behavior of the films [18].

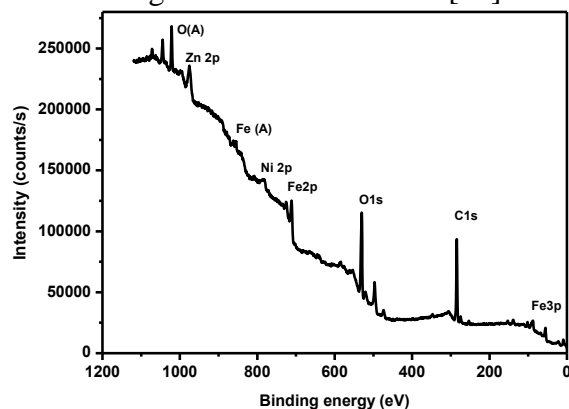


Fig. 5

The resistivity of $Ni_xZn_{1-x}Fe_2O_4$ (where $x = 0.0, 0.2, 0.4, 0.6, 0.8, 1.0$) films increases with the increasing Ni content. This is because, the Ni is more resistive than Zn. In case of ferrites, carrier concentration is almost constant but mobility of charge carriers increases with increasing temperature. For all of the samples, the graph shows the linear negative temperature coefficient of resistance (NTCR) attributed to semiconducting behavior. A break in the linearity is observed for all compositions. This break in linearity is due to the phase transition from ferrimagnetic to a paramagnetic state. The temperature at which this break occurs is called the Curie temperature. The conduction mechanism in ferrites can be explained on basis of polaron hopping [19]. When an electron moves in a crystal structure it induces some strain on neighbouring atoms. An electron coupled with strain field is called as polaron. If the strain field spreads beyond lattice constant it is called as large polaron and if the distance of strain field is less than the lattice constant, it is called as small polaron.

There are several experimental evidences for existence of polaron and polaron hopping [20, 21]. At low temperatures, small polaron behaves like a particle moving in a narrow conduction band. At elevated temperatures, small polaron absorbs one or two phonons resulting in hopping mechanism. As a result of this at high temperature resistivity decreases.

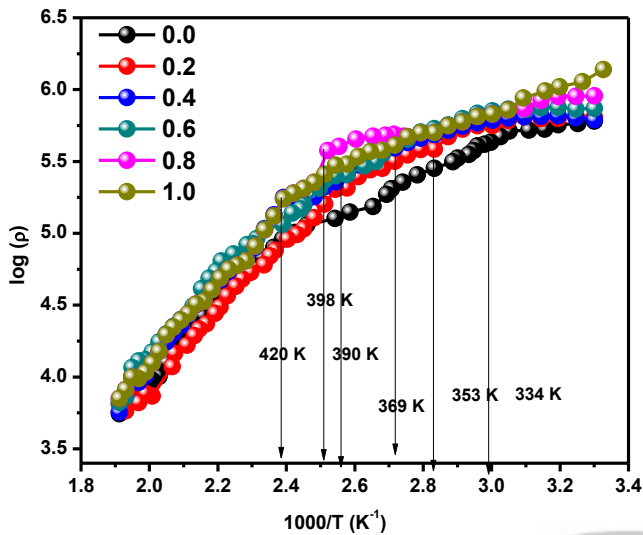


Fig. 6

The conduction mechanism in ferrites is explained on the basis of the Verwey and de Bohr [22] mechanism, which involves the exchange of electrons between the ions of the same elements present in more than one valence state and is distributed randomly over equivalent crystallographic lattice sites. These elements will act as centres for polaron generation. The decrease in DC resistivity with increase in temperature is attributed to an increase in the drift mobility of the charge carriers. Also, it is well known that conduction in ferrites is due to the hopping of electrons from Fe^{3+} to Fe^{2+} ions [23]. The resistivity in ferrites is controlled by the Fe^{2+} ion concentration at the B-site [24, 25]. Increase in resistivity is found to increase in Ni content. This increase may be attributed to the change in the cation distribution of the spinels. In $Ni_xZn_{1-x}Fe_2O_4$ the Zn ions prefer the occupation of tetrahedral (A) sites and Ni ions prefer the occupation of octahedral (B) sites while Fe ions partially occupy the A and B sites. On increasing Ni ion substitution at (B) sites, the Zn ion concentration at (A) sites will decrease. Increase in Ni^{2+} ions may replace Fe^{2+} ions at the B-site reducing conduction at the B-site. As a result, the number of ferrous and ferric ions at the B sites (which is responsible for electrical conduction in ferrites)

5. Conclusion

The $Ni_xZn_{1-x}Fe_2O_4$ (where $x = 0.0, 0.2, 0.4, 0.6, 0.8, 1.0$) thin films were successfully deposited by spray pyrolysis method. The X-ray diffraction study reveals that the films are due to polycrystalline in nature with spinel cubic structure. From AFM study, it is seen that formation of the cube like structure of grains all over the surface of the films. From XPS it is seen that all elements are present at surface the prepared thin films. As temperature increases the resistivity decreases which is attributed to the semiconducting behavior of the ferrite thin films. The resistivity of $Ni_xZn_{1-x}Fe_2O_4$ thin films increases with the increasing Ni content.

References

decreases. Thus, the resistivity increases on increasing Ni substitution [26].

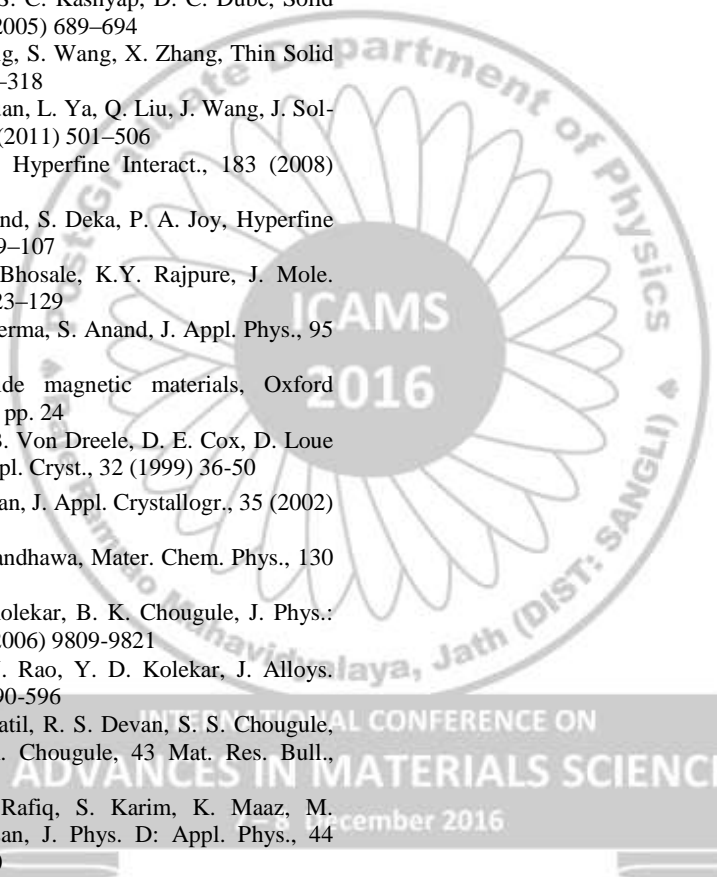
The activation energy is calculated by using Arrhenius equation. The DC resistivity of the ferrites, in general, depends on the density, porosity, grain size and chemical composition of the samples [27, 28]. In general, nickel ferrite demonstrates higher resistivity than that of zinc ferrite. Adding components with higher resistivity may also increase resistivity.

Table 2. Values of Curie temperature (K) and activation energy (eV) with different Ni content (where $x = 0.0, 0.2, 0.4, 0.6, 0.8, 1.0$)

Ni content (x)	Curie temperature (K)	Activation energy (eV)	
		Ferromagnetic	Paramagnetic
0.0	334	0.076	0.20
0.2	353	0.057	0.21
0.4	369	0.058	0.25
0.6	390	0.052	0.21
0.8	398	0.088	0.24
1.0	420	0.080	0.23

From Fig.6 it is clear that the transition from the ferromagnetic to the paramagnetic state shifted towards a higher temperature with increase in Ni concentration as shown in as shown in Table 2. As the concentration of Ni increases the Curie temperature also increases and is confirmed from the values of activation energies given in Table 2. The increase of T_C with an increasing Ni^{2+} concentration may be explained on the basis of modification of the A–B exchange interaction strength. The increase of Curie temperature is due to the strengthening of A–B interaction. This could be attributed to the decrease in the distance between the moments of A and B sites which is confirmed in the XRD results by the decrease in the lattice parameter with increasing Ni concentration [29].

1. S. Sindhu, M. R. Anantharaman, B. P. Thampi, K. A. Malini, P. Kurian, Bull. Mater. Sci., 25 (2002) 599–607
2. L. Li, L. Peng, Y. Li, X. Zhu, J. Magn. Magn. Mater., 324 (2012) 60–62
3. K. Sun, Z. Lan, Z. Yu, X. Nie, Curr. Appl. Phys., 11 (2011) 472-475
4. V. Musat, O. Potecasu, R. Belea, P. Alexandru, Mater. Sci. Eng., B 167 (2010) 85–90
5. M. Sorescu, L. Diamandescu, R. Swaminathan, M. E. McHenry, M. Feder, J. Appl. Phys., 97 (2005) 10G1051-10G1053
6. J. S. Lee, T. W. Ha, J. H. Jeong, I. W. Kim, S. S. Yi, Thin Solid Films, 472 (2005) 217–221
7. R. C. Kambale, N. R. Adhate, B. K. Chougule, Y. D. Kolekar, J. Alloy. Compd., 491 (2010) 372-377
8. N. Gupta, A. Verma, S. C. Kashyap, D. C. Dube, Solid State Commun., 134 (2005) 689–694
9. Q. Tian, J. Li, Q. Wang, S. Wang, X. Zhang, Thin Solid Films, 518 (2009) 313–318
10. T. Yuan, Z. Wei, J. Yuan, L. Ya, Q. Liu, J. Wang, J. Sol-Gel. Sci. Technol., 58 (2011) 501–506
11. B. Ghosh, S. Kumar, Hyperfine Interact., 183 (2008) 163–169
12. V. Sreeja, S. Vijayanand, S. Deka, P. A. Joy, Hyperfine Interact., 183 (2008) 99–107
13. S. S. Shinde, C. H. Bhosale, K.Y. Rajpure, J. Mole. Struct., 1021 (2012) 123–129
14. C. Upadhyay, H. C. Verma, S. Anand, J. Appl. Phys., 95 (2004) 5746-5751
15. K. J. Standley, Oxide magnetic materials, Oxford University Press 1962, pp. 24
16. L. B. Mc Cusker, R. B. Von Dreele, D. E. Cox, D. Loue Ęr and P. Scardi, J. Appl. Cryst., 32 (1999) 36-50
17. S. Bid and S. K. Pradhan, J. Appl. Crystallogr., 35 (2002) 517-525
18. M. Gupta and B. S. Randhawa, Mater. Chem. Phys., 130 (2011) 513–518
19. R. S. Devan, Y. D. Kolekar, B. K. Chougule, J. Phys.: Condens. Matter, 18 (2006) 9809-9821
20. R. C. Kambale, A. V. Rao, Y. D. Kolekar, J. Alloys. Compd., 492 (2010) 590-596
21. S. A. Lokare, D. R. Patil, R. S. Devan, S. S. Chougule, Y. D. Kolekar, B. K. Chougule, 43 Mat. Res. Bull., (2008) 326–332
22. A. Rahman, M. A. Rafiq, S. Karim, K. Maaz, M. Siddique, M. M. Hasan, J. Phys. D: Appl. Phys., 44 (2011) 165404-165410
23. K. K. Patankar, P. D. Dombale, V. L. Mathe, S. A. Patil, R. N. Patil, Mater. Sci. Eng. B, 87 (2001) 53-58
24. C. N. Chinnasamy, A. Narayanasamy, N. Ponpandian, K. Chattopadhyay, K. Shinoda, B. Jeyadevan, K. Tohji, K. Nakatsuka, T. Furubayashi, I. Nakatani, Phys. Rev. B, 63 (2001) 184108-184114
25. T. Meaz, M. Amer, Egypt. J. Solids, 31 (2008) 147-156
26. U. Ghazanfar, S. A. Siddiqi, G. Abbas, Mater. Sci. Eng. B, 118 (2005) 132–134
27. I. Gul, W. Ahmed, A. Maqsood, J. Magn. Magn. Mater., 320 (2008) 270-275
28. S. M. Hoque, A. Choudhury, F. Islam, J. Magn. Magn. Mater., 251 (2002) 292-303
29. D. Ravinder, P. Shalini, P. Mahesh, K. Rao, M. Vithal, B. Boyanov, J. Alloys. Compd., 364 (2004) 17-22



Kinetics and Mechanism of Oxidation of Maltose by keggin type 12-tungstocobaltate (III) in hydrochloric acid medium

Babasaheb Bhosale^{*a} Sunil Zende^b Shashikant Sawant^b and Balasaheb Sargar^c V. M. Gurame^d

^aRajaram College, Kolhapur,

^bDoodh-Sakhar Mahavidyalaya, Bidri, Kolhapur

^cJaysingpur College, Jaysingpur, Kolhapur

^dShivaji College, Barshi, Solapur

Abstract

Kinetics and Mechanism of Oxidation of Maltose by keggin type 12-tungstocobaltate (III) in acidic medium has been investigated at 25°C for the first time. The value of pseudo-first-order rate constant remains constant with variation of Keggin type 12-tungstocobaltate (III) clearly indicating the order of reaction with respect to $[\text{Co}^{\text{III}}]$ is unity. First-order rate constant values were found to be increased with increase in $[\text{Maltose}]$ and $[\text{H}^+]$. The order with respect to maltose concentration was found to be one each. Variations in ionic strength (μ) and dielectric constant (D) of the medium have not influenced the oxidation rates. The proposed mechanism, involving most reactive activated complex formed as a result of interaction between the Keggin type 12-tungstocobaltate (III) and maltose is supported by kinetic orders, Michaelis-Menten plot and the main oxidation products of the reaction was identified as formic acid.

1. Introduction:

Carbohydrates are the fuel of life, being the main energy source for living organisms and the central pathway of energy storage and supply for most cells. The study of the carbohydrates and their derivatives has greatly enriched chemistry, particularly with respect to the role of molecular shape and conformation in chemical reactions [1]. These biological and economic importances of the carbohydrates and especially the monosaccharides and disaccharides have been largely responsible for the interest in the study of their biological and physiochemical properties along with reactivities [2]. The kinetics of oxidation of sugars by a variety of oxidants has been reported [3-4] in both acidic and alkaline media. Several different mechanisms showing the importance of enediols, cyclic forms of sugars, etc. have been established. The oxidations of different substrates by KMnO_4 in acidic medium are reported [5, 6]. N-Bromosuccinamide is reported for oxidation of [7-11] sugar (a biologically important substrate). These reports and recent publications concerning the oxidation of sugars by organic halo amines have prompted us to use the heteropolyoxometalate for the oxidation of maltose in perchloric acid medium. The oxidation kinetics of maltose in alkaline [12] and ammoniacal [13] media have been described, but few studies in acidic media have been reported. The kinetics of oxidation of maltose by thallium (III), in the presence of sulphuric acid, in aqueous acetic acid was reported [14]. Studies involving the oxidation of the sugars by polyoxometalates are scarce, therefore we have undertaken the study of oxidation of maltose sugar by showing the

importance of enediols, cyclic forms of sugars, etc. have been established. The oxidations of different substrates by KMnO_4 in acidic medium are reported [5, 6]. N-Bromosuccinamide is reported for oxidation of [7-11] sugar (a biologically important substrate). These reports and recent publications concerning the oxidation of sugars by organic halo amines have prompted us to use the heteropolyoxometalate for the oxidation of maltose in perchloric acid medium. The oxidation kinetics of maltose in alkaline [12] and ammoniacal [13] media have been described, but few studies in acidic media have been reported. The kinetics of oxidation of maltose by thallium (III), in the presence of sulphuric acid, in aqueous acetic acid was reported [14]. The first direct measurements of self exchange rates for electron transfer between POM anions in water using $[\text{Co}^{\text{II}}\text{W}_{12}\text{O}_{40}]^{6-}$ and its one electron oxidized derivative $[\text{Co}^{\text{III}}\text{W}_{12}\text{O}_{40}]^{5-}$ first synthesized and characterized by Baker and co-workers [4] has been extensively used as an oxidant both for organic and inorganic substrates [5]. The potential utility of $[\text{Co}^{\text{III}}\text{W}_{12}\text{O}_{40}]^{5-}$ as a well-defined probe for determining the nature of outer-sphere oxidations of alkyl aromatic hydrocarbons [6]. When it is complexed with polytungstate ions $[\text{Co}^{\text{III}}\text{W}_{12}\text{O}_{40}]^{5-}/[\text{Co}^{\text{II}}\text{W}_{12}\text{O}_{40}]^{6-}$ which is attributed to the distribution of the charge density of the cobalt ion over a large area. The complex of transition metal ions with polyoxoanions like polytungstates are well known outer-sphere electron transfer reagent [7]. The redox reaction of $[\text{Co}^{\text{III}}\text{W}_{12}\text{O}_{40}]^{5-}$ have been recently revived [4,5]. Among various heteropolyacids structural classes the keggin type heteropolyacids have been widely

used as homogeneous and heterogeneous catalysts for acid-base and oxidation reactions[8].The studies involving the oxidation of the sugars by polyoxometalates are scarce, therefore we have undertaken the study of oxidation of maltose sugar by 12-tungstocobaltate (III) in perchloric acid medium.

2. Materials and methods:

All the solutions were prepared in doubly distilled water. The solution of Maltose was prepared by dissolving D-maltose (SD Fine) in water. 12-tungstocobaltate (III) was prepared, by reported method. The solution of $[\text{Co}^{\text{III}}\text{W}_{12}\text{O}_{40}]^{5-}$ was standardized iodometrically with excess of As^{III} , and spectrophotometrically at 624 nm.

2.1 Kinetic Measurements:

The reaction between $[\text{Co}^{\text{III}}\text{W}_{12}\text{O}_{40}]^{5-}$ and maltose was studied under pseudo-first-order conditions at a constant temperature of $25.0 \pm 0.1^\circ\text{C}$. The reaction was initiated by mixing the previously thermostated solutions of maltose and $[\text{Co}^{\text{III}}\text{W}_{12}\text{O}_{40}]^{5-}$ which also contained the requisite amount of perchloric acid, and doubly distilled water. The reaction was followed by determining the concentration of remaining $[\text{Co}^{\text{III}}\text{W}_{12}\text{O}_{40}]^{5-}$ spectrophotometrically at 624 nm. The sample run is given in Table 1 and the graph of $\log(a/a-x)$ versus 't' is shown in Fig 1. Ionic strength was maintained using NaClO_4 and to vary hydrogen ion concentrations HClO_4 (BDH) was used. The pseudo-first-order rate constants were determined from the plots of $\log [[\text{Co}^{\text{III}}\text{W}_{12}\text{O}_{40}]^{5-}]$ against time and the rate constants were reproducible within $\pm 4\%$.

2.2 Test for free radicals:

The reaction was also studied in presence of added acrylonitrile to understand the intervention of free radicals [15,16] in the reaction. There was no effect of added acrylonitrile on the reaction and also no precipitate due to the polymerization of the added acrylonitrile was observed thus confirming the absence of any free radical formation in the reaction.

3. Results and discussion:

3.1 Stoichiometry and product analysis:

The stoichiometry was studied by keeping concentration of $[\text{Co}^{\text{III}}\text{W}_{12}\text{O}_{40}]^{5-}$ constant at $3 \times 10^{-3} \text{ mol dm}^{-3}$ and varying concentration of maltose from 0.2×10^{-3} to $3.0 \times 10^{-3} \text{ mol dm}^{-3}$. Different reaction mixtures containing varying concentration of maltose were prepared, which

also contained required amount of perchloric acid. The concentration of unreacted $[\text{Co}^{\text{III}}\text{W}_{12}\text{O}_{40}]^{5-}$ was determined spectrophotometrically at 624 nm after 24 hours. The stoichiometry was found to be one mole of maltose per two mole of $[\text{Co}^{\text{III}}\text{W}_{12}\text{O}_{40}]^{5-}$. The main oxidation product, formic acid was detected [17] by TLC and spot test methods [18,19].

3.2 Reaction order:

The reaction was carried out under pseudo-first-order conditions, keeping the concentration of perchloric acid constant at 0.3 mol dm^{-3} and varying either maltose from 0.01 to 0.1 mol dm^{-3} at constant [one mole of $[\text{Co}^{\text{III}}\text{W}_{12}\text{O}_{40}]^{5-}$ ($1.0 \times 10^{-3} \text{ mol dm}^{-3}$) or [one mole of $[\text{Co}^{\text{III}}\text{W}_{12}\text{O}_{40}]^{5-}$ from 2.2×10^{-4} to $1.8 \times 10^{-3} \text{ mol dm}^{-3}$ at constant methionine ($3.0 \times 10^{-2} \text{ mol dm}^{-3}$). The pseudo-first-order rate constants were found to be increased with increase in the concentration of the maltose and the order was found to be 0.88 as determined by plot of $\log(k_{\text{obs}})$ against $\log[\text{maltose}]$. The order in oxidant concentration was found to be unity as the pseudo-first-order plots were found to be linear and the pseudo-first-order rate constants were fairly constant as the concentration of oxidant is varied (Table 2).

The effect of hydrogen ion concentration on the reaction was studied to know probable prior protonation equilibria of either the oxidant or the substrate and to identify the active reactant species. The concentration of H^+ ion was varied from 0.1 to 0.5 mol dm^{-3} keeping all other concentrations constant. It was found that the reaction rate increases with the concentration of H^+ ions (Table 2) and the order in $[\text{H}^+]$ was determined from the plot of $\log k_{\text{obs}}$ against $\log[\text{H}^+]$ and was found to be 0.91.

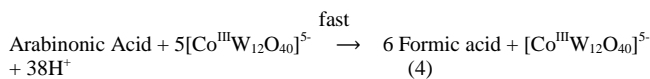
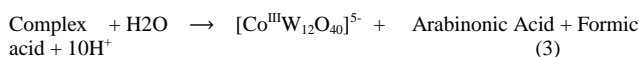
3.3 Effect of solvent polarity and ionic strength:

The effects of ionic strength and solvent polarity were studied keeping concentration of $[\text{Co}^{\text{III}}\text{W}_{12}\text{O}_{40}]^{5-}$, methionine and perchloric acid constant at $1.0 \times 10^{-3} \text{ mol dm}^{-3}$, 0.03 mol dm^{-3} and 0.35 mol dm^{-3} respectively at 25°C . Sodium perchlorate and acetonitrile were used to vary the ionic strength and solvent polarity, respectively. The rate of the reaction was unaffected by increasing ionic strength from 0.40 to 0.90 mol dm^{-3} .

3.4 Mechanism and rate law:

The mechanism according to Scheme 3 proceeds with the formation of a complex between

the maltose and $[Co^{III}W_{12}O_{40}]^{5-}$ in a prior equilibrium which then decomposes to give Arabinonic Acid, Formic acid and $[Co^{III}W_{12}O_{40}]^{8-}$ in a rate determining step. Arabinonic Acid reacts with five molecules of oxidants in fast step to give the product formic acid.



Scheme 3

$$\text{Rate} = \frac{k_1 K_2 [H^+] [\text{maltose}] [Co^{III}W_{12}O_{40}]^{5-}}{([H^+] + K_1)(1 + K_2 [\text{maltose}])} \quad (5)$$

$$k_{\text{obs}} = \frac{k_1 K_2 [H^+] [\text{maltose}]}{([H^+] + K_1)(1 + K_2 [\text{maltose}])} \quad (6)$$

4. Conclusions:

Kinetics of oxidation of maltose by protonated 12-tungstocobaltate (III) has been investigated at 25°C. Almost constant values of pseudo-first-order rate constant obtained during the variation of oxidant, 12-tungstocobaltate (III) clearly reveal that order of reaction with respect to $[Co^{III}]$ is unity. First-order kinetics with respect to $[Maltose]$ and $[H^+]$ is evident from the observed values of rate constants. Variations in ionic strength (μ) and dielectric constant (D) do not affect the rate of reaction. Protonated 12-tungstocobaltate (III) and unprotonated maltose have been postulated as the reactive species during the reaction. The main oxidation product of the reaction was identified as formic acid.

Table 1: Sample run for oxidation of maltose by 12-tungstocobaltate (III) in perchloric acid medium at 25°C. $[HClO_4] = 0.3 \text{ mol dm}^{-3}$, $[Co^{III}] = 1 \times 10^{-3} \text{ mol dm}^{-3}$, $[Maltose] = 0.1 \text{ mol dm}^{-3}$, $I = 0.4$.

$10^3 [Co^{III}W_{12}O_4]^{5-}$ mol dm ⁻³	$10 [HClO_4]$ mol dm ⁻³	$10 [Maltose]$ mol dm ⁻³	$10^3 k_{\text{obs}}$ s ⁻¹
0.2	3.0	1.0	1.20
0.4	3.0	1.0	1.10
0.6	3.0	1.0	1.12
0.8	3.0	1.0	0.99
1.0	3.0	1.0	1.23
1.0	1.0	1.0	0.43
1.0	2.0	1.0	0.90
1.0	3.0	1.0	1.23
1.0	4.0	1.0	1.86
1.0	5.0	1.0	2.30
1.0	3.0	0.1	0.16
1.0	3.0	0.3	0.56
1.0	3.0	0.5	0.85
1.0	3.0	0.7	1.05
1.0	3.0	1.0	1.23

Time in min	Absorbance at 624 nm	Log(a/a-x)
0	0.284	-
2	0.261	0.036678
4	0.226	0.09921
6	0.193	0.167761
8	0.163	0.241131
10	0.137	0.316598
12	0.114	0.396413
14	0.095	0.475595
16	0.077	0.566828
18	0.064	0.647138
20	0.053	0.729042

Table 2: Effect of concentration of maltose, perchloric acid and 12-tungstocobaltate (III) ion, on the reaction between maltose and 12-tungstocobaltate (III) at 25°C

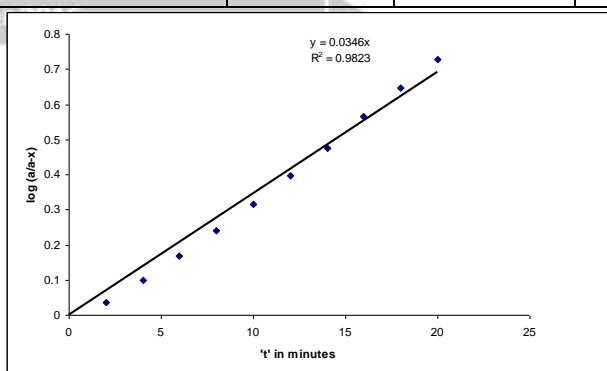


Fig:1 Pseudo first order plot for oxidation of maltose by 12-tungstocobaltate (III) in perchloric acid. (Conditions as in table 1)

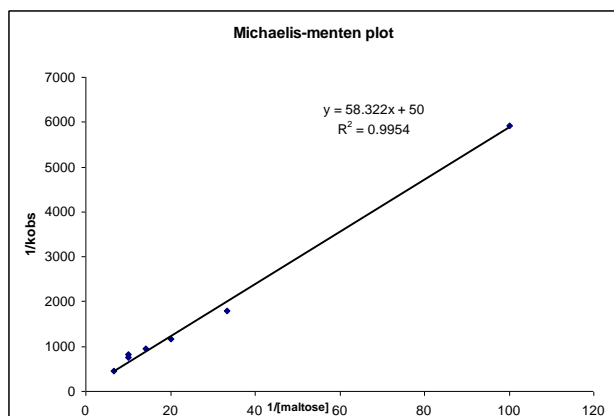


Fig: 2 Michaelis-Menten plot for oxidation of maltose by 12-tungstocobaltate (III) in perchloric acid. (Conditions as in table 2)

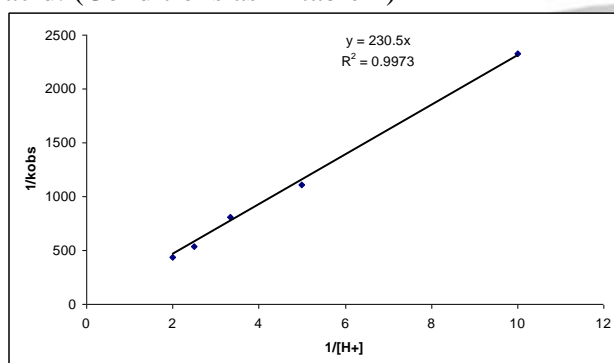


Fig. 3 Verification of rate law (Plot of $1/k_{obs}$ versus $1/[H^+]$)

Reference

1. Weinstock I. A, Chem Rev 1998, 98,113-170.
2. Saha S. K, Ali M, Banerjee, Coord Chem Rev 122 (1993) 41.
3. Chester A. W, J. Org. Chem 1970, 35, 1797-1800.
4. Nolan A. L, Burns R. C, Lawrance G. A, J. Chem Soc Dalton Trans 1998, 3041
5. Mizuno N, Misono M 1998 Chem Rev 98:199.



Surfactant Encapsulated Cobalt Complex Catalyst for Environmental Friendly Oxidation of Alcohols

Babasaheb Bhosale^a Sunil Zende^b Shashikant Sawant^b and Balasaheb Sargar^c

^aRajaram College Kolhapur, ^b DM Bidri and ^c Jaysingpur College Jaysingpur

Corresponding author: bdb_bhosale@rediff.com

Abstract

The surfactant encapsulated cobalt complex is prepared and characterized, which is used for Green oxidation of many simple aliphatic, aromatic and substituted alcohols. This encapsulated catalyst can be recycled number of times without losing its activity more than 5%. To understand the mechanism of the oxidation, kinetic study of oxidation is also studied.

Keywords: Encapsulated, Cobalt Complex, Alcohol, Oxidation

1. Introduction

Many of the present oxidizing agents used for oxidation of alcohols are hazardous and carcinogenic. In search of green and environmental friendly oxidation, we prepared surfactant encapsulated cobalt complex and used it for oxidation reactions as a catalyst using hydrogen peroxide as a green oxidizing agent

All the solutions required throughout the work were prepared in doubly distilled water, and standardized before starting the experiment. The cobalt complexes $[\text{Co}^{\text{III}}\text{W}_{12}\text{O}_{40}]^{5-}$ and $[\text{Co}^{\text{II}}\text{W}_{12}\text{O}_{40}]^{6-}$ were prepared¹ by the reported method. The solutions of $\text{K}_5[\text{Co}^{\text{III}}\text{W}_{12}\text{O}_{40}]$ and $\text{K}_6[\text{Co}^{\text{II}}\text{W}_{12}\text{O}_{40}]$ were standardized spectrophotometrically² (at 388 nm for $[\text{Co}^{\text{III}}\text{W}_{12}\text{O}_{40}]^{5-}$ and at 624 nm for $[\text{Co}^{\text{II}}\text{W}_{12}\text{O}_{40}]^{6-}$

respectively) using cystronic 119 UV-VIS spectrophotometer. All other chemicals were of analytical reagent grade used without further purification. The organic solvents like acetonitrile and 1-4, Dioxane were of spectroscopy grade used without further purification.

3. Results and Discussion

The oxidation of aliphatic alcohols by hydrogen peroxide catalyzed by surfactant encapsulated keggin type 12-tungstocobaltate (II), prepared by using cationic surfactant and characterized by IR, and C, H, N, analysis, has been carried out in buffer as well as weak acid solution. The oxidation of aromatic and substituted aromatic alcohols by hydrogen peroxide catalyzed by surfactant encapsulated keggin type 12-tungstocobaltate (II) has been studied in 50% aqueous acetonitrile solution

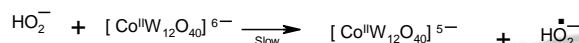
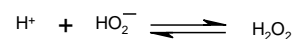
Alcohol (2.2 mmol) and Hydrogen peroxide (10 mmol) were taken in a buffer of pH = 4 and the catalyst $[\text{Co}^{\text{II}}\text{W}_{12}\text{O}_{40}]^{6-}$ (0.4gm) was added. In case of benzyl and substituted benzyl alcohols, 50-50% acetonitrile was used as solvent. The reaction mixture was stirred at 40°C for 5-10 h. The progress of the reaction was monitored by TLC. After completion of the reaction, the resulting solution was extracted with dichloromethane. The combined organic layer was washed with a solution of NaHCO_3 and dried over MgSO_4 . The products of oxidation of primary alcohols are respective aldehydes and secondary alcohols are ketones. The organic solution was then filtered and concentrated to obtain the crude carbonyl compound. The melting points of the 2-4 DNP derivatives of the products obtained agree well with the literature values (Some examples are given in table 1) confirming the aldehydes or ketones as the oxidation products in the case of all the alcohols studied.

To understand the mechanism of the reaction, various effects like effect of H^+ ion concentration,

Alcohol	Melting Point of 2,4 DNP	
	Observed	Literature
Methyl alcohol		
Ethyl alcohol	165	166
n-Propyl alcohol	170	168
Isopropyl alcohol	154	155
n-butyl alcohol	127	128
Isobutyl alcohol	120	123
Hexyl Alcohol	185	187
Benzyl alcohol	235	265
2-nitro-benzyl alcohol	264	265
	300	302
4- nitro-benzyl alcohol	263	265
4- chloro-benzyl alcohol	231	233

catalyst concentration and substitution concentration in case of benzyl alcohol is studied. With the help of kinetic results and activation parameters obtained, the following mechanism is proposed for the reaction.

The mechanism of oxidation of $[\text{Co}^{\text{II}}\text{W}_{12}\text{O}_{40}]^{6-}$ by hydrogen peroxide was studied separately in our laboratory and found to be as represented in *Scheme 1*



The kinetic data of both aliphatic and benzyl alcohols suggest that the initiation of the reaction occurs by interaction of the catalyst and oxidant generating oxidized form of the catalyst, 12-tungstocobaltate (III), which then oxidizes the substrate in a rate determining step.

In order to understand the nature of the active species of the reactants the effect of pH was studied. In case of aliphatic alcohols the time of reaction decreases with increase in pH of the solution which is due to prior protonation equilibria. Here unprotonated form the reactant, HO_2^- is an active species. Since catalyst, 12-tungstocobaltate(II), do not undergo protonation as evidenced by spectroscopic studies³ and alcohol also do not undergo protonation. It is protonation of the oxidant which affects the time of the reaction as the pH changes.

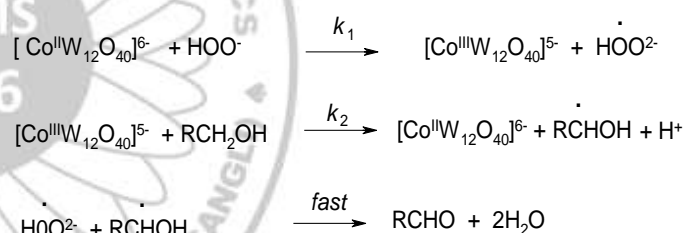
The oxidant, Hydrogen peroxide, in aqueous solution exists as HO_2^- and gets protonated as shown in equilibrium 1.



Since the rate of reaction increase with increase in pH or decrease in $[\text{H}^+]$, the unprotonated HO_2^- is the active species in the present study. There is no significant variation in the reaction time even when the nature of alcohol is changed; it indicates that the initiation of the reaction is due to the interaction of oxidant and the catalyst,

$[\text{Co}^{\text{II}}\text{W}_{12}\text{O}_{40}]^{6-}$. The detailed study of the mechanism reaction between oxidant and the catalyst was found to involve two single-electron transfer steps (*Scheme 1*) with HO_2^- as the oxidant species. In the $[\text{Co}^{\text{II}}\text{W}_{12}\text{O}_{40}]^{6-}$ catalyzed alcohol oxidation also, the reaction proceeds with the generation of $[\text{Co}^{\text{III}}\text{W}_{12}\text{O}_{40}]^{5-}$ in the slow step which then abstracts an electron from the alcohol to produce an alcohol-free radical. The concentration of the catalyst used is of the order of 4.0×10^{-5} and that of the oxidant is very high, of the order 3.0×10^{-2} , making dependence of the overall reaction on oxidant concentration negligible. The effect of pH on the reaction also justifies earlier results considering HO_2^- as the active oxidant species. The concentration of the species increases with pH leading to the enhancement of the rate of the reaction.

Therefore, the general mechanism of the $[\text{Co}^{\text{II}}\text{W}_{12}\text{O}_{40}]^{6-}$ catalyzed oxidation of alcohols by hydrogen peroxide can be represented as in *Scheme 2*.



Scheme 2

The catalyst, $[\text{Co}^{\text{II}}\text{W}_{12}\text{O}_{40}]^{6-}$ is recovered by simple filtration and it can be recycled number of times without losing its catalytic activity in measurable percentage or more than 5%. This catalyst can be stored without taking so much precaution and undergo heterogeneous reaction.

References

1. Sadakane, M.; Steckhan, E., *Chem. Rev.* 1998, 98, 219.
2. Baker, L. C.; McCutcheon, T. P. *J Am Chem Soc* 1956, 78, 4503.
3. Lawrence, G. A.; Burns, R. C.; Nolan, A. L., *J. Chem. Soc., Dalton Trans.* 2002, 3065.
4. Lawrence, G. A.; Burns, R. C.; Dunne, S. J.; Hambley, T. W., *Aust. J. Chem.* 1992, 45, 685.
5. Leparulo-Loftus, M. A.; Pope, M. T., *Inorg. Chem.* 1987, 26, 211.

Studies on Nano Crystalline $\text{Co}_{1-x}\text{Cd}_x\text{S}$ Thin Films

S. T. Mane^{*a}, R. S. Mane^a, D. G. Kanase^a, and L. P. Deshmukh^b

^aBharati Vidyapeeth's Dr. Patangrao Kadam Mahavidyalaya, Sangli- 416416, M.S., India.

^bThin Film and Solar Studies Research Laboratory, Department of Physics (Appl. Elect.), Solapur University, Solapur -413255,

M.S., India. *E-mail:* manesantosh7476@gmail.com

Abstract

$\text{Co}_{1-x}\text{Cd}_x\text{S}$ ($0 \leq x \leq 0.35$) thin films have been deposited by a chemical bath deposition process onto the glass and report their physical, microscopic and electrical transport properties. The deposition was carried out from a complex liquid phase formed by equimolar volumes of cobalt sulphate, triethanolamine, thiourea and cadmium sulphate; all AR grade. The film composition was decided by appropriate volume of cadmium sulphate. The preparative parameters, such as growth temperature (56°C), time (80 mins.), reaction pH (11 ± 0.2) and the rate of mechanical churning (70 ± 2) etc, were used as-optimized. The samples were thin, uniform, and tightly adherent with color changing from dark green to dark chocolate as x was varied from 0 to 0.35. Surface morphology of these films was determined by a Scanning Electron Microscopy (SEM). SEM's revealed a network of long elongated thread type crystallites tapered or pointed at both ends; randomly oriented and threaded into each other. The dc electrical conductivity and thermoelectric power were therefore measured in the 300 K -550 K temperature range and their temperature dependences have been studied to determine the various materials transport characteristics. The composition dependence of an electrical conductivity revealed increase in conductivity upto $x=0.1$ and thereafter conductivity decreased. Thermoelectric power measurements showed an increase in TEP with temperature showing n-type conduction.

Keywords: $\text{Co}_{1-x}\text{Cd}_x\text{S}$ thin films, surface morphology, Electrical transport, n-type.

1. Introduction

Nanomaterials have recently received much attention because of their unique physical, chemical and mechanical properties. The control on the fundamental properties of materials, such as magnetic, optical and electrical properties, can be achieved without altering their chemical composition by controlling the size, structure and surface morphology of the nanocrystalline materials. Nanostructured semiconductors show interesting electro-optical properties and catalytic behaviour, which imply that their surface properties significantly affect their structural and optical properties. Furthermore, modifying the surfaces of nanoparticles with various inorganic species removes their surface defects and influences their optical properties[1-18].

Our main intention is to develop the electrochemical PV-devices comprising ternary semiconducting materials that are known to exhibit excellent characteristic properties in tune with an ideal photovoltaic material. In the right perspectives, efforts need to be focused on improving the conversion efficiency and lowering the cost of the thin film based solar cell. For electrochemical PV- cell, the primary requirement for good solar energy conversion is that the photocathode or photoanode should have band gap close to the maximum in the visible spectrum of solar light. It has been found that the band gaps of

ternary materials can be adjusted using a solid state reaction with semiconductors with wide and narrow band gaps. In addition, cobalt sulfides are versatile materials with potential applications in solar cells, super capacitors, lithium-ion batteries and alkaline rechargeable batteries. The electrical, optical and microscopic properties make it extremely useful as potential candidate for many practical applications viz. electrochemical PV-devices, super capacitors and optoelectronic devices. Due to these important properties, many recent efforts have been dedicated to the synthesis and photoelectrochemical test of cobalt sulfides thin films. Furthermore CoS has remained a focus of the material science community due to its important band gap, conversion efficiency, high absorption coefficient and last but not the least its significantly low cost. Recently, incorporation of CdS into CoS to form $\text{Co}_{1-x}\text{Cd}_x\text{S}$ solid solution is one effective way to improve the activity of CoS by making conductive band edge of CoS more negative [7, 19, 28]. Both these semiconductors have appropriate band gaps, high optical absorption coefficients and similar crystallographic structures those can be tuned suitably for optical applications. Therefore, it is expected that, formation of solid solutions might take place when a small amount of CdS is mixed with CoS causing alterations in the energy gap, lattice parameters and materials properties making it more effective PV-material. Among the various

synthesis routes, chemical bath deposition is known to be one of the most convenient, versatile and matured technique for the preparation of thin films. It is the conventional method with the advantages of economy, convenience, ease of scaling up to large area deposition and high degree of composition control [7,8,22,23,28-35]. However, to the best of our knowledge, there has been no report on the synthesis of $\text{Co}_{1-x}\text{Cd}_x\text{S}$ thin films by chemical bath deposition method.

Keeping in mind this idea, in our present investigation we have prepared $\text{Co}_{1-x}\text{Cd}_x\text{S}$ thin film on glass substrate substrates by chemical bath deposition method and report their physical, microscopic and electronic properties.

2. Experimental details

2.1. Preparation of $\text{Co}_{1-x}\text{Cd}_x\text{S}$ thin films

$\text{Co}_{1-x}\text{Cd}_x\text{S}$ ($0 \leq x \leq 0.35$) thin films were prepared on mechanically cleaned glass substrates by chemical bath deposition method set by us [7, 19, 23, 28, 31] with analytical grade reagents. Equimolar (1M) volumes of cobalt sulphate, cadmium sulphate and thiourea (in proportion with x value) were taken in a reaction bath and allowed to react in an alkaline medium to produce $\text{Co}_{1-x}\text{Cd}_x\text{S}$ thin film deposits. Sufficient quantities of ammonia (16 ml) and triethanolamine (2 ml) were used as the complexing agents. For each material series prepared, the film stoichiometry was maintained by adjusting the ion concentration volumes of the basic reactants. The glass substrates were then positioned vertically on a specially designed substrate holder and were rotated in the reaction bath by means of a constant speed gear motor. To obtain good quality samples, the deposition time (80 mins.), reaction pH (11 ± 0.2), speed of substrate rotation (70 ± 2 rpm) and deposition temperature (56°C) were taken as optimized. The experimental details and preparation procedure are reported elsewhere [7, 19, 28, 31]. After deposition, the films were allowed to cool down to room temperature and then taken out for further characterization.

2.2 Characterization of the films

The films so obtained were then characterized through the electrical transport and microscopic properties. The thicknesses of the as-deposited layers were measured by an AMBOS-XP-1 profilometer. The electrical conductivity and

thermoelectric power measurements in the 300 -550 K temperature ranges were done on these samples using a two point probe technique. The area of the film was defined and silver paste was applied to ensure good electrical contact to the films. Cu-press contacts were used for the measurements. The working temperature was recorded using a Chromel-Alumel thermocouple. The current and voltage were recorded by DNM - 121, 4, 1/2 digit nanoammeter and a HIL - 2665, 4, 1/2 digit multimeter respectively. The surface morphology of the films was analyzed by a scanning electron microscope, SEM (JOEL 6360, JED 2300) operating an accelerating voltage of 30 kV and probe current of 1 nA with PHA mode T3.

3. Results and Discussion

3.1 Growth and physical observations

The CoS and $\text{Co}_{1-x}\text{Cd}_x\text{S}$ ($0 \leq x \leq 0.35$) thin films were obtained from a sufficiently high alkaline medium ($\text{pH} = 11 \pm 0.2$) on glass substrates which were previously degreased in concentrated nitric acid for 24 hours, washed with detergent solution and rinsed with double distilled water and dried ultrasonically. The reaction bath for deposition of CoS was composed of 10 ml (1M) CoSO_4 , 2 ml TEA, 16 ml ammonia, 10 ml (1M) thiourea and 150 ml double distilled water, which were added chronologically. During deposition cations and anions react each other to form neutral molecules, which either precipitate spontaneously or very slowly in high alkaline medium. Fast precipitation implies no film formation on the substrate surface. On the other hand, if the precipitation action is controlled slow (with reaction additives like TEA or NH_3), then neutral molecules could get sufficient time and chance to stabilize on the substrate surface that initiate the film formation process, which is favored energetically and enhanced by the reaction temperature and speed of the substrate rotation. The Co^{++} and S^{--} then condense on the surface of the substrate and get deposited as CoS. The formation of CoS occurs when the ionic product of Co^{++} and S^{--} exceeds the solubility product under the control of deposition conditions. The $\text{Co}_{1-x}\text{Cd}_x\text{S}$ thin composite films with various x values ($0 \leq x \leq 0.35$) were obtained by the co-deposition of Co^{2+} , Cd^{2+} , S^{2-} ions from the reaction mixture consisting of triethanolamine

complex of cobalt and cadmium ions under the same conditions of deposition. The quality deposition results only when a number of preparative parameters (such as temperature, time, pH, speed of the substrate rotation, concentration of basic ingredients, etc) are optimized. Therefore the film growth was examined as a function of few of the deposition parameters that were optimized and are time (80 minutes), temperature (56 °C), pH (11±0.2) and speed of the substrate rotation (70 ± 2 rpm).

As deposited films appear thin, uniform, tightly adherent and diffusely reflecting with colour changing from dark green to dark chocolate as x was varied from 0 to 0.35. The change in colour with increased Cd-concentration in CoS lattice indicates that Cd²⁺ forms an alloy with CoS under certain controlled experimental conditions. The compositional studies may strengthen these observations. In present investigation the film thicknesses of the various Co_{1-x}Cd_xS composites were measured using an AMBOS-XP-1 profilometer. It was found that the film thickness increased initially with increasing Cd content up to 0.1 and thereafter decreased with further increase of Cd concentrations in CoS. This behavior can be understood first, from role of the cadmium atom as a nucleation centre that enhances the growth process and therefore the thickness. Secondly at higher concentrations (>0.1), cadmium may occupy interstitial sites causing an impurity scattering and thereby preventing the further film growth.

3.2. The surface morphological studies

The surface morphologies of the CoS and Co_{1-x}Cd_xS thin films were therefore examined through a scanning electron microscope. Fig. 1 shows the SEM micrographs of various Co_{1-x}Cd_xS thin films. The SEM of CoS (micrograph a) shows a network of long elongated thread type crystallites tapered or pointed at both ends; randomly oriented and threaded into each other [19,28]. This is true for the values of x equal to 0, 0.025, 0.05 and 0.1. Further, upon addition of Cd in CoS improved the crystallite size with well defined grains and grain boundaries. In general, it has been seen that there is a significant improvement in the grain structure with a considerable grain boundary improvement

for the solid solution regions from both sides (0 ≤ x ≤ 0.1).

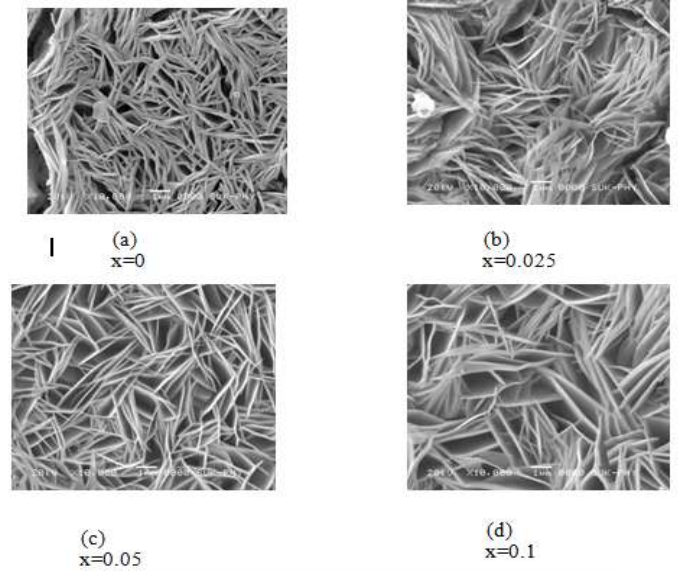


Fig.1 (a-d). Surface morphologies of CoS and Co_{1-x}Cd_xS thin films.

3.3.1 The electrical conductivity studies

Electrical behaviour of Co_{1-x}Cd_xS (0 ≤ x ≤ 0.35) thin films was studied in the temperature range 300–550 K, under constant voltage (10 V). The electrical conductivity of these as-deposited films was found to be dependent on the working temperature and film composition. The measurements showed an increase in electrical conductivity with increasing the working temperature. This indicates semiconducting nature of the material. The electrical conductivity is found to be composition dependent and it revealed increase in conductivity with increase in x for 0 ≤ x ≤ 0.1 and remained more or less constant upto x=0.35. The increasing amount of Cd-content in Co_{1-x}Cd_xS (0 ≤ x ≤ 0.35) thin films lead to an increase in the conductivity, which is due to the improved microstructure of the films. When Cd-content in the CoS bath was increased (0 ≤ x ≤ 0.1), the film content (Cd) also increased. As Cd²⁺ is more conductive than Co²⁺, an increase in electrical conductivity is obvious. This is further supported by the decreased dislocation density in this region. Hence addition of Cd into CoS increased the conductivity up to x=0.1 and thereafter conductivity decreased due to the structural disorder and mixed phases obtained between x=0.2 to x=0.35. The variation of log σ with the reciprocal of temperature for few of the typical Co_{1-x}Cd_xS films is shown in

Fig. 2. Activation energy of electrical conduction was calculated in both the regions and has been seen that the activation energy continuously decreased from 0.68 eV to 0.64 eV as x was increased from 0 to 0.1. The decrease in activation energies is due to the enhanced grain structure that reduces the height of the barrier between the crystallites composing the films.

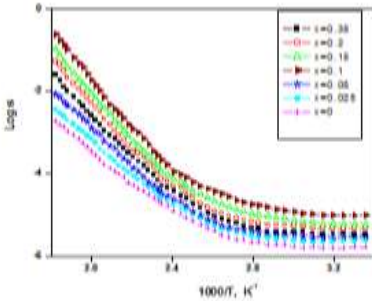


Fig. 2: Variation of an electrical conductivity with working temperature for $\text{Co}_{1-x}\text{Cd}_x\text{S}$ thin films ($0 \leq x \leq 0.35$).

3.3.2. The thermoelectric power studies

The thermo emf measurements were also carried out on these samples by establishing a temperature gradient and measuring the open circuit voltage across the ends of the sample. For all the samples, thermoelectric voltage is found to be

negative, which revealed n-type electrical conduction. For each temperature considered, the

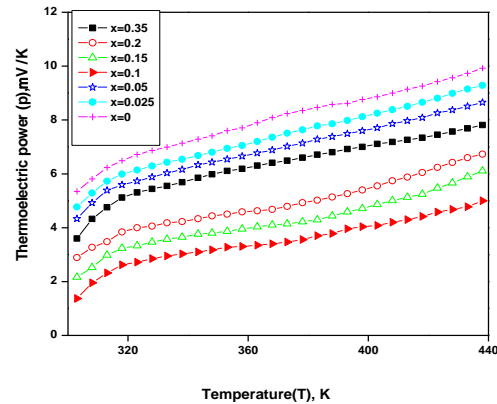


Fig.3 Variation in thermoelectric power with the working

increasing amount of Cd-concentration in $\text{Co}_{1-x}\text{Cd}_x\text{S}$ increases the magnitude of thermoelectric power (TEP) up to $x = 0.1$ and then it decreases. The temperature dependence of TEP (P) is shown in Fig. 3 for representative samples. From Fig. 3, it appears that the temperature dependence of TEP is quasilinear in the range of temperature studied.

4. Conclusions

The deposition of $\text{Co}_{1-x}\text{Cd}_x\text{S}$ ($0 \leq x \leq 0.35$) composite films is made possible with an inexpensive chemical bath deposition method. Thin, uniform, tightly adherent and diffusely reflecting films are obtained at our experimental conditions. The composites are Co-rich and addition of Cd causes improvement in the grain structure. SEM revealed that there is a significant improvement in the grain structure with a considerable grain boundary improvement for the solid solution regions ($0 \leq x \leq 0.1$). The electrical conductivity increased for the change of x from 0 to 0.1. TEP study revealed that all the samples are n-type semiconductors.

Acknowledgments

One of the authors (STM) is grateful to Dr. Vishwajit Kadam, Secretary and M.S. Sagare, Joint-Secretary Bharati Vidyapeeth, Pune, India for moral support and encouragements.

References

- [1] D. Jain, C.G.S. Pillai, ITAS Bulletin, 4(2011) 10-22.
- [2] P. Lala, Electronics maker, December (2011) 66-69.
- [3] V. Damodara Das, L. Damodare, Surface and Coatings Techno. 94-95 (1)
- [4] C. Tseng, C. Wang, K. Cheng, Sol. Energy Mater. Sol. Cells 96 (2012) 33
- [5] S. Chandra, In: Campbell, D. S. (Eds), Gordon and Breach, Science Publishers, New York, USA, 1985.
- [6] K.L. Chopra, P. D. Paulson, V. Dutta, Progress in Photovoltaics: Research and Applications 12 (2004) 69–92.
- [7] S.T. Mane, et al Proc.International Conference On Advanced Materials and Nanoparticles, Oct 21-23, 2011, Kathmandu,
- [8] L.P. Deshmukh, S.G. Holikatti, Journal of Physics D: Applied Physics 27
- [9] L.P. Deshmukh, S.T. Mane, Digest Journal of Nanomaterials and Biostructure 6(3) (2011) 931- 936.
- [10] M. Gratzel, Nature 421 (2003) 586 – 587.
- [11] F. Huang, C. Yang, D. Wan, Front. Physics 6(2) (2011)177- 196.
- [12] P.D. More, L.P. Deshmukh, Materials Chemistry and Physics 80 (2003)
- [13] A. Aruchamy, G. Aramudan, G.V. Subba Rao, Bulletin Material Science
- [14] A.G. Aberle, Thin Solid Films 517 (2009) 4706–4710.
- [15] P.K. Mahapatra, A.R. Dubey, Sol. Energy Mater. Sol. Cells 32 (1994) 29–
- [16] M. Sharon, K. S. V. Santhanam, UNESCO Training Workshop, 6 (1986).
- [17] T.M. Razykov, C.S. Ferekides, D. Morel, E. Stefanakos, H.S. Ullal, H.M. Upadhyaya, Sol. Energy 85(8) (2011) 1580-1608.
- [18] D. Wei, G. Amaratunga, International J. of Electrochem. Sci. 2 (2007)
- [19] S.T. Mane, P.C. Pingale, S.S. Kamble, V.S. Karande, L.P. Deshmukh, Advance in Appl. Sci. Research 2(5) (2011) 8-18.
- [20] N. Bahadur, A. K. Srivastava, S. Kumar, M. Deepa, B. Nag, Thin Solid Films 518(2010) 5257-5264.
- [21] R. Sathyamoorthy, et. al. J. Alloys Compd. 493 (2010) 240–245.
- [22] G. Hodes, Phys. Chem. Chem. Phys. 9 (2007) 2181–2196.
- [23] V.S. Karande, S.H. Mane, V.B. Pujari, L.P. Deshmukh, Mater. Lett. 59
- [24] K.R. Murali, K. Thilagavathy, S. Vasantha, P. Gopalakrishnan, P. Rachel Oommen, Sol. Energy 84 (2010) 722- 729.
- [25] E. Bacaksiz, M. Tomakin, M. Altunbas, M. Parlak, T. Colakoglu, Phys. B 403 (2008) 3740-3745.
- [26] Z.R. Khan, M. Zulfequar, M. Shahid Khan, Mater. Sci. Eng. B 174 (201)
- [27] R. Sathyamoorthy et al, J. Alloys Compd. 493 (2010) 240–245.
- [28] S.T. Mane, S.A. Lendave, S.S. Kamble, L.P. Deshmukh, Mater. Lett. 67
- [29] N.K. Allouchea, et. al., Mater. Chem. Phys. 123 (2010) 620–624.
- [30] A. Kassim, H.S. Min, T.W. Tee, L.K. Siang, S. Nagalingam, Research J. Appl. Sci. Eng. Tech. 3(6) (2011) 513-518.
- [31] S.T. Mane, S.S. Kamble, L.P. Deshmukh, Mater. Lett.65 (2011) 2639

Wetting properties of Rose petals

D.M. Chougule, A.S. Yadav, P.P. Zambre

Department of Physics, Raje Ramrao Mahavidyalaya, Jath-416404, Maharashtra, India

Abstract

The wetting of rough surfaces remains a subject of active investigation by scientists. since several modes or regimes of wetting of a rough surface can exist, including the Rose and petal. However, it was found recently that high with strong adhesion between water and a solid surface in the case of the so-called 'rose petal' effect. Understanding the wetting of rough surfaces is important in order to design non-adhesive surfaces for various applications.

1. Introduction

The wettability of a rough surface, has been active area of research because these micro-, nano- and hierarchical structures bring about many properties. low or high adhesions to water drops, for applications as diverse as self-cleaning surfaces.

The superhydrophobicity have high droplet cohere adhesion are found on the leaves of many plants, most famously the red rose. The water droplet on the rose leaf then do not stay stably on this surfaces, where they can spontaneously roll off with slight tremble. Here we show that this does not apply to a high adhesive superhydrophobic rose petal surface. Superhydrophilic can be used for high adhesion surface ,more difficult to create superhydrophobic surface. When two hydrophilic bodies are brought into contact, any liquid present at the interface forms menisci, which increases adhesion/friction and the magnitude is dependent upon the contact angle. Wettability and hydrophilicity phenomenon are usefull in solving practical issue as well as scientific concerns on both molecular and microscopic scals under static and

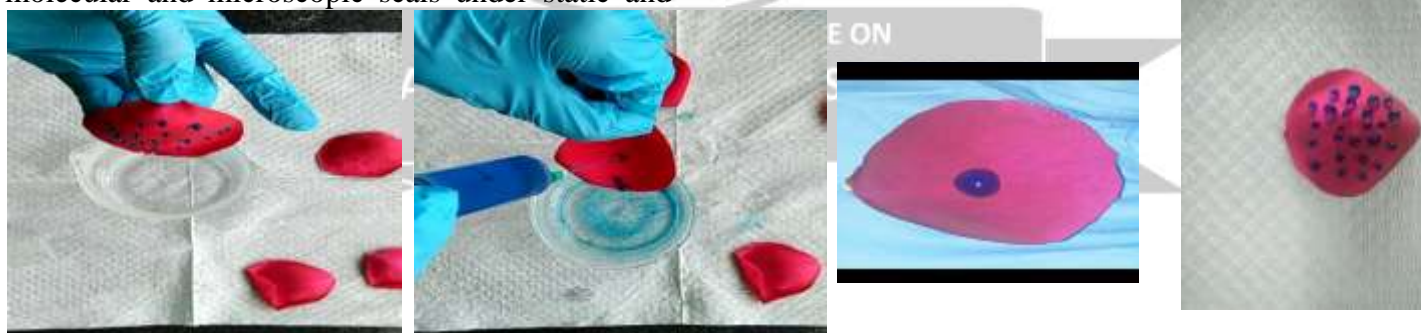
dynamic conditions. These micro and nanostructures provide a sufficient roughness for superhydrophobicity and yet at the same time a high adhesive force with water .A water droplet on the surface of the petal appears in spherical shape, which cannot roll off even when the petal is turned upside down.

2. Experimental Details

The purpose of the study is to create rose petal effect surface using hydrophobic and hydrophilic nanoparticle .The study and properties of superhydrophobic can be observed on a rose petal with high adhesion.

Take some water in beaker and blue colour added in water. . The water droplet on the rose leaf then does not stay stably on these surfaces, where they can spontaneously roll off almost effortlessly. During this process dust particles are removed.

One side petal of rose to show the sticky hydrophobic and another side observe non-sticky hydrophobic .



3. Conclusion

In this study the understanding of the petal effect provides us with an example of the nature of a superhydrophobic surface with a high adhesive force to water. In this work, several modes of wetting of rough surfaces were investigated. Rose petals have different hierarchically organized surface microstructure and can exhibit high and low adhesion to water. The pitch spacing and height of the microstructures controls the wetting regime, since it controls the penetration of water into the microstructure.

References

1. Bharat Bhushan, Michael Nosonovsky Bharat Bhushan, Michael Nosonovsky Published 20 September 2010. DOI: 10.1098/rsta.2010.0203
2. Daniel Ebert, Bharat Bhushan Wear-resistant rose petal- effect surface with superhydrophobicity and high droplet adhesion using hydrophobic and hydrophilic nanopartiels 19th Avenue, Columbus, OH 43210-1142USA
3. L Feng, Y Zhang, J Xi, Y Zhu, N Wang, F Xia, L Jiang - Langmuir, Petal effect: a superhydrophobic state with high adhesive force. 2008 - ACS Publications

Synthesis, characterization and photocatalytic application of Cr substituted ZnMnFeO₄

R. P. Patil^{a*}, A.D.Pinjarkar^a, B.V.Jadhav^c, R.R.Sawant^b, S.B.Patil^b

^a Department of Chemistry, M.H.Shinde Mahavidyalaya, Tisangi 416206, MH, India

^b Department of Physics, Krantisinh Nana Patil College Walwa, Sangli- 416313, MH, India

^c Department of Chemistry, C.K.T.College, Panvel, Mumbai,410206, MH, India

Abstract

Nanocrystalline ZnMn_{1-x}Cr_xFeO₄ (1.0 ≥ x ≥ 0) ferrites were prepared by sol-gel route. The synthesized material was characterized by various physicochemical methods. X-ray diffraction (XRD) method was used to confirm the formation of single phase cubic spinel lattice for all the composition. Lattice parameter shows a decreasing trend with an increase in Cr content in the compositions. Formation of spherical nanoparticles was revealed by scanning electron microscopy (SEM) analysis. Photocatalytic activity studies for thymol blue degradation indicate an enhanced activity for the composites when the maximum chromium is present in ZnMnFeO₄. The detailed results of physicochemical properties and photocatalytic application have been discussed so as to bring out the role of chromium substitution in determining structural and photocatalytic application of Zn-Mn ferrites.

Keywords: Ferrites, Sol-gel method, XRD, SEM, Photocatalysis

1.0 Introduction

Mixed-metal oxide nanoparticles have been intensively studied in the last decade for their unusual physical and chemical properties owing to their extremely small size, large specific surface area and number of promising applications. Among various classes of nanomaterials, metal oxides are very common, most diverse and possess richest class in terms of physical, chemical and structural properties. The result and prospects of numerous applications of metal oxides, such as fabrication of microelectronic circuits, sensors, piezoelectric devices, fuel cells, dielectrics, lasers, magnets and catalysts have been discussed in literature [1-13].

Recently, considerable effort has been made on the preparation of surface modified nanoparticles of different types of metal oxides. Various methods are available for the synthesis of metal oxides, such as microwave refluxing [14], sol-gel [15-16], hydrothermal [17-18], co-precipitation [19-20], citrate-gel [21] and spray pyrolysis [22] etc. The selection of appropriate synthetic procedure often depends on the desired properties and final applications. Among these synthesis techniques, sol-gel autocombustion method has several advantages over others for preparation of nanosized metal oxides as the process begins with a relatively homogeneous mixture and involves low temperature conditions and results a uniform ultrafine porous powders [23]. This method was employed by us to obtain improved powder characteristics, better homogeneity and narrow particle size distribution, thereby influencing structural, electrical and magnetic properties of spinel ferrites [24-26]. Spinel ferrites find potential applications in electrical components, memory devices, magnetostrictive and microwave devices over a wide range of frequencies because of their high resistivity and low losses [27-31]. The field of

ferrites is well explored, due to their potential applications and the interesting physics involved in them.

In this article, we report preparation of nanosized chromium substituted Zn-Mn ferrites by sol-gel method. It is a simple process, which offers a significant saving in time and energy consumption over the traditional methods, and requires lower sintering temperature. This method was employed to obtain improved powder characteristics, more homogeneity and narrow particle size distribution, thereby influencing their structural, electrical and magnetical properties.

2.0 Materials and Methods

2.1. Synthesis Technique

Analytical grade chromium nitrate [Cr (NO₃)₃.9H₂O], iron nitrate [Fe ((NO₃)₃.9H₂O)], zinc nitrate [Zn (NO₃)₂.6H₂O], manganese nitrate [Mn (NO₃)₂.4H₂O] and citric acid [C₆H₈O₇.H₂O] were used to prepare ZnMn_{1-x}Cr_xFeO₄ (where x = 0.0, 0.25, 0.50, 0.75 and 1.0) by sol-gel method and flow diagram for autocombustion technique is shown in Fig.1. Metal nitrates and citric acid were dissolved in minimum quantity of deionized water with 1:1 molar ratio. The pH of the solution was adjusted to about 9.0 to 9.5 using ammonia solution. The solution was transformed to dry gel on heating to 353K. On further heating the dried gel burnt in a self propagating combustion manner until all the gel completely converted to a floppy loose powder. The as burnt precursor powder was then sintered at 973K for 8 h for confirmation of phase formation. The sintered powders were granulated using 2 % polyvinyl alcohol as a binder and uniaxially pressed at a pressure of 8 ton /cm² to form pellets. These pellets were gradually heated to about 773K to remove the binder material.

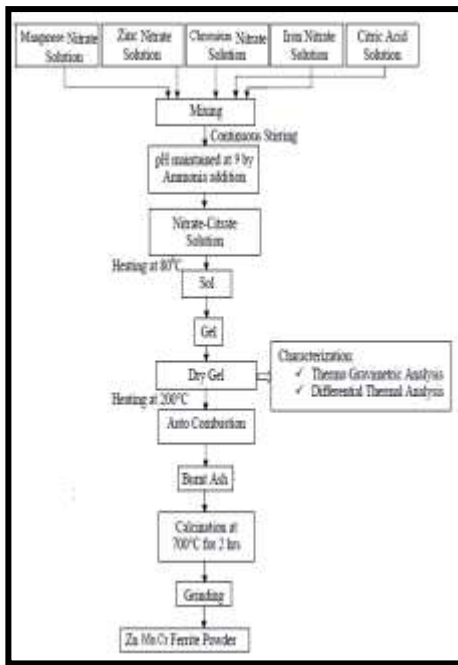


Fig.1. Flow diagram for sol-gel autocombustion technique

The phase formation of the samples calcined at different temperature was confirmed by X-ray diffraction studies using Philips PW-1710 X-ray diffractometer with CuK α radiation ($\lambda=1.54056\text{\AA}$). The lattice parameters were calculated for the cubic phase using following relations.

$$a = d (h^2 + k^2 + l^2)^{1/2} \quad \dots 1.0$$

where, a = Lattice parameter, (hkl) = Miller indices, d = interplanar distance

The crystallite size of sintered ferrites was calculated from the full width at half maxima of the most intense (311) peak by using Scherrer's formula.

$$t = 0.9\lambda / \beta \cos \theta \quad \dots 2.0$$

Where, symbols have their usual meaning.

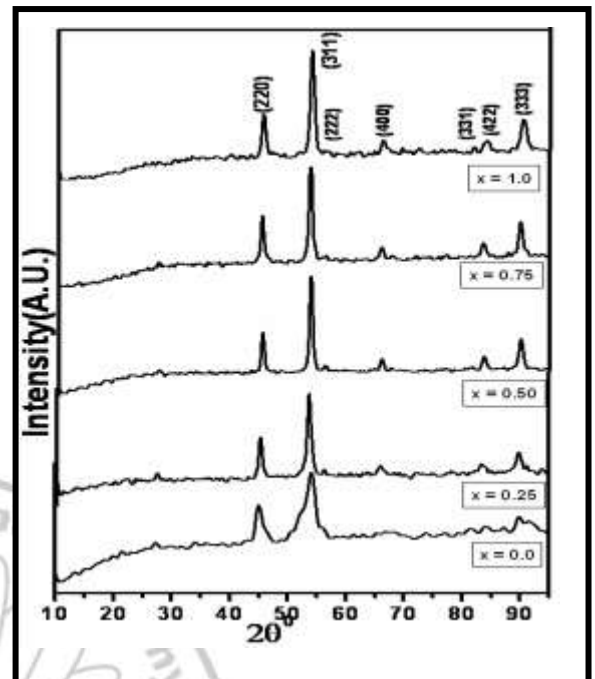


Fig.2 X-ray data for the system $ZnMn_{1-x}Cr_xFeO_4$

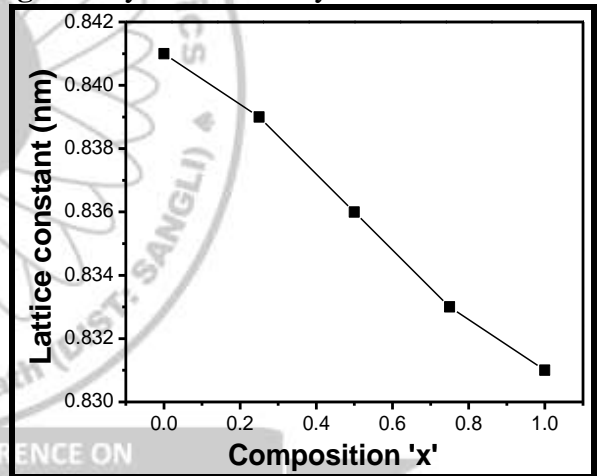


Fig.3 Lattice constant (nm) vs composition (x) for the system $ZnMn_{1-x}Cr_xFeO_4$

The X-ray density was calculated according to the formula

$$dx = 8M / Na^3 \quad \dots 3.0$$

where, N = Avagadros number (6.023×10^{23} atom/mole)

M = Molecular weight, and

a = lattice constant which was calculated from the X-ray diffraction pattern. X-ray density is sometimes also called 'theoretical density'.

The SEM micrograph of the samples was obtained using scanning electron microscope (JEOL JSM 6360).

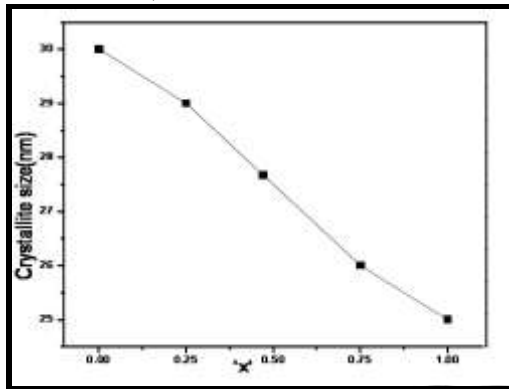


Fig.4 Variation of crystallite size with x in $ZnMn_{1-x}Cr_xFeO_4$ ferrites

Photocatalytic performance studied by using hazardous dyes like Thymol blue. Thymol blue is a well known dye and is considered as a model of a series of commonly used dyes in the industry. The photocatalytic activity of the samples was studied for Thymol blue dye in presence of Ultra-violet light with different times of exposure. The role of chromium in modifying structural and photocatalytic properties of these ferrites has been explained.

3.0 Results and Discussion

3.1 X-ray diffraction study

The structure and phase purity of the products were confirmed by analyzing the X-ray diffraction patterns. **Fig.2.** depicts the XRD patterns of the different $ZnMn_{1-x}Cr_xFeO_4$ compositions and all x-ray parameters are summarized in **Table 1.** All the observed reflections could be assigned to cubic spinel lattice indicating their single phase nature. Unit cell parameters were determined by indexing the diffraction peaks in the XRD patterns. The variation of unit cell parameter with chromium content is shown in **Fig.3.** It is observed that the unit cell parameter gradually decreases with increasing Cr content in the composition obeying Vegard's law. The slow linear decreasing trend in the lattice parameter is attributed to the replacement of Mn^{3+} (0.65\AA) ions by Cr^{3+} ions, a slightly smaller ion (0.62\AA), in the system [32]. From the X-ray diffraction peaks, average particle size was

estimated by using Scherrer's formula. The crystallite size decreases with increase in Cr content as shown in **Fig. 4** and it is observed to vary in the range of 30-25nm. The slow decreasing trend of unit cell parameter due to incorporation of lighter Cr^{3+} ion in place of Mn^{3+} leads to a gradual decrease in the x-ray density with increase in chromium content (**Fig.5**). The x-ray density (dx), lattice constant (a) and crystallite size (t) of the compositions are given in **Table.1.**

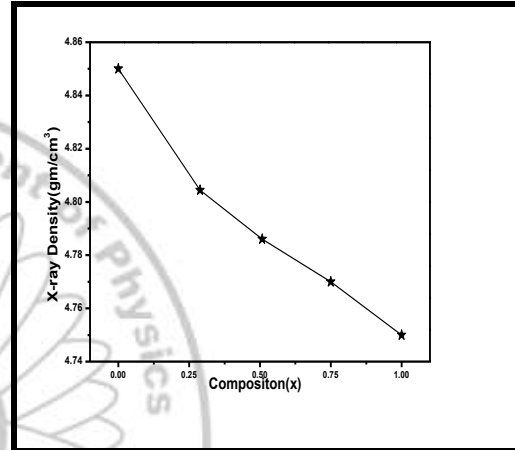


Fig.5 Variation of X-ray density with x in $ZnMn_{1-x}Cr_xFeO_4$ ferrites

3.2. Scanning Electron Microscopy

The SEM images of chromium substituted Zn-Mn ferrites are shown in the **Fig.6(a-d)**. It is observed that the average grain size goes on decreasing with substitution of Cr content. The average grain size is smaller than $0.1\mu m$ for all the compositions..

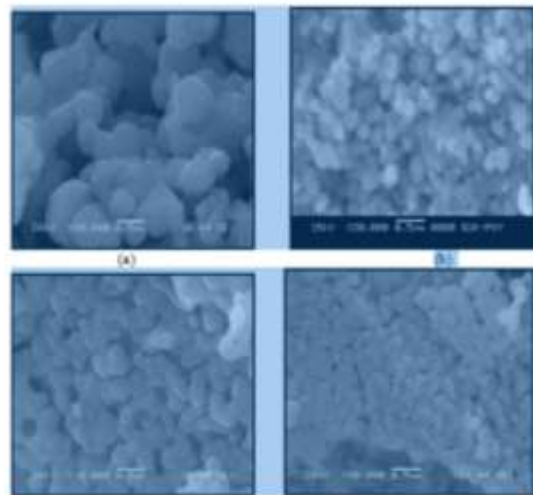


Fig.6 SEM micrographs for the system $ZnMn_{1-x}Cr_xFeO_4$ a) $x=0.0$, b) $x=0.25$, c) $x=0.75$ and d) $x=1.0$

3.3. Photocatalytic application

It can be seen that the grain size and crystallinity decrease significantly with increasing chromium content since the ionic radius of chromium is smaller than the ionic radius of manganese. The particle size becomes more uniform at higher chromium concentration

In recent years, the wide spread presence of chemicals such as heavy metals, herbicides, pesticides, aliphatic and aromatic detergents, arsenic compounds, solvents, degreasing agents, volatile organics, and chlorophenols pose a serious threat to the environment. When such chemicals contaminate water sources, they become really hazardous. For instance, waste waters produced from textile and dyestuff industrial processes contain large quantities of azo dyes. It is estimated that 15% of the total dye is lost during dyeing process and released in waste waters. Oxidation of these organic pollutants at the surface of different metal oxides catalyst is an important photocatalysis application.

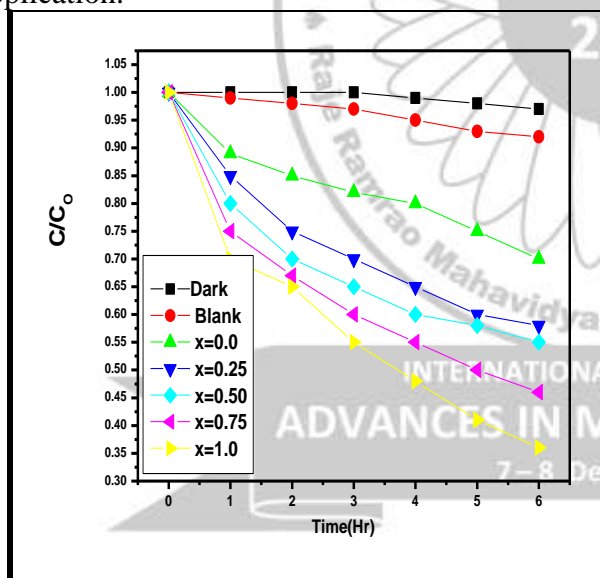


Fig.7. Photocatalytic study ZnMn_{1-x}Cr_xFeO₄ for system

Heterogeneous photocatalysis is a process in which a combination of photochemistry and catalysis are operating together. It implies that both light and catalyst are necessary to bring out the chemical reaction. UV light illumination over a semiconductor like metal oxides produces electrons and holes. The valence band holes are powerful oxidants (+1 to +3.5V versus NHE depending on

the semiconductor and pH), while the conduction band electrons are good reductants (+0.5 to -1.5V versus NHE). In 1977, Frank and Bard examined the possibilities of decomposing cyanide in water by Titania. Since then there is an increasing interest in semiconductor-mediated photo-oxidative processes.

There are number of different semiconducting materials which are readily available, but only few are suitable for sensitizing the photo-mineralization of wide range of pollutants. The semiconductor to be used as photocatalyst for photo-mineralization of wide range of organic pollutants must be (i) photoactive (ii) able to utilize visible and or near UV light (iii) biologically & chemically inert and (iv) photo-stable. It is generally found that only n-type semiconductor oxides are stable towards photo-anodic corrosion, although such oxides usually have bandgaps sufficiently larger than the semiconductors only absorb UV light. The textile dyes and dye intermediates with high aromaticity and low biodegradability have emerged as major environmental pollutants and nearly 10-15% of the dye is lost in the dyeing process and is released in the wastewater which is an important source of environmental contamination. Considerable amount of water is used for dyeing and finishing of fabrics in the textile industries. The wastewater from textile mills causes serious impact on natural water and land in the surrounding area. As dyes are designed to be chemically and photolytically stable, they are highly persistent in natural environments. The improper handling of hazardous chemicals in textile water also has some serious impact on the health and safety of workers putting them into the high-risk bracket for skin diseases like chemical burns, irritation, ulcers, etc. and respiratory problems.

The catalytic activity study of the Cr substituted Zn-Mn ferrite photocatalyst was carried by photodegradation rate of thymol blue. The experiment of photocatalytic reaction was conducted in a 100-ml Pyrex glass vessel with magnetic stirring and a UV lamp (8W) with the main wavelength of 253.7 nm. The as-prepared ferrite was used as photocatalyst during the study. It was, therefore, concluded that enhanced photodegradation is directly related to the reduced

particle size of the ferrites, which implies photosensitization as the primarily involved process. It is seen from Fig.7 that photocatalytic activity increasing with the increasing substitution of Cr content. ZnCrFeO₄ shows better photocatalytic activity towards Thymol blue as compared to other Cr substituted ZnMn ferrites.

Table 1 Data on lattice parameter, crystallite size, x-ray density, Physical density, Porosity of ZnMn_{1-x}Cr_xFeO₄ ferrite samples.

Composition (x)	Lattice constant (a) nm	Crystallite size (t) nm	X-ray density (d _x gm/cm ³)	Physical density (d _p gm/cm ³)	Porosity
0.0	0.841	30	4.85	4.95	4.89
0.25	0.839	29	4.80	4.87	5.21
0.50	0.836	28	4.78	4.83	5.67
0.75	0.833	26	4.77	4.82	5.97
1.0	0.831	25	4.75	4.78	6.23

3.4 Conclusions

Chromium-substituted nanocrystalline Zn-Mn ferrite samples were synthesized by sol-gel method. X-ray diffraction studies confirm the cubic spinel structure formation of the samples. The lattice constant and crystallite size decrease with increase of Cr content. Scanning electron micrographs indicate the formation of uniform and fine grained samples. The photocatalytic degradation of thymol blue indicates that ZnCrFeO₄ powders can effectively photodegrade thymol blue under ultraviolet plus visible light irradiation.

References

- [1] M.H. Sousa, F. Atourinho, J. Depeyrot, G.J. da Silva, M.C. Lara, J. Phys. Chem. B 105 (2001) 1168.
- [2] K. Raj, R. Moskowitz, R. Casciari, J. Magn. Magn. Mater. 149 (1995) 174.
- [3] T. Hyeon, Y. Chung, J. Park, S.S. Lee, Y.W. Kim, B.H. Park, J. Phys. Chem. B 6 (2002) 6831.
- [4] R.V. Mehtha, R.V. Upadhyay, B.A. Dasanacharya, P.S. Goyal, K.S. Rao, J. Magn. Magn. Mater. 132 (1994) 153.
- [5] M.H. Kryder, Mater. Res. Soc. Bull. 21 (17) (1996) 184.
- [6] D.G. Mitchell, J. Magn. Reson. Imaging 7 (1997) 1.
- [7] P.P. Hankare, P.D. Kamble, S.P. Maradur, M.R. Kadam, U.B. Sankpal, R.P. Patil, K. Nimat, P.D. Lokhande, J. Alloys Compd. 487 (2009) 730.
- [8] T. Mathew, K. Sreekumar, B.S. Rao, C.S. Gopinath, J. Catal. 210 (2002) 405.
- [9] G. Blasse, Philips Res. Rept. (Netherlands) 20 (1965) 528.
- [10] J.B. Goodenough, Magnetism and the Chemical Bond, John Wiley, New York, 1966.
- [11] J. Smit, Magnetic properties of materials, in: Intra-University Electronics Series, vol. 13, 1971, p. 89.
- [12] G.R. Dube, V.S. Darshane, Bull. Chem. Soc. Jpn. 64 (1991) 2449.
- [13] V.A. Chaudhary, I.S. Mulla, K. Vihaymohanana, Sens. Actuators, B 55 (1999) 127.
- [14] J. Giri, T. Sriharsha, D. Bhadur, J. Mater. Chem. 14 (2004) 875.
- [15] M. George, A.M. John, S.S. Nair, P.A. Joy, M.R. Anantharaman, J. Magn. Magn. Mater. 302 (2006) 190.
- [16] S. Giri, S. Samanta, S. Maji, S. Gangli, A. Bhaumik, J. Magn. Magn. Mater. 288(2005) 296.
- [17] S. Thompson, N.J. Shirtcliffe, E. O'keefe, S. Appleton, C.C. Perry, J. Magn. Magn. Mater. 292 (2005) 100.
- [18] J. Wang, Mater. Sci. Eng., B 127 (2006) 81.
- [19] A.S. Albuquerque, J.D. Ardisson, W.A.A. Macedo, J.L. Lopez, R. Paniago, A.I.C. Persiano, J. Magn. Magn. Mater. 226 (2001) 1379.
- [20] P.P. Hankare, V.T. Vader, N.M. Patil, S.D. Jadhav, U.B. Sankpal, M.R. Kadam, B.K. Chougule, N.S. Gajbhiye, Mater. Chem. Phys. 113 (1) (2009) 233.
- [21] P.P. Hankare, U.B. Sankpal, R.P. Patil, I.S. Mulla, P.D. Lokhande, N.S. Gajbhiye, J. Alloys Compd. 485 (2009) 798.
- [22] S.Z. Zhang, G.L. Messing, J. Am. Ceram. Soc. 73 (1990) 61.
- [23] J.A. Rodriguez, M. Fernandez-Garcia, Textbook of Synthesis, Properties and Applications of Oxide Nanomaterials, Wiley Interscience, A John Wiley and Sons, Inc., Publication, 2007, p. 95.
- [24] A.T. Raghavender, D. Pajic, K. Zadro, T. Milekovic, P. Venkateshular Rao, K.M. Jadhav, D. Ravinder, J. Magn. Magn. Mater. 316 (2007) 1-7.
- [25] P.P. Hankare, R.P. Patil, U.B. Sankpal, S.D. Jadhav, P.D. Lokhande, K.M. Jadhav, R. Sasikala, J. Solid State Chem. 182 (2009) 3217.
- [26] P.P. Hankare, R.P. Patil, U.B. Sankpal, S.D. Jadhav, I.S. Mulla, K.M. Jadhav, B.K. Chougule, J. Magn. Magn. Mater. 321 (2009) 3270.
- [27] T. Nakamura J. Magn. Magn. Mater. 168 (1997)285
- [28] R. C. Kambale, P. A. Shaikh, C. H. Bhosale, K. Y. Rajpure, Y. D. Kolekar, Smart Mater. Struct., 18 (2009) 85014.
- [29] P.P.Hankare, U.B. Sankpal, R.P. Patil, A.V.Jadhav, K.M.Garadkar, B.K.Chougule, J. Magn. & Magn. Mat., 323 (2011) 389.
- [30] P.P.Hankare, R.P.Patil, U.B.Sankpal, I.S.Mulla, K.M.Garadkar, R.Sasikala, A.K.Tripathi, J. Magn. & Magn. Mat., 322 (2010) 2629.
- [31] A. M. Shaikh, C.M.Kanmadi, B.K.Chougule, J.Mater.Chem.Phys, 93(2005) 548.
- [32] A. R. Denton and N. W. Ashcroft 1990 Phys. Rev. A 43, 3161.

Microwave Permittivity for Sunflower Seeds Using Non Resonant Ag Thick Film Microstripline as a Sensor

Vaishali Mane, Swati Patil, Vijaya Puri*

Thick and Thin and Film Device Lab, Department of Physics,
Shivaji University, Kolhapur. 416004. India.

Abstract –

In this paper the studies in the Ku band (13-18 GHz) of non resonant Ag thick film microstripline overlaid with moisture laden sunflower (*Helianthus Annuus*) seed is reported. The perturbation obtained in the transmittance and reflectance of the thick film microstripline due to the sunflower overlay has been used to obtain permittivity. Using the amplitude data the permittivity of moisture laden sunflower seed has been obtained by overlay technique. As moisture content increases microwave dielectric constant, dielectric loss and conductivity of sunflower increases. A non-resonant Ag thick film microstripline has been used for the first time for permittivity prediction in sunflower seeds. Ag thick film microstripline is sensitive to very low moisture content in the overlay material. From the permittivity calibration factor for moisture sensing has been predicted.

1. Introduction

Every natural and synthetic object reflects and emits electromagnetic radiation, according to the chemical composition and physical state. Agricultural biomaterials are basically materials consisting of organic and inorganic inclusions along with water. In the microwave region of the electromagnetic spectrum, dielectric properties of the moist granular materials depends on frequency, moisture content, bulk density and temperature [1-3]. Oil seeds form a major constituent of the agricultural and food sector. The dielectric properties of the grains due to the presence of water in varying quantities can be detected using microwave methods [4,5].

The simple nondestructive and miniaturized microstripline is a non resonant component. The perturbation due to leafy vegetation overlay has also been investigated by the authors group [6-8]. In this paper, the overlay technique has been used on a non resonant Ag thick film microstripline to predict the permittivity of the sunflower seeds (*Helianthus Annuus*). To the authors knowledge there are no reports on the use of non-resonant Ag thick film microstripline to predict dielectric constant of granular materials like oil seeds.

2. Experimental Procedure

The width of thick film microstripline was 25mil. The Ag thick film microstripline (figure1) was delineated by screen printing silver on 96% alumina (Kyocera, Japan) substrate and fired at 700°C by conventional thick film firing cycle in the three zone furnace. The microwave transmittance (S_{21}) and reflectance (S_{11}) measurements were

made point by point in the frequency range 13-18 GHz with the help of microwave bench consisting of Gunn source, isolator, attenuator, directional coupler and detector.

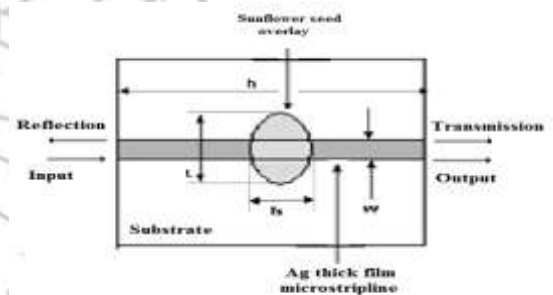


Fig.1: The schematic of Ag thick film microstripline with sunflower seed overlay

The geometry of microstripline showing a cross section (not to the scale): w, width of the microstripline= 0.0635cm; h, length of substrate = 2.54cm; L, length of sunflower seed; T_s , thickness of the sunflower seed.

In this technique, the change in transmission and reflection of the microstripline with a single sunflower seed with different moisture contents kept at the center the microstripline were measured. The investigations were done for as it is seeds, fully soaked for 24 hours and dried naturally upto 144 hrs. The moisture content was measured on wet basis using gravimetric method.

The sunflower seed was held in place with pressure block of thermocol on it to ensure better contact

between circuit and seed and to avoid air gap. For this thermocol block was used. The thermocol block did not change the characteristics of microstripline when placed over them. Three identical thick film microstriplines were investigated and six sunflower seeds with same moisture content were used as overlay. All sunflower seeds had ellipsoidal shape and the sample to sample variation in thickness was $\sim 0.006\text{cm}$ and variation in length was $\sim 0.008\text{ cm}$. The seed to seed variations were of the order of ~ 0.02 in transmittance. Due to excellent source of dietary fiber, protein and rich in cholesterol lowering phytosterols sunflower seed was chosen. The as obtained seed had a moisture content of 4.22%. These were soaked in distilled water for 24 hrs for maximum moisture absorption as confirmed by no further weight increase of the seed as

measured by microbalance (K-16Micro, accuracy 0.001 mg). Eight moisture levels from 4.22% to 34.78% were measured for all the six sunflower seeds. Due to moisture the thickness of the seed varied from 0.46-0.58cm, length from 1.22-1.46cm and bulk density from 0.18-0.24g/cm³. All the measurements were conducted at room temperature (27⁰C).

3. Results And Discussions

Since overlay technique was used for permittivity measurement, the characteristics of the Ag thick film microstripline without overlay was studied. The transmittance of the thick film microstripline is between 0.6 and 0.7 and reflectance is between 0.03 and 0.05 for the microstripline without overlay with almost no dispersion.

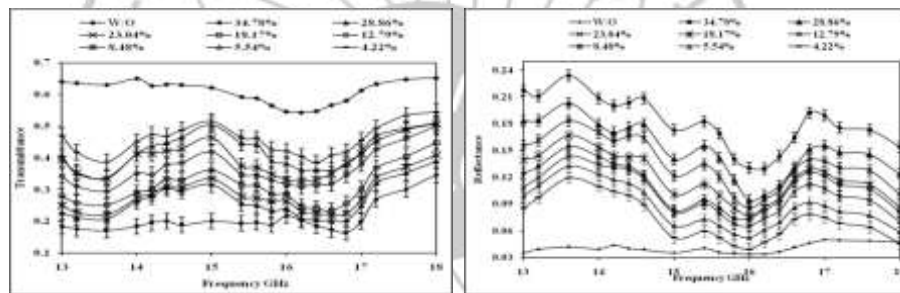


Fig.2. Perturbation in transmission and reflection due to sunflower overlay with error bars W/O –Without overlay, % - Moisture content %

The perturbation in transmission and reflection due to sunflower overlay and without the overlay on Ag thick film microstripline in the frequency range 13-18GHz is shown in Fig. 2 with error bars indicating \pm one standard deviation from mean value. Due to the moisture laden sunflower overlay the average (average of six seeds) transmittance decreases and reflectance increases.

Figure 3 shows the reflectance as a function of moisture content only for 13GHz, 15GHz and 18GHz frequencies. From the figure, it is seen that

the vertical spread of the data points indicates the seed to seed variations. The slope of the reflectance curve appears to be larger only for 13GHz and 15GHz indicating better moisture sensitivity while as 18GHz indicating lower moisture sensitivity.

From the reflection coefficient, the dielectric constant was calculated using the curve fit equation suggested by Gouker et al. [18]. Using the data of change in transmittance of the microstripline due to sunflower overlay the dielectric loss (ϵ'') was calculated using the

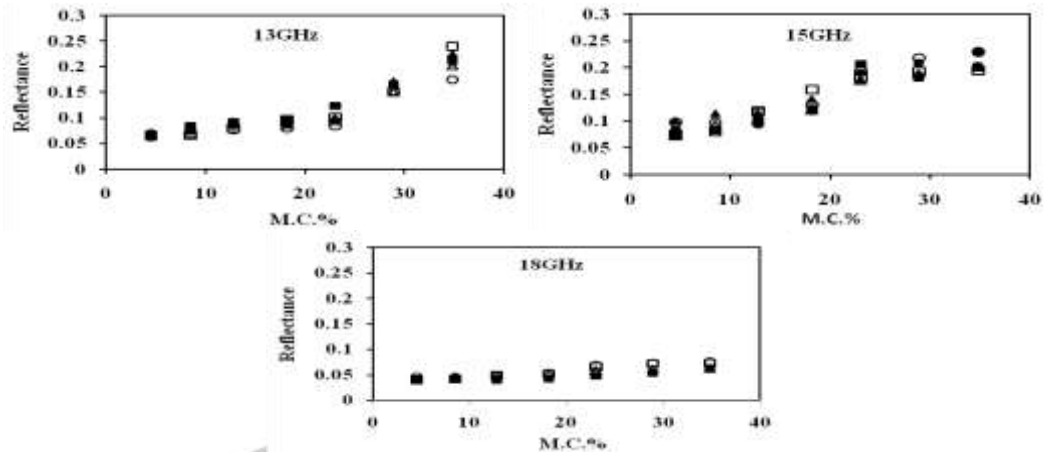


Fig.3. Reflectance as a function of moisture content for 13, 15 and 18 GHz frequencies.

M.C. % - Moisture Content
 expression by Kim et al. [6]. From this figure [4], it is seen that as moisture content (%) increases dielectric constant (ϵ') and dielectric loss (ϵ'') also increases. Only for 13 and 18 GHz frequency data of all the six seeds are plotted and for 14 -17 GHz only data of one seed is plotted. The vertical spread

of the data points is due to the variation of frequency. The dielectric loss shows behavior similar to dielectric constant. The sunflower seed exhibit low dielectric constant. The dielectric constant (ϵ') of the seed varies from 2 to 6 and dielectric loss (ϵ'') \sim 0.04 to 1.2.

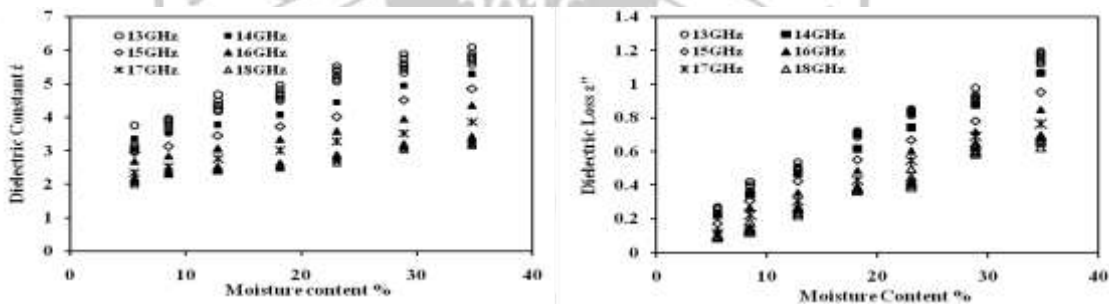


Fig.4. Dielectric constant (ϵ') and Dielectric loss (ϵ'') as a function of moisture content (%) for Sunflower at different frequencies.

The microwave conductivity of sunflower seed was calculated using the equation according to Nelson et al. [4] using the dielectric loss.

$$\sigma = \omega \epsilon'' \epsilon_0 \quad \text{Where } \omega =$$

$2\pi f$ here f is frequency in GHz.

$\epsilon_0 =$ permittivity of free space $= 8.85 \times 10^{-12}$

SI unit And $\epsilon'' =$ dielectric loss

The microwave conductivity value obtained by this method varies from 0.04 to 0.86 S/cm. As frequency increases conductivity decreases while as moisture content increases conductivity also increases. The microwave conductivity due to sunflower seed overlay for all frequencies and moisture contents (%) is tabulated in Table 1.

Table 1: Data of microwave conductivity(S/cm) for different frequencies and moisture contents

Microwave conductivity(S/cm)								
Moisture content %	→							
Frequency GHz	↓							
	34.78	28.86	23.04	18.17	12.79	8.48	5.54	4.22
13	0.86	0.70	0.60	0.51	0.38	0.28	0.19	0.13

14	0.83	0.68	0.57	0.48	0.36	0.26	0.18	0.10
15	0.79	0.65	0.55	0.45	0.35	0.25	0.14	0.08
16	0.75	0.64	0.53	0.43	0.31	0.23	0.12	0.07
17	0.72	0.62	0.51	0.40	0.29	0.21	0.10	0.05
18	0.68	0.61	0.49	0.38	0.26	0.18	0.09	0.04

4. Conclusion

Our results are indicating that overlay technique on a non resonant microstripline can be used to fabricate a nondestructive dielectric for granular bio materials. The perturbation causes changes in electrical parameters which are governed by the dielectric constant and size of overlay. The thick film component along with overlay can be cost effective dielectric and moisture sensor especially for biomaterials, since any size and shape of the overlay can be used. The permittivity of seeds increases with increase in moisture. . A non resonant cost effective miniaturized microwave component can be used as a non destructive sensor for measuring dielectric constant and moisture content in individual sunflower seed that is easy to use.

Acknowledgement

The author Vijaya Puri gratefully acknowledges the award of research scientist “C” by the University Grants Commission India and UGC DRS-SAP-II.

References

1. S.O.Nelson, L.E.Stetson, “Frequency and moisture dependence of the dielectric properties of hard red winter wheat,” *J. Agric. Eng. Res.*, vol. 21, 181-192, 1976.
2. S.O.Nelson “Review of factors influencing the dielectric properties of cereal grains,” *Cereal Chem.* vol.58, 487-492, 1981.
3. A.Kraszewski, “Microwave aquametry – a review,” *J. Microwave Power*, vol.15 209-220, 1980.
4. S.O.Nelson, “Measurement and applications of dielectric properties of agricultural products,” *IEEE. Trans. on Instr. Meas.*, vol.41, 116-122, 1992.
5. A.W. Kraszewski, S.O.Nelson, “Microwave Techniques in agriculture,” *Journal of Microw. Pow. Em. Energy*, vol.38, 13-35, 2003.
6. R.Ghorpade, and V.Puri, “Leaf overlay effects on the transmittance of thick and thin film microstripline,” *Int. J. Elec.*, vol.92, 683-696, 2005.
7. R.Ghorpade, and V.Puri, “X band response of thick and thin film microstrip patch antenna to leaf overlay,” *J.of Active and Passive Elec. Devices*, vol.2, 105-115, 2007.
8. P.D.Kamble, V.Puri, “Prediction of microwave permittivity of leafy vegetation using Ag thick film microstripline,” *Microelec Int.*, vol. 25, 37-40, 2008.
9. V.Mane, V.Puri, “Response of Ag thick film microstrip equilateral triangular patch antenna to overlay of moisture laden soybean,” *Microelec. Int.*, vol.26, 56-59, 2009.

Corresponding Author: Prof. Vijaya Puri (e mail:

vrp_phy@unishivaji.ac.in)

Author: Ms. Vaishali Mane (vv_mane@rediffmail.com)

Monitoring the physical properties of Bismuth Selenide thin films by electromagnetic wave as a special tool: Holographic Interferometry

P. M. Kulal^a, V. J. Fulari^b

^aDepartment of Physics, Shivaji Mahavidyalaya, Renapur

^bHolography and Material Research Laboratory, Department of Physics, Shivaji University, Kolhapur
E-mail address: pmkulal@gmail.com

ABSTRACT

Thin films of Bi_2Se_3 have been prepared by electrodeposition method from aqueous medium at room temperature using selenium dioxide and bismuth nitrate as anionic and cationic source deposited on stainless steel substrate. Micro structural, optical and surface wettability measurements were carried out. X-ray diffraction pattern indicates that the Bi_2Se_3 thin films possess polycrystalline nature with rhombohedral crystal structure. The surface morphology is determined using scanning electron microscopy (SEM). The optical band gap, which is direct allowed to 1.37eV for Bi_2Se_3 thin films. The static water contact angle of the Bi_2Se_3 is 120° revealed hydrophobic nature. The thickness, stress to substrate of the deposited thin films is determined using Double Exposure Holographic Interferometry (DEHI) technique.

Keywords: Bismuth Selenide, Electrodeposition, Double Exposure Holographic Interferometry (DEHI) technique, and Contact angle.

1. Introduction:

Bismuth (III) selenide is a semiconducting material, member of the V-VI binary semiconductor group, with a narrow band gap (Lovett et al 1977). The study of bismuth (III) selenide thin films is motivated from their suitable optical and electrical properties for construction of optical and photosensitive devices, modern thermoelectric devices, Hall effect magnetometer, high-frequency power sensor-thermopiles wide bond radiation detectors and humidity sensors using the Seebeck and Peltier effects (Giani et al 2000, Bhattacharya et al. 1982, Bates et al 1996, Hyun et al 1998). In the literature, several methods for bismuth (III) selenide thin-film deposition have been published, such as chemical bath deposition (Bhattacharya et al. 1982, Pramanik et al 1980, Garcia et al 1997), successive ionic layer absorption and reaction (Sankapal et al 2000), electrodeposition (Torane et al 1998, Torane et al 2001), molecular beam epitaxy (Boyer et al 1991), reactive evaporation (John et al 1993) and metal organic chemical vapor deposition (Giani et al 2000), for chemical deposition of Bi_2Se_3 thin films (Pejova et al 2002) and reported a preliminary study of their optical and electrical properties. The double exposure holographic interferometry technique has been widely accepted as a viable tool for non-destructive

testing of materials. This technique is sufficient to form a permanent record of relative surface displacement of object occurring after a fixed interval of time. As a result, the DEHI technique can be applied to many engineering problems, especially, continuous comparison of the surface displacement relative to an initial position (Dongare et al 1999). The technique has been successfully employed to study the surface deformation of stainless steel with Ti–Ba–Ca–Cu thin film deposition (Thokale et al 2002).

The present study concentrates on the synthesis and characterization of electrodeposited Bi_2Se_3 thin films prepared from aqueous acidic bath. The thickness and stress of the films have been determined by DEHI technique for various deposition times. The samples are characterized by X-ray diffraction (XRD), scanning electron microscopy (SEM), contact angle measurements and optical absorption.

2. Experimental:

2.1 preparation of Bi_2Se_3 thin film

Bi_2Se_3 thin films were deposited onto stainless steel substrate by electrodeposition technique. The metallic substrates were mirror polished by zero grade polish paper, detergent powder, brass and finally by an ultrasonic cleaner. The inert polished graphite plate was used as a counter electrode. The solutions of bismuth nitrate ($\text{Bi}_2\text{NO}_3 \cdot 5\text{H}_2\text{O}$) and selenium

dioxide (SeO_2) were prepared in double distilled water. Electrodeposition of Bi_2Se_3 thin film was carried out using Potentiostat (Princeton Perkin-Elmer, Applied Research Versa-stat-II; Model 250/270) in potentiostatic mode. The 20 ml of an electrolyte was used without stirring. Pure graphite was used as an anode and cathode was stainless steel. The deposition potential measurement was carried out with respect to

saturated calomel electrode (SCE) as a reference electrode. Gray colored, uniform and stoichiometric Bi_2Se_3 thin films were deposited onto stainless steel. After the deposition, the films were washed with double distilled water and preserved in desiccators to avoid the oxidation.

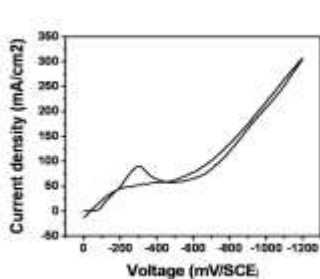


Fig. 1

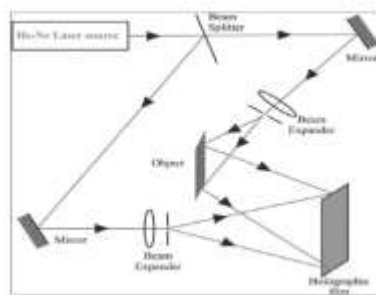


Fig.2

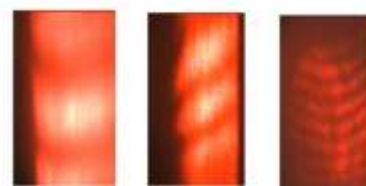


Fig. 3

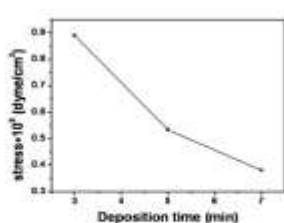


Fig.4

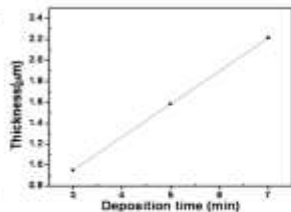


Fig. 5

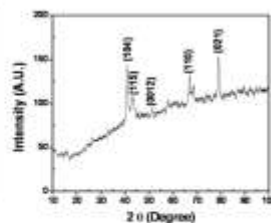


Fig. 6

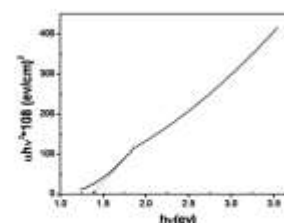


Fig.7

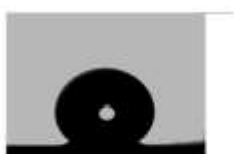


Fig. 8

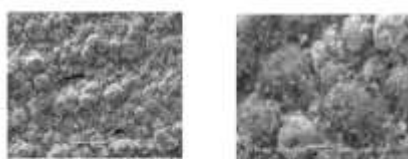


Fig. 9

Fig.1. Cyclic voltammogram on stainless steel substrate in the solution containing 0.1 M $[\text{Bi}_2\text{NO}_3 \cdot 5\text{H}_2\text{O} + \text{SeO}_2]$, **Fig.2** Actual experimental set up of the double exposure holographic interferometry technique, **Fig. 3** Recorded holograms of Bi_2Se_3 thin films at different time (a) 5 min. (b) 10 min. (c) 15 min, **Fig. 4** The variation of Bi_2Se_3 film stress to the substrate with deposition time. **Fig.5** The variation of Bi_2Se_3 film thickness with deposition time, **Fig.6** XRD pattern of Bi_2Se_3 thin film, **Fig.7** Plot $(\alpha h\nu)^2$ vs. $h\nu$ of Bi_2Se_3 thin films, **Fig.8** Contact angle of Bi_2Se_3 thin film, **Fig.9** scanning electron micrographs of Bi_2Se_3 thin film at two different magnifications

Table 1 Thickness and stress of Bi₂Se₃ thin films for different deposition times

Deposition time t [min]	No. of fringes	Thickness of film t _f [μm]	Calculated stress S*10 ⁹ [dyne/cm ²]
5	3	0.9492	0.889
10	5	1.5820	0.533
15	7	2.2140	0.381

Films were characterized for structural analysis by using X-ray diffractometer (Philips, Model PW-3710) using Cr-K α radiation ($\lambda=2.2896$ Å). The surface morphology was investigated using a JEOL, JSM-6360 scanning electron microscope (SEM). Optical properties were recorded by using Systronic-119 spectrophotometer model. In order to study interaction between liquid and thin film surface contact angle measurement was carried out by Rame-hart USA equipment with CCD camera.

2.2. Double exposure holographic interferometry (DEHI) technique

Holograms are recorded using double exposure holographic interferometry technique. The holograms were recorded by conventional two beam off-axis technique using 10 mW He-Ne laser having wavelength $\lambda=6328$ Å. The holograms were recorded on the holographic film (Kodak 8E 75 HD) before and after the deposition of Bi₂Se₃ thin films. The reconstructed image of substrate was observed with the reference beam which shows the localized fringes.

Table 2 Comparison of observed and standard 'd' values of Bi₂Se₃ thin films

Sr. No	Observed 'd' values	Standard 'd' values	(hkl)
1	3.5750	3.5590	(101)
2	3.2710	3.2050	(115)
3	2.3670	2.3860	(0012)
4	2.0749	2.0700	(110)
5	1.7975	1.7893	(1013)

INTERNATIONAL CONFERENCE ON
ADVANCES IN MATERIALS SCIENCE
7 – 8 December 2016

2.3. Measurement of thickness of the thin films and stress to the substrate

The simple non-destructive technique, for the quantitative measurement of stress in thin films by the use of DEHI technique is reported by (Magill et al 1967). While recording the hologram, if the object is illuminated with a beam of light making an angle θ_1 with the normal and is viewed at an angle θ_2 during reconstruction, the reconstructed image has a superimposed fringe pattern corresponding to a displacement of the surface. The displacement in the normal direction is given by

$$d = \frac{n\lambda}{\cos \theta_1 + \cos \theta_2}$$

Where n is the number of fringes and λ is the wavelength of light. In general θ_1 and θ_2 are sufficiently small, so that

$$d = \frac{n\lambda}{2}$$

The stress to the stainless substrate is given by the formula (Pawar et al 2007)

$$s = \frac{t_s^2 Y_s \Delta}{3l^2 t_f}$$

Where, S is stress in dyne/cm², t_s is substrate thickness, t_f is film thickness, Δ is deflection of the substrate equal to $4\lambda/2$, Y_s is Young's modulus, l is length of the substrate on which the film is deposited.

3. Result and Discussion

3.1 Cyclic Voltammetry

Cyclic Voltammetry was used to monitor the electrochemical reactions in solutions of 0.1 M [Bi₂NO₃.5H₂O] + 0.1 M SeO₂ to find the suitable Bi₂Se₃ deposition potential. All Voltammetry curves were scanned first in the cathodic direction and the current density indicates a cathodic current. Fig.1 shows the cyclic voltamograms measured for the SS electrode in the electrolytic bath of 0.1 M [Bi₂NO₃.5H₂O] + 0.1 M SeO₂. It is clearly seen that the cathodic current increases sharply from -0.65 V/SCE, which belongs to simultaneous reduction of both bismuth and selenium ions. The films deposited at -0.65 V/SCE potential are homogenous, uniform and well adherent to the substrates. The crossover between anodic and cathodic current curves appears on the reverse potential sweep which indicates that

nucleation and growth process exist on the substrate in electrolytic bath.

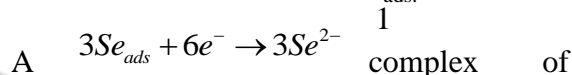
3.2. Reaction and growth mechanism

Electrodeposition of Bi₂Se₃ was carried out from aqueous acidic bath. The Bi₂Se₃ films were cathodically deposited from an aqueous solution containing bismuth and selenium ions. The electrodeposition of Bi₂Se₃ had been carried out from an aqueous acidic solution containing bismuth and selenium ions.

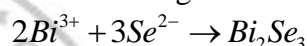


Se²⁺ is converted into Se_{ads}.

The electron reacts with Se_{ads}.



Bi³⁺ reacts with Se²⁻ to give



3.3. Double exposure holographic interferometry

The actual experimental of double exposure holographic interferometry technique is shown in fig. 2. The recorded holograms of Bi₂Se₃ thin films deposited onto stainless steel substrate at different deposition times are shown in Fig.3 from the hologram study, it is observed that as the deposition time increases, the number of fringes localized on the surface of stainless steel substrate goes on increasing; also thickness is dependant on the deposition time (Fulari et al 1996). From the Fig.4 and Fig.5 it is observed that thickness increases and stress to the substrate decreases with increasing deposition time respectively as shown in Table 1. Janseen et al reported that decrease in CrN thin film stress with thickness (Janseen et al 2006). This may be due to scattering or interference of incident light.

3.3. Structural study

Fig.6 shows the XRD pattern of as deposited Bi₂Se₃ thin film using complex bath on stainless steel substrate for 0.1 M bath concentration having rhombohedral crystal structure. The observed 'd' values are in good agreement with standard 'd' values (JCPDS. 33-0214) depicted in Table 2. The crystalline size of the as deposited thin film was calculated for (101) plane using Scherrer's formula:

$$D = \frac{0.9\lambda}{\beta \cos \theta}$$

Where λ is the wavelength of X-ray, β the full width in radians at half maximum of the peak and θ Bragg's angle of the X-ray diffraction peak. The crystalline size is about 49 nm for (110) plane.

3.4. Optical absorption studies

The optical absorption of the films has been studied in the wavelength range 350–850 nm, without accounting for reflection and transmission losses. The nature of the transition is determined using classical relation for absorption coefficient.

$$\alpha = \frac{A(h\nu - E_g)^n}{h\nu}$$

Where the symbols have their usual meaning. For allowed direct transition, $n = 1/2$ and for allowed indirect transition, $n = 2$. The value of absorption coefficient in the present case is of the order of 10^4 cm^{-1} which supports the direct band gap nature of the material. A typical plot of $(\alpha h\nu)^2$ versus $h\nu$ for deposited Bi_2Se_3 thin film on FTO coated glass substrate is shown in Fig.7. It is linear, indicating the presence of direct transition. The linear portion is extrapolated to $\alpha = 0$, on the energy axis giving the direct band gap energy of Bi_2Se_3 to be 1.37eV.

3.5. Surface wettability test

Wettability test is carried out in order to investigate the interaction between liquid and Sb_2Se_3 thin films. If the wettability is high, contact angle (θ), will be small and the surface is hydrophilic. On the contrary, if the wettability is low, θ will be large and the surface is hydrophobic. A contact angle of 0° means complete wetting and a contact angle of 180° corresponds to complete non-wetting. Both superhydrophilic and superhydrophobic surfaces are important for practical applications. Fig.8 shows the water contact angle of the Bi_2Se_3 thin film. Bismuth selenide thin film shows the hydrophobic behaviour since water contact angle is greater than 90° ($\sim 120^\circ$).

3.6 Scanning Electron Microscopic study

Fig.9 shows scanning electron micrographs of Bi_2Se_3 thin film at two different magnifications. Scanning electron micrographs shows that the surface is well covered with porous nanograins along with spongy clusters. Film shows randomly distributed spherical grains having some pits. Average size of these nanograins is about ~ 1300 nm. Such type of porous morphology provides large surface area and large volume for many applications.

4. Conclusion

Bi_2Se_3 thin films were deposited by electrodeposition in aqueous acidic bath using potentiostatic mode. Electrodeposition for synthesis of Bi_2Se_3 thin film is feasible technique. Nearly stoichiometric polycrystalline Bi_2Se_3 thin films were deposited from a bath containing bismuth nitrate and selenium dioxide. Thin films deposited at optimized preparative parameters are dark grayish in color and well adherent to the substrates. DEHI technique used for the characterization of Bi_2Se_3 thin films deposited on to a stainless steel substrate shows that as the deposition time increases, the number of fringes localized on the surface of stainless steel increases. Increase in deposition time, increases thickness of the film but decreases stress to the substrate.

Acknowledgement

Authors are grateful to the University Grants Commission (UGC), New Delhi for financial support through the scheme no. 36-209/2008 (SR).

References

1. Bates C W, England L 1996 Appl. Phys. Lett. **14** 390
2. Bhattacharya R N, Pramanik P 1982 J. Electrochem. Soc. **129** 332
3. Boyer A, Charles E, Le 1991 Vide Couches Minces **47** 99
4. Dongare M B, Fulari V J, Thokale R N, Kulkarni H R 1999 Asian Chem. Lett. **3** 52
5. Fulari V J, Kulkarni H R, Dongare M B 1996 J. Opt. **25** 249.
6. Garcia V M, Nair M T S, Nair P K, Zingaro R A 1997 Semicond. Sci. Technol. **12** 645
7. Gianì A, Bayaz A A, Foucaran A., Pascal-Delannoy F, Boyer A 2002 J. Cryst. Growth **236** 217
8. Hyun DB, Hwang J S, Oh T S, Shim J D, Kolomoets N V 1998 J. Phys. Chem. Solids **59** 1039
9. Janseen G C A M, Tichelaar F D, Visser C C G 2006 J. Appl. Phys. **100** 093512.
10. John K J, Pradeep B, Mathai E 1993 Solid State Commun **85** 879
11. Lovett D R 1977 Semi-metals and Narrow Band-gap Semiconductors, Pion Limited, London. p. 181
12. Magill P J, Young T 1967 J. Vac. Sci. Technol. **4** 47
13. Pawar S J, Chikode P P, Fulari V J, Dongare M B 2007 Mater. Sci. Eng. B **137** 23
14. Pejova B, Grozdanov I 2002 Thin Solid Films **408** 6
15. Pramanik P, Bhattacharya R N, Mondal A 1980 J. Electrochem. Soc. **127** 1857
16. Sankapal B R, Mane R S, Lonkhande C D 2000 Mater. Chem. Phys. **63** 230
17. Thokale R N, Patil P S, Dongare M B 2002 Mater. Chem. Phys. **74** 143
18. Torane A P, Bhosale C H 2001 Mater. Res. Bull. **36** 1915
19. Torane A P, Lokhande C D, Patil P S, Bhosale C H 1998 Mater. Chem. Phys. **55** 51



Thank You !

INTERNATIONAL CONFERENCE ON
ADVANCES IN MATERIALS SCIENCE
7-8 December 2016